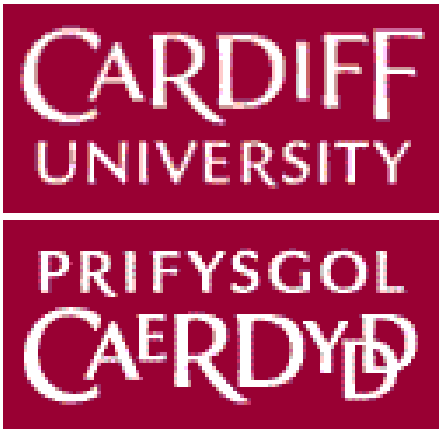

PODIFORM CHROMITE AT VOSKHOD, KAZAKHSTAN

Caroline Johnson

Submitter in partial fulfilment of the requirements for the degree of Ph.D.

November, 2012

Somewhat unconventionally, this thesis is *for me*.

Caroline Johnson

"I love deadlines. I like the whooshing sound they make as they fly by."

Douglas Adams (1952-2001)

Abstract

The Voskhod podiform chromitite is one of more than 30 chromitite deposits that collectively form the Main Ore Field (MOF) within the Kempirsai Massif, in Kazakhstan. The MOF is the largest podiform chromitite ore-field in the world. The Voskhod deposit, encased in a serpentinised dunite halo, is situated within harzburgite units that comprise the mantle sequence of the Kempirsai ophiolite. This study arose from a unique opportunity to work on drill core samples through an un-mined podiform chromite deposit and investigate its internal structure, composition and genesis.

The 18Mt ore-body has a strike of 600 m, is 170 m to 360 m wide and has an average thickness of 39 m. It has an immediate dunite halo between 1 m and 5 m thick. The ore body is made up of multiple stacked chromitite layers. Mineralised layers are separated by barren dunite or by weakly disseminated dunite lenses ranging from <1 m to 50 m. The style of mineralization varies throughout the ore body; the central region is dominated by thick (>5 – 45 m) units of massive chromite (>80% chromite), with progression towards the south west disseminated chromite (10 – 40% chromite) becomes increasingly abundant. Drill core logging and cross-section profiling of the internal structure of the ore body has identified an intricately connected network of what appear to be chromite-filled channel-ways.

Outside of the halo the host rocks are inter-layered harzburgite and dunite. Accessory chromite in harzburgite has an average Cr# of 0.31 compared to Cr# 0.49 in the dunite. The harzburgites are depleted, having formed from intermediate degrees of partial melting (~15 – 18 %) of a fertile mantle source at a mid-ocean ridge (MOR) setting. The dunite units have transitional geochemical fingerprints that imply they formed from the interaction of MOR mantle harzburgite with both mid ocean ridge baslt-melt and an arc derived-melt. They are not the products of extremely high degrees of partial melting.

The encasing dunite halo is extensively serpentinised (>80%). Chromite is only present as an accessory phase having an average Cr# of 0.62. The dunite has a geochemical signature indicating that it formed by reaction between residual harzburgite and a boninite melt in supra-subduction zone (SSZ) tectonic setting.

A variety of geochemical fingerprints have been identified; residual MOR harzburgite, reacted-MOR dunite, reacted-SSZ dunite and harzburgite, indicating that the mantle section has had a

polygenetic tectonic evolution, recording both ocean basin opening (MOR setting) and closing (SSZ setting) events.

Trace element and REE whole rock geochemistry of the chromitites and associated host rocks provide evidence of depletion and a later-stage LREE-enrichment event. LREE-enrichment is most intense within and immediately adjacent to the chromitite.

Chromites from the ore zone are at the Cr-rich extreme for podiform chromites (Cr# ave. 0.80-0.85) and are TiO_2 poor (ave. 0.16 wt%), similar to chromite in boninite worldwide and nearby. Al/Ti ratios have been used to calculate the composition of the parent melts from which the Voskhod podiform chromitite crystallised: compositions that are synonymous with a boninite melt composition.

Chemical variation in chromite is systematic and on a much smaller scale than was anticipated. Even variations in a single thin section provide key evidence for different magmatic processes. An apparent melt-rock reaction in harzburgite has been examined in freeze-frame.

The chromite chemistry has been investigated at 50 cm, 1 cm and 1 mm scales. Compositional differences were identified on the basis of MgO% and $FeO_{(t)}$% compositions. Diagrams FeO-Fe_2O_3 and Cr# - Mg# were used to demonstrate the variations and identify relationships. Broad cryptic layering on a 50 cm scale has been found as well as fine-cryptic layering on a 1 – 8 cm scale. The variations are interpreted to reflect differences in the mineral phases crystallised from the melt; periods when on chromite only crystallised are distinguished from periods when both chromite with olivine crystallised. It seems likely that the deposit is made up of thousands of episodes of chromite accumulation that formed in an intermittently replenished open-system.

It also seems likely that the conduit was never a single melt-filled cavity; instead melt flow was focused through the mantle over an extended period. The conduit appears to be comprised of multiple branches, as chromite (± olivine) crystallised from the melt the channel-way became blocked and the melt was forced to deviate and make a new pathway through the mantle. As time elapsed the process resulted in the formation of stacked chromitite lenses, creating an orebody that has an internal arrangement of chromitite and dunite unites which resemble a stacked braided 'delta'.

ACKNOWLEDGEMENTS

Sincere thanks to Iain McDonald for his patience, time and encouragement.

Thank you to my supervisors, Chris Neary, Julian Pearce and Hazel Prichard as well as my industry mentor Nic Barcza for their help and advice.

I owe a large debt of gratitude to; Nic Barcza, Chris Powers, Matt Boyes, Simon Apps, Kevin Alexander and Lisa Pereira for all their technical help, logistical support and kindness – it was a pleasure to work with you. Without their efforts this project would not have been possible.

Peter Fisher has been of invaluable assistance and equally patient during the long periods of time I have spent on the SEM. Lawrence Badham and Peter Greatbatch were responsible for making hundreds of polished thin sections between them.

Iain McDonald and Ley Woolley were efficient at running many sample solutions on the mass spectrometers at Cardiff and very kind to teach me the methods for sample preparation in the geochemistry laboratory.

A big thank you to Ian Parkinson and Andy Tindle, who supervised my use of the EMP at the Open University. Extra thanks to Millie and Anna, who “on-the-day” agreed to accommodate me during my time at the O.U and were really very lovely.

Thank you to; Matthew Minifie, Tracy Aze, Tom Gregory, Alan Hastie, Bryan Hatton, Sarah Dare, Freddie Spyre, Aggie Georgeopoulou, Ruth Liley, Namaste Nicolai and David Thornalley for your unending moral support and more importantly - the laughter. Thanks is also expressed to my magma process group officemates Chris Brough, Kerry Howard and Iain Neill.

I acknowledge the funding for this project from Cardiff University, Oriel Resources Plc. and an additional annual contribution from SRK. Travel grants from the SEG, GSSA, MDSG and IOM^3 Andrew Carnegie fund to attend conferences and field trips have been greatly appreciated.

Finally, thank you to my parents, Geoffrey and Gillian as well as to my sisters, Bertie and Minnie, who have been gracious enough to express continual faith in my ability.

Table of Contents

List of Figures

Chapter 2

Chapter 3

Chapter 4

Chapter 5

Chapter 6

Chapter 7

Chapter 8

Chapter 9

Chapter 1: Introduction

This study was set-up as a co-operative research project between Oriel Resources Plc. (a subsidiary of Mechel) and Cardiff University, Earth and Ocean Sciences department. In May 2006, the Voskhod mine plan had recently received approval for mine development. The collaboration was driven by an industry initiative to further understand the ore geology of the deposit; the ore types, their spatial distribution and, in particular, how the affect of mineralogical and compositional variation impacted mineral processing.

The inter-disciplinary nature of the project was difficult to take forward. During the first year several months were spent working at the High Temperature Technology department laboratories at Mintek in Johannesburg, South Africa. Thermo-gravimetric and smelting testwork studies were conducted to thermally characterise the ore types and determine the most efficient smelting recipes. In light of the complexities and difficulties experienced in combining the geological and metallurgical research deliverables, a decision was made at the end of the first year, to reduce the scope and focus purely on geological aspects.

Active collaboration with Oriel Resources Plc. included; three, two month field seasons working at the Voskhod mine in Kazakhstan. Work undertaken included; core logging, core sampling, data entry and ore body modelling. Unlimited access to drill core, drill core logs, assay results and use of ore-body modelling software was provided by the company. This provided a wealth of sample material and information that made this study possible.

The research focused on the geochemical variations in chromite. The processes responsible for the formation of podiform chromitite have been a point of long standing debate (e.g., *Irvine, 1967; Thayer, 1969; Malpas & Strong, 1975; Lago et al., 1982; Johan et al., 1983; Stowe, 1987; Paktunc¸, 1990; Zhou et al., 1994, 1996*). Attempts to draw analogies between crustal-hosted stratiform chromitite and mantle hosted podiform chromitite have previously proved contentious. A fundamental problem being that many large podiform chromitites have been mined out, leaving little in situ chromite. Access to an unmined podiform chromitite, Voskhod being one of the largest of its kind in the world, provided a unique opportunity to look at an intact podiform chromitite deposit.

Initial studies of the ore chromite geochemistry revealed that there was little variation with depth through, or between relative positions across the ore body. From these early results it was realised that detailed systematic analytical studies were required. Subsequent work focused on three aspects. To:

- Determine the tectonic setting associated with the ore body formation.
- Investigate the hanging wall, footwall and dunite halo adjacent to the ore body and assess how these lithologies had been affected by the ore forming process.
- Identify the characteristics of, and constrain the controls on, chromitite formation to develop a genetic model.

These objectives were achieved by studies on;

- A dense, complete chromite core, 45 m long, selected from the most intensely mineralised zone at the centre of the ore body (drill core V05-13).
- Three continuous drill core sections; two of massive chromite and one of massive grading into disseminated chromite, each 15 cm long.
- Numerous small (5cm) samples selected from across the ore body, dunite halo, hanging wall and footwall units.

A range of analytical techniques were used to collect data including, scanning electron microscopy, electron microprobe microscopy, laser ablation and whole rock geochemical analysis.

This thesis presents the results of these studies, linking together the outcomes to form a model that explains where, how and under what geological conditions this giant podiform chromitite, the Voskhod deposit, formed.

Chapter 2: Ophiolites

The early use and development of the terms close to 'ophiolite' was reviewed by Amstutz (*1980*). The term was initially used to describe different types of serpentinite. This lead to the development of the slightly more restricted model by Steinmann which included the collective association of peridotite, basalt and radiolarite, present in the Alps and Apennines, as characteristic of the deep-ocean floor. Bailey (*1936*) placed Steinmann's interpretation into the context of continental drift and orogeny.

In the 1960's an ophiolite was regarded as an on-land fragment of fossil oceanic lithosphere formed at the site of a palaeo-spreading centre (*Hess, 1965; Gass, 1968* and *1990*). This lead to the Penrose statement of the ophiolitic stratigraphy (*Anon, 1972*). Between this and the mid 1980's the view developed that most ophiolites were formed in a subduction zone environment (*Pearce, 2003*). However, many ophiolitic terranes did not have all the rock groups of the Penrose ophiolite, leading to a revised 9-fold classification of ophiolites (*Dilek, 2003*) each with a type locality. These all contained a simple 'trinity' of rock types - pillow lavas, gabbros and ultrabasic rocks or peridotites. Ophiolites were recognised to have a wide time distribution (Table 1) though the concept of a Pre-Cambrian ophiolite is still debated (*Klusky, 2003*). Many ophiolites are polygenic, recording the imprint of more than one tectonic environment.

Ophiolites record one or more of the progressive stages of a Wilson cycle, from early stage continental rifting and sea floor spreading, to late stage subduction and obduction events associated with ocean closure (*Dilek 2003*). The occurrence of ophiolites correlate with major orogenic events, resulting in sections of ocean crust being tectonically emplaced onto continental crust, or older oceanic crust by overthrusting or obduction at converging plate boundaries (*Coleman, 1971; Dewey & Bird, 1971; Dewey, 1976)* during the closing stage of an ocean basin. They are typically found situated in the fault zones of orogenic belts. Such fault zones are suggested to represent suture zones that link plate collision events, typically between continents and island arcs (*Burke et al., 1977*) as well as supercontinent formation events.

Event resulting in ocean crust formation	Ocean crust formed	Continent formed/orogenic event (Ophiolite emplacement)	Timing of orogeny
Assembly of Rodina	Proterozic 1040-960 Ma	Rodina	~1000 Ma
Collision between E. and W. Godwana	Proterozoic ~680 Ma	Pannotia	700-600 Ma
Rodina break-up, W. Gondwana assembly	Proterozoic 820 - 740 Ma	Pan-African – Brasiliano	520-500 Ma
East Iapetus Ocean Closure	Palaeozoic ~500 Ma	Caledonian – Famatinian	460-440 Ma
Rheic Ocean Closure	Palaeozoic ~380 Ma	Appalachian – Hercynian	300-270 Ma
Pleionic Ocean closure	Palaeozoic ~408 Ma	Altaid - Uralian	~240 Ma
Alpine Orogeny	Mesozoic ~180Ma	Africa-Europe	~120 Ma

Source: Dilek, 2003b

Table 1: Ophiolites and Associated Orogenic Events

2.1 Ophiolite stratigraphy

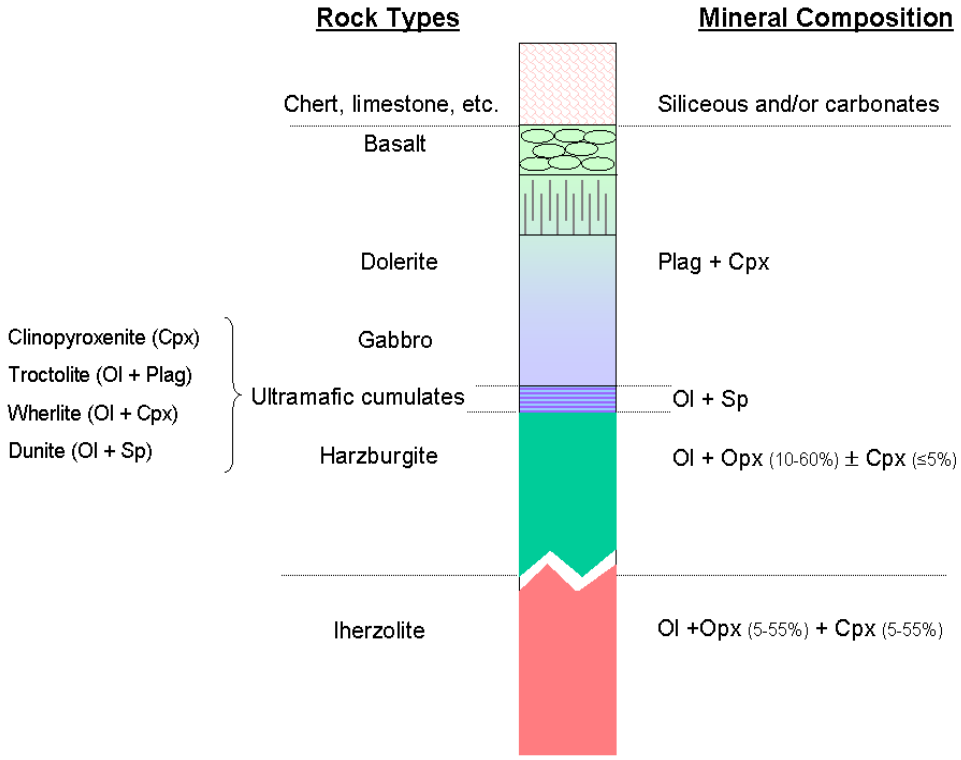

Figure 2.1.1: Ocean crust idealised stratigraphic section

Illustration is not drawn to scale

An idealised ocean floor sequence determined by geophysical surveying and ocean drilling (*Moores & Vine, 1971; Moores, 1972; Moores & Jackson, 1974*), is shown in Figure 2.1.1; it is similar to the Penrose pseudo-stratigraphy. The interface between the crustal ultramafic cumulate units and mantle ultramafic tectonites (harzburgite and lherzolite) is termed the Petrological Moho and can be identified in an ophiolite stratigraphic sequence (e.g. *White, 1988*). An ophiolite stratigraphic sequence includes; pelagic sediments, basalt pillow lavas, a dolerite sheeted dyke and sill complex, a gabbro plutonic intrusion, mafic progressing to ultramafic cumulates and mantle harzburgite and/or lherzolite at the base of the sequence.

2.1.1 Crustal units

Pelagic sediments, formed from biogenetic marine material, accumulate in the abyssal plain of the deep ocean typically in a back-arc setting. If situated close to a continental source, a terrestrial component may also be present. The uppermost igneous unit is typically basalt. Pillow lavas form when basaltic lava flows are expelled onto the ocean floor. They are sack like bodies typically 0.2 -2 m in diameter, separated by rapidly cooled, fine-grained rinds (*Benson, 1926; Steinmann, 1927*). Sheeted dykes and sill complexes of dolerite underlie the pillow lava unit. The dykes and sills are feeder conduits, responsible for transporting magma to the surface (e.g. *Gass, 1968; Moores, 1969*). Within the sequence, gabbro forms massive, isotropic, plutonic intrusions (non-cumulate), where minerals have crystallised at the periphery of the magma chamber (e.g. *Maxwell, 1969; Marsh, 1989*). Additionally, gabbroic horizons, possessing cumulus textures have been reported towards the top of the crustal ultramafics (e.g. *Church & Stevens, 1970*).

Ultramafic rock types are present towards the base of the crustal (e.g. *Maxwell, 1969; Moores, 1969; Anon, 1972*), these include; clinopyroxenite, troctolite, wehrlite and dunite. The mineral compositions and relative abundances of these rock types (Figure 2.1.1) are determined by the tectonic environment and the parent magma chemistries associated with their formation (see Section 2.2). Dunite is most abundant at the Petrological Moho, at the base of the crust. Lenses and discontinuous layers of dunite, are frequently observed parallel to or cross cutting the foliation of the harzburgite mantle rock.

2.1.2 Mantle units

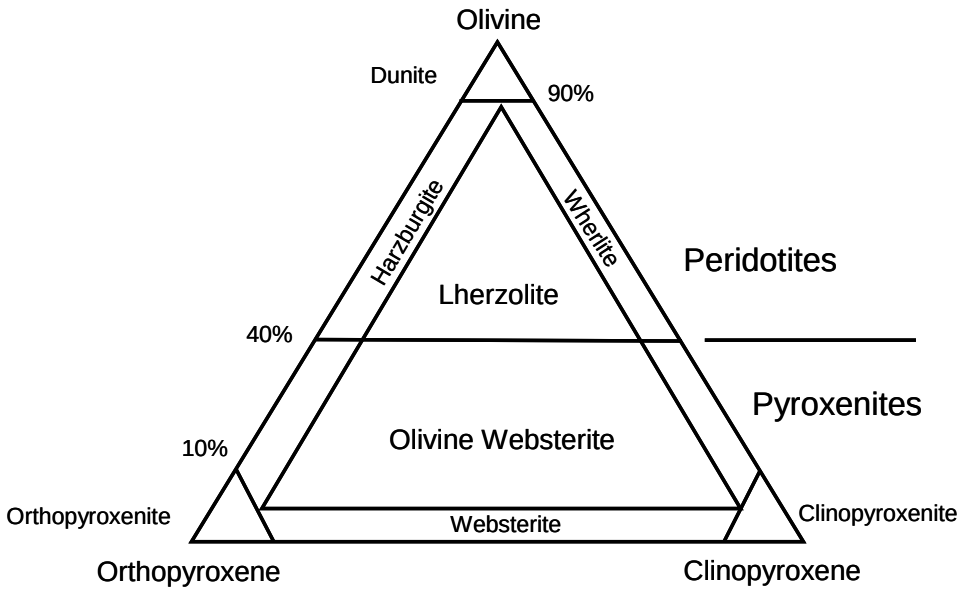

Figure 2.1.2: Pyroxenites, peridotites and dunite compositions.

Adapted from Bodinier & Godard 2004

The classification of mantle peridotites, harzburgite and lherzolite, is based on mineral proportions of olivine, orthopyroxene and clinopyroxene, Figure 2.1.2. Amphibole is present in some mantle rocks (typically <10 % of the rock composition) formed by the hydration of the primary mineral phase clinopyroxene.

Mantle harzburgite is a refractory, residual rock that stratigraphically overlies fertile mantle lherzolite. It forms by convection of the upper mantle, which causes lherzolite to rise and, by adiabatic decompression, partially melt. The partial melting process preferentially extracts clinopyroxene forming a residue depleted in clinopyroxene. Increased degrees of partial melting and/or prolonged periods of mantle melting, lead to a progressively more depleted residue, eventually forming a clinopyroxene-poor harzburgite or in extreme cases, dunite.

Lherzolite ⟶ Harzburgite (+ Cpx) ⟶ Harzburgite (- Cpx)

Increasing degree of mantle melting

Lherzolite is most commonly present stratigraphically below harzburgite. However, lherzolite may also form by the 'refertilisation' of harzburgite (*Ringwood, 1982; 1986; Ringwood & Irifune, 1988*), a process where upwelling melt, impregnates residual mantle harzburgite crystallising clinopyroxene, with or without orthopyroxene and plagioclase, changing the mineralogical composition (*Godard et al., 2000*; *Takazawa et al., 2003*). When lherzolite is created in this way it typically forms narrow bands several centimetres wide, with diffuse boundaries grading into the host harzburgite (*Lippard et al., 1986*).

2.1.3 Chromite in the ophiolite sequence

Two types of chromite are associated with peridotite rocks:

Accessory chromite, where grains comprise <3 % of the rock by volume, is commonly associated with crustal dunite and the mantle rocks, harzburgite and lherzolite.
Concentrated accumulations of chromite; these are found in almost all ophiolites, examples include; the Thetford Mines ophiolite complex in the southern Quebec Appalachians, the Loubusa ophiolite in Tibet and the Tari-Misaka Ultramafic Complex, south west Japan, numerous others have been documented in Cyprus, Oman, Turkey, Philippines, China, New Caledonia, Cuba, (*e.g. Stowe, 1994*).

Chromitite refers to a rock that is dominated by chromite co-existing with olivine, with or without clinopyroxene, orthopyroxene and plagioclase. When chromite concentrations form in the mantle units of an ophiolite as pod-, sack-, lensoid- or disc-shaped masses, they are termed podiform chromitite. Podiform chromitite is a characteristic feature of harzburgite mantle sequences, but are less common in lherzolite mantle sequences (*Roberts & Neary, 1993*). Laterally extensive, planar layers of chromitite may form in the lowermost crustal layers of some ophiolites, although generally these are not referred to as podiform chromitite.

Chromite and chromitite genesis is discuss further in Chapter 3.

2.2 Ophiolite formation and emplacement

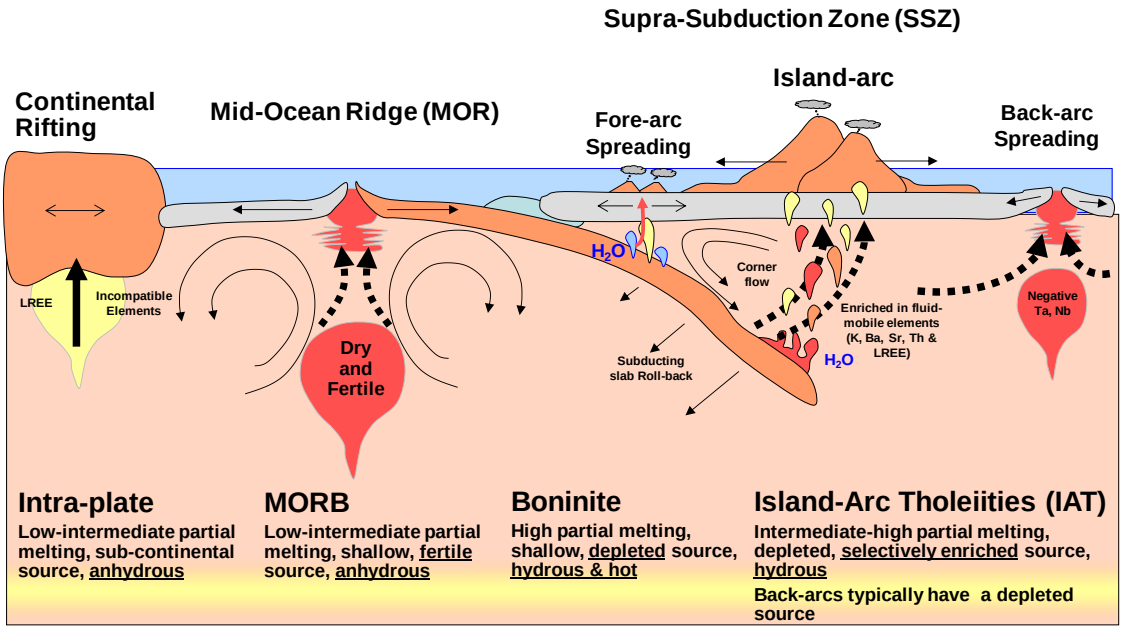

Figure 2.2.1: A schematic detailing the differing melt-types and the tectonic settings associated with their formation.

Adapted from R. Lilly, 2006

The sequential events resulting in ophiolite formation are; i) ocean crust genesis, ii) slab detachment within the ocean basin, iii) plate collision and iv) emplacement onto older, more dense crust, can occur in a short time frame of 2 Ma (*Hacker et al., 1996*). Young, hot, thin (3.5 km thick) ocean crust is buoyant, so resists subduction and is obducted (Dewey*, 1976*). Emplacement occurs most readily at a convergent plate system boundary e.g. a supra-subduction zone setting. For an ophiolite to form from mid-ocean ridge-type crust a divergent plate system must be reversed to a convergent system while the ocean crust is still young and buoyant. Buoyancy analysis of subducting lithosphere suggests that oceanic lithosphere 10 Ma or older has an increased susceptibility to deep subduction (*Cloos, 1993*). This provides an explanation for the lack of MOR (normal oceanic lithosphere) preserved in the geological record; such lithosphere would have undergone deep subduction and been reincorporated into the mantle (*Coleman, 1977*).

Older basement material, either continental margin or older oceanic crust, is comprised of platform sediments and carbonate sequences. The process of emplacement results in the formation of characteristic features including; a

metamorphic sole, nappes (intact thrust sheets) and/or a mélange (a complex tectonic mix of both continental and oceanic derived rock fragments) (*Moores et al., 2000*).

2.2.1 Tectonic settings: Mantle and melt geochemistry

Ocean crust forms in extension-related tectonic settings, sites include; mid-ocean ridge (MOR), e.g. the Mid-Atlantic Ridge, incipient rifts e.g. the Red Sea (*Bischoff, 1969*) and island arc settings; back arc basins e.g. East Scotia back-arc basin (*Dilek, 2003a*), forearc basins e.g. the Izu-Bonin-Mariana forearc, Western Philippine Basin (*Parkinson & Pearce, 1998; Pearce et al., 2000; Ishiwatari et al., 2003*) and incipient arcs.

Differences between tectonic settings affect the mantle conditions and subsequently the melts produced. These differences manifest as geochemical signatures that can be identified in lavas as well as mantle rocks where evidence of depletion or enrichment, owing to interaction between mantle and melts, may be recorded.

	Mid Ocean Ridge	**Fore-Arc**	**Island-Arc**	**Back-Arc**
Environmental Setting	MOR Sea floor spreading	Supra-Subduction Zone	Supra-Subduction Zone	Back-arc spreading
Nature of Mantle	Fertile	Depleted	Depleted	Depleted
Depth of melting	Shallow	Shallow	Deep	
Presence of water	Anhydrous	Hydrous	Hydrous	
Degree of Partial Melting	Low-Moderate	High	Moderate-High	
Melt-type	Mid Ocean Ridge Basalt (MORB)	Boninite (BON)	Island Arc Tholeiite (IAT)	Island Arc Tholeiite (IAT)
Element Signature	Depleted: LREE	Enriched: Mg. Depleted: REE and HFSE	Enriched: K, Ba, Sr, Th and LREE	Depleted: Ta and Nb

Source: Lilly, 2006

Table 2: Ocean Basin Tectonic Settings and Characteristics of Melts Generated

The initiation of a continental plate break-up is marked by the formation of an incipient rift, the resulting plate divergence marks the boundary between two continents. As rift extension progresses a major ocean basin forms that has a central submarine ridge

system, a MOR. The fresh basalts erupted onto the seafloor associated with these systems are termed mid-ocean ridge basalts (MORB).

At MOR localities the mantle source is fertile lherzolite containing 0.01-0.04 wt% water *(Pearce et al., 1992).* The mantle is subject to low-moderate degrees of partial melting (<25%) under anhydrous and reducing conditions, typically ±1 fO_2 of the quartz-fayaltie-magnetite (QFM) boundary (*Haggerty, 1976*; *Christie et al., 1986; Carmichael & Ghiorso, 1986*). A MORB melt containing ~0.33 wt% water *(Jambon, 1994)* forms and a moderately depleted mantle residue of either, lherzolite or clinopyroxene-rich harzburgite.

In contrast, a supra-subduction zone (SSZ) forms when two ocean plates converge. Initial subduction-related magmatism occurs at a localised spreading centre forming a forearc (*Pearce et al., 1984*). Subduction of the downward moving slab introduces water, at depth into the mantle wedge. This enriches the mantle source with up to 0.5 wt% water (*Pearce et al., 1992)*. Water is present either as hydrous minerals (e.g. the decomposition of amphibole) or fluids that flush through the melting zone. Water promotes hydrous melting of the mantle wedge by lowering the solidus and increasing oxidising conditions (*Kushiro, 1990*). Consequently, higher degrees of melting may be achieved, up to 30% (*Jacques & Green, 1980*). Island arc tholeiite (IAT) forms when the mantle wedge is fertile or boninite (BON) when the mantle source is depleted and a mantle residue of depleted harzburgite is remnant (*Dilek, 2003b*).

The development of a SSZ and associated forearc magmatism is the first stage in the formation of an intra-oceanic arc. As the tectonic regime evolves a complex series of arc terrains, separated by inter-arc basins form (Figure 2.2.1). The initial SSZ fore-arc setting evolves to form an island arc and with further maturation a back-arc. Melts with distinctly different chemical compositions are associated with each of the three settings (Table 2). Thus, the composition of an igneous rock provides information relating to the tectonic setting it formed in.

The concept to distinguish between ophiolites started with the work of Rocci et al. (1975) and was based on studies of the Tethyan ophiolites. This work was developed further by Pearce et al. (1984). Their findings showed that geochemical characteristics and crystallisation sequence differences could be used to distinguish between ophiolite types and interpret formation histories. A comparison of the mineralogical compositions of SSZ and MOR ophiolite mantle sequences show that SSZ ophiolites

more commonly possess podiform chromite, with economic sized chromite deposits only present in SSZ-ophiolites. In terms of the crustal sequences, clinopyroxenite and wehrlite are present in the ultramafic cumulates of SSZ-ophiolites, these units crystallised out of melts derived from depleted (clinopyroxene-poor) residual mantle. In contrast, troctolite and gabbro units are present in the lower crustal cumulates of MOR ophiolites crystallising from melts derived from fertile mantle comprised of lherzolite and clinopyroxene-rich harzburgite. The differences between the cumulate sequences result from the different melt source mantle compositions.

In addition to the crustal cumulates compositions, the order of crystallisation is also an indicator of the melt composition and tectonic setting associated with melt genesis. For boninites the order is olivine – orthopyroxene – clinopyroxene, for island arc tholeiites: olivine – clinopyroxene – plagioclase (*Pearce et al., 1984; Cameron, 1985*) and for MORB: olivine – plagioclase – clinopyroxene (*Bryan, 1983; Pearce et al., 1984*) . Pearce et al., (1984) proposed that the differences in crystallisation sequences and melt compositions was a reflection of the higher CaO/Al_2O_3 ratios of SSZ melts (boninites and island-arc tholeiites) than of primary melts (MORB) formed in MOR settings. This hypothesis is supported by the relative abundance of Ca-bearing clinopyroxene present in the fertile mantle units observed in MOR-ophiolites.

Although the differences between MOR- and SSZ-ophiolite mantle control the melt compositions, changes to the pressure, temperature and oxygen fugacity (fO_2) conditions during melting also have an effect. Melts formed under high pressure and temperature conditions (e.g. boninites) have greater abundances of Mg, Fe and Ti in comparison to lower pressure and temperature melts (primary MORB melts) that are higher in Si and Al (*Danyushevsky et al., 1987; Sobolev & Shimizu, 1993; Kamenetsky et al., 2001*).

2.2.1.1 *Mid-Ocean Ridge Basalt (MORB)*

MORB lavas are the product of the low-moderate partial melting of an upwelling fertile, asthenospheric mantle source, the result of adiabatic decompression (e.g. *Cawthorn, 1975*). Their chemistry reflects the anhydrous melting conditions present in a MOR setting (*Green, 1973*).

Oceanic basalts include Normal-MORB (NMORB), Enriched-MORB (E-MORB), Ocean Island Basalt (OIB) and Large Igneous Province (LIP) type lavas. The

differences between these lavas are a function of differing mantle compositions, melting conditions (e.g. pressure, temperature and fO_2), spreading rates and/or fractional crystallisation (*Stracke & Bourdon, 2009*). MORB is predominantly tholeiitic in composition (e.g. *Engel et al., 1965; Melson et al., 1976*). The geochemical data for 2,499 MOR samples was compiled and interrogated by Metcalf and Shervais (2008). They showed that MORB compositions have a restricted range in major element composition characterised by; a limited range, low silica content 48-52 wt% SiO_2, moderate to high TiO_2 contents of ~0.5 wt% up to 3.6 wt% (typically greater than 1.2 wt% TiO_2), Al_2O_3 ~15.0 wt%, FeO_T ~10.0 wt%, CaO ~11.3 wt% and Na_2O ~2.6 wt% (*Metcalf & Shervais, 2008*).

The N-MORB mantle source is depleted in incompatible trace elements (i.e. Cs, Ba, Th, Ta, Nb, K, Pb, Sr, P, Zr, Hf, Ti, Y, REE) relative to the estimated primitive-mantle compositions. This depleted source is referred to as depleted MORB mantle (DMM) (*Hofmann, 1988; Sun & McDonough, 1989*) and is present in the shallow asthenosphere. In comparison, enriched basalt compositions (E-MORB < LIP < OIB) are elevated in incompatible trace elements (*Schilling et al., 1983, 1985; le Roex, 1987; Sun & McDonough, 1989)* (Chapter 5, Section 5.6).

A-typical MOR spreading centre activity has produced more evolved basalt compositions from MORB parent magmas, these have been interpreted to result from extreme fractionation e.g. Pacific-Antarctic Ridge (*Stoffers et al., 2002*). Although a MOR setting is the principal locality where MORB forms, MORB lava compositions may be detected in back-arc basin lavas when back-arc spreading is sufficiently extensive to access mantle that has not been contaminated by subducted oceanic lithosphere (*Pearce et al., 1984*).

2.2.1.2 *Boninite*

Boninites were first classified in Western Pacific intra-oceanic arc rocks (*Sharaskin et al., 1980; Crawford et al., 1981; Natland, 1981; Natland & Tarney, 1981; Hickey & Frey, 1982: Umino, 1986; Bloomer & Hawkins, 1987; Stern & Bloomer, 1992*) and have since been identified in a number of ophiolites located within mountain belts at a number of worldwide localities including; the Tethyan ophiolites (*Pearce et al., 1984, 2000; Thy, 1984; Cameron, 1985*), the Appalachian ophiolites (*Crawford & Cameron, 1985; Coish, 1989*) and the Ural ophiolite massifs (*Kuz'min & Kabanova, 1991; Spadea et al., 1998; Spadea & Scarrow, 2000; Brown et al., 2006*). This melt-type is

associated with the inception of new subduction systems (e.g. *Crawford et al., 1981, 1986, 1997; van der Laan et al., 1989; Stern & Bloomer, 1992; Hawkins & Castillo, 1998; Flower, 2003; Flower & Dilek, 2003*) and is found exclusively in arc-forearc terrains (e.g. *Reagan & Maijer, 1984; Bloomer et al., 1994*).

Geochemically, boninites have a primitive compositions that are characterised by; high-MgO, low-TiO_2 and low alkali contents, relative to basalts and andesites that possess equivalent SiO_2 contents, as well as, low high-field strength elements (HFSE) relative to large ion lithophile elements (LILE) K, Rb, Sr and Ba (*Meijer, 1980; Natland & Tarney, 1981; Crawford et al., 1989*). Their geochemically primitive nature results from high degrees of partial melting of a depleted source and the characteristic high LILE/HFSE ratios observed indicate that the rocks are generated from depleted mantle wedge material, influenced by the addition of a fluid component. Furthermore, boninites show evidence for being high temperature magmas >1300-1350°C, as inferred from petrochemical observations (*Duncan & Green, 1987; Crawford et al., 1989*).

The evolution of these magmatic products has been debated. One hypothesis is that boninites are the product of reaction between ascending basaltic melts, formed from melting of the mantle wedge, and refractory residual mantle (e.g. *Kelemen, 1995; Zhou et al., 1996*). Parkinson & Pearce (1998) proposed that this model could explain the ultra-refractory characteristics of forearc associated peridotites. An alternative theory put forward by Macpherson & Hall (2001) interpreted boninites to represent magmas formed by the interaction of thermally anomalous mantle plumes associated with active, hydrous subduction systems (*see also, Deschamps & Lallemand, 2003*). The modification of the upper mantle mineralogy and geochemistry, resulting from melt-rock interaction between percolating magmas and mantle wall rock, has been documented in numerous studies (*Fisk, 1986; Kelemen, 1990; Kelemen et al., 1995*). The studies show that melt-rock interaction results in the continual mineralogical and geochemical modification of both the reacting melt and the wall rock, where basaltic magma alters to a boninite chemistry and the peridotite wall rock to dunite, the result of pyroxene dissolution (*Zhou & Robinson, 1994*).

2.2.1.3 *Island-Arc Tholeiite (IAT) and Calc-Alkaline Basalt (CAB)*

Island arc tholeiite (IAT) lavas form during the early stages in arc development. Island arc tholeiite rocks are chemically analogous to, but also different from, calc-alkaline

basalt (CAB) rocks (*Jakes & Gill, 1970*). Calc-alkaline basalts are associated with more mature arc systems and also back-arc basin (BAB) systems.

IAT lavas mark the evolution of a SSZ, from the initial fore-arc setting, to that of an island arc. IAT melts are generated at depth, from moderate-high degrees of partial melting of a depleted mantle source. Melting is enhanced by the hydrous conditions associated with SSZ settings. They are found in intra-oceanic, island arc systems e.g. the Mariana arc, as well as in association with oceanic plateaus e.g. the Caribbean island arc tholeiites. Geochemically these rocks produce flat to light rare earth element (LREE) enriched rare earth element (REE) patterns. Comparatively, IATs are more LREE depleted than CABs, have a comparatively lower silica mode, increased iron content and higher Na_2O/K_2O ratios. Negative Nb and Ta anomalies are associated with both lava types.

2.2.2 Mantle peridotite types

Aside from the melt chemistry, melt-rock reaction is also a governed by the mantle peridotite geochemistry. Some types of peridotite form in, or are influenced by, similar tectonic settings e.g. abyssal peridotite and the mantle section of ophiolites. In such cases it is the locality of the peridotite exposure that distinguishes the peridotite-type characterisation.

2.2.2.1 *Abyssal peridotite*

Abyssal peridotite is the residual product of adiabatic decompression melting of a fertile mantle source at a MOR typically found tectonically exposed along fracture zones, within transforms and locally on rift valley floors at some slow spreading ridges (*e.g. Dick & Bullen, 1984*). Studies by Johnson et al., (1990) demonstrate that abyssal peridotite is the residue of fractional melting of a fertile mantle source. The more depleted the peridotite (the greater the extent of melting), the greater the MgO content will be (e.g. *Frey et al., 1985*) as MgO increases proportionately with the olivine content. Hellebrand et al., (2001) observed that HREE in abyssal clinopyroxenes correlated with the Cr/(Cr+Al) ratio of co-existing spinel, reflecting the degree of partial melting of the residual peridotite.

Abyssal peridotite that is subsequently influenced by a SSZ tectonic setting undergoes further melt extraction episodes. The melts ascend and are subsequently expelled to

form an island arc. The extensively depleted abyssal peridotite formed at such a setting is classified as forearc peridotite (*Ishii et al., 1992; Nui et al., 1997 and 2001; Nui, 2004; Monsef et al, 2010*).

2.2.2.2 *Forearc Peridotite*

Forearc peridotite is characterised by high degrees of partial melting and is more depleted than abyssal peridotite. The degree of mantle melting is greater in SSZ settings, as dewatering of the downward subducting slab creates hydrous melts that lower the mantle solidus (*Pearce & Parkinson, 1993*).

Chromite in forearc peridotite has a geochemistry where the Cr# (Cr# =[Cr/(Cr+Al)]) is between 0.3 and 0.6 and TiO_2 contents are low (<0.13 wt%) (*Monsef et al., 201*0). These chemical characteristics typify residual peridotite formed from >20% partial melting such as that exposed in depleted residual mantle and ophiolites e.g. the Izu-Ogasawara-Mariana forearc (*Ishii et al., 1992*), South Sandwich arc-basin system (*Pearce et al., 2000*), the Mariana back-arc basin (*O'Hara et al., 2002*), the Izu-Bonin-Mariana forearc (*Parkinson & Pearce, 1998*) and the Oman ophiolites (*Tamura & Arai, 2006*).

It should be noted that in some exceptional cases depleted peridotite may also form in MOR settings where MORB melt extraction has been extensive e.g. the Fifteen-Twenty Fracture Zone, the Mid-Atlantic Ridge, (*Godard et al., 2008*) and the East Pacific Rise (*Niu & Hekinian, 1997*). To fully appreciate the tectonic setting associated with the formation of depleted peridotite investigation into REE and trace element patterns should be considered in conjunction with whole rock major and minor element data (*Monsef et al., 2010*).

2.2.3 Ophiolite mantle peridotite

Exposed mantle peridotite units located at the base of an ophiolite sequence may be studied to determine the melting history and assist in distinguishing the tectonic setting associated with the ophiolite genesis and emplacement. Studies of mantle peridotites, cross-referenced with co-genetic crustal lavas, can be used to assess; i) the mantle potential temperature variation, ii) plate spreading rate variation and iii) mantle source compositional variation. An appreciation of these factors facilitates the interpretation

of; the extent of mantle melting, the MORB composition and the rate of ocean crust production (*Nui, 2004 and references therein*).

2.2.4 Limitations relating mantle peridotites and crustal lavas

Studying residual peridotite and genetically associated crustal lava relationships to interpreting geodynamic settings has limitations. Dick et al. (*1984*) demonstrated a qualitative complimentary relationship between abyssal peridotites and spatially associated MORB in terms of their associated varying extents of melting. However, in terms of quantitative melting models this relationship is difficult to constrain. Elthon (*1992*) reported that the bulk chemical compositions of abyssal peridotites are not consistent with residues from MORB formation, formed by either batch or fractional melting processes. Elthon (*1992*) proposed that the chemical trends of abyssal peridotites result predominantly from refertilisation processes rather than partial melting processes. Nui et al. (*1997*) undertook studies to quantitatively reconcile melting and crustal accretion processes at mid-ocean ridge settings, by outlining the significance of olivine accumulation in the mantle. Their research found that olivine accumulation in the mantle impacts the modal mineral proportions of abyssal peridotites. This distorts the resulting bulk chemical compositions, subsequently impacting the interpretation of mantle melting processes.

In addition to the first order direct relationship between abyssal peridotite and MORB composition, second order aspects of melt generation and crustal accretion also require consideration. Second order aspects (termed as mantle melting dynamics, (*Nui et al., 1997*) include the initial and final depths of melting, the melting rate, the extent to which melting is fractional or batch, extent and depth of melt-rock interaction and modal and chemical source variation (*Klein & Langmuir, 1987; Johnson et al., 1990 and Kelemen et al., 1995; Nui et al., 1997*). A competent understanding of the factors that influence mantle melting dynamics is required to be able to correctly interpret the tectonic setting.

The compositions of mineral phases present in peridotite have been used to compare and contrast peridotites from different tectonic settings (*e.g. Dick & Bullen, 1984; Bonatti & Michael, 1989*). Geochemical parameters, e.g. the Cr# of chromite, Fo of olivine and the Al_2O_3 content of orthopyroxene, can be used to assess differences in the modal and bulk composition between peridotites. It has been shown that with progressive change in tectonic environment, from passive continental margins, to mid-

ocean ridge settings, to mature oceans, to supra-subduction zone settings, the degree of peridotite depletion increases respectively. As the degree of depletion increases, compositional changes are observed in the peridotite mineralogy; i) the Cr# of chromite increases, ii) the modal content of clinopyroxene decreases, iii) the bulk content of Al_2O_3 decreases and MgO increases, iv) the Al_2O_3 content of orthopyroxene decreases yet the MgO content increases and v) the Fo of olivine increases. Subsequently, these compositional variations are indicators providing information about the tectonic setting to have influenced peridotite formation (*Pearce et al., 1984; Dick & Bullen, 1984; Bonatti & Michael, 1989*).

2.3 Geochemistry: A tool for tectonic reconstruction

Ophiolites retain mineralogical, geochemical and structural characteristics that enable the reconstruction and interpretation of the tectonic setting that was in effect during crust formation up to and including the point of emplacement onto the continent (*e.g. Pearce, 1980*) and it is the tectonic setting that governs the degree of mantle melting. Studies have shown that more refractory and chemically-depleted the mantle reflect higher degrees of partial melting and melt extraction (*Goddard et al., 1995; 2000; Vernières et al., 1997; Gruau et al., 1998; Girardeau et al., 2002; Le Mee et al., 2004; Monnier et al., 2006*).

Reaction between residual mantle and upwelling melts, termed melt-rock reaction, compartmentally refertilises the mantle (*Elthon, 1992; Niu & Hekinian, 1997*; *Niu, 2004*). The geochemistry of residual mantle peridotite, fertilised peridotite and, if present, the associated crustal lavas, can be used together to determine the tectonic model associated with the formation of the ophiolite complex.

The extent of melt-mantle interaction can be investigated, by studies of chromite derived from mantle peridotite. The composition of chromite and modal proportions of mineral phases olivine, clinopyroxene and orthopyroxene in the mantle peridotite, provide evidence of the mantle melting history and interaction with upwelling (deeper sourced) melts (*e.g. Kelemen et al., 1995; Edwards & Malpas, 1996; Edwards et al, 1996; Nui et al., 1997; Pearce et al., 2000*).

2.3.1 Monogenetic and polygenetic tectonic settings

When the composition of the crustal and mantle units of an ophiolite reflect having formed in multiple, different tectonic environments, it is said to have formed in a polygenetic tectonic setting (*e.g. Meffre et al., 1996; Portnyagin et al., 1997; Parkinson & Pearce, 1998; Pearce et al., 2000; Flower, 2003; Dare et al., 2008*). The implication being that the mantle residue and melt responsible for refertilisation could be derived from tectonically different settings. The alternative is a monogenetic setting, which defines a tectonic setting where the mantle lithosphere and interacting melt are derived from the same tectonic setting e.g. Hess Deep where residual MOR mantle harzburgite reacts with MOR melt creating dunite.

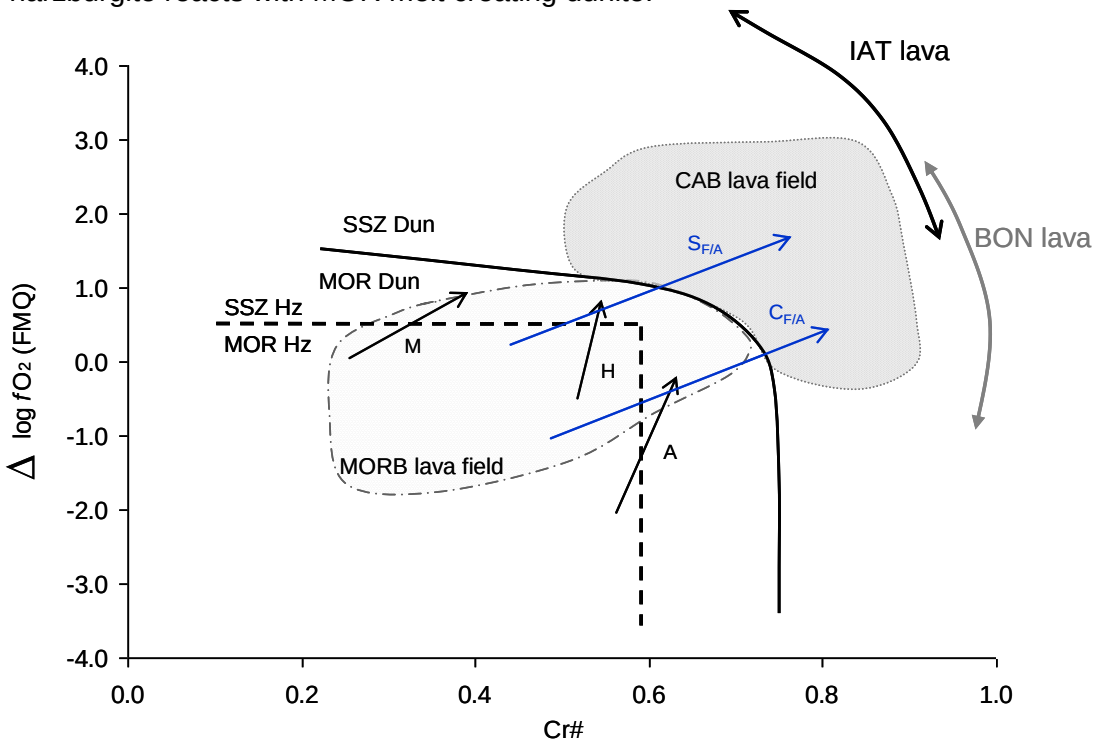

Figure 2.3.1: An annotated diagram of the Δ log fO_2 against Cr#.

Plot taken from the work of Dare et al., 2008 showing monogenetic and polygenetic reaction trend orientations between harzburgite and dunite pairs and discrimination boundaries for MOR and SSZ harzburgite and MOR and SSZ dunite. Cogenetic harzburgite-dunite pairs from mid-ocean ridge (MOR) and supra-subduction zone (SSZ) sites. MOR-SSZ discrimination boundaries for dunites (solid line) and harzburgites (dashed line) together with lava spinel fields for MORB, IAT, CAB and BON are shown. The vector for melt-rock reaction is marked by arrows between harzburgite-dunite pairs, for monogenetic settings arrows (black) are oblique to the peridotite discrimination boundaries, whereas for polygenetic settings arrows (blue) are sub-parallel to the boundaries. Sample notations for MOR sites: M = MAR (Mid-Atlantic Ridge), H = Hess Deep, A = Azores and for SSZ sites: SF/A = South Sandwich Forearc and CF/A = Conical Forearc Seamount. The SF/A and CF/A pairs formed diagonal interpreted to represent residual mantle (e.g. MOR or back-arc basin [BAB]) interacting with SSZ melts: the CF/A with a boninitic melt and SF/A with an IAT melt. Data sources: SF/A (*Pearce et al., 2000 and Dare et al., 2008*); CF/A (*Parkinson & Pearce, 1998*).

2.3.1.1 *Melt-rock reaction within monogenetic tectonic settings*

Dare et al. (*2008*) studied dunite-harzburgite pairs collected from a variety of monogenetic and polygenetic tectonic settings. Their investigations focused on the relationship between the Cr# (where Cr# = [Cr/(Cr+Al)]) of chromite present within each sample and the oxygen fugacity (Δ log fO_2), for each dunite-harzburgite pair (Figure 2.3.1). The monogenetic, mid-ocean ridge (MOR), sample pairs source localities included: the Mid-Atlantic Ridge (MAR), a slow spreading rate site; Azores, a plume influenced site and Hess Deep, a fast spreading rate site. Their findings showed that chromites from MOR dunites (the melt-mantle reaction product) typically have elevated fO_2 compared to the MOR harzburgite (the residual) counterpart. This was interpreted to be the result of the mantle residue and interacting melt being under anhydrous conditions, where comparatively Fe^{3+} would be depleted in the residue, yet relatively enriched in the melt. The Fe^{3+} component of chromite is a parameter involved in the calculation of Δ log fO_2 (*Wood & Virgo, 1989; Ballhaus et al., 1991*), the Cr# of chromite within a sample is intrinsically linked to the fO_2 of a sample (*Parkinson & Pearce, 1998; Parkinson & Arculus, 1999; Pearce et al., 2000*).

The vector drawn between the harzburgite and dunite pair end members for each sample set defines the melt-rock reaction trend (see the black arrows labelled M,H and A annotated on Figure 2.3.1). Melt-rock reaction between MOR harzburgite and MOR melt results in a greater increase in fO_2 than in Cr# (*Dare et al., 2008*). The vector trends produced are oblique to the fO_2 –dependent part of the discrimination boundary (the horizontal). This implies that the extent of melt-rock reaction is an important variable when determining a tectonic setting. Furthermore, the oblique orientation of the vector has been interpreted to reflect the extent of magmatic differentiation of the melt. The affect of magmatic differentiation on the composition of peridotite is an important consideration when interpreting a tectonic setting (*Sakuyama, 1978; Thy, 1983; Arai, 1992; Dare et al., 2008*).

2.3.1.2 *Melt-rock reaction within polygenetic tectonic settings*

A polygenetic tectonic setting is one where the mantle residue preserves a tectonic signature different to that of the interacting melt. The most common type forms by the interaction of MOR lithosphere with SSZ melts (published examples are the Conical Forearc Seamount in the Mariana forearc (*e.g. Ishii et al., 1992; Parkinson & Pearce, 1998; Pearce et al., 2000; Dare et al., 2008*) and the South Sandwich Forearc (*Pearce*

et al., 2000; Dare et al., 2008). Harzburgite-dunite pairs from polygenetic MOR-SSZ settings form diagonal trends on the Δ log fO_2 – Cr# diagram, (see the blue arrows labelled $S_{F/A}$ and $C_{F/A}$ on Figure 2.3.1). Both the Cr# and fO_2 values of chromite increase from harzburgite to dunite. This reaction trend has been interpreted by the authors cited above as consistent with pre-existing residual mantle (that possess lower Cr# and fO_2 values such as those associated with MOR or back-arc basin [BAB] settings) interacting with SSZ melts (that possess higher Cr# and fO_2 values owing to the hydrous nature of the SSZ melts).

2.4 Ophiolite types

Significant differences exist between ophiolites, even between those that occur in the same orogenic belt. Distinctive differences noted include; internal structures and micro-structures, chemical signatures and style of formation (*Nicolas, 1989; Dilek et al., 2000*).

The diversity in terms of ophiolite emplacement mechanisms and tectonic origins (*Wakabayashi & Dilek, 2003*) has resulted in the creation of type-subcategories to distinguish between ophiolites. Five ophiolite sub-types have been identified; Ligurian, Mediterranean, Sierran, Franciscan and Caribbean.

- Ligurian-type ophiolites (*Rampone & Piccardo, 2000*) are relics of continental rift basins and early-stage sea-floor spreading, the associated crustal units possess a mid-ocean ridge basalt (MORB) affinity. The mantle section is fertile lherzolite of exhumed subcontinental mantle lithosphere derived from an ocean-continent transition zone (*Dilek & Flower, 2003; Müntener & Piccardo, 2000*).
- Mediterranean-type ophiolites are derived from protoarc–forearc–backarc assemblages and possess supra-subduction zone affinities.
- Sierran-type ophiolites evolve from poly-genetic igneous histories associated with the development of ocean arc terrains resulting from multiple episodes of magmatism, rifting and tectonic accretion.
- Franciscan-type ophiolites are situated in ancient accretionary complexes, these are typically associated with mélanges and high-pressure metamorphic rocks. Genetic and temporal relationships between the melt and residua are not observed in the ophiolite stratigraphy, diverse chemical affinities, however, are noted.
- Caribbean-type (*Dilek, 2003a*) ophiolites are characterised by tectonically emplaced fragments of large igneous province generated oceanic crust.

2.5 Ophiolites of the Urals

The present day Ural mountains (the Uralides) are orientated approximately north-south and extend for a distance of 2,500 km from the islands of Novaya Zemlya in the Arctic Ocean (66°N) to the latitude of the Caspian Sea (48°N) (*Savelieva & Nesbitt, 1997; Brown et al., 2002, 2006; Spadea et al., 2003*). The Uralides are an orogenic fold-and-thrust belt that mark the Late Palaeozoic arc-continent collision event along the Eastern European palaeomargin of the Baltica plate (*Brown et al., 1998, 2002; Spadea et al., 2003*). The orogenic belt hosts in excess of 150 ophiolite masses derived from differing tectonic settings as identified by the geochemical variations between the oceanic lithosphere mantle sections (*Savelieva & Nesbitt, 1996;*). The majority of ocean crust fragments that constitute the Uralide ophiolites formed during the Palaeozoic in the Uralian Ocean basin (*Urals Papers*).

Given the vast length, the Uralides are divided geographically into the; Polar, CIS-Polar, North, Middle and South Urals (Chapter 4, Section 4.1, Figure 4.1.1). The Uralide ophiolites are not identical in terms of geochemistry, but record key stages of the Uralian Ocean basin evolution. Initiation of the ocean basin closure during the Silurian-Devonian led to the formation of island arcs; the Magnitogorsk island arc (MIA) in the South Urals and the Tagil-Schych'ya and Voykar island arcs of the Middle to Polar Urals region (*Yazeva & Bochkarev, 1996; Bosch et al., 1997; Saveliev et al., 1999; Savelieva et al., 2002; Herrington et al., 2005*).

Island-arc – continent (East European craton) collision during the Late Devonian – Early Carboniferous (*Spadea & D'Antonio, 2006*) caused the closure of back-arc-basins and emplacement of ophiolites along the formed suture zones. During the late Permian continent – continent collision (the Uralide Orogeny that occurred between Baltica – Eastern Europe and Kazakhstan – Siberia) the Uralian Ocean closed (*Brown et al., 1998; Condie & Sloan 1998*) and along with it the physical divide between Europe and Asia. This event contributed to the formation of the supercontinent Pangea.

Both Ligurian- and Mediterranean-type ophiolites are observed in the Uralides.

The Magnitogorsk arc is an intra-oceanic arc sequence, formed during the Middle to Late Devonian. Boninite and tholeiite magmas erupted in the forearc region, and younger (relatively) tholeiite to calc-alkaline volcanic rocks are found associated with

the mature arc (*Seravkin et al;. 1992; Brown & Spadea, 1998; Spadea er al., 2002; Herrington et al; 2005*). These volcanic units form the basement of the Magnitogorsk arc and are overlain by volcaniclastic sediments in the forearc basin, reaching thicknesses as great as 5,000 m (Brown et al., 2001). Located to the centre-west of the Magnitogorsk Zone in the South Urals, the Nurali, Mindyak and Kraka massifs are Ligurian-type ophiolites, dominated by fertile mantle lherzolite widely considered to have formed during early stage continental rifting and subsequent sea-floor spreading (*Savelieva et al., 1997; Spadea et al., 2003*). Further south of the Magnitogorsk zone are the Kempirsai and Khabarny massifs. These are Mediterranean-type ophiolites and possess mantle sequences comprised of depleted mantle harzburgite. Both the Kempirsai and Khabarny ophiolite massifs formed in association with the MIA accretionary complex, in a fore-arc – island-arc, supra-subduction zone setting (*Savelieva et al., 1997; Spadea & Scarrow., 2000 and Herrington et al., 2005; Brown et al., 2006*).

The Middle, North and CIS-Polar and Polar Urals host the Tagil zone (of the Tagil Arc). It is considered to represent an accreted intraoceanic arc and is comprised predominantly of Silurian andesites to the west and Early Devonian volcaniclastic rocks to the east. These units are overlain by 2,000m of Early and Middle Devonian limestone that, to the east, is inter-layered with calc-alkaline volcanics.

In the north, in the Polar Urals are the Voykar and Raiiz ophiolite massifs. These are also Mediterranean-type ophiolites and are considered the northern equivalents of the massifs such as Kempirsai and Khabarny. However, these ophiolites formed in the Tagil Arc, fore-arc – island-arc, supra-subduction zone setting (*Savelieva et al., 1997; Spadea & Scarrow., 2000 and Herrington et al., 2005; Brown et al., 2006*).

The Middle, North and CIS-Polar Urals host the Tagil zone (of the Tagil Arc). The east of the Tagil zone is characterised by the occurrence of rare, small, harzburgite-dominated, Mediterranean-type ophiolite complexes tectonically emplaced between the volcanic sequences (*Savelieva & Nesbitt; 1996; Savelieva et al., 2002; Herrington et al., 2005*). To the west are zoned ultramafic, Alaskan type, massifs that constitute the Platinum Belt. This belt extends over 900 km from the Arctic circle (60°N) south to Yekaterinburg (57°N) (Savelieva & Nesbitt, 1996; *Savelieva, 2002*). These massifs formed during the Mid-Silurian, intruding lower sequence basalts and sheeted dyke complexes of MORB affinity (*Schmeley et al., 1997; Herrington et al., 2005*). The

intrusions are considered to be co-magmatic with calc-alkaline, supra-subduction zone associated, lavas present higher in the sequence (*Bosch et al., 1997; Narkisova et al., 1999; Friberg, 2000; Savelieva et al., 2002; Herrington et al., 2005*).

The Uralian ophiolites mark progressive stages of the Wilson cycle and identify evolutionary differences in oceanic crust generation of the Uralian Ocean system; from the extension tectonic regime effective during the opening and growth of the Uralian Ocean during the mid Ordovician (*Spadea et al.,* 2003) to the compressive tectonics active during the closure of the Uralian Ocean in the late Permian.

Chapter 3: Chromite

Chromite ($FeCr_2O_4$) or chrome-spinel is an end member of the spinel group. The unit cell formula for spinel is AB_2O_4, where divalent cations substitute into "A", the tetrahedral site and trivalent cations into "B", the octahedral site. Major elements present in spinel are; Mg^{2+}, Fe^{2+}, Cr^{3+}, Fe^{3+} and Al^{3+}, the minor elements are; Mn^{2+}, Ti^{4+}, V^{3+}, Ni^{2+}, Co^{2+} and Zn^{2+}.

Chromite deposits are the primary ore source of chromium metal.

3.1 Chromium

Chromium was discovered in 1797 by Nicolas-Louis Vauquelin and Martin H. Klaproth as a component of the mineral crocoite ($PbCrO_4$) in a Siberian lead ore sample (*Donath, 1962*). Work by Vauquelin in 1798, led to the successful formation of chromium carbide by high temperature reduction of CrO_3, using charcoal as the reductant (*Vauquelin, 1974*). In 1798, J. T. Lowitz reported the discovery of chromium in Russian chromite samples.

The name chromium is derived from the Greek, "χρώμα", meaning "colour". The name was chosen because of the wide variety of colours possessed by chromium bearing compounds. The array of colours result from numerous oxidation states that the element exhibits, ranging from Cr^{+} to Cr^{+6} (*Rollinson, 1973*). However, in terms of chromium bearing minerals, oxidation states Cr^{3+} and Cr^{6+} are most prevalent, substituting readily into crystal structures, (*Burns & Burns, 1975*).

The cation Cr^{3+}, present as Cr_2O_3, is the most common oxidation state of Cr in chromium bearing minerals. This preferred oxidation state reflects the high crystal field and octahedral site preference energy of Cr^{3+} ions (*Burns, 1970*). The ionic radius of Cr^{3+} is 0.615 Å (*Shannon & Prewitt, 1969*) and is a similar size to cations Al^{3+} (0.53 Å), Fe^{3+} (0.645 Å), Ti^{4+} (0.68 Å) and Mg^{2+} (0.72 Å) (*Burns & Burns, 1975*). These similar ionic radii mean that for many minerals

where Cr^{3+} is a component of the crystal structure, isostructural phases form with Al^{3+} and Fe^{3+} in the place of Cr^{3+}. The reverse is also true; Cr^{3+} ions will substitute into the octahedral sites of many minerals containing Al^{3+}, Fe^{3+}, Ti^{4+} and Mg^{2+}. Burns & Burns (1975) identify that the most common chromium trivalent substitution is between Al^{3+} and Cr^{3+}, observed in the solid-solution series spinel-magnesiochromite and grossularite-uvarovite. In contrast, the substitution of Cr^{3+} for Fe^{3+} is less common with spinels, e.g. ishkulite, being comprised of chromite and magnetite mixtures ($FeCr_2O_3$ and Fe_3O_4, respectively). Similarly restricted is the substitution of Mg^{2+} for Cr^{3+} into minerals, e.g. chrome diopside and chrome tremolite. This substitution requires a compensation to accommodate the charge balance in these crystal structures.

Mao et al. (1972) proposed that Cr^{2+} is a constituent in blue diopsides. In addition, it has also been reported that olivine and pyroxene minerals from lunar samples possess chromium in the Cr^{2+} form (*Haggerty et al., 1970; Boyd & Smith, 1971; Boyd, 1972*). In the case of the lunar samples, the presence of Cr^{2+} reflects the reducing conditions in which these minerals formed. The substitution of Cr^{2+} in place of Fe^{2+} could, theoretically, occur in ferromagnesian silicates, owing to the similar ionic radii of Cr^{2+}, 0.82 Å and Fe^{2+}, 0.77 Å. However, Burns (1970) noted that Cr^{2+} is typically present in distorted octahedral sites of silicate phases and explained it to be the result of the Jahn-Teller effect (*Burns, 1970; Burns & Burns, 1975*

3.1.1 Uses of chromium

Initial concentrations of chromium in mantle peridotite can be as low as 0.2 wt.%, chromium may be concentrated up to 55 wt.% and when this happens the rock type chromitite forms (where chromite comprises a greater than 90 % volume of the rock). Chromitite is the most abundant source of chromium, a valuable element for alloying and refractory industries, and the reason it is mined. There are three principal categories of chromite ore;

i) Metallurgical ore (commonly Cr_2O_3 > 40%; Cr/Fe >2:2), which is smelted to produce ferrochrome for addition to the furnace charge for the manufacture of special steels, including stainless steel (18% Cr, 8% Ni and 74% Fe).

ii) Chemical ore (Cr_2O_3 >42%; Cr/Fe <2:2), the raw material for the production of Cr-chemicals used in a variety of applications such as paints and electroplating.

iii) Refractory ore (SiO_2 <10%, Al_2O_3 >20%, Al_2O_3 + Cr_2O_3 >60%), used for blast-furnace lining bricks.

Chromite ore or chromitite rock, forms as dykes, pods and layers up to several hundreds of metres long and several metres thick containing several tons of this element. For such mineralisation to form requires a concentration factor of approximately 300. Understanding the processes behind the genesis of this form of chromite mineralisation is an important part of mantle studies.

Chromite forms orthomagmatic ore deposits that take the form of layers, dykes or pods. Deposits vary across the globe in terms of size and chromium content of the chromites, that aggregate together to form chromite ore.

3.2 Chromite deposits

Chromite deposits occur where chrome-spinel concentrates in a localised area. Two principal economic deposit types of chromitite exist;

i) Stratiform chromite deposits are typically located in stable continental shield environments. Accumulations develop in layered igneous complexes e.g. the Bushveld Igneous Complex, S.A (*Barnes & Maier, 2002*).

ii) Podiform chromite deposits that occur in the ultramafic mantle and crustal rocks of ophiolites. These are present either as layers at the base of the magmatic cumulates or, more typically, as dykes, disc shaped lenses and pods

in upper mantle peridotites (*Jackson, 1961; Thayer, 1964; Jackson & Thayer, 1982; Stowe, 1994)*.

As the Earth has evolved, tectonic regimes have changed over time and consequently the environments favouring chromite concentration and deposit formation have varied. Five tectonic settings exist in which chromite accumulates, these are; *i*) ophiolite, lower crustal cumulates, *ii*) podiform chromite in mantle harzburgite, *iii*) Bushveld-type layered complexes in continental shields, *iv*) chromitite in serpentinised peridotite-metapyroxenite sills in Achaean greenstone belts, and *v*) Achaean anorthositic layered complexes in high-grade gneissic terrains (*Stowe, 1994*). Furthermore, there is a temporal relationship between the prevalence of each tectonic setting with four the key epochs of earth history: (i) the Achaean ~3,500 - 2,900 Ma a period of tectonic instability and high thermal gradients, (ii) 2,900 – 2,000 Ma when active extensive regions of continental shields with high thermal gradients became stable, favouring the formation and emplacement of large Bushveld-type complexes, (iii) 2,000 – 800 Ma the Cr/Fe ratios of chromite are low in layered complexes and ophiolites are unusual and (iv) since 800 Ma ophiolite-hosted podiform chromite deposits predominate.

Despite there being several different genesis models for the formation of chromite ore deposits, it is consistently observed that in all scenarios chromite formation is associated with ultramafic rocks (*Duke, 1983; Stowe, 1987*).

3.2.1 Stratiform chromitite

Stratiform chromite deposits are laterally extensive, thin (<1 cm up to 1 m) chromitite layers, e.g. the Bushveld Igneous Complex, South Africa and the Great Dyke, Zimbabwe. The layers can extend continuously over great distances, as much as 200 km. These chromite deposits are commonly found within early Precambrian continental shields or proximal to the margins of continental shields (*Stowe, 1994*).

Examples of layered intrusion complexes include: the Bushveld Igneous Complex, South Africa; Rhum, Scotland; Stillwater, Montana; Bird River Sill, Manitoba, Canada; Great Dyke, Zimbabwe; Bacuri Complex, Brazil.

The formation of chromitite bearing layered intrusions results from upwelling basaltic magma intruding continental crust. The magma penetrates upward until a point where the fluid pressure exceeds the pressure of the lithostatic overburden, at approximately 1-2 kbar (*Mudge, 1968*) at which point the magma migrates laterally. Typically the morphology of a layered complex is either, elongate and narrow in cross-section, tapering downward to a dyke-like feeder channel (e.g. The Great Dyke, Zimbabwe) (*Worst, 1958*) or sheet-like when the force of the magma has successfully breached the overburden, allowing it to spread laterally, e.g. Bushveld Igneous Complex, South Africa (*Sharpe et al., 1981*).

The Great Dyke, Zimbabwe and the Bushveld Igneous Complex, South Africa are located within the African continental craton and formed during the Precambrian, 2,460 Ma and 2050 Ma respectively. Both are immensely large, world famous, and host stratiform chromitite deposits (*Irvine, 1974)*. The Great Dyke is hosted within a graben structure 500 km long and up to 12 km wide; in cross-section it is a deep tapering conduit. The Bushveld Igneous Complex is comprised of five lobes and covers an area approximately 12,000 km^2 (*Von Gruenewaldt et al., 1985*).

Stratiform chromitite deposits form from the fractional crystallization of a picritic melt in a magma chamber. The precipitated crystals sink to the chamber floor and accumulate (*Lago et al., 1982*). Chromite layers crystallized in-situ, in a stable continental setting, form planar, continuous layers. Although, post-formation tectonic deformation may fault, tilt and cause brittle deformation, disrupting the continuity of the layers, while syncrystallization deformation may cause chromite layers to pinch and swell as observed at Kemi in Finland and in the Bushveld Igneous Complex within both the UG1 and UG2 layers (*Stowe, 1994*).

Associated mineral phases that crystallise prior to and following the crystallisation of monomineralic, chromitite layers are, olivine, clinopyroxene, orthopyroxene and plagioclase. The abundance of these minerals and thickness of the units formed is dependent on numerous factors including; environmental conditions, magma chemistry, volume and longevity of the magma pulse.

3.2.1.1 *Chromite crystallisation models: Stratiform chromitite*

For chromitite layered complexes to form a mechanism is required whereby chromite is the only phase to crystallise from the magma. A number of genesis models have been proposed.

Irvine (1977) demonstrated that by mixing fresh primitive magma with a comparatively more fractionated magma could produce a hybrid magma with a bulk composition that lay in the chromite crystallisation field.

Furthering the chromitite formation model of Irvine (1977), Sharpe and Irvine (1983) conducted a series of melting experiments on two samples from the Bushveld and identified a new chemical mechanism for chromitite formation. The liquidi of the two melts, one saturated with plagioclase and chromite (A_1) and the other with olivine and chromite (U_1), when combined lowered the crystallisation temperatures of the silicates yet chromite crystallisation was sustained. Thus, by mixing the two liquids that would independently crystallise cumulates dominated by silicates with only accessory amounts of chromite, formed a hybrid melt saturated in chromite, so forming chromitite.

Detailed modelling of the A_1 and U_1 melt compositions by Irvine (1977b) categorised them as spinel-saturated melts in the CaO-MgO-Al_2O_3-Cr_2O_3-SiO_2 system. Results showed that melt U_1 was significantly enriched in Cr_2O_3 compared to melt A_1 and that as the olivine content of U_1 increased, so too did the Cr_2O_3 content. In contrast, melt A_1, a primitive melt, was saturated with Al-rich chromite, there being only a trace amount of Cr_2O_3 present in the melt.

However, work by Mondal and Mathez (2007) demonstrates that the Irvine, 1977 model would result in chromitite forming at or near to the base of a cyclic unit, and that this in situ crystallisation of a thick chromitite layer should deplete the mixed magma of Cr. Consequently, the chemical composition of the orthopyroxene below a chromitite layer should be Cr-rich relative to that of the orthopyroxene crystallising above a chromitite layer. On the contrary, Mondal and Mathez show that orthopyroxene present in the units above and below the UG2 chromitite are chemically identical in terms of Cr content; results that conflict with the model of Irvine (1977) for in situ crystallisation.

Research by Eales, 2000, hypothesised that the silicates (olivine, orthopyroxene and plagioclase) and chromite crystallised within a magma and were carried to and deposited at the present location. He proposed that the chromite and silicate phases were separated by mechanical, postulating that chromite was introduced as a chromite slurry. Supporting Eales's (2000) work, Maier and Barnes (2008) and Voordouw et al. (2009) have put forward similar hypotheses to explain the genesis of the Bushveld, Upper Group chromitites.

Naldrett et al. (2009) draw on the primitive and fractionated (same parent source) magma mixing model of Irvine (1977), but acknowledge that the chromite and silicate phases may not have crystallised in situ. Instead they develop the model, suggesting that there were two ascent paths for the magma; one rapid, where fractionation of the magma did not occur, the other, slower, that permitted the fractionation of the magma, as well as interaction with and contamination by crustal material during ascent, so altering the initial composition. The differences between the evolution of the magma batches resulting from the different routes taken to reach Bushveld magma chamber, are recorded in the compositions of the mineral phases that crystallise from each magma batch.

3.2.2 Ophiolitic chromite

Two types of chromitite occur in the mantle peridotites of ophiolite complexes; pods of chromitite hosted by harzburgite and less commonly lherzolite, and chromitite layers present in the dunites of the lower cumulate and transition zone.

Podiform chromitites are most commonly located in the upper mantle tectonites of harzburgite ophiolite types (HOT) (*Pearce et al., 1984; Roberts, 1988; Boudier and Nicolas, 1985*) examples are; the Loubusa ophiolite, Tibet (*Bai et al., 1993; Zhou et al., 1996*), the Thetford Mines Ophiolite, southern Québec, Canada (*Gauthier et al., 1990; Bèdard et al., 2007; Pagé et al., 2008*) and the Vourinos Complex, Greece (*Rassios & Roberts, 1986; Roberts, 1992*). Podiform chromitite is uncommon in lherzolite mantle; when present chromitites are typically small (*Leblanc & Timagoult, 1989; Gervilla & Leblance, 1990*), examples include; the Trinity Complex northern California (*Quick, 1981; Noller & Carter, 1986*), the Horoman complex, Hokkaido, Japan (*Niida, 1984; Takahashi, 1992*) and the Oen complex, Spain (*Gervilla & Leblanc, 1990*). An exception is the Isabela ophiolite, the Philippines, which is a lherzolite-dominant mantle section that contains several podiform chromitites (*Morishita et al., 2006*)

Deposits form as either; i) tabular, sheet-like layers present in the peridotite units at the base of the crustal cumulates situated beneath magma chambers at the transition zone (*Nicolas & Prinzhofer, 1983*) or ii) as sack-like or pencil shaped pods hosted in the tectonite peridotites of the upper mantle (e.g. *Thayer, 1964; Dickey, 1975: Stowe, 1994; Ballhaus, 1998*). The petrological Moho is present at the dunite-harzburgite contact at the base of the magma chamber. Podiform chromitites tend to be focused at the Moho, both above and below. Deposits vary considerably in size, dimensions range from 5 to 1,200 m in length and 1 to 130 m in thickness (*Stowe, 1994*).

Although with respect to deposit morphology and stratigraphic position these two sub-categories of podiform chromite differ, the key similarities are that both

occur in the ultramafic units of ophiolites and both exhibit orbicular and/or nodular chromitite ore textures, a texture that is unique to podiform chromite deposits (*e.g. Thayer, 1969; Dickey, 1975*).

The genesis of podiform chromite is a complicated and controversial subject, numerous models have been proposed (*McElduff & Stumpfl, 1991; Arai et al., 2004; Uysal et al., 2005; Page & Barnes, 2009*). However, some aspects of podiform chromite genesis are agreed. It is widely accepted that the environmental setting responsible for podiform chromitite genesis is associated with the formation of oceanic crust. The extensive early crystal fractionation of olivine and chromite, such as that observed in the supra-subduction zone ophiolites, reflects mineralogically the association of podiform chromitite deposits with such a tectonic setting (*Pearce, 1984; Roberts, 1988; Edwards et al., 2000*).

Within Europe podiform chromites are associated with ophiolites dated Cretaceous age (95-80 Ma). Example localities include the Cyprus (*Blome & Irwin, 1985*) and Oman (*Pearce et al., 1981*) ophiolites. In a global context podiform chromite deposits as old as 500 Ma are known to exist e.g. the Thetford podiform chromite deposit, Canada ca. 480 Ma (*Clague et al., 1981*).

3.2.2.1 *Ophiolite chromite: Crustal cumulates*

The lower ultramafic crustal cumulates in ophiolite complexes are comprised of dunite, wehrlite and pyroxenite that grade upwards into gabbro, with the gabbro component progressively increasing in abundance at higher stratigraphic levels. These cumulate layers crystallise out from the melt fraction (olivine composition Fo_{85-87}) (e.g. *Haggerty, 1991*). Chromitites occur within this ultramafic sequence of crustal cumulates as thin (centimetre scale) horizons. However, alternating cumulate-chromitite sequences can be extensive, as in the case of the Orhaneli massif, Turkey that is 2,500 m thick (*Stowe, 1994 and references there in – Tankut, 1980*). As observed by Thayer (*1964, 1969*) the morphology of these deposits and the mineralogy of the associated overlying lithologies, that are dominated by progressive plagioclase enrichment up sequence, are features analogous to the continental layered complexes

(stratiform chromite deposits). Podiform chromitite genesis is associated with subduction zones and for arc spreading above a convecting mantle. Consequently, cumulates forming below the Moho are constantly deformed, being folded and dislocated. Casey and Karson, (*1981*) suggest that intermittent upwelling magma pulses cause changes to the shapes and distribution of overlying magma chambers from which the cumulate layers crystallise. This process may also contribute to the formation of discontinuous, irregular chromitite layers.

3.2.2.2 *Ophiolite chromite: Mantle hosted podiform chromitite*

Mantle hosted podiform chromitites differ in a number of ways from crustal cumulate podiform chromitites (Section 3.2.2.1). Arguably the most prominent difference is that podiform chromitite deposits are hosted by mantle residuum (olivine compositions Fo_{90-94}) most commonly harzburgite. The harzburgite mantle residue is depleted (compared to the underlying fertile lherzolite mantle) and is the source from which basaltic melts are derived, these melts migrate upwards to the ridge axis in the overlying crust (*Moores and Vine, 1971; Greenbaum, 1972; Menzies and Allen 1974; Paktunc, 1990; Roberts and Neary, 1993*). Comparatively, lherzolite-type ophiolites, where partial melting is less extensive, host significantly smaller amounts of podiform chromitite, if any. In lherzolite-type ophiolites chromium and aluminium are preferentially sighted in chrome-diopside or chrome-garnet (*Noller and Carter, 1986*). Similarly, podiform chromites are non-existent or small scale when present within highly refractory harzburgite (*Arai, 1997*).

A distinctive feature of mantle hosted podiform chromitite is the presence of a dunite halo. Irrespective of the size, shape, orientation or stratigraphic emplacement level, podiform chromitites are almost always enclosed by dunite (*Thayer, 1960*). The halo may be present as a sharp contact between massive chromite (mineralisation) and the dunite (selvedge of the orebody) or as a gradational contact passing from harzburgite to dunite into minor disseminated chromite mineralisation that progressively becomes more intense and massive with distance into the mineralised zone (*Zhou, 1994; Zhou et al., 2001*). The

size of the dunite halo varies between deposits, from a few centimetres to several tens of metres (*Thayer, 1964; Paktunc & Baysal, 1981; Christiansen, 1982; Paktunc, 1990*). To date there is no identified link between the thickness of the dunite halo and the size of the orebody or the grade of the ore contained within it (*Thayer, 1964, 1969; Peters and Kramers, 1974; Brown, 1980; Leblanc, 1987; Roberts and Neary, 1993; Zhou et al., 1994; Zhou et al., 1996*), although it seems reasonable to consider that the two are likely to be genetically linked.

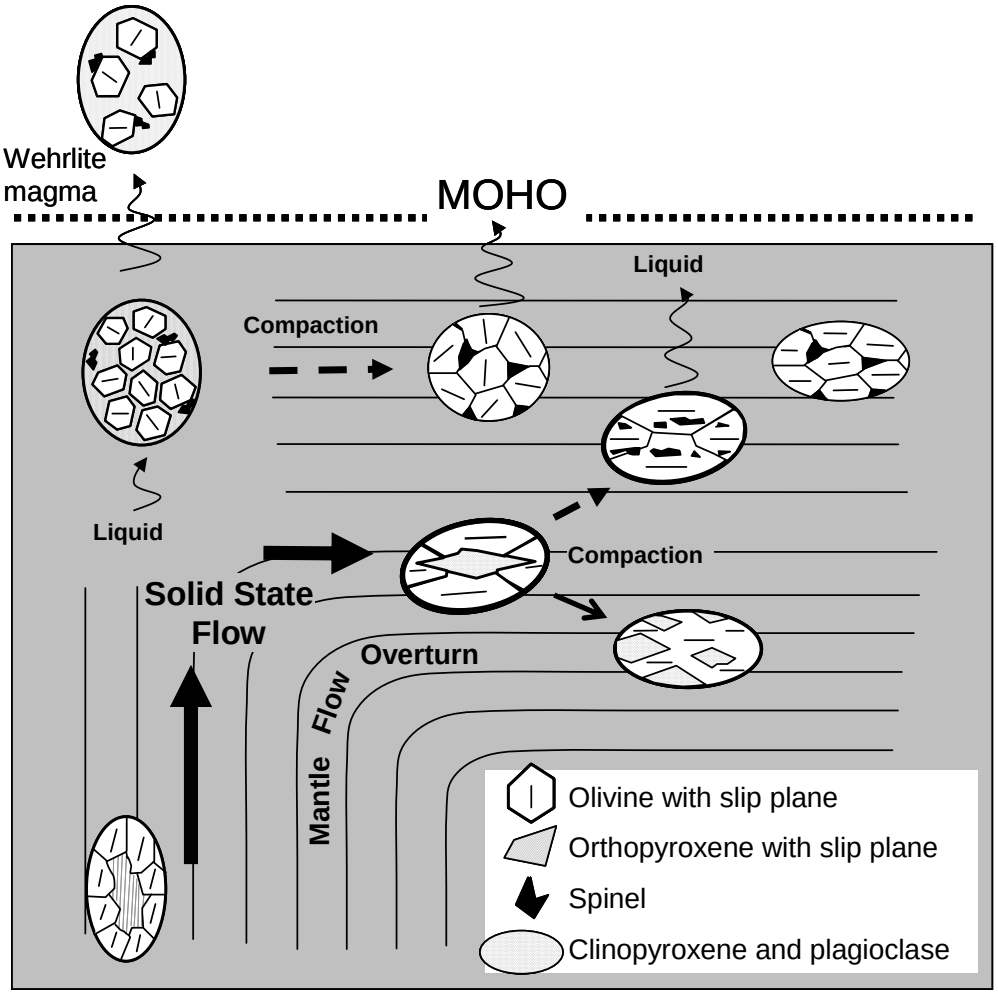

Figure 3.2.1: A sketch of textural evolution based on relationships of textures in mantle peridotite with mantle flow structures in the Maqsad Mantle Transition Zone (Adapted from Boudier & Nicolas, 1995)

When unaffected by emplacement-related deformation the mantle peridotite records, in structures produced by high temperature and low differential stress deformation, the history of solid-state mantle flow (Figure 3.2.1). Mapping of these structures provides insight into the asthenospheric flow geometry at the base of a ridge axis (*Ceuleneer et al., 1988; Nicolas et al., 1988*). Mapping of the Oman ophiolite by Leblanc and Ceuleneer (1991) has revealed areas, approximately 10 km in extension, where plastic flow lines are oriented perpendicular to the paleo-Moho. At the top of these palaeo-upwellings, the plastic flow structures rotate to the horizontal in a narrow transition zone a few hundred meters thick and diverge in all directions, primarily along the paleo-ridge axis. This flow pattern has been interpreted as the footprint of a small-scale mantle diapirism, possibly related to the segmentation of spreading centres (*Rabinowicz et al., 1987; Nicolas et al., 1988*).

The petrological Moho, which differentiates between the mantle (below) and the crust (above), is marked by cumulate dunite between the harzburgite (mantle) and cumulate gabbro (crustal) units. Preserved trapped melt is present in the dunite section in the form of melt pockets marking the pathway of melt to the surface of the upwelling asthenosphere. At the petrological Moho, characteristic flow lines in the country rock, which at depth were vertical, are rotated horizontal, along with any chromitite pods encapsulated in the section. The section is characteristically barren of melt extraction structures, although intrusive dikes are often prevalent. (*Leblanc & Ceuleneer, 1992*)

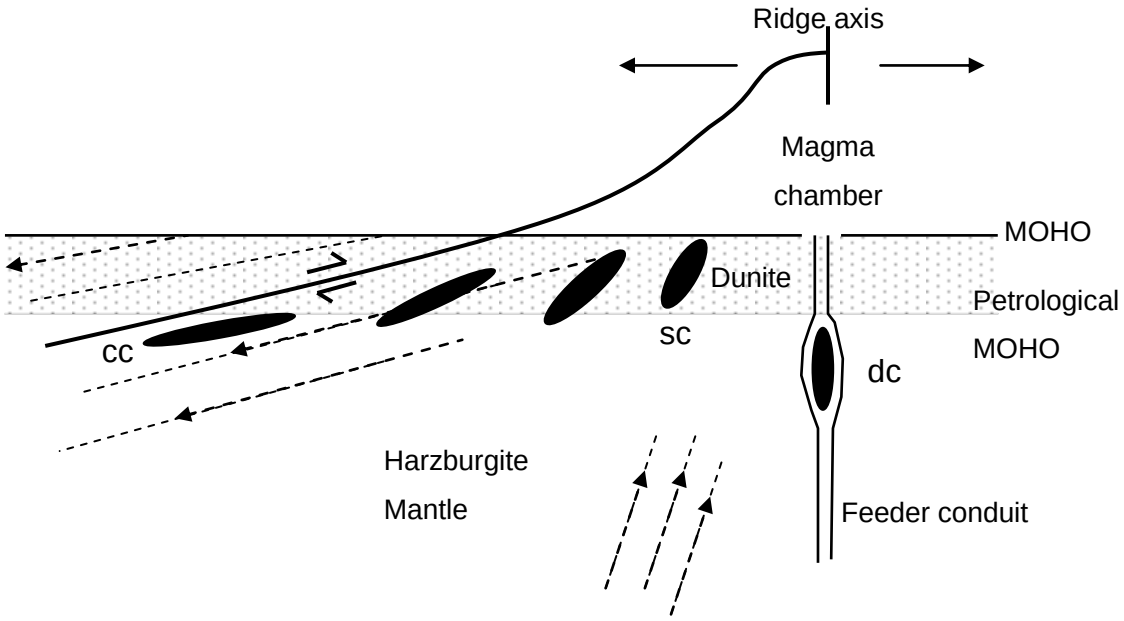

Figure 3.2.2: A sketch illustrating the positions of podiform chromitites (black) that are discordant (dc), subcordant (sc) and concordant (cc) in relation to mantle flow lines (black dashed arrows) in the upper mantle beneath a spreading ridge.

(*Adapted from Edwards et al., 2000 and references therein*)

The stratigraphic location and relative orientation of a chromitite pod is dependent on the post chromitite formation orientation changes that took place during mantle flow. The relationship between the orientation of the pod and the mantle flow lines preserved in the host peridotite make it possible to classify chromitite pods. Three categories are described, concordant, subcordant and discordant (C*assard et al., 1981*). As chromitites are deformed by asthenospheric flow processes their orientation changes progressively from discordant, to subcordant and finally concordant with the surrounding peridotite flow lineations (Figure 3.2.2).

Structures and fabrics identified within podiform chromitite are the result of solid-state flow and recrystallisation at relatively high temperatures (*Cassard et al., 1981*). Vertical flow structures record textures related to earlier mantle upwelling (discordant pods), and horizontal textures form subsequently during horizontal flow away from the ridge axis (concordant pods) (*Boudier & Nicolas, 1995*). Internal structuring within chromitite pods has been reported.

Observations include; i) banding differentiated between by varying compositions ratios of chromite and olivine minerals, ii) foliation identified by the alignment and flattening of minerals comprising the chromitites. and iii) lineation, determined either by the elongate direction of minerals within a foliation plane or the direction perpendicular to the plane of pull-apart structures (in massive ore) (*Cassard et al., 1981*).

Similarly, the chromite textures of podiform chromitites provide an indication of the extent of deformation. Chromite from discordant pods is often coarse and in some cases even pegmatitic (*Panayiotou et al., 1986; Georgiou, 1987*). It is interpreted to indicate magmatic crystallisation. However, the primary chromitite textures identified in discordant chromitite pods have often been affected by deformation, and are frequently distorted or overprinted. Although deformation of chromite ore is common, the nodular ore type is particularly effective at preserving a fabric. The orientation of chromite nodules, when compared with the host rock foliation, provides some indication of whether the chromitite is concordant, subcordant or discordant. Similarly with the orientated position of the ore body relative to the foliation of the host rock.

Lorand and Ceuleneer (1989) studied the presence of silicate inclusions in chromite from podiform chromitites. They observed that silicate inclusions are common in discordant podiform chromitite, however, are gradually lost diffusing out during strain-induced recrystallisation. Chromitite pods that are deformed and concordant with the host mantle are comprised of distorted chromite that has disrupted, lost or reformed grain boundaries and lack silicate inclusions, a result of the deformation process.

There is no characteristic morphology for a mantle hosted chromitite orebody, a result of the unstable environment in which these deposits form. However, orebodies are often described as lens-, tabular-, sack- or pipe-shaped (*Thayer, 1964*). Li et al., (1993) described that a typical chromitite orebody has a length of 20 to 250 m, width of 10 to 100 m, is between 0.5 and 5.0 m thick and has an average grade of 48 wt % Cr_2O_3. In more general terms, Thayer (1973) reported that an average sized podiform chromitite deposit would yield

approximately 1,000 tons of ore. However, there are exceptions; the Coto ore body in the Philipinnes consists of ~8,000,000 tons of ore, and the Tiebaghi in New Caledonia and Golalan in Turkey deposits each comprise in excess of 1,000,000 tons of ore (*Paktunc, 1990 and references there in*). The styles of mineralisation associated with these deposits also varies from small, centimetre sized patches of disseminated chromite grains, such as those observed in dunite channels cross cutting the harzburgite mantle unit at the Lizard in south west England, to enormous 1,800 m long massive chromite layers that reach up to 120 m in thickness, as exhibited by the economic deposits of the Main Ore Field within the Kempirsai massif, Kazakhstan (*Melcher et al., 1997*).

In the same way that the morphology of a podiform chromitite periphery is irregular, so too is the internal structure. Chromitite horizons occur interleaved with dunite. These horizons are rarely continuous, often folded or dislocated by syn-mineralisation or post-formation deformation events. Not only is the environment of formation, the mantle, unstable but the post-formation, exhumation, tectonic influences on the chromitites are also disruptive. At any time during the formation and emplacement process the chromitite pods might undergo distortion and lose their original form.

3.3 Podiform chromitite genesis models

The genesis of podiform chromitite is an controversial topic and one that is yet to be resolved; several genesis model exist.

In the early 1960's the works of Thayer started to address the development of a genesis model to explain the formation of podiform chromitite, Thayer (*1964, 1969, 1970*) suggested that mantle hosted chromite accumulations formed by differentiation of chromite from magma present in the lower crust and upper mantle, and that these chromite accumulations were subsequently emplaced within the underlying peridotite crystal mush (*Dickey, 1975)*.

The acceptance that ophiolites were segments of oceanic lithosphere (*deRoever, 1957; Vuagnat, 1963; Hess, 1965; Moores, 1969*) combined with the observation that podiform chromitites occur in the mantle tectonites units of ophiolites, led to the development of new formation models that associated their genesis with that of oceanic crust.

By the early 1970's it was agreed that the mantle section of ophiolites was residuum, formed from the extraction of basaltic melts (*Moores & Vine, 1971; Greenbaum, 1972; Menzies & Allen, 1974; Roberts & Neary, 1993*). The impossibility that mantle hosted chromitite deposits were also residuum, teamed with the numerous cumulate characteristics exhibited by the deposits, meant that a suitable genesis model had to explain how non-residual chromitite bodies occur in residual mantle units.

Attempts to create a model led to podiform chromitites being considered autoliths, formed from the accumulation of chromite crystallised in magma pockets at the base of the crustal cumulates (*Dickey, 1975; Greenbaum, 1977*). Dickey (1975) proposed that the chromite concentrations sank into the underlying residual peridotite due to the greater density of chromitite relative to the surrounding cumulate peridotite. Taking a similar approach Greenbaum (1977) proposed that the chromitite segregations were emplaced into the underlying mantle peridotite by tight in-folding. Both models were dispelled because of a lack of structural evidence (*Cassard et al., 1981*). Additionally, the models failed to explain the variation in Cr/Fe ratio seen in chromite with depth in many ophiolites (*Brown, 1980; LeBlanc, 1987*) or the presence of the dunite halo that characteristically surrounds chromitite pods.

Ideas progressed and it became accepted that the co-existence of olivine and chromite in the mantle represented early stage fractionates of picritic melts (*Menzies & Allen, 1974*) that ascended through the upper mantle, into the crust, at the site of palaeo-spreading centres (*Coleman, 1977*; *Neary & Brown, 1979; Brown, 1980; Lago et al., 1982; Roberts & Neary, 1993*). Throughout the late 1980's and 1990's the physico-chemical environmental controls that affect melts migrating through the mantle were studied to understand their influence

on the precipitation and composition of chromite (e.g. *Talkington et al., 1983; Murck & Campbell, 1986; Leblanc & Ceuleneer, 1991; Roeder & Reynolds, 1991; Zhou et al., 1996, 1997*). In addition, fluids and volatiles are thought to have played an important role in the crystallisation of chromite in the mantle (*Johan et al., 1983; McElduff & Stumpfl, 1991; Edwards et al., 2000; Matveev & Ballhaus, 2002*)

The cumulate textures and chromitite layers observed in ophiolitic chromitite deposits are indicative of crystallisation having played a significant role in the formation of podiform chromitite ore; especially for deposits located in the lower-crustal ultramafic cumulate sequence of ophiolites. Other characteristic features include; irregular form, random distribution within the mantle and geochemical composition variations between neighbouring deposits (*Auge & Roberts, 1982*)

3.3.1.1 *The chromitite-dyke hypothesis*

The chromitite-dyke model interprets podiform chromitites to be the product of early stage chromite crystallisation from a basaltic magma migrating through focused conduits in the mantle.*(Brown, 1980; Auge and Roberts, 1982; Lago et al., 1982; Cassard et al., 1983*; Leblanc, 1987; Leblanc & Ceuleneer, 1992). Brown (1980) suggested that chromite formed by fractional crystallisation of rising magma in periodically replenished, small chambers, situated beneath the main cumulate magma chamber, within the mantle harzburgite.

Lago et al., (1982) modelled the precipitation and accumulation of chromite within conduits for basaltic melt passing through mantle diapirs beneath a spreading ridge centre. The results showed that the melt and peridotite interaction produce dunite, and that active convection in cavities formed by local widening of magma conduits promotes crystallization, growth and accumulation of chromitite. The cumulates are deposited at the base of the mantle hosted chambers, blocking the conduit. According to this hypothesis the chromitite-bearing conduit initially cuts the structure of the surrounding peridotite. Subsequent intense deformation transforms the mass into a lens

which is rotated into concordance with the surrounding peridotite, such that the lens walls are aligned parallel to the foliation of the enclosing peridotite (*Nicolas, 1989*). A similar model was proposed by LeBlanc (*1987*) to explain the deposits in New Caledonia, who suggested that the dunite halo and the inter-layered dunite within the chromitite pods resulted from partial melting of the surrounding host peridotites by the high temperature magma.

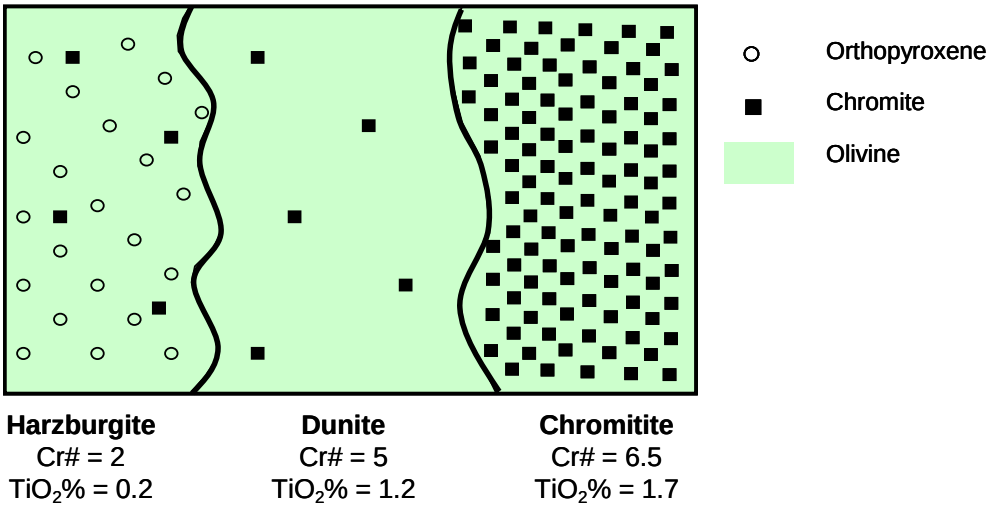

Figure 3.3.1: Harzburgite, dunite and chromitite labelled with example Cr# and TiO2 wt% values

Geochemically, the chromitite-dyke hypothesis is supported by the disparity between the Ti contents of chromite in the chromitite pod, the dunite envelope and the surrounding mantle harzburgite. Ti values for chromite in the pod and dunite halo are higher than those of chromite found in the host harzburgite, where it is considerably lower (Figure 3.3.1) (*Arai & Yurimoto, 1994*). This trend is observed even when the Cr# values for chromite in the chromitite pod, dunite halo and harzburgite are almost the same (*Arai and Yurimoto, 1994*). This implies that the Ti values of the podiform chromite reflect the composition of the inflowing melt chemistry.

Although this model goes some way towards providing an explanation of podiform chromitite genesis, it fails to address the problem that fractionating basaltic melts do not contain sufficient Cr to enable large volumes of chromite

to form prior to the onset of silicate-dominated crystallization (*Murck and Campbell, 1986; Roeder and Reynolds, 1991; Campbell and Murck, 1993*). For extensive horizons of chromitite to form chromite must crystallise without silicate phases, such a situation requires a mechanism to drive the melt composition into the liquidus field of chromite. This could be is controlled by advantageous chemistries between the melt and host wall-rock or by suitable and sustained environmental conditions. Furthermore, a podiform chromitite genesis model needs to explain the existence of the clino- and orthopyroxene depleted, dunite halo present around the podiform chromite pods.

3.3.1.2 *Mixing multistage-melts*

Mixing refractory (boninitic affinity) and fertile (mid-ocean ridge basalt affinity) melts produced by multistage melting and melt segregation in the mantle (*Paktunc, 1990; Ballhaus, 1998*) has been proposed as a model to explain chromite crystallisation in the mantle. However, field relationships in ophiolites have demonstrated that multistage melts would coexist and mix in a conduit, and that early MORB melts would leave a crystalline product rather than a melt in the conduit (*Edwards, 1991, 1995*).

Ballhaus *(*1998) has proposed a magma mixing model based on experiments combining a picritic melt (forsteritic, ol-norm, high-P, low-viscosity) with a boninitic melt (siliceous, low-P more viscous). Viscosity would inhibit instant mixing of the melts such that cumulus chromite would nucleate and grow only in the mafic melt where the chromite/melt interfacial energy was lowest. The siliceous melt would act as a diffusive chromium reservoir. It is proposed that the richest chromite ores form when the volume ratio of the melt nucleating chromite is small relative to the ambient melt. The experiments simulated, on a micro-scale, two characteristic features of podiform chromite deposits: the nodular texture, and the dunite envelope of chromite pods.

Some workers (e.g. *Auge 1987; Leblanc & Ceuleneer, 1992*) have considered the volume of magma required in order for accumulations of chromite, like those that comprise podiform chromitites, to form. In terms of magma chemistry

chromium is a minor component. In primitive MORB-type basalt the Cr content is typically 200-700 ppm (*Roeder & Reynolds, 1991; Leblanc & Ceuleneer, 1992; Roeder et al., 2006*), while naturally more chromium-rich boninitie magma has a Cr content between 1,000-1,500 ppm (*e.g. Kuroda et al., 1978; Jenner, 1981; Walker & Cameron, 1983*). Assuming the complete removal of Cr from a magma to form chromite, Leblanc and Ceuleneer (1992) calculated that to form a 3,000 t chromitite deposit (the equivalent of 900 t of chromium) would require a magma volume at least 300 to 400 times greater than the 3,000 t volumetric area of the final chromitite body (*Leblanc & Ceuleneer, 1992*). A similar calculation was considered by Auge (1987) using the average Cr crystal/liquid partition co-efficient derived from the works of Maurel and Maurel (1982b). He proposed that the volume of magma required to form chromitite would be at least 500 times greater that the volume of the ore formed. It is evident that substantial magma volumes (melt flow) are necessary to supply the Cr required for podiform chromite deposits to form.

The source of Cr-rich melt is important to consider. Such melts either form from second stage melt events, are boninitic or are derived from supra-subduction zone magmas. All are associated with a more extensively depleted mantle source (*Roberts, 1988, 1992*).

The hypothesis that multi-stage melts mix to form podiform chromitite would be a conceivable scenario if ongoing magmatism exploits a single conduit that remains open and is filled by melt at different stages during its chemical evolution (*Leblanc and Ceuleneer, 1992*).

3.3.1.3 *The melt-rock reaction models*

A more recent model hypothesis, the melt-rock reaction model, proposes that chromite crystallisation results from reaction between a migrating primitive melt and the mantle peridotite through which it percolates (*Kelemen, 1990; Arai & Yurimoto, 1994; Zhou et al., 1994, 1996; Edwards, 1995; Varfalvy et al., 1996,1997; Arai, 1997*). The concept of melt-rock interaction has been reported in several mantle sections (*Fisk, 1986; Kelemen, 1990; Kelemen et al., 1992*),

however the interaction does not always result in the crystallisation of chromite, let alone the formation of podiform chromitite (*Zhou & Robinson, 1997*). Furthermore, the reaction rationales that promote chromite precipitation vary between authors.

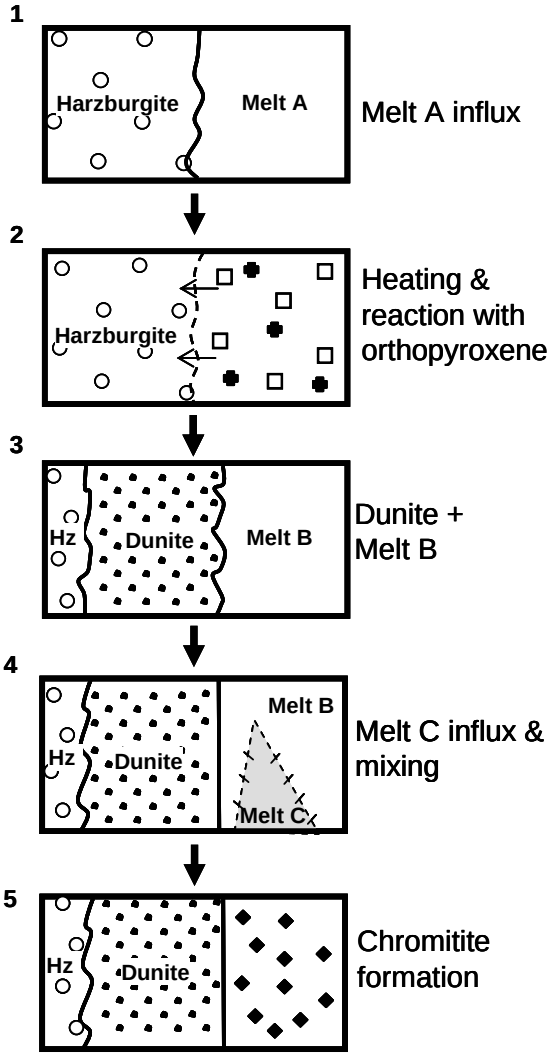

Figure 3.3.2: The melt mixing model from Arai and Yurimoto, 1994. Stage 1 Melt A reacts with the orthopyroxene (open circles) in harzburgite producing (stages 2 and 3) olivine and chromite and Melt B. The introduction of a new melt supply (melt C) mixes with melt B to precipitate chromite (stages 4 and 5)

Arai & Yurimoto, (*1994*) proposed that an exotic melt, formed at depth under higher pressure, is injected into mantle harzburgite and reacts with the wall-rock dissolving orthopyroxene to form dunite and a secondary Si-rich melt that is enriched in Cr (Figure 3.3.2). The Si-rich melt mixes with subsequent pulses of, relatively primitive melt and precipitates chromite. The authors also identified that large, Cr-rich podiform chromitites are typically found hosted in moderately refractory ($Cr\#_{\text{residual spinel}}$ ~0.5), clinopyroxene-bearing harzburgite,

whereas in lherzolite-dominant or refractory harzburgite mantle sections chromitites are small in size and limited in number, or altogether absent.

Arai (1997) further developed the concept that the composition of the host peridotite is a dominant control on podiform chromitite genesis. He proposed that the composition of the mantle peridotite wall-rock that controls the size and composition of the chromitites and identified the source of Cr to be from orthopyroxene in the mantle rocks.

A slightly different explanation of the melt-rock reaction model is given by Zhou et al., (1994). They attribute the composition modification of the ascending basaltic partial melts to result directly from reaction with the host peridotites. As with the model of Arai & Yurimoto (1994), this model relies on the incongruent dissolution of pyroxene from the host peridotite. The melt is altered becoming relatively enriched in SiO_2 driving the melt composition into the chromite stability field.

In both of the melt-rock reaction models melt dissolves pyroxene from harzburgite. A by-product of the dissolution of pyroxene is residual olivine. Field evidence in the form of a dunite selvedge encasing podiform chromitites and the dunite layers that coexist with chromitite layers in the mineralised zones, is the most conclusive evidence for this process (*Arai, 1994a*).

Irrespective of the subtleties between the melt-rock interaction systematics, there is agreement that pods of Al-rich chromite form where tholeiitic (Al-rich) melt reacts with lherzolite or harzburgite and Cr-rich chromitite pods form by reaction between harzburgite and boninitic (a Cr-rich melt) (*Zhou et al., 1994*; *LeBlanc, 1995; Rollinson, 2005*). In addition, aside from the compositions of the interacting melt and mantle the main control affecting the size and abundance of podiform chromitite is the extent of melt-rock interaction (*Zhou & Robinson, 1997*).

3.3.1.4 *Water and chromite formation*

All of the previous studies have incurred the problem of precipitating large volumes of chromite from basaltic melts where Cr has a very low solubility.

It is widely accepted that water is necessary for partial melting of supra-subduction zone mantle to produce melts capable of forming podiform chromitites with unfractionated Cr/Al ratios (e.g., *Pearce et al., 1984; Roberts, 1988; Zhou and Robinson, 1997; Robinson et al., 1997*). Water promotes the partial melting of refractory peridotites and will dissolve in the melt and remain present until after the crystallisation of podiform chromitite and pyroxenite. A hydrous melt has more octahedral sites as the presence of water lowers the degree of polymerisation of the silica network of the melt (*Edwards et al., 2000*). This promotes the solubility of Cr within hydrous melts owing to the high preference energy of Cr^{3+}, the major ion controlling Cr solubility *(Murck and Campbell, 1986; Roeder and Reynolds, 1991*). Cr is present in the melt until the melt and peridotite react, this raises the Si content of the melt inducing polymerisation of the melt. The result is a reduction in the number of octahedral sites available for Cr incorporation into the melt, thus Cr becomes an insoluble component of the evolved melt and is crystallised as chromite from the melt. To maximise the production of chromite, an open system is required to facilitate a continuous supply of Cr-rich melt during the melting stage. In the same way the presence of water favours chromium solubility in the melt, a sudden loss of water from the melt, which will lead to a drop in pressure (*Kushiro, 1969; Dickey, 1975*), promotes the crystallisation of chromite. In this event, chromium in the melt will partition into the solid phase chromite.

As outlined, several models have been proposed for the origin of podiform deposits hosted by the mantle tectonic section of ophiolites, however, none provide satisfactory accounts for all the observed features of chromite deposits, these being; the cumulate and deformation textures, the concordant to discordant disposition of the pods, the dunite envelope around the pods, and the variation of chromite composition with depth or host lithology.

It appears favourable that for chromitites to form, melt pathways must be available for melt to pass through the mantle. These melt channel ways provide a focal point for crystallised chromite to precipitate. The continual replenishment of chromium saturated melt passing through the pathways is essential for continuous chromite formation and deposition.

3.4 Chromite geochemistry

Podiform chromitite compositions range from Cr-rich to Al-rich. Chromite is a useful petrogenetic indicator, in terms of grain morphology and composition, the chemistry records the conditions at the time of crystallisation, these include; the geodynamic setting, melt composition (*e.g. Irvine, 1965, 1967; Evans & Frost, 1975; Fisk & Bence, 1980; Maurel & Maurel, 1982a, 1982b; Sack, 1982; Dick & Bullen, 1984; Allan et al., 1988; Allan, 1992, 1994; Arai, 1992, 1994b*), the peridotite source (*e.g. Dick & Bullen, 1984; Arai, 1987, 1994; Clynne & Borg, 1997*), the extent of melt and peridotite interaction (Kelemen et al., 1990; *Zhou et al., 1994; LeBlanc, 1995, 1997; Zhou and Robinson, 1997; Robinson et al., 1997*), as well as, the crystallisation conditions; temperature and cooling rate (*e.g. Fisk & Bence, 1980; Ozawa, 1984; Sack & Ghiorso, 1991; Scowen et al., 1991*), pressure (*e.g. Sigurdsson & Schilling, 1976; Jacques & Green, 1980; Ballhaus et al., 1991; Roeder & Reynolds, 1991*) and oxygen fugacity (fO_2) (*e.g. Hill & Roeder, 1974; Murck & Campbell, 1986; Ballhaus et al., 1991; Roeder & Reynolds, 1991*). The Cr# value (Cr# = [Cr/(Cr+Al+Fe^{3+})]) of chromite is frequently used to constrain the conditions and determine the mantle peridotite source and the degree of partial melting (*e.g. Jaques & Green, 1980; Duncan & Green, 1987; Bonatti & Michael, 1989*).

High-Cr chromitites are generally found in highly depleted mantle harzburgite (Arai, 1994). Their genesis is thought to be associated with high-Si, high-Mg magmas, boninites, the product of high degrees of partial melting (*Crawford et al., 1989*). In contrast, Al-rich chromitites are present in more fertile mantle peridotite, typically at higher levels within the ophiolite stratigraphic sequence (*Neary & Brown, 1979; Roberts & Neary, 1993; Stowe, 1994*) and are

considered to be produced from lower degrees of partial melting (*e.g. Dick and Bullen, 1984; Arai, 1992; Roberts & Neary, 1993; Zhou et al., 1994*).

3.4.1 Conditions that impact the composition of chromite crystallised from a melt

Research has been conducted, experimental petrology in the laboratory and natural geological analogues, to investigate the impact of melt composition, temperature, pressure and fO_2, on chromite composition. Studies have looked at; natural MORB lava samples (*Allan et al., 1988*) and komatiites (*Barnes, 1998*), chromium solubility and chromite crystallisation from basaltic melts (*Roeder & Reynolds, 1991*), as well as the effects of temperature, fO_2, and melt composition, on chromite equilibration with liquid and silicate phases in basic and ultrabasic melts (*Murck & Campbell, 1986; Klingenberg Kushiro, 1996*).

Typically these experimental studies have intended to further the understanding of crustal hosted chromite samples. The conditions simulated during these experiments are not analogous to the mantle conditions where podiform chromitite forms. However, the theoretical behaviour of a melt to condition changes and the impact of these changes on the melt chemistry and crystallisation of chromite, are none-the-less important to understand when studying the formation of podiform chromitite.

Chromite crystallises early from a basaltic melt. The principal variable controlling chromite composition, at liquidus temperatures, is the change in melt composition (*Allan et al., 1988)*. The contemporaneous crystallisation of other mineral phases, e.g. olivine, plagioclase, clino- and orthopyroxene alter the melt chemistry and change the composition of the chromite formed (*Allan et al., 1988, Roeder & Reynolds, 1991*); a result of the competition for trivalent and divalent cations between co-existing chromite, silicate and melt, as well as the efforts of the system to reach equilibrium.

Plagioclase

Crystallisation or melting of plagioclase changes the composition of the melt and co-existing chromite (*Irvine, 1977; Fisk & Bence, 1980; Roeder & Reynolds, 1991*). Plagioclase crystallisation consumes Al_2O_3 from the melt, while resorption of plagioclase into the melt increases the Al_2O_3 content. These processes effect the Cr/Al ratio of the melt and consequently the Cr# of coexisting chromite. Plagioclase crystallisation increases the Cr# of co-existing chromite, while resorption has the inverse effect (*Henderson, 1975; Henderson & Wood, 1981; Roeder & Reynolds, 1991; Roeder et al., 2000; Kamenetsky et al., 2001; Naldrett et al., 2009*) .

Olivine

Crystallisation of olivine from a melt increases the Fe^{2+}# content of the melt, consequently the Fe^{2+}# of contemporaneously crystallised chromite will also increase (*Roeder & Reynolds, 1991*). The Cr# of chromite is not significantly affected by olivine crystallisation because the trivalent cation content of the melt is unaffected, there being no trivalent cations in the olivine crystallographic structure. Thus, the composition of chromite is controlled only by the equilibrium between the chromite crystallised and the melt it crystallises from.

Clinopyroxene

The crystallisation of clinopyroxene removes Mg, Fe, Cr and Al from the melt. The Cr/Al ratio of clinopyroxene is higher than that of the parent melt (*Roeder & Reynolds, 1991*). Consequently, co-crystallising chromite will have a lower Cr# value. Early reports suggested that chromite crystallises over a small temperature range (*Hill & Roeder, 1974; Fisk & Bence, 1980*) and stops crystallising after clinopyroxene and plagioclase start to form (*Bowen, 1928; Irvine, 1965, 1967; Roeder & Hill, 1974; Dick & Bullen, 1984*). However, these hypotheses have since been dismissed. Kamenetsky et al. (2001) identified chromite inclusions in olivine, orthopyroxene, clinopyroxene and plagioclase and studied those present in olivine, where the Fo (Fo=[Mg/(Mg+Fe^{2+})]) values extended a wide range ($Fo_{75.0\text{-}94.4}$). Their findings support a hypothesis for continuous chromite crystallisation together with cotectic silicate phases, olivine, pyroxene and plagioclase, over a wide range of temperatures

(1,200°C–1,700°C). It is possible for the crystallisation temperature range to exceed 200-250°C (*Kamenetsky et al., 2001*).

Cooling rate

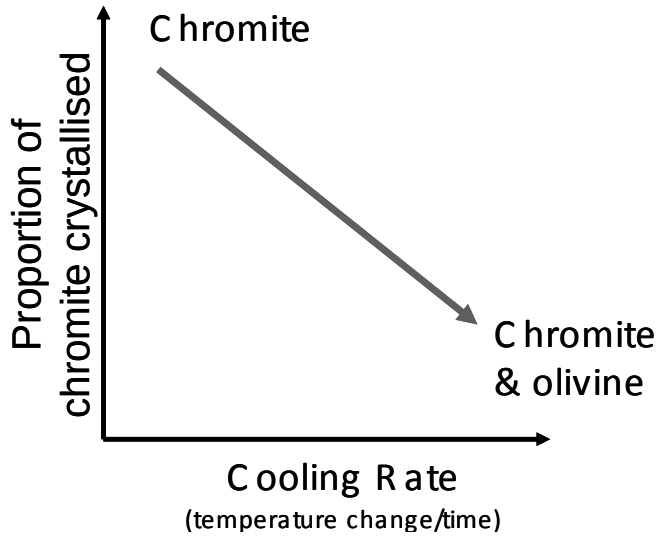

Figure 3.4.1: An idealised sketch to illustrate the effect of cooling rate on the crystallisation of chromite created using information from Campbell & Murck, 1986.

Campbell & Murck (*1986*) demonstrated that rapid cooling of a melt promotes chromite formation, crystallising a mixed chromite-olivine mineral assemblage. In contrast, lower cooling rates result in the crystallisation of chromite alone, forming chromitite horizons (Figure 3.4.1).

Pressure

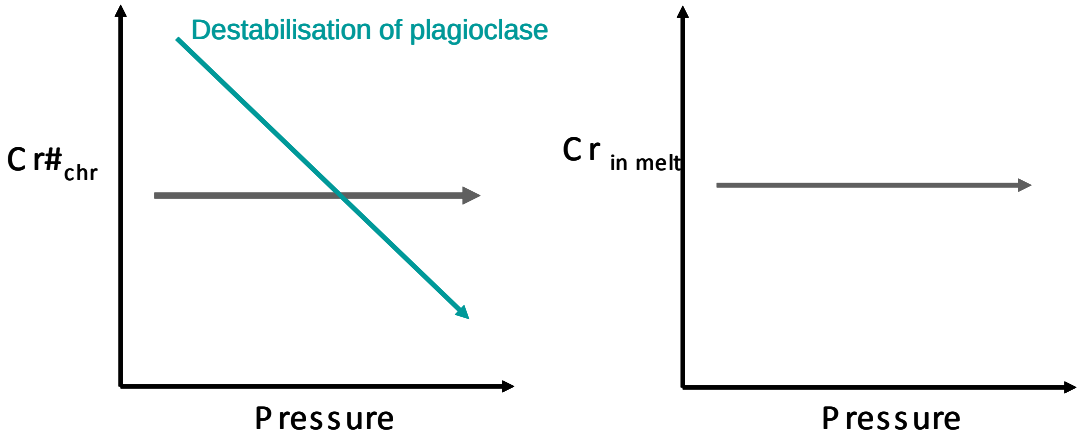

Figure 3.4.2: Idealised sketch of the relationship between pressure and chromium content of chromite (left) and chromium content of a melt (right) based on information from the literature (*Fujii & Scarfe, 1985; Falloon &Green, 1987; Roeder & Reynolds, 1991)*

Experimental studies of melt-chromite equilibrium dynamics by Roeder & Reynolds (1991) showed that increasing pressure raised the liquidus temperature favouring the crystallisation of chromite, although it did little to alter the solubility of chromium in the melt or change the composition of the chromite formed (Figure 3.4.2). The chromite-olivine-melt system was studied by Jaques & Green (1980) and demonstrated a pressure dependence for the residual $Fo_{olivine}$ - $Cr\#_{chromite}$ trend. Their results showed that the Cr# of chromites equilibrated with lower pressure melt were higher than those of chromites that had equilibrated with higher pressure melt for a given Fo value.

Fujii and Scarfe (1985) and Falloon and Green (1987) investigated the effect of peridotite melting under controlled pressure conditions and produced Al-rich chromites. The Al_2O_3 composition of a melt has a greater affect on the chromite composition than the influence of pressure (*Roeder & Reynolds, 1991*). However, that is not to say that pressure does impact the composition of chromite. When chromite, plagioclase and melt phases co-exist, an increase in pressure may cause the destabilisation of plagioclase, and consequently

increase the Al_2O_3 content of the melt. The co-existing chromite will equilibrate with the altered melt composition, increasing the Al_2O_3 content of the chromite, so lowering the Cr# value (*Allan et al., 1988; Naldrett et al., 2009*).

Oxygen fugacity

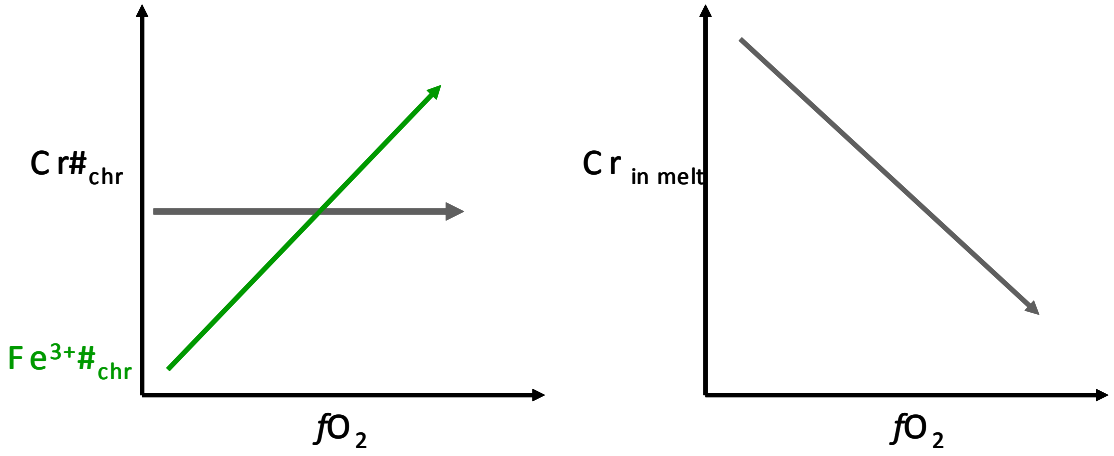

Figure 3.4.3: Idealised sketch of the relationship between fO_2 and chromium content of chromite (left) and chromium content of a melt (right) based on information from the literature (*Ulmer, 1969; Cameron & De-Borough, 1969; Maurel & Maurel, 1982a,b; Murck & Campbell, 1986; Roeder & Reynolds, 1991*)

The fO_2 is a function of the oxygen availability during chromite crystallisation. The chromite composition, specifically Fe^{3+}# and the Fe^{3+}/Fe_{total} ratio, give an indication, as the Fe^{3+} content of chromite is controlled by the oxidation of Fe^{2+} to Fe^{3+}. Chromium solubility increases under reducing conditions (lower fO_2) (at constant temperature) (Figure 3.4.3) as Cr^{2+} is more readily accommodated in the melt (*Murck & Campbell, 1986; Schreiber, 1976; Roeder & Reynolds, 1991*). When the conditions rapidly become more oxidising, reduced chromium (Cr^{2+}) oxidises to Cr^{3+} causing the melt to be super-saturated in Cr^{3+}. This promotes the instantaneous precipitation of chromite out of the melt, yet the Cr# does not appear to be sensitive to fO_2 variations (*Ulmer, 1969; Cameron & De-Borough, 1969; Maurel & Maurel, 1982a,b; Murck & Campbell, 1986; Roeder & Reynolds, 1991*). Although theoretically justified, there is difficulty applying the instantaneous precipitation of chromite hypothesis to a geological

context, as no geologic mechanism has been identified that produces a sudden increase in fO_2 at constant or near constant temperature (*Ulmer, 1969*).

Melt composition

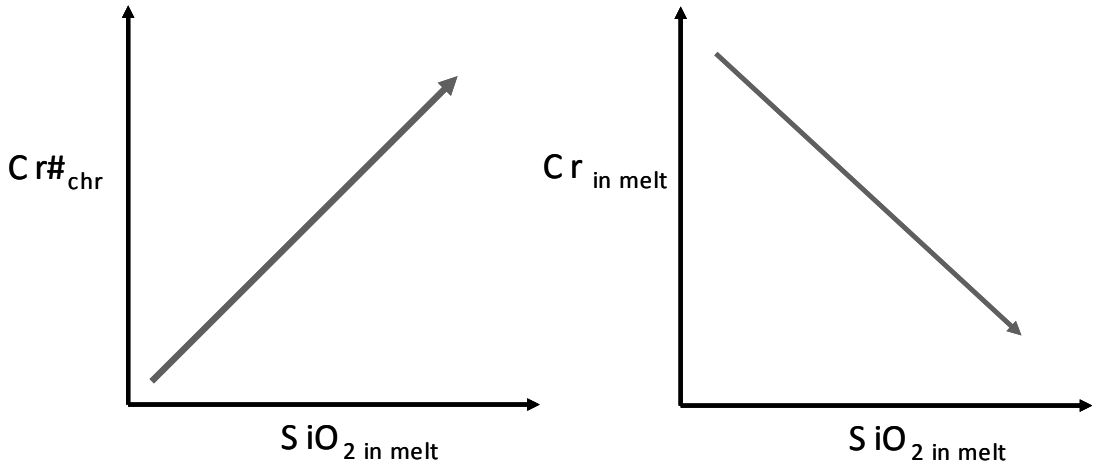

Figure3.4.4: Idealised sketch of the relationship between the SiO_2 melt content and chromium content of chromite (left) and chromium content of a melt (right) based on information from the literature (*Jaques & Green, 1980; Takahashi & Kushiro, 1983; Dick & Bullen, 1984; Murck & Campbell, 1986; Peck & Keays, 1990; Melcher et al., 1997; Edwards et al., 2000*)

The melt chemistry, in particular the solubility of Cr^{3+}, is controlled principally by the availability of octahedral sites. These are determined by the temperature and SiO_2 content of a melt. Chromium (Cr^{3+}) partitions into chromite when a melt is more SiO_2 -rich. The elevated SiO_2 content increases the polymerisation of the melt reducing the number of octahedral sites causing Cr^{3+} to become insoluble (Figure, 3.4.4), crystallising chromite (*Dick & Bullen, 1984; Murck & Campbell, 1986; Peck & Keays, 1990; Melcher et al., 1997; Edwards et al., 2000*). The SiO_2 content of a melt is sensitive to changes in pressure. Adiabatic decompression of upwelling mantle peridotite increases the SiO_2 content of mantle melts (e.g. *Jaques & Green, 1980; Takahashi & Kushiro, 1983*). Similarly, an increase in water vapour pressure (PH_2O) will favour an increase in the SiO_2 content of a melt (*Kushiro, 1969*).

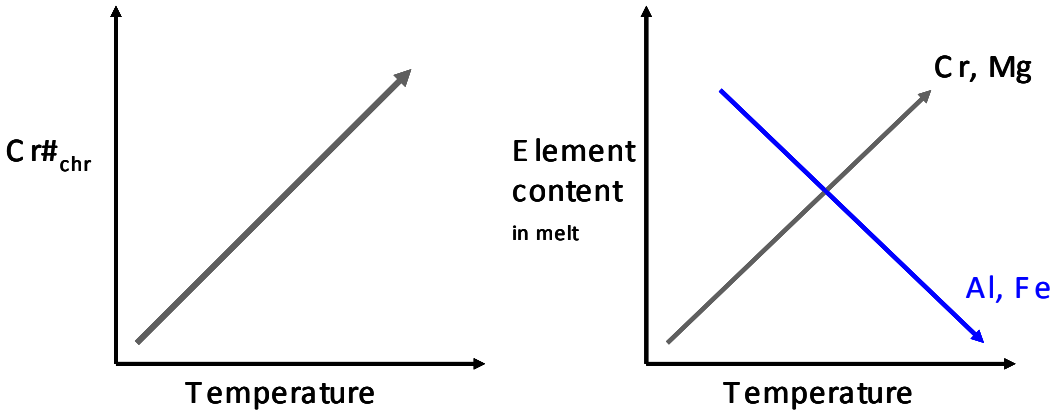

Figure 3.4.5: Idealised sketch of the relationship between temperature and chromium content of chromite (left) and chromium content of a melt (right) based on information from the literature (*Fisk & Bence, 1980; Ozawa, 1984; Murck and Campbell, 1986; Sack & Ghiorso, 1991; Scowen et al., 1991*)

An increase in temperature will increase the Cr^{3+} content of a melt, Figure 3.4.5 (*e.g. Fisk & Bence, 1980; Ozawa, 1984; Murck and Campbell, 1986; Sack & Ghiorso, 1991; Scowen et al., 1991)*. Two reasons have been suggested to explain this, i) an increase in temperature creates more octahedrally co-ordinated sites in the melt, or ii) at higher temperatures the structure of the melt is less rigid, such that a site may alter more readily to facilitate the substitution of elements that would not normally be accommodated (*Murck and Campbell, 1986*). Given that Cr^{3+} is more soluble in higher temperature melts, chromite precipitated and in equilibrium with melt at higher temperatures will have higher Cr# values (*Fisk, 1986; Murck & Campbell, 1986; Roeder & Reynolds, 1991*). In addition to Cr^{3+} the Mg^{2+} content of a melt also increases as temperature rises, while the Fe^{2+}, Fe^{3+}, and Al^{3+} contents decrease, in terms of relative abundance (*Murck & Campbell, 1986*).

It is important to note that the composition of chromite is considered to be proportionally representative of the composition of the melt phase at the time of chromite crystallisation. However, the composition does not necessarily correspond with the whole rock chemistry as coexisting minerals, e.g. olivine,

orthopyroxene and clinopyroxene, may distort the record of the chromite-melt equilibrium effective at the time of chromite crystallisation (*Maurel & Maurel, 1982*; *Roeder & Reynolds, 1991*).

3.5 Geochemical variation and trends in chromite

At a given pressure and temperature the modal proportions and respective composition of chromite and silicate phases, as well as the composition of trapped interstitial fluid or melt, all effect equilibration. The higher the modal percentage of a mineral the more it is buffered against subsolidus re-equilibration. The composition of chromitite (where chromite is the principal mineral phase comprising the rock) is analogous to the composition of the primary liquidus chromites (e.g. *Sack & Ghiorso, 1991; Poustovetov, 2000 and Barnes & Roeder, 2001*). The geochemistry of chromite and co-existing interstitial silicate phases, as well as the sequential order of crystallisation of these phases, provides a geochemical fingerprint by which to determine the parental melt composition. Experimental studies by Maurel & Maurel, (*1982*) and Roeder & Reynolds, (*1991*) have shown that chromite chemistry is fundamentally dictated by the composition of the parent melt from which it crystallises (*e.g. Crawford, 1980; Dick & Bullen, 1984; Allan et al., 1988; Arai, 1992; Della-Pasqua et al., 1995; Kamenetsky, 1996, 2001; Rollinson, 2008; Page & Barnes, 2009*).

Barnes and Roeder (*2001*) document the following geochemical trends; Cr-Al trend, the Fe-Ti trend and the Rhum trend, where the Al content of chromite increases primarily at the expense of Cr, and to a lesser extent Fe^{3+}. These can be identified when examining chromite data using the bivariate plots; Cr# - Mg# and Fe^{3+}# - TiO_2. These plots are used to examine the Voskhod sample datasets; F1925, F1964-65 and F1996-97 presented in Chapter 8.

3.5.1 The Fe-Ti Trend

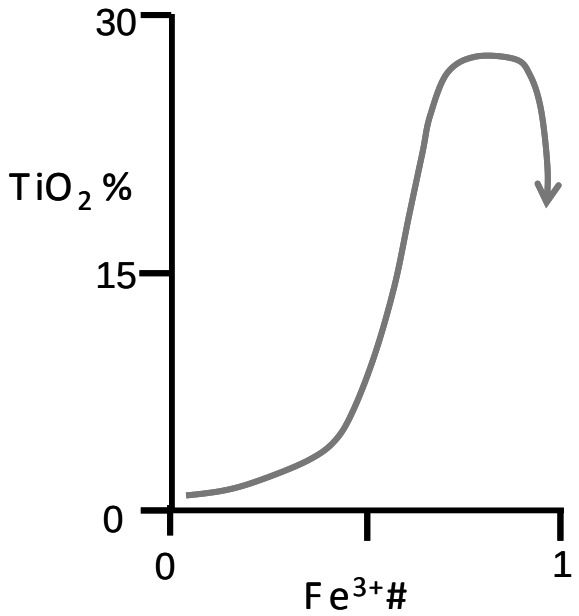

Figure 3.5.1: The generalised Fe-Ti trend for chromite based on the global terrestrial spinel dataset (adapted from Barnes & Roeder, 2001).

The Fe-Ti trend described by Barnes and Roeder (*2001*) identifies a positive relationship, where Fe^{3+} (and Fe^{2+}#) increases with TiO_2 wt%, (Figure 3.5.1). A negative correlation is observed between chromite Cr# and Mg#. The trend has been documented in Cr-rich chromites from basalt and differentiated mafic-ultramafic igneous bodies. The co-variation of Fe and Ti recorded in chromite provides evidence for the fractional crystallisation of olivine (and/or pyroxene, with or without plagioclase) out of the parent magma, promoting the Fe/Mg ratio and Ti content of the parent magma to increase (*Barnes & Roeder, 2001*). Chromites in orthocumulate rocks that interact with evolving, trapped, intercumulus liquid commonly display strong a Fe-Ti trend relationship (*Henderson, 1975; Henderson & Wood, 1981; Roeder & Campbell, 1985; Scowen et al., 1991*).

3.5.2 The Cr-Al Trend

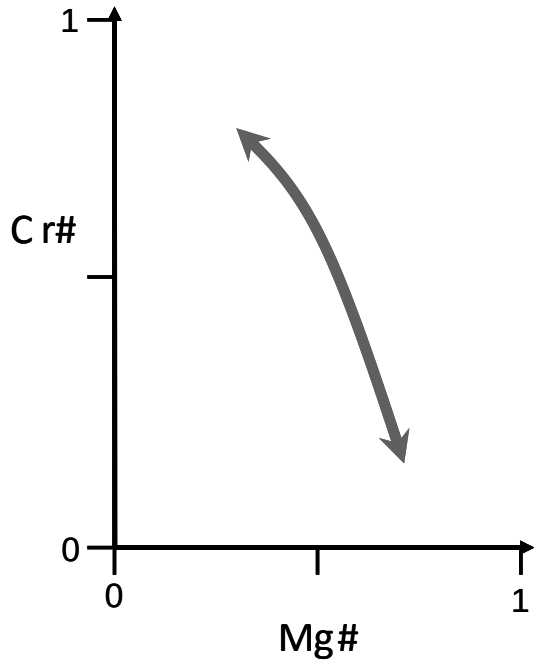

Figure 3.5.2: The generalised Cr-Al trend for chromite based on the global terrestrial spinel dataset (adapted from Barnes & Roeder, 2001).

The Cr-Al trend (where Cr# = [Cr/(Cr+Al)] and Mg#=[Mg/(Mg+Fe^{2+})]) is characterised by an increase in Cr# that is complimented by a decrease in Mg#, (Figure 3.5.2). It is described by Barnes and Roeder (2001) as extending a wide range of Cr#, low Fe^{2+}#, low Fe^{3+}# and low TiO_2 wt% values. The Cr-Al trend was first observed by Irvine (*1967*) in the Muskox layered intrusion located south of the Coronation Gulf in the Northwest Territories. Irvine (*1967*) proposed that the trend formed by equilibration of chromite and olivine at a constant temperature. The concept formed the theoretical basis for the olivine geothermometer where the gradient of the trend line is dependent on temperature. The gradient is formed by chromites that have re-equilibrated with co-existing olivine (*Sack & Ghiorso, 1991; Poustovetov, 2000*). This trend is inherent in mafic-ultramafic oceanic rocks (*Barnes & Roeder 2001*) and alpine ultramafic bodies (*Genshaft & Ilupin, 2002*).

3.5.2.1 *Sub-solidus re-equilibration between chromite and olivine*

Post cumulus and sub-solidus re-equilibration between chromite and olivine results in Fe-Mg exchange. The process is controlled by the more abundant mineral phase. When chromite dominates re-equilibration between chromite and olivine promotes the substitution of Mg into olivine at the expense of Fe^{2+} that is incorporated into chromite. Cooling a system where chromite and olivine co-exist promotes subsolidus re-equilibration (*Irvine, 1965*). Furthermore, the effect of Fe^{2+}-Mg^{2+} exchange is more pronounced in rocks where cooling rates have been slower (*Barnes & Roeder, 2001*) as the new equilibrium is more likely to be reached when the diffusional readjustments have had more time to reach conclusion. The extent of Fe-Mg exchange is determined when the closure temperature is reached and equilibration ceases (*Roeder et al., 1979; Sack and Ghiorso, 1991*). Sub-solidus re-equilibration affects the divalent cations, the trivalent ions, present in chromite, are essentially unaffected by the process.

3.5.3 The Rhum Trend

The Rhum trend is broadly similar to the Cr-Al trend. An increase in Al# (a decrease in Cr#) is complimented by an increase in Mg# (Figure 3.5.3). The Al# increases at the expense of Cr predominantly (although Fe^{3+} also decreases). In contrast to the Cr-Al trend that results from sub-solidus re-equilibration, Henderson (1975) (*and Henderson & Wood, 1981; Barnes & Roeder, 2001; Naldrett et al., 2009*) described the reaction of chromite with intercumulus trapped liquid, plagioclase and olivine as the mechanism responsible for the formation of the Rhum trend. In terms of a chemical reaction, as the Cr/Al ratio of chromite changes the Fe/Mg exchange co-efficient within the coexisting silicate phases alters to compensate, buffering the system (*Barnes & Roeder, 2001; Naldrett et al., 2009*). Hence, as the Cr/Al ratio of chromite decreases so too does the Fe/Mg ratio. This relationship reflects the preferential cation pairing of Cr^{3+} and Fe^{2+} that is complimented by the pairing of Al^{3+} and Mg^{2+}. Consequently, the Rhum trend is restricted to

mafic layered intrusions where chromite is present within gabbroic orthocumulate rocks.

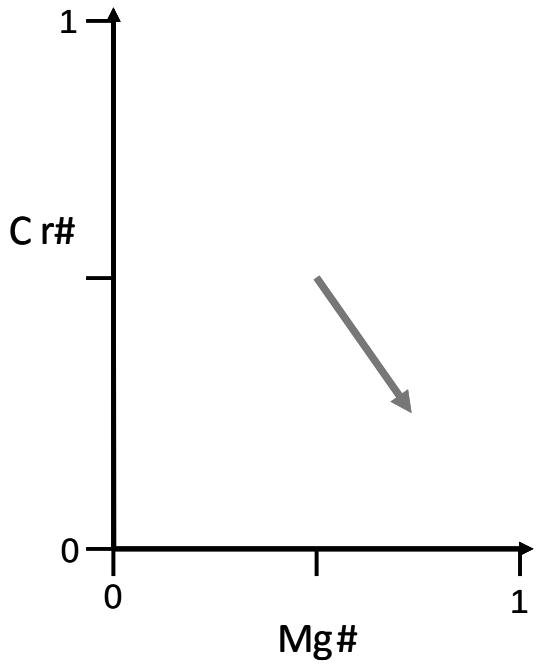

Figure 3.5.3: The Rhum trend present in chromite from the Rhum layered intrusion (adapted from Barnes & Roeder, 2001, after Henderson, 1975 and Henderson & Wood, 1981).

3.5.4 Mg#-Cr# relationships and understanding chromite genesis

The two principal Cr# and Mg# relationships documented in the literature on chromite; the Cr-Al and Rhum trends display an antithetic relationship, where Cr# increases as Mg# decreases are explained by two different processes (Sections 3.5.2 and 3.5.3); i) the influence of, and interaction between, co-existing chromite and an evolving melt phase, the Rhum trend and ii) subsolidus re-equilibration exchange of divalent cations Fe^{2+} and Mg between chromite and a co-existing silicate phase (most typically olivine), the Cr-Al trend.

Relationships between Cr# and Mg# in chromite have been used in support of models of chromite crystallisation (*e.g., Irvine, 1967; Henderson, 1975;*

Henderson & Wood, 1981; Cameron, 1977; and Naldrett et al., 2009). Naldrett et al., (2009) studied massive chromite samples collected from the Upper, Middle and Lower Groups of the Bushveld Complex. They identified two trends termed Trend A and Trend B. Trend A forms a negative correlation, where Cr# increases as Mg# decreases (the same relationship as exhibited by the Rhum trend). Trend B forms a positive correlation between Cr# and Mg#, where a decrease in the Cr# is accompanied by an decrease in the Mg#.

3.5.4.1 *Trend A*

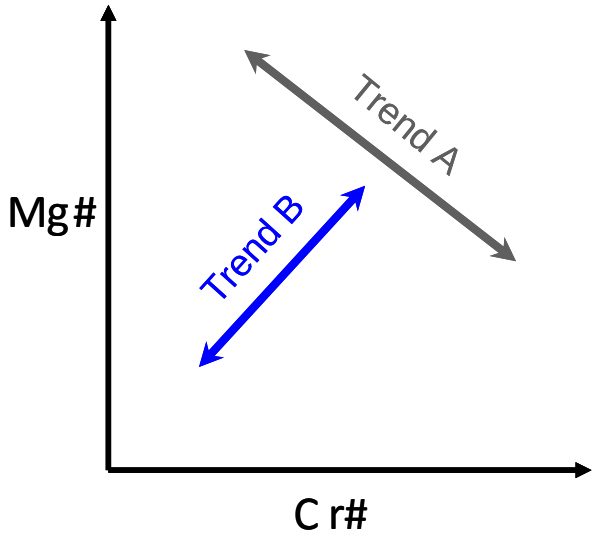

Figure 3.5.4: An idealised representation of the Mg#-Cr# relationships Trend A and Trend B as identified by Naldrett et al., 2009 in massive chromitite from the Bushveld Complex, South Africa.

Naldrett et al. (2009) analysed a set of massive chromite samples and identified Trend A within; i) the upper region of the Lower Group (LG) and ii) in the lower region of the Middle Group (MG) combined with the Upper Group (UG), of the Bushveld Complex. They reported that as the Cr# ratio increased and the Mg# ratio decreased, the Fe^{3+}/Fe_{tot} component remaining essentially constant. The trend (Trend A, Figure 3.5.4) was interpreted to result from rapid, sequential pulses of fresh magma entering the magma chamber, changing the

composition of the magma. The repetitive disturbance to the magma system prevented fractional crystallisation that consequently is not recorded by the chromite composition. Fundamentally Trend A forms by the same processes that are responsible for creating the Rhum Trend (Section 3.5.3).

To date Trend A has been most commonly documented in chromite samples sourced from layered mafic-ultramafic intrusions. The trend has been observed in massive chromite, where interstitial silicate minerals are minimal (e.g. the Bushveld Complex) as well as where chromite co-exists with olivine, orthopyroxene and plagioclase (e.g. the Rhum layered intrusion). Chromite analyses obtained from accessory chromite sourced from the dunite halo periphery (located immediately adjacent to podiform chromitite ore bodies) outward into the host peridotite and dunite units typically display a progressive decrease in Cr# that is complimented by an increase in Mg# (the Cr-Al trend) (*Irvine, 1965; Dick & Bullen, 1984*). The geochemistry of chromite sourced from within ore horizons internal to podiform chromitites has been reported to show a different trend of Cr# being stable as Mg# varies (e.g. *Ahmed, 1984*).

Trend A, first recognised and described by; Henderson, (1975) (and again later *Henderson & Wood, 1981*) identified in the Rhum layered mafic-ultramafic complex. Other localities where this trend has been observed include; the Bacuri Sill in Guyana (*Spier and Ferreira, 2001)*; the Bird River Sill, Manitoba (*Ohnenstetter et al. 1986*); the chromitites from the Upper Critical Zone of the Bushveld Complex (*Cameron, 1977*). Allan et al. (1988) observed the trend in quenched MORB-type lavas (the effect of quenching is deemed to minimise any post-accumulation reaction) sourced from the Lamont seamount chain, eastern Pacific. In addition to the Cr# - Mg# relationship produced by the MORB-type lava samples an inverse relationship between Fe^{3+}# and Mg was noted, where Fe^{3+}# increases as Mg# decreases (*Allan et al., 1988*).

3.5.4.2 *Trend B*

Trend B, the second trend identified by Naldrett et al. (2009), forms by a decrease in Cr# that is accompanied by a decrease in Mg#, producing a positive slope trend (Figure 3.5.4).

Trend B is interpreted by Naldrett et al. (2009) to correspond with periods when the composition of the magma in the magma chamber was dominated by fractional crystallisation, so promoting an increase in the Al_2O_3 content of the magma. This results in both a spinel and silicate (olivine and/or orthopyroxene (with ± plagioclase) phase precipitating from the magma. During periods when no new influxes of magma enter the chamber the composition of the magma systematically evolves, in doing so the chromite (and additional silicate phases) that crystallise and precipitate from the magma record the progressive compositional changes of the magma. The work of Hulbert & Gruenewaldt (1985) comments that the extremely high Cr# ratios observed in many of the disseminated chromites from the eastern Bushveld are likely to result from the co-crystallisation and precipitation of a plagioclase phase with chromite. The crystallisation and precipitation of plagioclase acts to buffer the abundance of Al_2O_3 in the melt such that Al is not incorporated into the chromite lattice, but is rather extracted from the magma through the formation of plagioclase.

Trend B has been less commonly identified in chromitites from layered intrusions. Wilson, (1982) found the trend in chromitites from the upper region of the Great Dyke, Zimbabwe and Naldrett et al. (2009) identified it in massive chromite samples sourced from the lower region of the Lower Group (LG) and in the upper region of the Middle Group (MG) of the Bushveld Complex. However, literature scans of the Cr# - Mg# plots created using chromite data from chromitites and disseminated chromite horizons identify additional localities where Trend B is exists, these include: chromite in chromitite from the Stillwater Intrusion, Montana (from data compiled by *Roach et al., 1998*. Sources: *Stevens, 1944, Howland, 1955; Sampson, 1966; Beeson & Jackson, 1968; Nicholson & Lipin, 1985*); chromite-rich zones of the Nazhny Tagil and Kachkanar Ultramafic Complexes, Urals, Russia, (*Auge et al., 2005*); chromitite

deposits hosted in the layered ultramafic bodies of the Nuasahi massif, Singhbhum Craton, India, (*Mondal et al., 2006*); chromite from i) the chromite and dunite dyke and ii) accessory chromite from the dunite and clinopyroxene dyke, in the Maqsad Diapir, Oman, (*Leblanc & Ceuleneer, 1992*); disseminated chromites from the Eastern Bushveld Complex (*Cameron, 1997*), the Merensky Reef and U.G.3 – (Maandagshoek), (*Hulbert & Von Gruenewaldt, 1985*); in the chromite composition of chromite sourced from “between” chromitite ore zones as well as in nodular texture ore from podiform chromite deposits of the Sakhakot-Qila ophiolite complex, Pakistan (*Ahmed, 1984*); in “between” the chromite ore seams of Panton Sill, Western Australia (*Hamlyn & Keays, 1979*).

3.5.5 Cyclic layering and chromitite layers

The close link between cyclic layering and chromitite layers in layered intrusions suggests a genetic link between chromitites and multiple injection. However, regardless of whether magma mixing causes chromite crystallise from the melt; a layer of pure chromitite will only form if the mixed melt “hybrid” lies in the primary field of chromite, as discussed by Irvine (*1977*) and Sharpe & Irvine (*1983*). If a primitive chromite-saturated melt mixes with a more evolved (fractionated) chromite-saturated melt the resulting hybrid melt will be super-saturated with respect to chromite. Consequently, mixing a primitive magma with a fractionated magma favours the formation of chromite-rich cumulates (*Murck & Campbell, 1986*).

3.6 Chromite alteration

It is widely accepted that chromite is a suitable petrogenetic indicator when olivine is the predominant co-existing silicate phase. The composition of olivine does not allow for the transfer or exchange of trivalent cations (Cr, Al), (*Irvine, 1967; Lehmann, 1983; Dick & Bullen, 1984; Hatton & Von Gruenewaldt, 1985; Scowen et al., 1991; Sack & Ghiorso, 1991; Poustovetov, 2000*). Subsolidus re-equilibration causes virtually no change to the abundance of Cr, Al or Fe^{3+} owing to their low diffusivity in olivine (*Roeder & Campbell, 1985; Scowen et*

al., 1991; Barnes, 1998). This is not true of the divalent cations, Fe^{2+} and Mg, that are interchangeable between olivine and chromite during subsolidus re-equilibration. If an appropriate carrier phase e.g. an intergranular fluid were present, it seems feasible that trivalent species could be mobilised out of chromite and across an olivine medium by intergranular flow.

Changes in chromite composition are not solely dependent on the diffusion of cations out of the lattice. Neary (1974) reports two co-existing chromite compositions within a grain, while evidence of unmixing textures and compositions are reported by Loferski and Lipin (1983), Sack and Ghiorso (1991) and Tamura and Arai, (2005). Furthermore, chemical changes e.g. the loss of aluminium, have been documented and attributed to events such as re-equilibration with, late stage magmatic fluids (*Frisch, 1971*), metamorphic fluids above 550°C (*Barnes S.J. 1998*) and at lower temperatures (*Arai et al, 2006*). There is insufficient evidence to support that these changes could not have taken place under conditions of decompression and decreasing temperature, such as those associated with the latter stages of a thermal cycle in the mantle where fluids are still present. Consequently, caution needs to be exercised when interpreting chromite compositions as being “original”. Reports of aluminium mobility are endorsed by the alteration of chromite to ferritchromit or chromian magnetite where it is evident that aluminium has been mobilised creating an end member composition that is absent of, or significantly lacking in, aluminium (*e.g. Ulmer 1974, Shen et al 1988 and Khalil and Makky 2009*). The silicates associated with these altered chromites are often notably chromian-rich and a testament to the mobility of chromium.

The presence of altered chromite phases are easily identified in reflected light and can be avoided when collecting data. In spite of the hindrance introduced by the composition of altered chromite, the trivalent cations in chromite are still considered to be the most effective to use when developing tectonic discrimination fingerprint models (Chapter 2, Section 2.3).

3.6.1 Accessory chromite morphologies: Proposed mechanisms of formation

A variety of chromite grain morphologies are associated with mantle peridotites. Terms to describe these shapes and textures included holly-leaf, cuspate, idiomorphic, subidiomorphic and euhedral.

Holly leaf chromite forms from the partial melting of peridotite (*Mercier and Nicolas, 1975)*. The shape results when the chromite phase is out of equilibrium with the melt and consequently subjected to aggressive resorption. This process produces the cuspate and concave embayment erosion features characteristic of a crystal formed out of equilibrium. The disruption to equilibrium may result from interaction with a new percolating melt or from localised, decompressional melting of clinopyroxene (e.g. *Augé, 1982*).

The formation of subidiomorphic and euhedral chromites is debated. Two mechanisms are proposed.
i) Magmatic crystallisation from a melt (*Pike and Schwarzman, 1977*)
ii) Melt-chromite reaction, where residual chromite interacts with a percolating melt (*Pike & Schwarzman, 1977; Leblanc et al., 1980*) where the reaction is not extremely aggressive resulting in rounding of the corners of the crystals.

Pike and Schwarzman (1977) propose that euhedral chromite grains develop when of a state of equilibrium is reached between a pre-existing chromite and a melt or fluid during recrystallisation of peridotite.

3.6.2 Silicate inclusions in chromite

Poikilitic textures develop from the growth of chromite around an earlier crystallised (or simultaneously growing) silicate grain. Silicate inclusions within chromitite chromite are common and deemed to form during magmatic crystallisation and/or melt-rock interaction (*Roberts, 1982; Lorand and Ceuleer, 1992*). It is debated that chromites with embayment features and deep cuspate

edges represent a precursor stage to poikilitic texture formation (*Barnes & Hill, 1995*). Insufficient chromium availability in the melt may result in incomplete growth of the crystal form and consequently, the chromite grain partially envelops the silicate grain around which it is growing.

3.6.3 Chromite ore types

Greenbaum (1977) created a classification to distinguish between different chromite bearing rock types on the basis of the modal variation of chromite comprising a rock. The categories are; massive chromitite (>90% chromite), olivine-chromitite (51-90% chromite), chromitiferous dunite (5-50% chromite) and dunite with accessory chromite (<5% chromite). Although this criteria is satisfactory for describing the compositional variation of the chromite/silicate ration of a rock, it fails to identify the vast variety of textures associated with podiform chromite ores.

There is no strict textural classification system used to describe chromite ores, however, some terms commonly used in the literature include; disseminated chromite, massive chromite, nodular, occluded silicate and chromite net textures and orbicular chromite ore-types (*Thayer, 1964, 1969; Greenbaum, 1977; Brown, 1980; Leblanc, 1980; Ahmed, 1982; Duke, 1983*). Nodular, orbicular and very coarse chromite ore textures are features unique to ophiolite chromitites (*Thayer, 1964; Leblanc, 1980; Brown, 1987*).

Disseminated chromite.
Weakly disseminate chromite is comprised of less than 5% modal proportion chromite. Grains are typically 0.1-2 mm and have euhedral, subhedral or anhedral forms. The grains may be scattered evenly throughout the olivine host silicate or form disorganised grain clusters in patches within the olivine.

Heavily disseminated chromite, where the rock is classified on the basis of modal variation as an olivine-chromitite, characteristically displays cumulate textures, evidence of layering and graded layers (*Duke, 1983*).

Nodular chromite, chromite net textures, occluded silicate, and orbicular chromite are all textures displayed by olivine chromitite or chromitiferous dunite.

Nodular chromite

Nodular chromite is comprised of interlocking, anhedral to subhedral chromite grains that form elliptical nodules approximately 2 mm to 20 mm in diameter, these are enclosed in a matrix of dunite (olivine or serpentine). Greenbaum (1977) describes that the rounded aggregates exhibit a variety of forms ranging from spherical to oblate and prolate spheroids. Within a single podiform chromite deposit nodules may vary in size, laterally and/or with depth throughout the deposit. Nodules will be in point contact with adjacent nodules with more densely packed nodules sharing a greater amount of surface contact between neighbouring nodules (*Greenbaum, 1977*) a feature that can ultimately result in nodules coalescing (*Brown, 1987*). Nodules may be elongate, the lineation defined by the long axis of the nodule preserves evidence of strain events, in such cases the nodules are normally aligned.

Nodules may possess cores comprised either of olivine (*Brown, 1980*), or in some cases of chromite dendrites inter-grown with olivine with or without clinopyroxene and/or feldspar (*Greenbaum, 1977; Leblanc, 1980; Brown, 1987; Malpas & Robinson, 1987*) although the host matrix silicate present between nodules is only composed of olivine. Silicate bearing cores may comprise as much as two thirds of the volume of some nodules, with the silicate proportion being as great as 60% (*Greenbaum, 1977*). Encasing the dendritic chromite and silicate core is a shell of massive, granular chromite.

Net textures and occluded chromite

The chromite net texture was first report by Thayer (1969), ore is comprised of small 1-2 mm subhedral to euhedral chromites present interstitially between larger, rounded olivine grains (that have since been altered to serpentine). The texture forms from the settling of large olivine and small chromite grains in a fluid magma (*Brown, 1980*). As the proportion of chromite crystallised

increases relative to that of olivine an occluded silicate texture forms (*Thayer, 1969*). An occluded silicate texture forms when grains of olivine are encapsulated in a matrix of smaller, interconnecting chromite grains that form a mesh .

Orbicular chromite

The mineral proportions and arrangement of orbicular chromite is the reverse of nodular chromite. The ellipsoids comprise a core of serpentinised olivine encased by one or multiple chromite shells alternating with olivine. Characteristically the chromite shells are very fine ranging from 0.2-2.0 mm in width. Multiple chromite shells are separated by comparatively thicker, irregular, coarse halos of olivine. The chromite grains forming the shells are anhedral to subhedral and range from 01.-2.0 mm in dimension (*Greenbaum, 1977*)

Massive chromite

Chromite comprises >90% of the modal proportion. Grains are coarse (up to 10 mm), euhedral to subhedral and coalesce to form granular aggregates. A small proportion (<10%) of inter-granular serpentinised olivine is present. Fluctuation in the proportion of serpentine results in a banded texture. When the proportion of serpentine exceeds 10% the rock is termed an olivine-chromitite.

3.6.4 Densification of chromite: Mechanisms and features

The low chromium contents in melts, even those considered relatively chromium-rich such as boninites and komatiites (Section 3.3.1.2, paragraph 3) mean that for a chromite deposit to form large quantities of melt are required. For a Cr-rich chromite deposit to form (as opposed to Al-rich chromite) requires that vast quantities of chromite to crystallise from the melt as well a high chromium availability and favourable physicochemical conditions to promote the incorporation of Cr^{3+} into the chromite lattice over that of Al^{3+} or Fe^{3+}.

The composition of podiform chromite ores, in terms of mineralogical composition is principally controlled by the ratio of chromite and olivine that

crystallise from the parent melt. This is governed by the melt composition and physical parameters e.g. fO_2 and the relative temperatures of the melt and wall-rock (*Mysen & Boettcher, 1975*). For massive chromite to form it is necessary either for chromite to be the sole crystallising phase from the melt or for a secondary, post-crystallisation process to aid the accumulation and concentration of the chromite grains. The latter process is referred to in the literature as densification (e.g. *Cameron & Emerson, 1959*), several theories have been proposed to explain this process.

3.6.4.1 *Mechanical separation: Drifting velocity*

Compared with olivine, chromite has a greater drifting velocity and this promotes the clustering of chromite in synneusis structures, as well as the separation of chromite from contemporaneously crystallised olivine within a melt (*Lago et al., 1981*). This mechanism has been proposed to explain the formation of chromite segregations in podiform chromite and requires that the chromite clusters are mechanically separated from olivine during settling in the melt conduit.

3.6.4.2 *Overgrowth – Postcumulus reaction with a chrome-rich liquid*

From the study of textures in chromite-rich rocks from the Bushveld Complex, Sampson (1929; 1931; 1932) concluded that the addition of a later-stage chrome-rich liquid had increased the initial chromite/olivine ratio. Proposed sources of a chrome-rich liquid include (i) partial re-melting of chromite crystals and subsequent chromite crystallisation, (ii) crystallisation of chromite from a chrome-rich residual magma or (iii) an intrusion of fresh chrome-rich magma that would permeate interstitially between the pre-existing settled chromites. A similar hypothesis was put forward by McDonald (1965; 1967a; 1967b) to explain the formation of massive chromite layers in the Bushveld Complex, citing the contemporaneous settling of chromite grains with chrome-rich melt droplets to explain the textures of massive chromite ore.

However, these theories invoking the later stage addition and reaction of a chrome-rich liquid with pre-existing chromites were rejected by Jackson (1966), Wager & Brown, (1968) and Cameron (1969). In addition, Golding (1975) also rejected this model as a means of explaining the massive chromite ore textures observed in podiform chromite from the Coolac ultramafic belt, New South Wales.

3.6.4.3 *Post-cumulus reaction between chromite, plagioclase and a late-stage liquid*

The formation of Al-rich massive chromite ore was explained by Henderson & Suddaby (1971) to result from post-cumulus reaction and equilibration between crystallised Cr-rich chromite, plagioclase and an interstitial trapped liquid. This reaction forms chromite with a lower Cr, higher Al content and causes an increase in the chromite volume.

3.6.4.4 *Compaction - Sintering*

Sintering is a process most commonly associated with the manufacturing of ceramics and powder metallurgy. However, it has been noted by several workers that the textures formed and the characteristic reduction in porosity that occurs as a consequence of the process are analogous to those seen in massive chromite ore, from layered intrusion deposits, e.g. the Bushveld Complex, South Africa (*Hulbert & Von Gruenewaldt, 1985*) and podiform chromite deposits, e.g. chromite from the Coolac ultramafic belt, New South Wales (*Golding, 1975*). Sintering has also been used in a geological context to explain the densification of magnetite layers in the upper zone of the Bushveld Complex (*Reynolds, 1985*) as well as the formation of monomineralic layers in layered intrusions (*Ulmer & Gould, 1982*).

Sintering results from the application of heat to a material and results in reducing the porosity; the temperature applied is not sufficiently high to melt the material. The process leads to the rearrangement of grains to optimise packing by maximising the number of grain boundary contacts. In addition, the

process increases the solubility, and consequently the transfer, of interstitial material away from the grain boundary contact areas towards regions of lower tensile stress. When pressure is applied to process it is termed pressure sintering and the packing order is further improved.

Typically, sintering changes the physical properties of a material without changing the bulk chemical composition. However, if the grains are not chemically homogenous then the compositions may be altered by solid-state diffusion. This results from the migration of atoms through a crystal lattice and transfer between neighbouring lattices. Grain boundary contacts provide a pathway for atoms to be exchanged between grains. Interstitial liquid can serve as a medium for the transfer of atoms between grains if the chemical composition permits. If the conditions for intergranular reaction prevail for a long enough time period it is possible for homogenization to be achieved, although long time periods are required (*Li, 1998*). The higher the sintering temperature the shorter the time required for homogenisation to be achieved (*Fischmeister & Exner, 1965*). It is noteworthy that the long time periods proposed by these authors are considered in terms of metallurgical processing and refer to timescales in excess of 500 hours; in a geological context, this time frame is very short.

Sintering and related processes such as Nabbaro-Herring creep (i.e. atoms diffuse through the crystal lattice resulting in grain elongation), Coble creep (i.e. atoms diffuse along grain boundaries causing grain elongation) and Ostwald ripening (i.e. small crystals dissolve and are adsorbed onto larger crystals) are all mechanisms that could take effect during the densification of chromite grains to produce enlarged, annealed grains, overgrowth textures and grain boundary interface adjustments. Furthermore, these are features that have been observed and documented in massive chromite ores from both podiform and stratiform chromite deposits (*Voll, 1960; Golding, 1975; Hulbert & Von Gruenewaldt,1985*).

3.6.4.5 *Deformation: Grain boundary features*

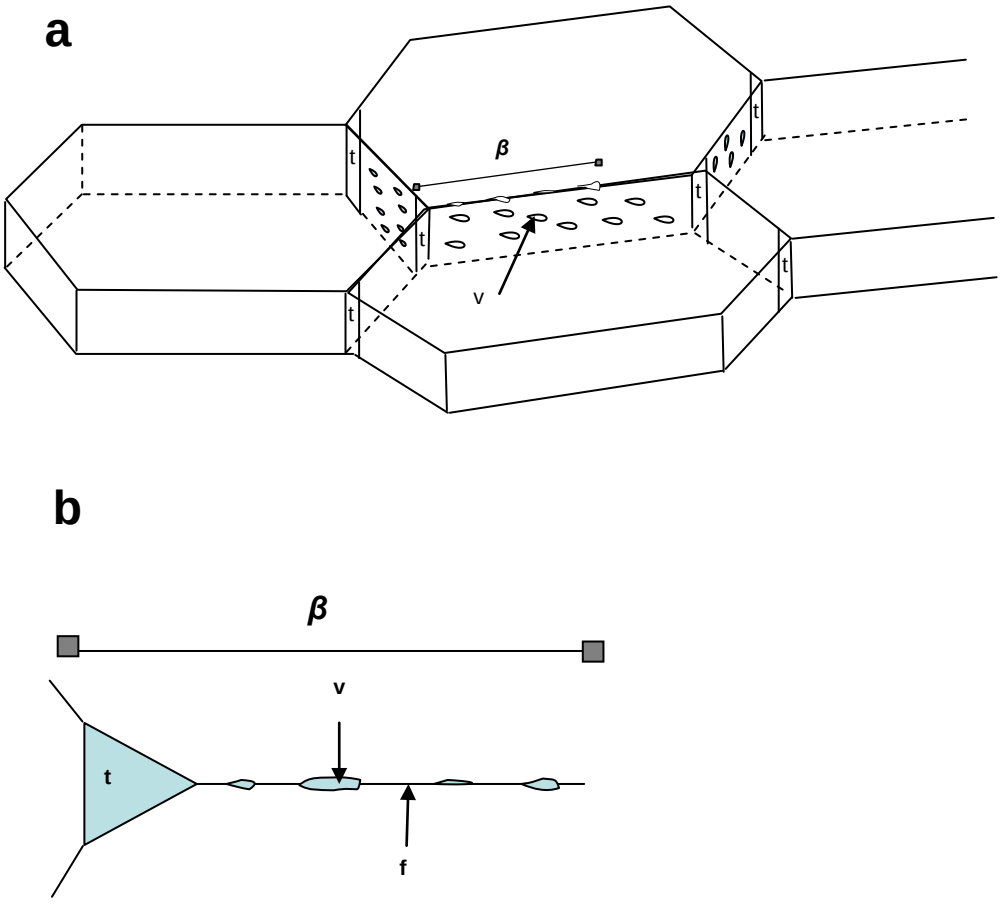

Figure 3.6.1: Grain boundary model schematic (after White & White, 1981)

[a] The grain boundary model is comprised of a grain boundary film (f) along this lie isolated voids (v), at grain triple junctions voids link to form tubes (t) or a series of interconnected micropores. [b] Illustrates the plan-view cross-section *β* of a grain boundary as defined in [a]

White and White (1987) studied grain boundary features to understand the effect of intercrystalline mass transport during deformation processes. The results documented observations made from the study of polycrystalline tectonites and a grain boundary model was developed to illustrate the principal findings. Features include, (i) grain junction tubules, (ii) isolated voids and (iii) a thin film of distorted crystal structure (Figure 3.6.1). Voids along grain boundaries shorten the effective diffusion path. The overall effect of the observed grain boundary features is to enhance the rate of intercrystalline transport processes.

Chapter 4. The Regional Setting of the Voskhod Podiform Chromite Deposit

4.1 Podiform Chromitites in the Kempirsai Massif

The Voskhod podiform chromitite is one of approximately 50 chromitite deposits and associated ore showings located within the Main Ore Field (MOF) of the Kempirsai Massif *(Distler et al., 2003; Herrington et al., 2005*). Collectively, these deposits form the largest occurrence of podiform chromitite in the world; both in terms of the number of recognised deposits as well as the unusually large size of the individual ore bodies. The MOF is situated in the south east of the Kempirsai Massif and is presently being mined for chromite. The Kempirsai Massif is an ophiolite complex that formed within the Magnitgorsk arc system, it is present within the Sakmara allochthon located in the south of the Ural mountains, Kazakhstan (see Figure 4.1.1).

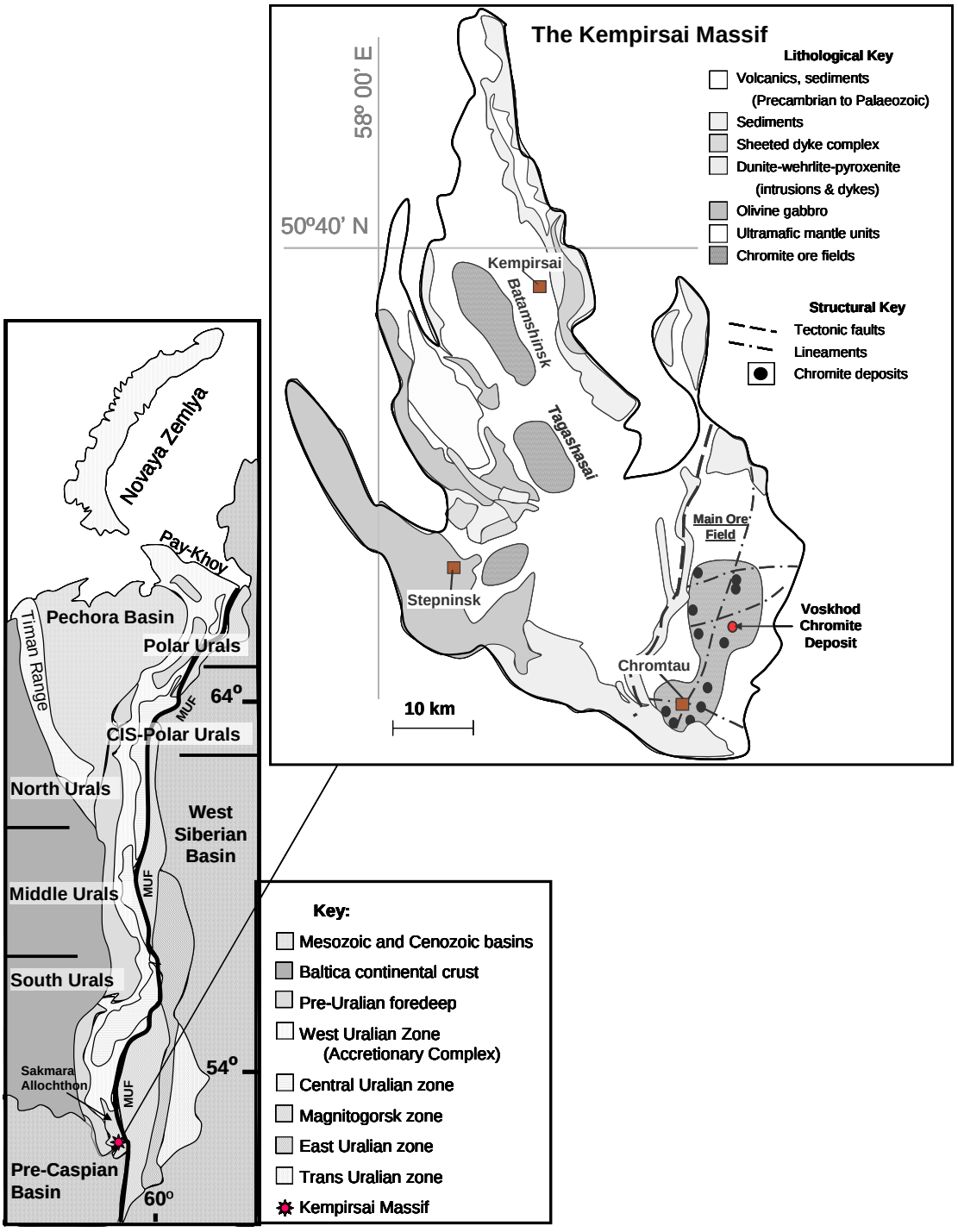

Figure 4.1.1: A map of the Ural divisions and corresponding geological units, with an enlarged map showing the Kempirsai Massif geology and orefields.

(Modified after Melcher et al., 1997; Herrington et al., 2005)

4.2 Regional setting: The Urals

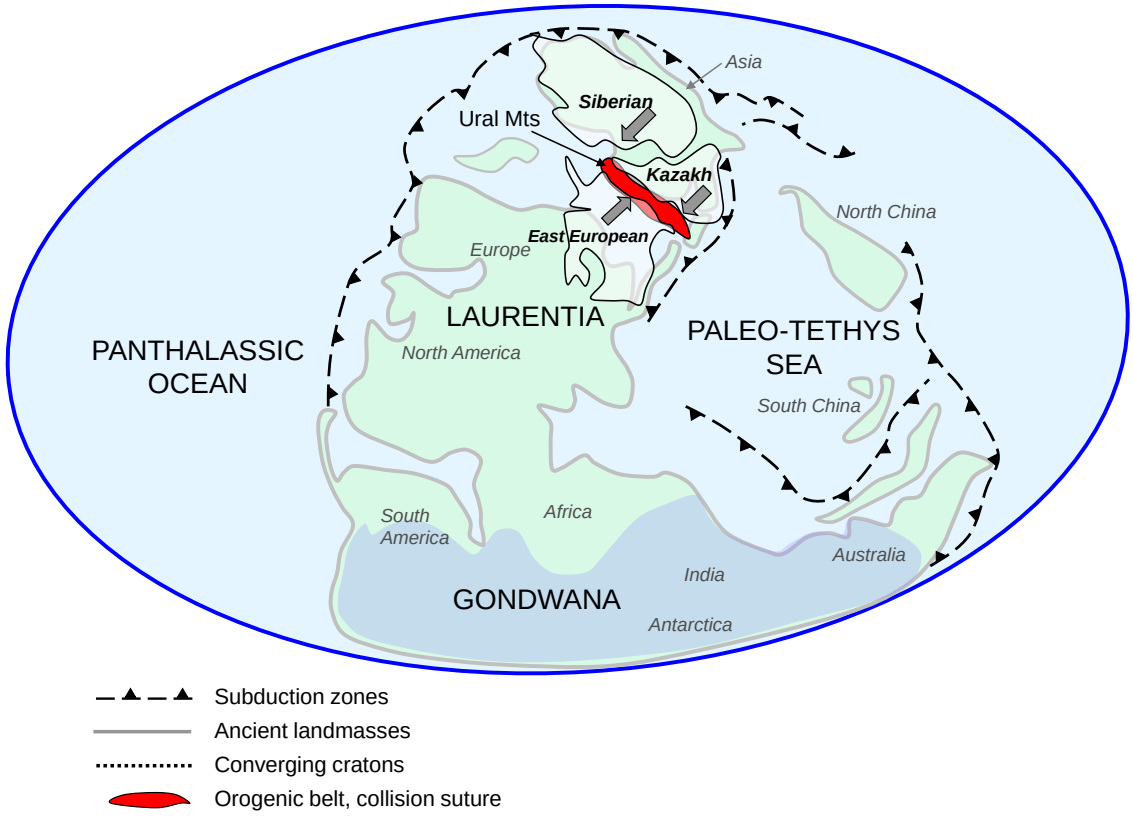

Figure 4.2.1: A late Carboniferous, palaeo-graphic world map to illustrate the construction of the Ural mountain chain.

Continent names, given in italics, landmass positions as at the time of the late Carboniferous. (After Dietz & Holden, 1970 and Windley, 1995)

The Ural mountains form the geographic divide between Europe and Asia. This orogenic mountain belt formed as a result of the Palaeozoic Uralide orogeny, an event that resulted in the collision of the East European, Siberian and Kazakh cratons throughout the Silurian to Carboniferous and concluded in the assembly of Pangea. The geological processes associated with the orogeny, are responsible for the formation of the diverse forms of mineralisation found in the Urals.

4.2.1 Tectonic evolution : Arc systems and structures of the Urals.

The Uralian orogenic cycle spanned from the Early Ordovician to the Early Triassic. The event was initiated by continental rifting at the passive plate margin boundary that existed prior to the split of the East European craton (EEC) and Kazakh, Siberian cratons, during the Late Cambrian to Early Ordovician. Throughout the Mid-Ordovician to Late-Silurian, extensional rift tectonics led to the development of a mid-ocean ridge (MOR) setting and associated sea floor spreading and ocean crust formation. This formed the palaeo-Uralian ocean basin, sited at the eastern edge of the EEC (*Herrington et al., 2005*).

An intra-oceanic thrust series developed during the onset of the Uralian palaeo-ocean basin closure in the early-Silurian. As basin closure progressed, ongoing compressional tectonic dynamics led to the development of a SSZ setting (*Savelieva & Nesbitt, 1996*) and subsequent formation of two intraoceanic volcanic arc systems; the Magnitogorsk (to the south) and Tagil (to the north) at the western margin of the ocean basin (Figure 4.2.2). Similarly, to the east of the basin a subduction zone and associated continental arc system, the Valerianovka arc, developed throughout the Late Devonian to Carboniferous at the western fringe of the Kazakh plate (see Figure 4.2.1).

The compressional tectonic regime progressed throughout the Late Devonian during which the continental margin of the EEC (East European craton) subducted eastward beneath the Magnitogorsk and Tagil ocean arcs. Simultaneously the Kazakh plate moved westward, encroaching and ultimately closing the paleo-uralian ocean, this was completed by the Late Carboniferous. Continent-continent collision continued throughout the Permian to the Early Triassic, forming the Ural mountains. The East Uralian zone (EUZ), situated east of the Magnitogorsk arc zone, represents the collision zone contact between the two cratons. To the west, the Main Uralian fault zone (MUFZ), separates the Magnitogorsk arc zone from the Central and West Uralian Zones (see Section 4.4, Figure 4.4.1,). (*Seravkin et al., 1992; Maslov et al., 1993; Melcher et al., 1994; 1997; Brown & Spadea, 1999; Brown et al., 2001; Spadea et al., 2002; Herrington et al., 2005; Brown et al., 2006*).

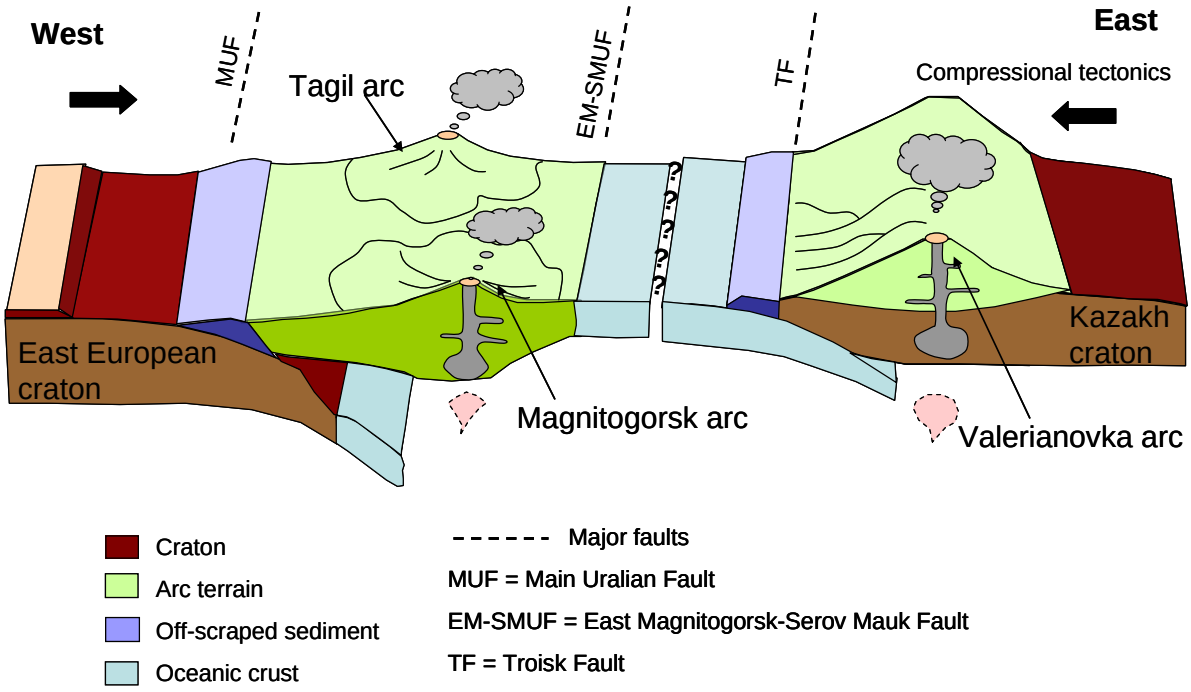

Figure 4.2.2: A schematic cartoon to illustrate the formation and relative positions of the Magnitogorsk, Tagil and Valerianovka arc systems during the Late Devonian.

Cartoon based on schemcatics from Melcher et al., 1997 Herrington et al., 2005 and Brown et al., 2006

Three major faults transect north to south along the Uralian Central, these are; the Main Uralian Fault Zone (MUFZ) to the west, the East Magnitogorsk-Serov Mauk Fault (EMSMF) in the centre and the Troisk Fault to the east Zone (Figure 4.2.2). The two major arc systems, the Magnitogorsk arc and the Valerianovka arc, present in the south Urals have sutured together along the EUZ (*Herrington et al., 2005*)**.**

4.2.2 The Main Uralian Fault (MUF)

The MUF is the suture contact between the EEC, to the west, and the Magnitogorsk and Tagil arcs (south and north respectively) present to the east (Figure 4.2.2 and Section 4.4 Figure 4.4.1,). Arc-continent collision between the Magnitogorsk island arc and the margin of EEC ceased in the Late Devonian (*Puchkov, 1997, 2000; Brown & Spadea, 1999; Alvarez-Marron, 2002; Brown et al., 2006*).

The MUF extends the entire length of the Urals, it is more than 2,500 km long. In the south Urals the MUF zone (MUFZ) is approximately 10 km wide and is comprised of an east dipping mélange unit. Lithologically this zone is dominated by serpentinites clastically bound with fragments of Devonian volcanics and arc derived sedimentary rocks as well as lenticular slabs of ultramafic mantle rock that vary from several hundred m^2 up to a km^2 in dimension (*Herrington et al., 2005 and refs therein; Brown et al., 2006)*.

4.2.3 The Tagil Arc - Middle to Polar Urals

The Tagil arc, an intraoceanic arc formation, accreted during the Silurian to Middle Devonian (*Yazeva and Bochkarev, 1996; Bosch et al., 1997*). To the west of the arc the basement units are comprised of Silurian andesitic lavas and in the east Early Devonian trachytes and volcaniclastic units. The basement units are overlain by approximately 2,000 m of Early to Middle Devonian limestone that to the east is inter-layered with calc-alkaline lavas that formed in a mature island arc setting *(Antsigin et al., 1994; Yazeva and Bochkareve, 1994).* The arc rock suite is intruded and cross-cut by dunite-clinopyroxene-gabbro massifs. Structurally the Tagil arc is an open synform (*Bashta et al., 1990; Ayarza et al., 2000*) that has been metamorphosed to a lower greenschist facies (*Herrington et al., 2005*).

4.2.4 The Magnitogorsk Arc – South Urals

The Magnitogorsk arc formed in a SSZ setting. The basement rocks consist of boninitic and tholeiitic lava assemblages and include the Baimak-Buribai Complex. These lavas erupted into a forearc setting in the Late Silurian – Early Devonian and are associated with incipient subduction; the primary stage of supra-subduction initiation. As the island arc system matured, during the Middle – Late Devonian, volcanism evolved to a tholeiitic - calc alkaline composition These lavas overly the boninitic and tholeiitic lavas (*Seravkin et al., 1992; Brown & Spadea, 1999; Spadea et al., 2002*). Up sequence are volcaniclastic sediments, that were deposited in a forearc basin and reach up to 5,000 m in thickness (*Maslov et al., 1993; Brown et al., 2001*). The top of the sequence is capped by Early Carboniferous, shallow-water, carbonates that unconformably overlie the island arc

rocks. Late-stage, Early Carboniferous granites intrude the arc sequence. Structurally the Magnitogorsk arc exhibits minor open folds and thrust deformation features (*Brown et al., 2001*). Herrington et al. (*2005*) report that the metamorphic grade does not reach greenschist facies.

4.3 Boninites of the Urals

Early to Mid-Devonian boninitic rocks (lavas, dikes and shallow-level intrusive rocks) have been recognised in the Baimak-Buribai Complex of the Magnitogorsk Zone island arc system. The Baimak-Buribai is comprised of volcanic and sub-volcanic units, including pillow lavas, hyaloclastites, dykes and volcanic terrigenous deposits and pelagic sediments. The lavas range from boninitic to calc-alkaline in composition and are the only documented boninite lavas present in the South Urals (*Ivanon et al., 1989; Seravkin et al., 1992; Brown & Spadea, 1999; Spadea et al., 2002*). The complex provides a record of the progressive evolution and development of the Magnitogorsk island arc (*Spadea et al., 1998*).

The Baimak-Buribai complex boninites are basic-intermediate lavas with compositional ranges of; 52-59% SiO_2, 7-19% MgO, 0.3-0.5% TiO_2, 4-10% CaO, low alkalis and relatively high Cr ≤ 1000 ppm and Ni ≤ 400 ppm. The rare earth element (REE) concentration characteristics include, low total abundances, depleted Ce concentrations, low La/Yb ratios and in some samples prominent depletion of the Middle REEs (MREEs) (*Spadea et al. 1998*).

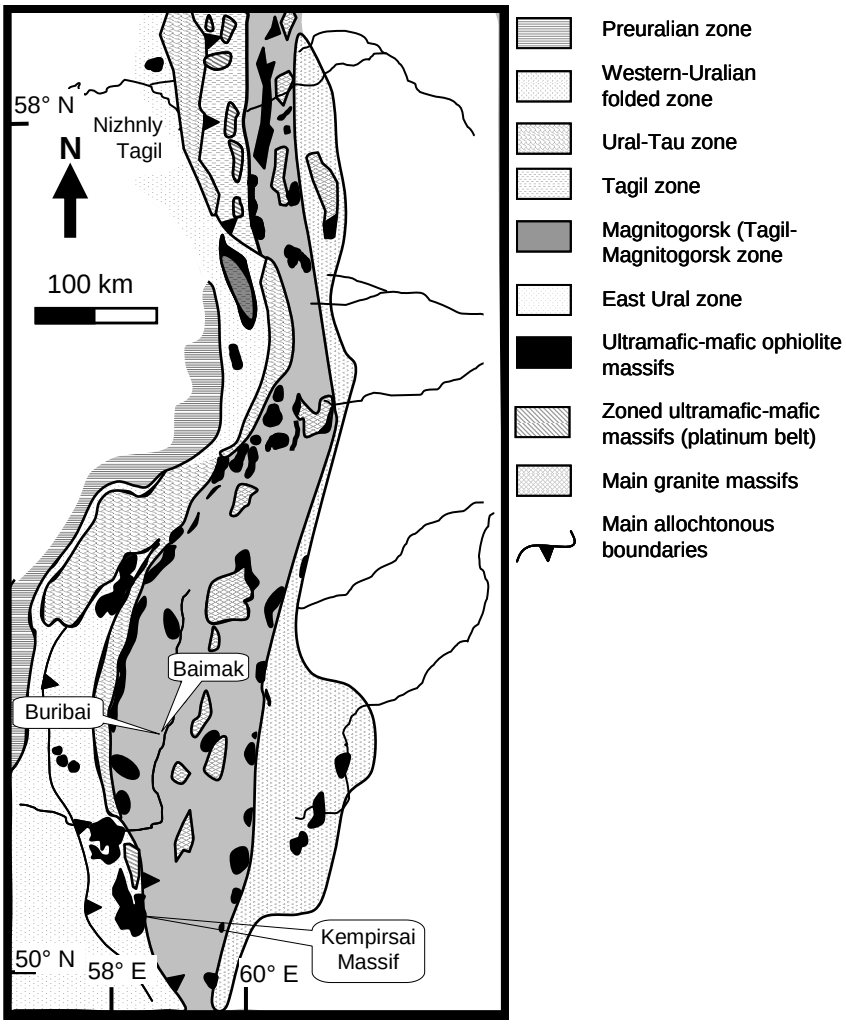

Figure 4.3.1: A geological map of the Urals showing the location of Baimak and Buribai the source localities for the boninite samples and the relative position of the Kempirsai Massif (host to the Voskhod deposit).

Adapted from Herrington et al., 2002

Three field localities were studied and sampled by Spadea et al. (*1998*); the Shankhai Stream sequence, the Tanalyk River sequence and the Baimak-Buribai type sequence near Samaskoe (listed in order from the base to the top of the Baimak-Buribai Complex).

The boninite samples were collected from horizons within the Shankhia Stream and Tanalyk River sequences. Of the 29 samples collected and studied by Spadea et al. (*1998*) five were identified as boninites; LK148-1, SU386, SU398, SU401 and

LK148-4. Petrographically these five samples split forming two groups termed 2b and 3a. The definition for each group given by Spadea et al. (*1998*) is as follows;

"Group 2b (LK148-1, SU386, SU398 and SU401) – are moderately porphyritic boninitic basaltic-andesites with olivine and/or orthopyroxene phenocrysts, and Cr-spinel included within olivine as micro-phenocrysts. Olivine is irregularly distributed, it is sometimes glomerophyric, and may be corroded. The secondary minerals are actinolite, chlorite, albite and epidote."

"Group 3a (LK148-4) – are aphyric, variably textured, spherulitic to dendritic and microlitic, commonly amygdaloidal, boninites. The secondary minerals are chlorite, actinolite, pumpellyite and epidote."

The literature portrays an apparent genetic association between boninite melts and the formation of mantle hosted, high-Cr, podiform chromitites present within ophiolites; e.g. the Troodos ophiolite, Cyprus - *Robinson et al., 1983*; the Luobusa ophiolite, southern Tibet - *Zhou, 1996*; the northern region of the Oman ophiolite in Wadi Rajmi - *Rollinson, 2005; 2008*; the Thetford Mines ophiolite, Québec, Canada - *Pagé & Barnes, 2009*. (Chapter 3, Section 3.3.1.4: Chromite crystallisation and melt type relationships, references: *Zhou & Robinson, 1994; Arai & Yurimoto, 1994; Zhou et al., 1996; Matsumoto et al., 1997; Zhou et al., 2001; Uysal et al., 2005; Morishita et al., 2007; Caran et al., 2010*). Consequently, it is becoming increasingly more common for authors to compare podiform chromitite and boninite lava data from genetically associated formations (e.g. *Rollinson, 2005; 2008; Pagé & Barnes, 2009*).

Boninite lavas have not been recorded within the crustal lava units of the Kempirsai Massif. The lava assemblages observed are Early Silurian dolerites, amygdoloidal basalts and siliceous tuffs (*Pavlov & Grigoryeva, 1977*). These Early Silurian lavas are too old to be related to the formation of the Magnitogorsk island arc system (Middle-Late Devonian). Instead, they are more likely MORB-type basalts that formed during the opening of the Uralian palaeo-ocean basin, in a MOR setting. Since the mantle units of the Kempirsai Massif have numerous, >15 Mt, high-Cr, podiform chromitite deposits in the Main Ore Field, it seems feasible that during subduction initiaition, when the Kempirsai Massif mantle would have been part of a developing fore-arc setting, interaction with a boninite melt may have occured.

Observed field and petrographic characteristics of the Baimak-Buribai complex boninites provide evidence for high temperatures typical of boninitic volcanism, ~1150°C – 1300°C (*Crawford et al., 1989*). Furthermore, the the abundance of vesicles within the boninite units indicate that the magmas were also volatile rich (*Spadea et al., 1998*).

Given that; i) the age dates of the Baimak-Buribai complex boninites are contemporaneous with the formation of the early stage Magnitogorsk arc, forearc setting (*Spadea et al., 1998*), ii) the evidence for the podiform chromitites (*Melcher et al., 1997*) and boninites (*Spadea et al., 1998*) being volatile rich and iii) the geographic proximity of the Kempirsai Massif and the Baimak-Buribai complex (*Spadea et al., 1998; Herrington et al., 2005; Brown et al., 2006*); a genetic relationship between the Baimak-Buribai boninites and the podiform chromitites of the Kempirsai Massif seems possible; a relationship that will be investigated further in the thesis.

4.4 The Sakmara Allochthon

The Sakmara allochthon accretionary complex is located in the South Urals. It is comprised of Cambrian and Ordovician sedimentary sequences rifted from the margin of the East European Craton (EEC). Fragments of oceanic-arc volcanic rocks and massifs, including the Kempirsai and Khabarny massifs, are incorporated within these sedimentary units (*Herrington et al., 2005*). Between the Sakmara Allochthon ophiolite massifs and the Main Ural fault (MUF) is a narrow belt comprised of metasediments and meta-ophiolites including eclogite-facies assemblages. The eclogites have been documented to record peak metamorphic conditions of 27 kbar and 615°C (*Melcher et al. 1997 and references therein*).

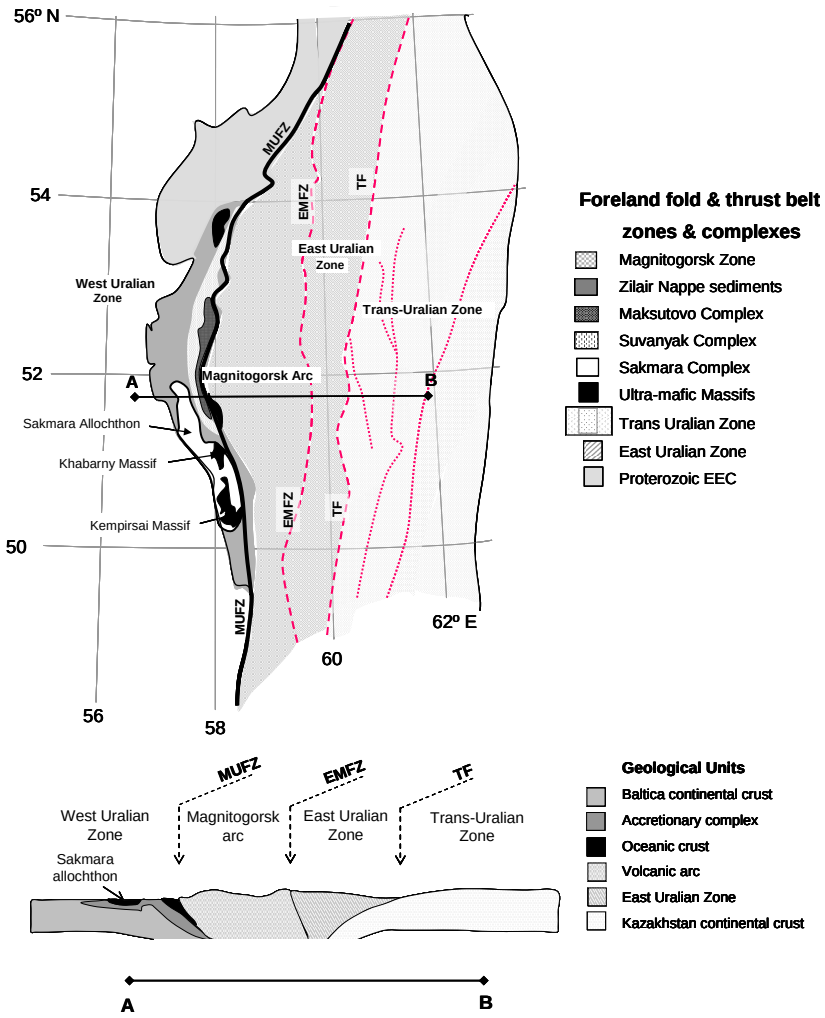

Figure 4.4.1: A map of the Sakmara Allochthon position in the south Urals, the regional geologic complexes and major faults.

The cross-section is representative (not to scale). Modified after Herrington et al., 2005.

The Sakmara Allochthon forms part of the Magnitogorsk arc-continent collisional suture. The unit was exhumed and obducted westwards onto the eastward subducting continental margin of the EEC during the Middle Devonian; a process associated with the closure of the palaeo-Uralian ocean basin (Figure 4.4.1) (*Herrington et al., 2005*). The Sakmara allochthon overlies the West Uralian zone which is comprised of continental shelf sediments and is bound to the east by the Main Ural deep-fault (*Melcher et al., 1997*).

4.5 The Kempirsai Massif

The Kempirsai massif is an ophiolite situated within the Sakmara Allochthon of the Central Uralian Uplift. It hosts the world's largest collection of podiform chromite deposits that form the Batamshinsk, Tagashasai, Stepninsk and Main Ore Field (MOF) orefields. The Voskhod deposit is located within the MOF (Figure 4.4.1).

The Kempirsai massif is an ophiolite complex of relict Palaeozoic ocean crust (*Dilek, 2003*). The massif was thrust westwards during obduction onto the Proterozoic and Palaeozoic shelf sediments of the EEC platform during the Variscan nappe tectonic episode of the Uralian orogeny. It is the largest of the Palaeozoic, ultramafic, ophiolite massifs, present in the southern Urals (*Melcher et al., 1994; Melcher et al., 1997; Savelieva et al., 1997*). Its elongate shape extends 90 km in a north-south direction and up to 32 km in an east-west direction, covering an area of approximately 2,000 km^2. The massif is comprised of a complete ophiolite sequence of; pillow lavas of MORB affinity, a sheeted dyke complex of gabbros and dolerites, cumulate layers of olivine gabbros, troctolites and dunites and a thick (up to 16 km) mantle sequence of residual harzburgite with minor dunite and lherzolite (*Melcher et al., 1997*) capped by Middle Ordivician black shales (*Herrington et al., 2005*). Late stage wehrlite, pyroxenite and gabbro dykes and intrusives cross-cut the crustal units (*Edwards & Wasserburg., 1985; Melcher et al., 1994*; *Savelieva and Nesbitt, 1996; Savelieva et al., 1997, 2002;* Melcher *et al., 1999 and references therein*).

It is reported by Melcher et al. (*1997*) that the formation of the giant sized podiform chromite deposits of the Kempirsai Massif are associated with vast quantities of volatile rich fluids likely to have been released from a hydrated subducting crust slab component. The hydrous regime is evident from visible, fluid and mineral inclusion assemblages present within the Kempirsai chromite. Furthermore, the oxidising conditions calculated by Melcher et al. (*1997*) do not conform with a magmatic model operating under an anhydrous upper mantle conditions (*Melcher et al., 1997*).

The chromite deposits present within the Kempirsai Massif account for the largest occurrence of podiform chromitite in the world and form the second largest

resource of chromite in world, after of the Bushveld chromite seams of South Africa.

4.6 Chromitite Orebodies of the Kempirsai Massif

The chromitite ore bodies within the Kempirsai Massif are divided into two groups based on chromite composition. High-Cr chromite chromitites are found in the MOF while the Stepninsk, Tagashasai and Batamshinsk ore fields host high-Al chromitites. The high-Al chromite chromitites associated with these orefields are collectively termed Batamshinsk-type (BAT) chromite ores (Melcher et al., 1997) (Figure 4.4.1).

4.6.1 The Batamshinsk-type (BAT) Chromite Ores

The high-Al chromite, BAT orebodies are situated in the west, central and northwest areas of the Kempirsai massif (*Melcher et al., 1994; 1997; Garuti et al., 2002*). To the north and west are the Batamshinsk and Tagashasai ore fields (respectively). The pod and lens shaped orebodies, which rarely exceed 100 m in length and 10 m in thickness (*Herrington et al., 2005*), are hosted in a layered series of serpentinised dunite-harzburgite mantle units underlain by tectonised harzburgites (*Melcher et al., 1994 and references therein)*. The Stepninsk orebodies are located to the southwest of the massif, within dunite cumulate layers, close to the inferred crust-mantle boundary near the village of Stepninsk. These orebodies are tens of meters in length and less than 3 m in thickness (*Herrington et al., 2005*).

To the south east of the massif is located the Main Ore Field (MOF), this region hosts the giant orebodies of Cr-rich, Al-poor chromian spinel. The Voskhod Chromite deposit, the focal study area of this thesis, is one such orebody from within the MOF.

4.6.2 The Main Ore Field (MOF)

The MOF is an elongate NNE-SSW trending anticline, the axial plane can be traced over 22 km and it is approximately 7 km wide. Two parallel ore zones of podiform chromite mineralisation can be traced, one on either side of the anticline, these ore zones meet in the south west (*Melcher et al., 1994*). The mantle sequenece in the MOF region is 16 km thick comprised of dunite, harzburgite and more rarely harzburgite interlayered with lherzolite horizons. Multi-orientated pyroxenite veins cross-cut the mantle stratigraphy. The massive chromite orebodies are frequently cross-cut by veins of amphibole and chromite. (*Melcher et al., 1997*; *1999 and references there in*)

The deposits possess a range of morphologies elongated in a north east orientation, occurring either as a single lens of chromite mineralisation (such as the Molodezhnoe deposit) or as a series of discrete lenses serparated by weakly mineralised dunite horizons (*Herrington et al., 2005*). Orebodies are generally orientated parallel to the mineral foliation visible in the host rocks of dunite and harzburgite. The deposits situated to the west side of the anticline dip to the west 5-50°, the largest deposits (>40 Mt) include Millionnoe, Diamond Pearl and 20 Years of Kazakh SSR in addition to 15 smaller deposits. To the east are large deposits 40 Years of Kazakh SSR, Mir, Molodezhnoe and Voskhod-Karagash as well as a further 30 smaller deposits recognised. These orebodies dip to the east 15-75°. The orebodies range in size from tens of meters to 1,800 m (Molodezhnoe) having thicknesses ranging from a few meters to 230 m (Diamond Pearl). Numerous, high angle faults (trending east-west) cross cut the MOF, these often displace and terminate the chromite orebodies (*Melcher et al., 1997*; *1999*; *Herrington et al., 2005*).

Chapter 5. Voskhod

This chapter presents the principal geological features of the Voskhod chromite deposit including; the location and spatial relationship to other chromite deposits in the Kempirsia Massif, the orebody morphology and broad chemical characteristics, as well as the mineralogical composition and geochemistry of the silicate rocks that comprise the hanging wall and footwall units.

5.1 The Voskhod podiform chromite deposit

The chromitite deposits of the Kempirsai Massif, Main Ore Field (MOF) are located proximal to the town of Chromtau. There are more than 50 identified deposits that cumulatively possess chromite reserves exceeding 300 Mt (*Melcher et al., 1994, 1997 and 1999*). The deposits form two parallel bands aligned with the north northeast-south southwest trending axial plane of the major anticline of the MOF. The largest are Voskhod, Mir and 40 Let located to the east of the axial plane and Millionnoe, Diamond Pearl and 20 Let to west. The MOF ore bodies are lens shaped and the long axes of the lenses are oriented parallel to the foliation present in the host rocks (*Melcher et al., 1997*). The deposits are always enveloped by serpentinised dunites, and are often offset and dismembered by east-west trending faults.

Typically ophiolite-hosted podiform chromitites rarely exceed 10 Mt of chromite, e.g. the classic ophiolite complex in the Troodos Massif of Cyprus. The Voskhod chromite deposit contains in excess of 18 Mt. Voskhod, located to the east of the MOF syncline, is separated from the neighbouring Karaagash deposit (sited to the north) by the east-west Karaagash fault, the surface expression of which dips to the north at 80º. The ore body is disc-shaped and comprised of a series of en echelon chromitite lenses. The hanging wall and, to a greater extent, the footwall contacts are highly irregular. Dipping to the northeast at 35-40º, it has a length of 600 m in this direction, a width varying between 170 m to 360 m and a thickness of between 2 m and 123 m (average 39 m). The median plane of the ore body is positioned at a depth of 102 m in the southwest that decreases to 452 m in the northeast, having an inclined dip of approximately 28°.

The deposit is comprised of multiple layers of stacked chromitite lenses orientated parallel to the dip of the ore body. These layers vary in thickness, ranging from centimetres to several metres thick. The thickest layer of continuous mineralisation is 123 m thick (comprised of massive and disseminated chromite ore types). The style of mineralisation varies from massive chromite (>80 chromite) to weakly mineralised, disseminated chromite (~10% chromite). The ores are comprised of two mineral phases, chromite and serpentine that represents altered primary olivine. The progression from massive chromite into disseminated ore or barren dunite horizons varies; sometimes the change is immediate with there being no evidence of a structural break in the core and other times the change is gradational with the modal proportions of chromite and olivine changing progressively over a depth interval, from one side of a layer to another.

The top soil overburden is composed of Palaeogene-Quaternary loams overlying sandy clays and rubble 0.5-0.7 m thick. The bedrock is comprised of alternating dunite and peridotite assemblages that have undergone varying degrees of serpentinisation. These units are weathered, heavily fractured and brecciated to depths of 60-80 m. Serpentinised dunite encompasses the ore body and is present between the stacked ore lenses. Sulphides are present in the dunite but are rare, they include pyrrhotite, pentlandite and chalcopyrite.

Samples were collected from six drill cores, five from the central region of the ore body extending to the west and east limits (V05-13, -21, -24, -28 and V06-48) and one to the southwest limit (V06-06).

5.1.1 Drill Collar Grid for the Voskhod License Area

Oriel Resources drilled a total of 53 holes during the 2005 drilling campaign; of these 43 intercepted chromite mineralisation. The average thickness of mineralisation intercepted is 63.80 m (Table 5.1.1). Information collected from the study of the drill cores was used to model the ore body; its size, shape, the ore type spatial variation and distribution. An overview of this data is presented.

Drill hole I.D.	Chromite mineralisation top	Chromite mineralisation base	Mineralisation thickness
V05-01	301.10	414.75	113.65
V05-02	392.10	461.60	69.50
V05-05	432.92	454.65	21.75
V05-06	405.90	443.60	37.70
V05-07	427.10	465.40	38.30
V05-08	398.25	447.20	48.95
V05-09	437.10	468.20	31.10
V05-10	341.00	379.59	38.59
V05-11	350.20	376.00	25.80
V05-12	332.80	398.80	66.00
V05-13	255.70	361.30	105.60
V05-14	285.00	409.70	124.70
V05-15	193.80	230.80	37.00
V05-16	415.05	456.30	41.25
V05-17	454.88	484.00	29.12
V05-18	409.00	435.10	26.10
V05-19	269.60	378.80	109.20
V05-20	333.90	421.70	87.80
V05-21	241.40	289.30	47.90
V05-22	249.50	358.70	109.20
V05-23	264.45	347.90	83.45
V05-24	266.40	377.50	111.10
V05-25	296.20	430.75	134.55
V05-26	326.30	435.55	109.25
V05-28	327.16	440.05	112.89
V05-30	401.30	413.20	11.90
V05-34	140.70	229.50	88.80
V05-35	138.00	189.45	51.45
V05-36	202.70	252.20	49.50
V05-37	104.00	179.20	75.20
V05-38	113.40	140.30	26.90
V05-39	116.70	153.45	36.75
V05-40	157.50	177.70	20.20
V05-41	85.00	133.10	48.10
	Average thickness(m) =		**63.80**

Table 5.1.1: Chromite mineralisation thicknesses observed across the orebody. The upper and lower limits are defined by a cut-off grade of 20% chromite.

Table 5.1.1 shows the of thicknesses of the mineralised zones intercepted, these range from 11.9 to 134.55 m, the average value is 63.8 m.

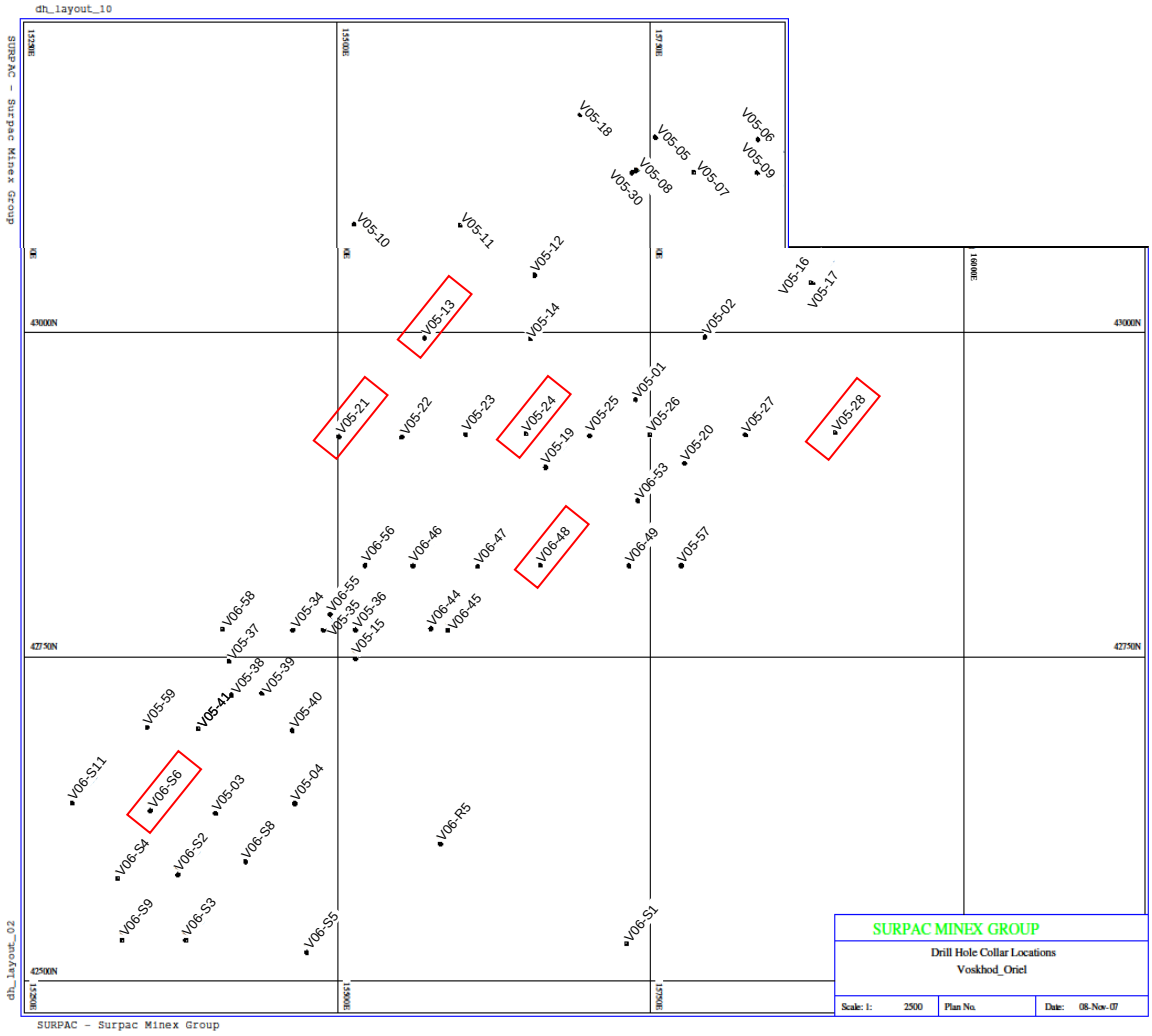

Figure 5.1.1 A map depicting the drill collar locations from the Voskhod license area.

The red squares around drill collars; V05-06, V05-13, V05-21, V05-24, V05-28, V05-48 and V06-S6 identify drill cores that were sampled for the purpose of this study.

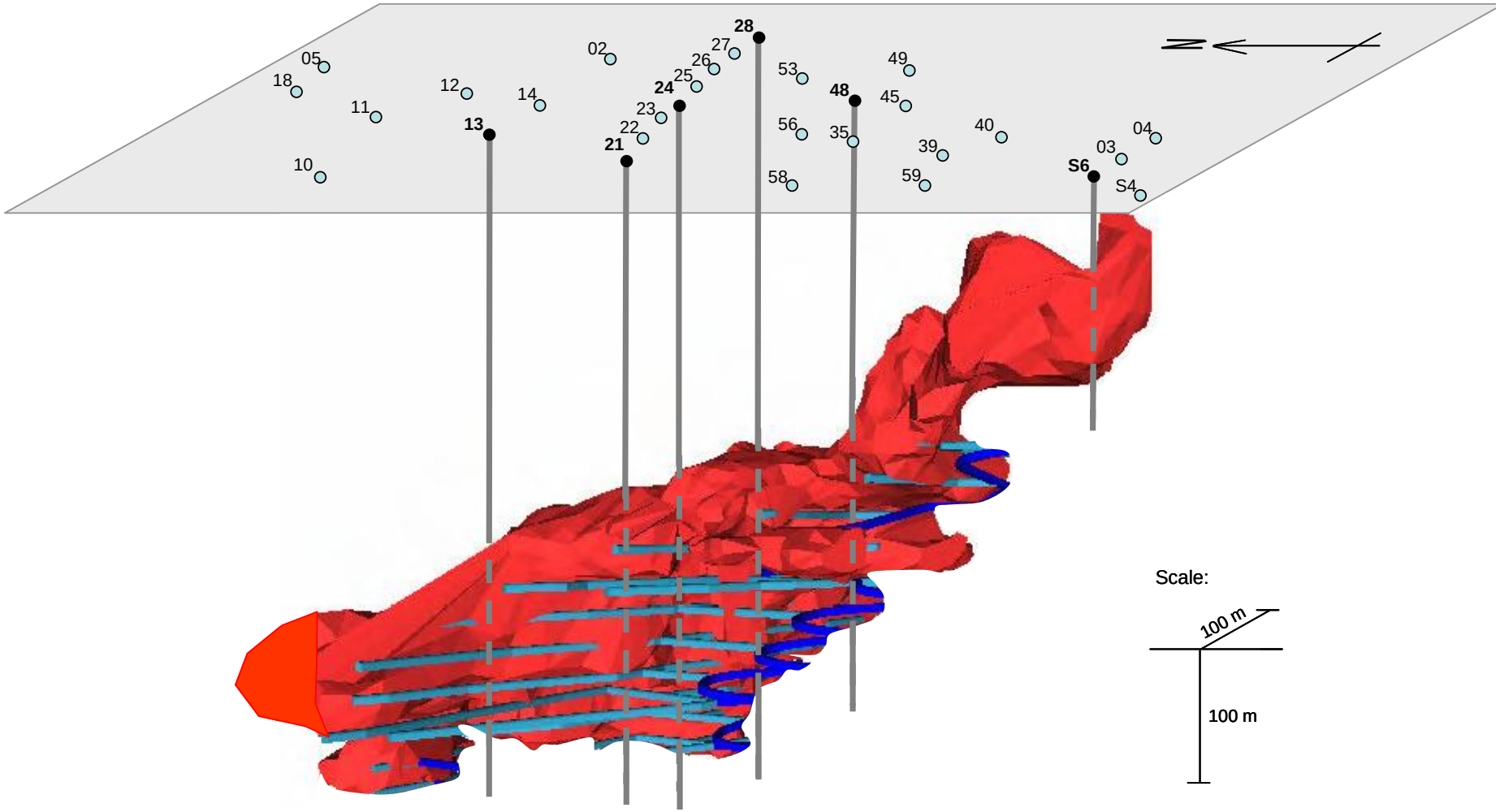

Figure 5.1.2: Drill collar locations and 3.D ore body model of the Voskhod podiform chromite deposit.

The samples that form the focus of this research were selected from drill holes V05-13, 21, 24, 28, 48 and S6 indicated as grey vertical lines. The reader should note that not every drill collar is surface expression is shown. The 3.D orebody model was created using GEMCOM software (*Matthew Boyes, 2006*). The ore zone (shown in red) was determined by the ore cut off grade of 20% Cr_2O_3. The blue lines are planned mining levels.

5.1.2 Morphology of the Voskhod podiform chromite ore body

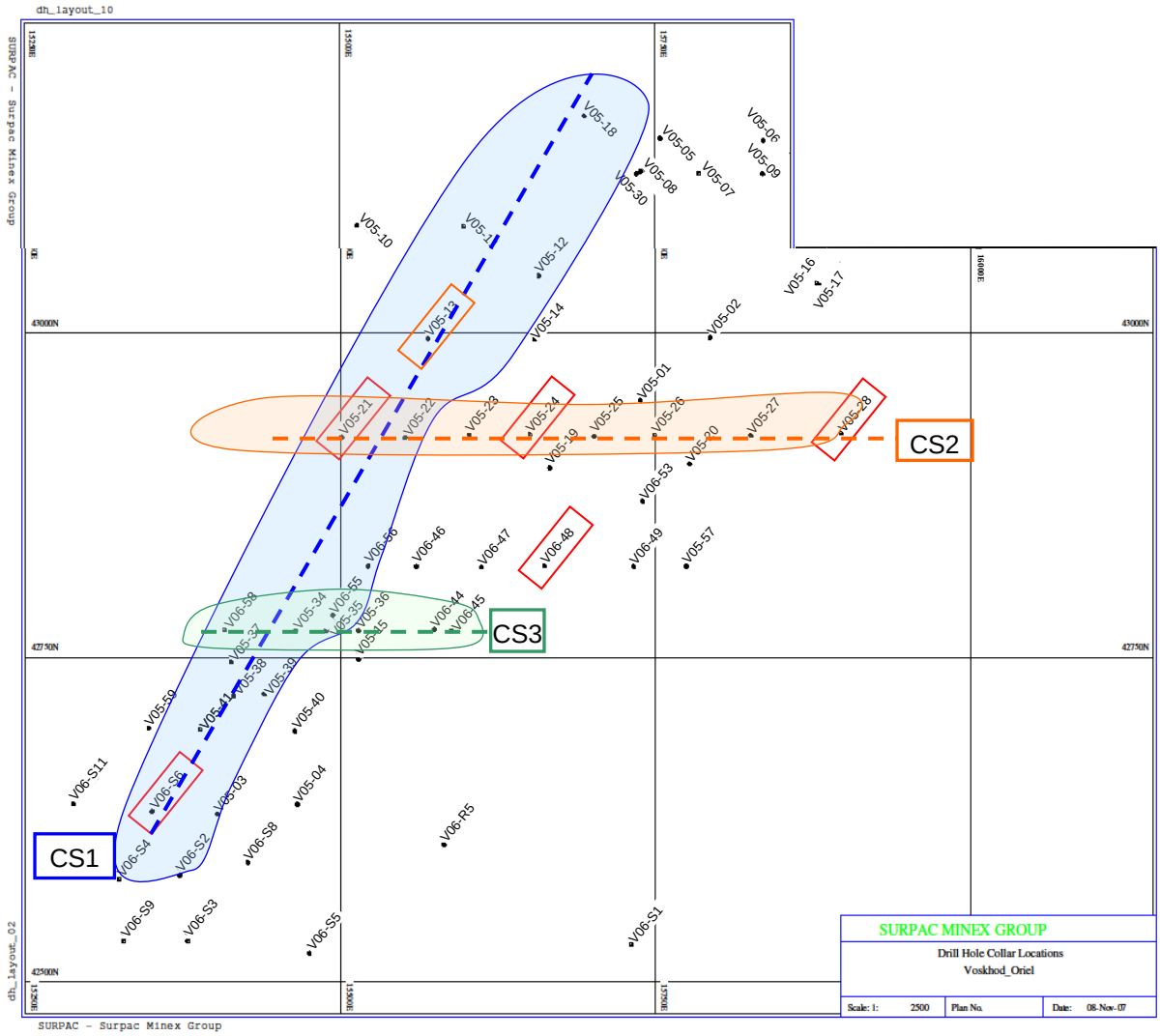

Figure 5.1.3 Drill collar map illustrating three cross sections constructed using drill core (by the author) from drill collars along the line of the section.

Cross section 1 (CS1) traverses southwest to northeast across the ore body.

Cross sections 2 and 3 (CS2 and CS3) traverse west to east across the ore body, CS2 transects the central ore zone of the ore body.

The broken lines indicate the surface expression of each transect presented as cross sections CS1, CS2 and CS3, the coloured shape outline encompasses additional drill collar identification numbers. Although these holes were not sampled in detail for geochemistry and mineralogy, they were logged by the author and the data have been incorporated into each cross section. The cross sections

(CS1 - Figure 5.1.4, CS2 -Figure 5.1.5 and CS3-Figure 5.1.6) provide a visual representation of the variation in mineralisation with depth in terms of principal ore type and continuity of the mineralised intervals

.

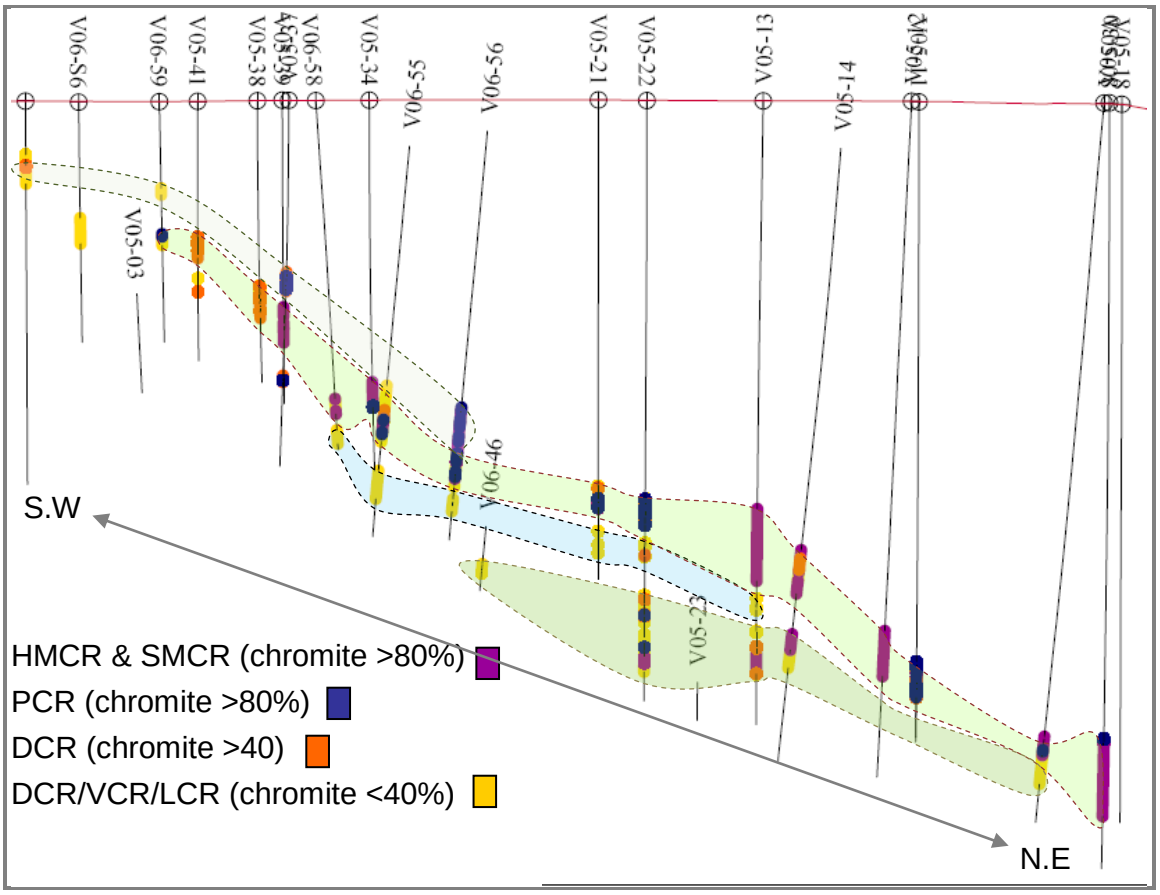

Figure 5.1.4 Cross section 1 - southwest to the northeast of the ore body (CS1).

The ore body dips at approximately 35° to the north east. The CS1 traverse intersects the western fringe of the ore body. Hard massive chromite (HMCR) - purple, soft massive chromite (SMCR) - purple and powdery chromite (PCR) – dark blue are ore types where chromite comprises more than 80% of the rock. For the purpose of modelling the other ore types vein- (VCR), lens- (LCR) and disseminated chromite (DCR) ore types were divided into two groups based on the percentage chromite content, of the rock mass, over a given interval. Greater than 40% chromite is coded orange and less than 40% chromite, yellow. The broken line shapes outline compositionally similar ore units present at similar depths. Created by the author using Surpac software.

The grade and thickness of mineralisation is greatest in the central region of the ore body, illustrated by drill cores V05-13, -22 and V06-56. The style of mineralisation varies throughout the ore body, from the centre to the periphery, as

well as with stratigraphic depth. It is common for there to be an interval of weakly disseminated chromite (<40% chromite) at the base of massive chromite. This may be immediately adjacent to the massive chromite mineralisation or separated by a unit of barren dunite. Typically the first appearance of mineralisation down hole is of massive chromite (purple or dark blue). Extensive drill core data collection and subsequent modelling of the relative proportions and relationships between the ore types, demonstrates that the deposit is not a singular, continuous massive chromite body. Instead, the mineralised intersections appear to link together forming a connected network. It has previously been documented that Voskhod is comprised of a series of stacked lenses (*Herrington et al., 200*5), modelling of the drill core data supports this. It is possible to connect similar styles of mineralisation present at similar depths and outline potential ore lenses, these may lie directly on top of one another or be separated by dunite (Figure 5.1.4).

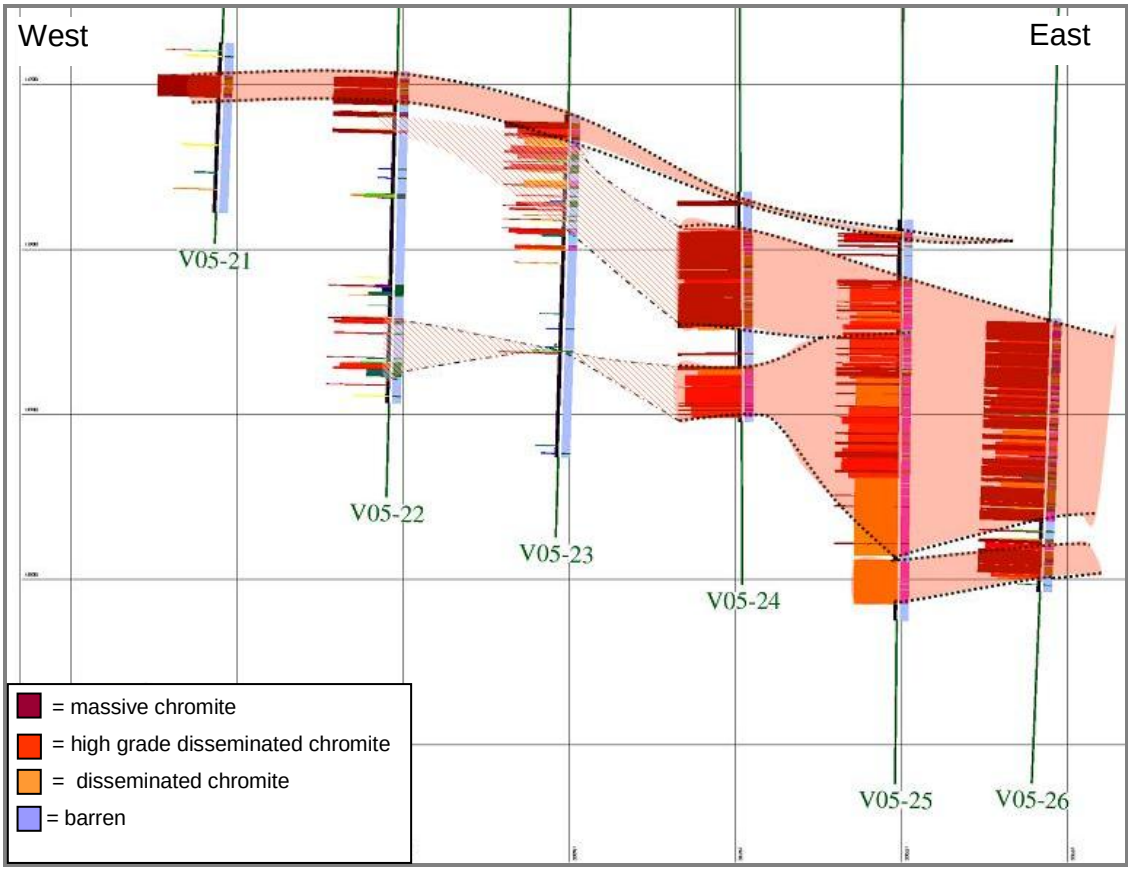

Figure 5.1.5: Cross section 2 (CS2) west-east cross section through the centre of the ore body.

Key as in Figure 5.1.4. The dashed outlines around selected mineral horizons indicate possible network relationships between neighbouring drill core mineralised sections. The small black dotted line with red shading represents network connections where the interpretation is confident. The dot-dashed black lines filled by oblique red stripes drawn to the west of the section indicate that the degree of confidence is less. Created by the author using Surpac software.

At the centre, verging towards the eastern margin of the ore body, is the most intensely mineralised region of the Voskhod deposit, drill holes V05-24, -25 and -26 (Figure 5.1.5). In drill cores V05-24, -25 and -26 more than one mineralised interval is identified. The start and end mineralisation contact in these drill cores is sharp. In contrast, to the west, the mineralisation present in drill cores V05-23 and -22 is comprised of numerous, comparatively small-scale, weakly mineralised intervals that are inter-layered with barren dunite and the cessation of mineralisation is gradual.

Figure 5.1.4 and Figure 5.1.5 show that unlike a stratiform chromite body the multiple 'layers' of different ore cannot be easily correlated between different drill holes. There is very little lateral continuity; rather the deposit seems to exhibit a spongiform structure with parts composed of massive ore surrounded on all sides, vertically and laterally, by less mineralised zones with higher silicate content.

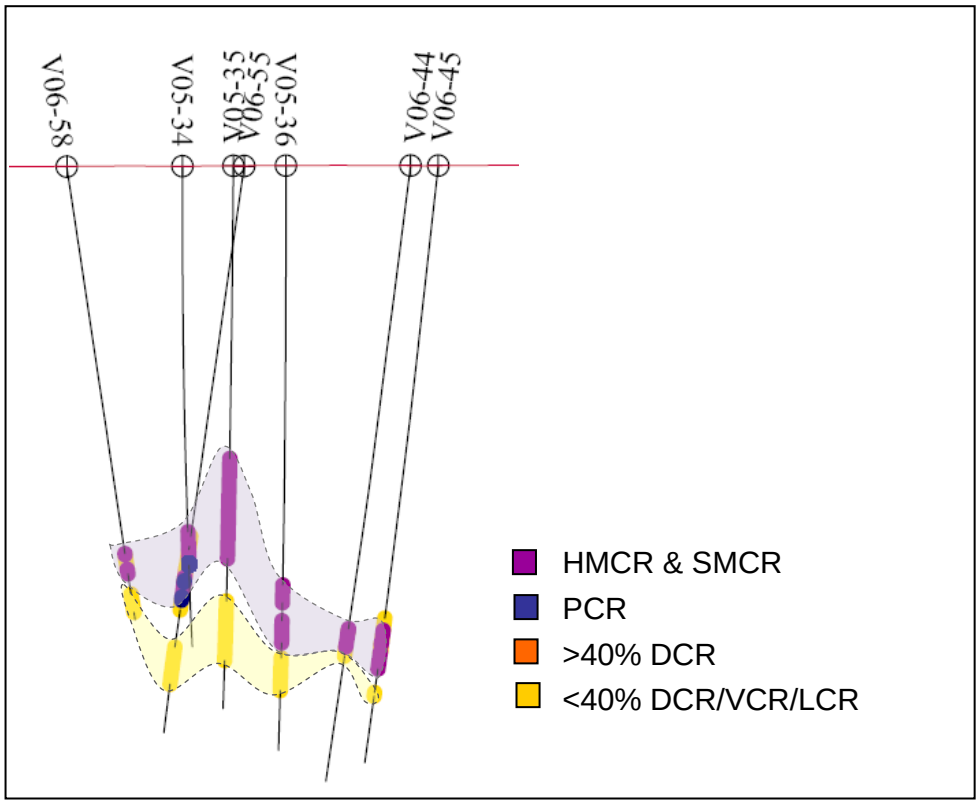

Figure 5.1.6 Cross-section 3 (CS3). East – west cross section south of the centre of the ore body south of CS2.

Key as in Figure 5.1.4. The broken line outlines identify two mineralised intervals. A stratigraphically higher, massive chromite horizon, shaded purple and a second, lower horizon of disseminated chromite that underlies the massive chromite, shaded yellow. Created by the author using Surpac software.

From the south to the centre of the ore body two intervals of different types of mineralisation are observed; a unit of massive chromite overlies disseminated chromite. At the edge of the ore body, drill holes V06-44, -45 and -58, the units are in contact, while towards the centre, a section of barren dunite separates the two intervals (Figure 5.1.6).

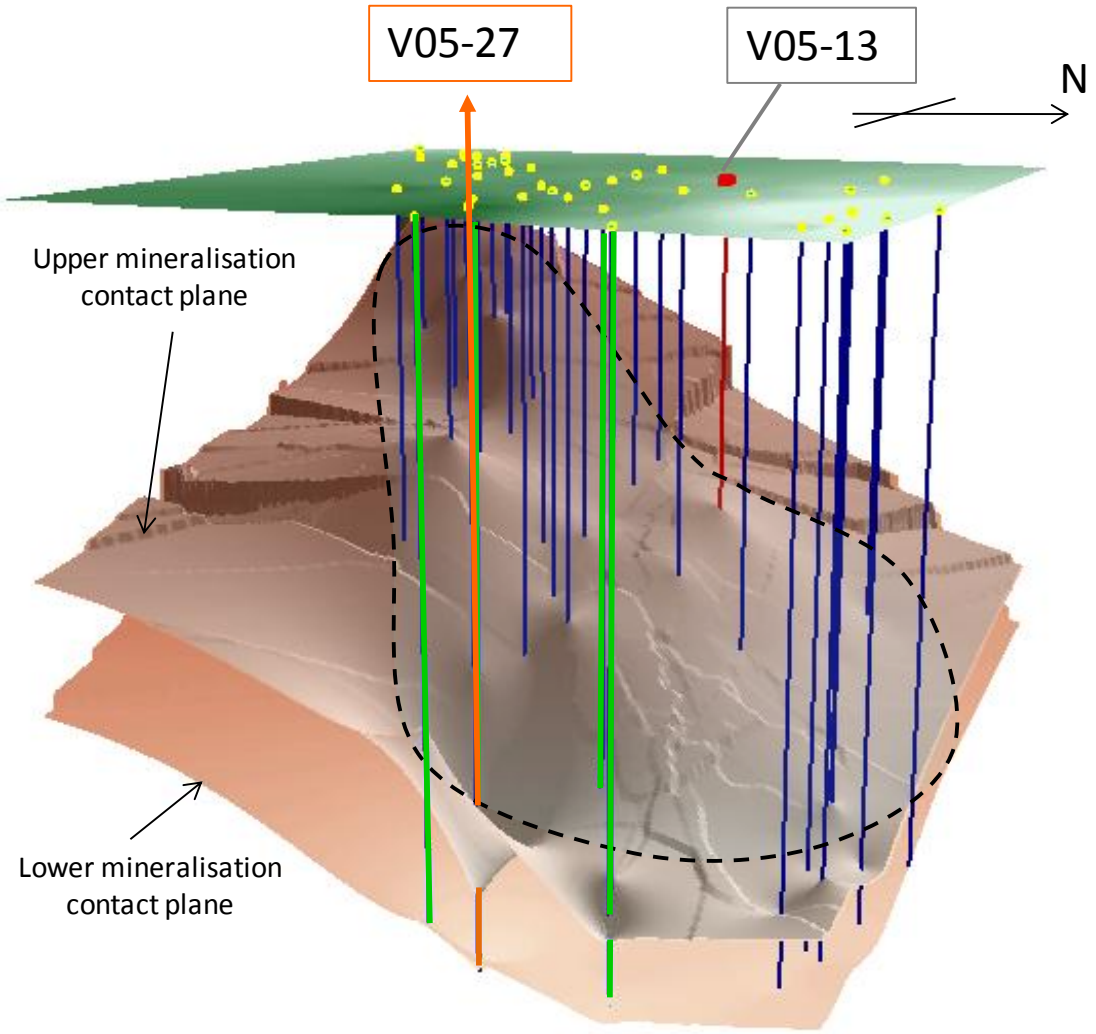

Figure 5.1.7: A 3.D schematic of the Voskhod chromite deposit ore body with drill holes produced by the author using Arc GIS software package.

The ore body model (Figure 5.1.7) shows i) the surface expression of the licence area and drill collar locations, ii) an upper plane that defines the start of mineralisation and iii) a lower plane representing the end of mineralisation. The ore zone, determined by a 20% Cr_2O_3 cut-off grade, is outlined by the black broken line shaded blue. The terrace features present at the edge of the diagram result from the interpolation of the data and are artefacts of the Arc GIS modelling program used.

The ore body outline is shown as a 3.D schematic with drill collars, drill holes and projections in Figure 5.1.7. Drill hole V05-27 did not intercept mineralisation, this is marked by a noticeable depression in the upper contact plane in Figure 5.1.7 (drill hole V05-27 is shown in orange). However, the four closest neighbouring drill holes; V05-02 (north), -20 (southwest), -26 (west) and -28 (east) are each

extensively mineralised with; 70 m, 88 m, 109 m and 113 m of chromitite respectively (shown in green). In fact, the extensive mineralisation reported in the area surrounding V05-27 forms the most ore-rich zone of the ore body. This observation is testament to the irregular, spongiform texture of the Voskhod chromite ore body and the one dimensional nature of sampling offered by drilling.

5.2 Mineralogy of the hanging wall and footwall ultramafics

The rock classification used is based on mineralogical modal proportions of olivine, chromite and clino- and orthopyroxene as shown in Chapter 2 Section 2.1.1. For the purposes of drill core logging a series of lithological codes and associated descriptions were produced. These are described below.

5.2.1 Overburden (OVB)

Several material types are included under this category, including; i) dark brown soil, ii) light khaki to ochre rubbly clays, iii) brown silt to sand grain size, clay, iv) rubble horizons consisting of disaggregated bedrock, v) rubble horizons containing fragments of bleached, light grey rock fragments that are porous, exhibit box-work cavities or are silicified, vi) loose sand with well rounded, well sorted grains and vii) fluviatile gravels.

5.2.2 Dunite (DUN)

Unaltered dunite is fine grained, dark grey to black, possessing a granular texture with no internal structure (Figure 5.2.1 a). Microscopy reveals relict olivine crystals set in a serpentine matrix, with fractures frequently filled with pale green or white lizardite. These fractures appear randomly orientated, are 5-8 mm thick and constitute <2 % of the modal volume. Additionally, small (3-5 mm) phenocrysts of orthopyroxene (or when altered, bastite) locally constitute 2-3% of the rock volume. The concentration and size of the phenocrysts gradually increases when the dunite units grade into harzburgite (HARZ).

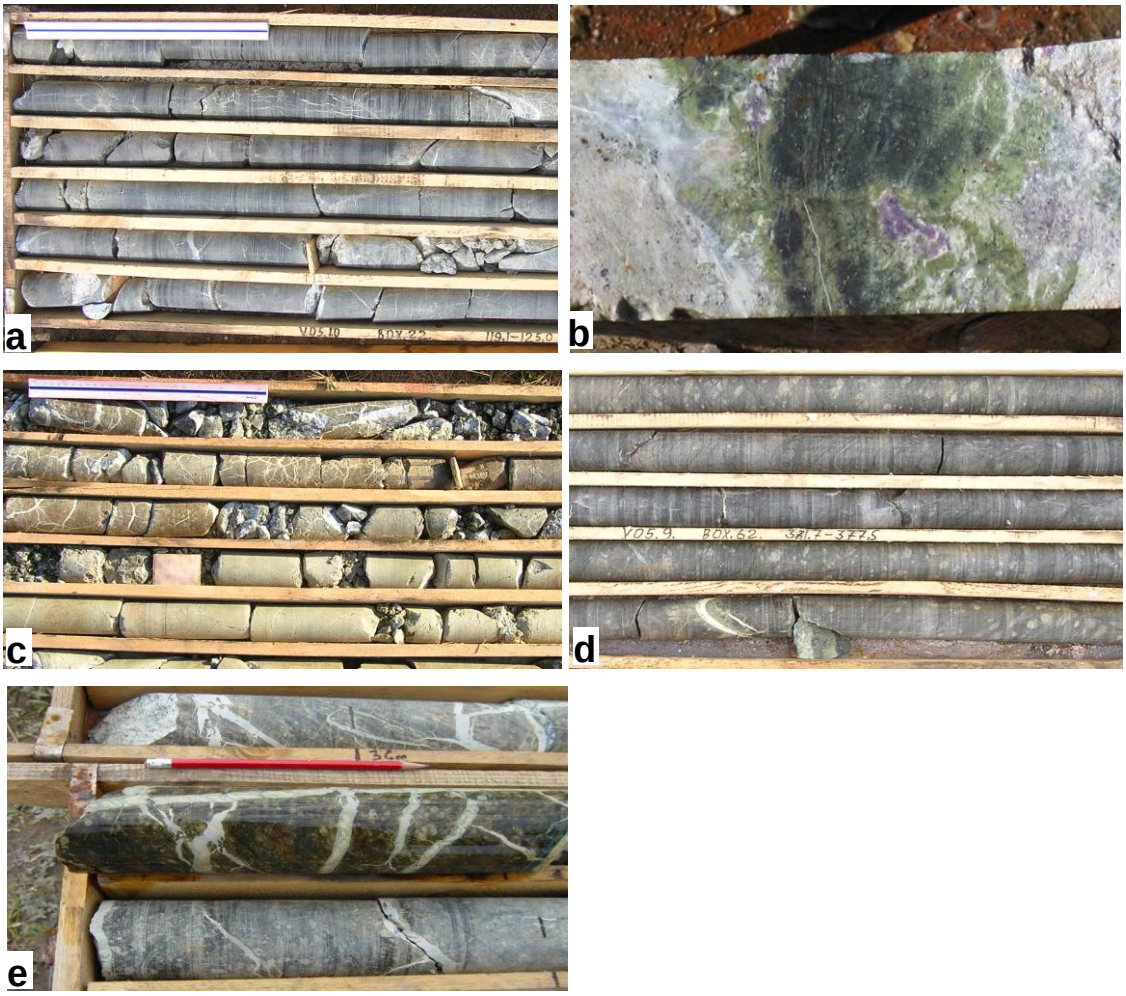

Figure 5.2.1: (a) Dunite (DUN), (b) grey serpentinised dunite (ADUN) with green dunite and purple kammererite, (c) bleached pale brown – cream altered serpentinised dunite (ADUN), (d) Harzburgite (HARZ) with porphyroblasts of orthopyroxene visible and (e) Altered harzburgite (AHARZ) with intense white lizardite veins.

A 30 cm ruler is shown for scale in (a) and (c).

5.2.3 Altered Dunite (ASDUN)

The extent of dunite alteration varies throughout the hanging wall, footwall and barren horizons within the ore body. Altered serpentinised dunite is present within and immediately adjacent to the mineralized zone, it is altered to a pale grey with centimetre sized regions of vivid green dunite often present, the rock is competent, fine-medium grained having a smooth powdery texture (Figure 5.2.1 b). A dunite

halo is a characteristic of podiform chromite deposits (e.g. *Thayer, 1964*). The Voskhod deposit dunite halo, composed of ADUN, ranges from <1m up to 3m in thickness. This type of altered dunite hosts the vein chromite (VCR) and disseminated chromite (DCR) mineralisation.

As the degree of alteration increases the ADUN rock is bleached pale brown to cream, has a very fine, powdery texture and poor rock competency that is characterised by intense fracturing (Figure 5.2.1 c). Where alteration is most intense the alteration of serpentine produces a powdery, cream-white smectite clay mineral assemblage.

Accessory minerals present in altered dunite include crystalline growths of bright green tremolite [$Ca_2(Fe^{2+},Mg)_5Si_8O_{22}(OH)_2$] and purple kammererite [$(Mg,Fe^{2+},Cr)_5Al_2Si_3O_{10}(OH)_8$] (the chromian-rich variety of clinochlore) (Figure 5.2.1 b). Veins of pale green and white lizardite, ranging from 2mm to 1 cm thick, are common in all cases of serpentinised dunite and altered serpentinised dunite.

5.2.4 Harzburgite (HARZ)

The hanging wall, and less obviously so the footwall, are comprised of a series of alternating harzburgite and dunite units. The harzburgite (HARZ) groundmass is olivine, comprising ~85% of the rock volume, it is grey, medium grained with a granular texture. The distinguishing feature of the harzburgite is the notable increase in the abundance and size of orthopyroxene porphyroblasts (crystals can be as large as 1.5 cm) that constitute >10% of the rock volume (Figure 5.2.1 d).

5.2.5 Altered Harzburgite (AHARZ)

Altered harzburgite (AHARZ) is present in the uppermost 65 m to 100 m of drill core, it is a pink-buff rock and centimetre-scale blue-black patches are common giving the rock a mottled appearance. Large (up to 1.5 cm) altered orthopyroxene phorphyroblasts (bastites), indicate that the harzburgite is altered. An abundance of highly irregular, randomly oriented lizardite veins cross-cut the AHARZ units. Veins range from 1 mm to 10 mm thick, consist mainly of white lizardite and in

some places exceeds 10% of the rock mass composition. They probably formed during the volume expansion process that is typically associated with serpentinisation. When veining is sufficiently intense a stockwork forms.

5.2.6 Alteration processes

The close relationship between the alteration and the development of veining (AHARZ) in the upper section of the hanging wall (the initial 65 m to 100 m of hard bedrock drilled) suggests that the two features are related by a common process. Several explanations have been proposed (*pers.comm. K. Alexander, Voskhod site geologist)*;

(i) A deep penetrating surface weathering event that altered and bleached the harzburgite and formed lizardite veins at low temperatures.
(ii) A localised hydrothermal event, spatially related to an overlying thrust zone, created brittle fractures.
(iii) Intense serpentinisation of the dunites and harzburgites causes brittle failure generating an intense fracture network. Bleaching of the rocks may be attributed to recent groundwater movement percolating through the units. However, if this is the case, the process has been selective as not all horizons have been affected.

5.3 Petrology of the hanging wall and footwall ultramafics

5.3.1 Dunite and altered serpentinised dunite

In the DUN and ASDUN rock types the degree of serpentinisation varies between 60% to 80% and >80% respectively. Serpentinisation forms the characteristic mesh-texture and relict olivine grains may be present at the centre, although many grains have been completely altered. Fine <1 mm veins of chlorite (e.g. Figure 5.3.2, V05-24-328) and lizardite cross-cut the dunite.

The intensity of serpentinisation increases down-hole with proximity towards the ore body. Accessory chromite (typically ~3%) is dark red/orange-black in plane polarised light; this colour is characteristic of high-chromium chromites.

The multiple bright birefringence colours of the olivine suggests that these relict grains have not crystallised under high strain conditions. Similarly, the mesh textures and grain fracture network are not aligned. There is a no evidence of a foliation in these units.

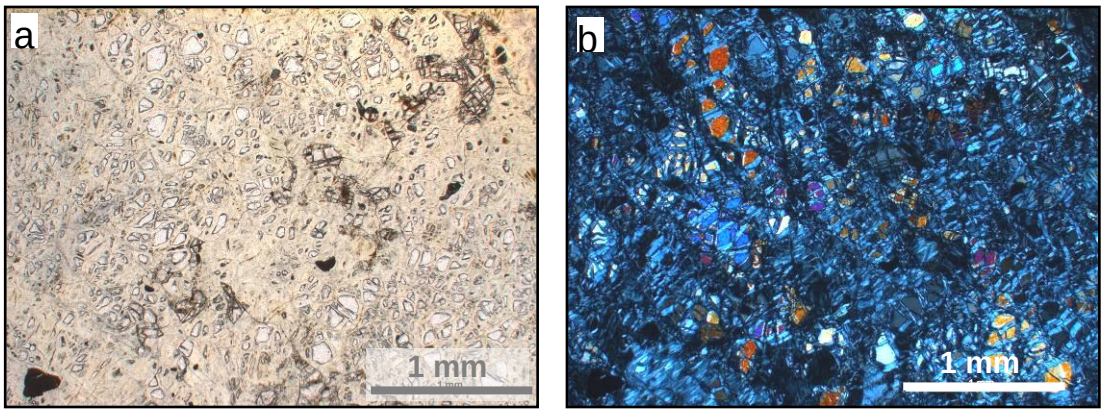

Figure 5.3.1: Dunite (DUN)

Sample V05-24-348, ~70% serpentinised dunite: a) plane polarised light, b) cross-polarised light The preserved olivine relicts at the centre of the mesh textures display characteristic, second order, bright birefringence colours.

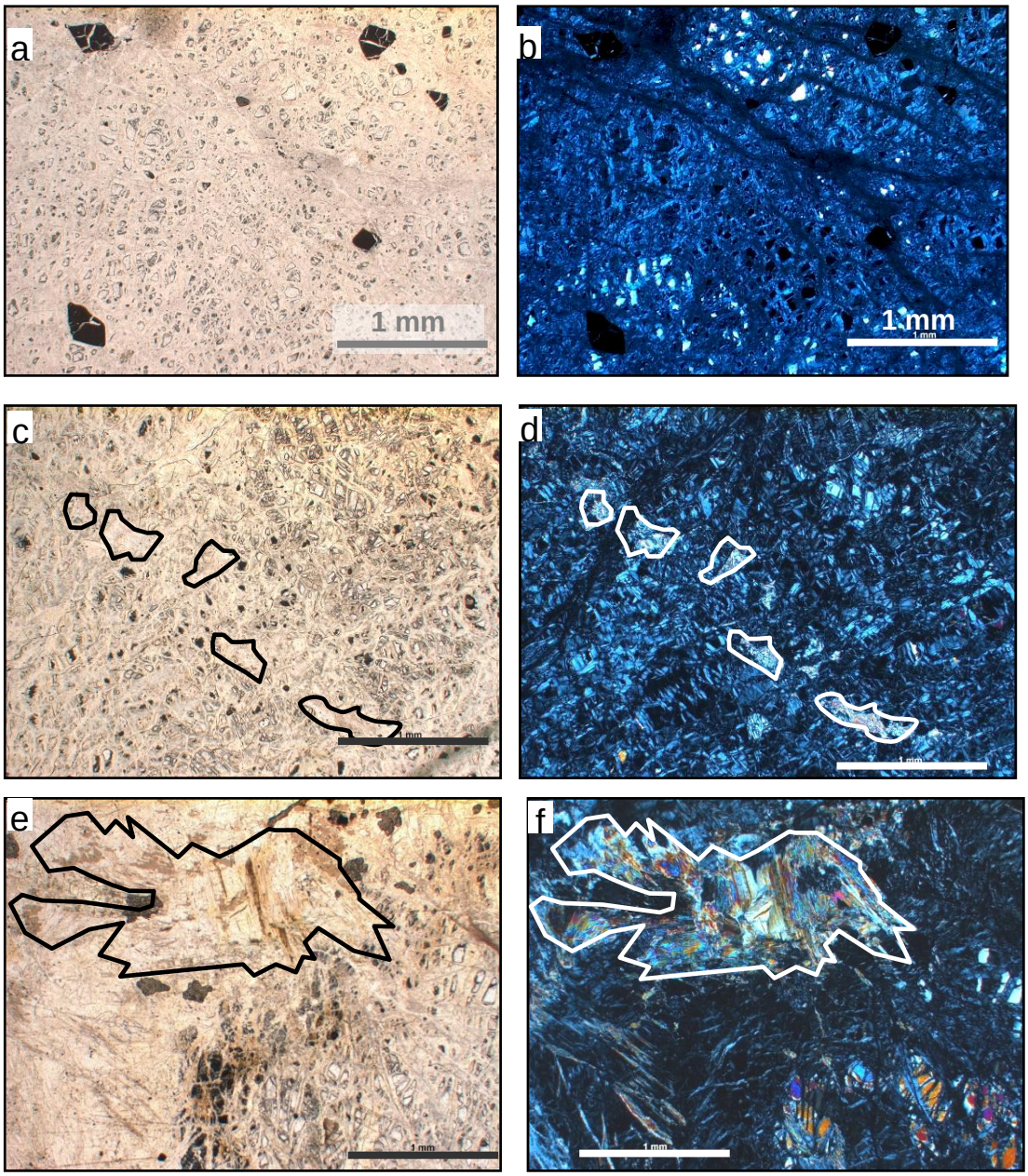

Figure 5.3.2: Altered serpentinised dunite (ASDUN)

(a) and (b) Sample V05-24-328: ~85% serpentinised dunite from the dunite halo at 375.00 m, of the Voskhod chromite ore body. A serpentine mesh texture dominates the thin section and microfractures are filled with serpentine. Euhedral chromite grains comprise ~5% of the rock. (c) and (d) Sample V05-24-301: ~85% serpentinised dunite from a dunite horizon at 249.53 m in the hanging wall of the ore body. A serpentine mesh texture is pervasive and micro-fractures are filled with serpentine. The small (<1 mm dimension) patches of a bright birefringence colour, platy mineral is actinolite, this constitutes <5% of the rock ground mass. (e) and (f) Sample V05-28-G1631: >90% serpentinised dunite from within the ore zone at 434.40m, extensively altered and deformed. The area of bright birefringence, fibrous mineral growth in the centre top of (f) is actinolite. To the bottom right are relict grains of olivine with bright, high birefringence colours.

5.3.2 Harzburgite

Serpentinisation of the harzburgite sections is >80% evidenced by serpentine mesh textures and 'bastites' formed from the alteration of orthopyroxene porphyroblasts (Figure 5.3.3). Of the original, unaltered mineral phases relict olivine constitutes ~20% and orthopyroxene ~5%. In some cases, an alteration selvedge surrounds the orthopyroxene porphyroblasts (Figure 5.3.3 b and f). In section DH-219A this halo is comprised of low temperature amphibole displaying bright birefringence colours (Figure 5.3.3 f). In section V05-24-327 the halo mineral is green in plane polarised light, displays low birefringence colours in crossed polarised light and is considered to be chlorite (Figure 5.3.3 b).

Prior to alteration the approximate modal composition of the harzburgite would have been 80% olivine, 15% orthopyroxene and up to 3% chromite and 2% clinopyroxene. The chromite grains vary from being pale golden and translucent (characteristic of high alumina-chromites) to deep red or brown-black (high chromium-chromites) in plane polarised light. Chromites, with diameters of up to 1 mm, are sometimes partially altered to ferrit-chromite or magnetite at the grain edges, these appear opaque in plane polarised light and are surrounded by chlorite e.g. DH 219A (Figure 5.3.3 e).

Evidence of a lineation fabric may be identified in some samples by the alignment of orthopyroxene porphyroblasts (bastites when altered), chromite grains and shear-foliated serpentine mesh textures e.g. DH-219A (Figure 5.3.3 e and f). Olivine grains in the serpentine mesh centres that display bright birefringence colours at different angles, when rotated under cross-polarised light, indicate a sheared foliation texture rather than a cumulate magmatic texture (Figure 5.3.4).

Pull apart textures are observed in the bastites and the resulting fractures are orientated perpendicular to the direction of the fabric lineation (e.g. sample DH 219A, Figure 5.3.3 e and f) or exploit the orthopyroxene crystal structure along the mineral cleavage plane (e.g. sample V05-24-327 Figure 5.3.3 a & b).

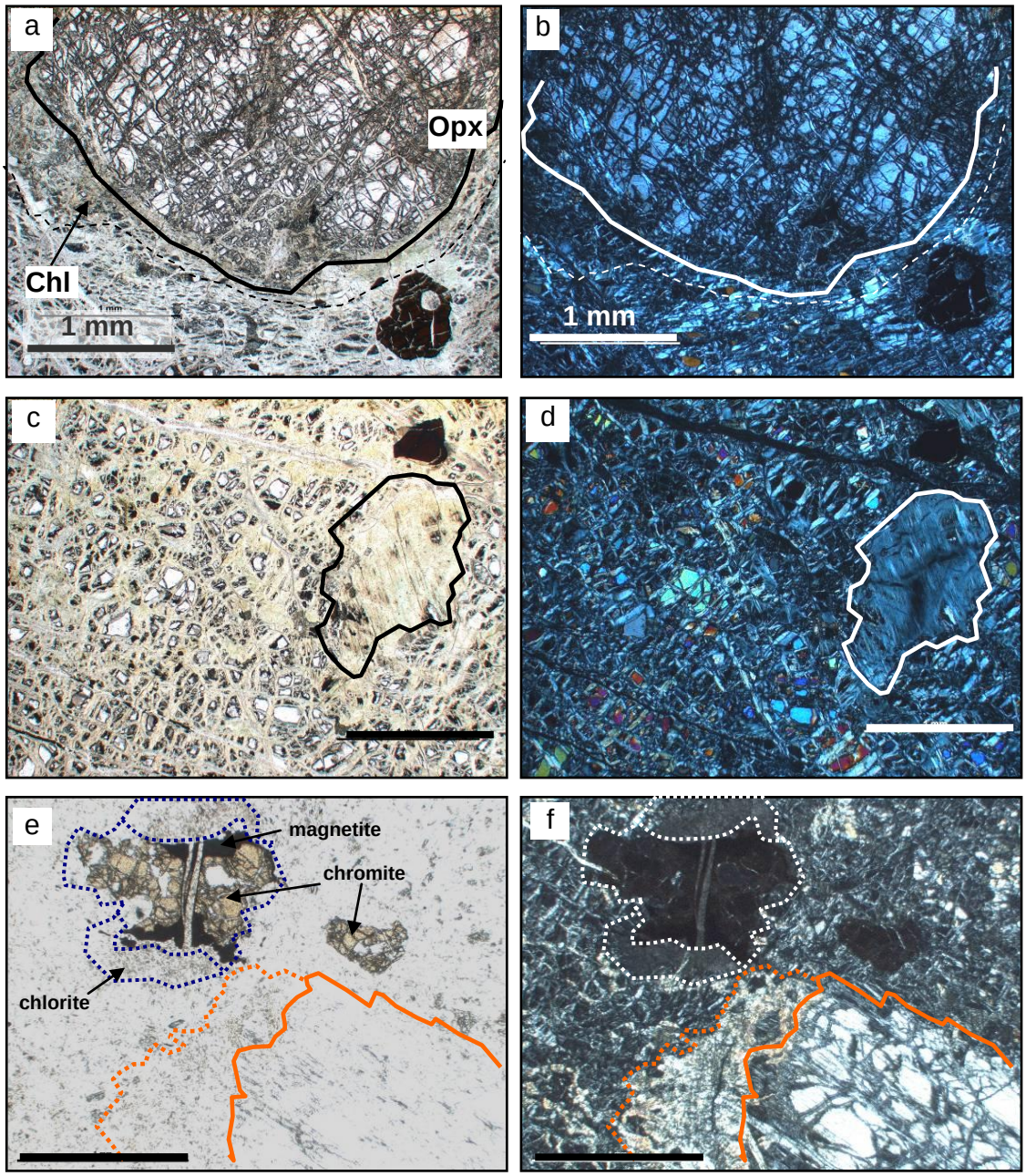

Figure 5.3.3: Harzburgite

(a) and (b) Harzburgite sample V05-24-327: a fractured, orthopyroxene (opx) porphyroblast selvedged by chlorite (chl), set in a serpentinised olivine groundmass (with <5% relict olivine) to the bottom right is a a subhedral chromite grain; (c) and (d) Altered harzburgite, sample V06-S6-179: right of centre is an altered pyroxene 'bastite' crystal, to the top right is a euhedral chromite grain, a serpentine mesh texture is present across the slide (~30% relict olivine); (e) and (f) Altered harzburgite sample DH 219A: in plane polarised light (e) An anhedral chromite grain partially altered at the edges to magnetite and chlorite and in cross polarised light (b) extensive serpentine alteration (>90%) with no relict olivine grains, bottom right is a fractured pyroxene porphyroblast partially selvedged by an amphibole halo. (Scale bar = 1 mm)

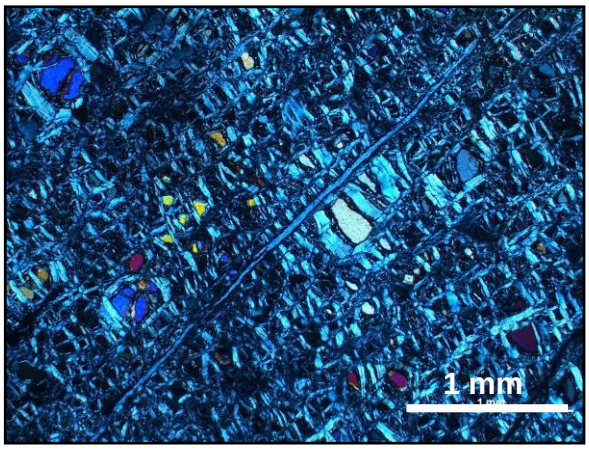

Figure 5.3.4: Altered harzburgite showing a shear foliation texture

Sample V05-24-327: Relict olivine grains (~25%) of differing birefringence colours indicate a shear foliation texture. (Scale bar = 1 mm)

5.4 Chromite grain types

A variety of chromite grain morphologies are seen developed in the harzburgite and dunite rocks where chromite is an accessory phase (see Chapter 3, Section 3.6.1). In contrast, the grains comprising the chromite ore are typically euhedral to subhedral. In the massive chromite ore grains are often densely packed and grain boundaries are difficult to distinguish.

5.4.1 Chromite grain morphologies in the harzburgite and dunite units of the Voskhod deposit.

Four chromite morphologies are identified in the Voskhod harzburgite and dunites; holly leaf and cuspate, subidiomorphic and euhedral. These correspond with the types identified and described in literature for the classification of ophiolite chromite (*Mercier, 1972; Dick, 1977; Augé, 1982; 1987*) (Chapter 3, Section 3.6.1).

Holly leaf chromite grains are uncommon, when present they appear as a transition phase seemingly half way between a holly leaf and cuspate grain, having smoother edges than are typical of the holly leaf shape, e.g. Figure 5.4.1 [d]. Cuspate chromite grains are characterised by smooth, intricate embayment features e.g. Figure 5.4.1 [a, b and c].

The holly leaf and cuspate morphologies are most prevalent in harzburgite, and dunite in the hanging wall and footwall. Subidiomorphic grains are most common in the dunite units, although occurrences in harzburgite are recorded (e.g. Figure 5.4.1 [e]). In the dunite halo and ore zone dunites, euhedral chromite is most common.

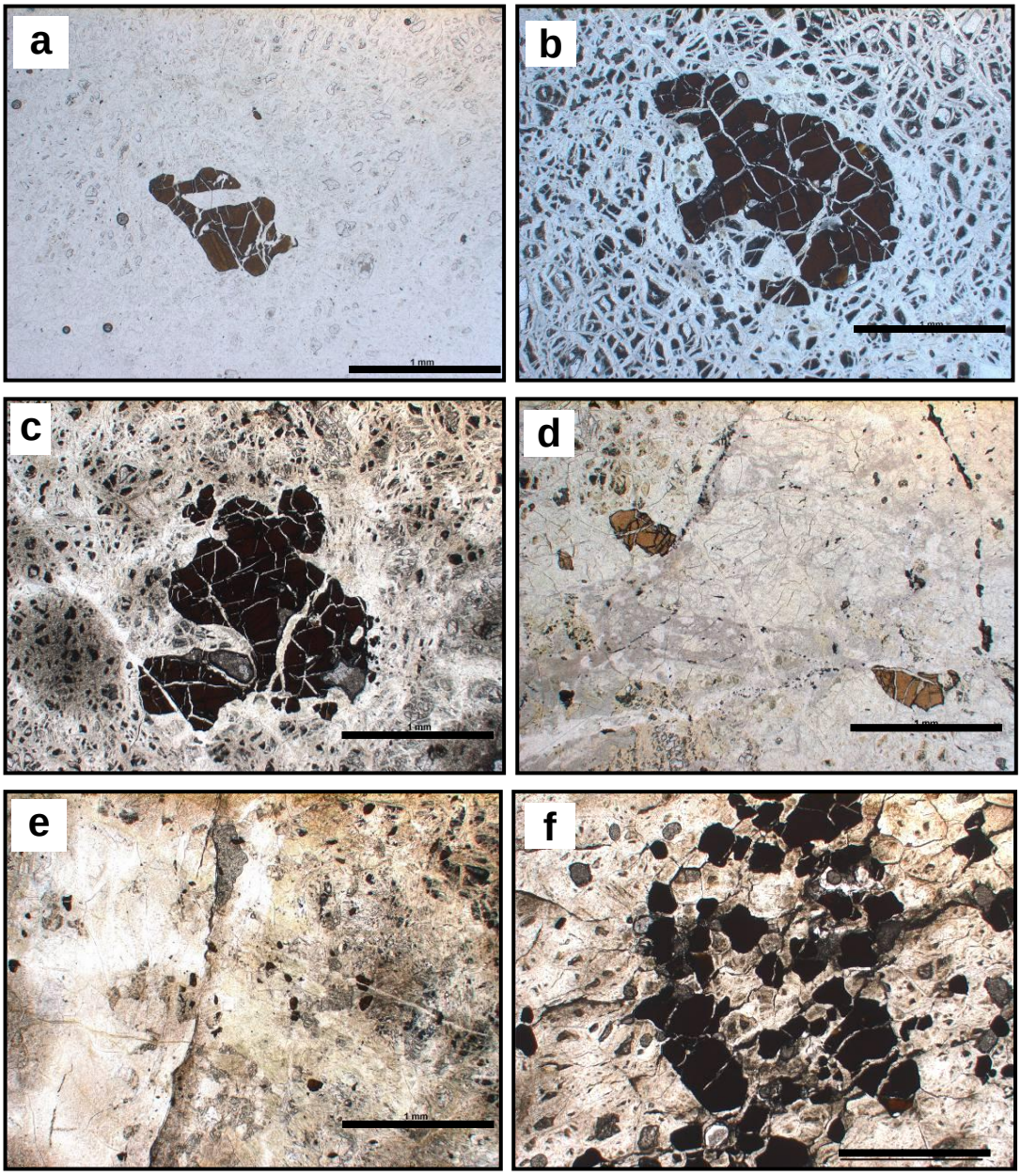

Figure 5.4.1: Cuspate, holly leaf and subidiomorphic chromites

(a), (b) and (c) Cuspate chromites; (d) holly leaf chromites; (e) and (f) subidiomorphic chromites. (a) V05-24-301 hanging wall dunite; (b) V05-24-306 upper contact dunite halo; (c) V05-24-309 upper contact dunite halo; (d) V05-24-341 footwall harzburgite; (e) V05-24-327 hanging wall harzburgite; (f) V05-24-F1971 ore zone dunite,. (Scale bar = 1 mm)

Subidiomorphic chromites range in size from small 10 µm (Figure 5.4.1[e]) to >1 mm. The grains are subhedral with rounded edges (*Auge, 1982*). Euhedral chromites have octahedral, hexagonal or cubic forms and rarely exceed 0.5 mm (Figure 5.4.2) (*Dick, 1977; LeBlanc et al., 1980*) In some sections two chromite morphologies co-exist within one slide, however, this is only observed in dunites (Figure 5.4.3 [d]).

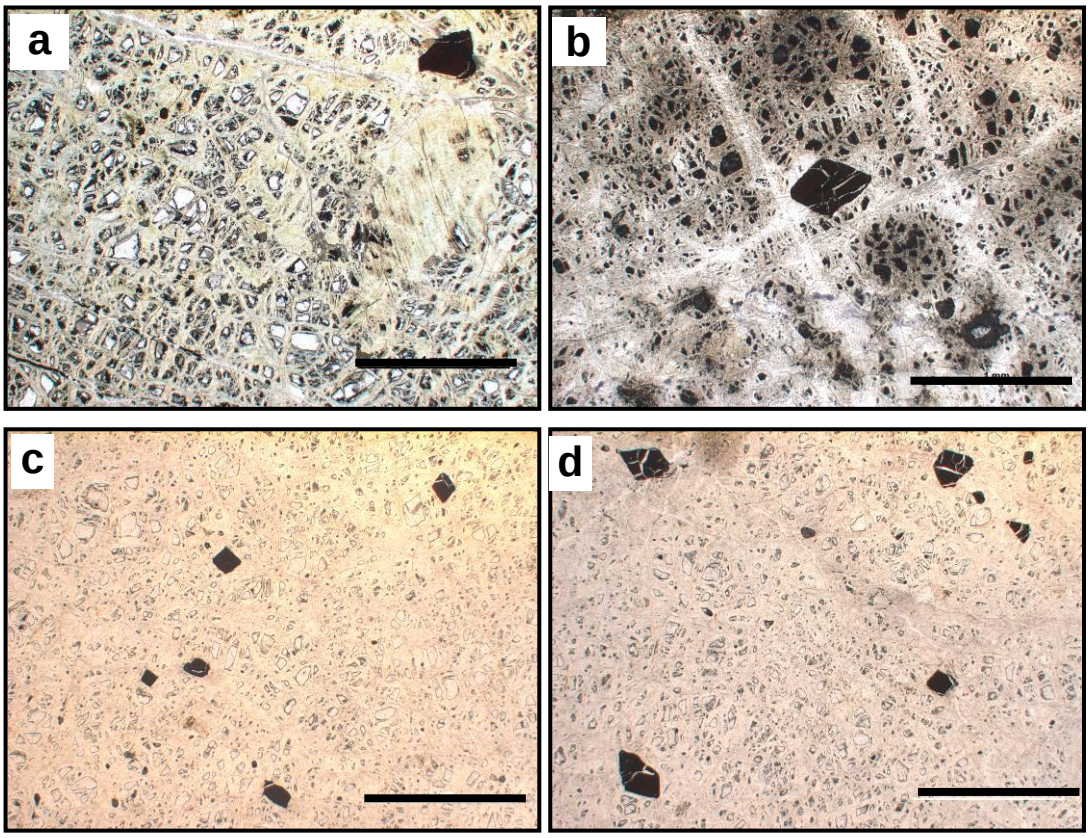

Figure 5.4.2: Euhedral chromites

Euhedral chromites (a) and (b) are from the hanging wall, samples (c) and (d) are from the footwall. Sample (a) is from drillcore V06-S6, while samples (b), (c) and (d) are from drill core V05-24.

(a) V06-S6-179 hanging wall dunite halo immediate prior to the start of the ore zone; (b) V05-24-309 hanging wall dunite halo; (c) and (d) V05-24-328 footwall dunite halo. (Scale bar = 1 mm)

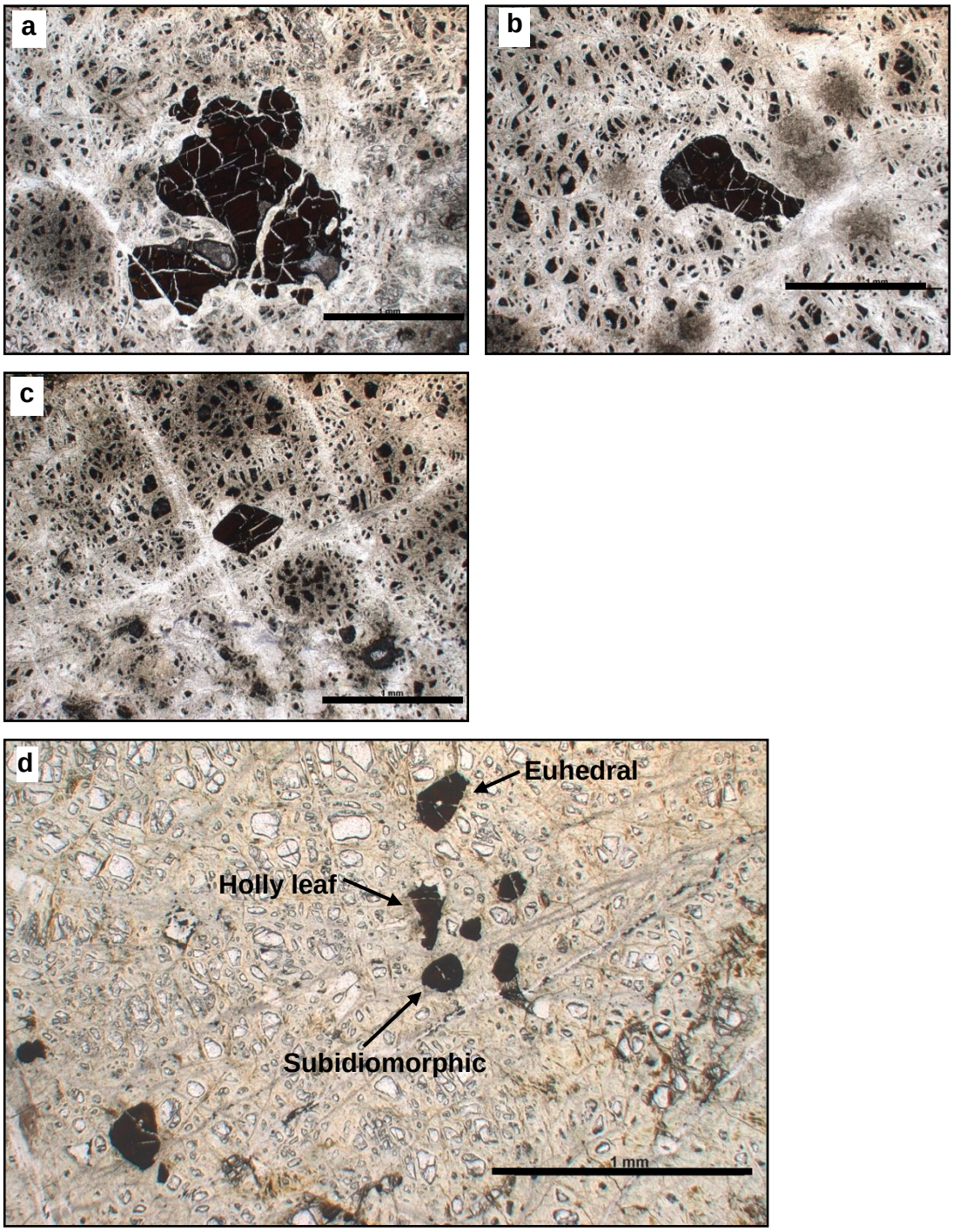

Figure 5.4.3: Co-existing chromite types in hanging wall dunite

(a-c) from V05-24-309 upper contact dunite halo; (a) holly leaf, (b) subidiomorphic and (c) euhedral; (d) V05-24-348 footwall dunite, co-existing holly leaf, subidiomorphic and euhedral morphologies. (Scale bar = 1 mm)

5.4.2 Poikilitic textures

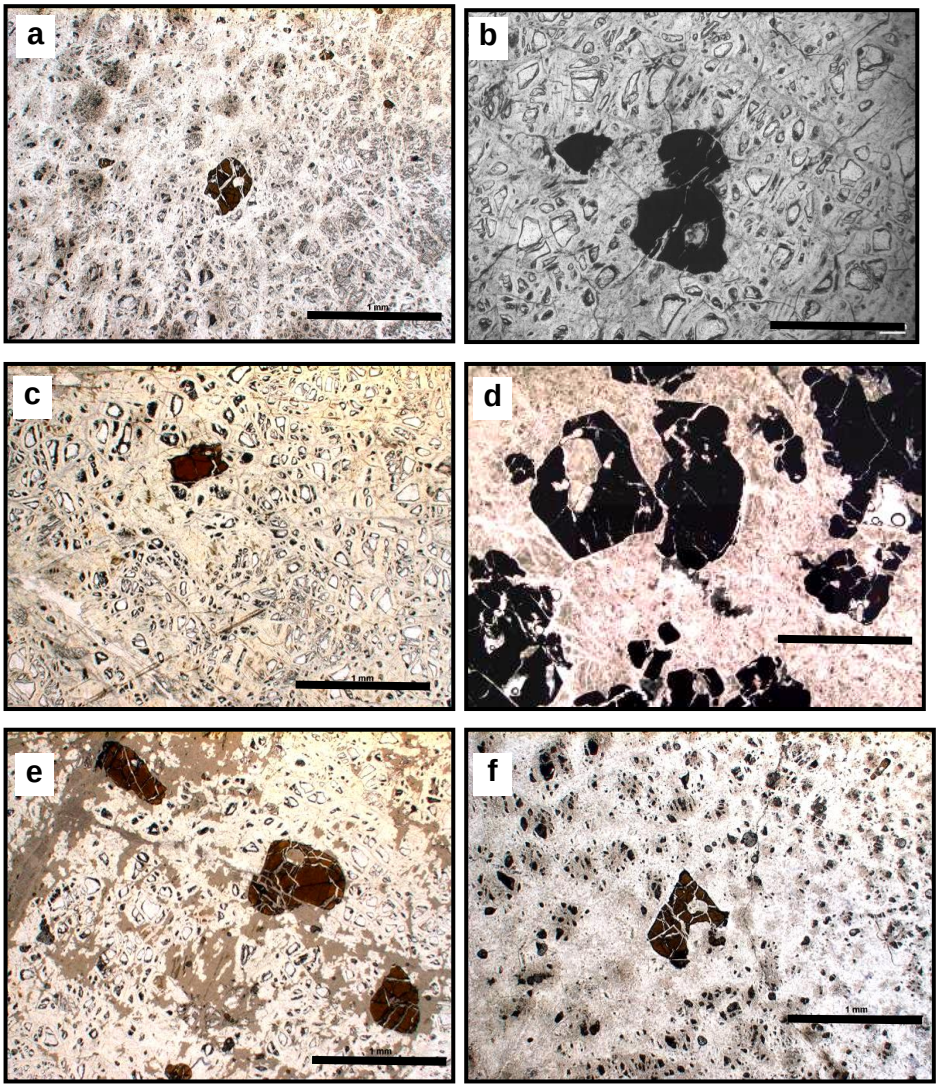

Figure 5.4.4: Poikilitic textures in holly leaf and subidiomorphic chromite types.

(a) V05-24-350 dunite footwall, (b) V05-24-F1907 upper contact dunite halo, (c) V05-28-G1601 hanging wall dunite, subidiomorphic chromite grain containing a single sub-rounded silicate inclusion; (d) V06-48-G1979 disseminated chromite ore (>40% chromite), subidiomorphic chromite with multiple, subhedral-angular, silicate inclusions; (e) V05-28-G1601 hanging wall dunite, subidiomorphic chromite with single sub-rounded-anhedral silicate inclusion; (f) V05-24-F1907 upper contact dunite halo, holly leaf-cuspate chromite with a single, rounded silicate inclusion. (Scale bar = 1 mm)

Poikilitic textures are commonly observed in holly leaf and subidiomorphic chromites from the Voskhod peridotites and dunites. Poikilitic chromites typically host one or more silicate inclusion (usually olivine). From the hanging wall and

footwall chromites studied, typically only a single, rounded silicate inclusion is present. However, dunite horizons from within the ore zone form subidiomorphic chromite that host multiple comparatively angular silicate inclusions (bottom left corner of Figure 5.4.4 b).

5.4.3 Recording the chromite morphologies of the Voskhod deposit

An intensive study of the chromite textures has not been conducted. However, based on the chromite grain morphologies identified, each sample analysed in this study was assigned to a category. These are presented in the data tables, Appendix B. The hanging wall and footwall harzburgite and dunite contain cuspate-holly leaf chromite, having concave embayment erosional edges. Subidiomorphic and euhedral grains (Figure 5.4.3), though less common in the hanging wall and footwall units are none-the-less present and may represent a second generation of chromite crystallised.

5.5 The Voskhod deposit chromitite ore types

The deposit Voskhod deposit is comprised of multiple chromite segregations encased in a dunite body. A variety of chromite ore types and textures were identified grading from barren dunites where chromite is an accessory phase (<5% chromite) to massive chromite comprised of >90% chromite. A classification criteria developed by Greenbaum (1977) to describe the range of chromite and olivine modal proportions common in chromitiferous rocks, given in Table 5.5.1, is used to distinguish between the Voskhod chromite ore types. However, this criteria alone is insufficient owing to the variety of ore textures observed. Consequently subcategories detailing textural features are presented for each ore type.

Chromite rock-type	**Modal proportion of chromite**
Dunite with accessory chromite	Less than 5% chromite
Chromitiferous dunite	5-50% chromite
Olivine-chromitite	51-90% chromite
Massive chromitite	More than 90% chromite

Table 5.5.1: Chromite rock classification criteria after Greenbaum (1977)

5.5.1 Massive Chromitite

Massive chromitite ore is comprised of more than 90% chromite with olivine, altered to serpentine, accounting for the remaining modal proportion (<10%). Sheared and brecciated zones of massive chromitite (Figure 5.5.1[d]) are often filled with serpentine, although in rare occurrences ferroan tremolite and kämmererite are seen. The ore comprises extensive zones of mineralisation up to 100 m thick. Three types of massive chromitite ore have been identified in the Voskhod deposit, these are; “Hard Massive Chromite”, “Soft Massive Chromite” and “Powdery Chromite”. These three ore types can be distinguished between on the basis of colour, chromite grain size and shape, as well as rock competence.

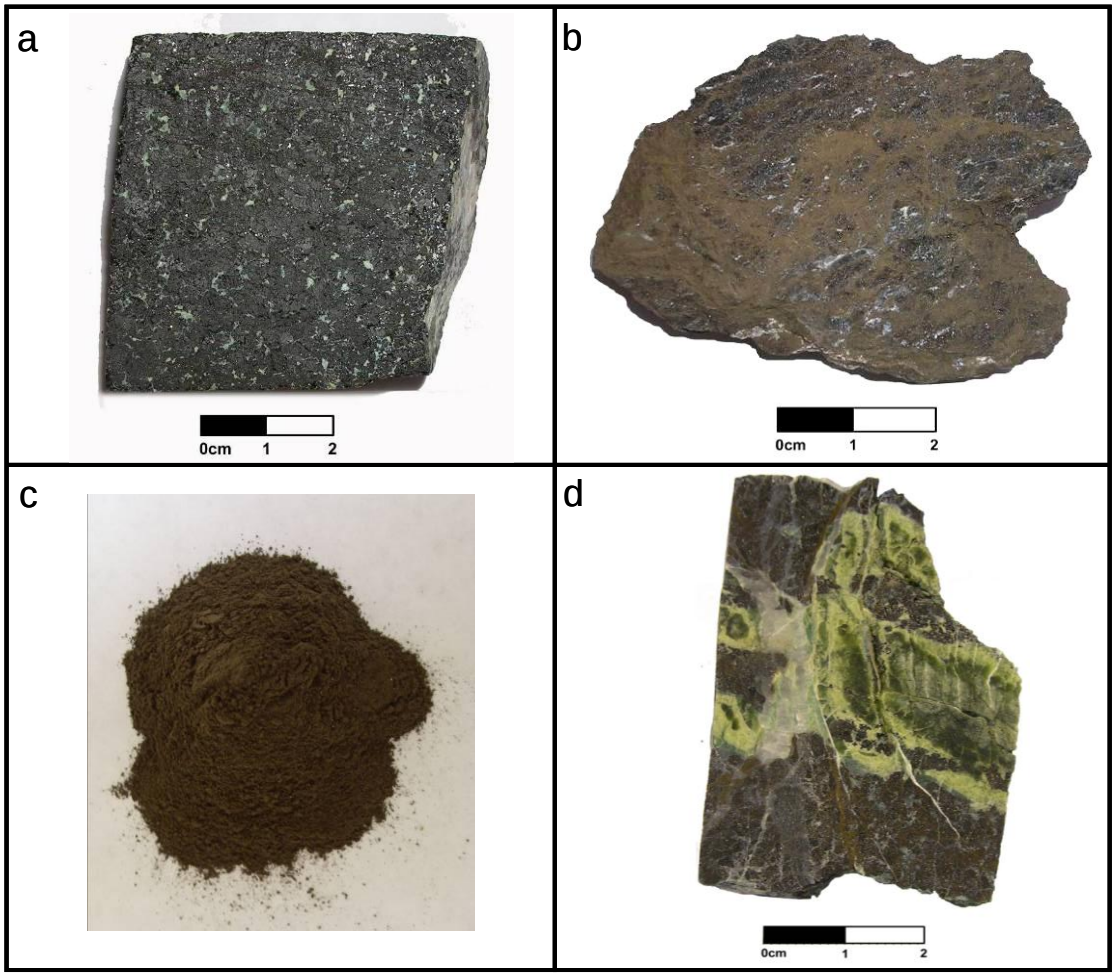

Figure 5.5.1: Massive chromite ore types

[a] hard massive chromite, [b] soft massive chromite, [c] powdery massive chromite and [d] brecciated massive chromite.

5.5.1.1 **Hard massive chromite (HMCR)**

HMCR ore is competent, dark grey-black, with a metallic lustre. It has a massive coarse granular texture with crystals ranging from 0.5-3.0 mm (Figure 5.5.1[a]). The whole rock Cr concentration is ~55% Cr_2O_3. Intersections of HMCR range from 20 cm to several tens of metres thick. Close to the base of HMCR intervals evidence of shearing and the development of a preferred fabric is common.

5.5.1.2 **Soft massive chromite (SMCR)**

SMCR is composed of a mixture of dull, mid-light brown, <1 mm ferrit-chromite grains and shiny, black, 0.5-1 mm grains of chromite (Figure 5.5.1[b]). This ore lacks competency and consists of poorly consolidated, small, competent fragments (1-3cm^2) that readily separate. The whole rock grade is ~55-60% Cr_2O_3.

5.5.1.3 **Powdery chromite (PCR)**

PCR ore is a fine grained (<1 mm wide), particulate ore that is silt-like, it has no structural integrity or competency (Figure 5.5.1[c]). The appearance varies from mid-brown, lacking lustre to grey-black with a metallic lustre. No silicate minerals are observed. In terms of ore grade, PCR is exceptionally high grade at > 60% Cr_2O_3 whole rock chemistry.

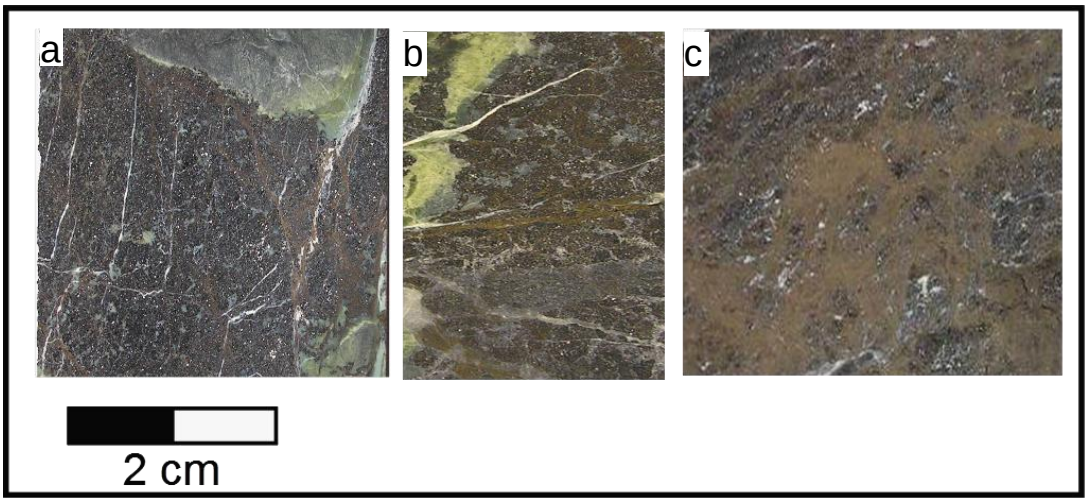

Figure 5.5.2: A micro-fracture network in HMCR ore: Alteration of chromite (black) to ferrit-chromite (brown).

An increase in the intensity of the micro-fracture network in HMCR and subsequent chromite alteration is seen from [a] to [c].

Studies of the three massive chromite ore types indicate that the formation of PCR seems to derive from a progressive sequence of physical disaggregation and chemical alteration of HMCR; HMCR → SMCR → PCR. The process involves the combined effect of structural deformation, resulting from stress events that create fractures in the HMCR ore, and subsequent chemical alteration by the introduction of fluids along the fracture network. This causes a dissociation of the chromite grains, sometimes altering the chromite to ferrit-chromite and dissolving the interstitial silicate minerals, which further reduces the rock competency.

5.5.2 Olivine-chromitite

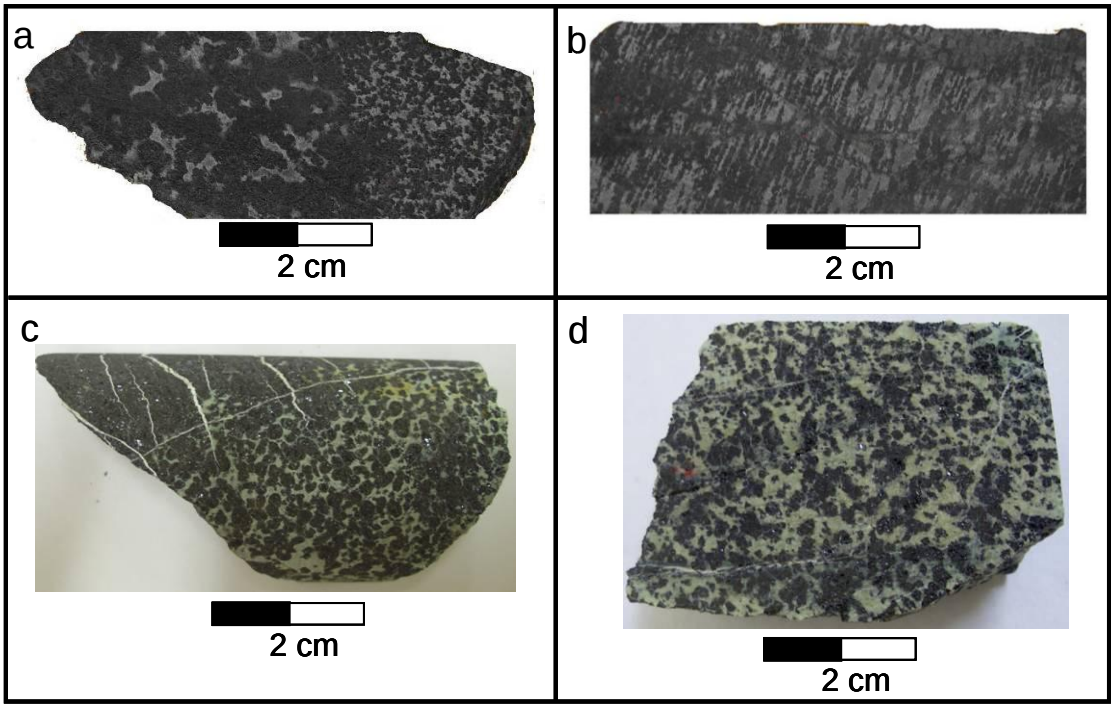

Figure 5.5.3: Olivine-chromitite ore types from the Voskhod ore body.

[a] Nodular, [b] spindle, [c] high-grade disseminated chromite grading into massive chromite and [d] high-grade disseminated chromite

Olivine-chromitite ore comprises 51-90% chromite. The remaining modal proportion is composed of olivine which, in the Voskhod ores, has been altered to serpentine. Olivine-chromitite ore sections form metre-thick (typically >5 m) zones within the ore-body. This style of mineralisation is most common in between massive chromite and dunite (barren) units. Three sub-types of olivine-chromitite

are present in the Voskhod deposit, these are; “nodular”, “spindle” and high-grade disseminated chromite ore. These three ore types are distinguished between by the shape and texture of chromite grain accumulations.

5.5.2.1 **Nodular chromite**

Nodular chromite ore is comprised of black, metallic, rounded to elliptical aggregates of chromite crystals present in a pale green-grey serpentinised olivine matrix. The nodules vary from 2 mm to 1 cm in diameter (Figure 5.5.3 [a] large nodules and [c] small nodules). There is no evidence, physical or chemical, of zoning in the nodules. The whole rock grade of this ore type is 45-55% Cr_2O_3. Nodular ore is rare in the Voskhod deposit, when present it occurs as narrow centimetre wide intervals located between high-grade disseminated chromite and massive chromite, e.g. Figure 5.5.3 [c], forming a densification, transition phase between these two ore types. A similar abrupt change in the style of chromite mineralisation is observed in Figure 5.5.3 [a] where aligned nodules (up to 1cm in diameter) sharply juxtapose high-grade disseminated chromite ore where the chromite shows no evidence of having a preferred orientation or fabric.

Although scarce in the Voskhod deposit, the nodular chromite texture is important to observe, as it is unique to ophiolite chromitite (*Thayer, 1960; 1964; 1969; Dickey, 1975; Greenbaum, 1977; Brown, 1980*)

5.5.2.2 **Spindle chromite**

Spindle chromite ore is characterised by thin, 1-3mm wide, elongate (up to several centimetres) bands of a chromite grains set in a serpentinised olivine (Figure 5.5.3 [b]). The bands are aligned parallel to one another forming a lineation in the rock. Wider bands appear to form ellipsoid shapes that may be genetically associated with nodular ore that has been subject to intense ductile-deformation resulting in the elongation and alignment of the chromite.

As with nodular chromite, spindle chromite is unusual in the Voskhod deposit and because of a lack of material it was not possible to study the composition.

5.5.2.3 **High-grade disseminated chromite (50-90% chromite)**

High-grade disseminated chromite is comprised of a mixture of individual black, metallic, euhedral chromite grains (1-2 mm wide) and angular grain aggregates (2 mm - 1 cm wide) set in serpentinised olivine Figure 5.5.3 [d]). The chromite grains and aggregates may link together to form chain network textures. This ore type typically forms thick metre scale horizons throughout which the modal proportion of chromite may vary between 50% and 90%, these horizons are typically located between massive chromite segregations. The whole rock grade is ~45-55% Cr_2O_3.

5.5.3 Chromitiferous dunite

There is only one ore type at Voskhod that fits the chromitiferous dunite category that is disseminated chromite. Olivine is the dominant mineral in this ore and technically the composition is a chromite dunite. However, when logging the mineralised intersections of drill cores the term disseminated chromite was used.

5.5.3.1 **Disseminated chromite (5-50% chromite)**

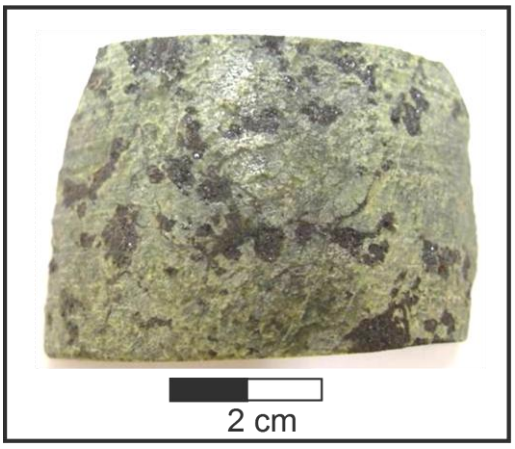

Figure 5.5.4: Chomitiferous dunite: Disseminated chromite

Disseminated chromite is prevalent throughout the Voskhod deposit. It is similar to high-grade disseminated chromite, the fundamental difference being the greater modal proportion of olivine. The ore is comprised of a mixture of individual black, metallic, euhedral chromite grains (1-2 mm wide) and angular grain aggregates (2

mm to 1 cm wide) set in serpentinised olivine (Figure 5.5.4). It is common for the aggregates to connect forming chains, while individual chromite grains tend to remain isolated in the olivine matrix. The ore type is most prevalent at the periphery of the ore body and is often the first form of mineralisation intercepted when drilling after passing through the dunite envelop. The extent of mineralisation varies forming both metre thick units and centimetre scale layers within barren dunite and massive chromite; furthermore, within a unit the modal proportion of chromite will range from 10-50%.

5.5.4 Dunite with accessory chromite

The dunite halo that encompasses the Voskhod ore body is composed of dunite with accessory chromite. Chromite accounts for less that 5% of the rock composition with serpentinised olivine forming the bulk of the mineralogy. Chromite grains are black, small (1-2 mm wide) and typically have anhedral-subhedral morphologies (Figure 5.5.5). In addition to the dunite halo, un-mineralised (barren) dunite horizons present within the defined limits of the ore body, separating the mineralised horizons, are composed of this rock type.

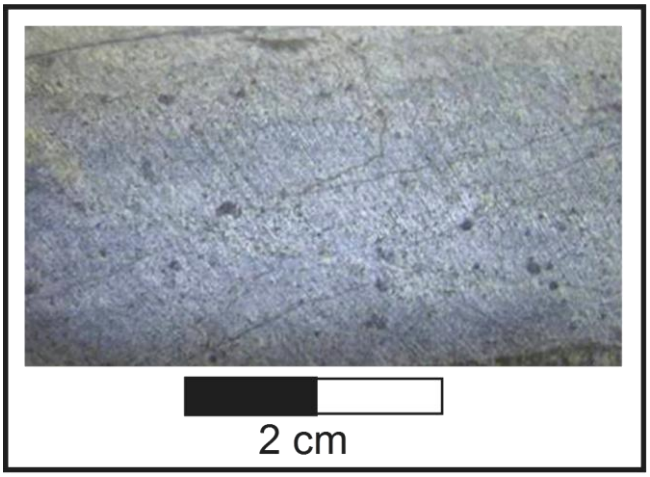

Figure 5.5.5: Dunite with accessory chromite

5.5.5 Vein and Lens Chromite

The Greenbaum (1977) classification addresses the relative mineral proportions of chromite and silicate in a chromite-bearing rock. However, in the Voskhod deposit

two additional categories have been developed these are “vein chromite” (VCR) and “lens chromite” (LCR). These forms of chromite identify intermittent occurrences of mineralisation present on a cm scale set within otherwise un-mineralised dunite.

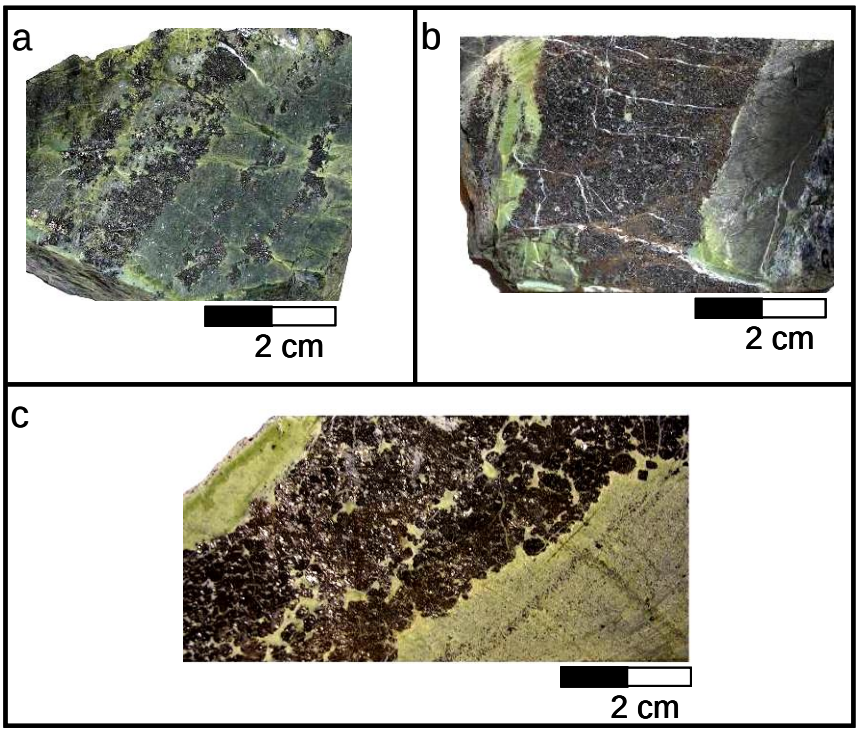

Figure 5.5.6: Vein chromite

[a] high-grade disseminate chromite veins, [b] massive chromite vein with altered serpentine (pale green) at the periphery of the dunite-chromite contact, [c] massive chromite vein, rounded small nodular aggregates can be distinguished along the contact edge and within the vein.

Vein and lens chromite form mineralised, bands ranging from 2 cm to 20 cm thick and may be comprised of massive chromite (Section 5.5.1) or disseminated chromite (Sections 5.5.2.3 and 5.5.3.1). They are often surrounded by a diffuse zone of altered serpentinised dunite that grades into progressively less serpentinised dunite, however, sharp edge contacts may also be seen, though are less common.

This style of mineralisation is typically found in the hanging wall and footwall of the ore body.

5.5.6 Reflected light petrology of massive chromite ore

In addition to being an extraordinarily large chromite reserve the Voskhod deposit contains unusually thick intersections of massive chromite mineralisation these can be as thick as 100 m.

Samples of massive chromite were studied under reflective light. Grain morphologies vary from euhedral to anhedral and sizes range from micron-scale (~0.10 mm) to >2 mm. The interstitial silicate mineral is serpentinised olivine. Observed features; grain boundary morphologies, grain organisation, inter-growth textures, compaction and annealing and silicate inclusions are described.

5.5.6.1 **Connecting grains: Contact grain boundaries**

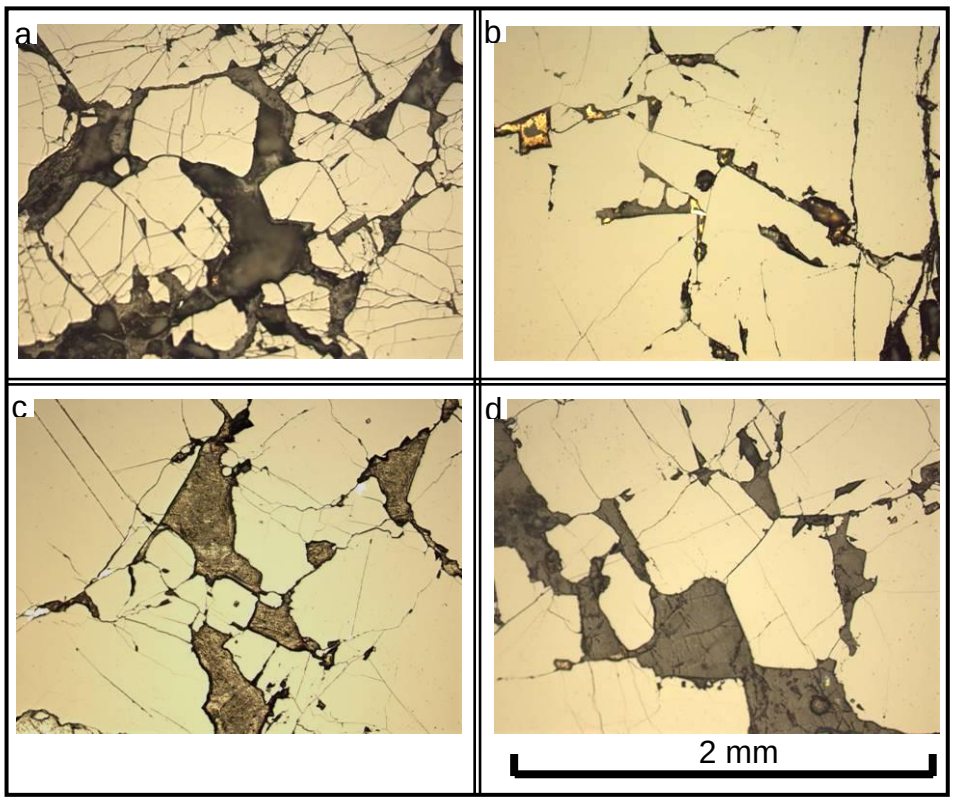

Figure 5.5.7: Connecting chromite grains present in interstitial silicate

[a] Two grains, one engulfing the other, are seen right of centre, to the left grains are linked along grain boundaries. [b] Two small subhedral grains in silicate, left of centre, surrounded by large, angular grains that lack clear grain boundaries. [c] A chain of subhedral to anhedral grains, in silicate, linked by boundary contacts, from left of centre to lower centre, other grains in the image are larger and grain boundaries are difficult to determine. [d] Inter-connecting grains where silicate material is present between grains.

In massive chromite samples contact relationships between chromite grains were studied. Grain edges in contact with silicate material can be straight, rounded or uneven, appearing sinuous, cuspate or pitted (Figure 5.5.7 [a-d]). Subhedral to anhedral grains present within interstitial silicate regions appear to connect together (Figure 5.5.7 [c]). Two textures are identified, one grain engulfs another (Figure 5.5.7 [a]) or more commonly, side-by-side grain contact forming a chain texture (Figure 5.5.7 [a-d]).

Surface adsorption can result when the boundaries of two grains connect leading the grains to fuse together. When this happens the grain boundary contact changes to a faint, sometimes indistinguishable line (e.g. Figure 5.5.7 [d]).

5.5.6.2 **Chromite grain inter-growths**

Having identified that in many samples grain boundaries are absent or poorly defined, as well as, “engulfing” textures where one grain encompasses another, evidence of inter-grown grains possibly provide an intermediate scenario.

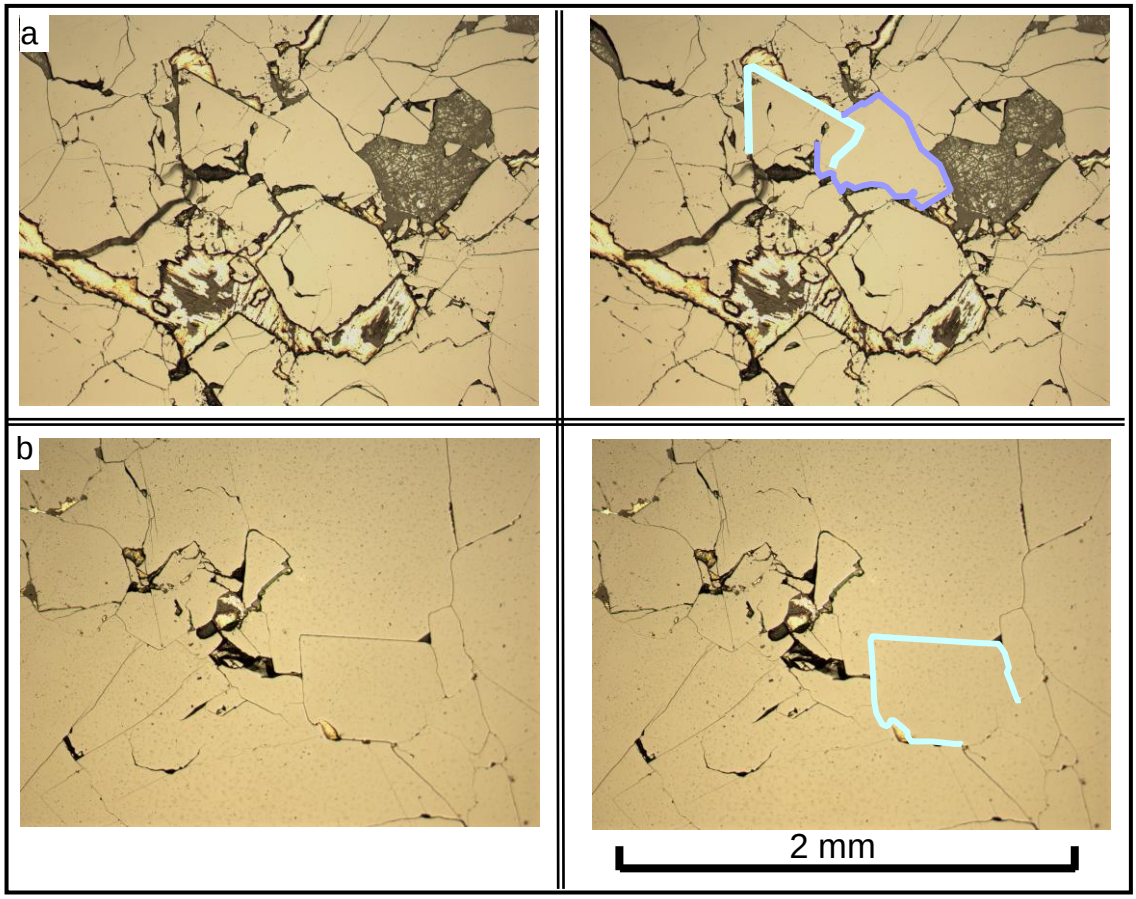

Figure 5.5.8: Grain inter-growths within massive chromite

[a] the intruding grain boundary edge of the upper left (outlined) grain appears faint. [b] a euhedral grain intrudes a larger, massive, neighbouring chromite.

Inter-grown grains show one chromite grain intruding into a neighbouring grain (Figure 5.5.8). Evidence that boundaries may start to fuse, resulting in the intergrowth of the two grains, can be seen in Figure 5.5.8 [a]. However, this is not

always the case, in another example the boundaries remain clearly evident, Figure 5.5.8 [b].

5.5.6.3 **Compaction and annealing**

The ergonomic organisation of the grains; evidence of coalescing grains forming diffuse boundaries and grain intergrowths, are features that reflect an efficient accommodation of space as would result from compaction.

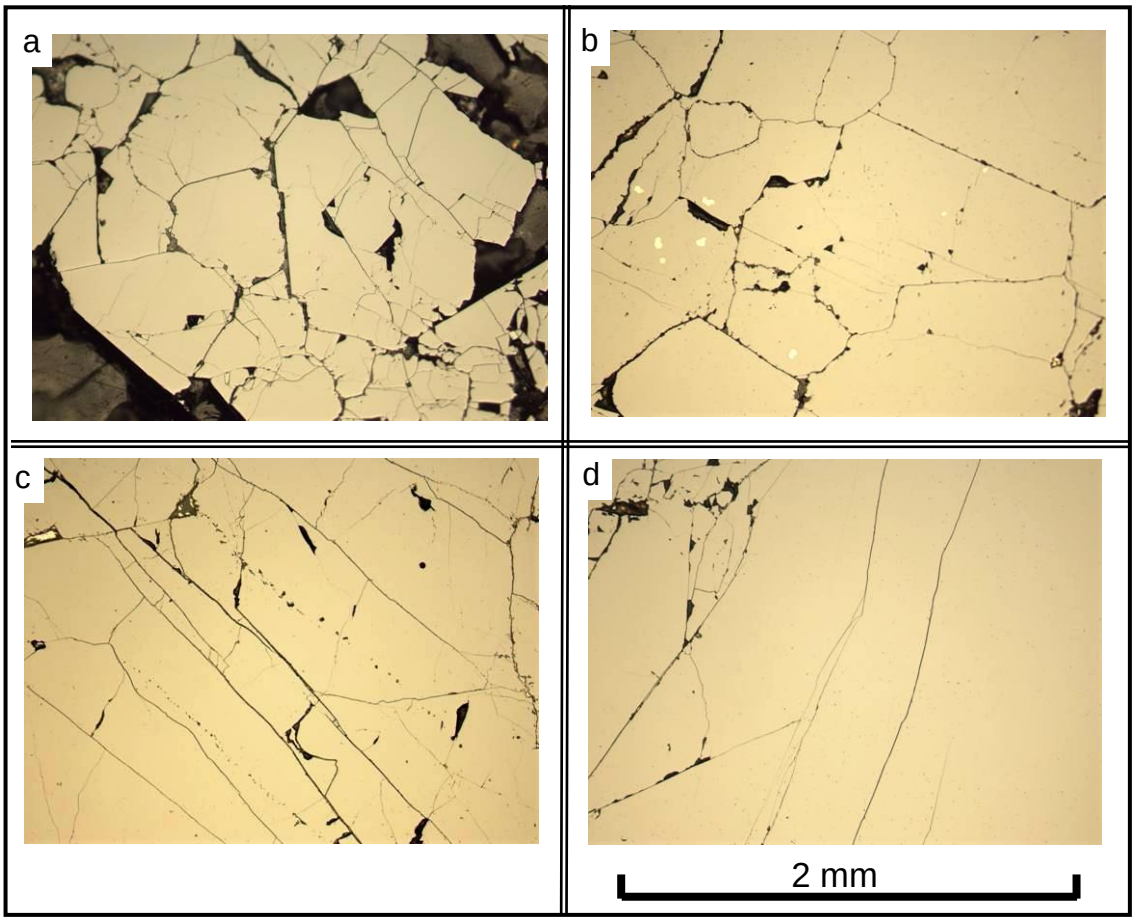

Figure 5.5.9: Compaction and annealing

Compaction intensifies (progressive examples [a] to [d]) grain boundaries fuse, grains merge and the boundaries anneal. The volume of interstitial silicate is reduced migrating along grain boundaries collecting in pockets or trapped within the chromite.

The mechanism governing compaction does not appear to have a preferred orientation, or rather no evidence is preserved in these samples. There is no textural evidence of alignment, stretching, shearing or compressive flattening of

the grains; where grain boundaries remain visible the grains are equant. This indicates that pressure, at least, was equal in all directions. Equally though, pressure appears to have been greater in the regions where grains are more tightly packed and greater still where grains have fused and annealed. As compaction increases the volume of interstitial silicate material decreases. The interstitial silicates migrate along grain boundaries forming pockets or less commonly are trapped as inclusions inside merged grains.

A sub-parallel fracture set is evident in some samples (e.g. Figure 5.5.9 [c] and [d]) indicating that a pressure event has affected these samples, the fractures crosscut grain boundaries indicating that they formed after compaction of the grains. In Figure 5.5.9 [c] two silicate inclusion trails are oriented parallel to the fractures and crosscut faint, annealed grain boundaries.

There is no apparent relationship between the extent of fracturing observed in a sample and the abundance of silicate material.

5.5.6.4 **Chromite grain organisation**

Chromite grain contacts and packing relationships show a variety of grain sizes.

Regions packed with small (0.1-0.3 mm) interlocking grains are often surrounded by massive chromite that lack evidence of grain boundaries, but where fracture networks are common forming straight edges (e.g. Figure 5.5.10 [a]). In areas where grain boundaries have been preserved, curved, undulate interlocking boundaries are common (e.g. Figure 5.5.10 [b]).

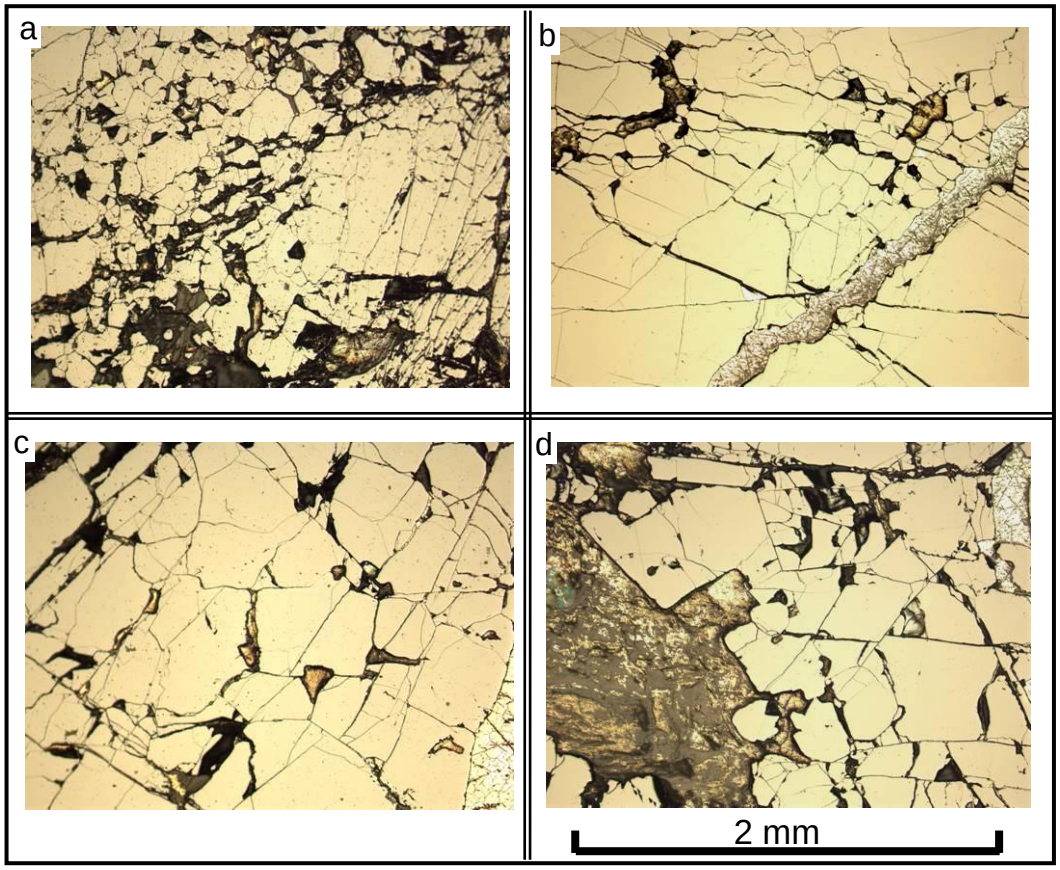

Figure 5.5.10: The organisation of chromite grains in massive chromite.

[a and b] Regions of small subhedral and anhedral interlocked grains coexist with massive chromite that shows only faint grain boundaries and is fractured. [c and d] Densely packed grains with faint grain boundaries and cross-cutting fractures, silicate inclusions are present along boundaries and at boundary junctions.

5.5.6.5 **Irregular grain edges; cuspate and embayment features**

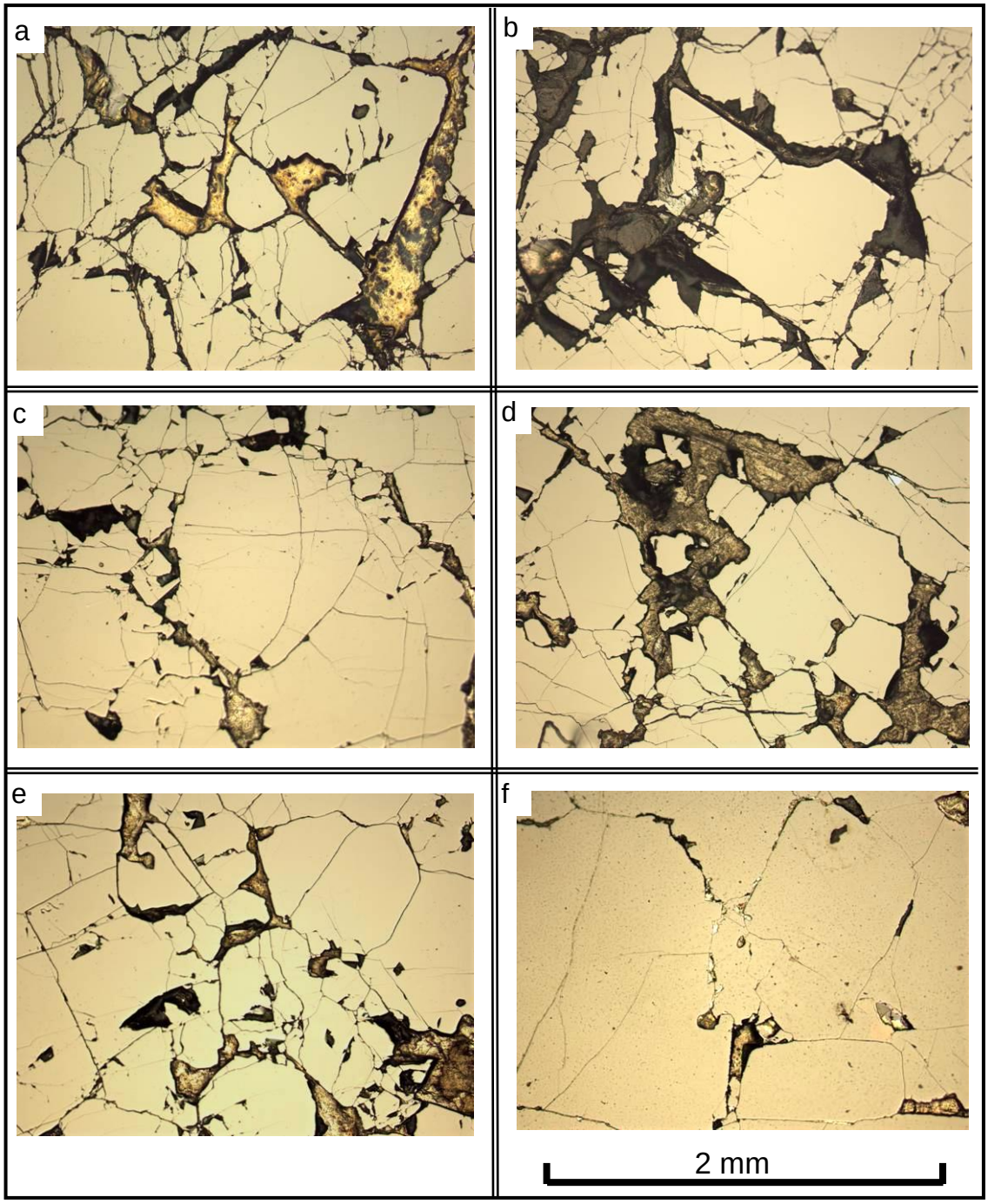

Figure 5.5.11: Cuspate, pitted and undulating chromite grain edges in contact with interstitial silicate.

Smooth chromite-chromite grain boundary contacts are common (e.g. Figure 5.5.11 [d]) and similar to the chromite grain boundary contacts seen in some chromitiferous peridotite samples (chromite morphology descriptions are given in Section 5.4.1). Euhedral and subhedral grains form when chromite is in equilibrium

or close to being in equilibrium with the surrounding mineral and melt phases (*Pike & Schwarzman, 1976*). In contrast, chromite grains in contact with other chromite grains typically have smooth edges, though not necessarily straight. Grains in contact with silicates often display along at least one edge rounded, sinuous or pitted features and in extreme cases deep cusps or embayments form (Figure 5.5.11 [a-f]). These corrosion textures are analogous to those of exhibited by cuspate accessory chromites present in peridotite (Section 5.4) and are characteristic of disequilibrium between chromite grains and the interstitial olivine (now serpentinised olivine) (e.g. *Mercier and Nicolas, 1975*) (as reviewed in Chapter 3, Section 3.6.1).

5.5.6.6 **Triple junctions and silicate-filled grain boundary voids**

Grain boundaries serve as a pathway for fluid flow during metamorphism (*Fyfe et al., 1978*) as well as provide diffusion interfaces for solid-state mass transfer during metamorphic reactions (*Fisher & Elliot, 1979; Lasaga et al., 1977*) and deformation (*White, 1976; Schmid et al., 1977*).

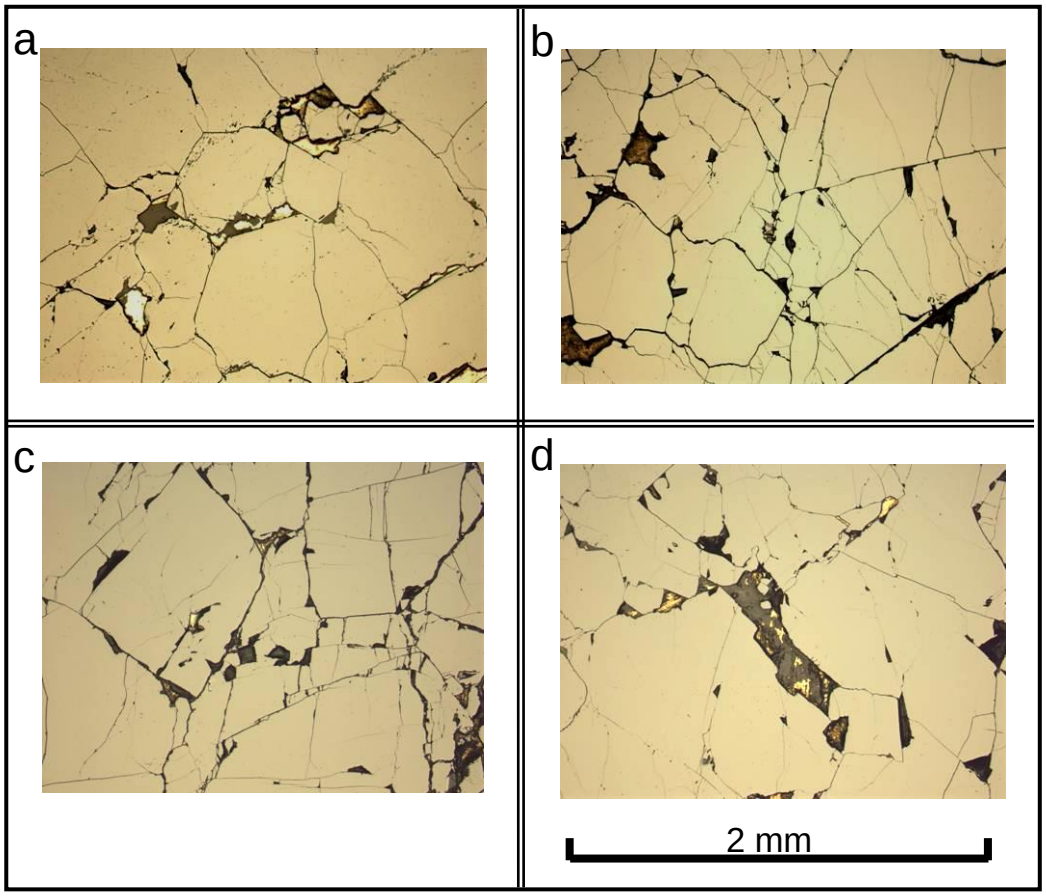

Figure 5.5.12: Triple junctions and boundary voids

[a] Several triple junctions are evident (e.g. top, left of centre), silicate filled voids between grains (right of centre); [b] Triple junctions formed between grains with curved, undulate grain boundaries (left of centre), equant orthorhombic and triangle-shaped voids present where multiple (≥ 3) grain boundaries meet; [c] equant orthorhombic and triangle-shaped voids present where multiple (≥ 3) grain boundaries meet and silicate filled voids between grains; [d] a series of silicate filled voids between grains and evidence of micron-size chromite grains present 'suspended' in silicate (centre).

Triple junctions between polygonal grains with straight or slightly curved crystal faces are frequently observed in the massive chromite. When triple junctions are

orientated at ~120° it is indicative of the system being in thermodynamic equilibrium. Such junction angles are characteristic of sintered grains (*Voll,1960; Hulbert & Von Gruenewaldt, 1985*) as are boundary curvatures that form as a result of triple junction migration (*Voll, 1960*). On the contrary, triple junctions where grain angles vary (are not 120°) signify that the system is not in thermodynamic equilibrium.

Triple junctions are observed in the massive chromites (Figure 5.5.12 [a]). In a single sample there is a diverse range in the size of chromite grains. It appears that the distortion of original grain boundaries during compaction, grain intergrowth and annealing has produced curved grain boundaries, evidence of triple-point migration or destroyed many triple junction boundaries. Golding (1975) observed and attributed similar features in podiform chromitite from the Coolac ultramafic belt in New South Wales, as evidence of the densification of chromite.

Where small amounts of interstitial silicate (serpentinised olivine) is present between some chromites, an inter-granular film forms. Cuspate and polygonal, typically orthorhombic or triangular shaped, silicate filled regions along grain boundaries and at triple-points are common. The presence of these films indicates that not all of the interstitial silicate material has been expelled during densification.

Silicate filled voids frequently observed along many grain boundaries (Figure 5.5.12 [a-d]) are analogous to the observations and resulting grain boundary model proposed by White & White (1981) that was developed from the study of a series of polycrystalline tectonite rocks (Chapter 3; Section 3.6.4). Triangular, silicate filled divots form at triple junctions while trapped olivine fills voids present along grain boundaries. Polygonal, diamond-, square- or orthorhombic-shaped silicate structures are sometimes seen, these may form when two triple junctions coalesce or are the result of a negative crystal structure.

5.5.6.7 **Silicate inclusions**

Silicate inclusions composed of olivine are located within grains and along grain boundaries, as singular inclusions, clusters or trails and form variety of shapes.

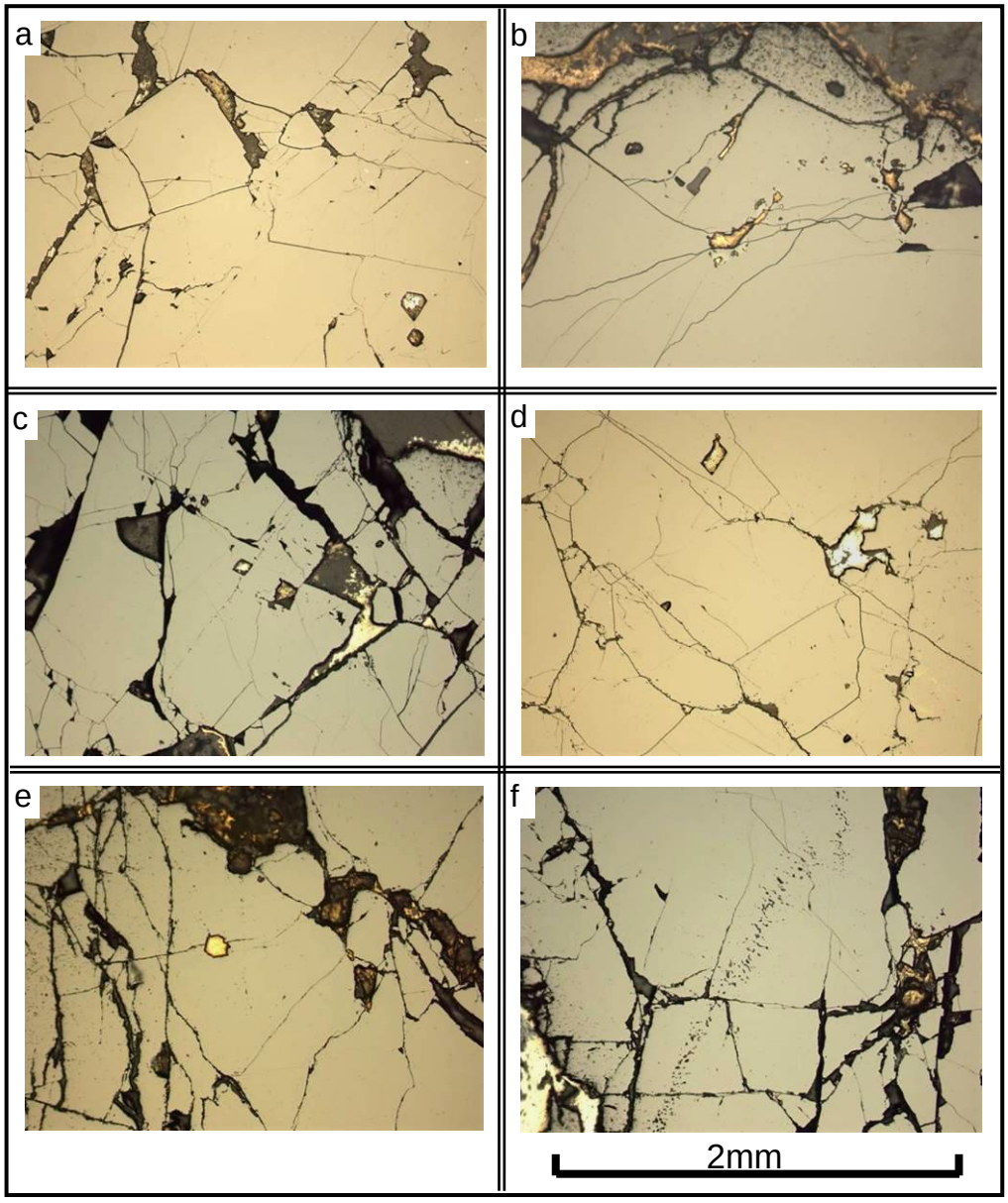

Figure 5.5.13: Silicate inclusions in massive chromite.

[a] Euhedral, negative crystal structure inclusion. [b] An arc-shaped cluster of anhedral and euhedral silicate inclusions, centre to right, elsewhere single inclusions (grey). [c] Two euhedral, square olivine inclusions. [d] Two euhedral olivine inclusions and a pool of trapped olivine at a multiple grain boundary junction. [e] single subhedral olivine inclusion. [f] multiple micron-sized inclusion trail extending across several fractures.

Micron-sized inclusion trails are common in the massive, annealed chromites where grain boundaries are weakly defined, discontinuous or non-existent. The trails are comprised of multiple inclusions that are cross-cut by fractures indicating they formed earlier. The shape of the trails vary in some cases straight (Figure 5.5.9 c) and in others creating a saw-tooth zig-zag pattern an apparent suture

texture (Figure 5.5.13 f). In some samples these inclusions appear to weakly outline possible, pre-existing chromite grains, which have since sutured together (Figure 5.5.13 f). In such circumstances the trail forms as a record of trapped olivine that was not expelled during compaction and annealing of the chromite grains.

Square, rectangular and hexagonal olivine inclusions form as chromite grains have grown or coalesced trapping the interstitial silicate. The shape of these inclusions is dictated by the crystal structure of the encompassing chromites.

5.6 Whole rock analyses

5.6.1 Covariation diagrams

To aid the interpretation of the Voskhod deposit peridotite and dunite units a whole rock geochemical study was performed for 15 hanging wall samples, 8 footwall samples and 7 dunite samples from barren horizons within the ore body. Of the 35 samples collected, 24 were sourced from drill core V05-24 ,the central drill hole and 9 samples were collected from drill cores V05-21 to the west, V05-28 to the east, V06-48 to the south of the centre and V06-S6 the furthest south drill hole (refer to Figure 5.1.3).

Lithologies studied included dunite, clinopyroxene-poor and -rich harzburgite and dunite. Samples of barren dunite from within the ore zone were included to enable the comparison of these results with those of the host rock dunite and the dunite halo surrounding the ore-body. Geochemical differences, in particular in the rare earth element (REE) patterns, could distinguish between different origins of the dunite groups, providing insight into the role of melts and associated fluids involved with the formation of the chromitite ore body.

The whole rock geochemistry was analysed using both ICP-OES (Induced Coupled Plasma-Optical Emission Spectrometry) and ICP-MS (Induced Coupled Plasma-Mass Spectrometry). The ICP-OES analysed for the abundance of major elements Si, Ti, Al, Fe, Mn, Mg, Ca, Na, K, P and Cr, these were reported as oxide percent, in addition the minor elements Sc, V, Co, Ni, Cu, Zn, Sr, Y, Zr and Ba,

were reported as elements in ppm concentrations. The ICP-MS analysed for rare earth elements (REE), Ti, V, Cr, Mn, Co, Fe, Ni, Cu, Zn, Ga, Rb, Sr, Y, Zr, Nb, Ba, Hf, Ta, Pb and Th, these values were reported as elements in ppm concentrations. A detailed description of the procedure for sample preparation and instrument use given in Appendix A and full results are given in Appendix C.

Sample I.D	Drill core I.D	Region	Depth down hole (m)	Distance from mineralisation (m)	Location	Rock type	Chromite modal %	Grain Shape
G1815	V05-21	West	286.60	n/a	n/a	OZ Dun	< 5%	Eu
G1823	V05-21	West	297.65	48.80	Footwall	Dist Dun	< 5%	SI
G1742	V05-24	Centre	141.30	142.92	Hanging wall	Harz	< 5%	HL/SI
G1763	V05-24	Centre	167.60	116.61	Hanging wall	Harz	< 5%	HL/SI
G1768	V05-24	Centre	176.94	107.26	Hanging wall	Harz	<5%	HL/SI
G1777	V05-24	Centre	185.60	98.56	Hanging wall	Dist Dun	< 5%	HL/SI
G1795	V05-24	Centre	231.90	52.30	Hanging wall	Harz	< 5%	SI/An
G1798	V05-24	Centre	240.00	44.70	Hanging wall	Dist Dun	< 5%	HL/SI
VOS-301	V05-24	Centre	249.53	34.67	Hanging wall	Dist Dun	< 5%	HL/SI
VOS-303	V05-24	Centre	252.00	32.50	Hanging wall	Dist Dun	< 5%	SI
VOS-306	V05-24	Centre	258.94	25.26	Hanging wall	Dun Halo	< 5%	HL/SI
VOS-315	V05-24	Centre	270.10	14.10	Hanging wall	Dun/Chr Stringer	~ 50%	SI/Eu
VOS-320	V05-24	Centre	274.59	9.61	Hanging wall	Dist Dun	< 5%	SI
VOS-322	V05-24	Centre	276.80	7.40	Hanging wall	Harz	< 5%	SI/An
VOS-327	V05-24	Centre	282.72	1.48	Hanging wall	Harz	< 5%	SI/Eu
F1907	V05-24	Centre	285.50	n/a	n/a	OZ Dun	<5%	SI
F1926	V05-24	Centre	296.70	n/a	n/a	OZ Dun	<5%	Eu
F1968	V05-24	Centre	341.70	n/a	n/a	OZ Dun	<5%	Eu
F1971	V05-24	Centre	343.00	n/a	n/a	OZ Dun	~ 15%	Eu
F1978	V05-24	Centre	348.00	n/a	n/a	OZ Dun	~ 35%	Eu
G1908	V05-24	Centre	373.42	n/a	Footwall	Dun Halo	< 5%	SI/Eu
VOS-328	V05-24	Centre	375.00	1.58	Footwall	Dun Halo	< 5%	SI/Eu
VOS-341	V05-24	Centre	389.23	15.81	Footwall	Harz	< 5%	HL
VOS-345	V05-24	Centre	394.00	20.69	Footwall	Harz	< 5%	HL/SI
VOS-348	V05-24	Centre	398.63	25.21	Footwall	Dist Dun	< 5%	HL/SI/Eu
VOS-350	V05-24	Centre	403.00	29.50	Footwall	Dist Dun	< 5%	HL/SI
G1601	V05-28	East	322.09	5.15	Hanging wall	Dun Halo	< 5%	An/SI
G1605	V05-28	East	325.52	1.72	Hanging wall	Dun Halo	< 5%	An/SI
G1609	V05-28	East	333.85	n/a	n/a	OZ Dun	< 5%	Eu
G1654	V05-28	East	369.70	n/a	n/a	OZ Dun	< 5%	SI/Eu
G1983	V06-48	S. Centre	298.45	1.75	Footwall	Dun Halo	< 5%	SI/Eu
VOS-185	V06-S6	South	93.95	8.08	Footwall	Harz	< 5%	An/SI

Table 5.6.1: Voskhod peridotite and dunite samples analysed for whole rock geochemistry.

"Distance from mineralisation (m)" refers to the vertical distance in the drill core.

Whole rock data assists in confirming the interpretation of the hanging wall and footwall unit rock types that were made from the inspection of hand specimens during drill core logging. In addition, some samples were selected as being representative of unit types, thin sections were made of these and the samples were optically classified.

The hanging wall and footwall peridotites of the Voskhod deposit have undergone extensive serpentinisation, consequently the rock samples exhibit high loss-on-ignition (LOI) values that range from 12-17 wt%. (Whole rock data tables including LOI values are given in Appendix C).

Whole rock data plots of Al_2O_3 wt% and CaO wt% against the incompatible, immobile trace element Y ppm (Figure 5.6.2) were used to investigate the mobility of elements during alteration. The Al_2O_3 against CaO co-variation plot (Figure 5.6.3) was used to classify dunite, harzburgite and clinopyroxene-rich harzburgite rock types by applying the peridotite classification strategy derived from the results of the study by Pearce and Parkinson (*1993*). Chondrite-normalised REE plots (presented in Section 5.6.2) of the ultramafic hanging wall, footwall and ore zone dunite and peridotite samples were used to further support the categorisation of the samples. These plots were normalised to chondrite values using the values published by Sun and McDonough (*1999*).

The Al_2O_3 wt.% and CaO wt% whole rock analysis values of the peridotite and dunite samples reflects the abundance of clinopyroxene (and to a lesser extent orthopyroxene) present in the samples; as the proportion of clinopyroxene decreases the Al and Ca contents also decrease. All of the harzburgites have elevated clinopyroxene contents compared to dunites and consequently have relatively higher Al_2O_3 wt.% and CaO wt.% contents. The dunite halo and ore zone dunites have lower CaO wt.% contents than the hanging wall and footwall dunites and peridotites. These findings conform with the documented reaction between a melt and host peridotite mantle that promotes clinopyroxene dissolution, a result of the de-stabilisation of the pyroxene stability field (*Kelemen, 1992; Arai, 1994*). In contrast, the dunite halo and ore zone dunites exhibit elevated Al_2O_3 contents owing to the increase in the proportion of chromite present in these samples.

The impact of serpentinisation on element mobility has been well documented (*e.g. Niu, 2004; Iyer et al., 2008; Deschamps et al., 2010*). High field strength elements (e.g. Ti, Zr, Al, Y and HREE) have been shown to be largely immobile during seafloor alteration processes (*Niu, 2004*) and serpentinisation of the fore arc mantle (*You et al., 1996*). Nui (*2004*) showed that in instances when serpentinisation effects only olivine, the major element geochemistry is largely unaffected with only MgO being slightly depleted. However, when clinopyroxene is altered CaO is removed (*Ulrich et al., 2010*).

Co-variation diagrams of HFSEs and major elements help to determine the mobility of these elements during hydrothermal alteration processes such as those associated with serpentinisation and seafloor alteration. By understanding the impact of alteration (if any) on the whole rock geochemical composition of the samples analysed it is possible to use geochemistry to aid and verify the classification of the peridotite and dunite units of the Voskhod deposit and investigate earlier geochemical signatures related to primary processes or tectonic setting.

5.6.1.1 Al_2O_3 against Y and CaO against Y co-variation plots

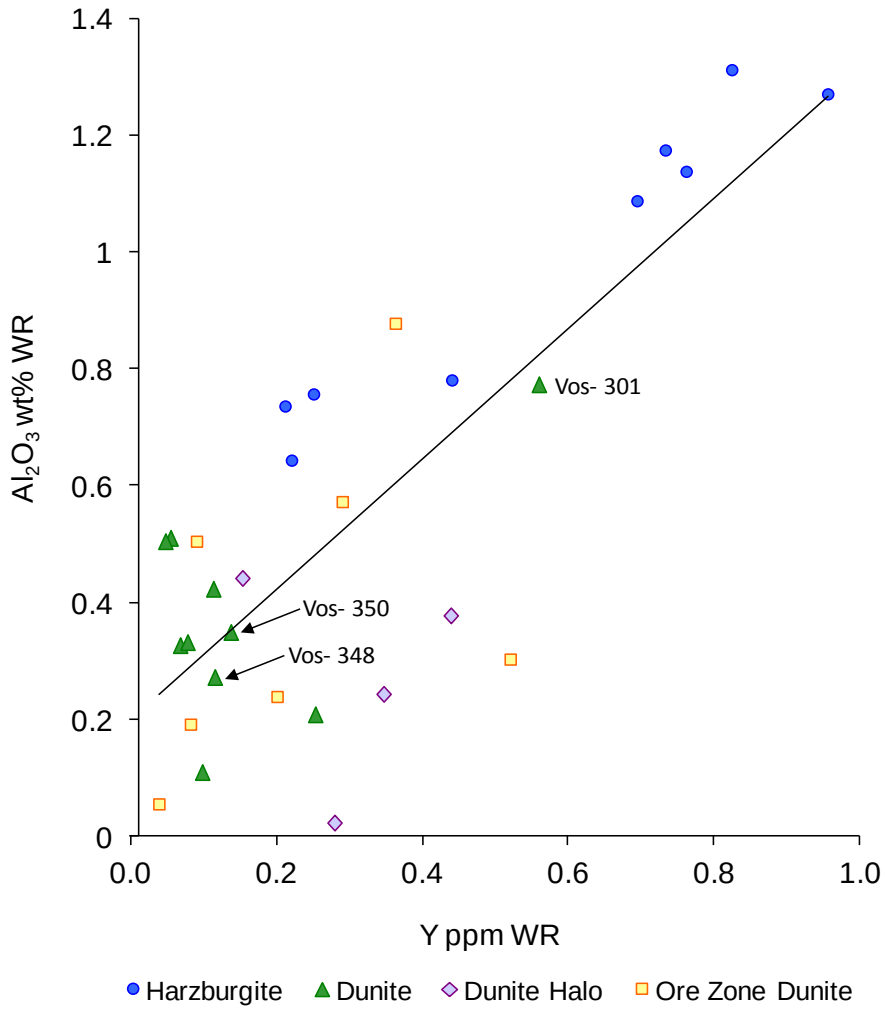

Figure 5.6.1: Al_2O_3 against Y whole rock co-variation diagram

Where "WR" denotes whole rock. The solid black line indicates the line of best fit through the data points.

A positive correlation is observed between Al_2O_3 and Y in Figure 5.6.1 (annotated by the black solid line) indicates that aluminium was largely immobile during alteration of the peridotite and dunite units (*Godard et al., 2000; Takazawa et al., 2002*). The "dunite" and "dunite halo" samples have lower Al_2O_3 contents (<0.5 wt%) than the "harzburgite", a reflection of the lower clinopyroxene content of dunite compared to harzburgite.

Harzburgite forms two groups, one having a higher Al_2O_3 wt% (>1 wt%) content than the other (<1 wt%). The more Al-rich harzburgite has correspondingly increased Y ppm contents, inferring that these samples have (or originally possessed) a higher proportion of clinopyroxene.

The dunite samples (green triangles) and the dunite halo samples (purple diamonds) have similar Al_2O_3 contents of <0.5 wt.% (true for 13 of the 14 samples, the exception being sample Vos-301). The dunite samples have lower Y ppm contents (8 of the 10 samples Y contents <0.14 ppm) compared with the dunite halo samples, where the Y ppm content is >0.15 ppm. In contrast to both of these groups, the ore zone dunite data (yellow squares) scatters across the graph, with data plotting close to harzburgite, dunite and dunite halo samples.

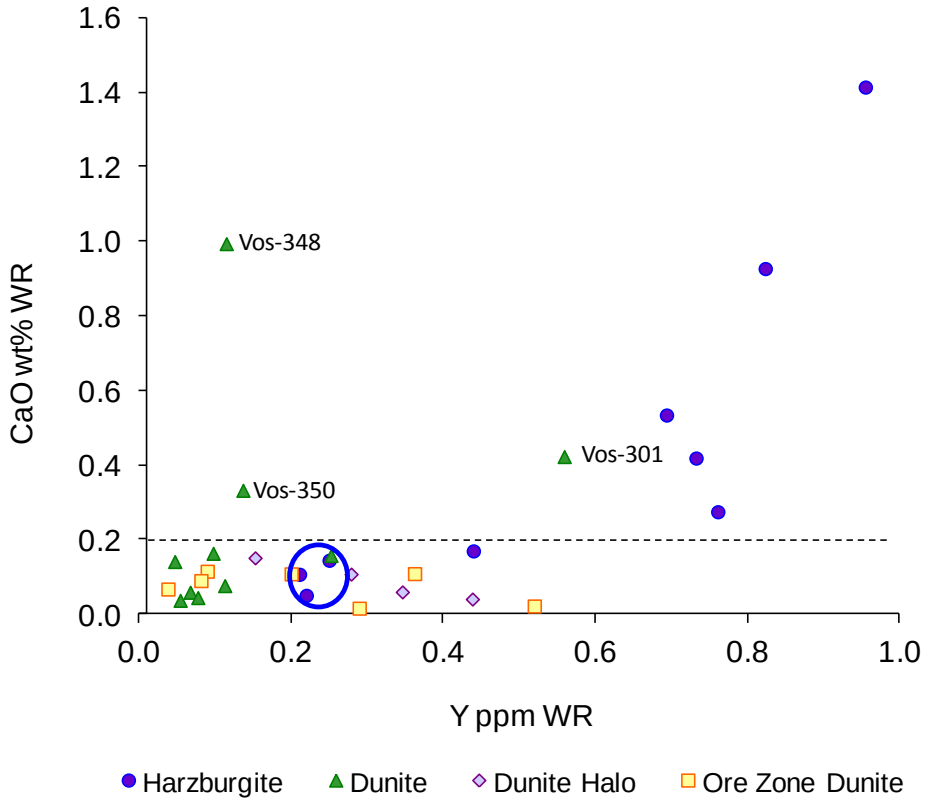

Figure 5.6.2: CaO against Y co-variation diagram

The plot CaO against Y (Figure 5.6.2) shows a weak positive correlation, inferring that CaO has been mobilised within the geochemical system (*Ulrich et al., 2010*).

The four cpx-poor harzburgite samples plot with lower CaO values <0.2 wt% (empty blue circles, Figure 5.6.2). Three of these (circled in blue in Figure 5.6.2) correspond with low Al_2O_3 and Y contents identified in Figure 5.6.1. The complimentary low Al_2O_3 and low CaO contents of these samples implies that they have a lower cpx content than the other harzburgites.

The dunite samples show no correlation between CaO wt% and Y ppm implying that CaO has been re-mobilised. Three samples from the hanging wall and footwall dunite exhibit anomalously high CaO wt% values lying above the annotated black dashed line in Figure 5.6.2, these are labelled Vos-301, Vos-348 and Vos-350. Of these anomalous samples Vos-348 and Vos-350 do not show a corresponding increased Al_2O_3 wt% content (Figure 5.6.1). This infers that these samples have been subject to the addition of carbonate material during later-stage alteration, possibly in the form of magnesite, which is a common mineral phase bi-product of serpentinisation. Sample Vos-301 has higher CaO and Al_2O_3 wt% values compared to the other dunite samples (labelled in both Figure 5.6.1 and Figure 5.6.2) and plots closer to the harzburgite samples.

5.6.1.2 **Co-variation plot Al_2O_3 against CaO**

Harzburgite and dunite can be distinguished between by the differing modal proportion of clinopyroxene. The plot Al_2O_3 wt% against CaO wt% can be used to chemically identify this compositional difference (Figure 5.6.3). The abundance of Al_2O_3 and CaO wt% in whole rock peridotite decreases as the clinopyroxene (and to a lesser extent orthopyroxene) content decreases. The peridotite type discrimination fields presented in Figure 5.6.3 are; lherzolite, clinopyroxene-rich harzburgite, harzburgite and dunite.

The Voskhod harzburgite and dunite samples were classified optically by visually estimating the mineral proportions of olivine, clinopyroxene and orthopyroxene observed in hand specimen and thin section. The samples were categorised into three groups, harzburgite, clinopyroxene-poor harzburgite and dunite.

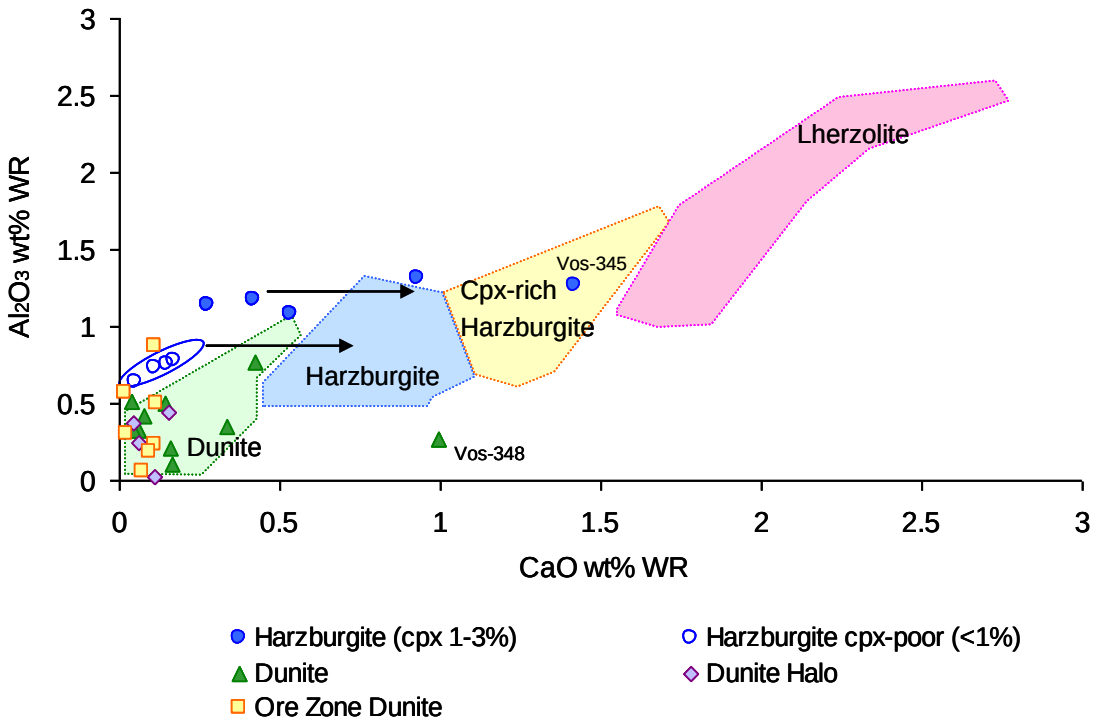

Figure 5.6.3: Al_2O_3 against CaO wt% co-variation plot

The discrimination fields are created using whole rock geochemical data from peridotite and dunite samples sourced from the Oman ophiolite ultramafic sequence. The mineral proportions of clinopyroxene were known having been calculated chemically by mass balance using whole rock composition data in conjunction with mineral compositions (*Takazawa et a., 2000; Godard et al., 2003; Dare, 2007*).The solid black arrows indicate displacement of samples from the rock-type discrimination field.

Harzburgite plots away from the harzburgite field as a result of low CaO values (indicated by the black horizontal arrows Figure 5.6.3), however, the Al_2O_3 values of these samples are sufficiently high that they do not plot in the dunite field. The cpx-poor harzburgite (<1% cpx, blue open circle) are the furthest removed from the harzburgite field having insufficient Al_2O_3 and CaO values, a reflection of a low clinopyroxene content. In contrast, Vos-345 plots in the cpx-rich harzburgite field, on optical examination this sample contains only ~2% clinopyroxene, consequently it is interpreted to exhibit elevated CaO wt%.

The dunite, dunite halo and ore zone dunite plot within the dunite discrimination field. Two ore zone dunites plot with elevated Al_2O_3, however, the CaO values are low and in keeping with dunite geochemistry. The elevated Al_2O_3 content reflects the presence of chromite (>3%) in the whole rock sample analysed. Vos-348 plots

away from the dunite field having a high CaO value of 1.00 wt%. The Al_2O_3 value is not high enough for it to plot in the harzburgite field, implying that the CaO increase results from an alteration process rather than an increase in clinopyroxene (similar to that seen in sample Vos-345).

A study conducted by Pearce and Parkinson (1993) examined the relationship between whole rock peridotite data and the percentage of non-exsolved clinopyroxene optically present in a sample series. The results showed that peridotite comprising 3% clinopyroxene has 0.08 wt% CaO in the whole rock while a peridotite with 0% clinopyroxene has <0.03 wt% CaO. The observations made and geochemistry presented on the Voskhod peridotites and dunites correspond well with the results of Pearce and Parkinson (*1993*).

5.6.2 REE patterns

Residual ultramafic rock formed by partial melting of the upper mantle is depleted in light rare earth elements (LREE = La to Nd). It has been reported that massive peridotite and dunite from ophiolites display chondrite-normalised ratios of LREE to heavy rare earth elements (HREE = Er to Lu) of less than one [$(LREE/HREE)_N < 1$] (*Melcher et al., 1999*). However, massive peridotites have the potential to exhibit ratios $(LREE/HREE)_N > 1$ if they have been subject to enrichment following interaction with metasomatic fluids, a process that may not significantly change the modal composition (*Boudinier et al., 1988; McDonough and Frey, 1989; Bodinier et al., 1990*).

Complex REE patterns have been identified in mantle peridotite and dunite rocks from the Kempirsai Massif (*Sharma et al., 1995, Sharma and Wasserburg, 1996, Savelieva et al., 1997, and Melcher et al., 1999*). Studies have reported U-shaped patterns characterised by variable LREE enrichment, low to middle REE (MREE = Sm to Tb) and increasing HREE contents. Chondrite-normalised REE values vary by up to five orders of magnitude. Dunites from the MOF have the lowest REE concentrations, while harzburgites show elevated HREE concentrations that approach compositions analogous to those of lherzolite. Ultramafic cumulates were also significantly enriched in LREEs relative to MREEs producing U-shaped patterns. The large variation in REE concentrations has been interpreted to reflect

strong compositional heterogeneities within the Palaeozoic mantle of the southern Urals (*Melcher et al., 1999*). The coexistence of depleted and enriched peridotites has been interpreted to result from either varying degrees of partial melting (ranging from <10% to >30%) (*Melcher et al., 1999*) or alternatively to require re-fertilisation of the mantle causing secondary enrichment (*Sharma & Wasserburg, 1996*). REE profiles presented in the literature for the Southern Urals mantle units are characteristic of LREE enrichment of depleted mantle that is associated with the infiltration of subsequent melts or fluids.

Fluid interaction with the mantle may be the result of fluids driven off from a downward subducting slab, or occur as a later-stage process by percolating waters associated with the obduction process of ophiolite emplacement. Deschamps et al. (2010) showed that the REE remain immobile during serpentinisation of abyssal and forearc peridotites and that the REE profiles reflect earlier magmatic processes or the effects of late-stage magmas or fluids..

Chondrite-normalised REE plots for representative harzburgite and dunite sourced from the hanging wall, footwall and ore zone of the Voskhod deposit are presented in Figure 5.6.4 [a-d]. The sample suite exhibits intermediate to low REE concentrations with Chondrite normalised value ranges; HREE 0.03-0.74, MREE 0.03-0.58 and LREE 0.03-2.18. The solid grey line shown in each plot represents depleted MORB mantle (DMM) (*Workman & Hart, 2005*) normalised to chondrite (*Sun & McDonough, 1989*). The DMM/chondrite line provides a comparison for the REE geochemistry profiles of the Voskhod deposit mantle peridotite and dunite rocks.

An important first order observation is that compared to the DMM REE profile, all lithologies in the Voskhod ore body and the host harzburgite and dunite samples are depleted in terms of REEs.

Although the Voskhod sample series studied lacks diversity in terms of mineralogical composition, the whole rock REE geochemistry identifies four different REE patterns in the suite.

(i) LREE depleted (Figure 5.6.4[a]), HREE>MREE>LREE

(ii) LREE enriched (Figure 5.6.4 [b]), HREE≥MREE<LREE

(iii) Flat (Figure 5.6.4 [c]), HREE=MREE=LREE

(iv) U-shaped (Figure 5.6.4 [d]), HREE>MREE≤LREE

Ulrich et al. (*2010*) reviewed the use of REE profiles for interpreting the petrogenesis of an ophiolite setting. Their findings showed that for chondrite-normalised REE profiles produced from the analysis of mantle peridotite rocks, progressively decreasing values from HREE through MREE to LREE result from mantle melting. In contrast, LREE enrichment patterns are interpreted to indicate post-melting refertilisation of the mantle produced by interaction of comparatively fertile uprising melts with depleted residual mantle.

5.6.2.1 **REE profiles grouped by shape**

Individual REE profiles for Voskhod rocks do not correspond exclusively to specific rock types or the location of the sample with respect to surface space or proximity to the ore body (i.e. whether the sample is sourced from the hanging wall or footwall, or central, north, south, east or west of the ore body).

Type (i) depleted LREE profiles (Figure 5.6.4 [a]) are produced by harzburgite and one ore-zone dunite sample. This pattern represents depleted country rock, the residue of mantle melting. Depleted LREE patterns are characteristic of rocks that have undergone melt extraction, as has been demonstrated by standard melting models (e.g. *Johnson et al., 1990*). A slight LREE enrichment is seen in several profiles. The negative Eu anomalies in some harzburgites may be attributed to differential mobility of the light (Sm-La) and middle (Eu-Tb) REE during alteration, rather than being a primary process signature (*Pearce., 2005*). The positive Sm anomaly has no obvious explanation.

Type (ii) enriched LREE profiles reflect varied levels of depletion combined with high levels of LREE re-enrichment (Figure 5.6.4 [b]). One sample of harzburgite is extremely enriched in LREE, more so than the dunite samples. If re-fertilisation of the mantle by interaction with an upwelling melt is responsible for the increase in LREE it implies that the LREE are trapped as LREE-enriched films along grain

boundaries (*Niu, 2004*). If this is the case, then the process of resorption of orthopyroxene from harzburgite is decoupled from the process by which the host rock is being enriched in LREE. From these observations it is proposed that magma in the conduit may not be the mechanism by which LREE enrich the mantle, but rather that an accompanying, unmixed volatile-rich fluid fulfils this role.

Type (iii) flat patterns in lithologies from the ore zones that do not contain clinopyroxene, may imply the entrapment of all REE along grain boundaries, in the proportion they are present in the new percolating melt (Figure 5.6.4 [c]). The approximately flat pattern in the harzburgite may comprise a slight decrease from HREE to MREE, the result of mantle melting and a slight increase in LREE by re-fertilisation (interaction with a new melt). This pattern may be transitional to the U-shaped pattern (Figure 5.6.4 [d]).

Type (iv) U-shaped patters are produced only by harzburgites and dunites from the host rocks. The pattern indicates that the rocks are depleted host-rocks (depleted-LREE) that have been subject to an intermediate level of LREE enrichment from interaction with a later stage melt (or melt derived fluid).

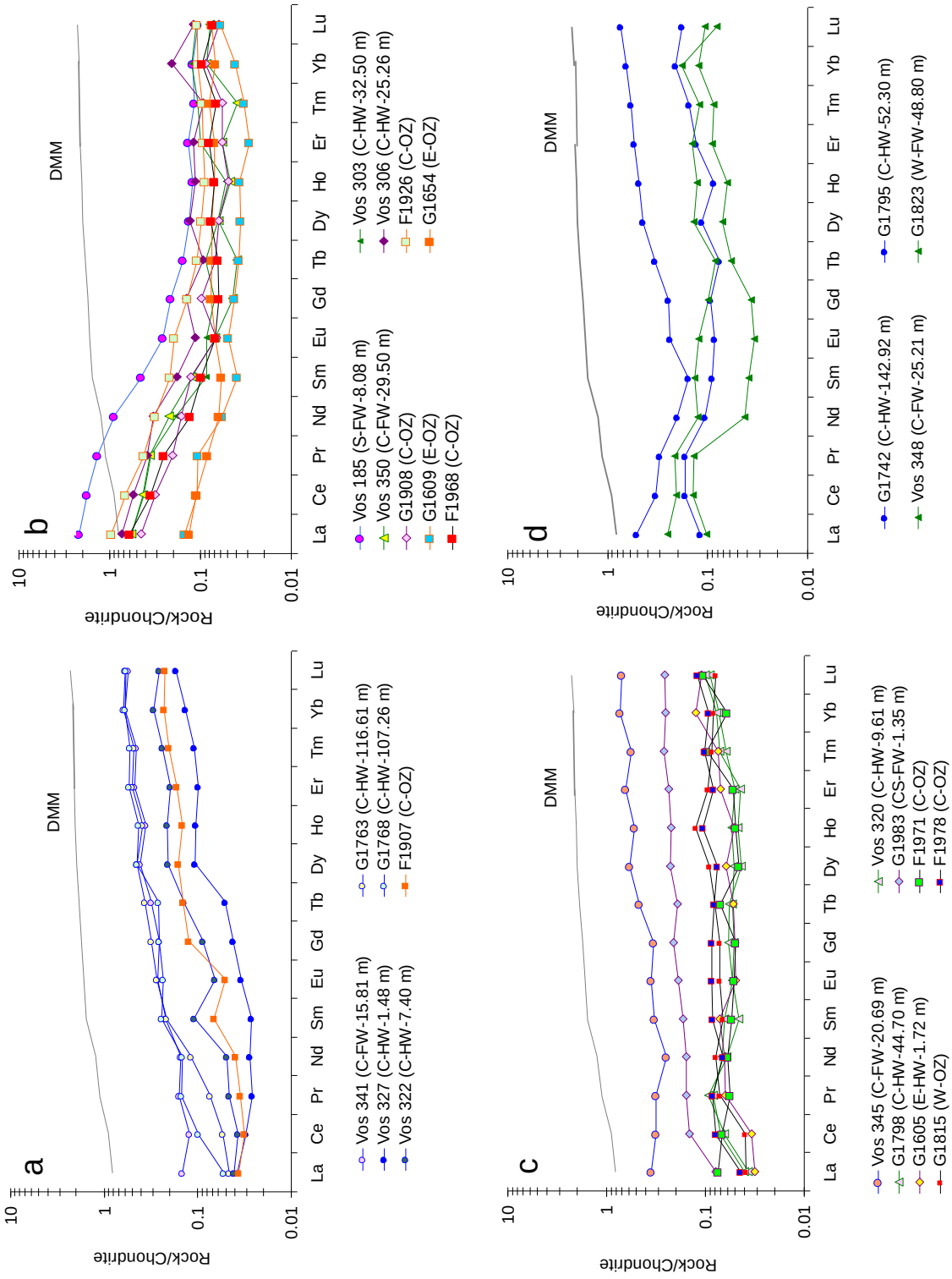

Figure 5.6.4: Chondrite-normalised REE patterns for Voskhod peridotites and dunite.

[a] LREE depleted, [b] LREE enriched, [c] Flat and [d] U-shaped REE profiles. C1 chondrite values from McDonough & Sun (1995). DMM (depleted MORB mantle) values from Workmann & Hart (2005). Sample number - (C=centre, E=east, CS=centre south, S=south, W=west - HW=hanging wall, FW=Footwall, OZ=ore zone - The distance from the orebody, perpendicular down hole is given in metres). Refer to Table 5.6.1 and Figure 5.1.3.

5.6.2.2 **REE profiles grouped by rock-type**

It has been demonstrated in Section 5.6.2.1 that four REE profile shapes exist but that these are not associated with specific rock-types or proximity to the ore body. To further understand the relationship between the REE profiles and rock-types the patterns have been grouped according by rock-type (Figure 5.6.5).

The harzburgite samples produce predominantly LREE-depleted profiles (Figure 5.6.5 [a]). However, sample Vos185, sourced 8.08 m into the footwall from the south of the deposit is particularly LREE-enriched, it is the only sample analysed from the south of the ore body, the others being sourced from the centre of the ore body (drill core V05-24). In comparison, the other footwall harzburgite samples (Vos-341 and -345) are LREE-depleted. This result may indicate that the south of the ore body has been subject to greater degree of LREE-enrichment, although from one sample it is difficult to confirm this.

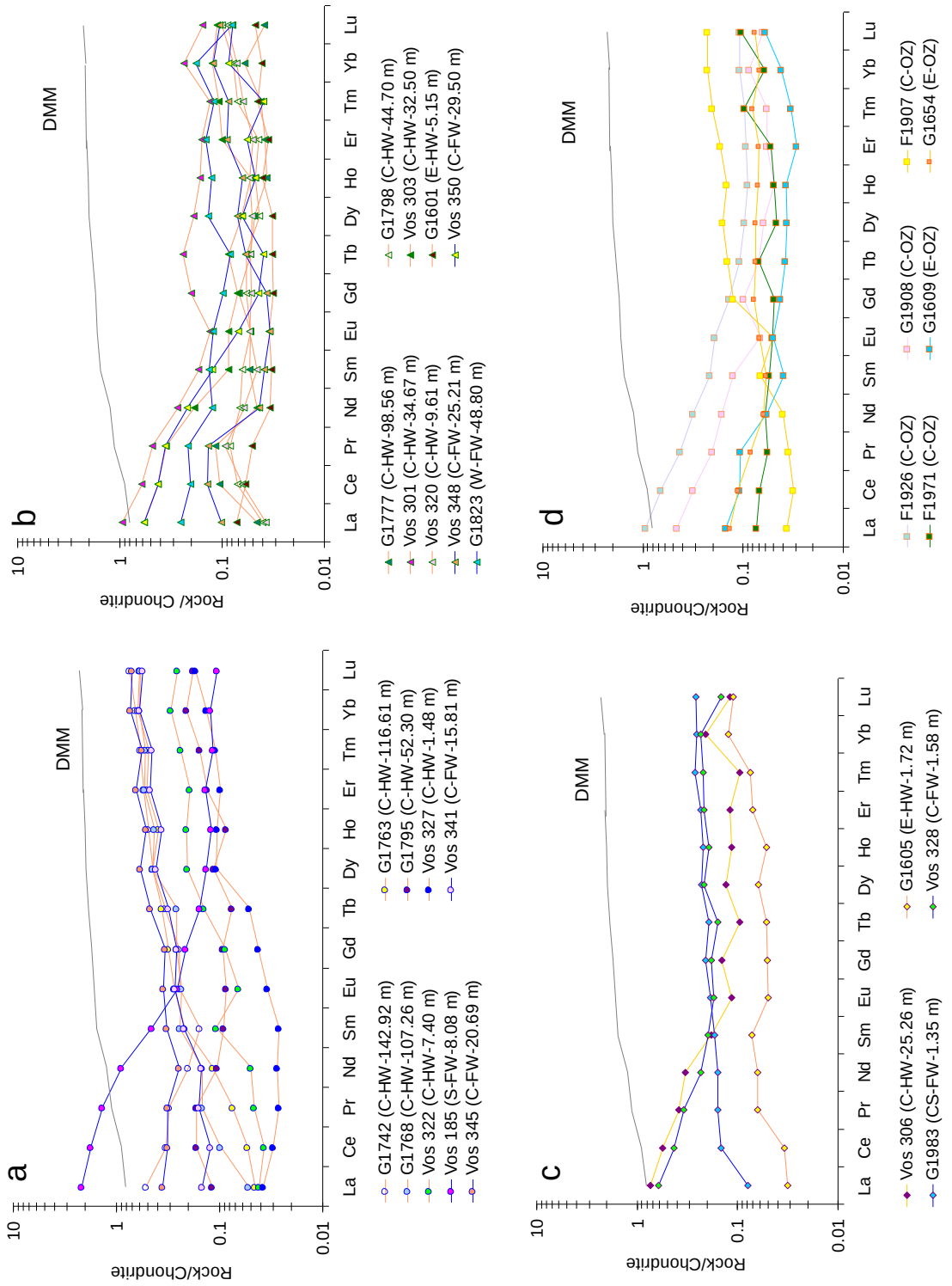

Figure 5.6.5: REE profiles grouped by rock-type.

[a] Harzburgite, [b] Distal dunite, [c] Dunite halo, [d] Ore zone dunite. Positions are given next to the sample number (C=centre, E=east, CS=centre south, S=south, W=west - HW=hanging wall, FW=Footwall, OZ=ore zone - The distance from the orebody, perpendicular down hole is given in metres). Refer to Table 5.6.1 and Figure 5.1.3. C1 chondrite values McDonough & Sun (1995).

The distal dunite samples form flat, U-shaped and LREE-enriched profiles (Figure 5.6.5 [b]). There are no LREE-depleted profiles indicating that all of these rocks have at some stage interacted, to variable extents, with a LREE-enriched liquid and are not solely the products of extensive degrees of partial melting, which would have formed LREE-depleted patterns. There is no apparent correlation with hanging wall or footwall localities, although it can be seen that generally samples sourced closer to the ore body have lower REE concentrations than those further away.

The dunite halo samples produce LREE-enriched or flat with slightly elevated HREE profiles (Figure 5.6.5 [c]). The former indicates interaction with a LREE-enriched liquid, while the slightly increased HREE concentrations of the flat profiles are evidence of melt extraction. There is no correlation with samples being collected from the upper or lower selvedge of the ore body, although sample G1605 is from the eastern periphery (drill core V05-28), upper selvedge of the ore body and has lower REE concentrations compared with those of dunite halo samples analysed from the centre of the ore body.

The ore zone dunites display LREE-enriched, LREE-depleted and flat profiles indicating a multiple processes involving melting (to produce the LREE-depleted profiles) and later-stage enrichment to produce the flat and LREE-enriched profiles. The LREE-enriched profiles form by more intense interaction with a LREE-enriching liquid, while less extensive reaction produced the flat profiles. Samples G1609 and G1654 from the east of the ore body and sample F1971 from the centre have overall lower REE concentrations compared with the other ore zone dunites and form flat profiles.

5.6.2.3 **Extended trace element plots (spidergrams)**

Spidergrams provide extended element profiles that include the large ion lithophile elements (LILE) K, Rb, Cs and Ba and the high field strength elements (HFSE) Nb, Ta, Zr and Hf in addition to REE. The inclusion of these elements assist in finger printing the chemical signature and consequently the source, of any fluids and/or melts that may have interacted with the mantle rocks.

In Chapter 4, Section 4.3, it is noted that previous studies have suggested that boninite lavas and mantle hosted podiform chromites are genetically linked. Furthermore, boninites are present in the Baimak-Buribai Complex (BBC) located ~150 km from the Kempirsai Massif. A genetic association between the two has never been established and there is some uncertainty whether these mantle and lava units are part of the same stratigraphic progression (mantle to crust) as the Main Uralian Fault transects between the two.

Typically boninites are rich in SiO_2, MgO, Cr, Ni, H_2O, LILE, U, Th, Pb, Sr and LREE, but poor in many HFSE and MREE-HREE (*Hickey & Frey, 1982; Pearce, 1982; Crawford, 1989; Saunders et al., 1991; Pearce et al., 1992; Taylor et al., 1994*). The hydrous nature of these melts promotes extensive melting of the mantle (*Dick & Bullen, 1984; Hamlyn et al., 1985; Bonatti & Michael, 1989; Dick, 1989; Arai, 1994*). This in turn can alter the relative proportions of the melt chemistry (*Gaetani & Grove, 1998; Bizimis et al., 2000*) and the ability of the melt to transport LILE and “hygrophile” elements (*Pearce, 1982; Saunders et al., 1991*). Boninite melt chemistry is further complicated by the unconstrained extent of melting required to form such a melt, the degree of depletion of the mantle source, the impact of melt-rock interaction during ascent to the surface and the undefined nature of associated fluids/melts produced by the devolatilisation and melting of sediment and/or crustal lavas brought down by the subducting slab, contributing what is a termed an ‘arc component’ to the melt signature (e.g. *Gill, 1981; Hickey & Frey, 1982; Pearce, 1982; Saunders et al., 1991; Pearce et al., 1992; Hawkesworth et al., 1993; Pearce & Parkinson, 1993; Arculus, 1994; taylor et al., 1994; Iwamori, 1998*).

Whole rock geochemical data for the BBC boninites (*Spadea et al., 1998*) has been plotted with the geochemical data collected from the Voskhod samples on the spidergrams for comparison.

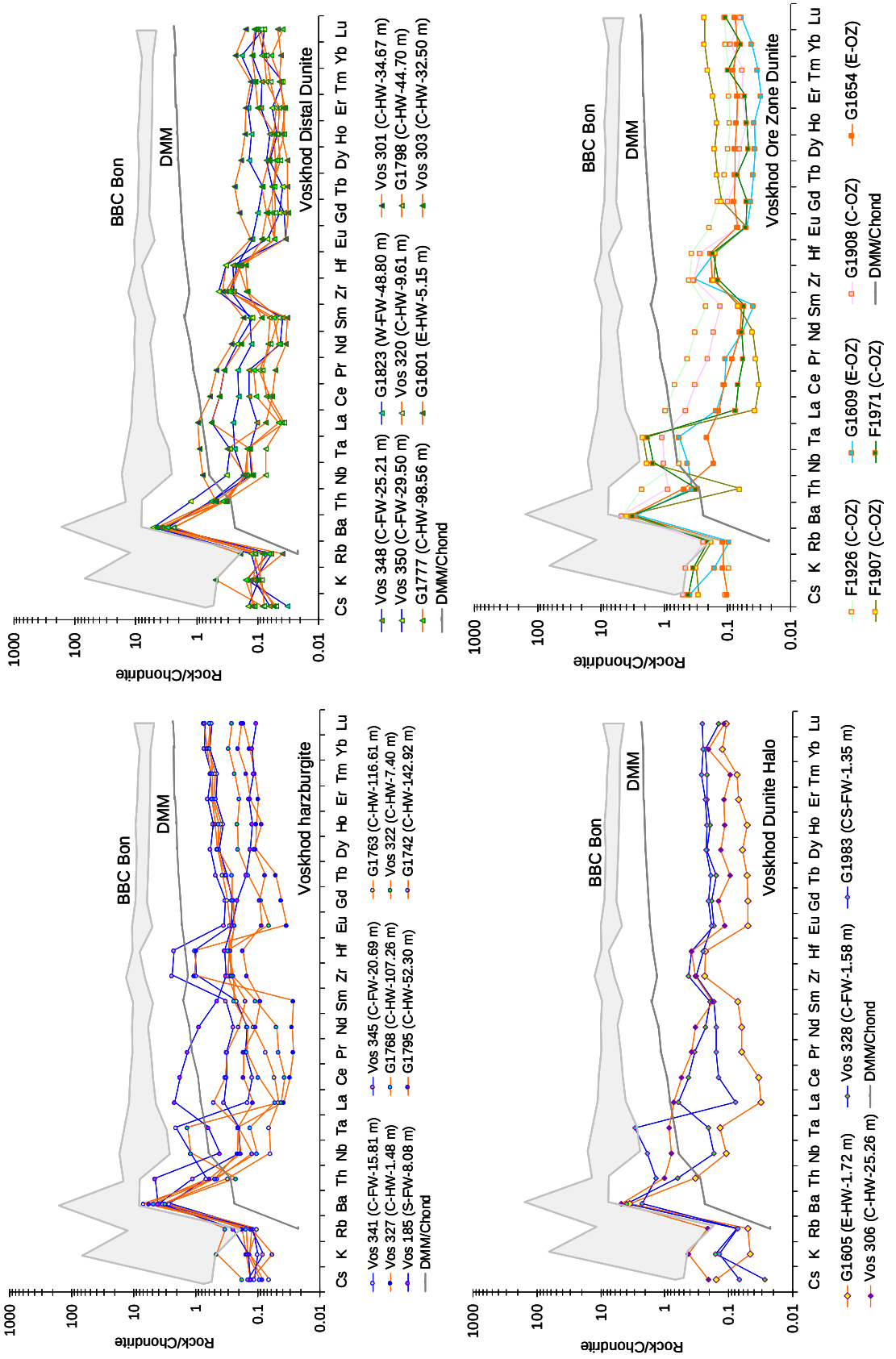

Figure 5.6.6: Extended trace element plots for the Voskhod samples grouped by rock-type and normalised to chondrite.

C1 chondrite values, McDonough & Sun (1995).

The chondrite-rock normalised spidergrams show that all of the Voskhod samples have positive Ba, Zr and Hf anomalies and many samples are anomalously enriched in the trace elements K, Th, Nb and Ta (Figure 5.6.6 [a-d]). The HFSE; Nb, Ta, Zr and Hf are immobile during alteration (*Godard et al., 2000*) and the values reported for the Voskhod samples are considered representative of the primary composition of these mantle rocks.

Relative to the chondrite-normalised DMM line, all of the Voskhod samples are enriched in the LILE; Cs, K, Rb and Ba, elements that are commonly associated with boninite melts. The presence of such high concentrations in otherwise depleted mantle rocks would suggest these components have been introduced to the mantle rocks after depletion. In all of the samples the LILE enrichment order is Ba>K>Rb≈Cs. Although the Rb and Cs values are approximately similar, in the ore zone dunites Cs>Rb is seen (Figure 5.6.6 [d]), yet in the other sample groups Rb>Cs is typical (Figure 5.6.6 [a-c]).

Increased Nb, Ta (±Th) values relative to LREE indicate that the mantle residue has been infiltrated by later-stage (post mantle melting and LREE-depletion), volatile-rich liquids such as those derived from the dehydration and/or melting of a downward sinking, subducting slab. This signature is present throughout the majority of the Voskhod sample series. Only samples: harzburgite; Vos-185, G1742 and Vos-345 (Figure 5.6.6 [a]), distal dunite; Vos-303 and -350 (Figure 5.6.6 [b]), dunite halo; Vos-328 (Figure 5.6.6 [c]) and ore zone dunite; F1926 (Figure 5.6.6 [d]) do not possess elevated Nb-Ta (±Th) values. Although the signature is present across the area sampled, it is not a rock-type specific signature. Instead it appears that the volatile-rich liquids may have formed isolated pathways and selectively enriched mantle regions of harzburgite and dunite as well as the ore zone.

The positive Zr-Hf anomaly appears to be independent of the Nb-Ta (±Th) signature, indicating that it is sourced from a separate fluid or melt event. When the data is scrutinised profiles showing the greatest Nb-Ta enrichment typically have the least pronounced Zr-Hf anomalies, e.g. samples, Vos-322 (harzburgite), G1983 (dunite halo), F1907 and F1971 (ore zone dunite). A remarkably similar positive Zr-Hf anomaly has been reported by Page et al. (2009) in the Thetford

Mines Ophiolite (TMO) mantle rocks (in harzburgite and dunite units). Similarly, the TMO mantle rocks are enriched in Nb and Ta relative to the LREE, although the extent of enrichment in these elements is not as great as that seen in the Voskhod mantle rocks. Page et al. (2009) were able to demonstrate that these anomalies resulted from the introduction of a sediment from the downward subducting slab at the site of mantle melting.

When the Voskhod rock suite spidergram plots are compared with the BBC boninite geochemistry (*Spadea et al., 1998*) there is a striking resemblance between the two. The BBC boninites show exceptionally strong positive Ba-K anomalies and positive Zr-Hf signatures. The Nb-Ta signature of the BBC boninites is more variable, however, the upper limit of the field indicates that some of the boninite samples analysed were enriched in Nb-Ta relative to the LREE.

For comparison the average trace and rare earth element compositions for Voskhod harzburgite and ore zone dunite and the BBC boninite field are plotted with the average TMO harzburgite and podiform dunite (dunite from the TMO chromite ore body) and TMO boninite compositions (Figure 5.6.7).

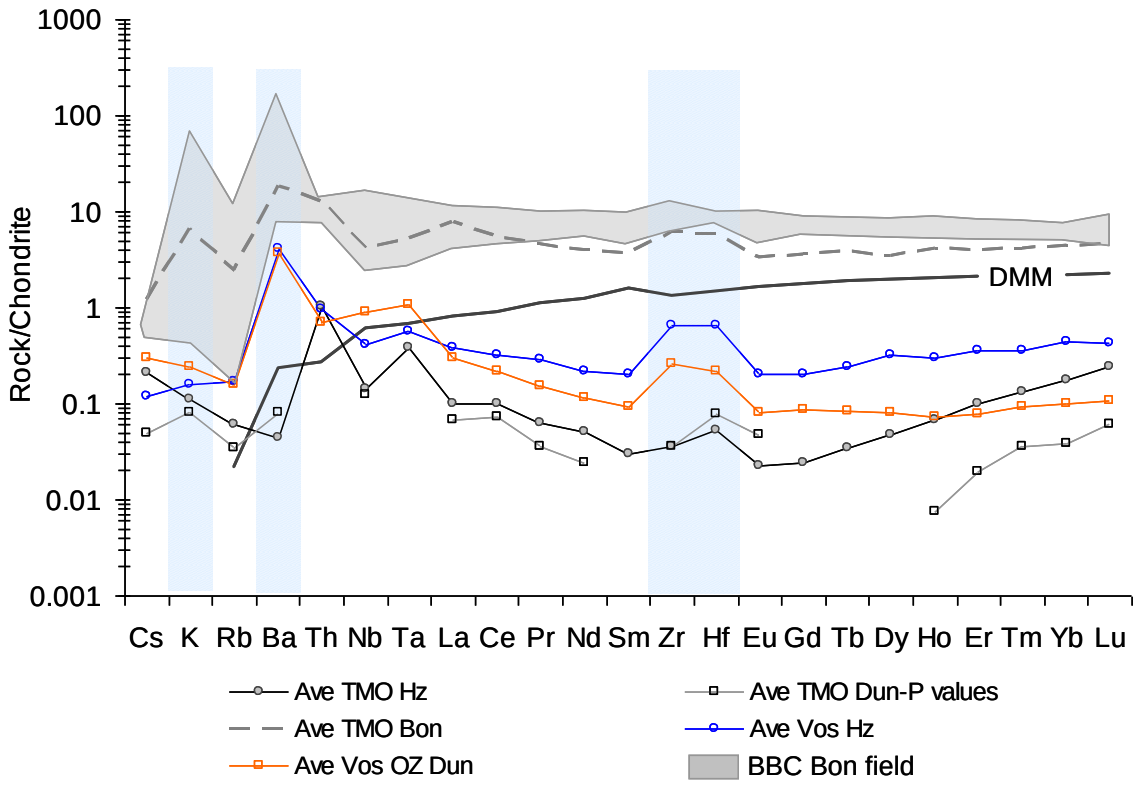

Figure 5.6.7: A comparison of the trace and rare earth element for the Thetford Mines Ophiolite and Voskhod mantle and boninite rock series.

C1 chondrite values from McDonough & Sun (1995). TMO data from Page et al. (2009). Hz= harzburgite, Bon= boninite, Dun-P= Podiform dunite, OZ Dun= Ore zone dunite.

The compositions of the BBC and TMO boninites are very similar. The BBC boninites are more enriched in MREE-HREE than the TMO boninites indicating that the source of the BBC boninites was either more fertile or underwent higher degrees of partial melting to liberate these elements from the mantle source. Both boninite series display positive K, Ba and Zr-Hf anomalies. However, the enriched Nb-Ta signature seen in the BBC boninites is not evident in the TMO boninites, in fact the TMO boninites are relatively depleted in these components compared to LREE concentrations.

The Voskhod and TMO mantle rocks form similar patterns and profile relationships; the harzburgite profiles have higher element concentrations than the ore zone dunite profiles. As seen in the boninite data comparison, the Voskhod mantle rocks are more enriched than the TMO mantle rocks. The positive Zr-Hf signature is clearly evident in the Voskhod mantle rocks and is comparatively less prominent, although still present, in the TMO mantle rocks. Additionally the

Voskhod harzburgite and ore zone dunite profiles record a strong Ba-enriched signature and elevated Th, Nb and Ta values. In contrast, despite the Ba spike in the TMO boninite, the TMO harzburgite and podiform dunite profiles are depleted in Ba. The Th, Nb and Ta concentrations compare well with the composition of the TMO boninite profile, Th and Ta are relatively enriched, while Nb is comparatively depleted. However, it is noted that in the TMO mantle rocks Nb concentrations are still greater than the LREE.

A steep increase in the HREE concentrations is seen in the TMO harzburgite and podiform dunite profiles, relative to the more gentle slope displayed by the Voskhod harzburgite and ore zone dunite profiles. This implies that the TMO mantle was subject to higher degrees of partial melting compared to the Voskhod mantle. Both display similar gradient LREE enrichment profiles, evidence of a LREE fluid or melt phase interacting with and re-enriching these rocks after the initial episode of melting and LREE depletion.

Large, Cr-rich podiform chromite deposits are present in both the Voskhod and TMO mantle units. The migration of boninite melt through the mantle is associated with the genesis of podiform chromite. The geochemistry, specifically the positive Ba, Zr-Hf, Nb-Ta signatures, of the TMO and BBC boninites is remarkably similar as is the geochemistry of the TMO and Voskhod mantle units. The extended trace element plots for the harzburgite and podiform (or ore zone) dunite from the TMO and Voskhod rocks form near identical profiles. Page et al. (2009) demonstrated that the anomalous positive signatures (Ba, Zr-Hf, Nb-Ta) result from the introduction, and subsequent melting, of a continental margin sediment in the subduction zone. The addition of this contaminant at the site of boninite melt production has been recorded in the compositions of the boninites as well as the mantle rocks through which the boninite melt migrated. Based on these observations it is evident that a common genesis process, involving a SSZ fore-arc setting and the addition of a sediment component to the melts formed therein, has formed the Cr-rich podiform chromites present at both localities.

A summary of the samples analysed for the data presented in this chapter is given in Table 5.7.1.

5.7 Summary of samples analysed and data presented in this chapter

Sample I.D	Drill core I.D	Region	Depth down hole (m)	Distance from mineralisation (m)	Location	Rock type	Chromite modal %	Grain Shape	REE Profile shape
G1815	V05-21	West	286.60	n/a	n/a	OZ Dun	< 5%	Eu	Flat
G1823	V05-21	West	297.65	48.80	Footwall	Dist Dun	< 5%	SI	U-shaped
G1742	V05-24	Centre	141.30	142.92	Hanging wall	Harz	< 5%	HL/SI	U-shaped
G1763	V05-24	Centre	167.60	116.61	Hanging wall	Harz	< 5%	HL/SI	LREE-Depleted
G1768	V05-24	Centre	176.94	107.26	Hanging wall	Harz	<5%	HL/SI	LREE-Depleted
G1777	V05-24	Centre	185.60	98.56	Hanging wall	Dist Dun	< 5%	HL/SI	LREE-Enriched
G1795	V05-24	Centre	231.90	52.30	Hanging wall	Harz	< 5%	SI/An	U-shaped
G1798	V05-24	Centre	240.00	44.70	Hanging wall	Dist Dun	< 5%	HL/SI	Flat
VOS-301	V05-24	Centre	249.53	34.67	Hanging wall	Dist Dun	< 5%	HL/SI	LREE-Enriched
VOS-303	V05-24	Centre	252.00	32.50	Hanging wall	Dist Dun	< 5%	SI	LREE-Enriched
VOS-306	V05-24	Centre	258.94	25.26	Hanging wall	Dun Halo	< 5%	HL/SI	LREE-Enriched
VOS-315	V05-24	Centre	270.10	14.10	Hanging wall	Dun/Chr Stringer	~ 50%	SI/Eu	LREE-Depleted
VOS-320	V05-24	Centre	274.59	9.61	Hanging wall	Dist Dun	< 5%	SI	Flat
VOS-322	V05-24	Centre	276.80	7.40	Hanging wall	Harz	< 5%	SI/An	Flat
VOS-327	V05-24	Centre	282.72	1.48	Hanging wall	Harz	< 5%	SI/Eu	LREE-Depleted
F1907	V05-24	Centre	285.50	n/a	n/a	OZ Dun	<5%	SI	LREE-Depleted
F1926	V05-24	Centre	296.70	n/a	n/a	OZ Dun	<5%	Eu	LREE-Enriched
F1968	V05-24	Centre	341.70	n/a	n/a	OZ Dun	<5%	Eu	LREE-Depleted
F1971	V05-24	Centre	343.00	n/a	n/a	OZ Dun	~ 15%	Eu	Flat
F1978	V05-24	Centre	348.00	n/a	n/a	OZ Dun	~ 35%	Eu	Flat
G1908	V05-24	Centre	373.42	n/a	Footwall	Dun Halo	< 5%	SI/Eu	LREE-Enriched
VOS-328	V05-24	Centre	375.00	1.58	Footwall	Dun Halo	< 5%	SI/Eu	LREE-Enriched
VOS-341	V05-24	Centre	389.23	15.81	Footwall	Harz	< 5%	HL	LREE-Depleted
VOS-345	V05-24	Centre	394.00	20.69	Footwall	Harz	< 5%	HL/SI	LREE-Depleted
VOS-348	V05-24	Centre	398.63	25.21	Footwall	Dist Dun	< 5%	HL/SI/Eu	U-shaped
VOS-350	V05-24	Centre	403.00	29.50	Footwall	Dist Dun	< 5%	HL/SI	LREE-Enriched

Sample I.D	Drill core I.D	Region	Depth down hole (m)	Distance from mineralisation (m)	Location	Rock type	Chromite modal %	Grain Shape	REE Profile shape
G1601	V05-28	East	322.09	5.15	Hanging wall	Dun Halo	< 5%	An/SI	LREE-Enriched
G1605	V05-28	East	325.52	1.72	Hanging wall	Dun Halo	< 5%	An/SI	Flat
G1609	V05-28	East	333.85	n/a	n/a	OZ Dun	< 5%	Eu	LREE-Enriched
G1654	V05-28	East	369.70	n/a	n/a	OZ Dun	< 5%	SI/Eu	LREE-Enriched
G1983	V06-48	S. Centre	298.45	1.75	Footwall	Dun Halo	< 5%	SI/Eu	Flat
VOS-185	V06-S6	South	93.95	8.08	Footwall	Harz	< 5%	An/SI	LREE-Enriched

Table 5.7.1: A summary of the Voskhod samples analysed and data presented in this chapter, including the results of the Cr# - Fo (OSMA) clasification diagram and REE profile types.

Rock type: Harz = Harzburgite, Dist Dun = Distal Dunite, Dun Halo = Dunite Halo, OZ Dun = Ore Zone Dunite, Dun/Chr Stringer = chromitiferous dunite (weakly mineralised) present outside of the classified ore zone region. Grain shape: HL = Holly Leaf, An = Anhedral, SI = Subidiomorphic, Eu = Euhedral. For the REE geochemistry results see Section 5.6.2.

Chapter 6: Tectonic setting discrimination using chromite from the Voskhod deposit peridotite, dunite and chromitite units

6.1 Aim of the Chapter

The aim of this chapter is to determine the tectonic setting associated with the genesis of the Voskhod podiform chromitite deposit in the Main Ore Field (MOF) of the Kempirsai Massif. The formation of the collective group of large ore-bodies present in the MOF can be interpreted to be the result of the mantle region having been subjected to large volumes of focused melt flow. In this chapter a data subset of the least altered samples of harzburgite, dunite and chromitite, selected from the hanging wall, ore zone and footwall of the Voskhod deposit, is interrogated in an attempt to understand what is distinctive about the formational history of this mantle region. The chromites in these samples have been analysed by electron microprobe analysis (EMPA) to obtain accurate Fe^{3+} values that may be used to determine oxygen fugacity and Ga contents collected by laser ablation induced coupled plasma mass spectroscopy analysis (LA-ICP-MS) (Appendix E). These new chromite data provide the opportunity to determine the tectonic setting as well as provide an insight into the genetic processes associated with the formation of this super-size (>18 Mt of chromite ore) podiform chromitite deposit.

6.1.1 Tectonic Settings

For a section of oceanic crust the tectonic setting changes during the process of ocean basin opening and closure (see Chapter 2, Section 2.2). Melts and residues formed in each setting have characteristic, genetic geochemical fingerprints.

6.1.2 Tectonic discrimination diagrams: An overview

Characterisation of the setting e.g. back-arc, forearc, island arc or MOR that ophiolitic peridotite formed in is integral to interpreting the tectonic setting in which the unit formed and its evolutionary history.

In this chapter the harzburgite and dunite samples, collected from the Voskhod deposit and encompassing host units, are investigated by studying the geochemical composition of chromite in an attempt to determine the genetic history associated with the formation of the Voskhod deposit.

6.2 Methodology

6.2.1 Sample selection

For the purposes of this study 46 samples, sourced from five drill cores, were selected for analysis. The sample number, location, rock-type (determined optically and verified by whole rock data analyses, see Chapter 5 Section 5.6), position relative to mineralisation, modal proportion of chromite and chromite grain shapes are provided for each sample in Table 6.2.1.

Table 6.2.2 details the samples analysed and the analytical methods used to analyse the chromite, and where possible the olivine, composition in each sample.

Analytical methods used are presented in Appendix A.

Sample No.	Drill Core I.D	Region in ore body	Depth (down hole) m	Rock Type	Position	Dist from Min (down hole) m	Chromite Modal %	Grain Shape
G1742	V05-24	Centre	141.30	Harz	Hanging wall	142.92	< 5%	HL/SI
G1791	V05-24	Centre	221.00	Harz	Hanging wall	63.17	< 5%	HL/SI
G1795	V05-24	Centre	231.90	Harz	Hanging wall	52.30	< 5%	SI/An
Vos-322	V05-24	Centre	276.80	Harz	Hanging wall	7.40	< 5%	SI/An
Vos-327	V05-24	Centre	276.80	Harz	Hanging wall	1.48	< 5%	SI/Eu
Vos-345	V05-24	Centre	394.00	Harz	Footwall	20.69	< 5%	HL/SI
Vos-341	V05-24	Centre	389.23	Harz	Footwall	15.81	< 5%	HL
G1798	V05-24	Centre	240.00	Dun	Hanging wall	44.70	< 5%	HL/SI
G1777	V05-24	Centre	185.60	Dun	Hanging wall	98.56	< 5%	HL/SI
Vos-301	V05-24	Centre	249.53	Dun	Hanging wall	34.67	< 5%	HL/SI
Vos-303	V05-24	Centre	252.00	Dun	Hanging wall	32.50	< 5%	SI
G1601	V05-28	East	322.09	Dun	Hanging wall	5.15	< 5%	An/SI
G1910	V06-48	S. Centre	200.75	Dun	Hanging wall	0.56	< 5%	SI/Eu
Vos-306	V05-24	Centre	258.94	Dun Halo	Contact	25.26	< 5%	HL/SI
Vos-309	V05-24	Centre	265.80	Dun Halo	Contact	18.40	< 5%	SI/Eu
F1901	V05-24	Centre	284.20	Dun Halo	Contact	0.00	< 5%	SI/Eu
Vos-174	V06-S6	South	66.45	Dun Halo	Contact	13.05	< 5%	SI
Vos-179	V06-S6	South	79.50	Dun Halo	Contact	0.00	< 10%	SI
G1989	V05-21	West	246.45	Dun Halo	Contact	2.40	< 5%	SI/Eu
G1991	V05-21	West	247.40	Dun Halo	Contact	1.45	< 5%	SI/Eu
G1605	V05-28	East	325.52	Dun Halo	Contact	1.72	< 5%	An/SI
Vos-348	V05-24	Centre	398.63	Dun	Footwall	25.21	< 5%	HL/SI/Eu
Vos-350	V05-24	Centre	403.00	Dun	Footwall	29.50	< 5%	HL/SI
Vos-328	V05-24	Centre	375.00	Dun Halo	Contact	1.58	< 5%	SI/Eu
G1983	V06-48	S. Centre	298.45	Dun Halo	Contact	1.75	< 5%	SI/Eu
G1988	V06-48	S. Centre	300.15	Dun Halo	Contact	3.45	< 5%	SI/Eu
F1907	V05-24	Centre	285.50	Dun	Ore Zone	n/a	< 5%	SI
G1908	V05-24	Centre	372.00	Dun	Ore Zone	0.52	< 5%	SI/Eu
G1631	V05-28	East	434.40	Dun	Ore Zone	n/a	< 5%	SI/Eu
G1623	V05-28	East	354.67	Dun	Ore Zone	n/a	< 5%	SI/Eu
G1624	V05-28	East	432.97	Dun	Ore Zone	n/a	< 10%	SI/Eu
G1956	V06-48	S. Centre	288.55	Dun	Ore Zone	n/a	~ 15%	SI/Eu
G1941	V06-48	S. Centre	231.35	Dun	Ore Zone	n/a	< 5%	SI/Eu
Vos-312	V05-24	Centre	266.88	Chromitite	Ore Zone	n/a	~ 30%	SI/Eu
Vos-315	V05-24	Centre	270.10	Chromitite	Ore Zone	n/a	~ 50%	SI/Eu
F1920	V05-24	Centre	290.50	Chromitite	Ore Zone	n/a	~ 10%	SI/Eu
F1925	V05-24	Centre	296.12	Chromitite	Ore Zone	n/a	~ 30%	Eu
F1935	V05-24	Centre	311.60	Chromitite	Ore Zone	n/a	> 90%	Eu

Table 6.2.1: The Voskhod sample suite used for the tectonic setting discrimination study.

"Region" refers to the area of the ore body the drill core intercepts. Rock-type code: Harz= Harzburgite, Dun= Dunite and Dun Halo= Dunite Halo. Chromite grain shape codes: HL= Holly Leaf, SI= Subidiomorphic, An= Anhedral and Eu= Euhedral.

Sample	Rock Type	Drill Core I.D	Analytical Techniques		
			LEO 360 SEM	CAMECA SX-50 EMP	LA-ICP-MS (Laser)
G1742	Harzburgite - HGWL	V05-24	Yes (+ Olivine)	Yes	Yes
G1791	Harzburgite - HGWL	V05-24	Yes (+ Olivine)	No	No
G1795	Harzburgite - HGWL	V05-24	Yes (+ Olivine)	Yes	Yes
Vos-322	Harzburgite - HGWL	V05-24	Yes (+ Olivine)	Yes	No - Failed Run
Vos-327	Harzburgite - HGWL	V05-24	Yes (+ Olivine)	Yes	Yes
Vos-345	Harzburgite - FTWL	V05-24	Yes	No	Yes
Vos-341	Harzburgite - FTWL	V05-24	Yes (+ Olivine)	Yes	Yes
G1798	Dunite - HGWL	V05-24	Yes (+ Olivine)	Yes - (n.d Olivine)	Yes
G1777	Dunite - HGWL	V05-24	Yes (+ Olivine)	Yes	Yes
Vos-301	Dunite - HGWL	V05-24	Yes (+ Olivine)	Yes	Yes
Vos-303	Dunite - HGWL	V05-24	Yes	Yes	Yes
G1601	Dunite - HGWL	V05-28	Yes (+ Olivine)	No	No
G1910	Dunite - HGWL	V06-48	Yes (+ Olivine)	No	No
Vos-306	Dunite Halo - HGWL	V05-24	Yes (+ Olivine)	Yes	Yes
Vos-309	Dunite Halo - HGWL	V05-24	Yes	No	No
F1901	Dunite Halo - HGWL	V05-24	Yes	No	No
Vos-174	Dunite Halo - HGWL	V06-S6	Yes (+ Olivine)	No	No
Vos-179	Dunite Halo - HGWL	V06-S6	Yes (+ Olivine)	No	No
G1989	Dunite Halo - HGWL	V05-21	Yes	No	No
G1991	Dunite Halo - HGWL	V05-21	Yes	No	No
G1605	Dunite Halo - HGWL	V05-28	Yes (+ Olivine)	No	No
Vos-348	Dunite - FTWL	V05-24	Yes (+ Olivine)	Yes	Yes
Vos-350	Dunite - FTWL	V05-24	Yes (+ Olivine)	Yes	Yes
Vos-328	Dunite Halo - FTWL	V05-24	Yes (+ Olivine)	Yes	Yes
G1983	Dunite Halo - FTWL	V06-48	Yes (+ Olivine)	No	No
G1988	Dunite Halo - FTWL	V06-48	Yes (+ Olivine)	No	No
F1907	Dunite - OZ	V05-24	Yes (+ Olivine)	Yes	Yes
G1908	Dunite - OZ	V05-24	Yes (+ Olivine)	Yes	Yes
G1631	Dunite - OZ	V05-28	Yes (+ Olivine)	No	No
G1623	Dunite - OZ	V05-28	Yes (+ Olivine)	No	No
G1624	Dunite - OZ	V05-28	Yes (+ Olivine)	No	No
G1956	Dunite - OZ	V06-48	Yes	No	No
G1941	Dunite - OZ	V06-48	Yes	No	No
Vos-315	Chromitite - OZ	V05-24	Yes (+ Olivine)	Yes	Yes
Vos-312	Chromitite - OZ	V05-24	Yes	Yes - (n.d Olivine)	Yes
F1920	Chromitite - OZ	V05-24	Yes	No	No
F1925	Chromitite - OZ	V05-24	Yes	No	No
F1935	Chromitite - OZ	V05-24	Yes	No	No
F1965	Chromitite - OZ	V05-24	Yes	No	No
F1967	Chromitite - OZ	V05-24	Yes	No	No
F1971	Chromitite - OZ	V05-24	Yes	Yes - (n.d Olivine)	Yes

Table 6.2.2: The Voskhod sample suite analysed and analytical methods used.

HGWL = Hanging wall, FTWL = Footwall and OZ = Ore Zone. For the SEM data (+ Olivine) indicates that olivine composition data was collected for these samples. For the EMPA data (n.d Olivine) signifies that no olivine composition data was collected. In the absence of EMPA data for olivine compositions it was not possible to calculate Δ log fO_2 values for samples.

6.3 The Voskhod Chromite Deposit: A Crustal or Mantle Chromitite?

Chromite is commonly found in a many geological settings. Barnes and Roeder (2001) compiled a global spinel database to investigate the diverse range of chromite compositions in terrestrial mafic and ultramafic rocks.

Chromite Type Category	Locality (chromite data source)
Stratiform Complex	Bushveld Complex, South Africa Stillwater Complex, Montana, USA
Ophiolite Complex	Kempirsai Massif, Kazakhstan Limmasol, Cyprus Troodos, Cyprus Oman Luobousa, Tibet Voskhod (Kempirsai Massif), Kazakhstan (this study)

Table 6.3.1: Chromite source locations

The location source for the chromite data of each chromite type category presented in Figure 6.3.1.Chromite type categories and chromite source localities are from Barnes and Roeder, 2001.

Barnes & Roeder used 50th percentile contours as a guideline to assist in the discrimination of chromite compositions and establish a parental source setting. It is evident from Figure 6.3.1 that Mg# is the key discriminatory value that distinguishes between podiform and stratiform chromitites. The podiform chromitites have elevated Mg# (0.56 – 0.80) in comparison to the stratiform chromitites (0.25 - 0.56). In terms of Cr# the podiform chromitites span a greater range of values (0.48 – 0.86) than the stratiform chromitites (0.56 – 0.77).

Chromite compositions from the Voskhod podiform chromitite are shown in Figure 6.3.1. Cr# ranges from 0.83 to 0.86 and Mg# from 0.77 to 0.46. The Voskhod chromitite data plots in the ophiolite field, confirming its classification as a podiform chromite deposit.

Chromite from Kempirsai and Voskhod possess the highest Cr# (average Cr# is 0.85) content when compared to the composition of chromite sourced from other podiform chromitites (Figure 6.3.1). The Voskhod deposit chromite compositions

represent an end member of the podiform chromitite group in terms of Cr# contents that extend to higher values than are common for ophiolitic chromite.

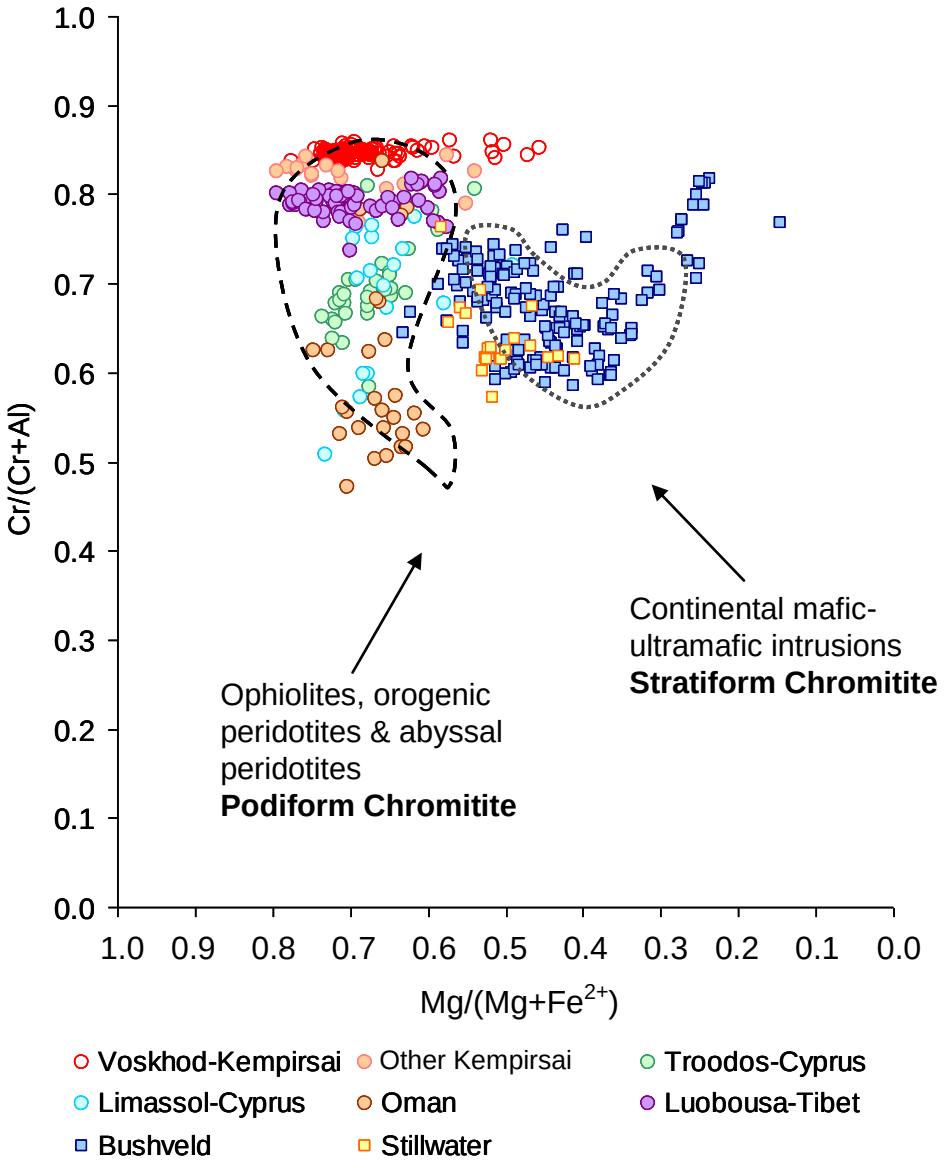

Figure 6.3.1: A plot of Cr# against Mg# to discriminate between chromitites of differing genetic origins.

The chromitites from the Voskhod deposit (this study), the Kempirsai Massif (*Melcher et al., 1997; Pavlov & Grigoryeva, 1977*), Troodos (*Greenbaum, 1977; Panayiotou et al., 1986*), Limassol (*Panayiotou, 1978*), Oman (*Leblanc & Nicolas, 1992*; *Peters & Kramers, 1974*) and Luobousa (*Zhou et al., 1994; Zhou & Robinson, 1994*) are all ophiolite hosted, podiform chromitites. The chromitites from the Bushveld (*Cameron, 1977; deWaal, 1975; Teigler & Eales, 1993; Scoon & Teigler, 1995)* and Stillwater complexes (*Howland, 1955; Stevens, 1944; Nicholson & Lipin, 1985*) are stratiform (mafic layered intrusion) hosted. (All fields are the 50th percentiles taken from *Barnes and Roeder, 2001)*.

Having identified the Voskhod chromitite host environment as being the mantle, the next questions are; in what geotectonic setting did the chromite pod and the immediately surrounding host rocks form in and what processes led to the formation of the deposit?

6.3.1 Petrogenesis of the Voskhod host peridotites using the Olivine-Spinel Mantle Array (OSMA) diagram

The composition of olivine and chromite coexisting in the same peridotite can be used to decide whether the rock is a residue remaining after partial melting or whether it crystallised from new melt rising through a pre-existing mantle sequence.

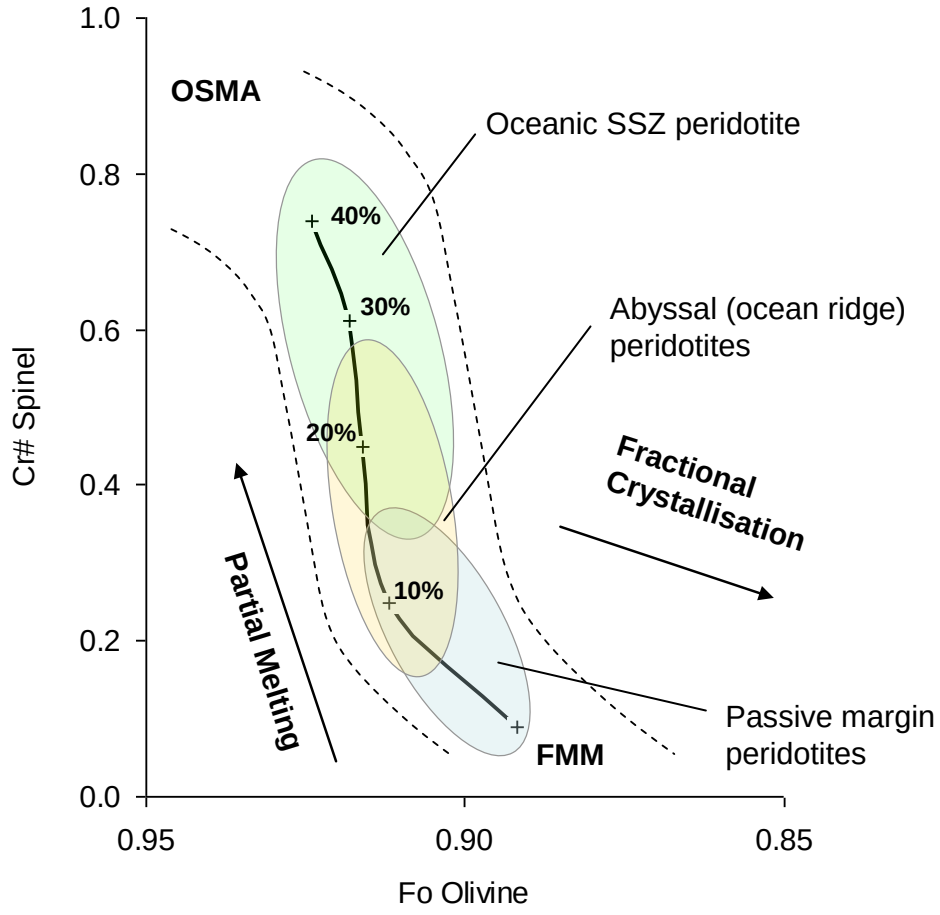

Figure 6.3.2: An illustration defining the fields given in the Cr#-Fo diagram

The dashed parallel lines define the olivine-spinel mantle array (OSMA), a spinel peridotite mantle restite trend as defined by Arai (1987,1994(a)). The FMM Fertile MORB mantle theoretical melting trend (Jacques and Green, 1980; Arai, 1994a). The abyssal (ocean ridge) field of Dick & Bullen (1984), the oceanic supra-subduction zone peridotite field and passive continental margin field estimated by Pearce et al. (2000) from published data.

In the $Cr\#_{(sp)}$-$Fo_{(ol)}$ diagram of Arai (*1987, 1990(a) Arai 1994a, b*), $Cr\#_{(sp)}$ is the Cr/(Cr+Al) ratio of chromite and $Fo_{(ol)}$ is the $100*Mg/(Mg+Fe^{2+})$ ratio in co-existing olivine (see Figure 6.3.2). During partial melting, the Cr# of chromite and Fo content of olivine comprising residual mantle increases; this trend forms the OSMA (olivine spinel mantle array). Residual peridotites plot within the OSMA. In contrast, olivine formed by fractional crystallisation from a magma has lower Fo values as the forsterite content of olivine decreases during fractional crystallisation. The chromite-olivine pair in this rock-type plot to the right, outside of the OSMA boundary, although Arai (*1994a*) acknowledged that such discrimination was not always effective and that in some instances 'new' olivine crystallising from a melt may form dunite that plots within the OSMA lines, provided that the liquid does not fractionate

Three peridotite-type fields are identified on the OSMA plot; passive margin peridotite, abyssal peridotite and SSZ peridotite (*Dick and Bullen, 1984; Pearce et al., 2000*) (Figure 6.3.2). Ophiolitic – SSZ mantle and sub-continental mantle have a wide range of Cr# values from 0.08 to 0.95 (*Arai, 1994a*). Peridotite sourced from the harzburgite-lherzolite boundary typically has chromite with Cr# ~ 0.5. Ophiolitic lherzolite with Cr# < 0.3 is rare. Such chromite values are more commonly associated with lherzolite derived from a subcontinental setting (*Arai, 1994a,b*).

The majority of the Voskhod samples plot within the abyssal (ocean ridge) peridotite field (Figure 6.3.3). However, peridotites from passive margins, oceanic arcs and marginal basins also have the potential to plot in this field (*Pearce et al., 2000*). One dunite footwall and three dunite halo samples plot in the oceanic SSZ peridotite field, indicating that these samples have experienced higher degrees of partial melting in comparison to those that plot in the abyssal peridotite field. The chromitites and remaining dunite halo samples plot within the OSMA, but outside of the three peridotite fields, these samples possess very high $Fo_{(ol)}$ and $Cr\#_{(sp)}$ values that are consistent with a SSZ origin (*Dick and Bullen, 1984; Bonatti and Michael, 1989, Arai, 1994a, 1997; Pearce et a., 2000; Tamura & Arai, 2006*)

The chemical composition of chromite allows the origin and evolution of its host peridotite to be constrained. This is achieved using the olivine-spinel mantle array

(OSMA) a field identified on the $Cr\#_{(sp)}$-$Fo_{(ol)}$ plot (*Arai, 1987, and 1994a*) that may be used to differentiate between residual mantle peridotite and peridotite formed by fractional crystallisation.

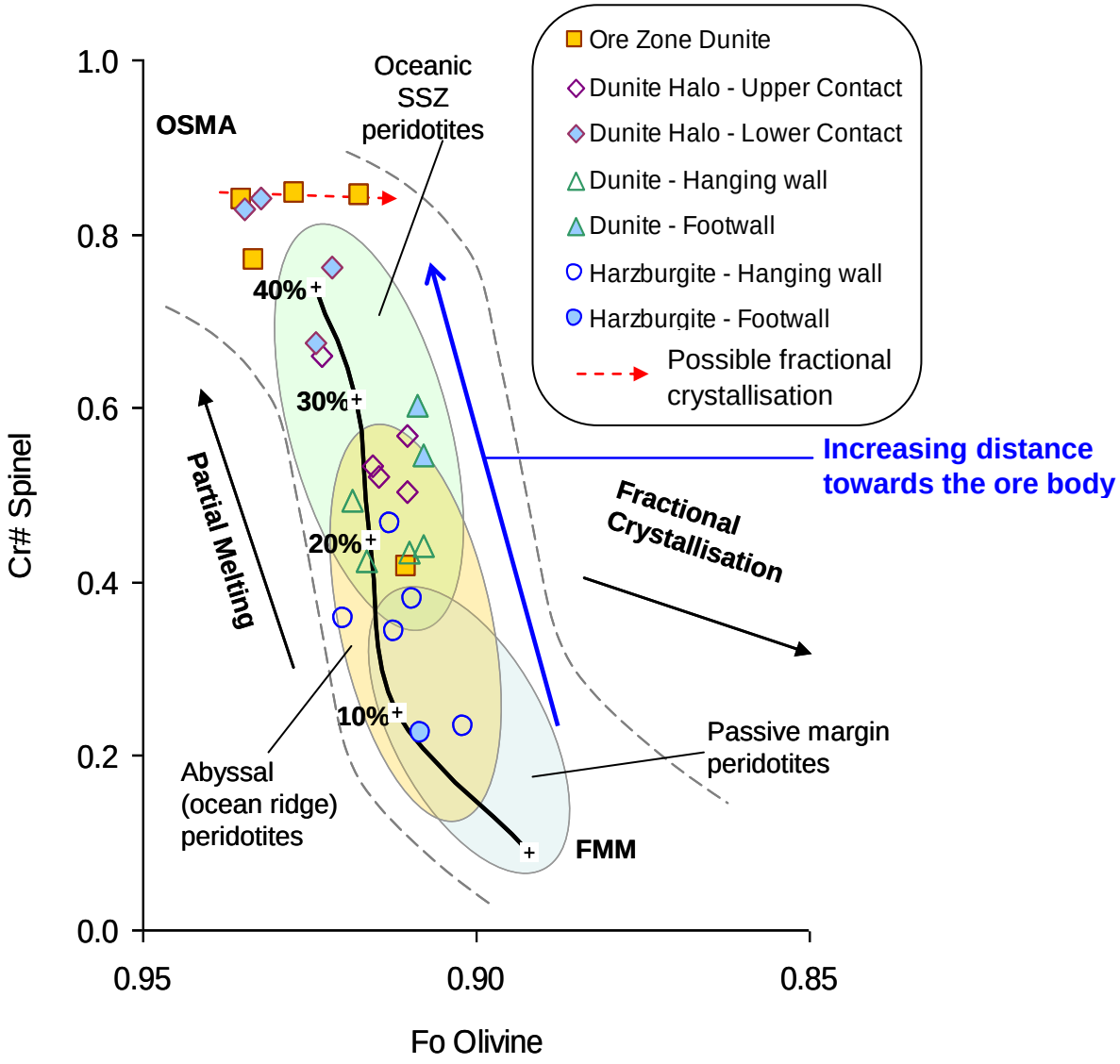

Figure 6.3.3: A plot of Cr# spinel against the Fo content of olivine from the host peridotites and dunite, dunite halo and chromitite rocks of the Voskhod deposit.

The dashed parallel lines define the olivine-spinel mantle array (OSMA), a spinel peridotite mantle restite trend as defined by Arai (*1987,1994(a)*). The FMM Fertile MORB mantle theoretical melting trend (*Jacques and Green, 1980; Arai, 1994a*). The abyssal (ocean ridge) field of Dick & Bullen (*1984*), the oceanic supra-subduction zone peridotite field and passive continental margin field estimated by Pearce et al. (*2000*) from published data. Data presented chromite compositions Appendix D, olivine Fo contents Appendix F .

The $Cr\#_{(sp)}$ compositions of the Voskhod silicate rocks range from 0.23 to 0.85 and $Fo_{(ol)}$ contents range from 90.2 to 93.5 (Appendix F). All 26 samples fall within the

OSMA (Figure 6.6.3) implying that these rocks are likely to be of mantle origin and at first sight it might be expected that they are residues of partial melting.

The rock types plot systematically in a progressive order along the OSMA, from low $Cr\#_{(sp)}$ and $Fo_{(ol)}$ values (harzburgite), to high $Cr\#_{(sp)}$ and $Fo_{(ol)}$ values (ore zone dunite). The sequence is as follows; harzburgite, dunite, dunite halo and ore zone dunite. The order may be considered to reflect an increase in the degree of partial melting of the host peridotite with increasing proximity towards the chromitite orebody; such that the peridotite immediately adjacent (dunite halo) and internal to the orebody (ore zone dunite) has been subject to the highest degrees of partial melting (as indicated by the blue arrow Figure 6.3.3). This is not to say that the chromitite formed by partial melting of the mantle or is itself residual; the high degrees of partial melting (>40%) required for chromitite to form (especially that of a monomineralic nature, possessing Cr# values >0.80 and forming an 18 Mt chromite deposit), would be unrealistically obtainable as results from experiments conducted by Jacques & Green (1980) demonstrate.

A theoretical melting trend shows the percentage melting of a fertile MORB mantle (FMM) source. This is illustrated on Figure 6.3.3 by the sigmoid trend shown as a solid black line that extends through the centre of the OSMA plot (*Jacques and Green, 1980; Arai, 1994a*). Considering this theoretical melting curve, the range of $Cr\#_{(sp)}$ values obtained for the Voskhod chromitite host peridotite samples indicates that 10 – 40% partial melting of the mantle peridotite has occurred. Arai (*1994a*) proposed that residual lherzolite would have a maximum $Cr\#_{(sp)}$ of 0.3 corresponding to ~10% partial melting, residual harzburgite to have $Cr\#_{(sp)} \leq 0.6$ associated with up to 30% partial melting and residual dunites, $Cr\#_{(sp)}$ values between 0.6-0.75, resulting from 30-40% partial melting (of fertile MORB mantle).

The harzburgite samples have the lowest $Cr\#_{(sp)}$ and $Fo_{(ol)}$ values with $Cr\#_{(sp)}$ 0.23 – 0.47 and $Fo_{(ol)}$ 90.2 – 92.0. Samples G1742, from the hanging wall and Vos-341, from the footwall, are offset from the other harzburgite samples having especially low $Cr\#_{(sp)}$ values that are comparable with chromites from a passive margin peridotite setting. From Table 6.2.1 it is seen that G1742 was collected furthest from the ore body, 141.30 m from the start of mineralisation (down hole), while Vos-341 at 15.81 m from the start of mineralisation is much closer to the ore body.

These $Cr\#_{(sp)}$ values correlate with ~10% partial melting of the mantle. Petrographically the harzburgite samples are clinopyroxene poor (where clinopyroxene constitutes <3% of the modal proportion mineral assemblage see Appendix G) this suggests that the harzburgite is depleted (whole rock analyses also support this interpretation, see Chapter 5, Section 5.6). These are the most fertile peridotites in the Voskhod sample series, having undergone the lowest degrees of partial melting.

The dunite and dunite halo samples have intermediate $Cr\#_{(sp)}$ and $Fo_{(ol)}$ values, $Cr\#_{(sp)}$ 0.42 – 0.66 and $Fo_{(ol)}$ 90.8 – 92.3. In the context of the OSMA diagram the higher $Cr\#_{(sp)}$ values of the dunite compared to the harzburgite, may indicate that these rocks have undergone higher degrees of partial melting, approximately 20-30%, or been subject to increased metasomatic interaction transforming orthopyroxene into olivine. The dunite halo samples have $Cr\#_{(sp)}$ 0.50 – 0.84 and $Fo_{(ol)}$ 91.0 – 93.5 which are higher than the dunite samples perhaps indicating increased metasomatic interaction between the host and products of the invading melt.

The ore zone dunite samples possess the highest $Cr\#_{(sp)}$ values 0.77 – 0.85 and $Fo_{(ol)}$ 91.7 – 93.5, and are offset at elevated $Cr\#_{(sp)}$ values from the partial melting curve. There is a suggestion of a horizontal trend in these samples consistent with early fractionates from the invading melt, if this is the case fractionation has been insufficient to take them outside of the OSMA.

Given that the compositions form a systematic trend (dunite appears to be an extension of harzburgite, and the dunite envelop an extension of dunite), with one group following on from the next, it is suggested that these sample groups are genetically linked. The trend formed by the series harzburgite, dunite, dunite halo corresponds with the rocks being progressively depleted. To distinguish between the effect of increased melting that produces increasingly depleted residue and late-stage melt-rock reaction that can further deplete existing residue, requires other geochemical evidence presented later in this chapter.

Despite the appearance of the samples forming a progressive partial melting trend this genesis model is theoretically infeasible. Instead, it raises the question of

whether the samples could be related by melt-rock interaction; with harzburgite being the least reacted and ore zone dunite being the most reacted. This possible model is examined later in this chapter.

The trend formed by the limited number of ore-zone dunite samples suggests that this rock-type is crystallising from a new melt and is beginning to form a crystallisation trend that if continued would progress outside the OSMA.

6.4 Peridotite-type Discrimination and Significance

The melt composition controls the Al_2O_3 content of mantle chromite (*Maurel & Maurel. 1982*). The melt composition may be influenced by several parameters; pressure, temperature, the extent of partial melting, the chemical nature of the source as well as phase compositions. Early stage melts derived from melting of a fertile mantle source are relatively more enriched in LILEs and LREEs with respect to HREEs and incompatible elements (e.g. LIP and OIB magmas) than melts produced by late stage melting of a depleted mantle source that are depleted in LREEs with respect to HREE (e.g. MORB magmas) (Chapter 5, Section 5.6). Changes to the pressure and temperature conditions at the time of melting impact the chemistry of the melts produced. Melts formed under high pressure and temperature conditions (e.g. boninites) have greater abundances of Mg, Fe and Ti in comparison to lower pressure and temperature melts (primary MORB melts) that are higher in Si and Al (*Danyushevsky et al., 1987; Sobolev & Shimizu, 1993; Kamenetsky et al., 2001*).

The TiO_2 against Al_2O_3 diagram (Figure 6.4.2) distinguishes between MORB and SSZ peridotite types and includes fields to differentiate between magma chemistries (determined by chromite compositions obtained from volcanic rocks) (*Kamenetsky et al., 2001*). Mantle chromite compositions that relate in terms of geochemical composition to a magma field (MORB, OIB, LIP, BAB and Arc) may provide evidence for reaction between the mantle and an ascending melt. Furthermore the diagram may be used to infer the chemistry of the reacting melt (*Page & Barnes, 2009*).

6.4.1 TiO_2-Al_2O_3 Chromite Composition Variation: Host Peridotite- and Reacting Melt-type Discrimination Diagram

TiO_2 content in chromite is a useful parameter to use when investigating melt-rock reaction and interpreting tectonic setting (*Arai, 1992; Kelemen et al., 1995; Edwards & Malpas, 1996; Edwards et al., 1996; Pearce et al., 2000*). The mantle TiO_2 component is progressively depleted during partial melting (preferentially partitioning into the melt fraction) and is enriched by interaction with a melt. The TiO_2 - Al_2O_3 content of chromite can be used to distinguish between different parent magma chemistries, by comparison with a set of fields from volcanic rocks and mantle peridotites (Figure 6.4.1). Mantle chromite compositions that are geochemically similar to chromites in lavas (e.g. mid ocean ridge basalt - MORB, ocean island basalt - OIB, large igneous provinces - LIP, back arc basin - BAB and island arc – ARC settings) may provide evidence for interaction between the mantle and ascending melts promoting the crystallisation of chromite in the mantle (*Zhou et al., 1998 ; Edwards et al., 2000; Rollinson, 2008; Page & Barnes, 2009*). Using the identified magma-type fields it may be possible to infer the parent of the reacting melt and subsequently constrain the tectonic setting with which the melt-type is associated (*Page & Barnes, 2009*).

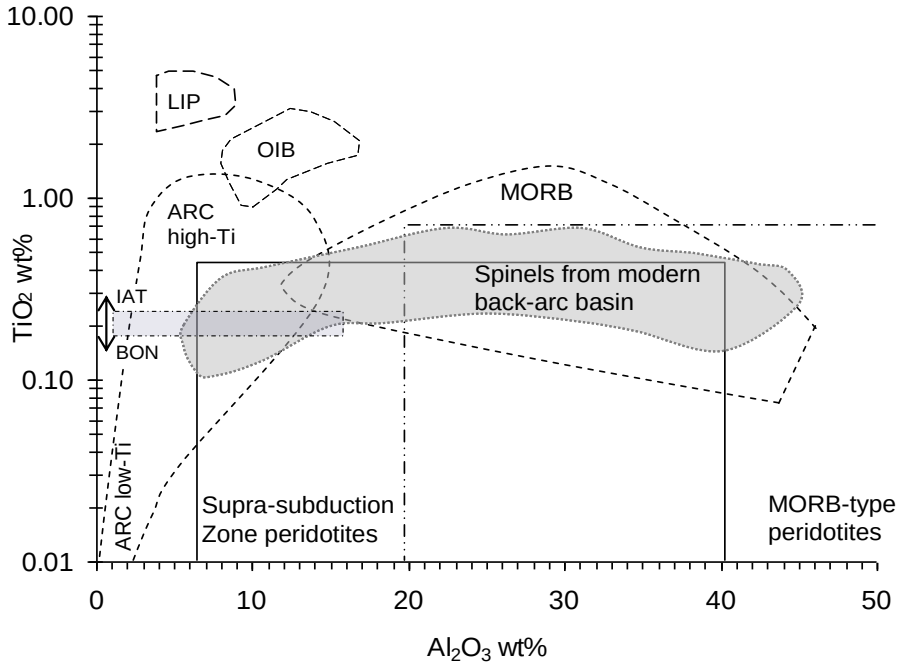

Figure 6.4.1: TiO_2 against Al_2O_3 illustrating the peridotite type and lava type defined field boundaries after Kamenetsky et al., 2001.

Kamenestsky et al., (*2001*) showed that the Al_2O_3 and TiO_2 content of chromite is controlled by the parental melt. The composition of chromite reflects the composition of the melt it is in equilibrium with (*Maurel & Maurel, 1982; Roeder & Reynolds, 1991*). The Al_2O_3 and TiO_2 contents of chromites from genetically-related peridotite, dunite and chromitite samples aids the interpretation of the tectonic setting in which they formed. Page and Barnes (2009) further investigated this theory for podiform chromitite from both MOR and SSZ tectonic settings. Their results showed that the composition of chromite from podiform chromitites ranges from arc to MORB melt type fields and they interpreted these findings as demonstrating that both melt types are capable of forming podiform chromitite (fields shown in Figure 6.4.2). A similar conclusion was reached by Rollinson (2008) who concluded that two different magma types were responsible for the stratigraphically low, high-Cr chromites and the stratigraphically high low-Cr chromitites in the Oman ophiolite.

On the TiO_2 -Al_2O_3 diagram (Figure 6.4.2) the Voskhod sample suite chromites plot in a progressive order with high-Al harzburgite chromite in the MORB-type peridotite field progressing into the transitional MORB-type – SSZ-type peridotite region as the Al_2O_3 content of the chromites increases. Chromites from all dunite and five dunite halo samples plot in the transitional MORB-type – SSZ-type peridotite region. The dunite halo chromites lie close to the SSZ-type peridotite field boundary. Eight chromite analyses from dunite halo, ore-zone dunite and chromitite samples plot in the SSZ-type peridotite field. Chromite from ore-zone dunite and chromitite plot in the boundary overlap between the SSZ-type peridotite, modern back-arc basin and arc fields. In terms of the arc field characterisation these chromites have low Al_2O_3 wt % and intermediate TiO_2 wt % compositions, that are comparable with the chemistry of a boninitie melt. (S*ee also, Menzies & Hawkesworth, 1987; Arai & Yurimoto, 1994; Arai, 1997, Page et al. 2008*).

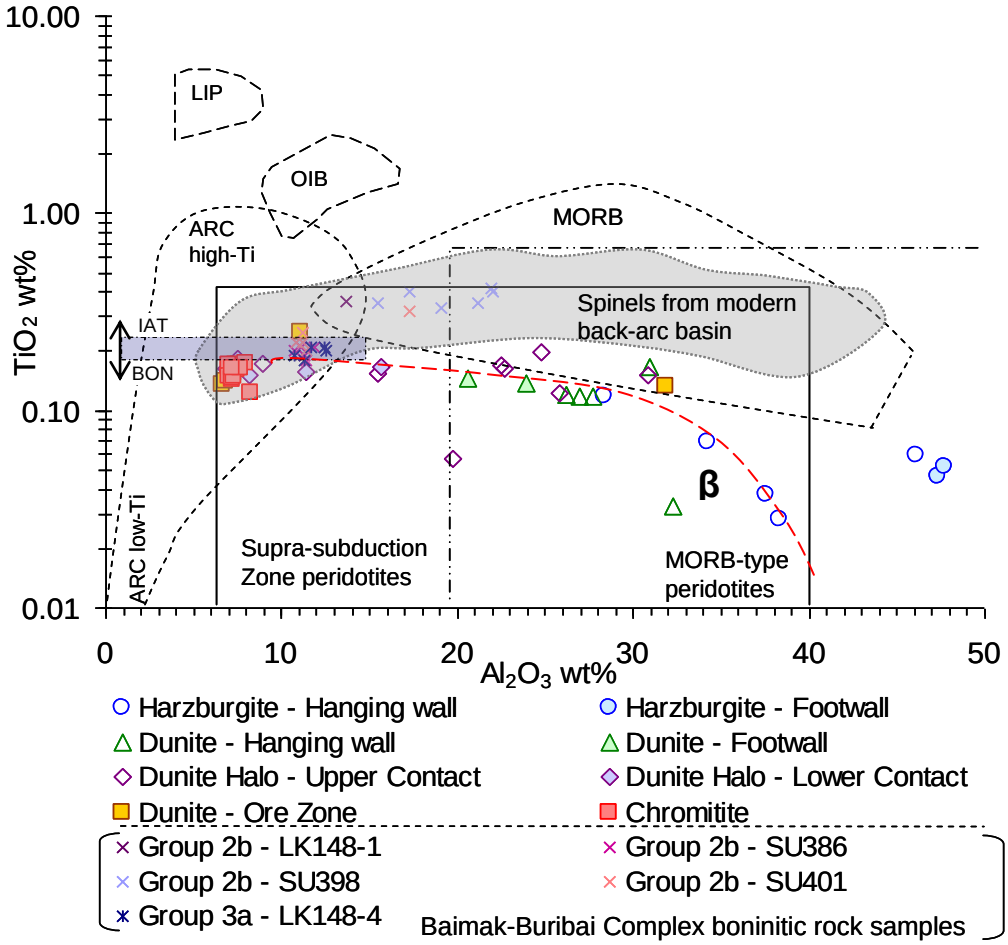

Figure 6.4.2: TiO_2-Al_2O_3 variation as seen in Cr-spinel with respect to modern day tectonic settings.

Composition of chromites from the Voskhod podiform chromitite plotted in Kamenetsky et al., 2001 fields for chromites from volcanic rocks. LIP = large igneous province basalt, OIB = ocean island basalt, MORB = mid ocean ridge basalt, ARC = arc related volcanic rocks (boninites = BON, island-arc tholeiites = IAT from Page and Barnes, 2009). Data presented in Appendix D.

Chromites in harzburgite have the lowest TiO_2 wt % (average, 0.06 wt%) and the highest Al_2O_3 wt % (average, 39.95 wt%) values of the dataset.

From the harzburgite to dunite chromites there is an increase in the average TiO_2 content from 0.06 wt % to 0.12 wt % respectively. Chromites from the dunite samples have an average Al_2O_3 content of 26.90 wt % and TiO_2 values ranging from 0.12 to 0.17 wt %. Within this sample subset is an anomalous data point with a low TiO_2 value of 0.03 wt %. This TiO_2 value is geochemically similar to that of chromite in harzburgite.

Between the dunite and dunite halo there is an increase in the average TiO_2 wt % from 0.12 wt % to 0.15 wt%, respectively. Furthermore, the dunite halo chromites have a higher average Al_2O_3 content of 16.94 wt %.

Chromites from the ore-zone dunite and chromitite samples both show average TiO_2 values of, 0.16 wt %. However, it is evident that the average TiO_2 wt% in the chromite of the ore zone dunite is skewed by an anomalous value of 0.25 wt %. Discarding this outlier, the average content of the ore-zone dunite chromite is 0.15 wt %. This value is in keeping with the progressive increase in TiO_2 composition seen with proximity towards the orebody and that peaks in the ore zone.

Compositions of chromites analysed from the Baimak-Burabai Complex (BBC) boninites are also included in Figure 6.4.2. (data from *Spaeda et al., 1998*). The chromite values for Groups 2b–SU386 and 3a–LK148-4 are the similar to those of dunite halo and ore zone dunite chromites. They plot in the SSZ-peridotite field and possess an arc signature that is intermediate between a boninite and IAT composition.

6.5 Cr# - TiO_2 wt% diagram: Melt-mantle interaction discrimination

The Voskhod samples are plotted on a Cr# - TiO_2 wt % diagram (Figure 6.5.1). The Cr#-TiO_2 composition relationships of chromite may be used to fingerprint the tectonic setting in which the samples formed. The diagram is effective at distinguishing between chromite formed by partial melting and melt rock interaction processes (*e.g. Arai, 1992; Zhou et al., 1996; Pearce et al., 2000*). The plot also provides information on the extent of partial melting of the mantle and the geochemistry of the melts associated with melt-rock interaction (*Pearce et al., 2000*).

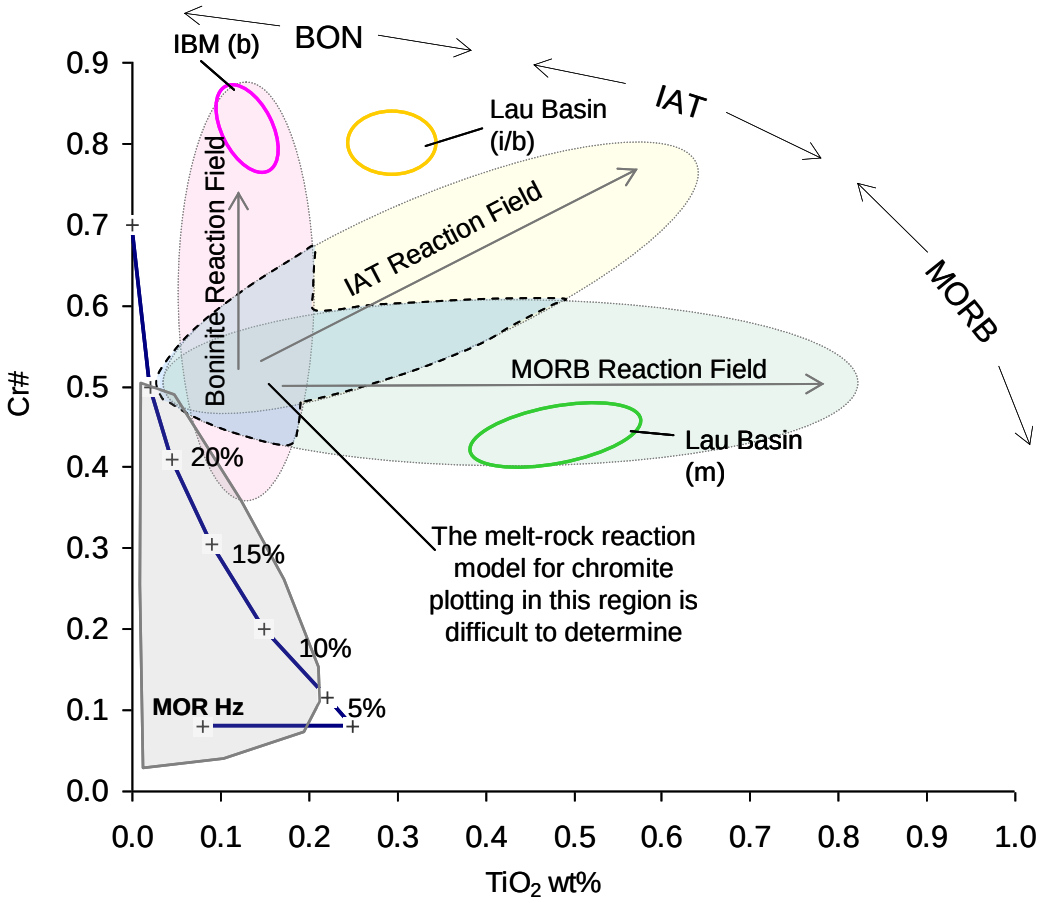

Figure 6.5.1: A plot of Cr# against TiO_2 wt% annotated with reaction fields.

Diagrammatic lava-type fields (MORB, IAT and BON), the theoretical fertile MOR mantle (FMM) melting curve and melt-mantle reaction trends (MORB and BON) after Pearce et al., 2000.

Interaction between a Ti-poor, depleted mantle peridotite and a Ti-rich melt will upgrade the Ti content of a peridotite. The extent of Ti incorporation into the peridotite is dependant on the availability of Ti from the melt (determined by the composition of the melt) and the extent of interaction between the melt and peridotite. Consequently, using chromite compositions obtained from dunites and harzburgites that are considered to be genetically linked (as a result of varying degrees of reaction between melt and residual mantle) it is possible to form a reaction trend that defines the composition of the reacting melt (*Pearce, et al., 2000*).

Pearce et al. (2000) modelled the change in the Ti component of chromite that results from fractional melting of a fertile MORB mantle (FMM). Typically a fertile

MOR mantle has chromite with approximately 0.08 wt % TiO_2 prior to melting. This value rises to 0.18 wt% as a result of equilibration with the initial melt but subsequently decreases as the degree of melting increases and as Cr# increases. Chromites that plot close to the FFM melting curve are derived from peridotite that has experienced little reaction with a melt. In contrast, chromites that plot far from the FFM melting curve are from peridotite that has undergone more extensive melt-rock reaction The varying degrees of Ti enrichment in peridotites result from the chromites equilibrating with melts of different compositions (*Kelemen et al., 1995; Edwards & Malpas, 1996; Edwards et al., 1996; Pearce et al., 2000*).

Data that plots away from the FMM fractionation curve provides evidence for melt-rock reaction, the reaction between mantle lithosphere and an infiltrating melt. Depending on the source of the reacting melt, which will be in part a reflection of the tectonic setting, the chromites will form a particular vector to the right of the FMM melting curve. Reaction between residual mantle and MORB melt is characterised by a reaction trend towards a composition with relatively low Cr# and higher TiO_2 wt % values (Figure 6.5.1). At the other extreme, reaction between residual mantle and a boninite melt is characterised by a trend extending to higher Cr# and very low TiO_2 wt % values.

Data from lava-fields representative of MORB, IAT and boninite lavas are shown in Figure 6.5.1. On this projection, chromites from the Voskhod peridotite, dunite and chromitite form a trend (Figure 6.5.2) from low Cr#, low TiO_2 wt% compositions, that lie close to the melting curve, to high Cr# and comparatively elevated TiO_2 wt% compositions displaced significantly from the melting curve. This trend is marked by an increase in Cr# from the harzburgite (that plots in the MOR harzburgite field), through the dunite, dunite halo and ore zone dunite to the chromitite (the zone of mineralisation). It is possible to extrapolate a trend line back to the FFM melting curve. The point at which the line intercepts the FFM partial melting curve provides an approximation of the composition (inferred from the degree of partial melting) of the residual mantle that has reacted with the melt.

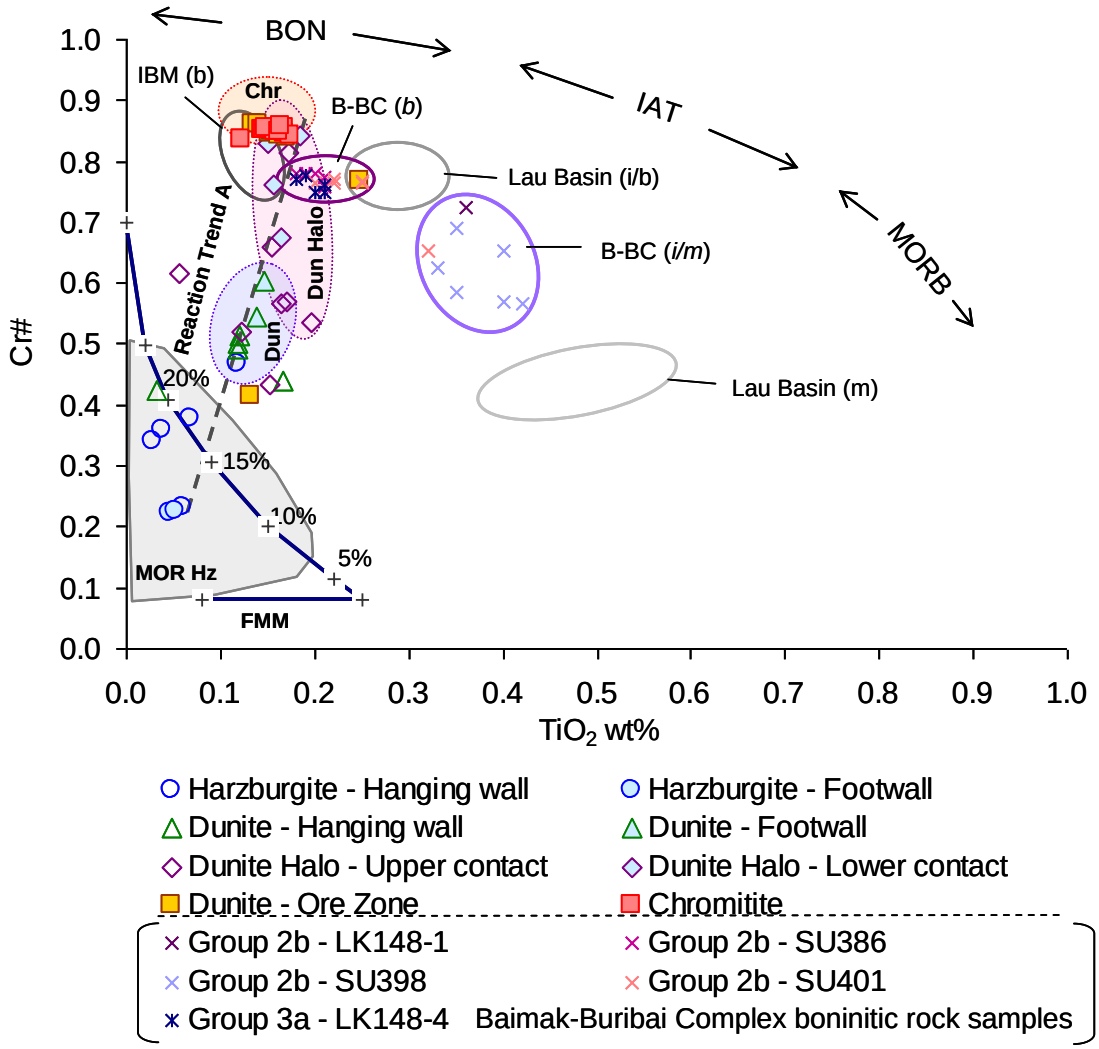

Figure 6.5.2: Plot of Cr# against TiO_2 wt% for chromite from the host units and ore zone of the Voskhod deposit.

The Cr# against TiO_2 wt % plot for chromite after Pearce et al., 2000. The diagram discriminates between partial melting trends and melt-rock reaction as modelled by Pearce et al., 2000. Reaction Trend A (the broken black line) provides evidence that, the Voskhod ore zone originates from, and the encompassing host peridotite and dunite units have been influenced chemically by, interaction between a boninitic (SSZ) melt and a mantle that has experienced 15-20% partial melting. Subscripts; *m* - MORB, *i* – island arc tholeiite and *b* - boninite refer to the chemistries of the arc-basin lava chromite reference. *IBM* refers to the Izu-Bonin-Mariana system. The *FMM* partial melting curve illustrates the theoretical partial melting of fertile MORB mantle. MOR Hz refers to the partial melt residue MORB harzburgite field. (Fields taken from Parkinson & Pearce, 1998; Pearce et al., 2000). Annotated fields Dun – Dunite, Dun Halo – Dunite Halo, Chr – Chromitite and B-BC – Baimak-Buribai Complex, are from this study.

The point of intersection on the FMM created by the Voskhod chromite data suite indicates that the mantle is the product of an intermediate degree of ~15% partial

melting (annotated by the black dashed line labelled “Reaction Trend A” on Figure 6.5.2). The trend to high Cr# and marginally increased TiO_2 wt.% content, can be explained by melt-mantle interaction through reaction or melt impregnation of the mantle as discussed. The end members are considered to be unreacted harzburgite (with Cr#=0.22 and TiO_2=0.06 wt%) and the extreme unreacted crystallate from the boninite melt, the chromitite (with Cr#=0.86 and TiO_2=0.13 wt%). Boninite melts typically characterise the forearc region of SSZ settings, indicating that the reacting melt associated with the genetic evolution of the Voskhod dunite halo, ore zone dunites and chromitite rocks, has a SSZ origin. This may or may not be the case for the residual harzburgite which has a Cr# consistent with both MOR and SSZ settings.

Chromite data for boninite lava samples from the southern Urals Baimak-Buribai Complex (B-BC) form two groups on Figure 6.5.2 (boninite data source *Spaeda et al., 1998*). One group has a borderline IAT-MORB chemistry (B-BC (*i/m*)) and the other a boninite chemistry (B-BC (*b*)). The B-BC (*b*) chromites overlap with the compositions of the Voskhod deposit dunite halo and chromitite chromites. This may imply a genetic link between the two groups.

The annotated reaction trend “A” in Figure 6.5.2 shows that the Voskhod chromite series is compositionally analogous to the Conical Seamount in the Izu-Bonin-Mariana forearc system. This trend has been explained by interaction between residual MOR mantle harzburgite and a melt of a boninite composition associated with a SSZ, forearc tectonic setting (*Parkinson & Pearce, 1998; Pearce et al., 2000*). A similar explanation could be invoked for the Voskhod mantle sequence.

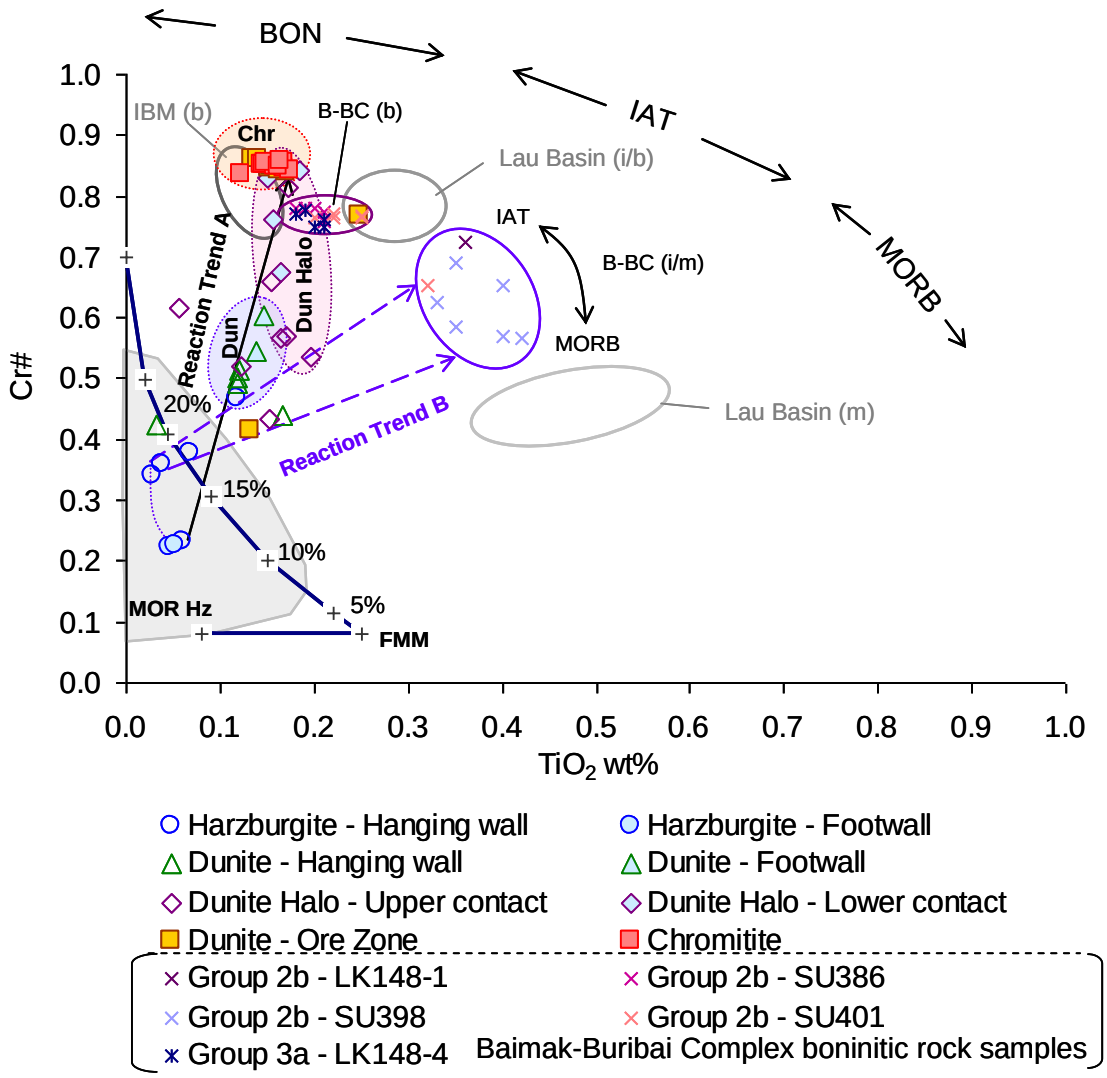

Figure 6.5.3: Plot of Cr# against TiO_2 wt% for chromite from the Voskhod deposit host units and ore zone annotated with a two-part reaction trend "A" and "B".

Plot of Cr# against TiO_2 wt% after Pearce et al., 2000. Reaction Trend "B" illustrates the reaction between residual mantle peridotite that has undergone ~18% partial melting and reacted with a SSZ melt of a borderline MORB-IAT chemistry (B-BC (*i/m*)). Reaction Trend "A" illustrates the reaction between mantle peridotite that has undergone ~15% partial melting and reacted with a SSZ melt of a boninite chemistry (B-BC (*b*)). Fields and subscripts are the same as those given in Figure 6.5.2.

An alternative interpretation of the results may be made to infer two distinct reaction trends. "A" and "B" (Figure 6.5.3), where Trend "A" extends from harzburgite to high chromite Cr# around 0.8 and Trend "B" extends from harzburgite with low to moderate chromite Cr# (0.3-0.4).

Trend "A" intercepts dunite, dunite halo and ore zone dunite lithologies. As a melt-rock reaction trend the direction (annotated by the solid black arrow) approximates

to the Lau Basin peridotite reaction trend (*Pearce et al., 2000*). In addition to the Voskhod samples, B-BC (*b*) chromite analyses cluster along this reaction trend line, with some plotting in the same space as the Voskhod chromitite values. This trend (A) results from melt-rock interaction between a boninitic melt (B-BC (*b*)) and residual mantle that has undergone ~15% partial melting.

In contrast, proposed Trend B would be created by a melt of an IAT-MORB composition reacting with MOR residual mantle that has undergone intermediate partial melting of ~17%. This trend (B) is supported by the abrupt increase in the TiO_2 wt% content of chromite observed between harzburgite (ave 0.06 wt% TiO_2) and dunite (ave 0.12 wt% TiO_2). Chromite compositions of the extrusive lava group B-BC (*i-m*) plot in a cluster at the far end of the trend B reaction vector (Figure 6.5.3) indicating that melts of this composition are preserved in the Southern Urals.

If this two-trend interpretation of the data is correct it implies that two, chemically different, melt compositions have percolated through the same region of the mantle. Of the extrusive B-BC rocks, samples that form the B-BC lava fields *i/m* and *b*, annotated in Figure 6.5.3, co-exist within the same stratigraphic horizons. For example, samples LK148-1 (B-BC(i*/m*)) and LK148-4 (B-BC(*b*)) were collected from the same stratigraphic horizon. Similarly, samples SU398 (B-BC(*i/m*)) and SU401 (BB-C(*b*)) were collected from the same, stratigraphically higher horizon (*Spadea et al., 1998*).

Additional evidence supporting the two-trend model is given in Figure 6.5.4 where podiform chromite values from the neighbouring Batamshinsk ore field located to the north west of the MOF have been plotted (values from *Pavlov & Grigoryeva, 1977*), reinforcing the bi-modality of the melt compositions as well as substantiating the likely polygenetic origin. The spread of the data points that comprise each field also suggests changing conditions within each geotectonic environment.

The TiO_2 -Al_2O_3 projection of Kamenetsky et al. (2001), in Figure 6.4.2, where TiO_2 plots on the vertical axis and Al_2O_3 on the horizontal axis, is very similar to the Cr#-TiO_2 plot. Cr# and Al_2O_3 contents of chromite are intrinsically linked, consequently, the TiO_2-Al_2O_3 diagram has a similar role in chromite fingerprinting, illustrating the

same progression that is observed in the Cr#-TiO_2 plot (Figure 6.5.4). A strength of the TiO_2 - Al_2O_3 plot is the identification of the IAT/BON discrimination zone within the "ARC" field; IAT melts are associated with higher TiO_2 contents in comparison to boninite melts that are characterised by lower TiO_2 contents. This enables the melt chemistry association of the end member group (chromitite) to be more firmly established.

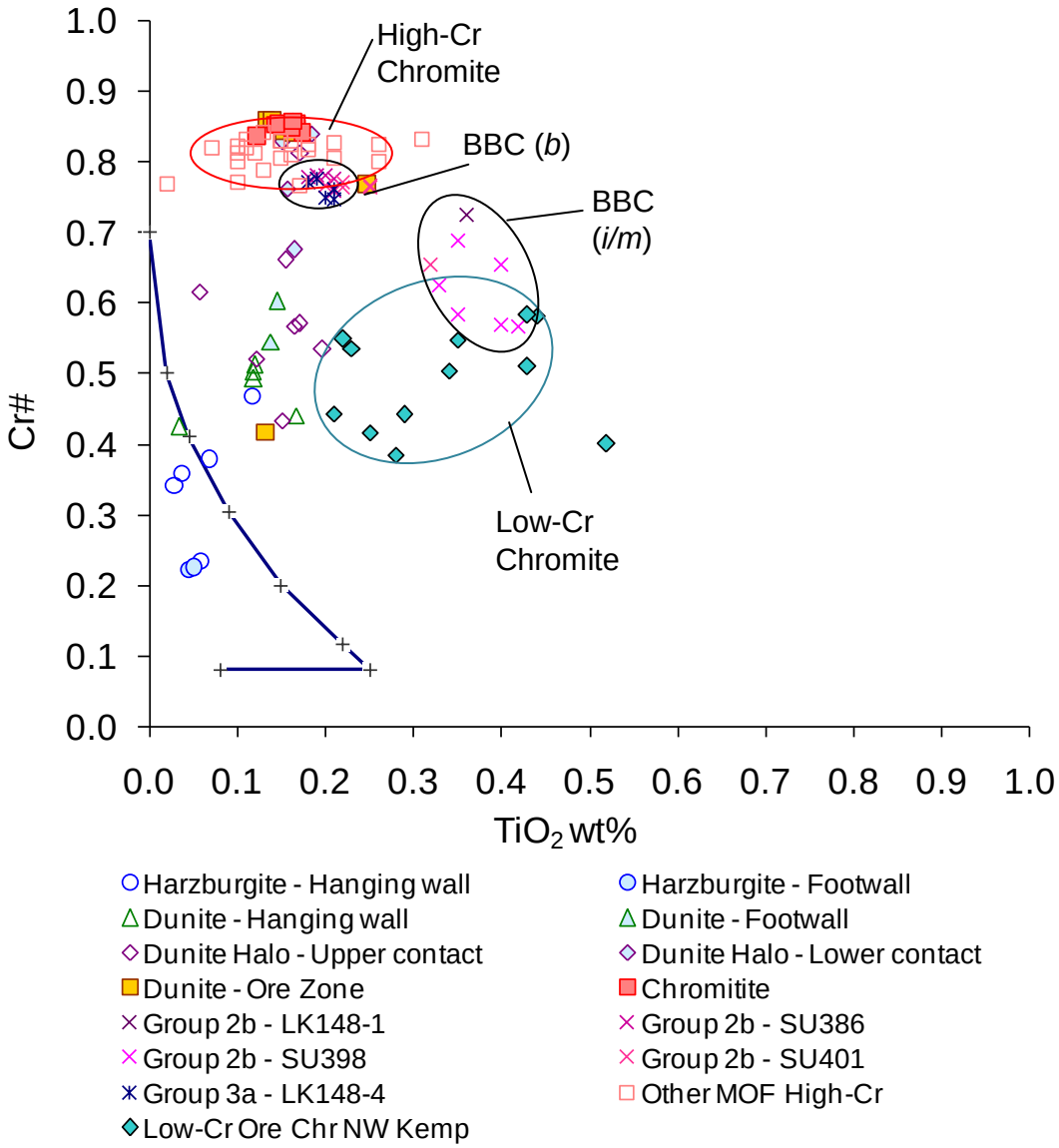

Figure 6.5.4: Chromite Cr#vsTiO2 plot with data added from nearby areas.

Low-Cr podiform chromite ore from north west Kempirsai data is sourced from Melcher et al., 1997 and Pavlov & Grigoryeva, 1977.

Although the Cr# - TiO_2 diagram provides a method with which to discriminate MOR from SSZ settings, there is ambiguity when using the diagram because of the significant overlap between the two fields, especially for Cr# values between 0.4 and 0.6 (Figure 6.5.1). The main reason for the overlap is that Cr# is strongly dependent on the degree of partial melting and melt-rock reaction in the two settings which themselves overlap. For this reason, oxygen fugacity has been found to be an important additional discriminatory variable. As oxygen fugacity is a function of water-content, it reduces the overlap between 'dry' MOR and 'wet' SSZ settings.

It is seen in Figure 6.5.1 that the MORB and arc fields (IAT and boninite) overlap prominently at low TiO_2 wt.% (0.1-0.4) and Cr# (0.4-0.7) values, causing uncertainty in the discrimination between differing early stages of melt-rock reaction.

Oxygen fugacity (fO_2) is a parameter that can be used to evaluate the oxidising conditions of a tectonic setting. The Fe^{3+} component of chromite is integral when calculating fO_2 values. The most direct evidence for high fO_2 conditions in SSZ settings is in the Fe^{3+} content: chromite in peridotites, dunites and lavas from SSZ tectonic settings tend to be more Fe^{3+} rich in comparison to the MORB equivalent (*Arai, 1992*).

6.5.1 TiO_2 – Fe^{3+}# Diagram

Arai (1992) used the TiO_2–Fe^{3+}# diagram to differentiate between MORB magma chromite phenocrysts that possessed high TiO_2/Fe^{3+}# ratios and arc magma chromites with comparatively lower ratios. Both TiO_2 and Fe^{3+}# increase during magmatic differentiation, Fe^{3+}# is elevated in arc melt relative to MORB melt because the presence of water associated with a SSZ setting promotes oxidising conditions (*Arai, 1992*).

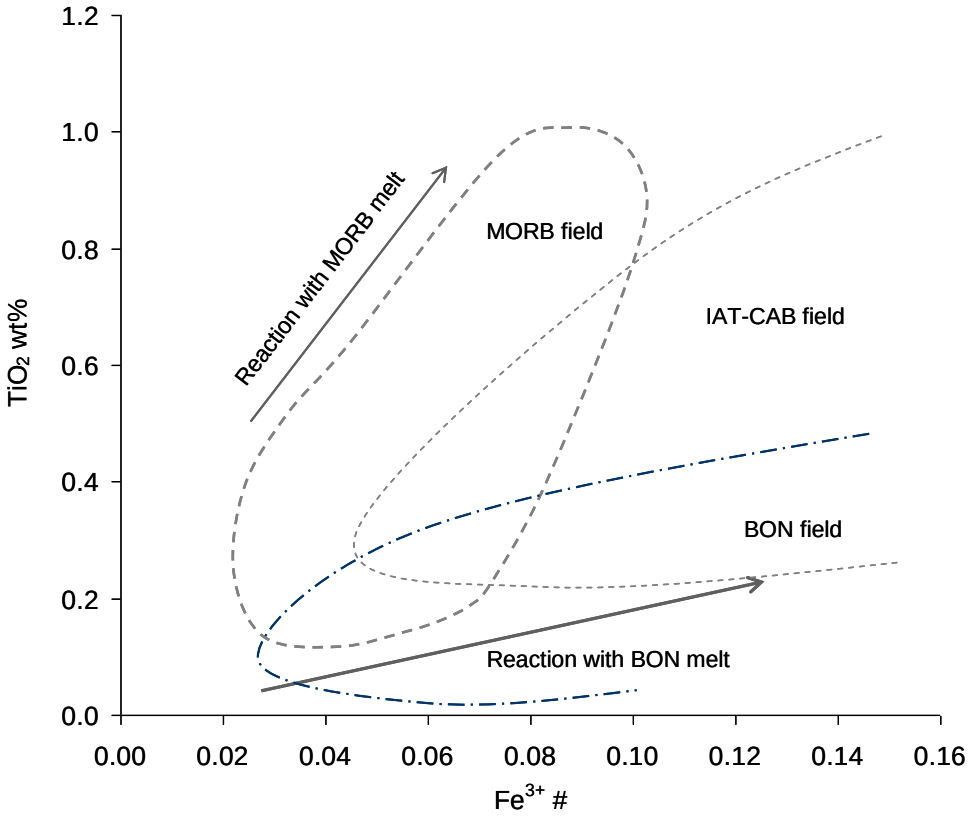

Figure 6.5.5: A schematic overview of the TiO_2 wt% against Fe^{3+}# plot.

Annotated with lava fields; Bon – boninite, IAT – island arc tholeiite, MORB – mid-ocean ridge basalt. Two arrows are shown illustrating melt-rock reaction trends between residual mantle and melts of BON and MORB chemistries (*Arai, 1992*).

The arrows annotated on the TiO_2–Fe^{3+}# diagram (Figure 6.5.5) show that it is possible to infer the chemical signature of a reacting melt (interacting with residual mantle) from the orientation of a trend line produced by harzburgite (less reacted) and dunite (more reacted) paired sample sets (*Arai, 1992*). In both mono- or polygenetic situations chromite from dunite samples (of the harzburgite-dunite pairs) typically have higher TiO_2 and Fe^{3+}# contents than the corresponding residual harzburgite samples (*Dare et al. 2009*).

The TiO_2/Fe^{3+}# ratio can therefore be used to assess melt-rock reaction as both Ti and Fe^{3+} increase during progressive melt-rock reaction. Residual harzburgite from a SSZ setting will possess progressively lower TiO_2/Fe^{3+}# ratios (see arrow labelled “reaction with BON melt” on Figure 6.5.5).

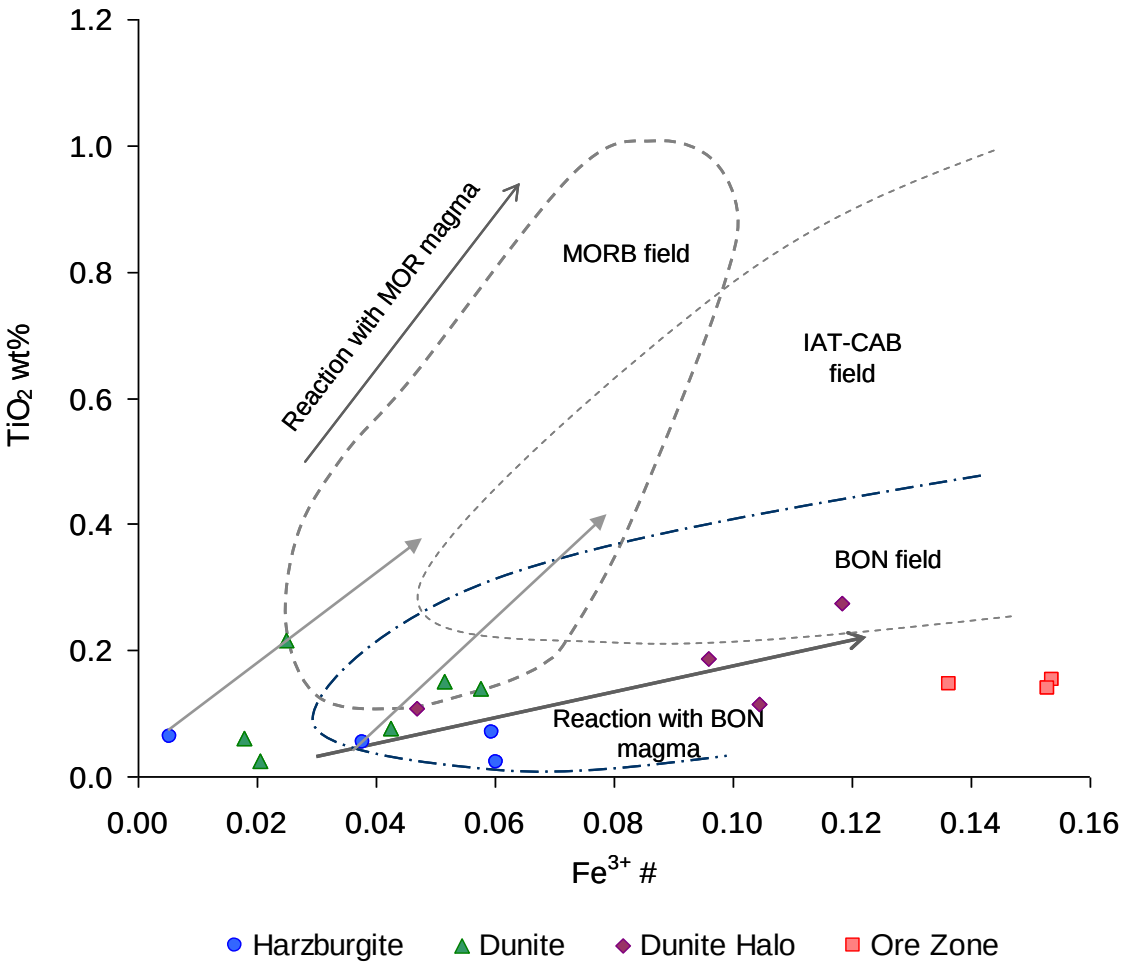

Figure 6.5.6: TiO_2 wt% against Fe^{3+}# in chromite from the Voskhod peridotite and dunite units.

Chromite fields for MORB and IAT/CAB chromites are reproduced from Arai (1992) and for BON chromites reproduced from Dare et al. (2009). Data presented in Appendix E.

The TiO_2 – Fe^{3+}# plot for the Voskhod sample suite (Figure 6.5.6) shows that there is a systematic increase in Fe^{3+}# from the harzburgite, dunite, dunite halo and ore zone samples at low TiO_2 compositions (<0.27 wt.%). This is analogous to the reaction between a residual mantle and a boninite melt as illustrated in Figure 6.5.6 by the black arrow labelled “reaction with BON magma”.

In addition, four of the six dunite samples show elevated TiO_2 contents relative to the harzburgite samples, and could indicate the onset of a reaction between residual mantle and MORB- or IAT-melt (see the grey solid arrows annotated on Figure 6.5.6). However, interpretation using this diagram is ambiguous for low TiO_2 and Fe^{3+}# values.

6.5.2 Fe^{2+}/Fe^{3+} - Al_2O_3 Chromite Composition: Peridotite-type Discrimination Diagram

The Fe^{2+}/Fe^{3+} - Al_2O_3 plot uses chromite geochemistry to provide a basic discrimination of the mantle source peridotite into MORB-type and SSZ-type (*Kamenetsky et al., 2001*). This provides further supporting evidence for the interpretation of the geodynamic setting associated with the genesis of the chromites present in host peridotite and ore zone at Voskhod. Low Fe^{2+}/Fe^{3+} values reflect an increase in oxidising conditions and may reflect the presence of water in a melt.

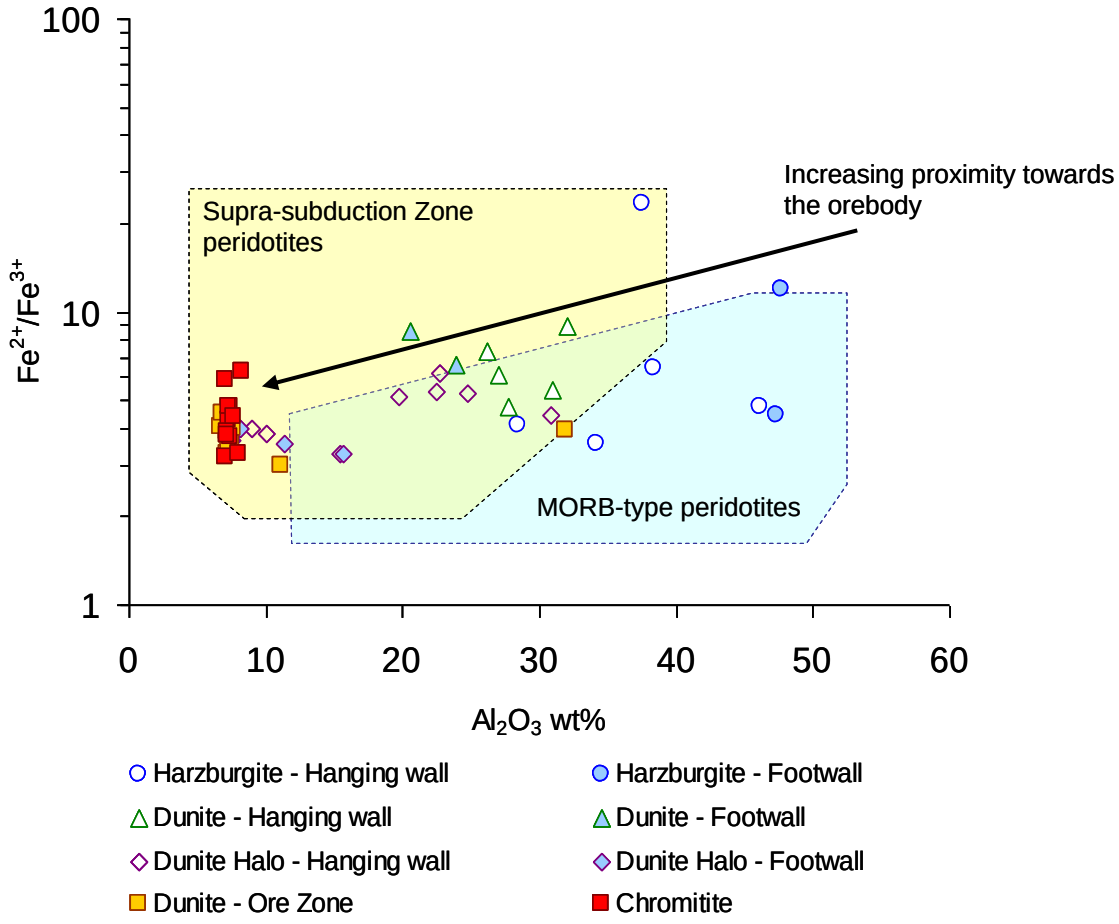

Figure 6.5.7: Fe^{2+}/Fe^{3+} - Al_2O_3 discrimination between SSZ-type and MORB-type mantle chromite.

(Discrimination fields are from Kamenetsky et al., 2001). Data presented in Appendix D.

Variation in Al_2O_3 has already been discussed in relation to figure 6.7.2 The Fe^{2+}/Fe^{3+} ratios range from 19.02 to 2.98. Fe^{2+}/Fe^{3+} values are highest in

harzburgite and dunite, being 5.51 and 6.62 respectively. The average Fe^{2+}/Fe^{3+} values decline in the dunite halo and ore zone to 4.18 and 3.97, respectively. Within the ore zone, the average chromitite Fe^{2+}/Fe^{3+} is elevated (ave. 4.55) compared to the ore zone dunite values (ave. 3.66).

Several observations can be made:
i) As an increasing Fe^{3+}/Fe^{2+} ratio in chromite is an indicator of rising fO_2, the oxygen fugacity increased with proximity towards the ore-body.
ii) A range of oxygen fugacity conditions are recorded within the ore-body chromitite, the most reduced of which are associated with massive chromite.
iii) Two samples from the ore zone dunite have elevated Al_2O_3, one of which is similar in chemistry to the harzburgite in the hanging wall. These either represent regions of the ore-body that have not been exposed to the same processes responsible for the formation of high-chromium chromite or that syn-formational structural discontinuity has incorporated host dunite or dunite halo into the ore zone.
iv) The Al_2O_3 contents of footwall and hanging wall harzburgite are not the same. The asymmetry of the chromite compositions, on either side of the ore-body, suggests that processes forming the ore have had a different effect on harzburgite above and below the ore-body.

6.6 Oxygen fugacity as a tool for fingerprinting tectonic settings

6.6.1 Δlog fO_2(FMQ) against Cr# diagram: Tectonic discrimination of the Voskhod peridotites and dunites.

The hydrous nature of SSZ environments promotes oxidation. Consequently, chromite formed in this environment is more oxidised and possesses higher fO_2 values than chromite formed in a MOR tectonic setting (*Ballhaus et al., 1991; Parkinson & Pearce, 1998; Pearce et al., 2000; Parkinson & Arculus, 1999; Elburg & Kamenetsky, 2007*). The work of Parkinson and Pearce (1998), identified the use of oxygen fugacity (fO_2) as a means to differentiate between peridotites from MOR and SSZ tectonic settings.

To obtain oxygen fugacity values required electron probe micro-analysis (EPMA) using Mossbauer-analysed probe standards. Using the EPMA result oxygen fugacity values were calculated for a subset of 15 Voskhod sample chromites using the method described in Appendix A. Values are reported as Δlog fO_2 (QFM) in Appendix E, Table E.1, where QFM refers to the deviation from the quartz-fayalite-magnetite (QFM) buffer at a specified temperature and pressure, expressed in log units. The plot, Δlog fO_2 (QFM) (a value commonly termed fO_2) against Cr# can be used to discriminate between tectonic settings and determine the formation environment of chromites from peridotites and dunites (*Wood & Virgo, 1989*).

The plot of fO_2 against Cr# (Figure 6.6.1) presents chromite data from Voskhod chromites. Discrimination fields and boundaries for lavas; island arc tholeiites (IAT), calc-alkaline basalts (CAB) and boninites (BON), as well as MOR- and SSZ-type mantle dunite (labelled as MOR Dun and SSZ Dun) and harzburgite (labelled as MOR Hz and SSZ Hz) are also provided. The dunite boundary is displaced to higher (~0.5 log units) oxygen fugacity at similar Cr# and extends to higher Cr# (up to 0.75) than the harzburgite boundary.

Chromite that formed under oxidising conditions, typical of SSZ settings, should be associated with IAT, calc-alkaline basalt (CAB) and boninite (BON) melts. Chromites crystallised from these subduction-related lavas, or formed in mantle units that have been subject to melt-rock reaction with subduction associated melts, exhibit higher fO_2 values (>1.5 fO_2). In contrast, chromites from mid-ocean ridge basalts or present in MOR mantle (either residual, or affected by melt-rock reaction with a MORB melt) are characterised by comparatively low fO_2 values (<1.5 fO_2), (*Ballhaus et al., 1991 and Elburg & Kamenetsky, 2007*).

Monogenetic SSZ melt-rock reaction trends e.g. the Torishima Forearc Seamount, in the Izu-Bonin forearc (*Parkinson & Pearce, 1998; Pearce et al., 2000*), form under the oxidising conditions of a SSZ setting (*Parkinson & Pearce, 1998*). Reaction trends formed between co-existing harzburgite and dunite pairs from monogenetic SSZ settings show an increase in Cr# (from harzburgite to dunite) that is accompanied by a negligible increase in fO_2 during interaction between SSZ harzburgite (residual mantle) and a SSZ melt (that forms the dunite).

Consequently, the orientation of the reaction trend vector is sub-parallel to the discriminating boundary for monogenetic SSZ settings. This is in contrast to the oblique orientation of the reaction trends of the monogenetic MOR settings (*Dare et al., 2009*).

The genesis of IAT, CAB and BON lavas are associated with the evolution of an arc setting. IAT arc lava chromites are characterised by Cr# (0.5 – 0.8) and exhibit fO_2 values ranging from QFM +1 to QFM +2. This range has been interpreted as a reflection of the increase in fO_2 during magmatic differentiation. In comparison, chromites sourced from boninites typically exhibit high Cr# values (0.75 - 0.9) and lower fO_2 (0 < QFM < +2) (*Ballhaus et al., 1991 and Elburg & Kamenetsky, 2007*). Chromites from CAB lavas have similar Cr# compositions to chromites from IAT and BON lavas (Cr# 0.5 - 0.85). However, the associated fO_2 values of the CAB chromites are typically much higher (+2 < fO_2 < +4, e.g. *Eggins, 1993*).

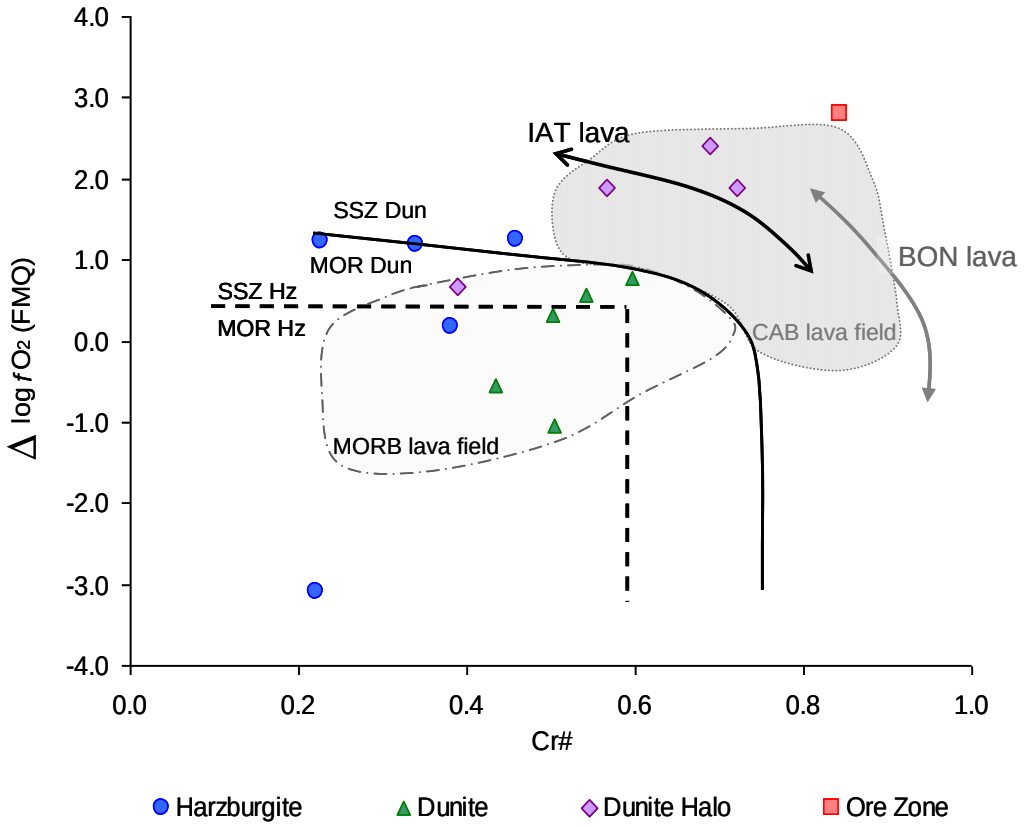

Figure 6.6.1: Δlog fO_2(FMQ) against Cr# diagram for chromites from the Voskhod peridotites and dunites.

fO_2 values were calculated at 1.0GPa. The discrimination boundaries for dunites (solid line), harzburgites (dashed line) and lava fields are taken from Dare et al. (2009). MOR Hz = MOR harzburgite, SSZ Hz = SSZ harzburgite, MOR Dun = MOR dunite and SSZ Dun = SSZ dunite. Data presented in Appendix E.

The harzburgite samples (solid blue circles) display a wide range in oxygen fugacity (Δlog fO_2 (QFM)) from -3.0 to 1.3 and a Cr# range of 0.22 to 0.46. One sample is an outlier which has an oxygen fugacity value of -3.0 (at Cr#, 0.22) plots in the MOR harzburgite (MOR Hz) region, indicating reducing conditions. The moderately elevated (0.2 to 1.3) oxygen fugacity values exhibited by the other four harzburgite samples indicate that these chromites formed under more oxidising mantle conditions, such as those likely to be associated with a SSZ setting. Three of the harzburgite samples plot as SSZ harzburgite (SSZ-Hz) with an additional sample lying just below the MOR-SSZ discrimination harzburgite boundary which would technically be characterised as a MOR harzburgite sample. One further harzburgite sample is well within the MOR field with oxygen fugacity of -3 and Cr# just above 0.2.

The dunite samples (solid green triangles) plot below the solid line that distinguishes between MOR-Dun and SSZ-Dun in Figure 6.6.1. Consequently, these samples are characterised as MOR dunite. This sample group has an oxygen fugacity range of -1.04 to 0.78 and a Cr# range of 0.43 to 0.60. The higher Cr# values clearly distinguish the chromites in dunite from those in harzburgite. The oxygen fugacity range of the dunites is slightly lower than that of the three SSZ harzburgites, implying that these dunites formed under low to intermediate oxidising conditions in the mantle. Such conditions may arise during interaction between residual MOR mantle and MORB-melt. This theory is further supported by the fact that the dunite samples plot in the MORB lava field, indicating that the compositions of these samples resemble MORB lava chromites.

Of the four dunite halo samples (solid purple diamonds), three plot in an oxygen fugacity range of 1.89 to 2.04 and a Cr# range of 0.57 to 0.72. These oxygen fugacities indicate a history of exposure to mantle conditions that were more oxidising than those that have affected the harzburgites and dunites. These dunite halo samples plot as SSZ dunites and plot in the IAT/CAB lava field. This is consistent with an origin by reaction with melts of arc lava affinities. There is a dunite halo outlier with an oxygen fugacity value of 0.67 and a Cr# of 0.39. This point plots in the MOR dunite region (within the MORB lava field) in close proximity to the dunite samples; this sample also lies close to the SSZ harzburgite samples.

The ore zone chromitite sample has the highest oxygen fugacity (2.81) and Cr# (0.84) values plotting as a SSZ dunite. This implies that the sample has been affected by the most oxidising conditions of all the samples analysed.

Across the entire sample series, a progression of increasing oxygen fugacity accompanied by increasing Cr# is seen. The most oxidising conditions are concentrated at the site of the ore zone, i.e. in the chromitite and dunite halo regions. Evidence of MOR harzburgite reacting with a SSZ melt is recorded. The harzburgite, dunite halo and ore zone samples record the SSZ melt signature. In contrast, the dunite and two of the harzburgite samples provide evidence to support a MOR tectonic history also having been preserved.

6.6.2 Limitations of the fO_2 –Cr# discrimination diagram

The fO_2 - Cr# diagram is an effective tool for discriminating between harzburgite and dunite in monogenetic settings. Care is needed when interpreting polygenetic settings where a data point plotting in the harzburgite domain could represent smaller degrees of melt-rock interaction (i.e. a harzburgite may not be a simple residue), while a dunite may form from a greater degree of melt-rock interaction (*Dare et al., 2009*) within a gradational melt-rock interaction process (*e.g. Pearce et al., 2000; Dare et al., 2009*).

There is also potential for some discrepancy in the interpretation of polygenetic settings, as the boundary between unreacted and reacted peridotites is dependent on the composition of the pre-existing mantle lithosphere. When MOR harzburgite interacts with a SSZ-melt the lesser-reacted MOR harzburgite may plot within the MOR harzburgite (MOR Hz) field. The intensity of the reaction between the MOR mantle and the reacting SSZ-melt can be traced by the least and most reacted sample end-members. In addition, reaction between MOR harzburgite and an evolving MORB melt (magmatic differentiation) can lead to an increase in the oxygen fugacity recorded by chromite without change to the tectonic setting e.g. Hess Deep dunites (*e.g. Allan & Dick, 1996; Arai & Mutsukage, 1996*). In light of these observations, the tectonic discrimination boundaries presented on the fO_2 – Cr# diagram are not independent of processes such as melt-rock reaction and magmatic differentiation.

The fO_2 – Cr# plot also has limitations in very altered rocks or detrital chromites. To calculate the fO_2 of a sample, co-existing chromite and olivine must be analysed (*Ballhaus, 1991; Nell & Wood, 1991*). This is not possible for samples where no fresh olivine exists, as is commonly the case with podiform chromitite and the encompassing dunite halo where olivine is often serpentinised. Equally, massive chromite with no co-existing silicate minerals is unsuitable for such analysis and cannot be plotted on the fO_2 – Cr# diagram.

To aid the tectonic discrimination of harzburgite and dunite using the oxygen fugacity of chromite, it is beneficial to conduct petrographic studies to look for; i) changes in the modal proportion of orthopyroxene, ii) evidence of melt impregnation textures and iii) chromite morphologies, these observation can provide evidence of melt-rock reaction (*Pearce et al., 2000*). However, the use of Ga, Ti and Fe^{3+} compositions from chromite as devised and implemented by Dare et al. (2009) potentially provides a more reliable method by which to separate a possible residual signature from a differentiating melt-rock reaction signature.

6.7 The tectonic discrimination of the Voskhod peridotites and dunites using Ga-Ti-Fe^{3+} systematics in chromite

Dare et al. (2009) devised and implemented the use of chromite Ga-Ti-Fe^{3+} systematics as a means to develop further the tectonic discrimination between peridotites and dunite. Gallium (Ga) occurs in trace quantities (e.g. 10-120 ppm) in chromite (*Kurat, 1980; McKay & Mitchell, 1980; O'Reilly et al., 1991; Griffin et al., 1993, 1994; Paktunc & Cabri, 1995; Paktunc & Hulbert, 1996*). The physical and chemical properties of Ga make it a practical tool to use in the tectonic discrimination of peridotite and dunite.

Ga is a trivalent cation capable of substituting into the Y^{3+}, octahedral site of the chromite lattice. As noted earlier, the chromite lattice Y^{3+} site occupants (Cr^{3+}, Al^{3+}, Fe^{3+}, Ga^{3+}, V^{3+} and Ti^{4+}) are recognised to have a low diffusivity through silicate minerals and consequently are considered unlikely to re-equilibrate during cooling (*Scowen et al., 1991*). Both Ga and Fe^{3+} have the same ionic radii of 0.62A; but, Ga is not redox-dependant (whereas Fe^{3+} is). Instead, its chemical behaviour is

similar to that of Al, which it neighbours in Group III of the Periodic Table (*Goodman, 1972; Norman, 1998*).

Dare et al. (*2009*) developed the use of Ga^{3+}-Ti^{4+}-Fe^{3+} systematics in chromite as a tool to discriminate between tectonic settings, creating an analytical technique affective for use on samples where no co-existing silicate minerals exist. The Ga^{3+}-Fe^{3+}-Ti^{4+} systematics of chromites provides a good opportunity to assess the origin and tectonic setting of the Voskhod chromitites and the co-genetic peripheral dunite halo and host mantle peridotite and dunite units.

6.7.1 TiO_2/Fe^{3+}# against Ga/Fe^{3+}# diagram

The plot TiO_2/Fe^{3+}# against Ga/Fe^{3+}# was devised and implemented by Dare et al. (2009). The diagram discriminates between low TiO_2/Fe^{3+}# residual harzburgite (residual mantle) and high TiO_2/Fe^{3+}# reacted harzburgite/dunite (residual mantle that has reacted with an upwelling melt) from MOR and SSZ settings. Typically MOR settings have higher Ga/Fe^{3+}# ratios than SSZ settings.

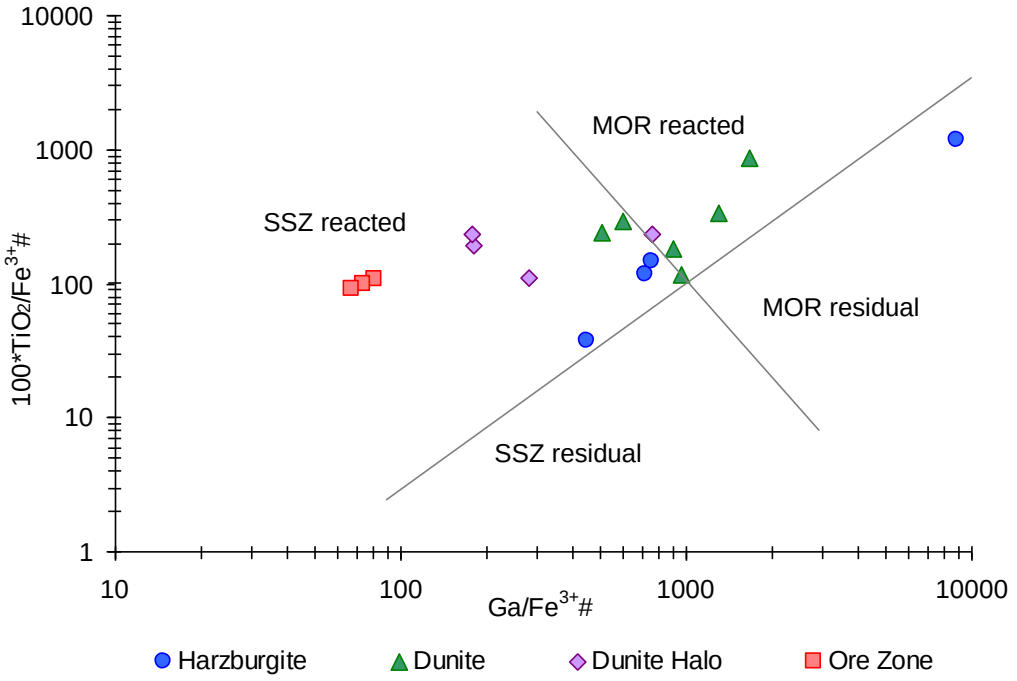

Figure 6.7.1: TiO_2/Fe^{3+}# against Ga/Fe^{3+}# in chromite from the peridotite and dunite units of the Voskhod deposit.

Field boundaries discriminating between MOR residual, MOR reacted, SSZ residual and SSZ reacted peridotite (and dunite) are from Dare et al., 2009. Data given in Appendix E

It is possible to determine whether a tectonic setting of a sample suite is mono- or polygenetic as harzburgite-dunite pairs from a monogenetic setting will plot only in the MOR residual and MOR reacted fields (or SSZ residual and SSZ reacted fields). In contrast, polygenetic harzburgite-dunite pairs will plot across the tectonic setting classification boundary that separates the MOR and SSZ fields (see Figure 6.7.1).

A strength of this diagram is that it is able to take into account both magmatic differentiation (an increase in TiO_2/Fe^{3+}# but with no change in Ga/Fe^{3+}#) and melt-rock reaction (an increase in TiO_2/Fe^{3+}# and a decrease in Ga/Fe^{3+}#). The insensitivity of Ga/Fe^{3+}# magmatic differentiation may be attributed to the similarity in ionic radii of the two ions. The increase in TiO_2/Fe^{3+}# may be attributed to the greater incompatibility of Ti than Fe^{3+} in the chromite lattice.

Of the four harzburgite samples, one plots in the residual MOR field and three plot in the reacted SSZ field. All harzburgite chromite morphologies are holly-leaf (HL) and/or subidiomorphic (with cuspate edges). Such chromite textures are characteristic of residual peridotites (*Nicolas, 1986; Monnier et al., 2006 Dare et al 2009*) and would normally be interpreted as such. However, observations made by Dare et al. (2009) where harzburgite samples plotted in reacted-MOR and –SSZ fields yet contained holly-leaf chromite were explained as chromite that had not undergone a morphological change from anhedral to euhedral or alternatively on altering to a euhedral morphology had subsequently been deformed into an anhedral shape. Despite the petrological observations, the harzburgite samples that plot in the SSZ-reacted field may be interpreted as residual mantle that has interacted with SSZ melt.

The dunite samples plot across two fields: four plot in the reacted-MOR field (one data point being on the MOR-SSZ reacted boundary); and two plot in the reacted-SSZ field. Interestingly all dunite chromites also exhibit holly-leaf and subidiomorphic morphologies that are characteristic of a residual origin. Yet the degree of melting required to produce dunite would be unfeasibly high. It is proposed that the subidiomorphic chromites form during the melt-mantle reaction process and that the pre-existing residual chromite is chemically altered by

interaction with the melt, without any change to the primary residual morphology of the chromites.

The dunite halo samples plot in two fields of the $TiO_2/Fe^{3+}\#$ - $Ga/Fe^{3+}\#$ plot. The dunite halo chromite, F1907, lies in the MOR-reacted field and is chemically similar to the dunite samples that also plot in the MOR-reacted region (this was also noted in the plot of $\Delta\log fO_2$(QFM) against Cr#, Figure 6.6.1). Sample F1907 displays holly-leaf and subidiomorphic chromite morphologies. The three dunite halo samples plot clearly inside the reacted-SSZ field. These chromites have formed by reaction between residual mantle and a SSZ melt and, unlike the other SSZ-reacted dunite halo sample, the melt-rock interaction may have been more extensive. The chromites in these samples are primarily euhedral with lesser amounts of the subidiomorphic chromite. The predominant presence of euhedral chromite is an additional indicator that these chromites formed either as a result of melt-rock interaction (*Nielson Pike & Schwarzman, 1976; Dick, 1977; Leblanc et al., 1980*) or by magmatic crystallisation from a melt (*e.g. Nielson Pike & Schwarzman, 1976*).

6.7.1.1 Anomalous distal dunite samples

From the $TiO_2/Fe^{3+}\#$-$Ga/Fe^{3+}\#$ plot two types of distal dunite, MOR-reacted and SSZ-reacted, are identified. In contrast, on the fO_2-Cr# plot, all distal dunites plot as MOR dunite. There is a discrepancy in the distinction of two distal dunite samples that have a SSZ-reaction origin on the $TiO_2/Fe^{3+}\#$-$Ga/Fe^{3+}\#$ plot and MOR origin on the fO_2-Cr# plot, this could be the result of analytical error. Another possibility is that the samples fingerprinted as being MOR in origin by the fO_2-Cr# plot, crossed the MOR-SSZ boundary on the $TiO_2/Fe^{3+}\#$-$Ga/Fe^{3+}\#$ plot as a result of reaction with an evolving SSZ melt. The two samples plot very close to the discrimination boundaries on both of the $TiO_2/Fe^{3+}\#$-$Ga/Fe^{3+}\#$ and fO_2-Cr# plots which supports the possibility that these are transitional MOR-SSZ reacted dunites. Alternatively, the discrepancy may be a consequence of uncertainty on the position of the lines annotated on these plots by Dare et al. (2009), as relatively few data points were used when the boundary lines were constructed.

6.7.2 Chromite Cr# against Mg# diagram

Use of the variation of Cr# and Mg# in considering the high temperature genesis of chromite containing ultrabasic rocks needs to acknowledge the possibility of lower temperature subsolidus re-equilibration between olivine and chromite. In this process Fe and Mg are progressively exchanged as the temperature falls, with olivine being enriched in Mg and chromite in Fe. The exchange process is predictable and the basis of a geothermometer that records the closing temperature of the system at which diffusional readjustment ceases (*e.g. Irvine 1967*). When mass-balance considerations are made, the effect of subsolidus re-equilibration on chromite composition (i.e. on Mg#) is greatest when the proportion of the chromite mineral phase in a peridotite or dunite sample is minor relative to the modal proportion of olivine (*e.g. Irvine, 1967; Dick & Bullen, 1984; Scowen, 1991*). The opposite is also true, that the effect on olivine composition is greatest when olivine is the minor phase.

Using only chromite compositions from chromitites where the chromite/olivine ratio is high, mantle chromite compositions plot at near constant Cr# values forming an array that extends parallel to the Mg# axis (*e.g. Zhou et al, 1996; Barnes & Roeder, 2001*).

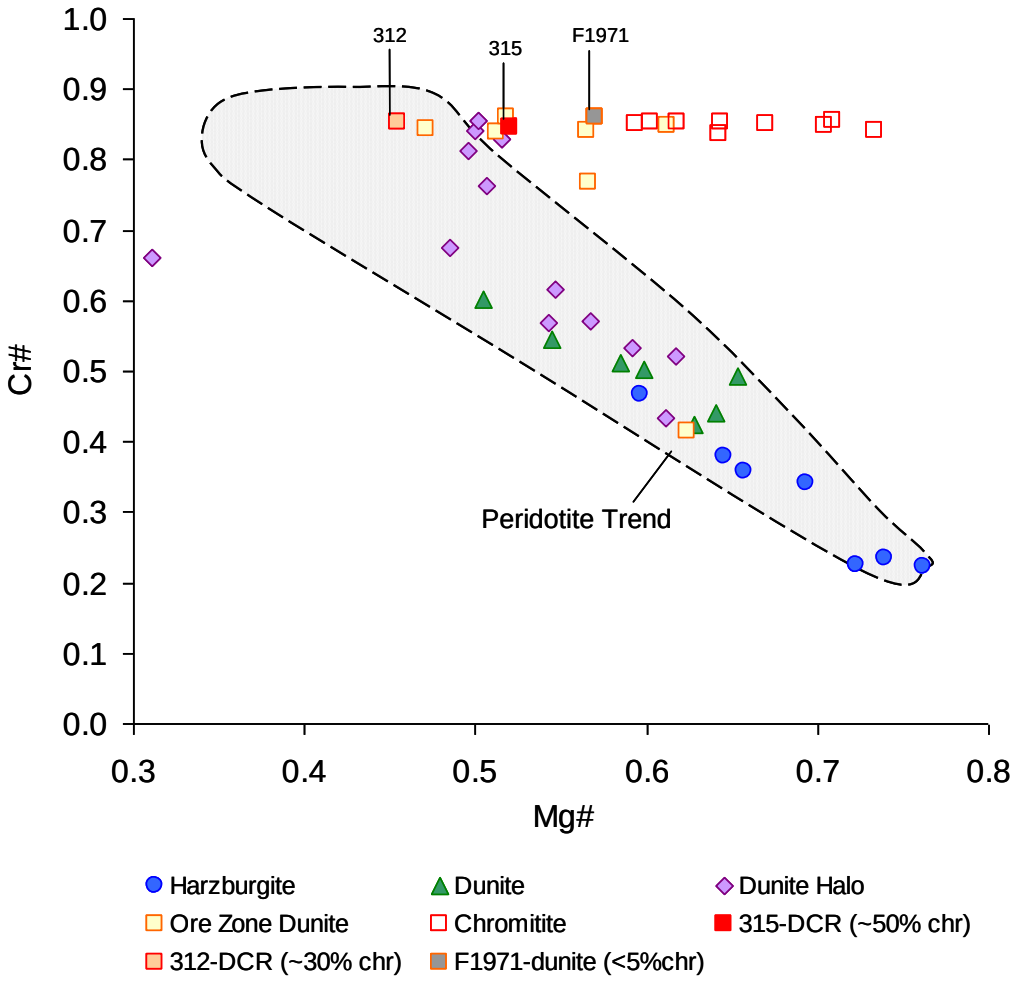

Figure 6.7.2: Cr# against Mg# diagram of chromites from peridotite, dunite and chromitite units.

The peridotites and dunites form a distinct field displaced to lower Mg# and Cr# than the chromitites. The chromitites exhibit a near constant Cr# [Cr/(Cr+Al)] yet a wide range of Mg# [Mg/(Mg+Fe^{2+})], a result of subsolidus re-equilibration and varying chromite/olivine ratios in chromitites. Data presented in Appendix D.

Chromite compositions from Voskhod harzburgite, dunite and chromitite samples are plotted on the Cr# against Mg# chromite diagram (Figure 6.7.2). The harzburgite, dunite and seven of the dunite halo samples plot in a systematic sequential order, seen in other plots, forming a negatively-sloped linear trend with Mg# decreasing (from 0.76 to 0.49) as Cr# increases (from 0.22 to 0.68). During refertilisation an increase in Cr# would be expected at any given Mg# (*Le Roux et al, 2007*). In addition, both Cr# and Mg# would be expected to change values towards the source of the refertilisation, irrespective of later subsolidus Fe-Mg

adjustments. The dunite halo sample group forms an end-member of the trend with the Mg# composition stabilising at 0.50, after which the Cr# increases from 0.68 to 0.86. In contrast, the ore zone dunite and chromitite samples have stabilised Cr# values that range from 0.84 to 0.86, and Mg# values that cover almost the same range as the host rock samples collectively, these extend from 0.46 to 0.73.

One sample from the dunite halo hanging wall group with a very low Mg#, 0.31 is the only outlier. The Cr# of this sample, 0.66, lies within the range for dunite halo samples. The low Mg# value is interpreted to result from the chromite having undergone some degree of alteration, gaining Fe^{2+} and Fe^{3+} at the expense of Mg^{2+} and Al^{3+} (*e.g. Evans & Frost, 1985*) to form ferritchromite. Petrographically the sample is extensively serpentinised (>85% serpentinisation). Chromite grains have morphologies that vary from subhedral to cuspate and the “spongy” surface texture is a characteristic of ferrit-chromite (e.g. *Ahmed & Hall, 1981*).

The high Mg# values of chromite seen in chromitite correspond to samples of massive chromite, where the olivine component is ≤ 5% of the rock composition.

In rocks where chromite and olivine co-exist it is possible to calculate the closure temperature, from the partitioning of Fe^{2+} and Mg^{2+} between these two minerals, and from this it is possible to calculate the oxygen fugacity conditions during the formation of chromite (*Ballhaus et al., 1991*). Using this method, temperatures were calculated for the Voskhod harzburgites, dunites and, where possible, chromitites. However, given the extensive serpentinisation associated with the dunite halo, ore zone dunite and chromitite units, it was particularly difficult to find samples where fresh olivine was present for analysis. The average calculated closure temperatures from the Voskhod sample set analysed are; harzburgite 650°C ± 28°C, dunite 657°C ± 26°C, dunite halo 678°C ± 39°C, ore zone dunite 648°C and chromitite 734°C (there being only one ore zone dunite and chromitite sample for which olivine was successfully analysed). The closure temperatures for each sample are given in Appendix E, row labelled “T°C Ballhaus 1991”.

The chromitite samples record a higher temperature than the dunite and harzburgite samples owing to the greater chromite content of this rock type. The

higher chromite/olivine ratio causes the effect of re-equilibration to be less extensive on mass balance grounds, as well as lower chromite having a lower diffusion rate compared to olivine (*Irvine, 1965, 1967; Ballhaus, 1991*).

Of the ore zone samples, two are considered to be ore and both of these samples are of disseminated chromite (DCR), one composed of ~50% chromite (sample 315- DCR) and the other ~30% chromite (sample 312-DCR). The third ore zone sample is from a barren dunite horizon where chromite constitutes less than 5% of the sample composition (sample F1971). It is noted that for all the groups presented in this plot, the ore zone group is the most tightly constrained in the $TiO_2/Fe^{3+}\#$ - $Ga/Fe^{3+}\#$ plot, despite being the most varied in terms of the olivine/chromite ratio. Furthermore, Dare et al., (2009) acknowledged that interpretation of chromitite samples on the $TiO_2/Fe^{3+}\#$ - $Ga/Fe^{3+}\#$ diagram is difficult, because the diagram is based on samples that have undergone a subsolidus exchange atypical for disseminated chromite. Their paper concluded that the samples should first have been subjected to a similar subsolidus re-equilibration history (with respect to both temperature of equilibration and olivine/chromite ratio) as that of the peridotite accessory chromite used for the calibration (i.e. the oceanic and ophiolite peridotite chromite standards). They proposed that selection of suitable samples may be achieved by first filtering the chromite compositions through the peridotite trend on the Cr#-Mg# diagram, as more olivine-rich chromitites may be suitable. However, in the case of the Voskhod ore zone chromite samples, this statement does not hold true. Two of the three ore zone samples fall outside of the peridotite trend and yet all three are observed to plot in close proximity to one another and well within the SSZ-reacted field of the $TiO_2/Fe^{3+}\#$ and $Ga/Fe^{3+}\#$ plot.

6.8 Parent melt composition

The composition of chromite reflects the geochemistry of either, the melt from which it crystallised or the last melt it equilibrated with (*Dick and Bullen, 1984; Arai, 1992; Barnes and Roeder, 2001; Kamenetsky et al., 2001; Page and Barnes, 2009*).

6.8.1 Al_2O_3 and TiO_2 in the parent melt

Relationships between the Al_2O_3 and TiO_2 contents of chromite and melt have been established, both experimentally (*Maurel and Maurel, 1982*) and through the study of natural systems (*Roeder and Reynolds, 1991; Kamenetsky et al., 2001*). Page and Barnes (2009) proposed that the Al_2O_3 and TiO_2 contents in chromite may be used to estimate the geochemical composition of a melt from which the chromite crystallised, as these components are not affected by subsolidus re-equilibration with olivine or postcumulus reaction. They also proposed that reaction with trapped interstitial melt would have a minimum effect on the chromite composition given the high proportion of chromite relative to the amount of trapped melt (*Page and Barnes, 2009*).

Kamenetsky et al., (*2001*) identified a relationship between the Al_2O_3 and TiO_2 content of chromite and the parent melt using chromite-olivine pairs and melt inclusion-chromite pairs from oceanic, arc and intraplate tectonic settings. Their work demonstrated that Al_2O_3 and TiO_2 compositions can be used to distinguish between tectonic settings in which chromite forms (Figure 6.8.1). Page and Barnes (2009) used this to reason that podiform chromitites may be formed from arc to MORB melt types.

The Al_2O_3 and TiO_2, chromite – parent melt composition relationship (Figure 6.8.1) has been applied to the Voskhod harzburgite, dunite and ore zone chromites. The equation used to link the Al_2O_3 content in chromite to the associated parental melt is derived from the power best fit line through the data compilation of Kamenetsky et al. (2001) determined from natural sample suites (Eq.1) (Figure 6.8.1).

$$Al_2O_3 \text{ wt\% in melt} = 5.356 \ln(Al_2O_3 \text{ wt\% in spinel}) - 1.7852 \quad \text{(Eq.1)}$$

The work of Kamenetsky et al. (2001 identified different relationship trends between Al_2O_3 and TiO_2 chromite contents of high-Al (> 19 wt% Al_2O_3) chromites and low-Al (<15 wt% Al_2O_3) chromites (Figure 6.8.2). Low-Al chromites are predominantly IAT-melt related and high-Al chromite, MORB-melt associated. Consequently, it is possible to determine two separate equations to calculate the TiO_2 content of the parental melt. Given the significant spread in Al_2O_3 values from

the Voskhod chromite dataset two equations were formulated one for chromite with Al_2O_3 values <15 wt% (Eq.2) and a second for those >15 wt% (Eq.3) (see Figure 6.8.2 for data trendlines and equations).

TiO_2 wt% in melt = 1.7336 (TiO_2 wt.% in High-Al spinel)$^{0.7096}$

(Eq.2)

TiO_2 wt% in melt = 1.1993 (TiO_2 wt.% in Low-Al spinel)$^{0.8259}$

(Eq.3)

Low Al_2O_3 contents are associated with chromite in the chromitite and dunite halo. These units (the ore body and encompassing halo) appear to represent a boninite melt flow channel-way. The calculated TiO_2 wt% melt content for the low Al_2O_3 chromites ranges from 0.21 to 0.38 wt.%. These values are consistent with TiO_2 wt% boninite melt contents (Figure 6.8.3). In contrast the high Al_2O_3 chromites present in the mantle host units (through which the boninite melt has percolated) show to have last equilibrated with a melt having a TiO_2 wt% content of between 0.14 to 0.55 wt.%. These values indicate that the high Al_2O_3 chromites which plot outside of the boninite field have not formed from, or equilibrated (fully) with, the boninite melt (Figure 6.8.3).

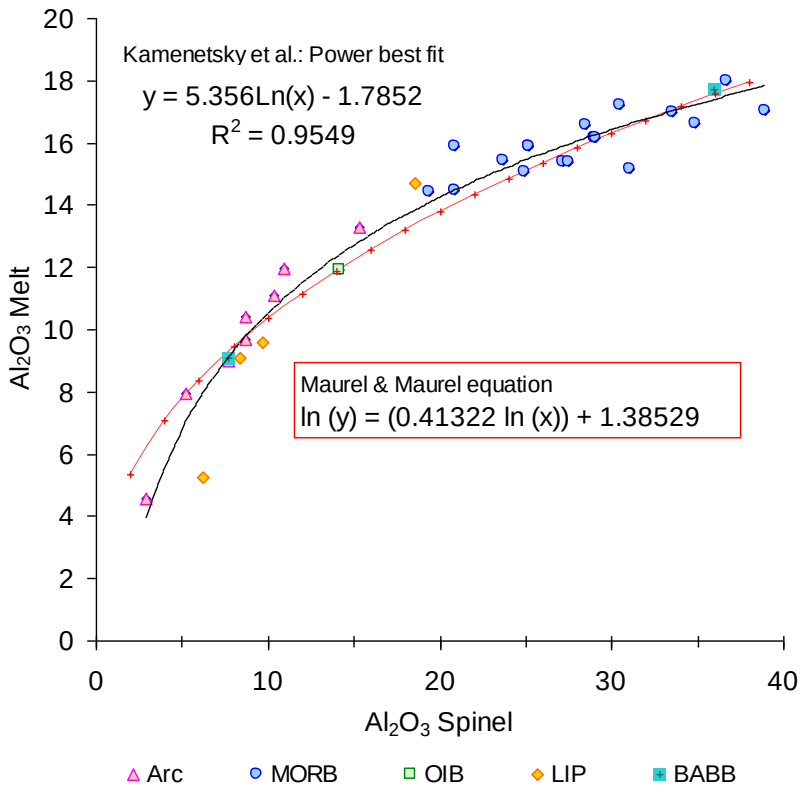

Figure 6.8.1: Al_2O_3 melt-spinel relationship

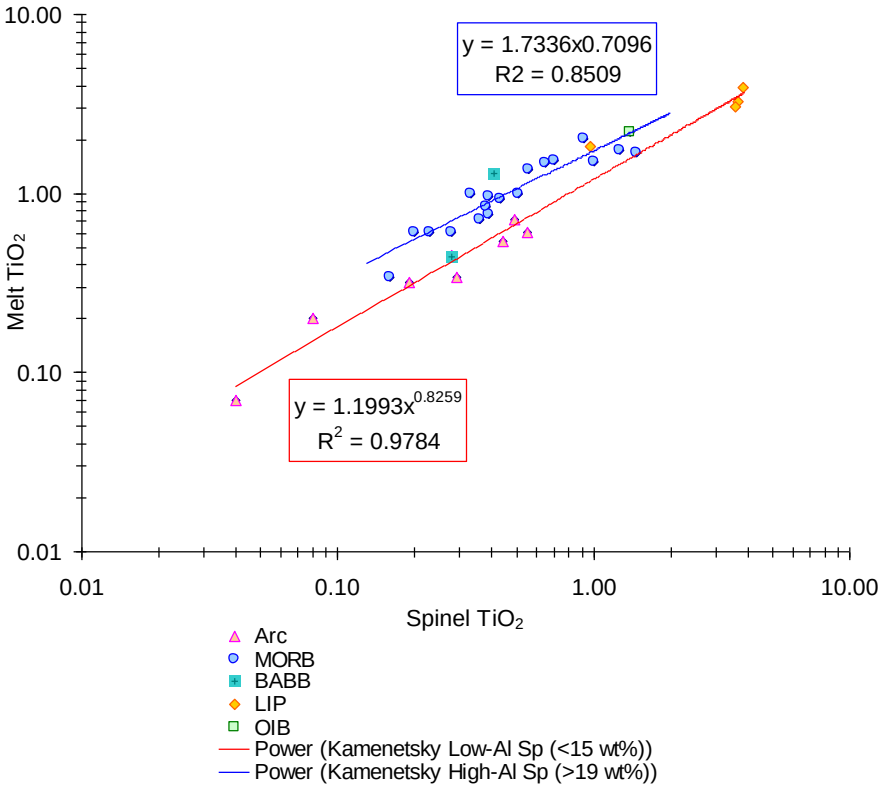

Figure 6.8.2: TiO_2 melt-spinel relationships for high- and low-Al_2O_3 spinel

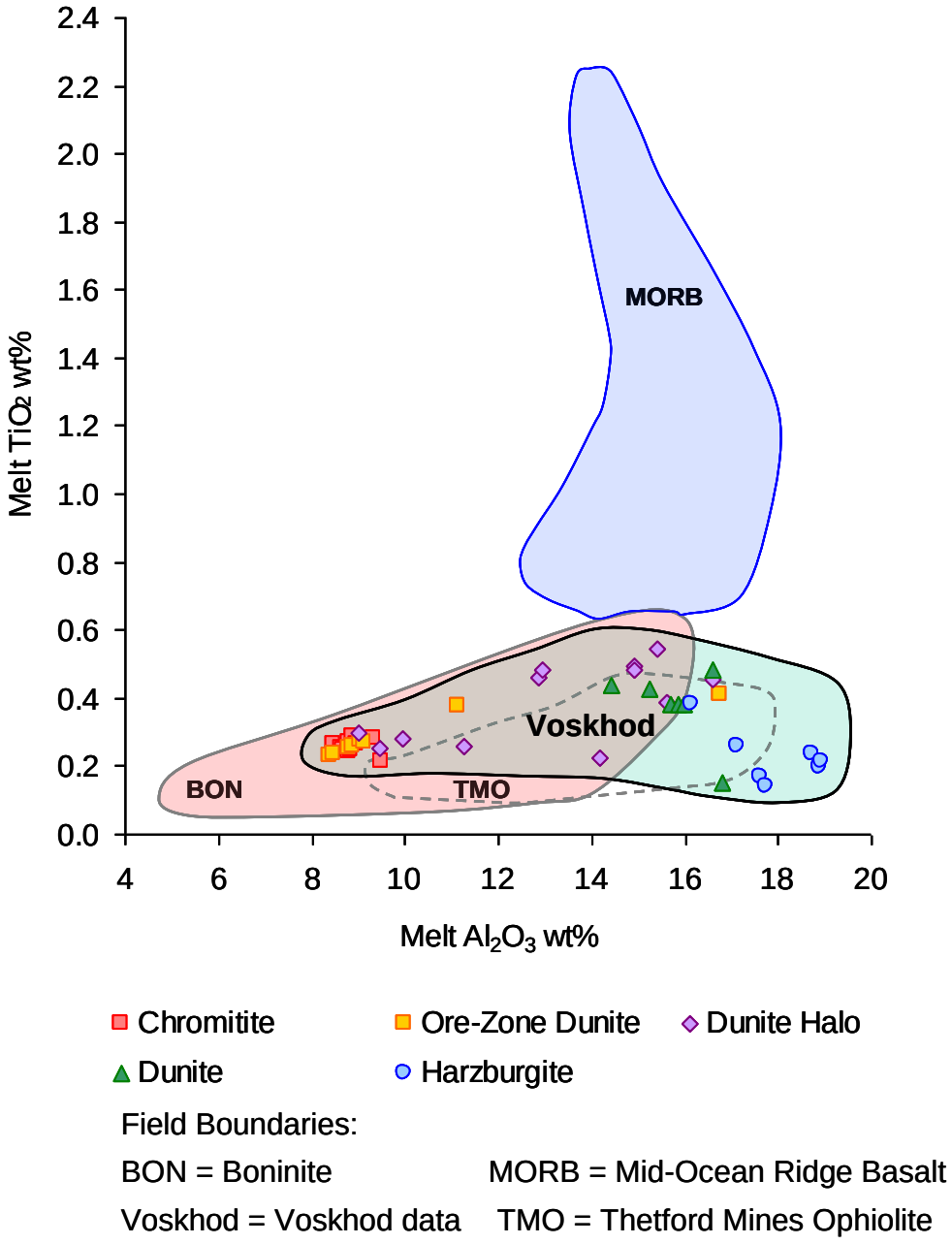

Figure 6.8.3: TiO_2 wt% versus Al_2O_3 wt% melt compositions

calculated to be in equilibrium with chromite from the Voskhod podiform chromite deposit and host rock. For comparison fields from the Thetford Mines Ophiolite (TMO), boninites (BON) and MORB as identified by Page and Barnes (2009) are shown.

The calculated parental melt compositions from which the Voskhod podiform chromite (and associated ore-zone dunite horizons) have crystallised, range from 8.37 to 9.52 wt% Al_2O_3 (average = 8.86 ± 0.29) and from 0.21 to 0.29 wt% TiO_2 (average = 0.26 ± 0.02). (These value ranges omit two ore-zone dunite anomalies that are geochemically similar to chromite from the dunite halo and dunite fields).

The calculated melt compositions are comparable with boninite lava values (BON field annotated in
Figure 6.8.3) as well as the boninite lavas of the B-BC (Figure 6.5.2)

The TiO_2 melt compositions for the harzburgite, dunite and the majority of the dunite halo samples are calculated using equation 2 as these chromites have a high-Al content.

There are at least two possible origins for the chromites in the Voskhod sample suite:

- They are residual from harzburgite that has had orthopyroxene removed and the chromite composition changed, with increasing Cr and Ti.
- They are chromite-bearing dunites, crystallised from the new percolating melt

Since dunite halo chromites have higher Ti contents than both ore-zone chromite and harzburgite chromite, melts or fluids associated with neither of these would seem to be the source of the Ti.

The increased TiO_2 wt% content relative to both end member chromite sample groups, the low-Al podiform chromitite (ore zone) chromites and the high-Al harzburgite chromites suggests that an additional TiO_2 source is required. It is proposed that this may be supplied by the selective dissolution of pyroxene from harzburgite, a reaction that could, as a result of environmental changes, cause the pyroxene field to destabilise and consequently form olivine. This would liberate Ti^{4+} and Cr^{3+}, that are present as minor element components in pyroxene, into the local system. These cations are not incorporated into the olivine structure however, the chromite structure can accommodate them.

It is proposed that the chemical gradient observed in the dunite halo chromites is created by the release of Cr^{3+} and Ti^{4+} from orthopyroxene forming chromite that has an Al^{3+} content intermediate between that of the ore-zone (low-Al) and harzburgite (high-Al) compositions as well as contributing to the elevated Ti content.

Chromite within the dunite halo also has higher Fe_2O_3 contents than chromite in the ore-zone. This implies that the $\int O_2$ conditions were higher in the halo than in the ore-zone. This may indicate that the melts or fluids which dissolved the orthopyroxene, and were responsible for element transfer between the melt and host-rock, are not the same as the boninite melt that is interpreted to have formed the podiform chromite (ore zone chromite). The liquid may either be, a volatile-rich melt or a volatile phase that is independent of the boninite melt.

6.8.2 FeO/MgO Melt Composition

Calculating the FeO/MgO ratio of the parent melt composition from the chromite composition is difficult because subsolidus re-equilibration of Mg^{2+} and Fe^{2+} cations between chromite and olivine has to be accounted for. Re-equilibration would alter the chromite composition significantly from its original composition, such that any calculated melt composition would not represent the parent melt. However, there should only be minimal changes to the Fe^{2+} and Mg^{2+} contents in samples where chromite is the primary mineral phase. In massive chromite, where chromite constitutes >90% of the modal composition, the primary geochemistry will be preserved during low temperature re-equilibration processes (e.g. *Maurel & Maurel, 1982*). Using equations determined by Maurel & Maurel (1982) the geochemical composition of massive chromite may be used to calculate FeO/MgO melt compositions.

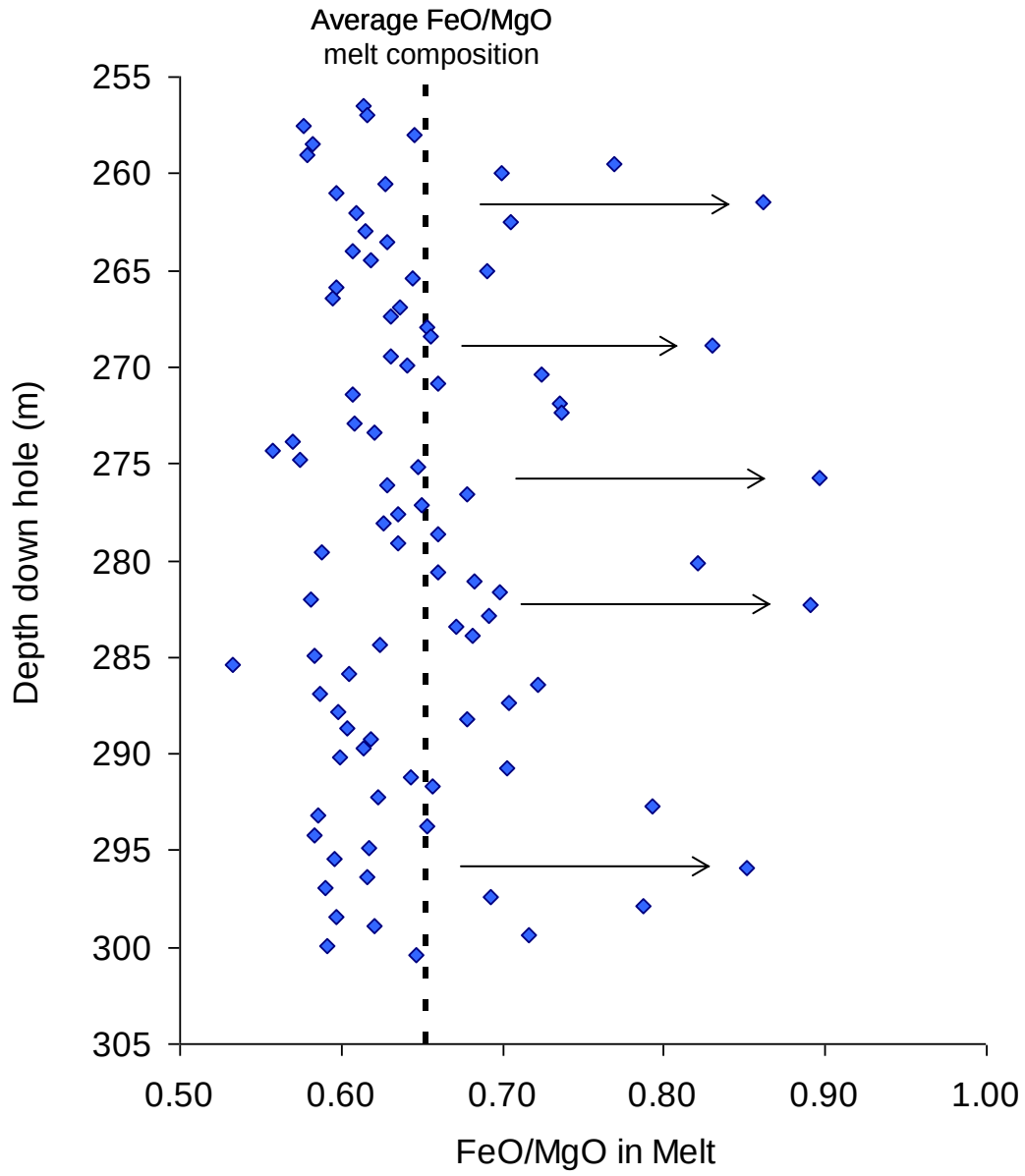

Figure 6.8.4: V05-13 chromite dataset: The calculated FeO/MgO content of the parent melt from which the chromite crystallised plotted against down hole depth.

The broken black line transects at the average FeO/MgO melt composition of all the samples. Black arrows indicate anomalously high FeO/MgO values. FeO/MgO melt composition values were aalculated using the equation of Maurel & Maurel, 1982. The FeO and MgO values used in the calculation were obtained from the massive chromite series V05-13, analyses were acquired using wave dispersive spectroscopy (WDS).

The melt compositions of FeO/MgO, Al_2O_3 and TiO_2 are calculated using equations that assume quartz-fayalite-magnetite (QFM) buffered fO_2 conditions. It is feasible that periodic pulses of volatile-rich boninite melt may have intermittently entered the system. These would cause the fO_2 of the melt to fluctuate (Chapter 3,

Section 3.4.1) which would affect the availability of Fe^{2+} (and Fe^{3+}) in the melt and consequently the partitioning of iron between the melt and crystallising chromite (*Roeder & Reynolds 1991*). Such changes would affect the results of the Maurel & Maurel (1982) calculation. This hypothesis provides one possible explanation for the fluctuations in the FeO/MgO of the melt seen in Figure 6.8.4. Variations in the Al_2O_3 and TiO_2 melt compositions of the V05-13 massive chromite dataset (Figure 6.8.5) do not correlate with one another or the FeO/MgO fluctuations (Figure 6.8.4). These melt components are not reported to be affected by changes in fO_2. A different process is required to explain the changes which reflect changes in the boninite parent melt chemistry.

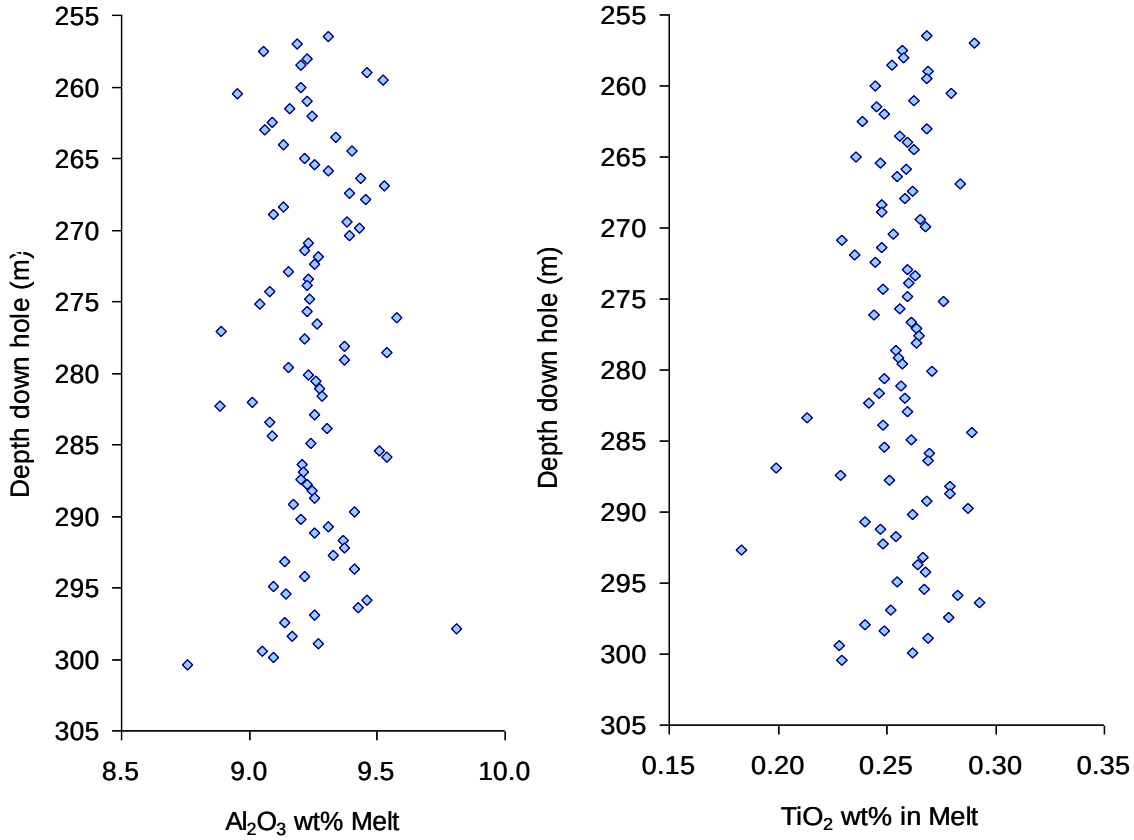

Figure 6.8.5: V05-13 chromite dataset: Variation with depth of the Al_2O_3 wt% and TiO_2 wt% content of the parent melt from which the chromite crystallised.

6.9 Results overview

- The Voskhod hanging wall, footwall and ore zone dunites plot inside the OSMA trend indicating that they are residual mantle rocks. However, as acknowledged, it is possible for dunite cumulates to crystallise from melts in the mantle and plot within OSMA. Regardless of the dunites being residual or having crystallised in the mantle, the Voskhod deposit is mantle hosted.

- The Voskhod podiform chromitite deposit plots in the same field as the Luobousa and Troodos podiform chromitites. The Kempirsai podiform chromitites (including Voskhod) have the highest Cr# values of podiform chromitite, being some of the most Cr-rich chromitites in the world.

- With distance from the ore body the chromite composition changes from 0.23 – 0.85 Cr#, this is consistent with reaction between a percolating melt and the residual mantle.

- The chromite compositions from chromitite and ore zone dunite are analogous to chromites from boninite lavas. The data presented infers that interaction between residual mantle and a boninite melt has formed the Voskhod deposit. This finding is supported by the parent melt composition calculations which are compositionally analogous with boninite melt. Boninite melts characterise supra-subduction zone settings in particular the formation of island forearcs.

- Dunite in the haning wall and footwall (distal dunite) has formed by reaction between mantle residue and a MORB melt (in a MOR setting) and appears unrelated to the SSZ-melt event responsible for the genesis of the Vokshod chromitite and the dunite halo.

- The mantle sequence represented by the Voskhod harzburgite and distal dunite samples analysed, records the transition of an evolving geodynamic setting from a MOR to a SSZ tetonic setting.

- Chromite in the dunite halo is comprised of primary phase chromite crystallised from the percolating boninite melt (euhedral) and residual chromite that is thought to have been "up-graded" by re-equilibration with the interacting melt or a melt associated fluid phase (subidomorphic and anhedral grains).

- The dunite and harzburgite samples have experienced less exposure to the melt and/or the melt associated liquids, consequently re-equilibration has been less extensive and possibly, in the case of some harzburgite samples, has not occurred at all.

- The observed MOR- and SSZ-reaction signatures recorded in these mantle units over a small distance (142 m from ore zone to the other most harzburgite sample) it seems plausible that the region preserved evidence of subduction initiation (water-rich boninite melt genesis) at the site of a redundant MOR setting, possibly along a transform fault, where the mantle section would have previously been subject to MORB melt percolation (forming the MOR-reacted dunite). This hypothesis also provides an explanation for the evidence of MOR-mantle residue harzburgite.

- Interaction between mantle residue derived from ~15% partial melting and a boninite melt is analogous to the present day tectonic setting of the Conical Seamount in the Izu-Bonin-Mariana forearc system.

Table 6.9.1 provides a summary of the samples analysed and results presented in this chapter.

Sample I.D	Drill core I.D	Region	Depth down hole (m)	Distance from mineralisation (m)	Rock type	Chromite modal %	Grain Shape	Diagram classification			
								$Cr\#_{(chr)}$-$Fo_{(ol)}$ [Peridotite type]	fO_2-Cr#	Ga-Fe^{3+}-Ti	REE Profile shape
G1815	V05-21	West	286.60	n/a	OZ Dun	< 5%	Eu	–	–	–	Flat
G1823	V05-21	West	297.65	48.80	Dist Dun	< 5%	SI	–	–	–	U-shaped
G1742	V05-24	Centre	141.30	142.92	Harz	< 5%	HL/SI	Passive margin/ Abyssal	MOR Hz	MOR-residual	U-shaped
G1763	V05-24	Centre	167.60	116.61	Harz	< 5%	HL/SI	–	–	–	LREE-Depleted
G1768	V05-24	Centre	176.94	107.26	Harz	<5%	HL/SI	–	–	–	LREE-Depleted
G1777	V05-24	Centre	185.60	98.56	Dist Dun	< 5%	HL/SI	Abyssal/SSZ	MOR Dun	MOR-reacted	LREE-Enriched
G1791	V05-24	Centre	221.00	63.17	Harz	< 5%	HL/SI	Abyssal	–	–	–
G1795	V05-24	Centre	231.90	52.30	Harz	< 5%	SI/An	Passive margin/ Abyssal	SSZ Hz	SSZ-reacted	U-shaped
G1798	V05-24	Centre	240.00	44.70	Dist Dun	< 5%	HL/SI	Abyssal/SSZ	–	MOR/SSZ-reacted	Flat
VOS-301	V05-24	Centre	249.53	34.67	Dist Dun	< 5%	HL/SI	Abyssal/SSZ	MOR Dun	MOR-reacted	LREE-Enriched
VOS-303	V05-24	Centre	252.00	32.50	Dist Dun	< 5%	SI	–	MOR Dun	MOR-reacted	LREE-Enriched
VOS-306	V05-24	Centre	258.94	25.26	Dun Halo	< 5%	HL/SI	SSZ	SSZ Dun	SSZ-reacted	LREE-Enriched
VOS-312	V05-24	Centre	266.88	17.32	Dun/Chr Stringer	~ 30%	SI/Eu	–	SSZ Dun/Chr	SSZ-reacted	–
VOS-315	V05-24	Centre	270.10	14.10	Dun/Chr Stringer	~ 50%	SI/Eu	*outside field*	SSZ Dun/Chr	SSZ-reacted	LREE-Depleted
VOS-320	V05-24	Centre	274.59	9.61	Dist Dun	< 5%	SI	–	–	–	Flat
VOS-322	V05-24	Centre	276.80	7.40	Harz	< 5%	SI/An	Abyssal/SSZ	SSZ Hz	–	Flat
VOS-327	V05-24	Centre	282.72	1.48	Harz	< 5%	SI/Eu	Passive margin/ Abyssal/SSZ	MOR Hz	SSZ-reacted	LREE-Depleted
F1907	V05-24	Centre	285.50	n/a	OZ Dun	<5%	SI	Abyssal/SSZ	MOR dun	MOR-reacted	LREE-Depleted
F1926	V05-24	Centre	296.70	n/a	OZ Dun	<5%	Eu	–	–	–	LREE-Enriched
F1968	V05-24	Centre	341.70	n/a	OZ Dun	<5%	Eu	–	–	–	LREE-Depleted
F1971	V05-24	Centre	343.00	n/a	OZ Dun	~ 15%	Eu	–	–	SSZ-reacted	Flat
F1978	V05-24	Centre	348.00	n/a	OZ Dun	~ 35%	Eu	–	–	–	Flat
G1908	V05-24	Centre	373.42	n/a	Dun Halo	< 5%	SI/Eu	SSZ	SSZ Dun	SSZ-reacted	LREE-Enriched
VOS-328	V05-24	Centre	375.00	1.58	Dun Halo	< 5%	SI/Eu	SSZ	SSZ Dun	SSZ-reacted	LREE-Enriched
VOS-341	V05-24	Centre	389.23	15.81	Harz	< 5%	HL	Passive margin/ Abyssal	SSZ Hz	SSZ-reacted	LREE-Depleted
VOS-345	V05-24	Centre	394.00	20.69	Harz	< 5%	HL/SI	–	–	–	LREE-Depleted
VOS-348	V05-24	Centre	398.63	25.21	Dist Dun	< 5%	HL/SI/Eu	SSZ	MOR Dun	SSZ-reacted	U-shaped
VOS-350	V05-24	Centre	403.00	29.50	Dist Dun	< 5%	HL/SI	Abyssal/SSZ	MOR Dun	SSZ-reacted	LREE-Enriched

Sample I.D	Drill core I.D	Region	Depth down hole (m)	Distance from mineralisation (m)	Rock type	Chromite modal %	Grain Shape	Diagram classification			
								$Cr\#_{(chr)}$-$Fo_{(ol)}$ [Peridotite type]	fO_2-Cr#	Ga-Fe^{3+}-Ti	REE Profile shape
G1601	V05-28	East	322.09	5.15	Dun Halo	< 5%	An/SI	Abyssal/SSZ	–	–	LREE-Enriched
G1605	V05-28	East	325.52	1.72	OZ Dun	< 5%	An/SI	Abyssal/SSZ	–	–	Flat
G1609	V05-28	East	333.85	n/a	OZ Dun	< 5%	Eu	–	–	–	LREE-Enriched
G1623	V05-28	East	354.67	n/a	OZ Dun	< 5%	SI/Eu	*outside field*	–	–	–
G1654	V05-28	East	369.70	n/a	OZ Dun	< 5%	SI/Eu	–	–	–	LREE-Enriched
G1624	V05-28	East	432.97	n/a	OZ Dun	< 10%	SI/Eu	*outside field*	–	–	–
G1631	V05-28	East	434.40	n/a	OZ Dun	< 5%	SI/Eu	*outside field*	–	–	–
G1910	V06-48	S. Centre	200.75	0.56	Dun Halo	< 5%	SI/Eu	SSZ	–	–	–
G1983	V06-48	S. Centre	298.45	1.75	Dun Halo	< 5%	SI/Eu	*outside field*	–	–	Flat
G1988	V06-48	S. Centre	300.15	3.45	Dun Halo	< 5%	SI/Eu	*outside field*	–	–	–
VOS-174	V06-S6	South	66.45	13.05	Dist Dun	< 5%	SI	Abyssal/SSZ	–	–	–
VOS-179	V06-S6	South	79.50	n/a	OZ Dun	< 10%	SI	Abyssal/SSZ	–	–	–
VOS-185	V06-S6	South	93.95	8.08	Harz	< 5%	An/SI	–	–	–	LREE-Enriched

Table 6.9.1: A summary of the Voskhod samples analysed and the results of the tectonic setting discrimination diagrams and REE profile types.

Rock type: Harz = Harzburgite, Dist Dun = Distal Dunite, Dun Halo = Dunite Halo, OZ Dun = Ore Zone Dunite, Dun/Chr Stringer = chromitiferous dunite (weakly mineralised) present outside of the classified ore zone region. Grain shape: HL = Holly Leaf, An = Anhedral, SI = Subidiomorphic, Eu = Euhedral. The tectonic discrimination diagram results (plots fO_2-Cr# and Ga-Fe^{3+}-Ti) of the underlined samples Vos-327, 348 and 350 are in disagreement. These samples plot close to discrimination boundaries. The REE geochemistry is presented in Chapter 5, Section 5.6.2.

Chapter 7. Major and minor element geochemistry variation on a 50 cm spaced scale, across a 45 m section of massive chromite from drill core V05-13

This chapter presents data that was collected to investigate the variation in chromite composition with depth down hole. A 45 m intersection of continuous, massive chromite ore, from drill core V05-13 of the Voskhod deposit, was sampled at 50 cm intervals; 90 samples were collected. The extensive intersection of continuous, monomineralic chromite, mineralisation presents a unique opportunity to examine the geochemistry. The lack of olivine (<5% modal proportion) in the samples means that the potential for divalent cation (Mg^{2+} and Fe^{2+}) exchange to take place between olivine and chromite is limited. Thus, the divalent cation compositions obtained from the chromite analyses are considered representative of the primary composition.

The interval of massive chromite studied starts at 255.70 m (vertical depth down hole) and extends to 301.20 m. Samples were collected between 256.50 m and 300.40 m; 87 were hard massive chromite (HMCr) and 3 were powdery chromite (PCr), taken from depths 259.0 m, 266.4 m and 285.4 m.

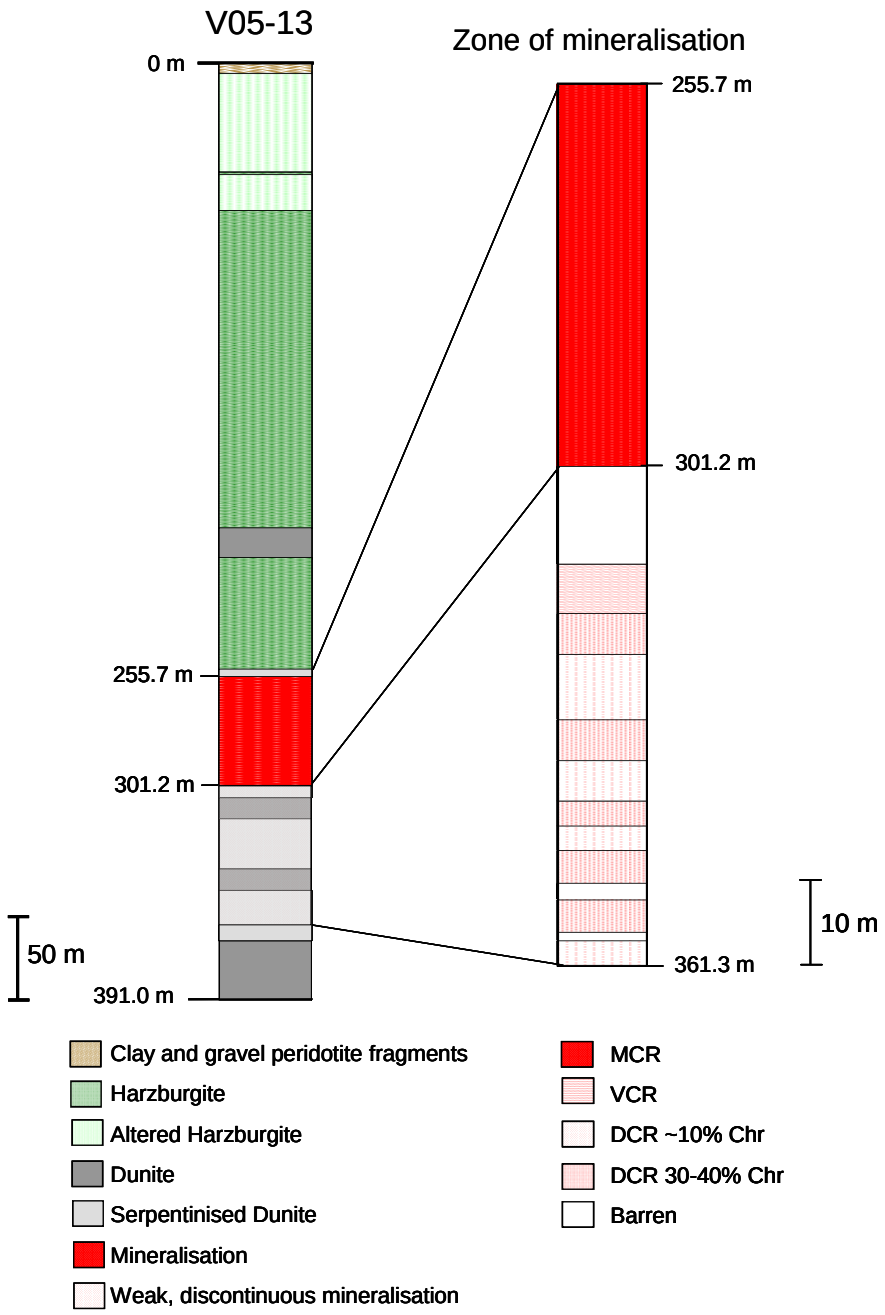

Figure 7.1.1: Drill core V05-13 lithological units log.

Core V05-13 was drilled just off centre, to the northwest, of the Voskhod orebody (Chapter 5, Section 5.1.1, Figure. 5.1.1). The start of the 45 m intersection of massive chromite, at 255.70 m, is the first occurrence of mineralisation in the core. Overlying the mineralisation, the hanging wall is comprised of serpentinised harzburgite and dunite. At the base of the intersection are two further mineralised intervals of disseminated chromite, one 18 m thick and the other 22 m thick.

Mineralisation ceases at 361.3 m down hole. The footwall is comprised of dunite and serpentinised dunite units (Figure 7.1.1).

From each of the 87, V05-13 samples of HMCr ore, a small, millimetre dimension sample was taken, these were mounted in resin blocks and polished. Each block held four sample fragments and careful note was taken of the position of each sample within the blocks. The PCr samples were prepared as polished thin sections, where the chromite ore powder was mixed with resin on the surface of a glass section slide, allowed to set and then polished.

The major elements Cr^{3+}, Al^{3+}, Fe^{2+} and Mg^{2+} and trace elements V^{5+}, Ti^{4+}, Mn^{2+}, Ni^{2+}, Zn^{2+}, Co^{2+} were analysed using a LEO 360 scanning electron microscope attached with a wavelength dispersive spectroscopy (WDS) analytical capability (Appendix A, Methods). From each sample three chromite grains were analysed twice at the grain centre, avoiding proximity to the grain boundaries where post magmatic alteration may have affected the composition.

The chromite compositions were calculated by stoichiometry using the Barnes and Roeder (2001, amended 2004) spinel calculation spreadsheet to determine the cation concentrations.

7.1 Interrogation of the V05-13 data series

Variation in the chromite geochemistry will reflect changes in the melt composition and/or oxygen fugacity conditions either at the time of chromite crystallisation, or present during the most recent re-equilibration event, which could have occurred after the primary crystallisation event. Changes to temperature and pressure are unlikely to have affected the composition, as at the mantle depths where this chromite formed such conditions are deemed to have been constant over a distance of 45 m.

7.1.1 Data reliability

The ranked, systematic order of the major element oxide compositions, of the V05-13 chromite dataset, from most to least abundant are; Cr_2O_3, MgO, $FeO_{(t)}$, Al_2O_3. The range of each major element, as acquired by WDS, is shown in Table 7.1.1.

Dataset	V05-13			
No. of analyses	270 grains			
Values (%)	**Al_2O_3**	**Cr_2O_3**	**$FeO_{(t)}$**	**MgO**
High	8.95	65.46	16.41	16.42
Low	6.70	62.03	11.85	12.37
Average	7.86	63.78	13.00	14.49
RSD%	3.67	0.91	6.77	4.71

Table 7.1.1: The data range of the major element compositions obtained from the analysis of the V05-13 chromites.

$FeO_{(t)}$ denotes total iron compositions presented in the divalent form Fe^{2+}. For each major element the relative standard deviation (RSD%) was calculated and is presented as a ratio of the sample standard deviation to the sample mean expressed as a percentage.

From each sample three grains were analysed, the compositions collected were averaged and the RSD% calculated for the major element oxide values; Cr_2O_3, Al_2O_3, MgO, $FeO_{(t)}$ and the trace element oxides MnO, TiO_2, V_2O_5 and NiO. The Co and Zn analysis values were frequently below detection limit and are not presented. The highest, lowest and average RSD% value for a sample are presented in Table 7.1.2. The dataset was also considered in entirety and the RSD% was calculated for the same major and trace elements. The premise being that if the RSD% for the composition of the entire dataset (considered as one "sample") was greater than the RSD% for the composition of a single sample it would demonstrate that the dataset was more heterogeneous than a single sample.

Dataset V05-13

	Major elements				Trace elements			
	Al_2O_3	**Cr_2O_3**	**$FeO_{(t)}$**	**MgO**	**MnO**	**TiO_2**	**V_2O_5**	**NiO**
Average composition	7.86	63.78	13.00	14.49	0.23	0.15	0.10	0.16
Average RSD% of a sample	2.06	0.45	1.39	1.28	5.85	6.36	16.15	10.83
Max RSD% of a sample	7.59	1.30	5.90	6.61	15.91	23.95	84.55	33.91
Min RSD% of a sample	0.21	0.08	0.18	0.11	0.49	0.29	0.49	1.63
RSDev of the dataset	3.67	0.91	6.77	4.71	11.97	10.38	20.00	15.35

Table 7.1.2: The average chromite composition of the V05-13 dataset and the maximum, minimum and average relative standard deviation values for a sample compared with that of the entire dataset.

The results show that the RSD% for a single sample can be as great, if not greater than that of the entire dataset (Figure 7.1.1), indicating that the composition within a sample can be varied. Consequently, each grain should be examined individually and the data collected from a sample should not be averaged. There is one exception, the values for $FeO_{(t)}$, where the variation in a single sample is always less than that of the dataset (or more tightly constrained) (Figure 7.1.1).

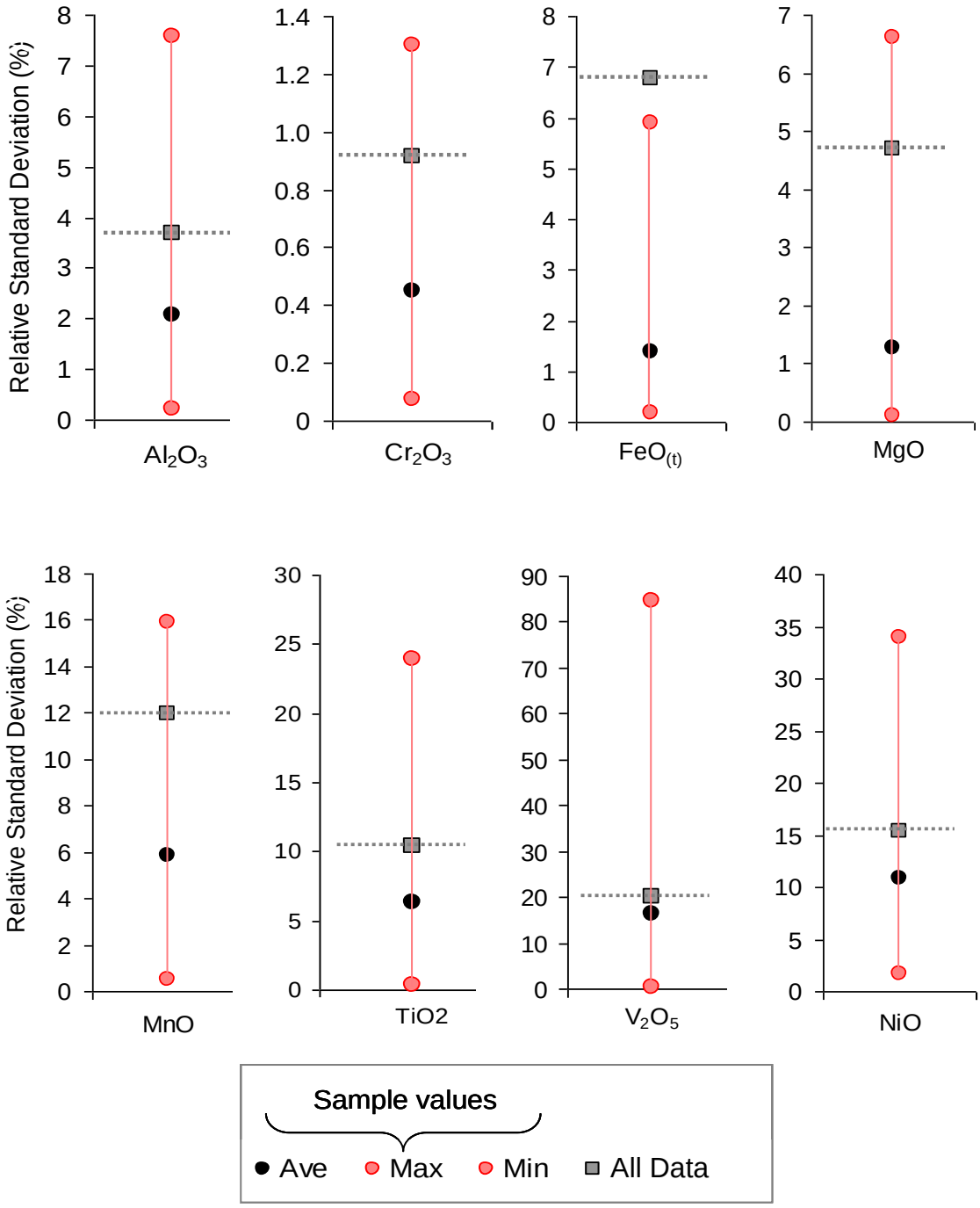

Figure 7.1.1: The major and trace elements, maximum, minimum and average RSD% values from samples compared with the complete dataset RSD%.

7.1.1.1 Comparison of the Voskhod sample variation with natural standards

To investigate the composition homogeneity of the V05-13 dataset, comparisons were made with data collected from five chromite grains; MBD-7-G1, MBD-7-G2, MBD8-Std, C51 Std and Vos-Std (Table 7.1.3). These were sourced from podiform chromitites and were deemed to have formed under similar conditions in similar tectonic environments as Voskhod and served as natural standards.

Sample	Ophiolite Source	No. Analyses	2σ			
			$FeO_{(t)}$	MgO	Cr_2O_3	Al_2O_3
MBD-7-G1	Berit, Turkey	256	0.43	0.60	1.41	0.83
MBD-7-G2	Berit, Turkey	28	0.40	0.45	1.37	0.83
MBD8-Std	Berit, Turkey	34	0.56	0.47	0.73	0.77
C51 Std	Al'Ays, Saudi Arabia	81	1.29	0.47	0.95	0.67
Vos-Std	Voskhod, Kazakhstan	56	0.19	0.31	0.35	0.23
V05-13 - dataset	Voskhod, Kazakhstan	270	1.76	1.36	1.16	0.58

Table 7.1.3: Natural chromite standard samples, source localities, number of analyses and 2σ values for each of the major elements analysed using WDS.

The data for grains MBD-7-G1, MBD-7-G2, MBD8-Std and C51 Std are from Brough (2011).

Samples MBD-7-G1, MBD-7-G2 and MBD-8-Std were from podiform chromite in the Berit ophiolite, Turkey and C51-Std was from Al'Ays, Saudi Arabia. These data are taken from a study carried out by Brough (2011) that used the same SEM-WDS analytical facilities that were used to collect the chromite data presented in this study. The Vos-Std chromite grain was sourced from the Voskhod podiform chromite deposit, Kazakhstan and analysed as part of this study.

Each standard grain was analysed multiple times (between 28 and 256 times). The results provide some indication of the natural composition variation that can be present within a single grain, as well as the effect had by instrumental drift (during data acquisition) on the analyses collected. It is not possible to differentiate between the effects of these two variables, however, it is not of particular importance to be able to do so, as the dataset featured in this study could

potentially be affected by either, or both, of these factors. Thus, having an understanding of the effect had on the data acquired is important.

The $FeO_{(t)}$% composition of the V05-13 dataset is the only variable where the RSD% within a sample is consistently less than that of the RSD% for the whole dataset (Figure 7.1.1). Consequently, it is the best parameter to use to interrogate the dataset and it is important to compare this value with that obtained from the standards. The Cr_2O_3% composition of the V05-13 dataset, in contrast, is exceptionally uniform, with the greatest relative standard deviation of a sample being 1.30%.

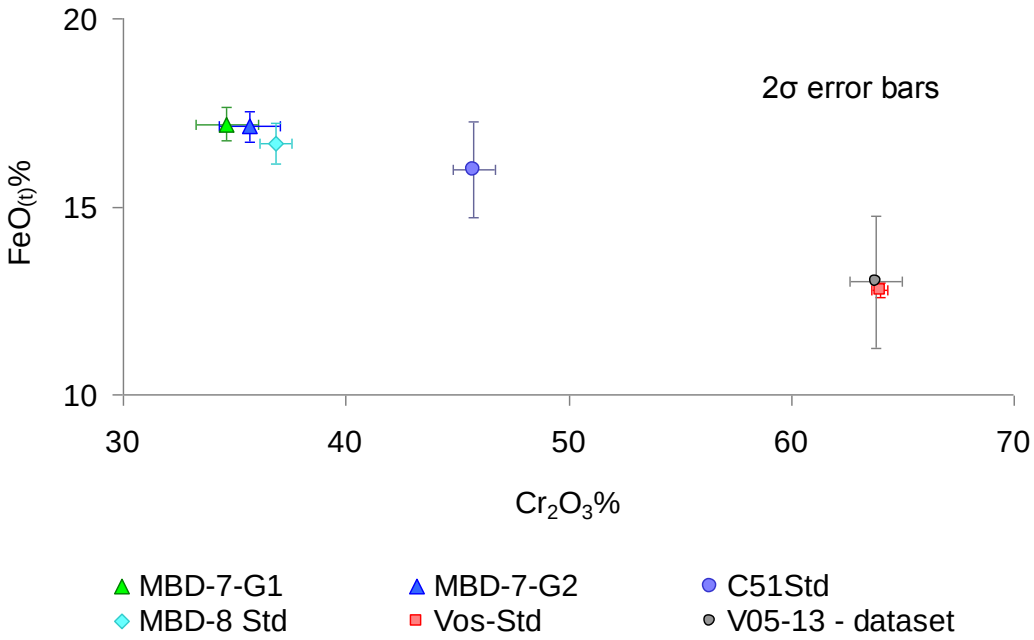

Figure 7.1.2: $FeO_{(t)}$% against Cr_2O_3% compares the composition variation of single chromite grain standards with the V05-13 chromite dataset.
Error bars presented are to 2σ (2 standard deviation).

Comparison of the standards MBD-7-G1, MBD-7-G2, MBD-8 Std, C51Std with Vos-Std (the Voskhod standard, red data point), shows that the composition of the Voskhod sourced standard, Vos-Std is the most homogeneous, both in terms of $FeO_{(t)}$ and Cr_2O_3% content (Figure 7.1.2).

The 2 sigma range for the Cr_2O_3% content of the V05-13 dataset (grey data point) is similar to that of the standards MBD-7-G1, MBD-7-G2, MBD-8 Std and C51Std;

in fact, compared with the standards MBD-7-G1 and MBD-7-G2 the Cr_2O_3% 2 sigma range of the V05-13 dataset is smaller. In contrast, the $FeO_{(t)}$% 2 sigma range for the V05-13 dataset is significantly larger than those of the standards, although, as standard C51Std demonstrates, in a single grain this composition can vary. The 2 sigma range of the standards and dataset V05-13 for the other major element compositions Al_2O_3% and MgO% are presented in (Figure 7.1.3).

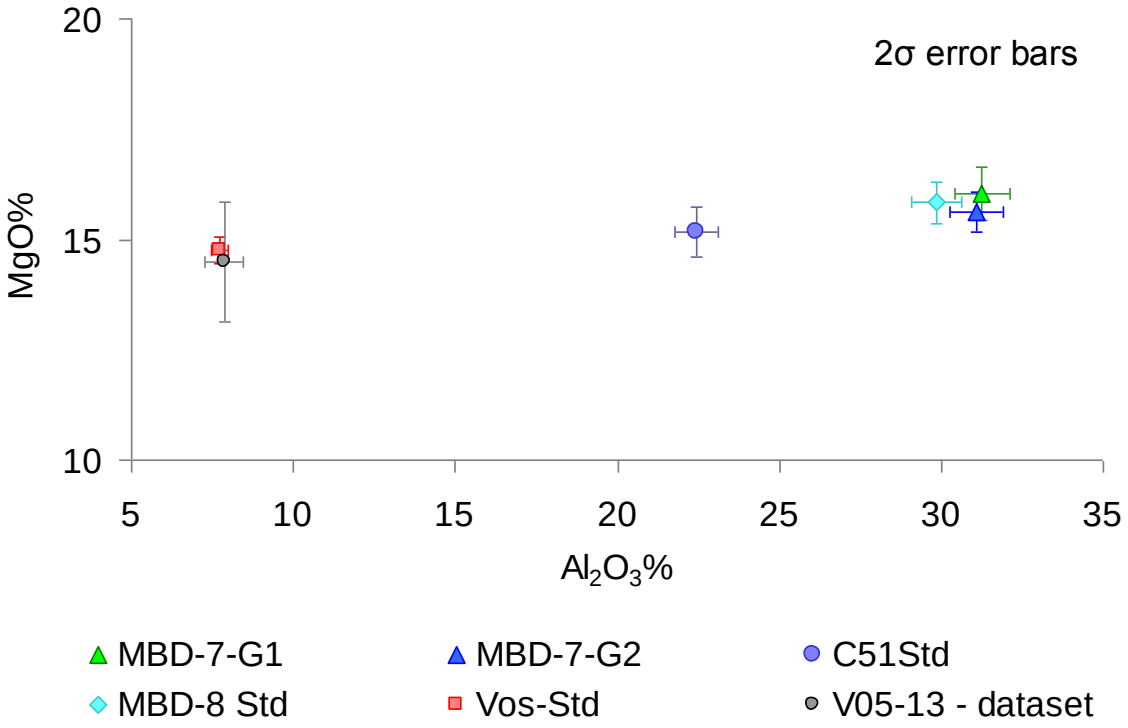

Figure 7.1.3: MgO% against Al_2O_3% to compare the composition variation of single chromite grain standards with the V05-13 chromite dataset.

Error bars presented are to 2σ (2 standard deviation).

In the plot MgO% against Al_2O_3% (Figure 7.1.3) the 2 sigma error bars for the standard Vos-Std (red data point) are once again much smaller than the other standards, indicating that the composition of the grain analysed is comparatively more homogeneous.

The Al_2O_3% 2 sigma range for dataset V05-13 (grey data point) is similar to the error bar range of the standards MBD-7-G1, MBD-7-G2, C51Std and MBD-8Std, demonstrating that the Al_2O_3% composition of the dataset is similar to that of a single grain. The MgO% 2 sigma range of dataset V05-13 is much greater than that of the standards error bars, reflecting greater compositional variation within the V05-13 dataset than is seen in a single grain.

The major element plots (Figure 7.1.2 and Figure 7.1.3) show that the variation in the Voskhod standard grain Vos-Std is consistently the smallest . This does not appear to be the consequence of a greater number of analyses as standards C51Std and MBD-7-G1 were analysed 81 and 256 times, respectively. In comparison, the Voskhod standard was analysed 56 times. The homogeneity of the Voskhod chromite composition appears to be the exception and not the rule. It is reasonable to assume that the Voskhod sourced standard (Vos-Std) has been exposed to the same formation process history as that of the V05-13 chromite samples and so is most likely to have an equally well constrained, comparable composition. This is supported by the comparisons made with the other standards. So as not to discard the small, but potentially significant, compositional variations that are present in the V05-13 dataset it is highlighted that the major element 2 sigma error bar values for Vos-Std are much smaller than those presented by the V05-13 dataset or those of the other chromite grain standards. On this premise, all of the major elements will be considered when examining the V05-13 dataset, although it is recognised that the $FeO_{(t)}$ and MgO compositions are the most varied.

The chromite analyses report iron values as $FeO_{(t)}$% a value that represents the combined abundance of iron (total iron), both FeO% and Fe_2O_3%, expressed as FeO% ($FeO_{(t)}$ is the nomenclature used to express the value obtained). The FeO% and Fe_2O_3% values can be calculated from the $FeO_{(t)}$% value using the ideal stoichiometric unit cell formula of chromite, an equation given in the Barnes and Roeder spinel calculation spreadsheet (2001, amended 2004).

Of the calculated iron constituents FeO% and Fe_2O_3% (calculated for each grain analysed), the average FeO% composition for the V05-13 dataset is 10.98 (RSD% 18.50) and the average Fe_2O_3% composition is 2.25 (RSD% 52.03). The Fe_2O_3% content of chromite records changes in the oxidising conditions effective during chromite crystallisation. Increased Fe_2O_3% values infer more oxidising conditions, resulting from the conversion of FeO to Fe_2O_3, to accommodate the additional oxygen available in the system.

7.1.2 V05-13 Chromite: Major element geochemistry

The major element compositions for each of the V05-13 chromite samples were plotted against depth (Figure 7.1.4). The Al_2O_3% and Cr_2O_3% compositions are well constrained. In contrast, the MgO% and $FeO_{(t)}$% composition variation is much greater.

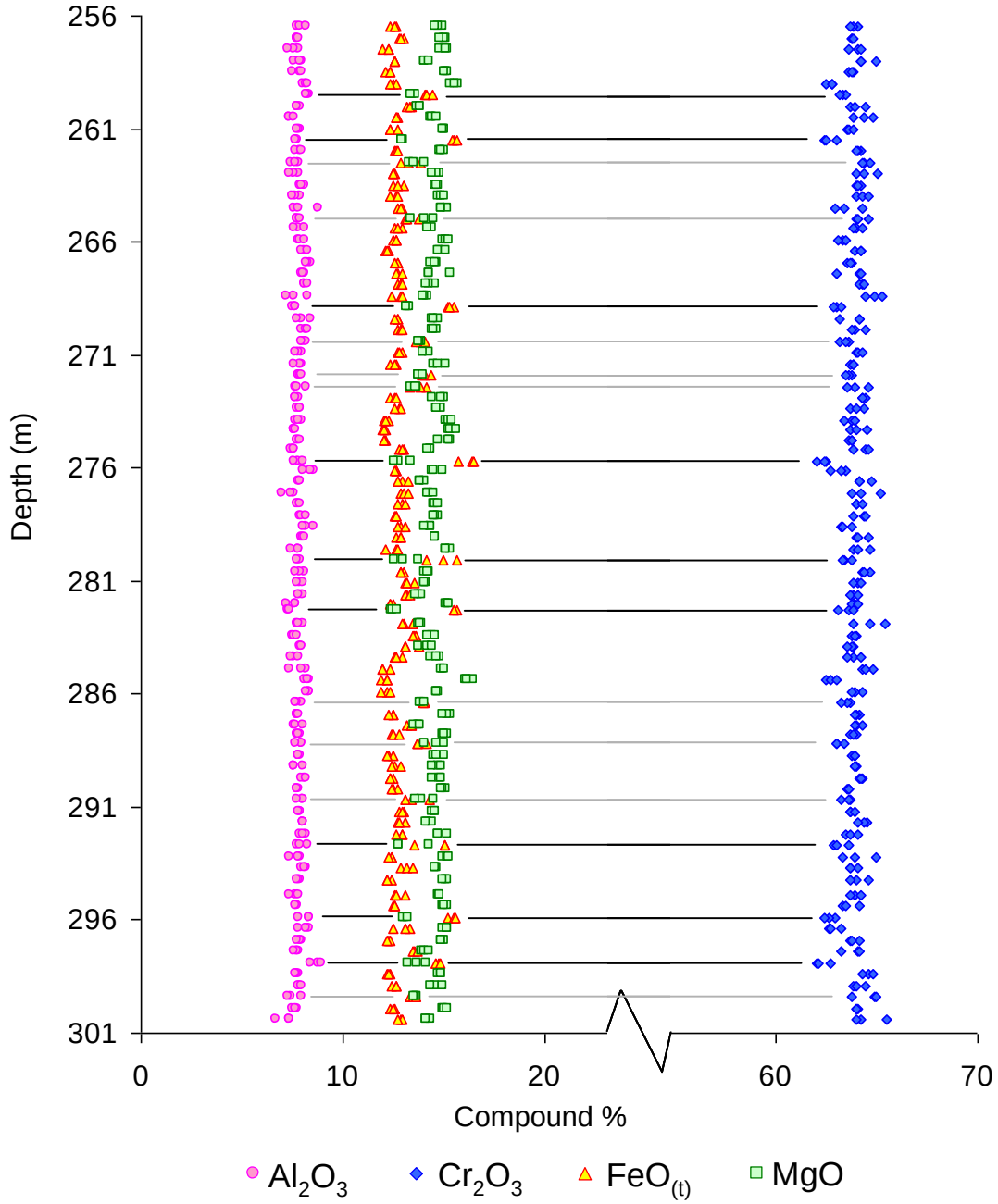

Figure 7.1.4: The major element geochemistry of chromite analyses from drill-core V05-13 versus depth.

Black filled symbols are 13 chromites where the $FeO_{(tot)}$ value exceeds the MgO value.

Typically, MgO% is greater than $FeO_{(t)}$%, however, there are 9 samples where each of the three grains analysed have $FeO_{(t)}$% compositions greater than MgO% (these samples are identified with solid black lines in Figure 7.1.4). Furthermore, there are 9 samples where one or two of the three grains analysed have compositions where $FeO_{(t)}$% is greater than MgO% (these samples are identified with solid grey lines in Figure 7.1.4).

It appears that for some of the samples where $FeO_{(t)}$% exceeds MgO%, the Cr_2O_3% composition is slightly lower, but this is not a consistent observation. Additionally, there does not appear to be any relationship between depth and the variations seen in the chromite compositions that is to say, not all of the samples where $FeO_{(t)}$% is greater than MgO% form groups at specific depth intervals or cluster together, on the contrary the spacing of these samples appears to be random. The greatest distance between two iron-rich chromites is 7.4 m (between points 261.5 m and 268.9 m) and the smallest interval is 0 m, where points 271.9 m and 272.4 m are adjacent to one another in the series.

Recognising that samples can contain grains of mixed compositions, i.e. grains where the MgO% content is greater than $FeO_{(t)}$%, co-exist with grains where the $FeO_{(t)}$% content is greater than MgO%, further validates the case for not averaging the sample compositions (Table 7.1.4). This observation also demonstrates that the samples are not compositionally homogeneous. Consequently, the composition of each grain must be considered independently. In terms of formation this observation identifies a process that causes some grains to be iron-rich and others to be magnesium-rich and for the two differing compositions to co-exist.

Using the difference in the $FeO_{(t)}$% and MgO% compositions, it is possible to distinguish two chromite types within the data series these are termed the MgO>$FeO_{(t)}$ chromite (where MgO% exceeds $FeO_{(t)}$%) and the $FeO_{(t)}$>MgO chromite (where $FeO_{(t)}$% exceeds MgO%). These two groups are examined further to investigate whether additional geochemical characteristics exist.

Sample	Number of chromites in group		
Depth (m)	$MgO>FeO_{(t)}$	$FeO_{(t)}>MgO$	(FeO>MgO)
259.50	0	3	0
261.50	0	3	2
262.50	2	1	0
265.00	2	1	0
268.90	0	3	0
270.40	2	1	0
271.90	0	3	0
272.40	1	2	0
275.70	0	3	2
280.10	0	3	2
282.30	0	3	3
286.40	1	2	0
288.20	2	1	0
290.70	2	1	0
292.70	1	2	2
295.90	0	3	1
297.90	0	3	0
299.40	2	1	0

Table 7.1.4: The 18 samples from the V05-13 dataset (location depths given) where results reported one or more $FeO_{(t)}>MgO$ chromite analysis.

7.1.3 Determining the ferrous and ferric iron contents of $MgO>FeO_{(t)}$ and $FeO_{(t)}>MgO$ chromites

The presence of iron-rich, $FeO_{(t)}>MgO$ chromites, distinguished on the basis of total iron content (i.e. combined Fe^{2+} and Fe^{3+}) poses the questions; i) What has caused the increase in iron composition? ii) Do the values stem from increased FeO or Fe_2O_3 contents (or possibly both)?

The plot FeO% against Fe_2O_3% is used to establish whether increased ferrous or ferric iron contents are responsible for high $FeO_{(t)}$ values (Figure 7.1.5). High $FeO_{(t)}$% compositions resulting from increased FeO% would indicate that more iron was present in the reduced form (Fe^{2+}) when the most recent closure temperature for chromite crystallisation and/or equilibration was achieved. This could be when the chromite crystallised from the parent melt, in which case it

would indicate that these chromites crystallised from a more iron-rich pulse of melt compared with the MgO>$FeO_{(t)}$ chromites. An alternative hypothesis may be that there has been a post-crystallisation, sub-solidus re-equilibration event that has caused localised, iron enrichment within the chromitite pod. High $FeO_{(t)}$% values that result from increased Fe_2O_3% contents would indicate that the most recent equilibration conditions were both iron rich and oxidising.

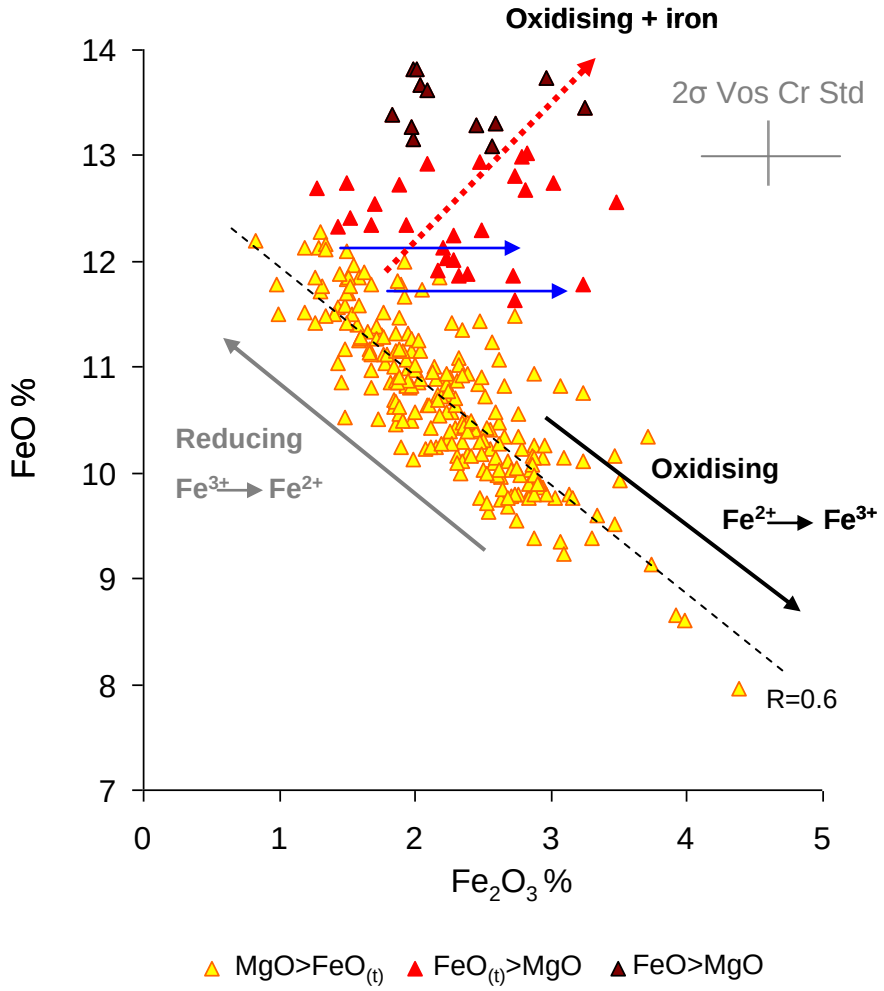

Figure 7.1.5: FeO% against Fe_2O_3%

The red filled triangle symbols represent the $FeO_{(t)}$>MgO group and the yellow filled triangle symbols, the MgO>$FeO_{(t)}$ group. The black triangles are $FeO_{(t)}$>MgO chromites with FeO values greater than MgO values. The R^2 values provide an indication of the strength of correlation between the two variants.

It is seen in the plot FeO% against Fe_2O_3% that the dominant trend of the V05-13 dataset is for the FeO% content to increase as Fe_2O_3% decreases (Figure 7.1.5).

This is most readily seen from the negative correlation of the MgO>$FeO_{(t)}$ chromite data (yellow triangles, Figure 7.1.5). This relationship may be explained by changes to the oxidising conditions; as the oxygen availability in the melt decreases (conditions become reducing) iron will preferentially stabilise as FeO to optimise bonding with the limited available oxygen. The strength of this relationship is verified by the R^2 value of 0.69 (black broken line, Figure 7.1.5) .

The $FeO_{(t)}$>MgO chromites behave differently (red triangles, Figure 7.1.5) plotting away from the main trend formed by the MgO>$FeO_{(t)}$ chromites (yellow triangles, Figure 7.1.5). Of the 39 $FeO_{(t)}$>MgO chromites identified, 12 have FeO% compositions greater than MgO% (red/black triangles, Figure 7.1.5). The Fe_2O_3% compositions extend the same range as those of the MgO>$FeO_{(t)}$ chromites. In comparison to the MgO>$FeO_{(t)}$ chromites, the $FeO_{(t)}$>MgO chromites possess higher Fe_2O_3% contents for FeO% values that are the same as, or greater than the MgO>$FeO_{(t)}$ chromites (blue arrows, Figure 7.1.5). This observation reaffirms that the Fe_2O_3% component is integral to the characterisation and genesis of the $FeO_{(t)}$>MgO chromites.

The relationship between the FeO% and Fe_2O_3% compositions of the $FeO_{(t)}$>MgO chromites lack correlation, implying that there are at least two independent processes that control the partitioning of these components into chromite. It is proposed that the composition of the MgO>$FeO_{(t)}$ chromites results from a single process, where the system evolves resulting in the observed trend.

Having established that the two chromite groups are at compositionally different, at least in terms of iron content, the respective major and trace element average compositions were calculated for each group (Table 7.1.5).

Dataset V05-13 $FeO_{(t)}$>MgO	No = 39									
	Major elements						Trace elements			
	Al_2O_3	Cr_2O_3	MgO	$FeO_{(t)}$	FeO	Fe_2O_3	MnO	TiO_2	V_2O_5	NiO
Average	7.89	63.22	13.28	14.79	12.72	2.30	0.28	0.15	0.10	0.15
RSD%	4.69	1.06	3.48	5.22	4.92	22.90	10.63	15.43	18.25	23.57

MgO>$FeO_{(t)}$	No = 231									
	Major elements						Trace elements			
	Al_2O_3	Cr_2O_3	MgO	$FeO_{(t)}$	FeO	Fe_2O_3	MnO	TiO_2	V_2O_5	NiO
Average	7.85	63.95	14.63	12.70	10.68	2.24	0.23	0.16	0.10	0.16
RSD%	3.48	0.78	3.39	3.26	6.88	26.56	8.27	9.18	20.33	13.64

Table 7.1.5: The average major and trace element compositions of the MgO>$FeO_{(t)}$ and $FeO_{(t)}$>MgO chromite groups and relative standard deviation for each value.

The FeO and Fe_2O_3 values presented have been calculated using the Roeder & Barnes (2001, amended 2004) spinel calculation spreadsheet. No. denotes the number of grains analysed in each group.

It is evident from the data presented in Table 7.1.5 that the effect of the MgO% and FeO% composition variations, which determine these two groups, have a negligible effect on the Cr_2O_3% and Al_2O_3% compositions. When compared with the composition variation seen in the chromite standards (Section 7.1.1) these data values are remarkably uniform.

7.1.4 V05-13 Chromite: Trace element geochemistry

The V05-13 chromites were analysed for the trace elements MnO, V_2O_5, TiO_2 and NiO. The relative standard deviation expressed as a percentage (RSD%) of the trace elements is high (Appendix D, Table D2). Analyses show that there are no differences between the V_2O_5%, TiO_2% and CoO% compositions of the two groups (Table 7.1.5), however, a difference is seen between the MnO% compositions.

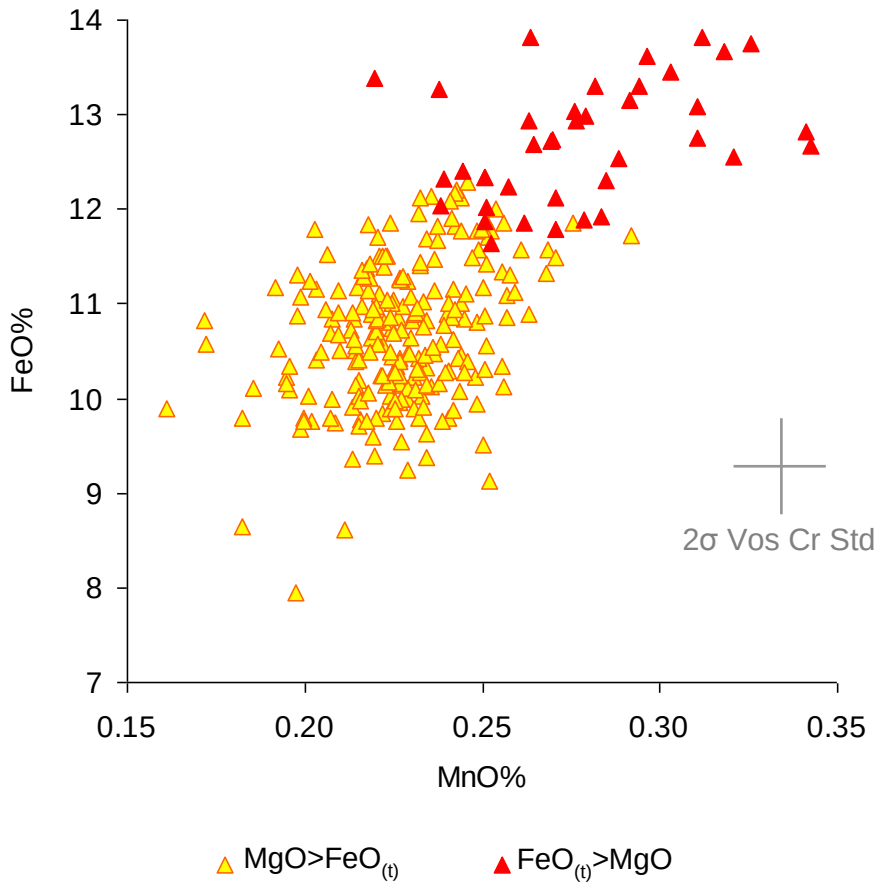

Figure 7.1.6: FeO% against MnO% showing the chromite groups MgO>$FeO_{(t)}$ and $FeO_{(t)}$>MgO

MnO% is the most abundant, consistently detectable, trace element. Concentrations (across the whole V05-13 dataset, i.e. both chromite groups) range from 0.18% to 0.33%. Furthermore, the MnO% values stand up best to the scrutiny of relative standard deviation that ranges from 0.5 % to 16.0 % (*pers comm. Dr. I. McDonald*).

The $FeO_{(t)}$>MgO chromites have a higher average MnO% content of 0.28% compared with the MgO>$FeO_{(t)}$ chromites, where the average compositions is 0.23%. The groups are formed based on the relative proportions of the divalent cations Mg and Fe^{2+}. As Mn is also a divalent cation, it will substitute into the same tetrahedral sites as those filled by Mg and Fe^{2+}. The MnO% content is seen to correlate positively with FeO% (Table 7.1.5 and Figure 7.1.6).

7.1.5 Mg#-Cr# diagram

The Mg#-Cr# diagram shows the relationship between the divalent (Mg#) and trivalent (Cr#) cation ratios for the chromites (Figure 7.1.7). This plot provides an additional geochemical tool to study the chromite groups. Using the Mg#-Cr# diagram, Naldrett et al. (2009) documented trendlines, termed Trend A and Trend B (Chapter 3, Sections 3.4.4 and 3.4.5) that formed when a sample series of massive chromite compositions, sourced from the Bushveld Complex, were plotted. Magmatic processes were assigned to explain the compositional variation controlling the relationships observed. In this study the Mg#-Cr# diagram is used to compare and contrast the V05-13 data array with the observations made by Naldrett et al. (2009) to aid the interpretation of the processes responsible for the compositional variation and genesis of the massive chromite in the Voskhod deposit.

The geochemical plots presented in this chapter illustrate that the V05-13 chromite compositions differ, principally in terms of the divalent cations, Mg, Fe^{2+} and Mn. Furthermore, it is evident from the scatter of the data points, seen in the plots presented, that the compositions do not vary systematically throughout the dataset, i.e. the groups do not plot in well constrained clusters along a single trend-line.

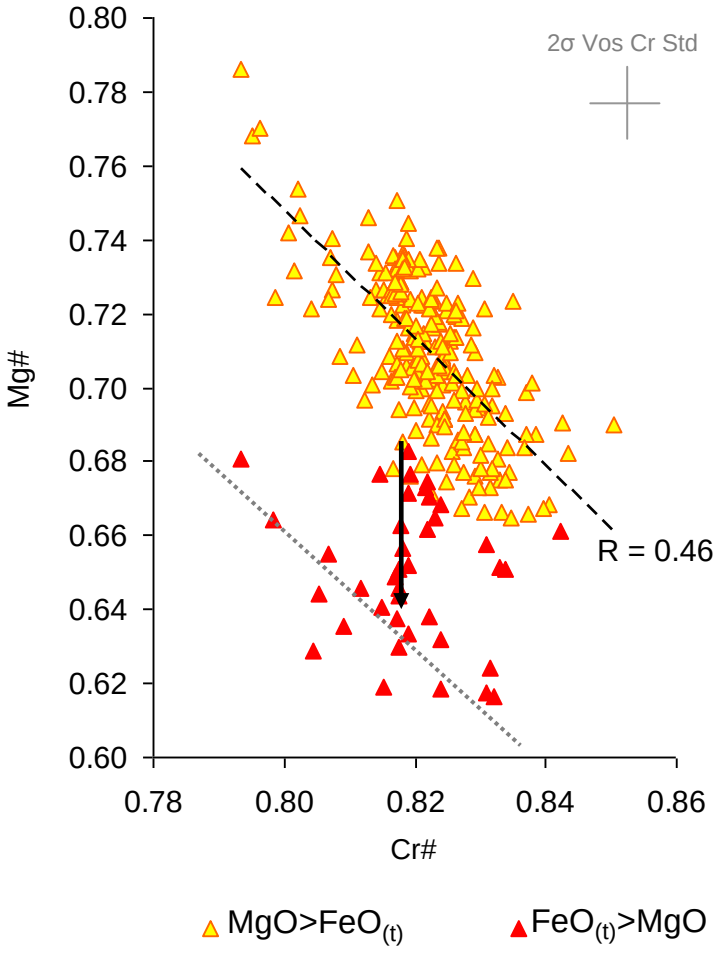

Figure 7.1.7: Mg# versus Cr# plot

Where Mg# = [Mg/(Mg+Fe^{2+})] and Cr# = [Cr/(Cr+Al+Fe^{3+})]

The Mg#-Cr# relationships for the two chromite groups identified in the V05-13 dataset are shown in (Figure 7.1.7). The Cr# range is tightly constrained, extending from 0.79 to 0.85, (a range of 0.06 Cr#). This range is covered by the data arrays of both groups. The Mg# range is much greater; the $FeO_{(t)}$>MgO chromites plot to lower Mg# values, between 0.62 to 0.68 and the MgO>$FeO_{(t)}$ chromites plot at higher Mg# values, from 0.67 to 0.79. There is little overlap between the data spread of the two groups.

The MgO>$FeO_{(t)}$ group forms a weak negative correlation (R = 0.46); as Mg# increases, Cr# decreases (illustrated by the broken black trend line that passes through the data (Figure 7.1.7). A similar relationship is displayed by some, but not all, of the $FeO_{(t)}$>MgO chromite data points forming a trend parallel to that of the MgO>$FeO_{(t)}$ chromites, but displaced to lower Mg# values (illustrated by the

broken grey line, (Figure 7.1.7). The $FeO_{(t)}$>MgO chromite data points that form the parallel trend at lower Mg# values appear to be connected by a series of vertically aligned $FeO_{(t)}$>MgO data points that descend from the MgO>$FeO_{(t)}$ chromite group (illustrated by a black arrow, Figure 7.1.7).

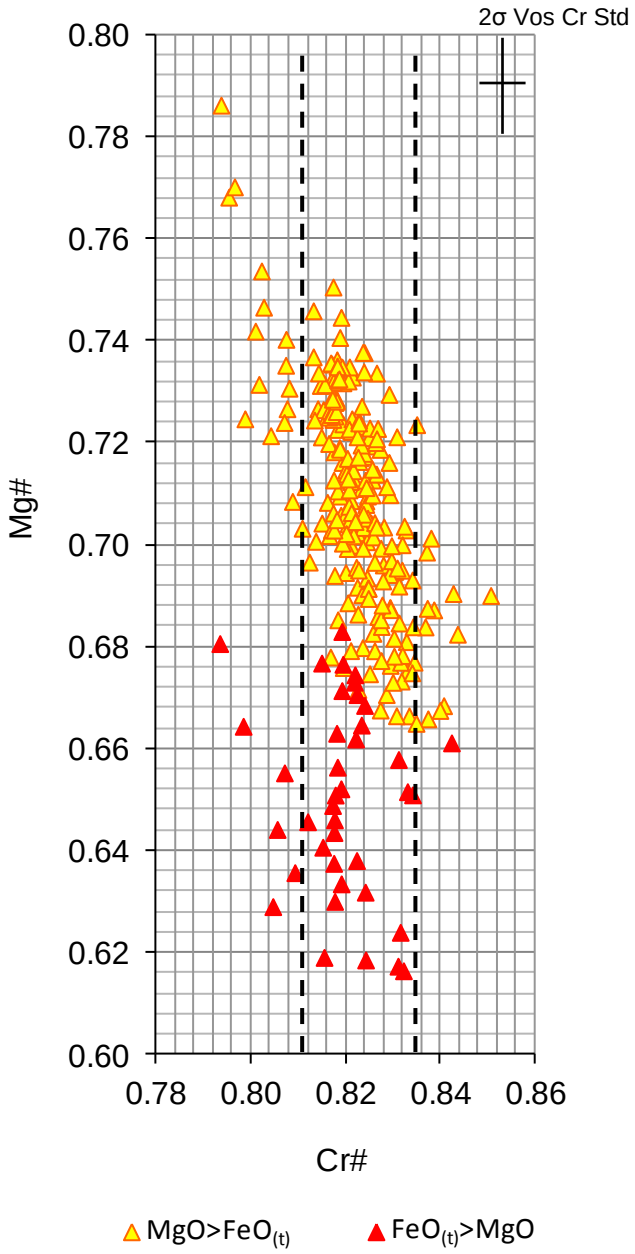

Figure 7.1.8: Data point population density of the Mg# versus Cr# plot
Here the plot is presented with equal scale x- and y-axes for clarity.

When the V05-13 dataset is considered collectively, rather than as two groups, it is seen that the majority of the data (90%) plots between 0.812 to 0.836 Cr#, a range

of 0.024 (illustrated by broken black tram lines, Figure 7.1.8). As seen in Section 7.1.3, Table 7.1.5, the Cr_2O_3% and Al_2O_3% compositions of V05-13 chromites are exceptionally uniform, so inevitably the Cr# values will be equally uniform. In light of this, the data is described as plotting within a well constrained Cr# range where the groups are readily distinguished on the basis of Mg#. Furthermore, it is noted that the vertical line of $FeO_{(t)}$>MgO points that plot with decreasing Mg# from the MgO>$FeO_{(t)}$ chromite group, also plot in the Cr# region comprised of 90% of the chromite data. For the remaining 10% of data, which plot outside of the 0.812-0.836 Cr# range, it is generally the case that Mg# and Cr# correlate negatively.

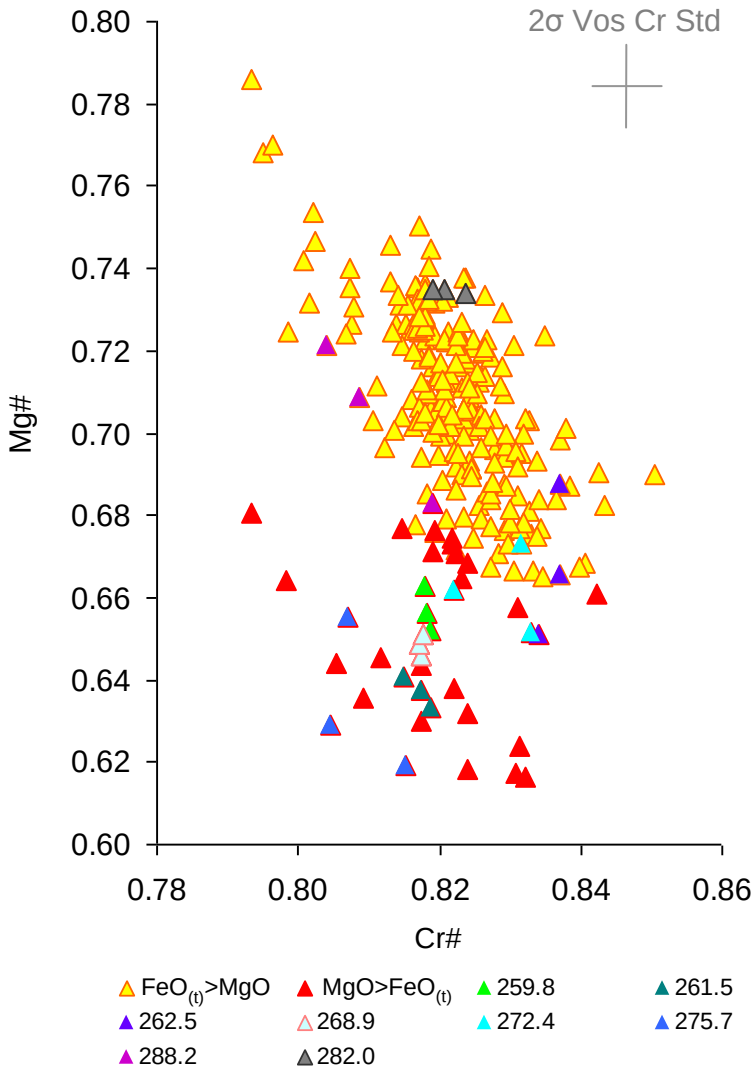

Figure 7.1.9: Mg# against Cr# annotated with individual grain analyses from seven samples to demonstrate compositional variation within a sample.

To demonstrate the compositional variation present within a sample, as well as between samples, the data collected from eight samples is shown on the Mg#-Cr# plot (Figure 7.1.9). For each sample the respective number of $FeO_{(t)}$>MgO and MgO>$FeO_{(t)}$ chromite analyses obtained are given in Table 7.1.6.

Dataset V05-13	**No. of grains**	
Sample depth (m)	**MgO>$FeO_{(t)}$**	**$FeO_{(t)}$>MgO**
259.8	0	3
261.5	0	3
262.5	2	1
268.9	0	3
272.4	1	2
275.7	1	2
282.0	3	0
288.2	2	1

Table 7.1.6: The depth interval and corresponding number of $FeO_{(t)}$>MgO and MgO>$FeO_{(t)}$ grains for each of the samples presented in Figure 7.1.9.

It is seen in Figure 7.1.9 that two samples, 259.8 and 268.9, form the vertical line present between the MgO>$FeO_{(t)}$ and $FeO_{(t)}$>MgO chromite data clusters. These samples demonstrate the possibility for the Cr# of a sample to be nearly homogenous. In contrast, sample 282.0 plots horizontally showing that a sample can have a near constant Mg# composition. Samples 261.5 and 288.2 plot obliquely, aligned parallel with the extension of the two data groups, while samples 262.5, 272.4 and 275.7 plot in no particular organised fashion. No systematic, compositional variation is seen within or between samples (e.g. with depth) irrespective of the chromite compositions ($FeO_{(t)}$>MgO or MgO>$FeO_{(t)}$). Furthermore, results of nine samples from the dataset indicate a mixed composition being comprised of both $FeO_{(t)}$>MgO and MgO>$FeO_{(t)}$ chromites (Table 7.1.4).

In light of the findings presented in this chapter the immediate questions are:

1) Why is the Voskhod chromite composition so homogenous?
2) What causes the change in iron content?
3) How is it possible for MgO>$FeO_{(t)}$ and $FeO_{(t)}$>MgO chromites to co-exist in a sample?

Chapter 8. Variation on a 1 cm spaced scale, in the major and minor element geochemistry of the Voskhod massive chromite.

Chapter 7 documented the discovery of two different chromite compositions within a 50 m intersection of massive chromite from the Voskhod deposit; $FeO_{(t)}$>MgO chromite, where the $FeO_{(t)}$% content exceeded that of MgO% and MgO>$FeO_{(t)}$ chromite where the MgO% content was greater than $FeO_{(t)}$%. From the results it appeared that a chromite sample could be comprised of one chromite group ($FeO_{(t)}$>MgO or MgO>$FeO_{(t)}$ chromite) or a mixture of both i.e. $FeO_{(t)}$>MgO and MgO>$FeO_{(t)}$ chromite. The Cr_2O_3% and Al_2O_3% contents were remarkably uniform throughout the intersection.

This chapter presents chromite geochemistry obtained from sections spaced 1 cm apart. The aim is to investigate whether small scale cryptic layering can be identified and whether this resembles in any way layering in stratiform chromitite deposits such as the Bushveld Complex, in South Africa (*Naldrett et al., 2009*).

Drill hole V05-24 intercepts a mineralised zone 88.40 m thick starting at 284.20 m and ending at 372.60 m. Three chromitite samples; F1925, F1964-65 and F1996-97, each 15 cm long, were selected from this drill hole. The samples were selected from intervals to examine the compositional variation in chromite from the upper, middle and base of the mineralised zone.

Sample	Start (depth m)	End (depth m)	Description
F1925	296.05	296.18	massive chromite (8 cm) grading into disseminated chromite (6 cm) where chromite constitutes <20%
F1964-65	341.45	341.59	massive chromite
F1996-97	359.01	359.15	massive chromite

Table 8.1.1: The sample numbers, start and end depths of the sample lengths (in meters) and chromite mineral content description.

The core lengths were cut into 1 cm thick sections, perpendicular to the vertical axis of the drill core. Each 1 cm thick section was prepared as a polished thin section and analysed for the major elements; Cr, Al, Fe^{2+} (expressed as $FeO_{(t)}$) and Mg and trace elements V^{5+}, Ti^{4+}, Mn^{2+}, Ni^{2+}, Zn^{2+}, Co^{2+}. From each section three chromite grains were analysed twice at the grain centre. Grain boundary edges, where post magmatic alteration may have occurred were avoided.

Cation concentrations and the partitioning of Fe^{2+} and Fe^{3+} concentrations were calculated using 'spincalc' the Barnes and Roeder spinel calculation spreadsheet (*Barnes & Roeder, 2001, updated 2004*). The results are given in Appendix D, Tables D3, D4 and D5 for sections F1964-65, F1996-97 and F1925 respectively.

8.1 Data reliability and the data distribution of samples F1964-65, F1996-97 and F1925

In order to establish whether the three samples F1964-65, F1996-97 and F1925 are compositionally distinct from one another, as well as examine the extent of compositional diversity within each sample, the average compositions annotated with 2σ distribution bars are plotted on the FeO%- Fe_2O_3% and Mg#-Cr# diagrams (Figure 8.1.1 and Figure 8.1.2). These diagrams were selected because in Chapter 7, where the two chromite groups $MgO>FeO_{(t)}$ and $FeO_{(t)}>MgO$ were identified, the discrimination between these groups was most effectively observed using these plots.

The compositions of the 5 standards (see Chapter 7, Section 7.1) with error bars of 2σ are included in the plots to compare the compositional variation in a grain with that of the samples examined in this chapter.

8.1.1 The standard error and sample data distribution for FeO % against Fe_2O_3 % diagram

The average composition for each standard and samples F1964-65, F1996-97, F1925-massive chromite and F1925-disseminated chromite are shown on the FeO% against Fe_2O_3% diagram (Figure 8.1.1).

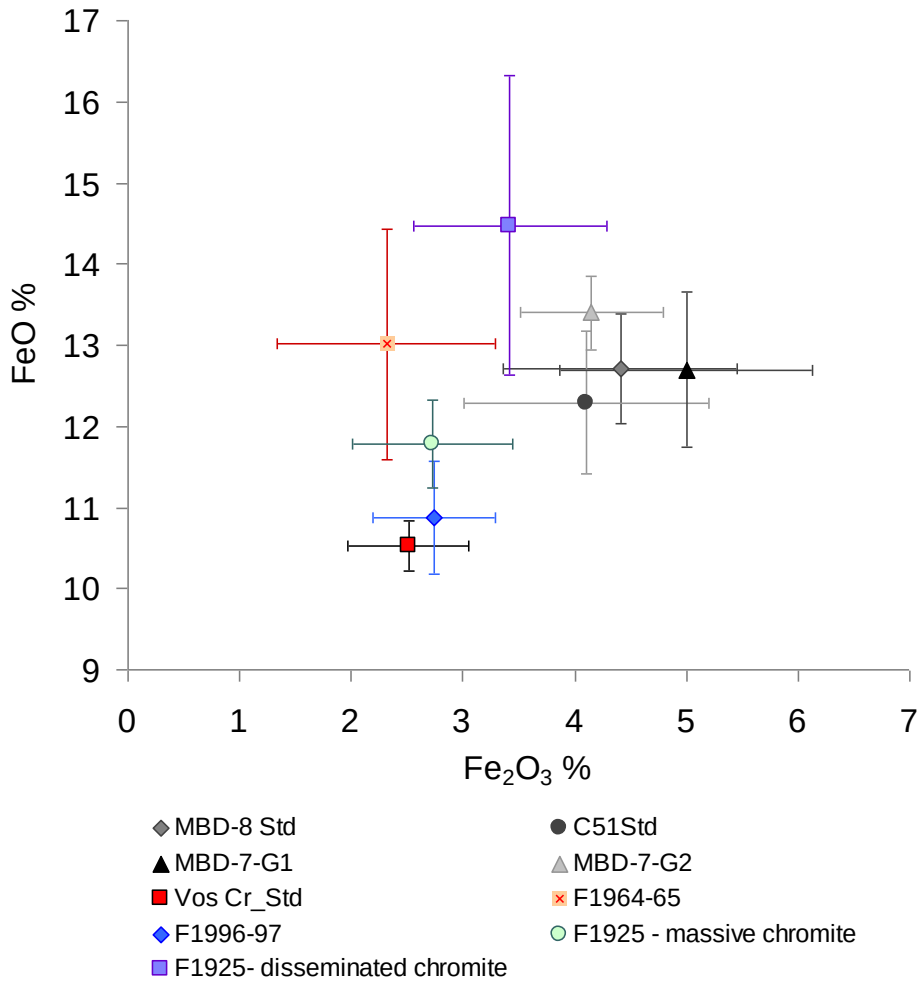

Figure 8.1.1: FeO% against Fe_2O_3% showing the average compositions of the standards and samples F1964-65, F1996-97, F1925-massive chromite and F1925-disseminated chromite.

For the purpose of this plot F1925 is divided into two as the sample is composed of two mineralogically distinct portions; massive chromite and disseminated chromite where olivine is the dominant mineral phase. The error bars given for the standards are 2σ and the data distribution of each sample, shown as bars, is the calculated 2σ. Details of the natural podiform chromite standards MBD-7-G1, MBD-7-G2, MBD-8 Std and C51 Std (*Brough, 2011*) are given in Chapter 7, Section 7.1.1.1.

Standards, C51Std, MBD-8 Std and MBD-7-G1 are compositionally more varied than standards MBD-7-G2 and Vos-Std (Figure 8.1.1). The 2σ of Fe_2O_3% is consistently greater than that of FeO%. The Voskhod standard (Vos-Std) has the smallest error bars, most notably the 2σ of FeO%. This reflects the compositional homogeneity of the grain.

The average compositions of the samples F1964-65, F1996-97, F1925-massive chromite and F1925-disseminated chromite, plot separate from one another. There is some overlap of the 2σ data distribution between the samples e.g. F1996-97 and F1925-massive chromite have near identical Fe_2O_3% compositions and the FeO% 2σ values overlap. Similarly the 2σ of the Fe_2O_3% and FeO% compositions for samples F1964-65 and F1925-disseminate chromite partially overlap. However, although one sample may overlap with another, no two samples plot in exactly the same region. Furthermore, some clear distinctions are noted, e.g. F1996-97 is compositionally different from both F1964-65 and F1925-disseminated chromite, and F1925-massive chromite differs from F1925-disseminated chromite, there being no overlap between these samples.

The 2σ of Fe_2O_3% for F1996-97 and F1925-massive chromite is comparable with that of the Voskhod standard. Samples F1964-65 and F1925-disseminate chromite show greater Fe_2O_3% variation, although when compared with the standards MBD-8 Std, C51Std and MBD-7-G1 it is evident that the compositions are fairly well constrained. Instead, it is the FeO% contents that most clearly distinguish the samples from one another. Whereas the 2σ of FeO% for the standards is typically smaller than the 2σ of Fe_2O_3%, for the Voskhod samples the reverse is seen, with FeO% being consistently the more variable component.

Evaluation of the geochemical diversity of the standards and samples demonstrates:
i) The Voskhod standard is compositionally the most homogeneous standard
ii) The Fe_2O_3% variation of the standards is greater than the FeO% variation
iii) In contrast, the FeO% variation of the Voskhod samples is greater than the Fe_2O_3% variation (the exception being F1925-massive chromite)

As previously documented in Chapter 7 (Section 7.1) the Voskhod standard composition, which is the most uniform of all the standards, has been subject to the same (or most similar) genetic process history as that of the samples presented in this study. When compared with the standards C51Std, MBD-8 Std and MBD-7-G1 the 2σ

Fe_2O_3% variation of the Voskhod samples are similarly diverse. This implies that the variation within the samples could either result from instrumental drift or be similar to the natural variation present within a single grain. However, when compared with the Voskhod standard 2σ values the sample variations are clearly greater, particularly for samples F1964-65 and F1925-disseminated chromite. It is proposed that the variation seen results from genuine compositional diversity within the sample, but that the Voskhod chromite is apparently more homogeneous than other chromite (i.e. the standards).

The FeO% and Fe_2O_3% composition variation seen in the samples (F1964-65, F1996-97 and F1925-massive chromite and F1925-disseminated chromite) is taken to reflect true geochemical variations present within and between the groups showing them to be distinct from one another.

8.1.2 The standard error and sample data distribution on the Mg# - Cr# diagram

The average compositions for each standard and samples F1964-65, F1996-97 , F1925-massive chromite and F1925-disseminated chromite are presented on the Mg#-Cr# diagram (Figure 8.1.2).

The Cr# values of the Voskhod samples are well constrained, ranging from 0.794 to 0.834. The Cr# variation of the Voskhod standard (ranging from 0.814 to 0.828) is only slightly less. It is the Mg# variation, which ranges from 0.542 to 0.723, that distinguishes the samples from one another, in much the same way as the FeO% composition was the principal discriminating variable in Figure 8.1.1 (the author acknowledges that the Mg# and FeO% compositions are intrinsically related).

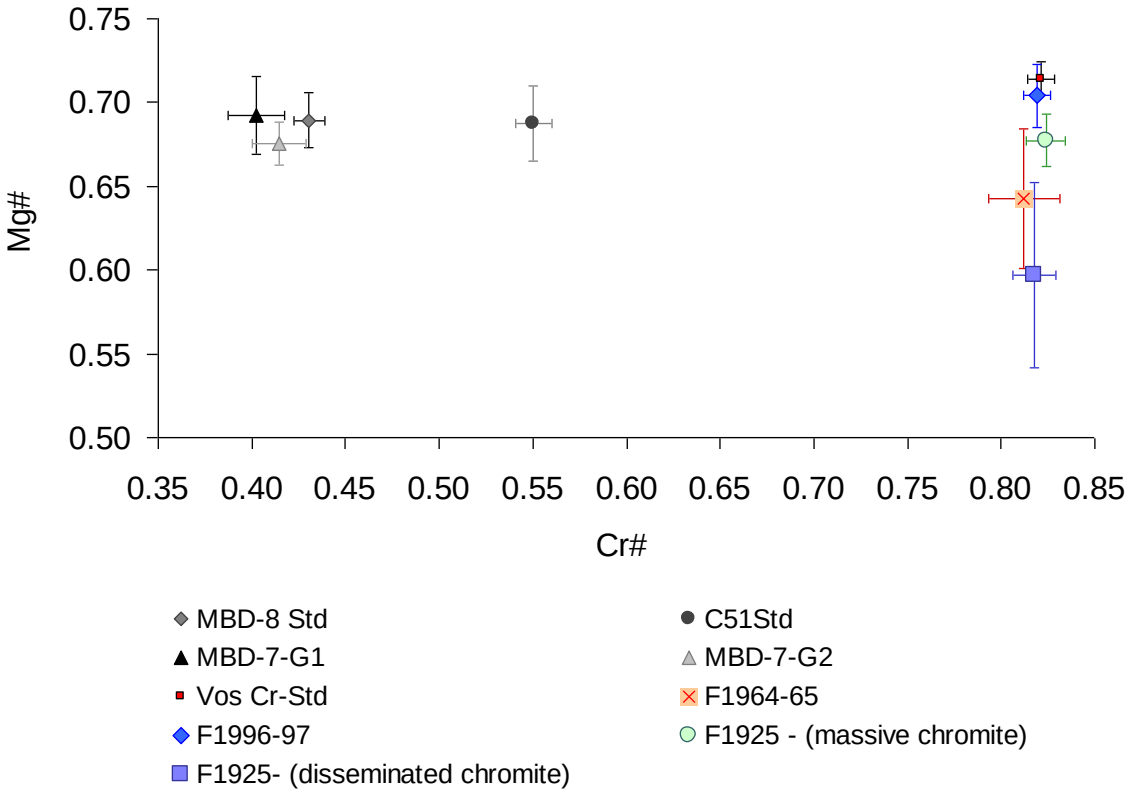

Figure 8.1.2: Mg# against Cr# showing the standard compositions and the average data for samples F1964-65, f1996-97, F1925-massive chromite and F1925-disseminated chromite.

For the purpose of this plot F1925 is divided into two as the sample is composed of two mineralogically distinct portions; massive chromite and disseminated chromite where olivine is the dominant mineral phase. The error bars given for the standards are 2σ and the data distribution of each sample, shown as bars, is the calculated 2σ. Cr# = [Cr/(Cr+Al+Fe^{3+})] and Mg# = [Mg/(Mg+Fe^{2+})].

The Voskhod standard has the smallest error bars. In comparison, the other standards have Cr# and Mg# error bar sizes that are similar to the 2σ data distributions of samples F1996-97 and F1925-massive chromite. Samples F1964-65 and F1925-disseminated chromite are compositionally the most diverse, more so in terms of Mg# than Cr#. Sample F1964-65 has the greatest Cr# distribution.

The compositional diversity of the standards and samples shown on the Mg#-Cr# diagram, is similar to that seen on the FeO%-Fe_2O_3% diagram (Figure 8.1.1), reinforcing the deductions made in Section 8.1.1.

8.1.3 Examination of the trivalent cation geochemistry

The Fe_2O_3% and Cr# compositions presented in Sections 8.1.1 and 8.1.2 both demonstrate that the trivalent cation, major element oxide geochemistry of the Voskhod samples and standard have a restricted range. The 2σ distributions of the Voskhod chromite analyses are comparable with that of the error bars (2σ) of the standards.

The composition variation of the major elements, Cr_2O_3, Al_2O_3 and Fe_2O_3, provides information required to interpret the environment that the chromites form in. Thus, it is important to examine the analyses of these major elements, obtained from the standards, to identify the factors that could have caused the variation.

The variation of these major element compositions could result for two possible reasons, either i) the instrument used to acquire the analyses or ii) the result of natural compositional variation within a grain or sample. In the event that the analytical instrument is responsible for the composition variations then a systematic compensation of one of the trivalent elements for another might be expected.

The Al_2O_3%-Cr_2O_3% and Fe_2O_3%-Cr_2O_3% relationships for each standard are shown in Figure 8.1.3 the R-squared value is given on each plot as an indication of the strength of correlation.

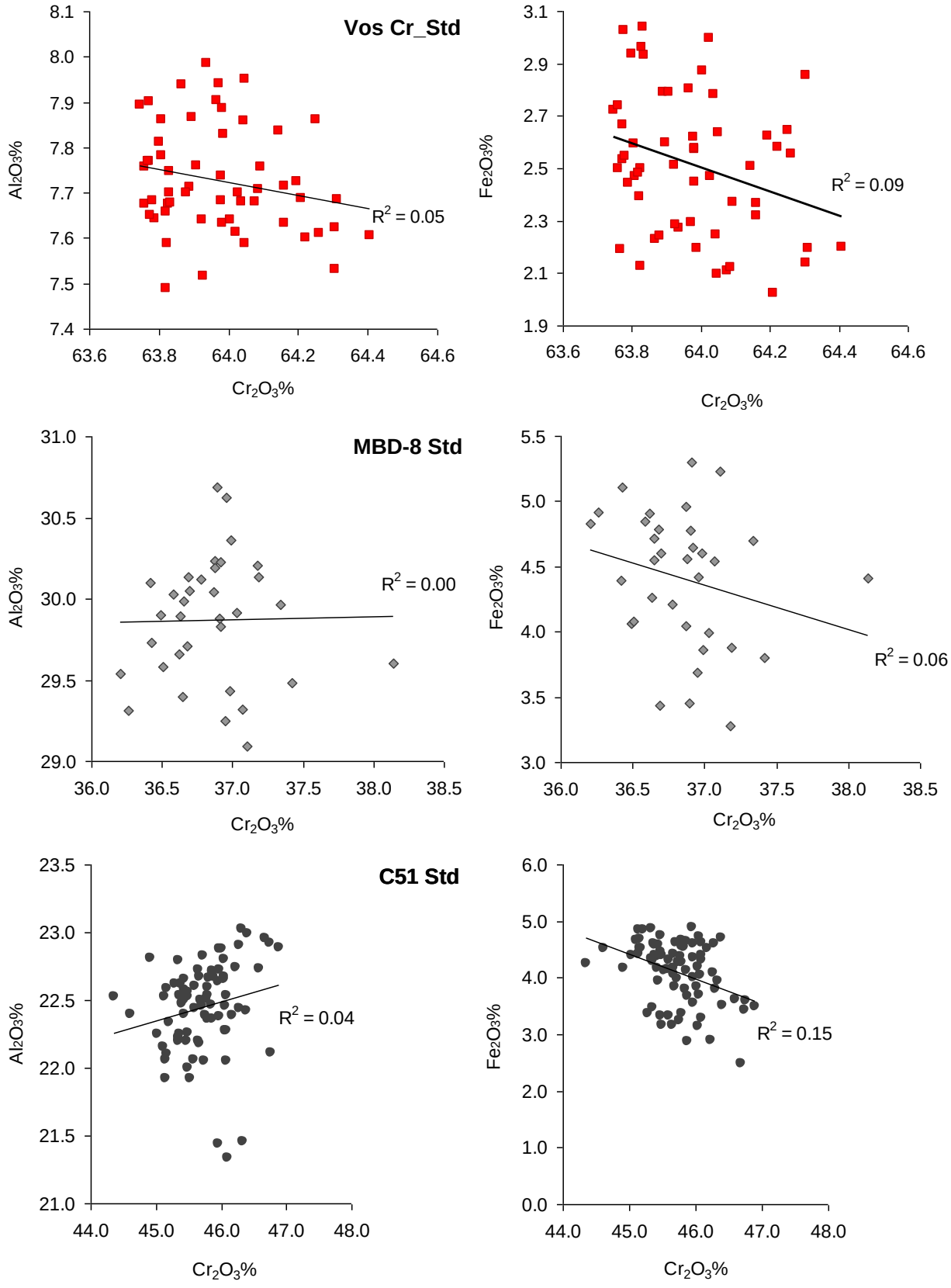

Figure 8.1.3: Comparison of the trivalent, major element oxide compositions, Cr_2O_3, Al_2O_3 and Fe_2O_3 obtained from the analysis of the standards.

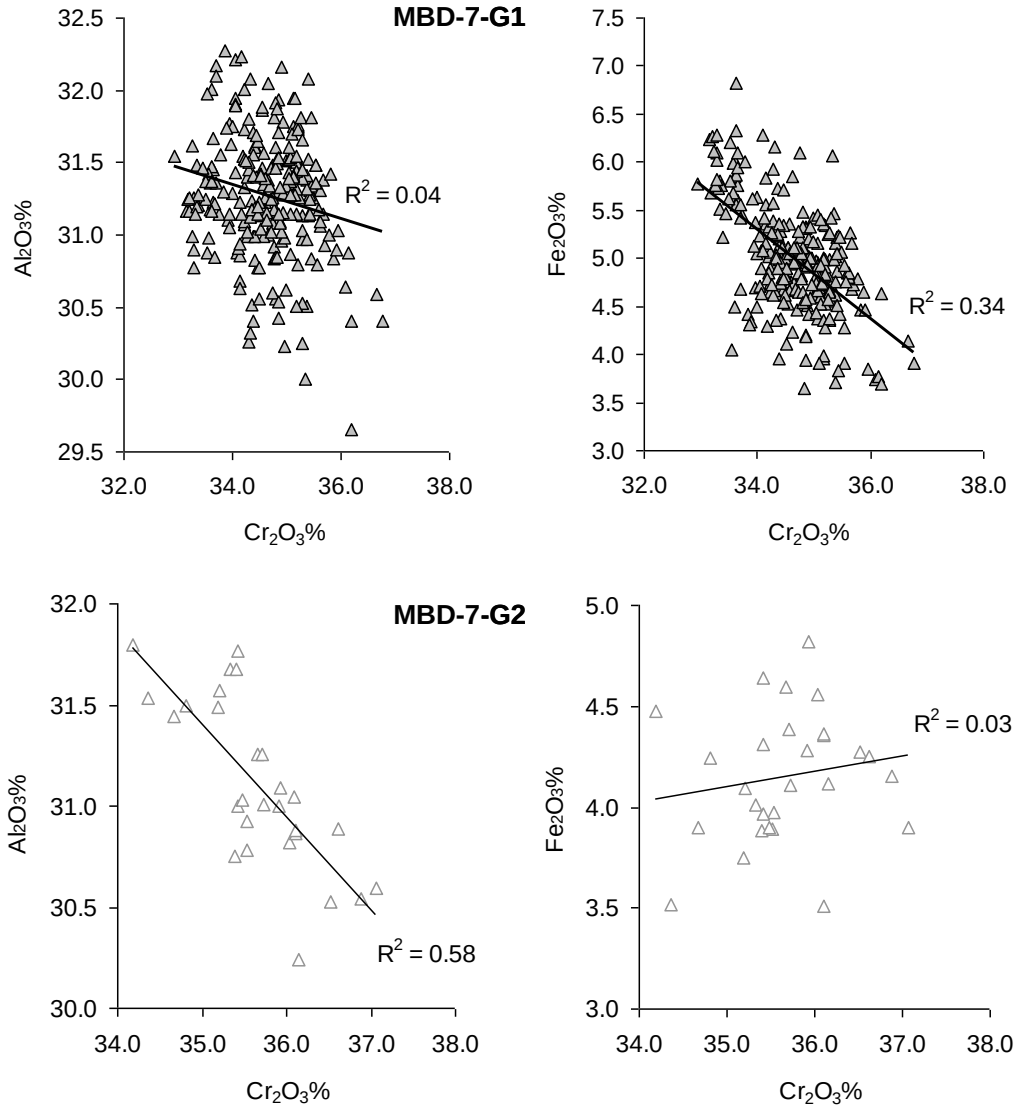

Figure 8.1.3 (cont): Comparison of the trivalent, major element oxide compositions, Cr_2O_3, Al_2O_3 and Fe_2O_3 obtained from the analysis of the standards.

A black trendline and the corresponding R-squared value is shown on each plot.

From the Al_2O_3%-Cr_2O_3% and Fe_2O_3%-Cr_2O_3% plots given for each standard (Figure 8.1.3) no systematic or consistent relationship between the elements is seen. In standards Vos Cr-Std, MBD-8 Std and C51Std there is no apparent reciprocal relationship between either Al_2O_3%-Cr_2O_3% or Fe_2O_3%-Cr_2O_3%, this is supported by R-squared values of less than 0.15. Standards MBD-7-G1 and –G2 are two separate grains sourced from the same sample, it is of interest to note that in MBD-7-G1 there is a weak negative relationship between Fe_2O_3%-Cr_2O_3% (R = 0.34) , while in MBD-7-G2 a negative relationship between Al_2O_3%-Cr_2O_3% is evident (R=0.58).

No systematic or consistent chemical variation is seen between the standards. Furthermore, the trends identified within standards MBD-7-G1 and –G2 are different indicating that when present, systematic geochemical variation is detectable. These results indicate that the compositional variation does not result from the analytical instrument used to acquire the data. It is most likely that the variation in composition is a manifestation of subtle geochemical differences present within the standard grains analysed.

From these observations it is proposed that the data distribution range (2σ) seen in the Fe_2O_3% and Cr# values of the Voskhod samples, despite being similar to the 2σ error bar values of the standards (MBD-8 Std, C51Std, MBD-7-G1 and –G2), does in fact represent a true geochemical variation preserved in the chromite. The homogeneity of the Voskhod standard supports that the small variations between and within the Voskhod sample groups are real and may provide information about changes to the conditions during the chromite formation. These variations should not be dismissed as analytical error.

8.2 The geochemical distinction between samples F1964-65, F1996-97 and F1925

Each dataset for samples, F1925, F1964-65 and F1996-97 is geochemically different, as demonstrated by the relative positions of the Mg# and Cr# for each sample, shown in Figure 8.2.1. Samples F1925 and F1964-65 are seen to have a bi-modal distribution that is defined by the Mg#, whereas sample F1996-97 plots in a comparatively well constrained cluster. The variation between the samples is principally controlled by the Mg# that ranges from 0.56 to 0.72, while the Cr# is well constrained between 0.78 and 0.83, of which 90% of the data plot between 0.81 and 0.83. The Cr# range of 0.02 that encapsulates 90% of the data is comparable with the variation seen in a natural standard (refer to Section 8.1.2) and reflects the homogeneity of the trivalent cation compositions of the Voskhod samples. The chemical variation within and between the datasets is scattered, there is no single trend displayed by any one group, or by all the groups when viewed together.

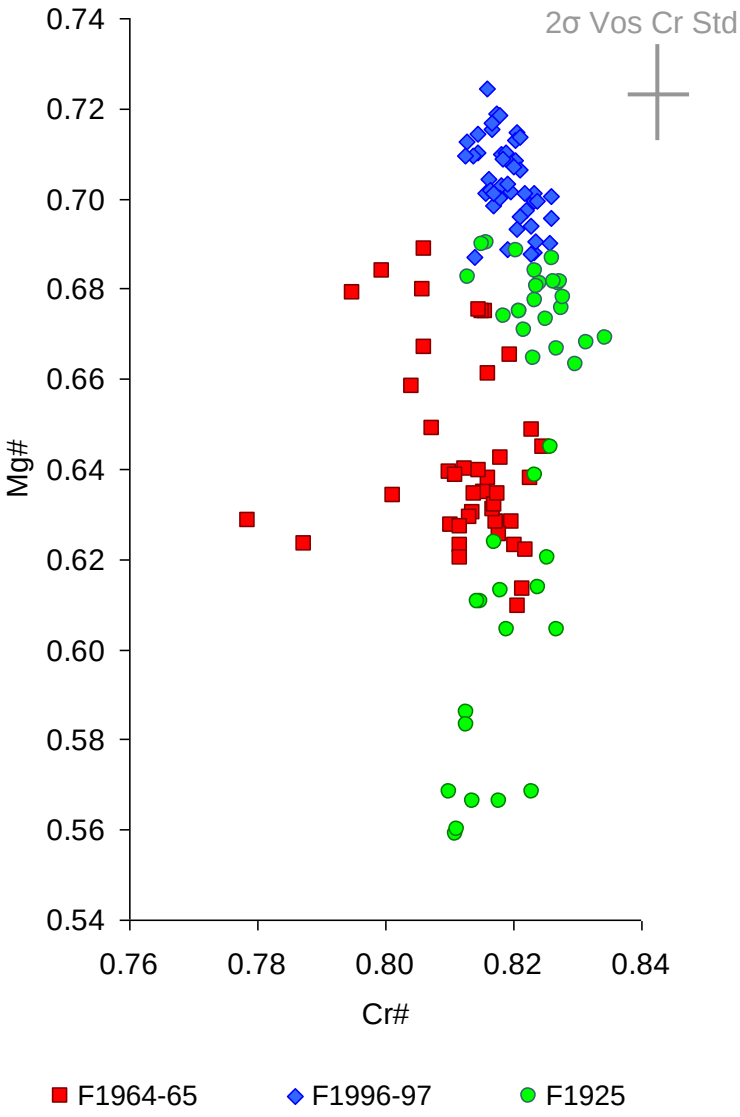

Figure 8.2.1: The major element composition of chromitite samples F1964-65, F1996-97 and F1925 presented on the plot Mg# against Cr#

The data for each sample is displayed using the diagrams; depth vs. major element composition, FeO% vs. Fe_2O_3%, Mg# against Cr# and modal chromite mineral proportion in a section against Mg#.

8.3 Examination of dataset F1964-65

The major element data for the three grains analysed in the 14 sections from F1964-65 is given in Appendix D, Table D3. The average chromite composition for the whole sample is given in Figure 8.3.1. The element order, from most to least abundant, is Cr_2O_3 > MgO > FeO > Al_2O_3 > Fe_2O_3 (the same order is seen in the V05-13 chromite series). $FeO_{(t)}$% is consistently greater than MgO% throughout the data set.

Sample		Al_2O_3	Cr_2O_3	Fe_2O_3	MgO	FeO	$FeO_{(t)}$	MnO
F1964-65	**Average (%)**	**8.25**	**62.77**	**2.32**	**13.13**	**13.01**	**15.10**	**0.30**
	RSDev	4.86	1.05	21.04	3.69	5.46	3.83	5.91

Table 8.3.1: The average major element and manganese compositions for chromite sample F1964-65

The RSD values show that Cr_2O_3% is the most constant major element (RSD, 1.05%) and iron, as both FeO% and Fe_2O_3%, is the most variable with RSD values of 5.46% and 21.04%, respectively.

8.3.1 Variation with depth

The major element chromite composition variation with depth for sample F1964-65 is shown in Figure 8.3.1.

Following the chromite classification devised from the data presented in Chapter 7, the chromites in F1964-65 are $FeO_{(t)}$>MgO chromites. Within a single section the greatest composition range is in Cr_2O_3%, seen in 46, 47 and 49 (the numbers refer to the depth in centimetres from 341 m, indicated by the grey arrows in Figure 8.3.1). The Al_2O_3% contents of the grains analysed in these sections, although more tightly constrained, also show a spread in composition that compliments the Cr_2O_3% variation.

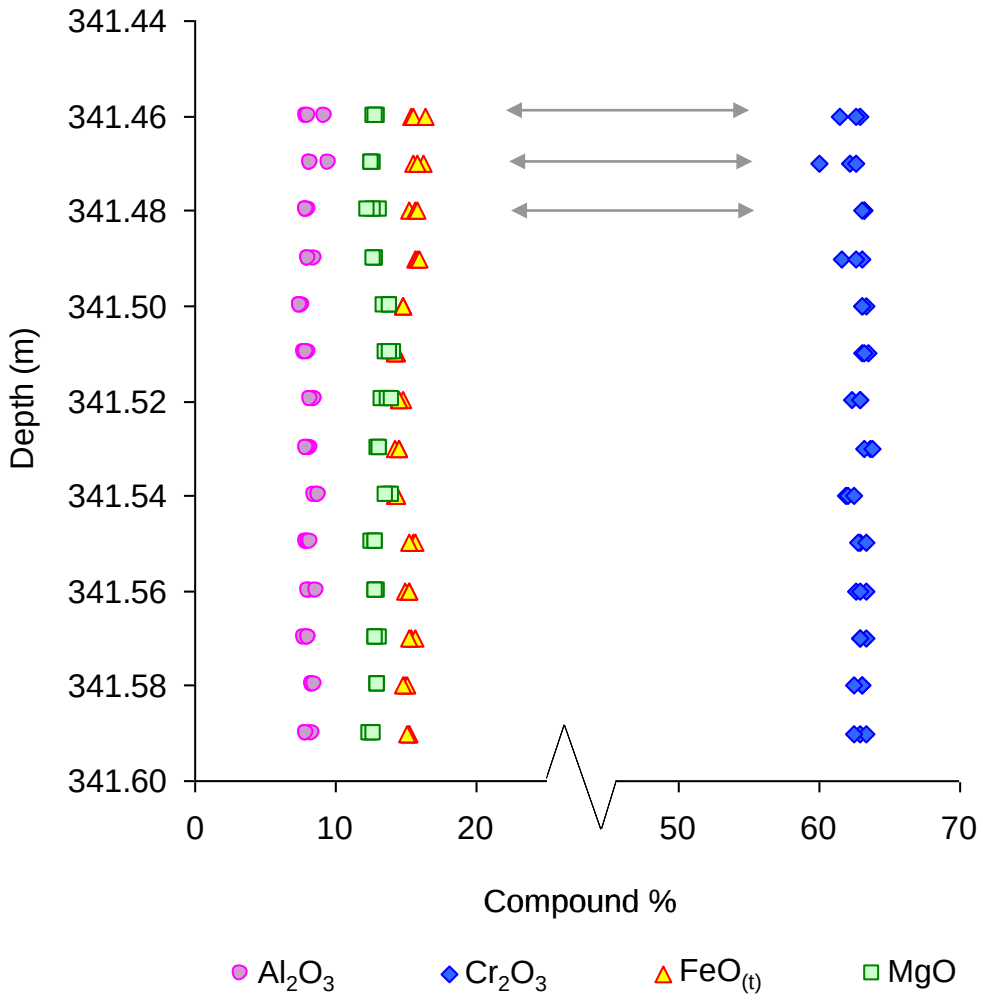

Figure 8.3.1: Variation of the chromite major element chemistry with depth in sample F1964-65.

Grey arrows indicate the sections with the greatest compositional diversity within the sample.

The compositional variation between the sections is characterised by pronounced differences in MgO% and $FeO_{(t)}$%. Sections 46 to 49 and 55 to 59 have higher $FeO_{(t)}$% contents and lower MgO%, whereas in sections 50 to 54 the difference between MgO% and $FeO_{(t)}$% is notably less.

Further investigation of the $FeO_{(t)}$% and MgO% relationship is made by assessing the FeO% and MgO% compositions.

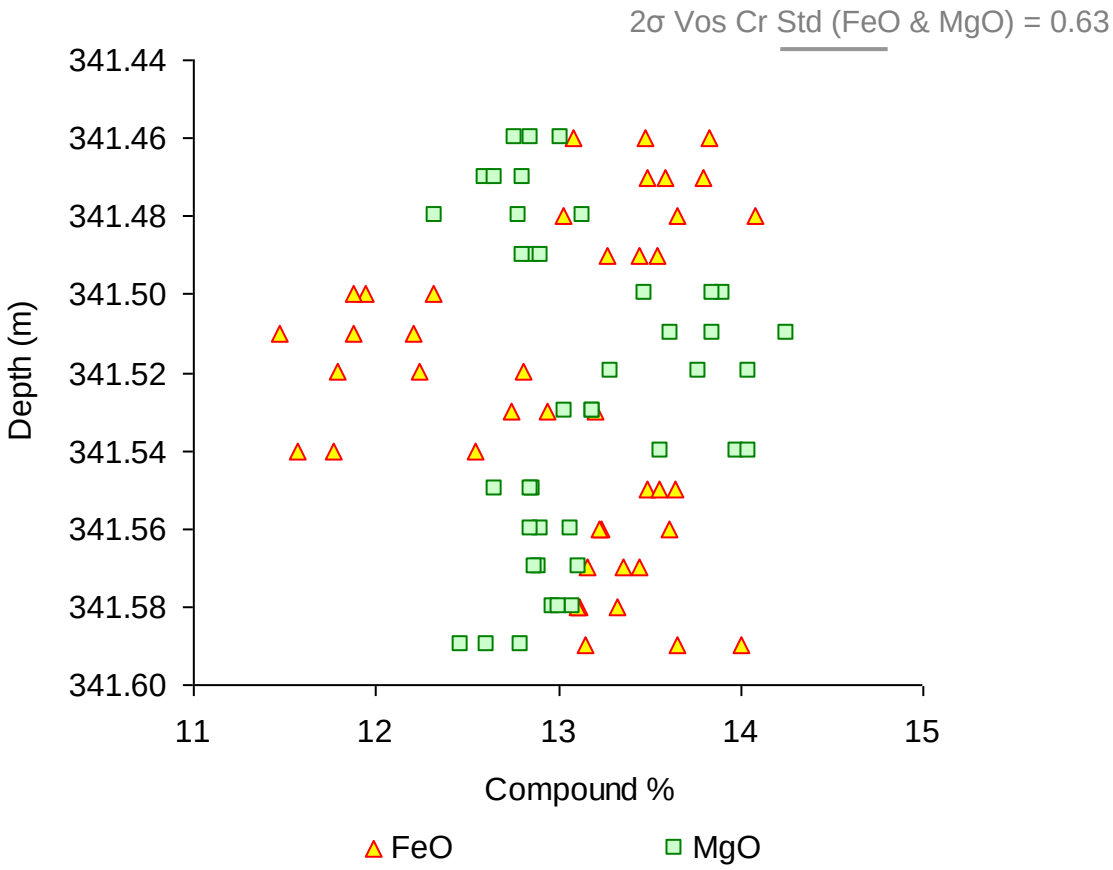

Figure 8.3.2: The variation of FeO and MgO with depth in sample F1964-65

The 2σ error bar value for both FeO and MgO is 0.63.

The variation between FeO% and MgO% with depth (Figure 8.3.2) shows that sections 46-49 and 55-59, where the difference between $FeO_{(t)}$% and MgO% was greatest, have FeO% contents greater than MgO%. In contrast, sections 50-54 have MgO% contents greater than FeO%. The switch in composition is very clear and takes place over a distance of less than 1 cm. Furthermore, it is noted that none of the sections contain grains of mixed compositions; that is to say when FeO% is greater than MgO%, it is so for every grain analysed in a section and *visa versa*.

For sections 50-54, the $FeO_{(t)}$>MgO classification is evidently governed by the Fe_2O_3% content, indicating that these grains either crystallised from or last equilibrated with a melt under conditions that were comparatively more oxidising than those that sections 46-49 and 55-59 were subject to. Given the close spaced proximity of the sections and the fact that no structural discontinuity is visible in the sample, it is suggested that the

geochemical signatures preserved are either remnant of the parent melt from which the grains crystallised or are a localised (centimetre-scale) post-crystallisation subsolidus artefact.

On the basis of the chromite group classification developed in Chapter 7, all 14 of the F1964-65 chromitite sections are $FeO_{(t)}$>MgO chromites. The only way that these chromites can be part of the same group in terms of $FeO_{(t)}$%, yet in different groups when FeO% is examined, is if the partitioning of the iron oxidation state is altered by varying fO_2.

The variation with depth seen in the FeO%-MgO% plot (Figure 8.3.2) is used to form sub-groups within sample F1964-65. Sections 46 to 49 and 55 to 59 form a MgO>FeO group and 50 to 54 form an FeO>MgO group.

8.3.2 FeO% vs. Fe_2O_3%

The chromite grain compositions from the F1964-65 sections are plotted on the FeO% - Fe_2O_3% diagram, Figure 8.3.3.

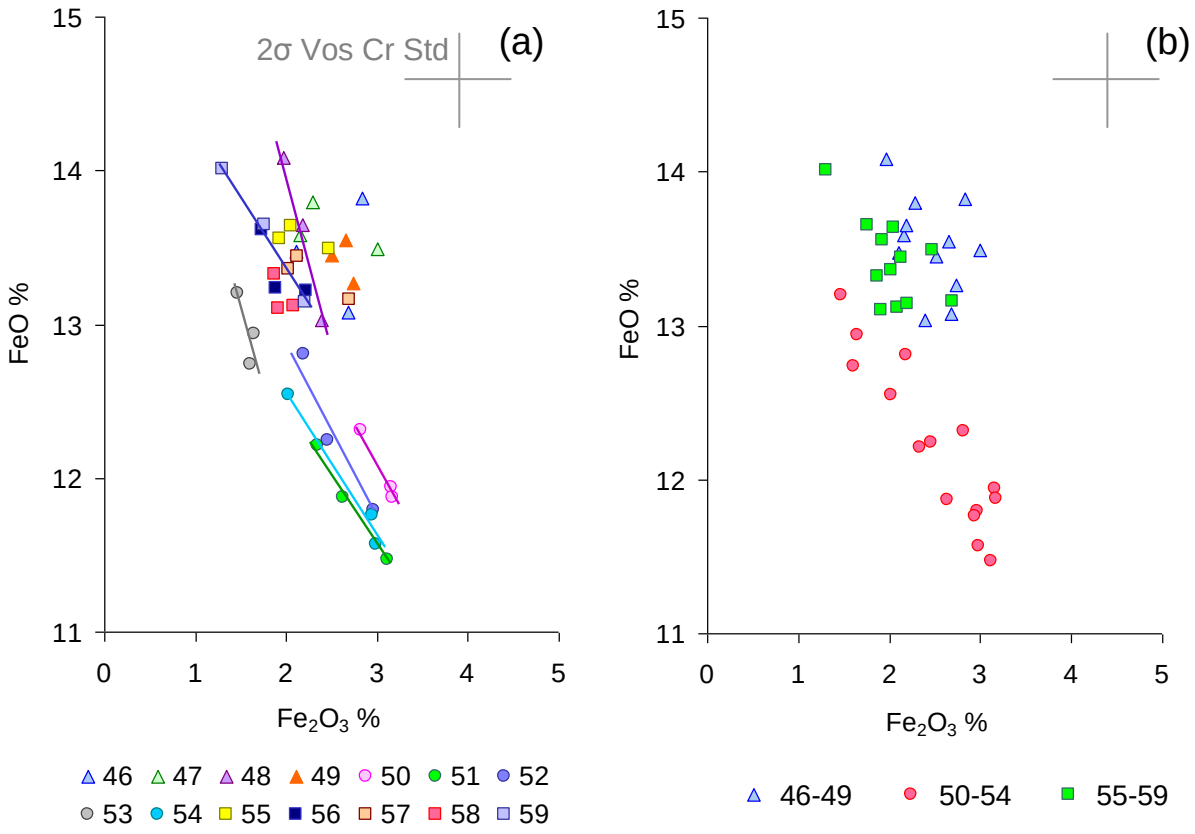

Figure 8.3.3: FeO% against Fe_2O_3% showing the F1964-65 chromite compositions.

(a) The three chromite grains analysed from each F1964-65 section are plotted and colour coded. The numbers given correspond with depth from 341.0 m. Triangles represent sections from the depth interval 46-49, circles 50-54 and squares 55-59. Oblique lines connect the grain compositions for sections 50-54 as well as sections 48 and 59. (b) the three groups are plotted; 46-49 - triangles, 50-54 - circles and 55-59 – squares. Grey cross-lines represent the 2σ range of the Vos_Cr Std single grain composition.

The three chromite groups identified cluster in two regions on the FeO% - Fe_2O_3% diagram, the positions of which are principally controlled by the FeO% content. In contrast, the Fe_2O_3% compositions of each group are similar.

The 50-54 chromites are displaced to lower FeO% values that align to form a negatively correlated trend (where R=0.84) characterised by increasing FeO%, from 11.47% to 13.20%, at the expense of Fe_2O_3% which depreciates from 3.17% to 1.46%. This trend is formed collectively by the group, as well as being apparent from the chromite compositions of each section, indicated by the oblique lines that connect the grains (Figure 8.3.3 a).

The chromites comprising Groups 46-49 and 55-59, which are separated by 5 cm (positioned immediately above and below the down-hole position of Group 50-54), have higher FeO% values, yet similar Fe_2O_3%. This indicates that the oxidising conditions for the genesis of all three intervals of massive chromite were similar and that the compositional control is the result of a greater (Groups 46-49 and 55-59) or lesser (Group 50-54) availability of Fe^{2+} in the melt. Unlike the Group 50-54, the chromites in Groups 46-49 and 55-59 do not have aligning compositions, but plot scattered.

A pronounced overlap in the Fe_2O_3% compositions is seen with Group 46-49 chromites plotting at marginally higher Fe_2O_3% values (1.97%-3.00%) than Group 55-59 chromites (1.30%-2.69%). In contrast, the Fe_2O_3% compositions of Group 50-55 chromites extend the range covered by these groups combined (1.46%-3.17%). It is noted that the Fe_2O_3% composition range of each group is only slightly greater than the 2σ range of Fe_2O_3% calculated for the Voskhod standard (annotated by the grey cross-lines Figure 8.3.3 b) which is 1.08%.

A comparison of the F1964-65 chromites is made with the V05-13 dataset (Figure 8.3.4). It is seen that Groups 46-49 and 55-59 plot in the same region as the V05-13 FeO>MgO chromites (black and dark red triangles), while Group 50-54 plot in the same space as the V05-13 $FeO_{(t)}$>MgO chromites (open red triangles). The negatively correlated V05-13 MgO>$FeO_{(t)}$ chromites (yellow filled triangles and solid black line) are aligned near parallel to the negative correlation of the Group 50-55 chromites from sample F1964-65 (red circles and grey broken line). From this it might be suggested that the genesis mechanisms resulting in the formation of the V05-13 MgO>$FeO_{(t)}$ chromites were similar to those that formed the Group 50-55 chromites, although the melt chemistry composition, specifically the iron availability, would have been different.

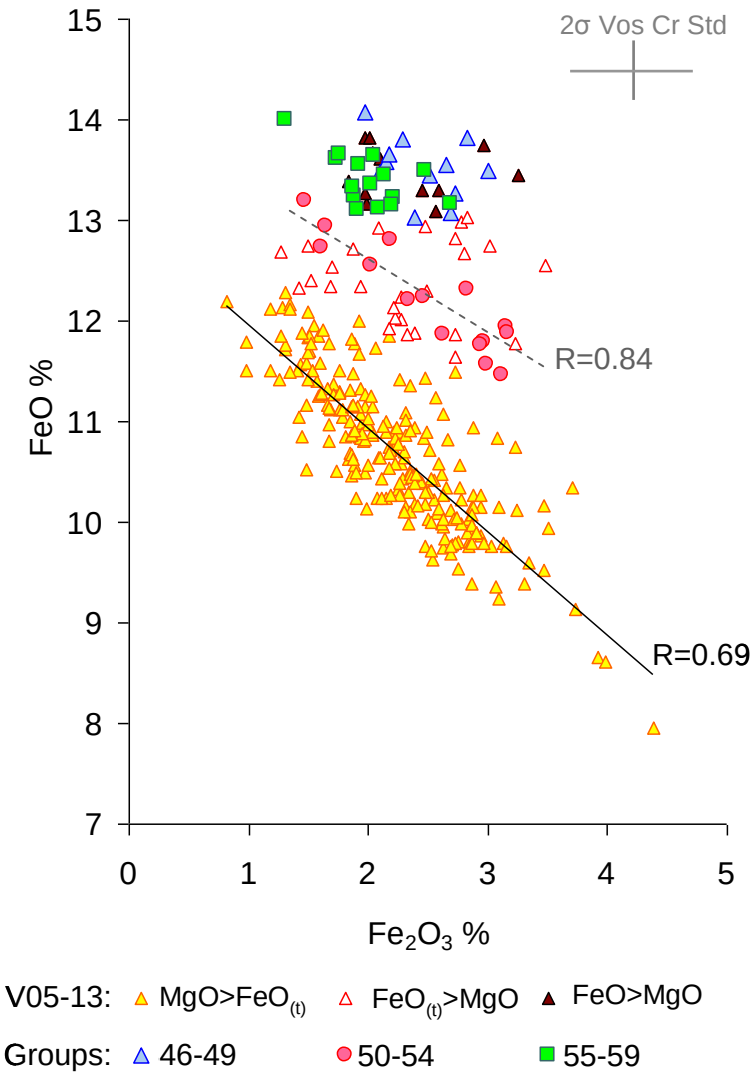

Figure 8.3.4: FeO% against Fe_2O_3% a comparison of the V05-13 massive chromites with the three chromite groups identified in sample F1964-65.

The solid black line is the trendline of the V05-13 $MgO>FeO_{(t)}$ chromites, yellow triangles. The grey broken line is the trendline for the F1964-65, Group 50-55 chromites. The R values are given respectively beside each trendline.

Two questions are apparent:

What controls the changes in the total iron content?

What controls the inter-group fO_2 variation which is most pronounced in Group 50-55?

8.3.3 Chromite mineral proportions vs. chromite Mg#

The F1964-65 sections are composed of massive chromite, however, chromite is not the only mineral phase as small quantities of serpentinised olivine co-exist interstitially. Olivine coevally crystallising from a melt with chromite, will incorporate Mg reducing the availability of Mg for chromite. Thus, a greater the proportion of olivine co-existing with chromite will the lower the Mg# of chromite (see sample F1925 in Sections 8.4 and 8.5 of this Chapter).

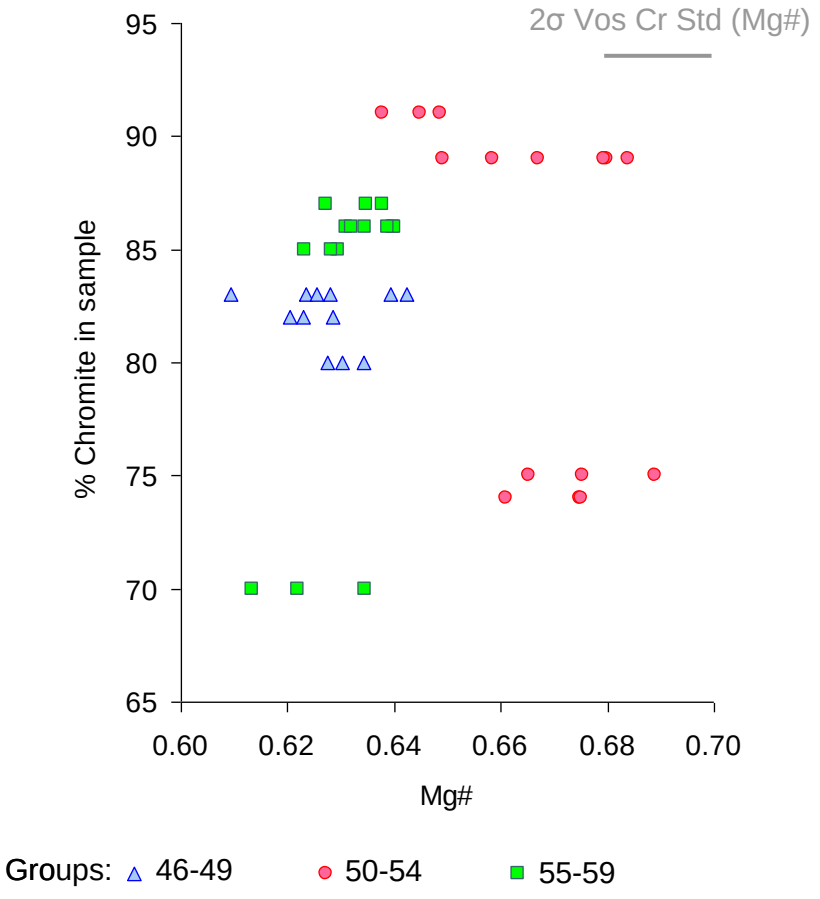

Figure 8.3.5: The chromite content in a section against the chromite Mg# values for each section of sample F1964-65.

The relationship between the percentage of chromite in a section and the Mg# does not strictly conform with the hypothesis, as is evident from Figure 8.3.5. The general trend is for the chromite content to increase as the Mg# of the chromite increases. However, there are anomalous points, and no single trend satisfies the data.

As these results demonstrate, it is not possible to explain the MgO%-FeO% contents of the chromites from the relative proportions of chromite and olivine that (presently) comprise the sections. That is to say, although contemporaneous crystallisation of olivine and chromite from a melt could account for the variation in Mg# seen, a subsequent, post crystallisation process resulting in the separation or the redistribution of the two mineral phases under subsolidus conditions, is required to explain the present mineral proportions seen. If such a process took place then it would explain how the chromite has inherited a composition characteristic of the co-crystallisation of chromite and olivine from a melt, while the mineral proportions seen are indicative of chromite crystallisation alone.

8.3.4 Mg# vs. Cr#

F1964-65 is comprised of three distinguishable chromite groups that differ in terms of trivalent and divalent cation ratios. The Mg#-Cr# diagram shows the relationship between the divalent (Mg#) and trivalent (Cr#) cation ratios for each sample and each chromite group (Figure 8.3.6). The compositional changes are persistent over incremental, centimetre scale, depth intervals that may be interpreted as chromite layers present within the podiform ore body. Changes to the processes responsible for chromite crystallisation affect the chromite chemistry and the chromite layers record these changes.

The most obvious variation is that with depth (i.e. the inter-group variation) and the changes in Mg# which are more prominent than those of Cr#. Such changes may result from sub-solidus re-equilibration between olivine and chromite. Alternatively the changes could be caused by fluctuations in the relative proportions of chromite and olivine crystallising contemporaneously from a melt. The latter introduces a complication when applied to this scenario where massive chromite is being examined as a post-crystallisation process that separates the two mineral phases, is required to explain the formation of massive chromite e.g. densification of the chromite (see Chapter 3, Section 3.6.1). Such a process would need to take place under tectonically stable conditions, such that the fine-scale layering and structural continuity identified could be preserved.

In the literature, regarding work on stratiform intrusions, there is comparatively little information presented on the variation in total iron, which is the main inter-group

variation in this core-section. However, Hulbert and Von Gruenewaldt (1985) noted that variation in total iron (as $Cr/Fe^{2+}+Fe^{3+}$) is linked to a variation in the $\mathit{f}O_2$ (see also Hill and Roeder, 1974). This is comparatively difficult to achieve within the constraints of a stratiform magma chamber in the crust, but is more easily achieved in a SSZ ophiolitic setting where the water content is high and the confining pressure changes as magma ascends through the mantle.

The Mg#-Cr# diagrams presented illustrate the geochemical variation in chromite of sample F1964-65 (Figure 8.3.6). From the evidence that fine, centimetre scale compositional changes are present within the F1964-65 chromitite sample, parallels can be drawn with the fine scale layering documented in stratiform chromitites e.g. the Bushveld Complex, S.A (e.g. *Jackson, 1969; Cameron, 1975,1977; Hamlyn & Keays, 1979; Naldrett et al., 2009*) these aide the interpretation of the genesis history of the chromitite.

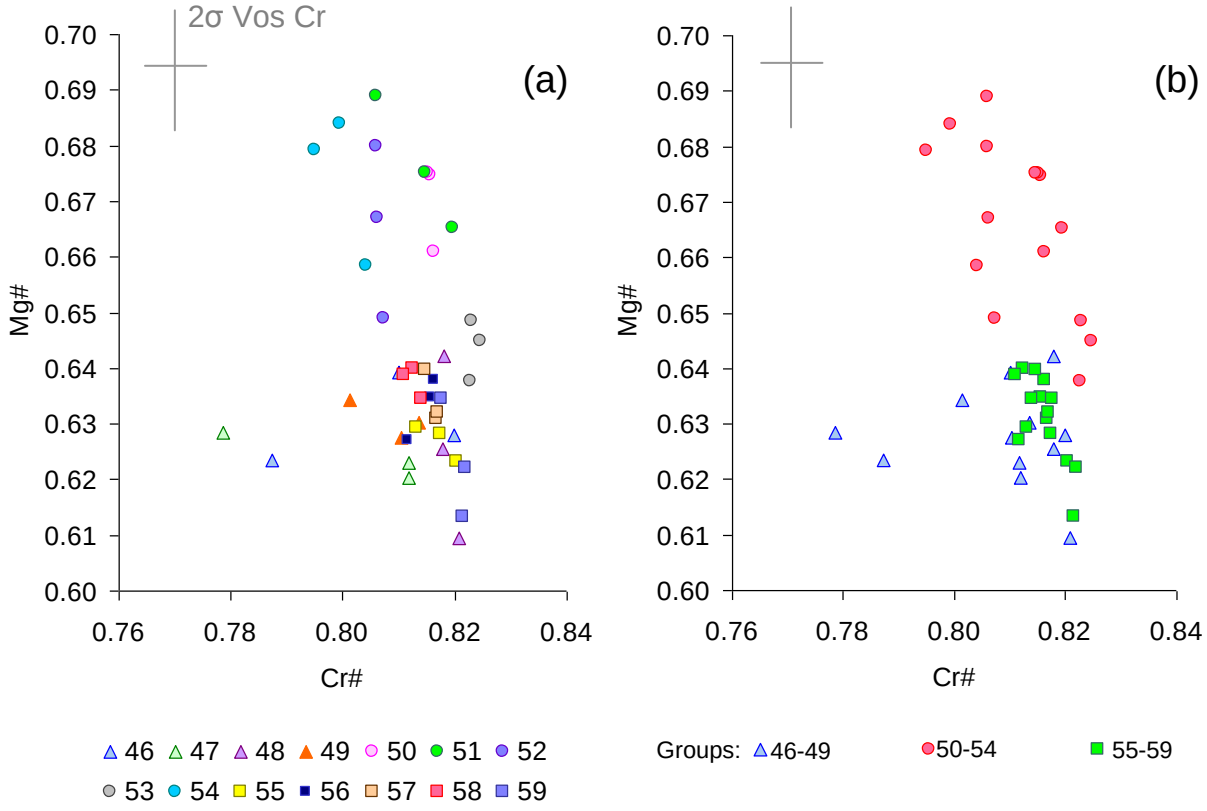

Figure 8.3.6: Mg# against Cr#

(a) the individual chromite grain analyses obtained from each section are presented on the Mg#-Cr# diagram. (b) The three groups identified in sample F1964-65 are shown.

The Mg#-Cr# diagram supports the interpretation of there being three groups (Figure 8.3.6b). The Cr# data spread of Group 46-49 is greater than that of Group 55-59, yet both have similar Cr# and Mg#. Group 50-54, on the other hand, has higher Mg# that spreads over a greater range, yet a Cr# range that is the same as that covered by Groups 46-49 and 55-59 combined. Distinction between the groups is based principally on the change in Mg#, no Mg#-Cr# varying trends are visible within any of the groups or formed by all the groups when viewed together.

In terms of the individual chromite grain compositions (Figure 8.3.6a) no systematic variation in composition with depth down hole is seen. It may be suggested that the Group 50-54 chromites plot to form near vertical lines indicative of changes to Mg# at constant Cr#, this would seem reasonable in light of the alignment of this group on the FeO%-Fe_2O_3% diagram (Figure 8.3.3). The individual grain compositions from each section plot scattered and it is only when viewed as groups determined by depth and FeO%-MgO% composition that clusters are apparent.

When compared with the V05-13 dataset the Groups 46-49 and 55-59 plot in the same space as the FeO>MgO chromites (black-red triangles, Figure 8.3.7), Group 50-55 chromites plot in the vicinity of the $FeO_{(t)}$>MgO chromites (red-white triangles, Figure 8.3.7). Groups 50-54 and 55-59 form weak negative trends. In Group 55-59 this trend extends over a Cr# range of 0.01, given that the group is comprised of 12 analyses the degree of confidence is not considered sufficient to validate the trend. Group 50-54 extends over a greater Cr# range of 0.03 that, as similarly observed in the FeO%-Fe_2O_3% diagram, aligns parallel with the V05-13 MgO>$FeO_{(t)}$ chromites. This negative trend (R=0.40) is analogous with the Trend A identified by Naldrett et al. (2009).

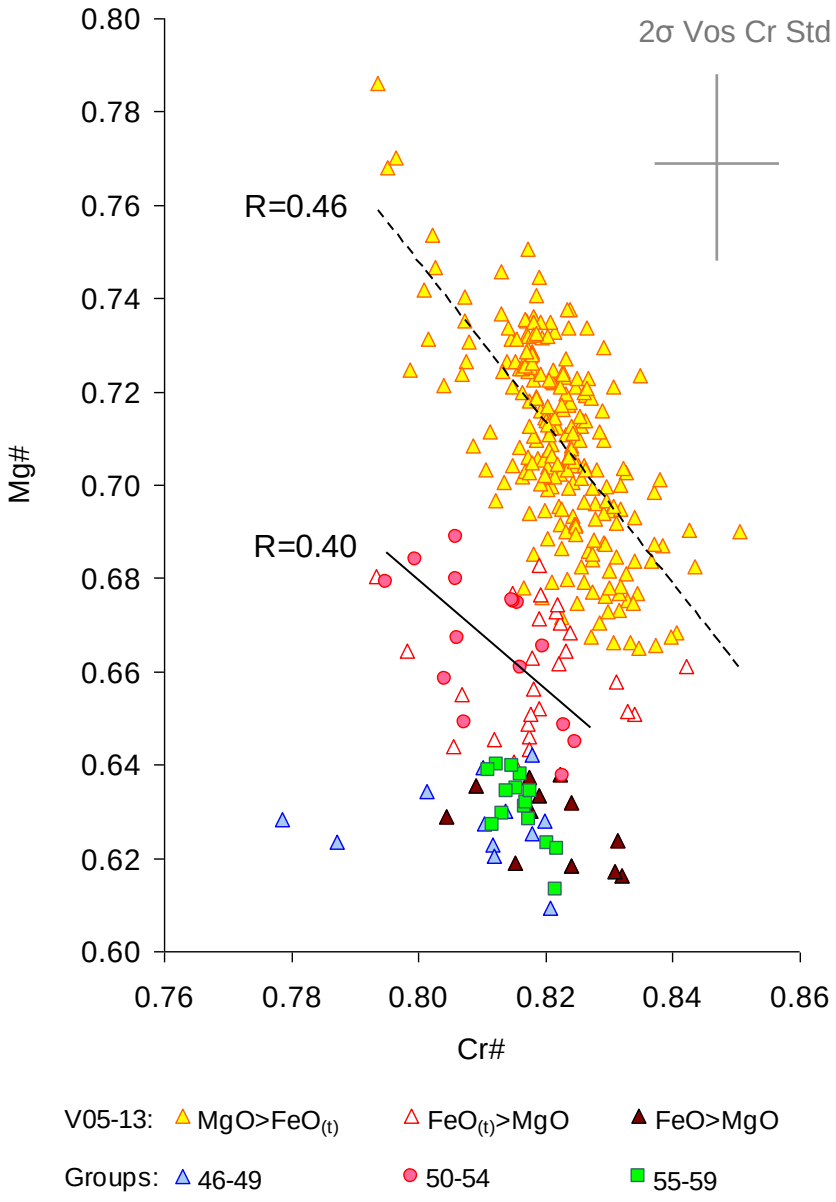

Figure 8.3.7: Mg# against Cr# a comparison of the V05-13 massive chromites with dataset F1964-65, Groups 46-49, 50-54 and 55-59

The trendline for the V05-13 MgO>$FeO_{(t)}$ chromites (yellow triangles) is shown as a broken black line.

The spatial association of the groups is the same as that observed in the FeO%-Fe_2O_3% diagram and reiterates the minimal effect had by the Al_2O_3 and Cr_2O_3 contents on the characterisation of the groups identified. The constrained Cr# range (0.78-0.83), with 75% of the data plotting between Cr# 0.80 and 0.82, is only slightly greater than that of the Voskhod standard and is comparable with, and in some instances more uniform than, the 2σ error bars of the chromite standards analysed (i.e. MBD-7-G1 and –G2) .

This further exemplifies the homogeneous nature of the Al_2O_3 and Cr_2O_3 compositions in the F1964-65 chromites, across all groups.

8.4 Examination of dataset F1996-97

Sample F1996-97 is located at 359.01 m, 17.5 m down hole from sample F1964-65. In comparison with sample F1964-65, the average composition of these chromites is higher in Cr_2O_3, Fe_2O_3 and MgO, and lower in Al_2O_3, FeO and MnO (Table 8.4.1). Here the MgO content is greater than FeO(t). In relation to the chromite groups presented in Chapter 7, the F1996-97 chromites are classified as MgO>$FeO_{(t)}$ chromite (Figure 8.4.1).

Sample		Al_2O_3	Cr_2O_3	Fe_2O_3	MgO	FeO	$FeO_{(t)}$	MnO
F1996-97	**Average (%)**	**7.66**	**63.59**	**2.75**	**14.52**	**10.88**	**13.35**	**0.24**
	RSDev	2.18	0.52	10.01	1.36	3.19	2.27	6.19
F1964-65	**Average (%)**	**8.25**	**62.77**	**2.32**	**13.13**	**13.01**	**15.10**	**0.30**
	RSDev	4.86	1.05	21.04	3.69	5.46	3.83	5.91

Table 8.4.1 Comparison of the average compositions for the chromite datasets F19964-65 and F1996-97.

The ordered element abundance of the F1996-97 chromite is Cr_2O_3> MgO>> FeO> Al_2O_3> Fe_2O_3. This is the same order as the majority of the V05-13 chromites (the MgO>$FeO_{(t)}$ chromites) and the F1964-65, Group 50-59 chromites. As seen in the other datasets, Cr_2O_3 is the most constant major element in sample F1996-97 having an RSD of 0.52% and Fe_2O_3 is the most variable having a RSD of 10.01%.

8.4.1 Variation with depth

The major element chemistry variation with depth in core-section F1996-97 is shown in Figure 8.4.1.

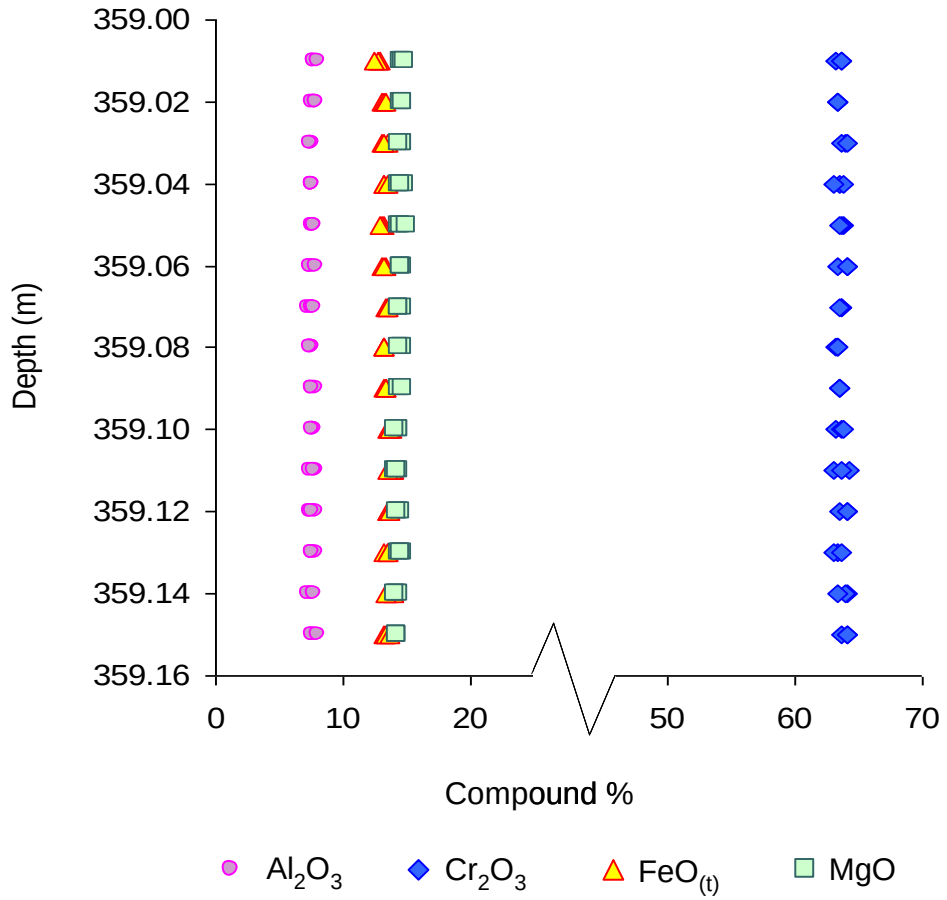

Figure 8.4.1: Variation of the chromite major element chemistry with depth down hole in sample F1996-97.

The composition of the 15 sections that comprise sample F1996-97 is remarkably homogenous, both the variation within a sample and between samples. MgO% is consistently greater than $FeO_{(t)}$%, although it is seen that towards the base of the intersection, from 359.10 to 359.12 (inclusive), the difference between these compositions is less (the FeO% and MgO% data points appear to merge).

Sample		Al_2O_3	Cr_2O_3	Fe_2O_3	MgO	FeO	$FeO_{(t)}$	MnO
F1996-97	**Average (%)**	**7.66**	**63.59**	**2.75**	**14.52**	**10.88**	**13.35**	**0.24**
	RSDev	2.18	0.52	10.01	1.36	3.19	2.27	6.19
Vos-Std	**Average (%)**	**7.73**	**63.97**	**2.51**	**14.76**	**10.53**	**12.79**	**0.24**
	RSDev	1.51	0.27	10.73	1.06	1.50	0.74	5.24

Table 8.4.2: Comparison of the F1996-97 dataset composition with the Voskhod standard chromite.

To evaluate the homogeneity of the chromite compositions in sample F1996-97 the relative standard deviation values for the average composition of the dataset are compared with those of the Voskhod standard chromite grain (Table 8.4.2). A striking similarity between the values is seen, in particular the value for Fe_2O_3% which is less than that obtained from the Voskhod standard. The comparably low standard deviations of the two datasets imply that the chromite compositions of all the sections that comprise sample F1996-97 is nearly as well constrained as the composition obtained from a single grain. Furthermore, it is reiterated that the Voskhod standard analyses were considerably more uniform than those obtained from any other standard analysed (see Chapter 7, Section 7.1.1), this further confirms the exceptional homogeneity of sample F1996-97.

The subtle, yet evident shift in MgO% and $FeO_{(t)}$% compositions (Figure 8.4.1) is examined further in the plot depth against MgO% and FeO% (Figure 8.4.2).

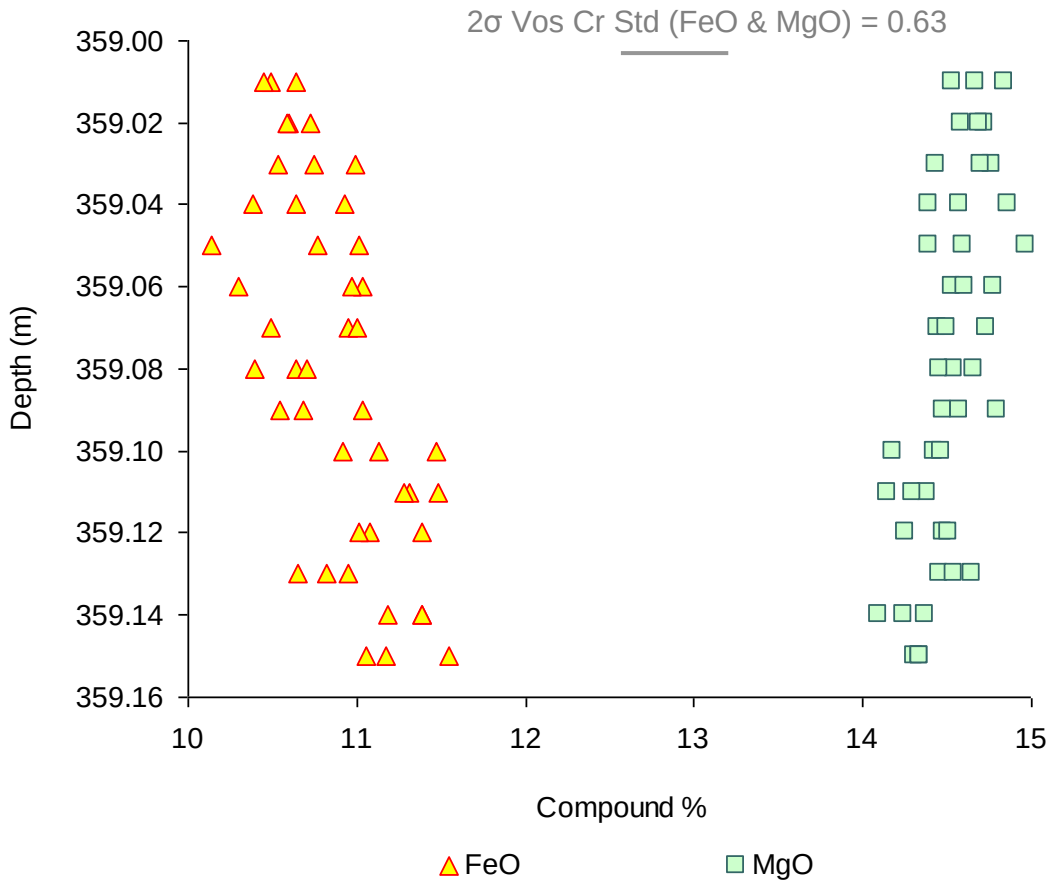

Figure 8.4.2: Variation of FeO and MgO contents in F1996-97

The 2σ error bar value for both FeO and MgO is 0.63.

The comparison of the calculated FeO% composition with MgO% demonstrates that from the depth interval 359.01 to 359.08 the composition is most uniform, after which there is greater variability (depth interval 359.09 to 359.15) (Figure 8.4.2). However, the increased variation fluctuates within a very small compositional range of 1% for both MgO% (14.1-14.8%) and FeO% (10.5-11.5%).

The homogeneous composition of the F1996-97 chromites propagates through into the plots FeO%-Fe_2O_3% (Figure 8.4.3 and Figure 8.4.4) and Mg#-Cr# (Figure 8.4.5 and Figure 8.4.6) that have been used previously (Chapter 7 and this chapter, Section 8.2) to identify differences in chromite geochemistry.

8.4.2 FeO%- Fe_2O_3%

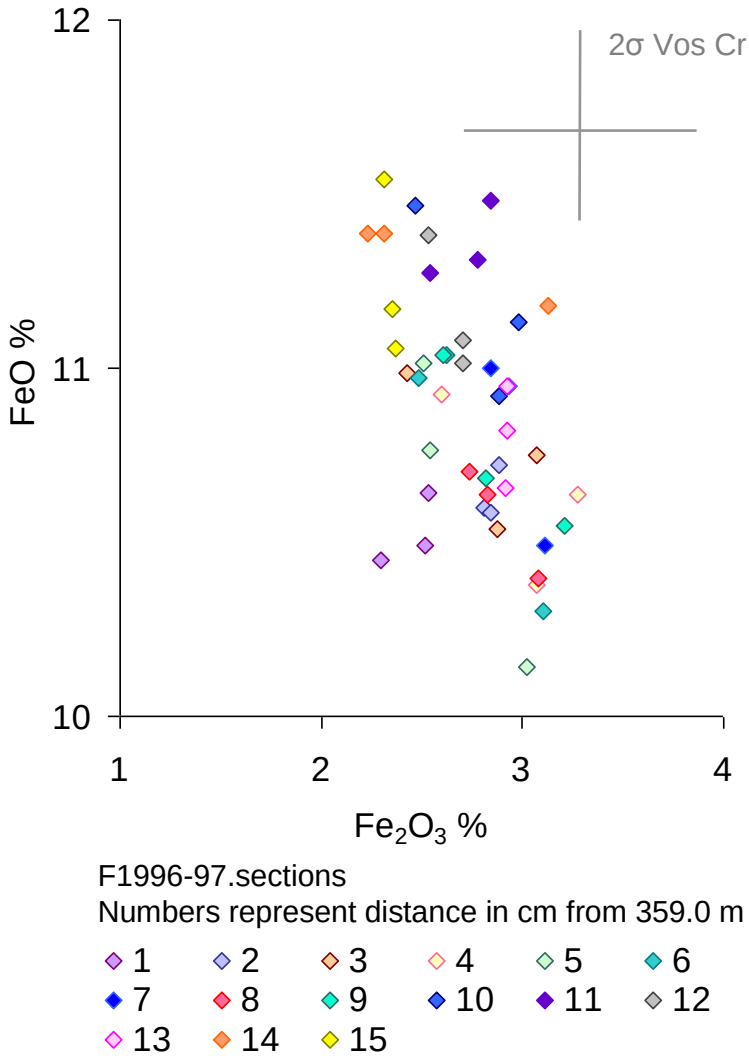

Figure 8.4.3: FeO% against Fe_2O_3% showing the composition of sample F1996-97.

The FeO% and Fe_2O_3% compositions of the chromite grains from each section of sample F1996-97 studied are plotted in Figure 8.4.3. Whereas previously trends and/or groups have been identified using the FeO%-Fe_2O_3% plot, in sample F1996-97 the data forms one group that has an FeO% range 10.14-11.54% and Fe_2O_3% range 2.23-3.28%. The analyses scatter randomly, no outliers are noted and no systematic trends are seen within the individual sections.

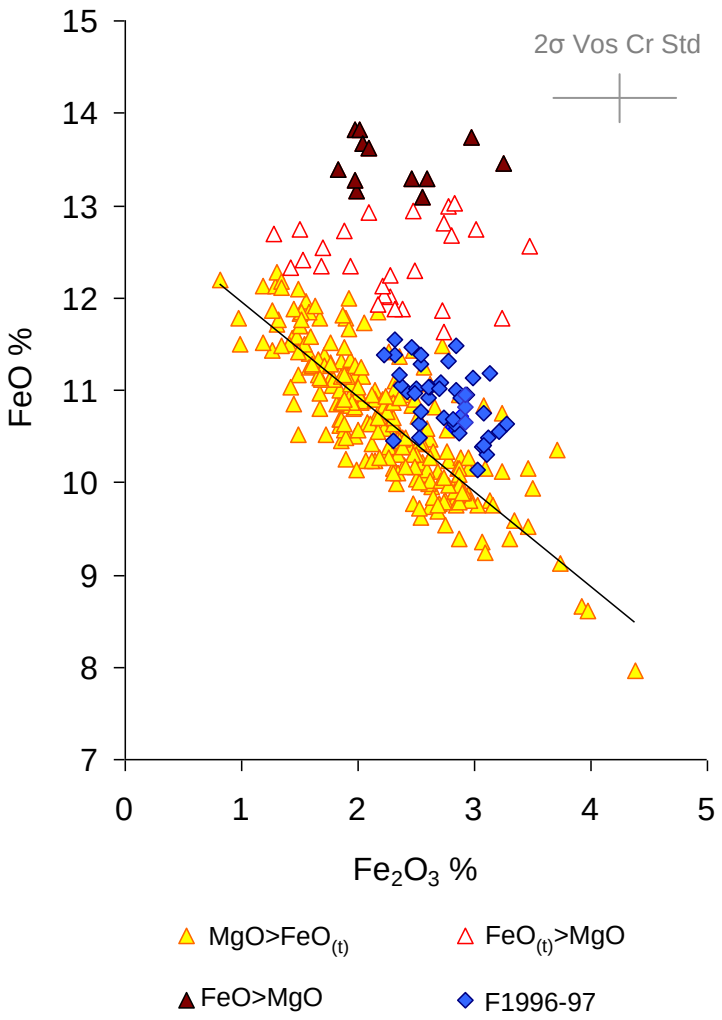

Figure 8.4.4: FeO% against Fe_2O_3% diagram a comparison of the V05-13 massive chromites with the composition of sample F1996-97.

When compared with the V05-13 MgO>$FeO_{(t)}$ chromites (yellow triangles, Figure 8.4.4), the F1996-97 chromites plot at intermediate FeO% and have slightly higher than average Fe_2O_3% compositions for the same FeO compositions, being displaced to the right of the main V05-13 MgO>$FeO_{(t)}$ chromite group.

8.4.3 Mg#-Cr#

When the F1996-97 data is plotted on the Mg#-Cr# diagram the uniform composition of the sample is once again confirmed (Figure 8.4.5). The data plots scattered within a confined Mg# range of 0.687-0.724 and a Cr# range of 0.81-0.826, the greatest variation being in the divalent cation compositions.

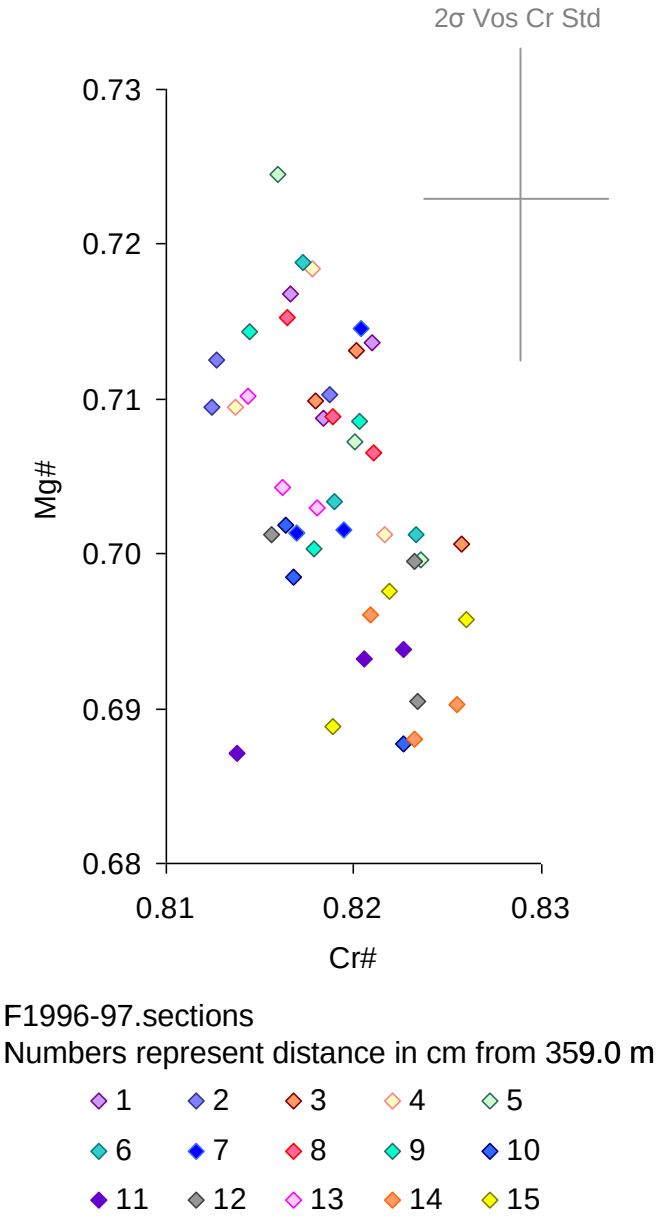

Figure 8.4.5: Mg# against Cr# diagram for sample F1996-97

No groups are established between samples and no relationships or patterns are evident within individual sections. When the entire dataset is viewed collectively, there may be some inclination to propose a weak negative trend (R=0.23, Figure 8.4.6). However, the Cr# range (0.013) is very small and is comparable with the Cr# range recorded from the Voskhod standard.

When plotted with the V05-13 chromite dataset on the Mg#-Cr# diagram (Figure 8.4.6), the F1996-97 chromites (blue diamonds) lie close to the centre of the MgO>$FeO_{(t)}$ chromite field, the group is displaced to slightly lower Cr# values than those that typify the V05-13 MgO>$FeO_{(t)}$ chromites (yellow triangles, Figure 8.4.6). The negatively correlated trendline shown for the F1996-97 chromites (solid black line, Figure 8.4.6), although weak (R-squared = 0.23), aligns almost parallel with the trendline of the V05-13, MgO>$FeO_{(t)}$ chromites (broken black line, Figure 8.4.6).

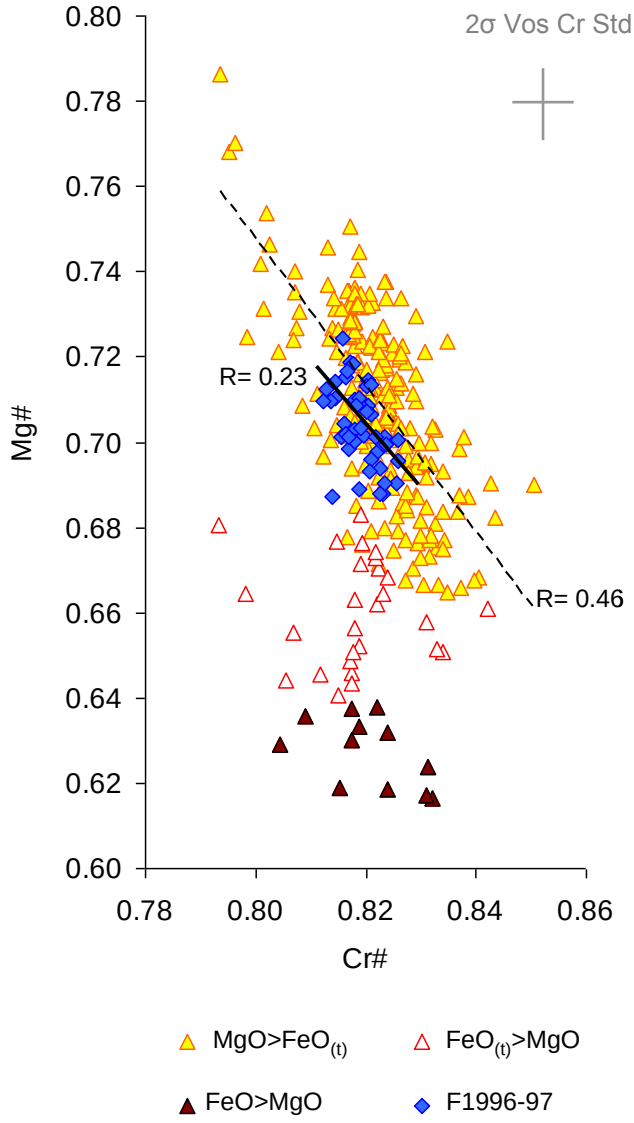

Figure 8.4.6: Mg# against Cr# diagram a comparison of the V05-13 massive chromites with the composition of sample F1996-97.

8.5 Massive chromitite grading into a silicate-rich horizon

The compositional variation of massive chromite has been examined on a centimetre scale from the study of samples F1964-65 and F1996-97. Sample F1925 is located at 296.05 m down drill core V05-24, stratigraphically higher (in terms of the present day position) than samples F1964-65 and F1996-97.

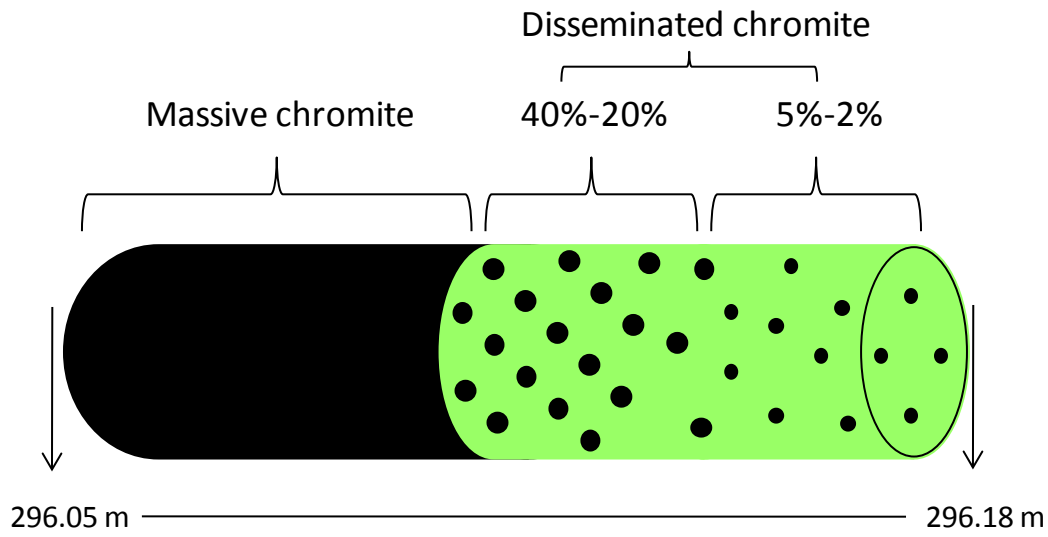

Figure 8.5.1: Schematic of sample F1925 illustrating the change in style of chromite mineralisation across the drill core intersection.

The sample was collected from the base of a 25 cm thick lens of massive chromite. It is a transitional chromite ore sample comprised, at the top, of massive chromite that grades into disseminated chromite becoming progressively chromite-poor (from 40% - 2% chromite content) over a 6 cm interval, (Figure 8.5.1).

Sample: F1925		
Depth from 296 m in cm	**Chromite %**	**Olivine %**
5	80	20
6	88	12
7	87	13
8	93	7
9	95	5
10	95	5
11	90	10
12	82	18
13	40	60
14	30	70
15	24	76
16	5	95
17	2	98
18	3	97

Table 8.5.1: Chromite and olivine mineral proportions and corresponding down hole depth intervals of sample F1925.

Table 8.5.1 provides the chromite-olivine proportions with depth for sample F1925. The 14 sections, spaced 1 cm apart, were analysed to assess the chromite composition variation, traversing from massive chromite to disseminated chromite. Extensive serpentinisation of the olivine meant that it was not possible to obtain olivine analyses.

8.6 Examination of dataset F1925

The 14 sections from sample F1925 can be divided into two groups based on the modal proportions of chromite and olivine. Group 1 consists of massive chromite (296.05 m to 296.12 m) and Group 2, disseminated chromite, where chromite constitutes less than 40% of the section (296.13 m to 296.18 m). The change in the chromite geochemistry affects both the divalent and trivalent cation species and corresponds with the changing modal proportions of chromite and olivine. This implies that the composition variation is not simply a result of re-equilibration between olivine and chromite that would affect only the divalent species. It is inferred that the process responsible for the crystallisation of a

silicate phase affects the melt composition from which chromite is contemporaneously crystallising.

The study of sample F1925 aims to identify the geochemical changes in chromite that take place as a result of increasing the silicate modal proportion. Three genesis scenarios are to be considered when examining co-existing chromite and silicate phases:

1) The olivine present in the disseminated chromite intervals originates from residual mantle, through which a chromite bearing melt has percolated and crystallised chromite interstitially, at some localities more extensively forming massive chromite.

2) The olivine may be a contemporaneous mineral phase that has crystallised from the melt with chromite when conditions have permitted two mineral phases to crystallise.

3) The infiltrating melt interacts with and absorbs the mantle olivine through which it is percolating, this could cause the melt to enter the chromite stability field, resulting in the crystallisation of chromite (with or without olivine).

Examination of the chromite composition variation with increasing silicate proportion will assist with explaining; i) changes in conditions that took place during chromite crystallisation; ii) the process required for the crystallisation of a contemporaneous silicate phase and iii) what controls the chromite and olivine mineral proportions.

Sample		Al_2O_3	Cr_2O_3	Fe_2O_3	MgO	FeO	$FeO_{(t)}$	MnO
F1925 ALL	**Average (%)**	**7.26**	**63.02**	**3.02**	**13.08**	**12.93**	**15.65**	**0.28**
	RSDev	3.05	1.39	17.20	7.78	11.53	11.84	11.89
F1996-97	**Average (%)**	**7.66**	**63.59**	**2.75**	**14.52**	**10.88**	**13.35**	**0.24**
	RSDev	2.18	0.52	10.01	1.36	3.19	2.27	6.19
F1964-65	**Average (%)**	**8.25**	**62.77**	**2.32**	**13.13**	**13.01**	**15.10**	**0.30**
	RSDev	4.86	1.05	21.04	3.69	5.46	3.83	5.91

Table 8.6.1: The average composition of the F1925 chromite compared with samples F1964-65 and F1996-97.

Comparing the average chromite compositions for samples F1964-65 and F1996-97 with the average composition of sample F1925 shows that it is geochemically most similar to F1964-65 in terms of the divalent cation proportions (Fe^{2+}, Mg and Mn), yet is distinct from both in terms of the trivalent cations, having the lowest Al_2O_3%, intermediate Cr_2O_3% and highest Fe_2O_3% values (Figure 8.6.1).

However, the F1925 average chromite composition combines both the massive chromite and disseminated chromite compositions, this obscures the average. When the composition of the massive chromite portion alone, is compared with the other samples, it is evident that it is compositionally intermediate between samples F1964-65 and F1996-97 (Table 8.6.2).

Sample		Al_2O_3	Cr_2O_3	Fe_2O_3	MgO	FeO	$FeO_{(t)}$	MnO
F1925 Massive Chromite	**Average (%)**	**7.38**	**63.64**	**2.73**	**13.88**	**11.77**	**14.23**	**0.26**
	RSDev	2.38	0.61	13.08	1.39	2.30	1.48	7.82
F1925 Disseminated Chromite	**Average (%)**	**7.11**	**62.21**	**3.42**	**12.03**	**14.47**	**17.55**	**0.30**
	RSDev	2.49	1.04	12.64	5.12	6.38	7.03	5.12
F1996-97	**Average (%)**	**7.66**	**63.59**	**2.75**	**14.52**	**10.88**	**13.35**	**0.24**
	RSDev	2.18	0.52	10.01	1.36	3.19	2.27	6.19
F1964-65	**Average (%)**	**8.25**	**62.77**	**2.32**	**13.13**	**13.01**	**15.10**	**0.30**
	RSDev	4.86	1.05	21.04	3.69	5.46	3.83	5.91

Table 8.6.2: The average composition of the F1925 massive chromite and disseminated chromite portions compared with samples F1964-65 and F1996-97.

In contrast, the chromite in the disseminated portion of F1925 has a composition that, compared with the massive chromite portion of the sample, is higher in FeO%, MnO% and Fe_2O_3% and lower in Cr_2O_3% and Al_2O_3% (Table 8.6.2).

When compared with the chromite groups determined in Chapter 7, the F1925 massive chromite portion is categorised as $FeO_{(t)}$>MgO chromite. The Cr_2O_3% content is the most constant major element having an RSD of 0.61% and Fe_2O_3% is the most variable, having a RSD of 13.08%. This observation is consistent with that seen in the other massive chromite samples V05-13, F1964-65 and F1996-97.

8.6.1 Variation with depth

The major element chemistry for F1925 chromite is shown with depth and corresponding chromite content in Figure 8.6.1.

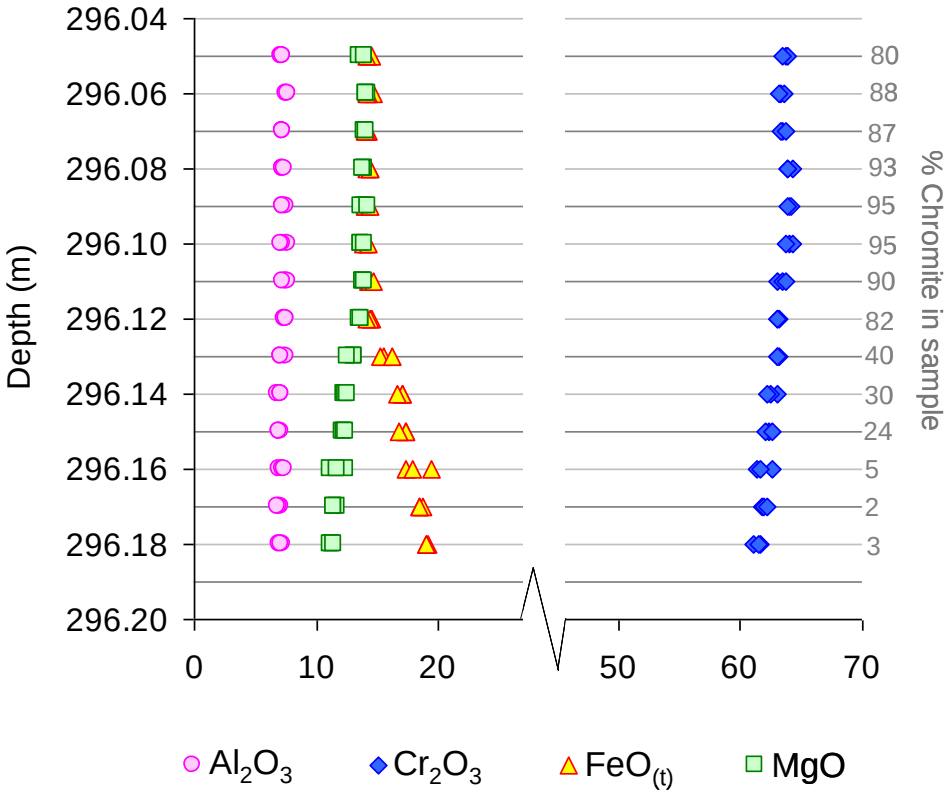

Figure 8.6.1: Variation of the chromite major element chemistry with depth down hole in sample F1925.

Throughout the massive chromite portion, from 296.05 m to 296.11 m (inclusive), the MgO% and $FeO_{(t)}$ % values are similar. At 296.12 m $FeO_{(t)}$ % starts to increase and continues to do so systematically with depth to 296.18 m. This relationship is examined further looking the MgO% and FeO% contents (Figure 8.6.2).

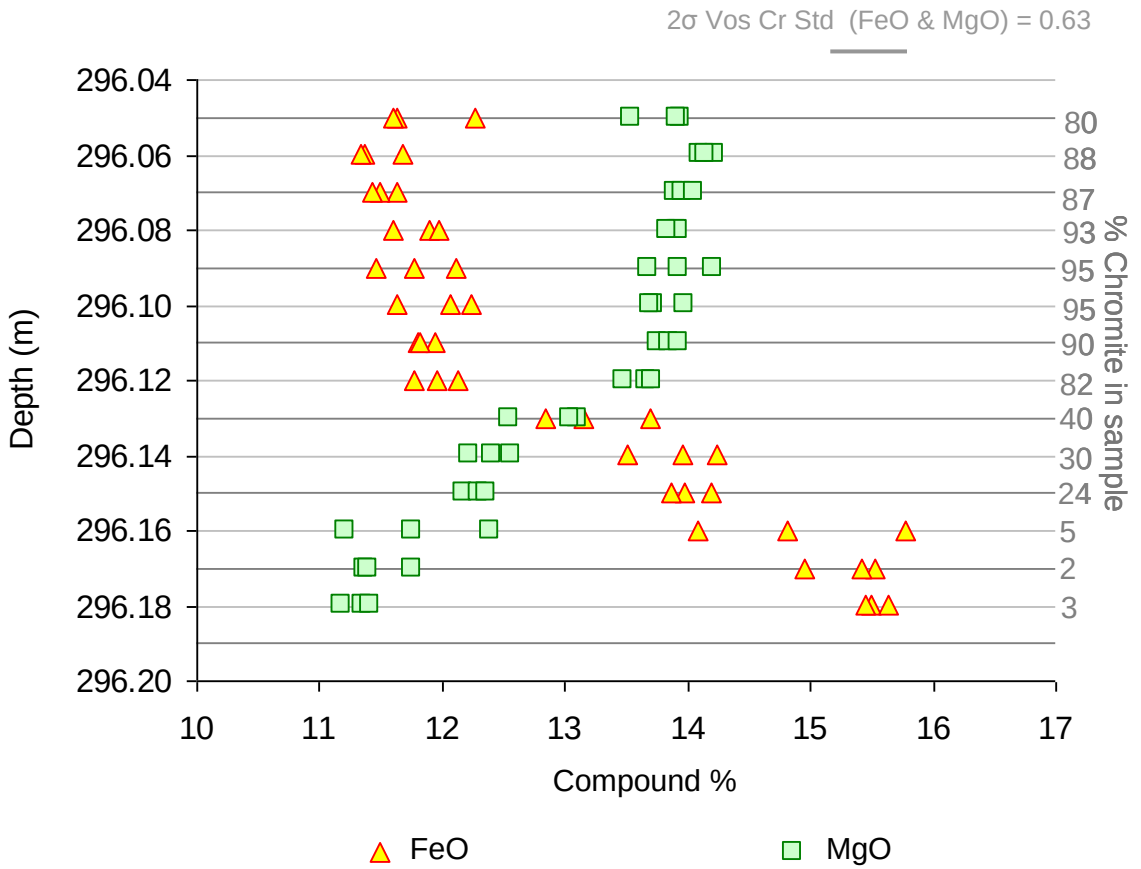

Figure 8.6.2: The variation of MgO and FeO with depth in sample F1925

The chromites comprising the massive chromite, from 296.05 m to 296.12 m, have higher MgO% than FeO% compositions (Figure 8.6.2). In contrast, chromites from the disseminated chromite portion (296.13 m to 296.18 m), where the chromite modal proportion is less than 40%, have FeO-rich compositions. MgO% depreciation starts at 296.12 m, this trend corresponds with the increasing modal proportion of silicate. It is at the centimetre interval between 296.12 m and 296.14 m that FeO% first exceeds MgO%, it is also at this point where the modal proportion of chromite decreases substantially, from 82% to 40% and olivine becomes the abundant mineral phase.

Also evident from the major element geochemistry (Figure 8.6.1) is a subtle relationship between Cr_2O_3% and MgO%. In the massive chromite Cr_2O_3% and MgO% vary in opposition, this relationship changes at 296.11 m, and continues to 296.18 m, with Cr_2O_3 and MgO varying in unison, decreasing together (Figure 8.6.3).

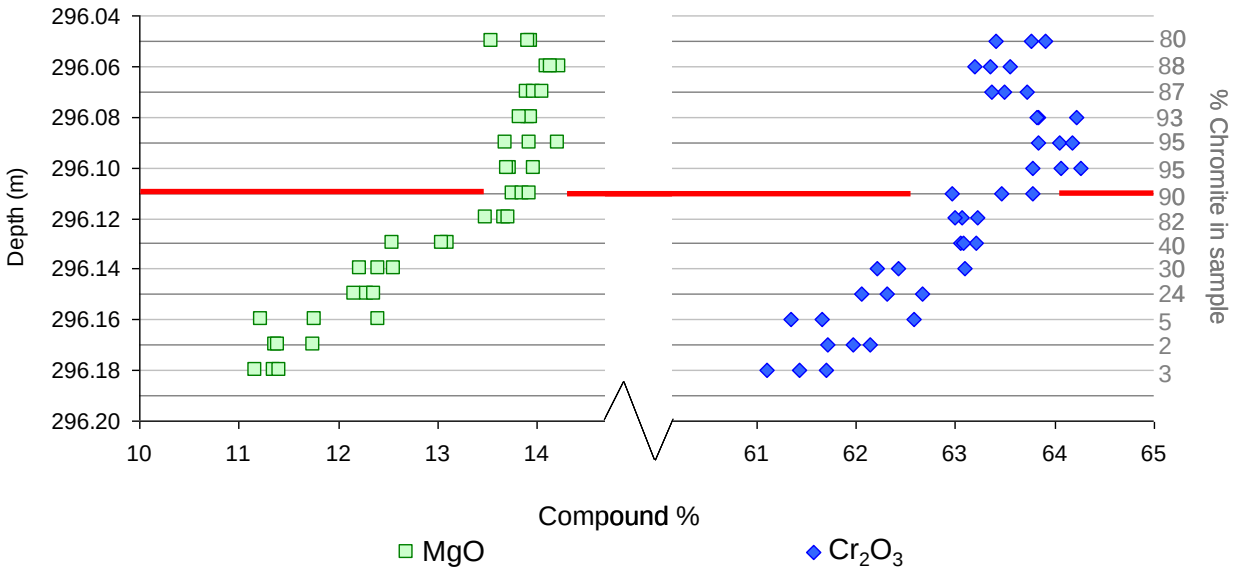

Figure 8.6.3: The variation of Cr_2O_3 and MgO with depth in sample F1925.

The red line drawn at 296.11 m indicates where the Cr_2O_3-MgO relationship changes.

Furthermore, Cr_2O_3 is seen to vary antithetically with Fe_2O_3 (Figure 8.6.1).

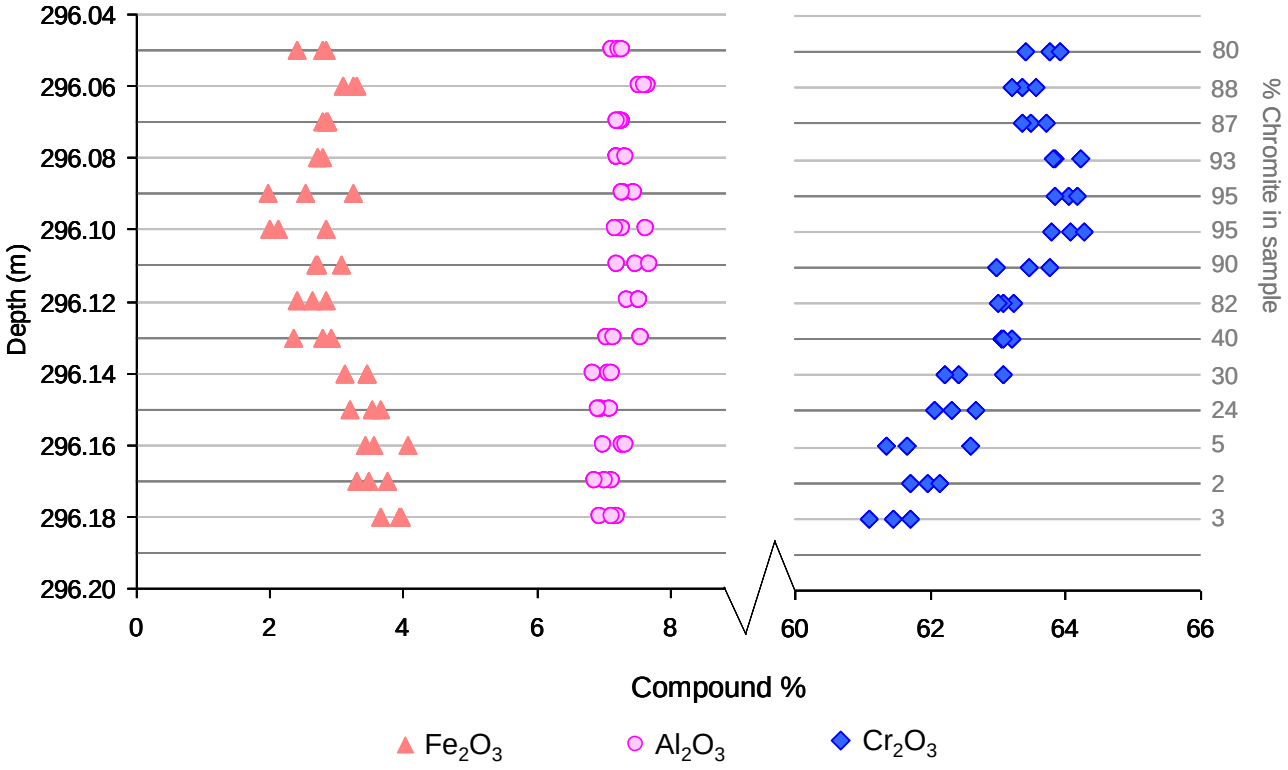

Figure 8.6.4: The variation of Cr_2O_3, Al_2O_3 and Fe_2O_3 with depth in sample F1925

The relationships between Cr_2O_3, Al_2O_3 and Fe_2O_3, presented in Figure 8.6.4, show that the antithetic relationship between Cr_2O_3 and Fe_2O_3 is evident in both the massive and disseminated chromite compositions of F1925, consistent with the substitution of Fe^{3+} for Cr. In contrast, a sympathetic relationship between Al_2O_3 and Fe_2O_3, that is seen in the massive chromites, is not apparent in the disseminated chromites. The relationships produced by variations in the chromite major element geochemistry indicate that the conditions in the melt, from which chromite was being crystallised, changed.

8.6.2 FeO%-Fe_2O_3%

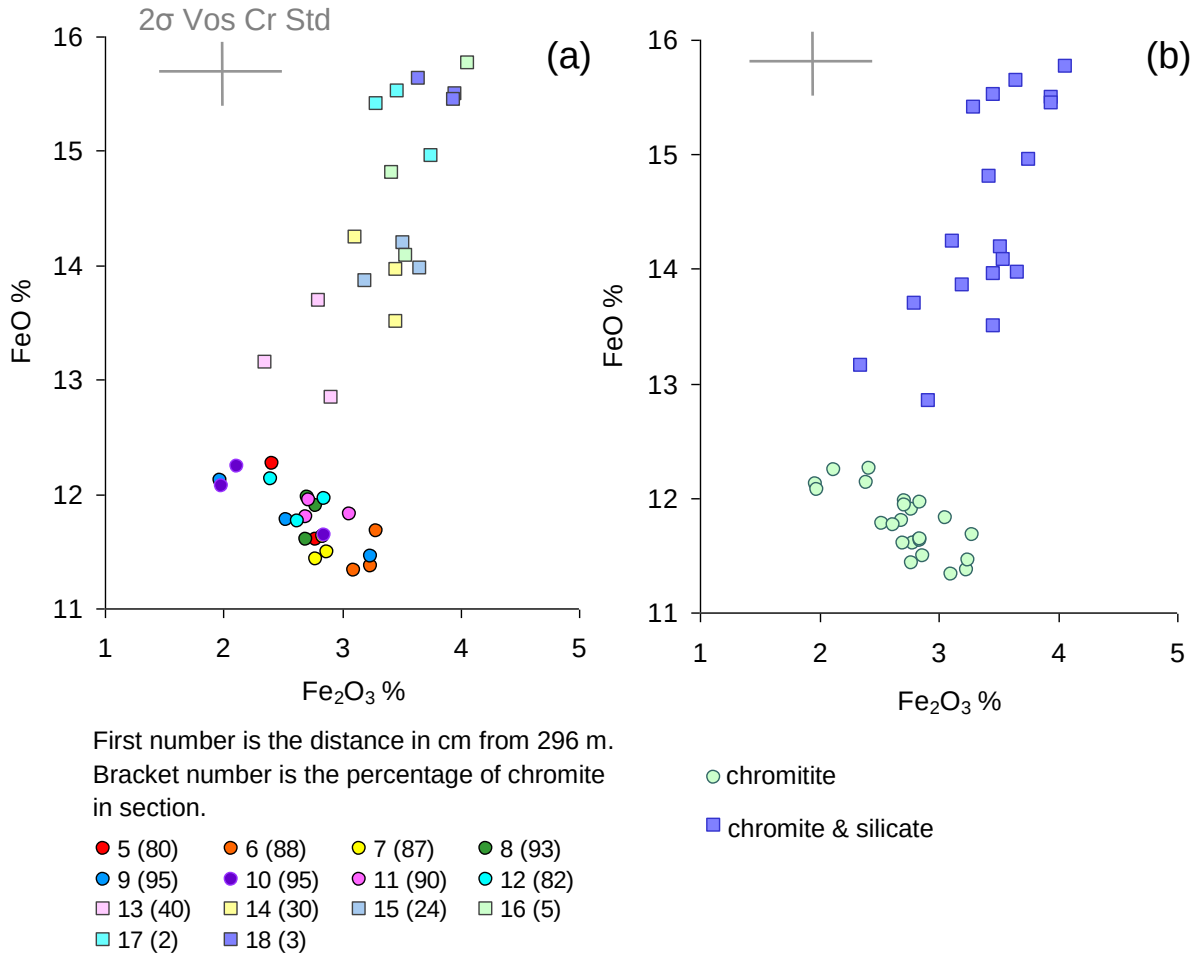

Figure 8.6.5: FeO% against Fe_2O_3%

(a) The chromite analyses for each section of sample F1925 are plotted individually. Circles correspond with massive chromite and squares with disseminated chromite. (b) The sections are plotted by rock types 'chromitite' – massive chromite, green circles and 'chromite & silicate' - disseminated chromite, purple squares.

It has been established that the chromite composition of the massive chromite sections classifies them as $FeO_{(t)}$>MgO chromites (Table 8.6.2), however, the MgO% content is greater than the FeO% content. In contrast, the silicate-rich, disseminated chromite sections (≥60% silicate), which are also classified as $FeO_{(t)}$>MgO chromites have FeO% contents greater than MgO%.

The FeO-Fe_2O_3 plot shows that the high $FeO_{(t)}$% composition of the disseminated chromites results from an increase in both the FeO% and Fe_2O_3% contents. These increase together forming a positive trend (purple squares, Figure 8.6.5b).

The high $FeO_{(t)}$% contents of the massive chromite sections are the result of high Fe_2O_3% contents. The data for these sections form a negative trend, as FeO% increases, Fe_2O_3% decreases (green circles, Figure 8.6.5b). When the chromite compositions from each section analysed are plotted independently there is an indication that the negative trend is evident within some of the sections e.g., 296.09 and 296.10 (blue and purple circles, Figure 8.6.5a) however, not every section produces this trend e.g., 296.06 (orange circles, Figure 8.6.5, Figure 8.6.5a).

The F1925 and V05-13 chromite data is compared on the FeO%-Fe_2O_3% diagram, (Figure 8.6.6). The $FeO_{(t)}$>MgO chromite compositions of the F1925 massive chromite sections (green circles, Figure 8.6.6) plot to high Fe_2O_3% values in the region of overlap between the V05-13 MgO>$FeO_{(t)}$ and $FeO_{(t)}$>MgO chromites (solid yellow and solid red triangles, respectively). The Fe_2O_3-rich compositions imply that the chromite crystallised (or last equilibrated) with a melt under oxidising conditions. The compositions align parallel with the V05-13 MgO>$FeO_{(t)}$ chromite trend. This may indicate that the two chromite groups formed by a similar process, but that the conditions were comparatively more iron-rich and oxidising when the F1925 massive chromite formed.

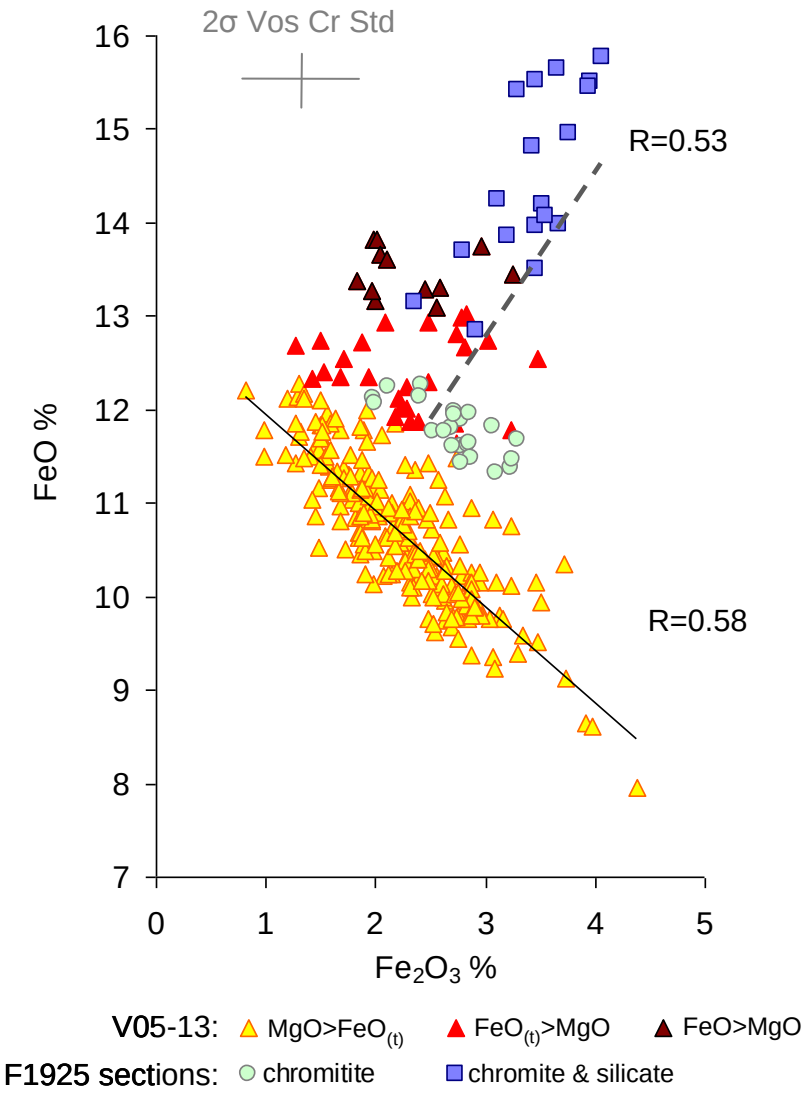

Figure 8.6.6: FeO% against Fe_2O_3% comparison of the V05-13 massive chromite dataset with sample F1925.

The massive chromite green circles, disseminated chromite, purple squares. The V05-13 MgO>$FeO_{(t)}$ chromites, yellow triangles with trendline given as a solid black line, the V05-13 $FeO_{(t)}$>MgO chromites, red triangles and the V05-13 FeO>MgO chromites dark red/black triangles.

The disseminated chromite data (purple squares, Figure 8.6.6) form a positive trend characterised by increasing FeO% and Fe_2O_3% (R-squared value, 0.53). The FeO% and Fe_2O_3% values are higher than those seen for any of the other chromite analyses that have been obtained from massive chromite samples. The disseminated chromites plot in the same region, and beyond to higher FeO% and Fe_2O_3% values, as the V05-13 FeO>MgO chromites (black outline, dark red triangles). One data point plots in the $FeO_{(t)}$>MgO chromite region (solid red triangles). It is suggested that the progressive

trend that correlates with the increasing abundance of olivine in the disseminated chromite sections, is the hallmark of a genesis process involving the co-existence of both chromite and olivine. However, although these results demonstrate that the introduction and subsequent increase of silicate co-existing with chromite increases the FeO% and Fe_2O_3% compositions of the chromite, it is not possible to determine with certainty the relative timings of crystallisation of the two mineral phases (chromite and olivine).

8.6.3 Mg#-Cr#

The Mg#-Cr# plot for sample F1925 (Figure 8.6.7), further supports the identification of the two chromite trends (Figure 8.6.4). Two well formed, differently orientated relationships can be seen, a negative trend that is formed by the massive chromites and a positive trend formed by the disseminated chromites. The trends form across a very small Cr# range, of approximately 0.02 Cr# for both groups and is only slighter greater than the 2σ error bar range for the Cr# of the Voskhod standard. None-the-less, the variation is genuine and is explained by changes in the abundance of Fe_2O_3 (demonstrated in Section 8.6.1, Figure 8.6.4).

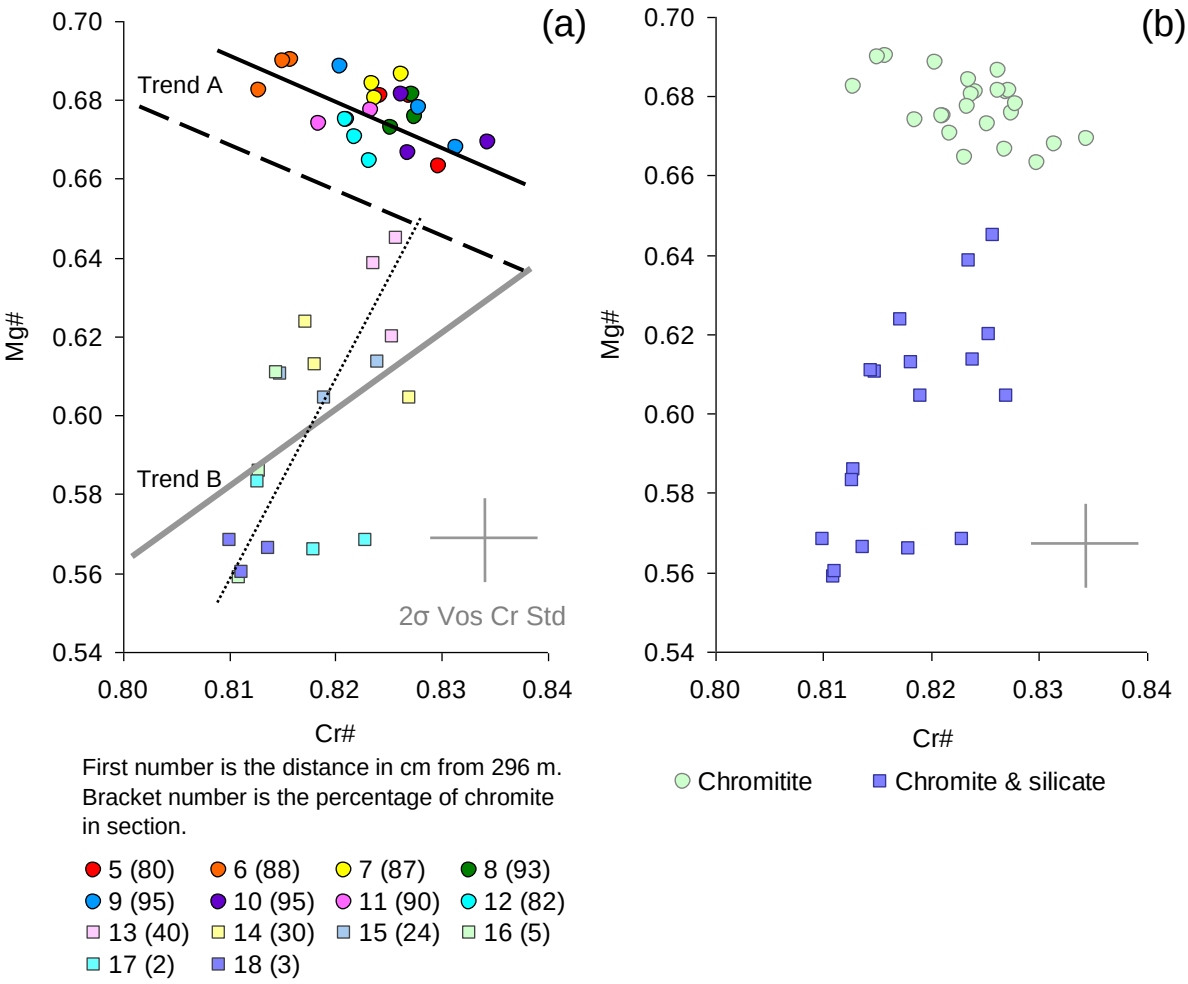

Figure 8.6.7: Mg# versus Cr#

The black dashed line represents the orientation of Trend A and the grey solid line Trend B, after Naldrett et al., 2009. The fine black dotted line is the line of best fit through the F1925 disseminated chromite, the black solid line is the line of best fit through F1925 massive chromite.

The Mg#-Cr# relationship formed by the massive chromites has an orientation similar to that of Trend A described by Naldrett et al. (2009) (refer to Chapter 3, Section 3.5.4). It is consistent with the earlier observation that Cr and Mg vary antithetically (Section 8.6.1, Figure 8.6.3). Between points 12 and 13, where the silicate content increases rapidly from 18% to 60% over a 1 cm interval, Trend A terminates. The relationship formed by the disseminated chromites is analogous with Trend B (*Naldrett et al., 2009*; refer to Chapter 3, Section 3.5.4) where Cr and Mg vary together (Section 8.6.1, Figure 8.6.3).

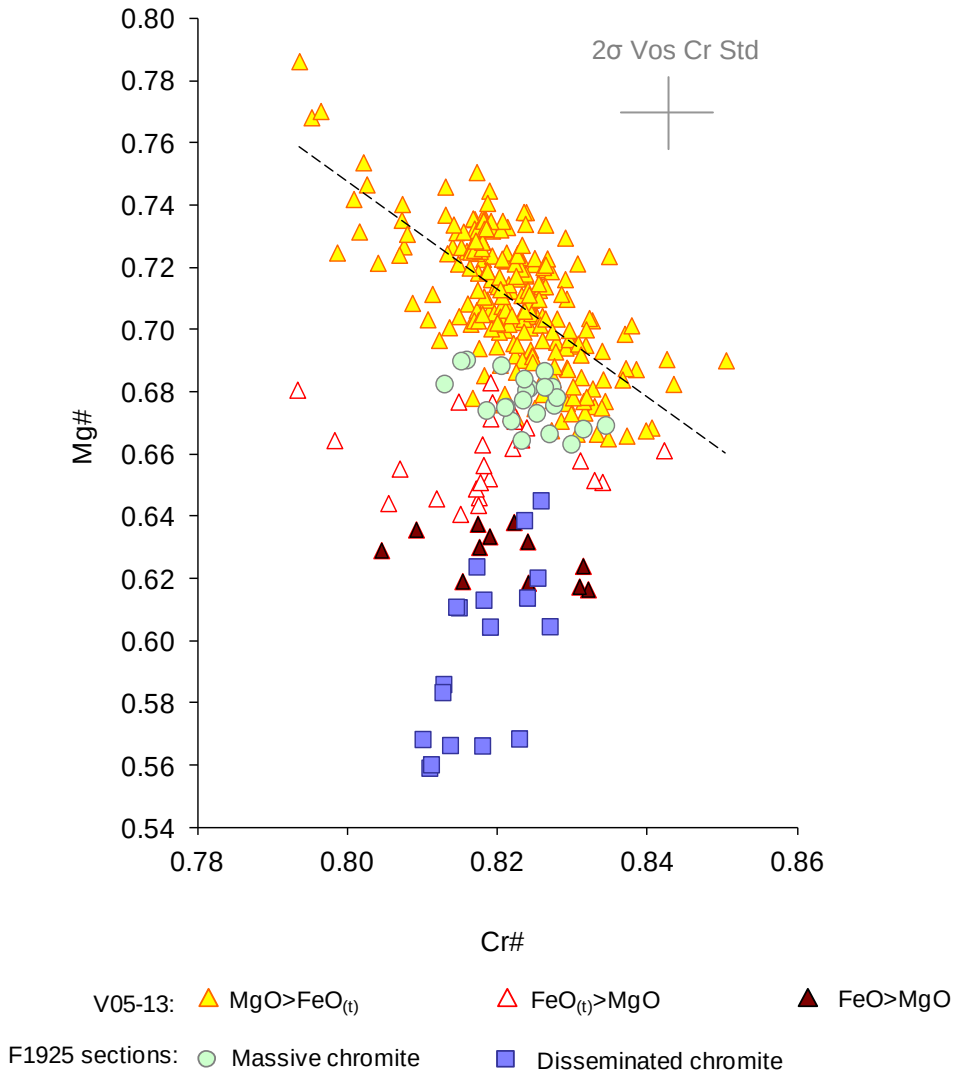

Figure 8.6.8: Mg# against Cr#; comparison of chromite composition datasets V05-13 and F1925.

When compared with the V05-13 chromite dataset, the massive chromites plot predominantly in the same space as the MgO>$FeO_{(t)}$ chromites (yellow triangles, Figure 8.6.8) although some data points fall in the region of overlap between the MgO>$FeO_{(t)}$ and $FeO_{(t)}$>MgO chromite groups (yellow and red-white triangles, Figure 8.6.8). The disseminated chromites plot in the same region as the V05-13 FeO>MgO chromites (dark red-black triangles) as well as to lower Mg# values. The Cr# of both the massive and disseminated chromites plot in the same range as the majority (~90%) of the V05-13 dataset, and the Cr# range of the disseminated chromites is more tightly constrained than that of the massive chromites.

8.7 Summary

Sample F1964-65 (massive chromite)

Fine, centimetre-scale geochemical layering is identified within sample F1964-65. Three groups are identified on the basis of geochemistry and depth. Groups 46-49 and 55-59 are comprised of MgO>$FeO_{(t)}$ chromite and are each 4cm thick and Group 50-55 is comprised $FeO_{(t)}$>MgO chromite and is 5 cm thick. The switch in composition occurs with depth, such that the $FeO_{(t)}$>MgO chromites (Group 50-55) is sandwiched between the two MgO>$FeO_{(t)}$ chromite groups (Groups 46-49 and 55-59, respectively).

In Group 50-55 (MgO>$FeO_{(t)}$ chromites) as the Fe_2O_3% increases the FeO% decreases, the trend aligns sub-parallel to that formed by the V05-13 MgO>$FeO_{(t)}$ chromites. Whereas Groups 46-49 and 55-59 (composed of $FeO_{(t)}$>MgO chromites) cluster, and do not form trends.

On the Mg#-Cr# diagram, Group 55-59 forms a trend that is oriented similar to Trend A described by Naldrett et al. (2009).

Sample F1996-97 (massive chromite)

No geochemical layering is observed in sample F1996-97. The compositions of each of the 15 sections analysed are classified as MgO>$FeO_{(t)}$ chromites and are considered to be nearly homogeneous, no trends or clusters are observed in any of the plots used to examine the data.

Sample F1925 (massive chromite grading to disseminated chromite)

The massive chromite portion of sample F1925 is comprised of $FeO_{(t)}$>MgO chromite. The high $FeO_{(t)}$% contents result from high Fe_2O_3% values. The iron content of the chromite increases (both FeO% and Fe_2O_3%) as the modal proportion of olivine increases, while the MgO% and Cr_2O_3% contents decrease.

On the FeO%-Fe_2O_3% and Mg#-Cr# diagrams the massive chromite compositions align parallel with the V05-13 MgO>$FeO_{(t)}$ chromites. This could indicate that the genesis of these two groups, although chemically different, may be related by a common process.

On the Mg#-Cr# diagram the massive chromites form a negative trend that aligns with Trend A and the disseminated chromites form a positive trend that is similar to Trend B described by Naldrett et al. (2009). Furthermore, the differences in the modal proportions of chromite and olivine and the compositions of the chromites comprising sample F1925 is evidence of two different formation processes (or a change in the formation process).

The effect of chromite and olivine modal proportions on chromite compositions

Examination of the chromite Mg# and modal proportion of olivine present in a section (for samples F1964-65 and F1925) has shown that the two do not correlate. Contemporaneous crystallisation of chromite and olivine from a melt could explain the variations in Mg# seen. To explain how these compositional changes are recorded in massive chromite, where the olivine proportion is less than 20%, requires a post crystallisation process to have taken place. The process would need to physically separate the chromite and olivine, without altering the geochemistry. Such a process would explain how the massive chromite has, in places, inherited a composition characteristic of the co-crystallisation of chromite and olivine from a melt, while the mineral proportions infer that only chromite has crystallised. It is suggested that a densification process, e.g. sintering, could produce this effect (see Chapter 3, Section 3.6.4). From the samples studied evidence for sintering, resulting in the separation of olivine and chromite (to form massive chromite) is further evidenced in the textures of the massive chromite ore (Chapter 5, Section 5.5.6). The effect of this process on the composition of chromite and grain textures is addressed further in the discussion, Chapter 9.

Chapter 9: Discussion

9.1 The tectonic evolution of the Uralian basin recorded by the mantle hosted Voskhod chromite deposit

Evidence of the tectonic processes responsible for the opening and closure of the palaeo-Uralian ocean basin are recorded in the mineralogy and whole rock geochemistry of the mantle harzburgite and dunites that host the Voskhod deposit. These same processes have contributed to the genesis of the Voskhod deposit.

9.1.1 Whole rock geochemistry

Rare earth element profiles

Whole rock geochemistry of the Voskhod harzburgite and dunite suite can be used to identify and discriminate between mantle depletion and enrichment processes. REE profiles show that host rocks have undergone varying degrees of depletion, the result of mantle melting, prior to being re-enriched with LREE, a signature imparted by interaction between the mantle and SSZ derived melts and associated liquids. Four REE profile types have been identified; LREE depleted, LREE enriched, flat and U-shaped. These do not correlate systematically with a particular lithology (harzburgite or dunite) or distance from the ore-body (distal, halo or ore zone dunites). LREE-enrichment of peridotite mantle has been shown to result from post-melting refertilisation by new melts that percolate upwards through overlying mantle lithosphere during ascent to the crust (*Niu, 2004*). Accounting for the extent of depletion or enrichment in terms of the characteristics resulting from partial melting or melt-rock reaction and magma transport, as well as identifying the process and source of LREE enrichment, is extremely complex (e.g. *Vernieres et al., 1985; Page et al., 2009*) and beyond the scope of this thesis. Some general observations can be made.

The Voskhod harzburgite and dunite units are depleted mantle rocks forming REE profiles that plot below the DMM line (*Workmann & Hart, 2005*) (Chapter 5, Section 5.6.2, Figures 5.6.4 and 5.6.5). The differences between the REE profile

shapes and concentrations, demonstrate that depletion and enrichment processes have varied in intensity (Chapter 5, Section 5.6.2, Figure 5.6.4). The different lithologies have not formed simply by partial melting, as ratios of light to heavy REE are too high to be explained in terms of residue of equilibrium partial melting (*Prinzhofer and Allegre, 1985; Nicolas, 1989*) (Chapter 5, Section 5.6.2, Figure 5.6.5).

It is widely documented that mantle harzburgites typically produce U-shaped profiles (e.g. *Van der Wal & Bodinier, 1996; Parkinson & Pearce, 1998; Proenza et al., 1999; McDonough & Frey, 1989*). However, four harzburgite samples produce LREE-depleted profiles and a further three form weakly LREE-enriched U-shaped profiles (Chapter 5, Section 5.6.2, Figure 5.6.5 [a]). The dunites (distal, halo and ore zone) typically have a LREE-enriched component forming either LREE-enriched or U-shaped profiles (Chapter 5, Section 5.6.2, Figure 5.6.5 [b, c and d]).

REE mobilisation episodes are recorded in the ore zone, dunite halo, distal dunite and harzburgite units.

- The first event is LREE depletion caused by incremental partial melting forming residual mantle harzburgite (*Johnson et al., 1990*).
- The second is LREE-enrichment that has an arc component signature, formed by reaction with a SSZ melt (e.g. a boninite melt). This signature is particularly prominent in rocks sourced from within, and close to, the ore zone, inferring that the ore zone was a conduit through which the SSZ-melt migrated.

LREE-enriched signatures in ophiolite peridotites have been explained by secondary processes relating to serpentinisation, oceanic alteration or contamination by crustal fluids contemporaneous with ophiolite obduction (*Sharma & Wasserburg, 1996; You et al., 1996; Gruau et al., 1998; Niu, 2004; Iyer et al., 2008; Deschamps et al., 2010*). The Voskhod rocks are recognised to be highly serpentinised. The Al_2O_3 wt% - Y ppm diagram showed that Al was largely immobile during alteration of the harzburgite and dunites (Chapter 5, Section 5.6.2, Figure 5.6.1), whereas the CaO wt% - Y ppm plot inferred that Ca had been remobilised (Chapter 5, Section 5.6.2, Figure 5.6.2). It cannot be discounted that LREE-enrichment has resulted from late-stage, ophiolite emplacement associated

processes. Throughout the hanging wall and footwall LREE-depleted rocks are inter-layered with LREE-enriched rocks, both are serpentinised to approximately the same extent and are typically no more than 50 m apart (vertically down hole). No obvious structural discontinuities or faults are identified between the units. These observations indicate that LREE-enrichment resulted from focused melt or fluid flow pathways that were constrained to metre-wide specific horizons within the mantle. There is no apparent relationship between the extent of serpentinisation and LREE enrichment or depletion.

LREE-enriched signatures permeate beyond the confines of the ore zone into the host rocks (Chapter 5, Section 5.6.2, Figure 5.6.4 [b]). This indicates that there has been diffusion of a LREE-bearing melt (or liquid) away from the main conduit into the wall rock.

Partial melting and interaction between percolating melts and residual mantle removes orthopyroxene from harzburgite (*Boudier & Nicolas, 1972; Boudier, 1978; Cassard et al., 1981; Quick, 1981; Fisk, 1986; Kelemen, 1990; Arai & Yurimoto, 1994; Arai, 1997*). The resulting mantle residue is depleted in the REEs with the LREEs lost preferentially first (*Johnson et al., 1990; Johnson & Dick, 1992; Seyler et al., 2001; Hellebrand et al., 2001, 2002*). LREE-depleted profiles in mantle residue (Chapter 5, Section 5.6.2, Figure 5.6.4 [a]) are characteristic of dry stage melting such as that associated with a MOR setting (*Frey, 1984; McDonough & Frey, 1989; Rampone et al., 1996, Zhou et al., 2001; Urlich et al., 2010*), the LREE-depleted profiles produced by the harzburgites at Voskhod are consistent with this model. These REE profiles are the same as those seen in lherzolites that host the Sartohay high-Al chromite deposits in the Dalabute ophiolite (NW China) (*Zhou et al., 2001*) as well as mantle peridotites from massifs in the western Alps (*Frey, 1984; McDonough & Frey, 1989; Rampone et al., 1996*).

U-shaped profiles cannot be explained by batch melting or fractional melting (*Prinzhofer & Allegre, 1985*) (Chapter 5, Section 5.6.2, Figure 5.6.4 [d]). The apparently selective MREE-depletion requires a two stage process (at least), one of depletion and a subsequent refertilisation process. Interaction between depleted mantle and a percolating arc derived melt, will destabilise and scavenge ortho- and clinopyroxene but will also enrich the rocks in the LREEs, forming U-shaped or

LREE-enriched profiles (*Prinzhofer & Allegre, 1985; Stopler, 1987; Bodinier et al., 1990; Takazawa et al., 1992, 2003; Nui, 2004; Li & Lee, 2006; Ulrich et al., 2010*).

LREE enriched harzburgite (Chapter 5, Section 5.6.2, Figures 5.6.4. [d] and 5.6.5 [a]) has been documented in other ophiolites e.g. the Finero massif (western Alps), the Zabargad peridotites of the Red Sea, the Oman ophiolite (Oman) (*Bodinier, 1988; Bodinier et al., 1988*) and the Dalabute ophiolite (NW China) (*Li et al., 1987*). LREE-enrichment is attributed to the post-melting addition of highly incompatible elements by interaction between a metasomatic fluid or melt with the mantle (*Bodinier, 1988. 1990; McKenzie, 1984; Navon and Stolper, 1987;Bodinier et al., 1988; Bodinier et al., 1990; Vasseur et al., 1991*) and is a signature that typifies the addition of an arc component derived from melting of a subducting slab in a SSZ setting (*Gill, 1981; Pearce, 1982; Saunders et al., 1991; Bédard, 1999*). The addition of a hydrous component at the site of slab subduction is commonly proposed for arc and boninite melt sources (*e.g. Hickey and Frey, 1982; Woodhead et al., 1998; Bédard, 1999; Kimura and Yoshida, 2006*) that are formed by hydrous melting of refractory, depleted peridotite (e.g. *Crawford et al., 1981; Bizimis et al., 2000; Arndt, 2003*). Furthermore, melts generated by fluid circulation through forearc mantle typically display U-shaped REE profiles, similar to those of boninites (*Urlich et al., 2010*).

Determining how the LREE-signature is retained in the rocks is unclear. Owing to the dissolution of clinopyroxene (and orthopyroxene) it is not possible that the LREEs are accommodated in these mineral structures. Olivine, the most abundant mineral does not readily incorporate REE into its structure. Nui (*2004*) proposed that LREEs could be present trapped along mineral grain boundaries as thin films.

It is proposed that the LREE-enriched profiles seen in the Voskhod rocks (Chapter 5, Section 5.6.2, Figure 5.6.4 [b]) result either from i) interaction between highly LREE-enriched melt (or melt associated fluids) and residual mantle that has been subject to varying degrees of depletion, or ii) olivine that has crystallised directly from a melt generated from, or that is contaminated by, subducting slab LREE-enriched fluids (*Takahashi, 1991, 1992*; *Niu, 1997*).
U-shaped profiles are more LREE- and HREE-enriched than flat profiles (Chapter 5, Section 5.6.2, Figure 5.6.4 [c and d]). The variability in the MREE-HREE

portions of these profiles, the U-shaped having HREE>MREE and the flat, MREE≈HREE, result from differing degrees of partial melting and primary extraction of REE. Flat profiles, seen in all of the rock types studied, have been subject to more extensive partial melting and consequently have lost more MREE and HREE than U-shaped profiles. This implies that the extent of mantle melting (and REE depletion) in the region around the ore body has not been uniform.

In general terms the LREE-depleted harzburgite and LREE-enriched ore zone dunite profiles represent REE-profile end members. The rocks correspond with the two processes; depletion by partial melting (harzburgite) and enrichment by interaction with an arc derived liquid (ore zone dunite). The distal dunite and dunite halo display a range of REE profiles; U-shaped, flat or LREE-enriched. There is no characteristic “type” profile that defines these units.

Spidergrams

Positive Ba and Zr-Hf anomalies are present in all of the extended trace element plots for the Voskhod harzburgite and dunite rocks (Chapter 5, Section 5.6.2, Figure 5.6.6). Similarly, a positive Nb-Ta (±Th) signature (relative to the LREE) is also evident in the majority of samples, but not every sample. Some samples have extremely enriched Nb-Ta anomalies that are more than an order of magnitude greater than the LREE concentrations. In other samples the signature is less prominent and concentrations are greater than, but still similar to, the LREE concentrations. The positive Ba and Zr-Hf anomalies appear to be independent of the Nb-Ta (±Th) signature. The elements Th, Nb and Ta are reported to be immobile during alteration (e.g. *Godard et al., 2000*) so it seems unlikely that some samples underwent selective depletion in these elements, removing the positive signature. Consequently, the positive Ba, Zr-Hf and Nb-Ta (±Th) signatures are considered to be derived from two different melt events.

The BBC boninite spidergram profile possesses the same positive anomalies (Ba, Zr-Hf, Nb-Ta ±Th) as those seen in the Voskhod mantle rocks (Chapter 5, Section 5.6.2, Figure 5.6.7). The Ba anomaly appears to have survived in the melt to the surface where the signature is equally prominent as that retained in the mantle rocks. In contrast, the Nb-Ta (±Th) anomaly is less prominent. The Nb-Ta

concentration range covered by the BBC boninite composition field shows that concentrations can be less than the neighbouring LREEs. This is similar to the composition variation seen in the mantle rocks and demonstrates that some of the boninite samples possess a positive Nb-Ta signature, while others do not. The positive Zr-Hf anomaly is present in all the BBC boninites. It is possible that enrichment of the LILE (Cs, K, Rb, Ba and Sr) may result from a secondary remobilisation process, such as serpentinisation (*Godard et al, 2000*). This is one explanation for the prevalent and strong Ba signature seen in both the BBC boninites and Voskhod mantle rocks.

A comparison of the Voskhod mantle units and BBC boninite geochemistry with the TMO mantle units and boninites shows that both possess the same positive Ba, Zr-Hf, Nb-Ta ±Th signatures (*Page et al., 2009*) (Chapter 5, Section 5.6.2, Figure 5.6.7). Page et al. (2009) were able to demonstrate that the addition of a distal continental margin sediment contaminant (the Caldwell sediment), at the site of melting in the subduction zone, would produce a melt with a highly enriched LILE, Th, Nb, Ta, LREE profile, a strong positive, Zr-Hf anomaly and depleted in HREE. Their study concluded that this accounted for the geochemical signatures seen in the TMO mantle and boninite units. Furthermore, it was noted that the proposed continental margin sediment contaminant produced similarly shaped REE profiles as those formed by sediments from the Marianas Trough (*Elliott et al., 1997*), although the Caldwell sediment geochemical profiles formed slightly higher Rb, Ba, Th, Nb and Ta, and much higher Zr and Hf anomalies.

An alternative explanation for the positive Nb-Ta (±Th) signatures could be infiltration of late-stage (post mantle melting and LREE-depletion) volatile-rich liquids. Such liquids could be derived from the dehydration and/or melting of a subducting slab in a SSZ setting (*Eggler, 1987; Schiano & Clochiatti, 1994; Bodinier et al., 1996; Proenza et al., 1999*). However, such a process does not account for the positive Zr-Hf anomaly.

Boninites are hydrous melts rich in SiO_2, MgO, Cr, Ni, the LILE (K, Rb, Cs, Ba), U, Th, Pb and Sr, and in LREE (La, Ce and Pr); yet poor in many HFSE (Nb, Ta, Zr, Hf, Ti) and MREE and HREE (e.g. *Hickey and Frey, 1982; Pearce, 1982; Crawford, 1989; Saunders et al., 1991; Pearce et al., 1992; Taylor et al.,1994*).

Brenan et al. (1995) reported that LREEs, Th, Nb and Ta are immobile in hydrous fluids, as are the HFSE (which include Zr and Hf) (*Pearce et al., 2000)*. Consequently, the enriched Zr-Hf signature seen in the Voskhod mantle rocks and BBC boninites cannot be attributed solely to the presence of water in the melt (Chapter 5, Section 5.6.2, Figure 5.6.7).

On the basis of the findings presented in this study and the comparison with the TMO complex rocks, it is proposed that the positive element anomalies; Ba, Zr-Hf, Nb-Ta ±Th, characterise boninite lavas formed when a distal continental margin sediment component is added to the mantle wedge at the site of slab subduction and melt generation. Furthermore, the apparent associated formation of large Cr-rich podiform chromitites with these enriched boninite melts implies that the chromium availability may be enhanced as a result of the added sediment contaminant.

The BBC boninites and Voskhod mantle rocks: A proposed genetic relationship

It is recognised that the BBC boninites and mantle rocks of the Kempirsai massif (in which Voskhod is located) are separated by a major geological fault, the MUF. From this it might appear, spatially, that the two are not genetically associated. However, the formation of both the BBC boninites are Kempirsai massif are associated with the evolution of the Magnitogorsk island arc system (*Zonenshain et al., 1984; Lennykh et al., 1995; Melcher et al., 1997*). The initiation of subduction within the palaeo-Uralian basin, which marked the start of the ocean basin closure, led to the development of a SSZ and a fore arc setting where boninite melts formed (preserved as the BBC boninites, *Spadea et al., 1998, 2002; Brown & Spadea, 1999*). With maturation of the SSZ-setting the Magnitogorsk island arc formed. It has been proposed by Melcher et al. (1997) that the boninite melts were the parent melt source from which the MOF podiform chromite crystallised. Until now, no evidence has been presented to show the geochemical association between the BBC boninites, the only occurrence of boninite reported in the southern Urals (*Ivanon et al., 1989; Seravkin et al., 1992; Brown & Spadea, 1998; Spadea et al., 2002*), and the mantle rocks that host the giant chromite deposits of the MOF (hosted in the Kempirsai massif). The similarity between the geochemical signatures is indisputable. The genetic association is further endorsed by the similarities between the TMO mantle and boninite rocks and the Voskhod mantle

and BBC boninite rocks. In the TMO complex the stratigraphic relationship and genetic association of the mantle to crust progression is well preserved and clearly exposed (*Page et al., 2009a, 2009b*).

A complete ophiolite stratigraphy is reportedly preserved in the Kempirsai massif where the lava units documented are of MORB compositions (*Savelieva and Nesbitt, 1996; Savelieva et al., 1997, 2002; Melcher et al., 1999*). No boninites have been documented. The MORB composition pillow lavas are reported to be of Mid-Ordovician age (*Ivanov, 1988; Fershtater et al., 1997*) while the BBC boninites formed later during the Early to Mid-Devonian (*Spadea et al., 1998; Brown et al., 2006*). Neither the geochemistry nor the Mid Ordovician age of the MORB pillow lavas are compatible with the timing of SSZ initiation and the subsequent Magnitogorsk formation. The BBC boninites are dated as Early to Mid-Devonian in age. A possible explanation for the separation of the BBC boninite lavas from the Kempirsai mantle section, through which it is proposed the melts migrated, is that the boninite melt did not ascend upwards through the mantle but instead migrated at an oblique angle, moving both upwards and laterally through the mantle, before being expelled onto the ocean floor. Subsequent uplift, thrust development, obduction and emplacement of the Kempirsai massif resulted in the separation of the preserved mantle conduit pathway (the podiform chromitite) from the crustal expression of the boninite lavas.

In terms of the lava types geochronology; the MORB lavas preserved in the Kempirsai Massif are the products of fertile mantle melting associated with the opening of the palaeo-Uralian ocean basin during the Mid-Ordovician. The BBC boninites and, from the findings of this study the formation of the podiform chromitites that are preserved in the Kempirsai Massif, formed during the Early to Mid-Devonian. The BBC boninites are the product of depleted mantle melting (the depleted mantle being the residue left from the extraction of the MORB melts) in a fore-arc setting and mark the onset of the development of the Magnitogorsk island arc.

9.1.2 The OSMA

Harzburgite and dunite, which host the Voskhod ore body, plot as mantle residues inside of the OSMA field (*Arai, 1994*) (Chapter 6, Section 6.3.1, Figure 6.3.3). These rocks form a systematic trend with both Cr# and Fo increasing from harzburgite (passive margin peridotite), through distal dunite, dunite halo to ore-zone dunite. It appears that the rocks are increasingly residual and that the degree of partial melting intensifies with proximity towards the ore body. However, it is extremely unlikely that the 18 Mt Voskhod chromite deposit formed by extreme partial melting of the mantle. Experiments have shown that 20% partial melting of fertile lherzolite forms harzburgite and dunite forms at ~50-60% melting (*Jaques & Green, 1980; Duncan & Green, 1980, 1987; Bonatti & Michael, 1989; Kostopoulos, 1991*). To satisfy these results the degree of melting required to form chromitite would have to exceed 60% partial melting of a fertile lherzolite. The degree of partial melting and the longevity of the partial melting event required to form a chromite volume of this size is considered to be unfeasibly high.

It has been proposed that early crystallised dunite cumulates could also plot within the OSMA, provided that fractionation has not been significant (*Quick, 1980; Lago et al., 1982; Arai & Yurimoto, 1994*). On these grounds, the application of the diagram to infer formation processes, particularly those associated with the dunite rocks, yields limited information.

9.1.3 Chromite composition: The Cr#-TiO_2 relationship

The Cr# of chromite increases as the degree of partial melting of the mantle increases (*e.g., Dick & Bullen, 1984;Arai, 1991, 1992, 1994a, 1994b, Arai & Abe, 1994; Ninomiya & Arai, 1992*). Partial melting of fertile mantle lherzolite forms harzburgite and at high degrees, >40% partial melting, residual dunite may form (*Arai, 1987, 1994a*). Melt-rock interaction has also been shown to raise the Cr# of mantle chromite (*Arai, 1992; Zhou et al., 1996; Pearce et al., 2000; Dare et al., 2008*). Variation in the composition of chromite in the Voskhod harzburgite and dunite suite plot on the Cr#-TiO_2 diagram forming a trend characteristic of a reaction between depleted MOR harzburgite and boninite melt (*Arai, 1992; Zhou et al., 1996; Pearce et al., 2000*) (Chapter 6, Section 6.5, Figure 6.5.2). The boninite

melt signature is most prominent in the ore zone dunites and chromitite, and is less so in the distal dunite and harzburgites. Harzburgite plots in the residual MOR harzburgite field close to the FMM partial melting curve having undergone 15-20% partial melting. Dunite plots away from the partial melting curve indicating that it is not a product of extreme mantle melting, but rather a reaction product.

It is widely reported that podiform chromite genesis, especially that of high-Cr chromitite, is associated with the migration of boninite melt through mantle harzburgite (*Paktunc, 1990; Zhou et al., 1994; Leblanc, 1995; Ballhaus, 1998; Ishikawa, 2002; Rollinson, 2005; 2008*). The Cr#-TiO_2 plot identifies this association at the Voskhod deposit.

9.1.4 Chromite composition: fO_2-Cr# and TiO_2/Fe^{3+}#-Ga/Fe^{3+}# relationships

The fO_2-Cr# and TiO_2/Fe^{3+}#-Ga/Fe^{3+}# diagrams identify MOR- and SSZ-type, harzburgite and dunite (Chapter 6, Section 6.6, Figure 6.6.1 and Section 6.7, Figure 6.7.1, respectively). The diversity of the tectonic signatures determined from the 15 samples, collected over 260 m (down hole vertical depth) indicate that the region has been subject to a polygenetic tectonic evolution that is recorded by these mantle units.

The residual-MOR harzburgite and MOR-reacted dunite, provide evidence of a MOR setting that would have formed as the palaeo-Uralian ocean basin opened and spread. The SSZ-reacted harzburgite and dunites record the onset of basin closure and the formation of a SSZ and associated fore-arc, a setting with which boninite melts are typically associated.

Residual-MOR Harzburgite

Residual-MOR harzburgite is located furthest from the chromitite ore body (142 m). It represents the original mantle residue formed from decompressional, partial melting of a fertile mantle source. It marks the tectonic evolution from a passive continental margin (fertile mantle lherzolite) to a spreading centre mid-ocean ridge

system. The upwelling of a fertile mantle diapir would have undergone partial melting of ~15% creating MORB melts and mantle residue of harzburgite.

MOR-reacted Dunite

The distal dunites are MOR-reacted dunites. These formed by interaction between residual mantle harzburgite and a MORB melt. Referring to the Cr#-TiO_2 diagram the reaction trend indicates reaction with a boninite melt, not a MORB melt, where higher TiO_2 values would be anticipated (Chapter 6, Section 6.5, Figure 6.5.2). However, the Cr#-TiO_2 plot also identifies an increase in TiO_2 between the residual harzburgite and distal dunite. This is interpreted to represent a reaction between mantle residue and a percolating MORB melt in channel-ways at a mid-ocean ridge spreading centre.

The distal dunites are not residual dunites formed by high degrees of partial melting of the mantle as might be inferred from the OSMA diagram (Chapter 6, Section 6.3.1, Figure 6.3.3).

SSZ-reacted harzburgite and dunite

The dunite halo and ore zone dunites plot as SSZ-reacted dunites, formed by reaction between mantle harzburgite and a SSZ arc derived melt, identified as a boninite melt, e.g. the Cr#-TiO_2 diagram (Chapter 6, Section 6.5, Figure 6.5.2). Spatially, these samples are closest to the chromitite ore body, inferring that the chromitite marks the focus of a boninite melt passage through the mantle. Melt has diffused through and reacted with the harzburgite wall rock.

The SSZ-reacted harzburgites record having undergone ~18% partial melting. This appears to be the result of localised enhanced melting of the host peridotite wall-rock which the melts have interacted with.

The implication that the Voskhod mantle units preserve a boninite-melt interaction signature, where boninites characterise forearc settings, provides further evidence that the mantle units formed in a SSZ setting. The Kempirsai Massif (in which Voskhod is located) is interpreted as the mantle units of the Sakmara Allochthon (*Savelieva et al. 1997*), an accretionary complex that formed during the early stage

evolution of the Magnitogorsk island arc system; a setting synonymous with boninite melt genesis.

Discrepancy using the fO_2-Cr# plot to determine melt composition

On the fO_2-Cr# diagram the chromitite and dunite halo chromites have high fO_2 values (+1.5< QFM > +3.0) plotting in the composition field of CAB lava spinel (Chapter 6, Section 6.6 Figure 6.6.1). However, the very high Cr# values ≥0.80 are characteristic of boninite. It is reported that chromites formed in oxidised environments, such as those associated with arc settings, possess higher fO_2 values than chromites formed in a MOR setting (*Ballhaus et al., 1991; Parkinson & Pearce, 1998; Pearce et al., 2000; Parkinson & Arculus, 1999; Elburg & Kamenetsky, 2007*). Additionally, studies on IAT lavas have shown that fO_2 can increase as a result of magmatic differentiation (*Ballhaus et al., 1991 and Elburg & Kamenetsky, 2007*). It is proposed that the boninite parent melt that crystallised the Voskhod chromitite pod was especially water-rich, hence the fO_2 values are higher than expected for a boninite melt. This may, in part, contribute to the unique physico-chemical conditions required for the genesis of such an unusually large chromitite.

9.1.5 Host rock geochemistry: A record of the palaeo-Uralian ocean basin evolution.

Inter-layered harzburgite and dunite intervals comprise the hanging wall and footwall host units of the Voskhod chromite deposit. Decompression induced partial melting of fertile mantle forms harzburgite and MORB melt. The presence of this rock type in the host units is interpreted as a record of the tectonic setting transition from a passive continental margin to a MOR setting. It marks the split of the East European craton from the Kazakh and Siberian cratons, during the Late Cambrian to Early Ordovician and subsequent opening of the palaeo-Uralian ocean basin during the Mid-Ordovician to Late-Silurian.

Harzburgite

Mineralogically the harzburgites are cpx-poor (<3% cpx modal proportion) indicating that they are depleted rocks. The whole rock major element chemistry

supports this interpretation as seen from the Al_2O_3-CaO diagram (Chapter 5, Section 5.6.1, Figure 5.6.3). The chromite Cr# range is 0.23-0.47. Two harzburgite samples have a particularly low Cr# of 0.23 (Vos-341 and G1742), a value that is typically associated with fertile mantle rocks such as passive continental margin peridotite or lherzolite (*Arai, 1994a*). This observation contradicts the mineralogical evidence which infers that the harzburgites are highly depleted. No relationship is seen between the Cr# of the harzburgites and the proximity or distribution of the samples relative to the ore body, although mineralogically lower Cr# are associated with comparatively higher cpx modal proportions (though still cpx-poor). These findings cannot be explained readily by a single localised event associated with mantle melting or the genesis of the podiform chromite ore body.

The chromite grains in samples Vos-341 and G1742 (Cr# 0.23) are holly-leaf shaped and are characteristic of aggressive resorption. This implies that during the most recent liquid-mantle interaction event, equilibrium between the chromites and liquid was not reached. The disparity between the Cr# compositions and the mineralogy of the harzburgites results from the chromite compositions retaining a fertile mantle signature, possibly the result of mantle conditions restricting the grains from equilibrating during partial melting or interaction with subsequent liquids that have infiltrated the mantle. The mineralogy is consistent with mantle melting and depletion.

In contrast, harzburgites with higher Cr# (>0.40) chromites, which are more typical compositions for depleted harzburgite (*Arai, 1994a; Arai & Yurimoto, 1994*), tend to be subidiomorphic or anhedral. These morphologies indicate that the grains have equilibrated, at least to a greater extent than the holly-leaf shaped grains, during the most recent liquid-mantle interaction event. It is proposed that the greater extent of equilibration achieved accounts for the higher Cr# seen.

Distal dunite

Inter-layered between intervals of harzburgite in the hanging wall and footwall is dunite (distal dunite). These units are comprised of olivine which has been altered to serpentine, the absence of pyroxene porphyroblasts distinguishes the rock type from harzburgite in hand specimen. In thin section, patches of fibrous actinolite are seen. On the Al_2O_3-CaO diagram these samples plot in the dunite field.

The chromite Cr# range is 0.42-0.60, values that increase systematically from the harzburgite Cr# range. The mineralogy and Cr# ratios could be interpreted to result from high degrees of partial melting of the mantle. However, as demonstrated by the tectonic discrimination diagrams, this is not the case. The fO_2-Cr# and TiO_2/Fe^{3+}# - Ga/Fe^{3+}# plots show that the dunites formed by interaction between residual mantle and a percolating melt, i.e. by melt-rock reaction.

The dunites record a pathway of melt through the mantle. The source of the melt, whether a MOR- or SSZ- setting derived melt, is not clear. From the fO_2-Cr# plot it appears that the reacting melt has a MORB composition, with fO_2 values approaching the MOR-SSZ discrimination boundary. On the TiO_2/Fe^{3+}# - Ga/Fe^{3+}# diagram the compositions appear to be transitional having formed from the reaction of melts derived from both a MOR- and SSZ-setting. The samples plot either side of and close to the MOR- and SSZ- discrimination boundaries on both plots. The ambiguous classification of the distal dunite results from the low Fe^{3+} chromite compositions that reflect the chemistry of the melt that the grains last equilibrated with. The Fe^{3+} contents are lower than are expected from equilibration with a melt produced in a SSZ setting. In comparison, three harzburgite samples have higher fO_2 values implying that they have interacted with a more oxidising melt than the dunites, although the Cr# of the harzburgite chromites are lower.

Subidiomorphic chromite morphologies are most common in distal dunites, although, holly-leaf and euhedral shaped grains are also seen. In the distal dunite samples it is common for more than one type of chromite grain morphology to be identified within a single section, despite being compositionally similar. The mixture of grain shapes identified in a sample implies that equilibrium between the chromites and melt was not always achieved, yet the similar compositions of the grains within a sample indicates that chemical equilibrium was reached. It is proposed that the different grain shapes represent multiple generations of chromite that either crystallised from, or equilibrated with, melts of differing compositions. As new melts infiltrated chromites crystallised from previous melt events equilibrated chemically with the new melt composition. The equilibration process is not one of dissolution and re-crystallisation but of chemical exchange, consequently, the

structure of earlier chromite phases are affected by the compositional change causing the grain shape to be distorted (*Mercier and Nicolas, 1975; Auge, 1982*).
The units of distal dunite inter-layered with harzburgite provide evidence of multiple, and based on the geochemistry, compositionally different melt events. Had the melt events infiltrated outwards from the podiform chromitite then a systematic, concentric rock-type progression might be expected as follows;

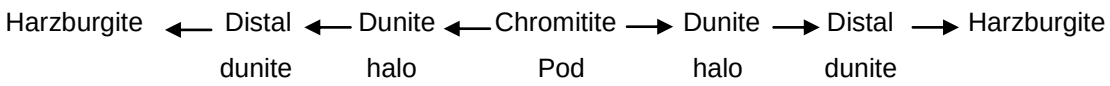

This is not the case. Consequently, the distal dunites are not considered to have formed from the same process as that which formed the chromitite and peripheral dunite halo.

From the TiO_2/Fe^{3+}#-Ga/Fe^{3+}# diagram the distal dunites are interpreted to have formed by interaction between residual mantle harzburgite and a MORB melt. It would not be expected for these units to show significant REE enrichment relating to this event. The reduced pressures in the upper mantle (relative to the lower mantle) result in the destabilisation of orthopyroxene. However, this is at the expense of olivine which crystallises from the melt, forming the dunite melt-rock reacted pathways seen. Furthermore, the REE remain partitioned in the MORB melt. Consequently although MORB melts are primary and LREE-enriched (relative to the residue they form and percolate through) this signature is not inherited by the MORB-reacted dunite formed. In contrast, boninite melts are extremely LREE-enriched, derived from higher degrees of hydrous partial melting they are capable of partitioning greater quantities of LREE into the melt phase (*Pearce et al., 2000*). It is proposed that the REE-enriched profiles seen in the distal dunites, in particular the LREE-enriched profiles, result from a later-stage over-print by the boninite melt or fluids associated the melt. Alternatively it could be that metasomatic fluids introduced during ophiolite emplacement resulted in the remobilisation of these elements and subsequent enrichment profiles seen. A requirement of the LREE-enrichment process is that it occurred without impacting the chromite composition so as to explain why these dunites, in terms of chromite composition and melt-rock reaction model results, possess characteristics of MORB melt-mantle reacted dunite.

The whole rock geochemistry REE patterns and spidergrams indicate that the distal dunite units have been infiltrated by one or more of the liquid events associated with the genesis of the podiform chromitite. On the contrary, the chromite compositions apparently record a different melt-rock reaction event, one that is not associated with the SSZ melt-related podiform chromitite genesis event. The intervals of distal dunite range in thickness from 10 m to approximately 100 m (vertical down hole). They are interpreted to represent focused melt channel-ways where multiple, compositionally different melt events have percolated and reacted with the mantle harzburgite. This explanation accounts for the transitional MOR- and SSZ-melt signatures present in the chromite compositions, the range of chromite morphologies seen, as well as the varying levels of REE depletion and subsequent LREE re-enrichment identified. These dunites record the change between the MOR-setting associated with the palaeo-Uralian ocean basin opening and the SSZ-setting associated with the Magnitogorsk island arc formation.

Dunite halo and ore zone dunite

The halo of dunite that surrounds the chromitite pod is formed of highly serpentinised olivine (>80% serpentinisation). On the Al_2O_3-CaO diagram these samples plot in the dunite field close to the distal dunites and ore zone dunites.

The dunite halo chromites have a Cr# range of 0.50-0.76, they are more chromium-rich than the distal dunite and harzburgite chromites, but less so than the ore zone dunites (Cr# range, 0.77-0.84). A progressive increase in chromite Cr# is noted from the outermost edge of the halo towards and into the ore zone and as the units are located next to one another they are thought to be genetically linked. The Cr#-TiO_2 diagram shows that these dunites formed from the interaction of residual mantle harzburgite with a boninite melt. The ore zone dunites plot in the same field as chromites in peridotites sourced from the present day Izu-Bonin-Mariana fore-arc system. The fO_2-Cr# diagram shows that the chromites record equilibration and/or crystallisation under oxidising conditions, approximately Δlog fO_2 (QFM) 2, values that are synonymous with melts of arc lava affinities. On the TiO_2/Fe^{3+}#-Ga/Fe^{3+}# diagram the samples plot in the SSZ-reacted field also supporting the arc signature interpretation.

The REE profiles of both the dunite halo and ore zone dunite are typically LREE-enriched and are characteristic of an arc derived REE signature. The dunite halo chromite grains are either subidiomorphic or euhedral. The euhedral grains will have crystallised from a boninite melt. In contrast, the subidiomorphic grains result from re-equilibration between earlier stage chromite grains (e.g. chromites in the residual harzburgite) and the infiltrating boninite melt. This would explain the difference between the co-existing morphologies as well as the elevated chromium contents. Only euhedral chromites are seen in the ore zone dunites and it is interpreted that these either crystallised directly from the boninite melt, or that melt through-flow in the ore zone was sustained long enough for total equilibration of any residual chromites (low Cr#) present to be achieved.

9.2 Parental melt composition of the high-Cr Voskhod chromitite

High-Cr chromitite deposits have been interpreted to form from high-Mg boninitic melts (e.g. *Zhou & Robinson, 1994, 1997; Rollinson, 2005, 2008; Page & Barnes, 2009*). The Voskhod chromite ore body is characterised by high-Cr chromite (Cr# ≥ 0.80) having high Mg# and low Ti contents, a composition indicative of having formed from a boninitic parent melt.

Chromite composition is controlled by several factors, the most influential being; oxygen fugacity, pressure and temperature (*Barnes, 1986; Murck & Campbell, 1986; Roeder & Reynolds, 1991*). Additionally, subsolidus equilibration drives divalent ion exchange between co-existing chromite and olivine phases changing the Mg# of chromite and Fo of olivine (*Irvine, 1967; Lehmann, 1983*). The trivalent ion contents of Cr and Al in chromite are considered relatively immobile, although this is a point of some debate. Chromite in equilibrium with a melt will have a Cr/Al ratio that is determined by the Cr_2O_3 and Al_2O_3 composition of the melt (e.g. *Maurel & Maurel, 1982*)

9.2.1 The role of boninite in forming podiform chromitite

Boninite melts characterise forearc settings, forming as a result of intra-oceanic subduction initiation. The melts are typified by high-Mg and high-water contents. The solubility of Cr increases as a function of increasing water content (*Wood & Fraser, 1984; Lange, 1994; McMillan, 1994; Richet et al., 1996*), hence boninites are more Cr-rich compared to other melt types. The BBC boninite lava assemblages located in the south Urals formed in the forearc setting of the Magnitogorsk arc complex. Although not found within the Kempirsai Massif ophiolite sequence, this is the only boninite complex identified in the south Urals to date. The BBC boninites show evidence of having been especially water- and volatile-rich (*Spadea et al., 1998*) and it is inferred that these boninites would have been capable of transporting high Cr contents in the melt phase. It has been reported that boninites are capable of carrying up to 1,200 ppm Cr in the melt (*Cameron & Nisbet, 1982; Malpas et al., 1997*) and experimental melts similar to boninites in composition have been shown to have contents of nearly 2% Cr_2O_3 (*Klingenberg and Kushiro, 1996*). Freeman (1996) calculated that the melting of highly refractory mantle harzburgite could generate melts with Cr contents as great as 3,250 ppm. The potential for high chromium contents mean that a boninite melt is capable, more so than any other arc derived melt, of generating significant quantities of chromite if conditions permit crystallisation. However, even at high Cr concentration levels a significant volume of melt will be required.

Simple calculations of Cr_2O_3 melt content show that for a melt with a Cr_2O_3 content of 2%, to form an 18 Mt chromite deposit with an average Cr_2O_3 grade of 58% would require, 10.44 Mt of Cr_2O_3 and 522 Mt of melt. A melt with a Cr_2O_3 content of 1,200 ppm to form the same sized deposit would require 8,696 Mt of melt.

High-Cr podiform chromitites are considered to have formed deep in the mantle while high-Al chromitites are emplaced at stratigraphically higher levels in the mantle closer to the Moho (*Leblanc & Violette, 1983*). The extremely high Cr content of the Voskhod chromitites (Cr_2O_3 ≥60 %) implies that the deposit is located deep in the mantle.

9.2.2 Water and chromite crystallisation

It has been established that the hydrous component of boninite melts increases the solubility of the Cr in the melt. So it is that a loss of water from the melt would lead to a reduction in the chromium solubility and promote crystallisation. Observations by Pearce et al. (1984) and Roberts (1988) proposed that lavas erupted in SSZ settings had fractionated greater quantities of chromite during ascent through the mantle than lavas that had erupted in MOR settings. However, work by Edwards et al. (2000) predicts that water contained in the melt will not be dissolved prior to the onset of chromite crystallisation, they predict that water will remain dissolved in the melt until after the crystallisation of pyroxenite. Instead of water loss their proposed model causes water to destabilise orthopyroxene which will simultaneously increase the stability field of olivine. The destabilisation of orthopyroxene will increase the SiO_2 content of the melt which will increase the polymerisation network of the melt and decrease the availability of octahedral sites in the melt. The result is that Cr will no longer be soluble in the melt and chromite crystallises. However, the system can change to favour the retention of Cr in the melt if olivine should start to crystallise, this reduces the SiO_2 content of the melt, having the reverse effect on the melt polymerisation network causing Cr to remain soluble.

9.2.3 Melt-rock reaction

Melt-rock reaction, as a mechanism for initiating chromite crystallisation, requires melt to react with mantle harzburgite (or lherzolite) and dissolve pyroxene. The percolation of melt allows for interaction with pyroxenes which increases the Cr and SiO_2 content of the melt providing the chemical conditions required for the crystallisation of chromite (e.g. *Arai 1997*). According to an unpublished calculation by Page (pers comm., 2010) the quantity of orthopyroxene required to cause the precipitation of 18Mt of chromitite is some 7,200 Mt. This raises the question as to whether the reaction between melt and host rock can be maintained. Once the initial wall-rock reaction has taken place there will be a buffer zone of dunite between the channel-way and harzburgite, preventing further interaction. This would seem to hinder continued wall-rock reaction (*Brough pers*

Comm 2010), unless the melt channel-way migrated around the edge of the dunite buffer zone to regain contact with the outer harzburgite.

In relation to the Voskhod deposit there are other possible difficulties with this model. Most crucial is the presence of harzburgite in the hanging wall, situated below a chromite stringer prior to the start of the main ore zone (identified in the down hole profile of drill core V05-24). Had melt-rock reaction accounted for the formation of the 18 Mt Voskhod chromite deposit it would seem likely that this harzburgite unit would have been involved with the melt rock reaction event that took place immediately next to chromite forming channel that required additional silica to continue precipitation of chromite in each new batch. Nevertheless, the addition of silica must be continuous somewhere during the transit to the chamber. It could be argued that this harzburgite unit remained unscathed and that it's reaction with the melt was not required. However, chromite composition and REE data infer otherwise. The chromite in the harzburgite present between the stringer and ore zone has Cr# compositions of 0.47 and 0.36. In contrast, harzburgite further away from the ore zone, in the hanging wall, has Cr# compositions of 0.23, 0.33 and 0.36. Given the difference in composition and the proximity to the ore body, one possibility is that this section of harzburgite has an altered chromite composition that results from buffering between the boninite melt and the residual mantle, however the question still remains why has dunite not formed.

A counter argument may be that the melt has scavenged Cr and SiO_2 through melt interaction with a distal harzburgite source. However, this theory would put the proposed explanation for the formation of the characteristic dunite halo into dispute. The dunite halo that shrouds podiform chromitite deposits, is thought to form by interaction between the melt and country rock. The dissolution of pyroxene phases is deemed to add to the supply of Cr in the melt as well as enhance the SiO_2 content, so promoting the crystallisation of chromite. Given that it is widely noted that the thickness of the dunite halo and chromite deposit size are independent of one another, it seems unfeasible to suggest that the dissolution of pyroxene from the halo would account for the concentrations present in chromitite. However, the increase in SiO_2 in the melt from the dissolution of pyroxene could initiate chromite crystallisation. The crystallisation of chromite from the melt would maintain the silica levels perhaps to those required to sustain chromite

crystallisation. In this sense, once chromite crystallisation is initiated (by an increase of SiO_2 in the melt) the reaction could be self maintaining depending on the availability of Cr in the melt and whether or not olivine also crystallises.

It appears that melt-rock reaction is instigated and driven by the presence of a hydrous component that leads to changes in the melt which promote the crystallisation of chromite

9.3 The Voskhod orebody

The Voskhod chromite deposit is an elongate, sack-like shape ore body, orientated at an oblique angle that narrows (stratigraphically upwards) towards the south west. The encompassing harzburgite host lithology, the internal layering of chromitite and dunite lenses combined with the chromite composition (ore chromite Cr#>0.8) and relative stratigraphic position within the ophiolite sequence are features that characterise this deposit as a podiform chromitite. The data available on the Voskhod ore body has provided a unique opportunity to study the genesis of this massive chromitite deposit, recognised as being one of the largest in the world, contributing to the world's largest podiform chromite ore field, the MOF.

9.3.1 The Voskhod orebody: A record of melt migration through the mantle.

Melcher et al. (1997) documents that the MOF chromite deposits (including the Voskhod deposit) are concordant, deformed type orebodies (following the chromite pod classification of Cassard et al., 1981). Although the majority of the cores drilled from the Voskhod deposit were angled perpendicular, the attempts to retrieve orientated core by drilling at an oblique angle failed. Consequently, it has not been possible in this study to document the relationship between the mineral foliation preserved in the host harzburgite and the orientation of the orebody.

Irrespective of the present day orientation of the orebody relative to the host mantle harzburgite (reportedly concordant (*Melcher et al., 1997*) the Voskhod

chromite pod would originally have been aligned discordant to the mantle mineral foliation (*Cassard et al., 1981*). It is the effect of tectonic rotation, post formation at depth in the mantle, that aligns the pods concordant with the host rock mineral foliation (*Cassard et al., 1981; Nicolas & Jackson, 1982*). This has implications for the formation and emplacement of the chromitite pod.

If the Voskhod chromitite pod is considered as a dyke-like structure, as other authors have previously proposed podiform chromitite pods to be (e.g. *Lago et al., 1982; Leblanc & Ceuleneer, 1992*), then the mechanisms of dyke emplacement in the mantle may provide insight into the genesis of these deposits.

The orientation of a mantle hosted dyke preserves the stress field controlling deformation (*Boudier & Nicola, 1972*). Paterson (1978) and Shaw (1980), proposed that melts could be extracted from the mantle by high pressure, hydraulic fracturing and that this process would create discordant dyke structures. Fluid pressure plays a fundamental role in hydraulic fracturing; the greater the fluid content of the melt the higher the pressure. High fluid pressures can be achieved by melting mantle peridotites (*Nicolas & Jackson, 1982*). If mantle melting is enhanced by the addition of fluids, as is the case in the melting of the mantle in a SSZ setting, then the fluid pressure of the melt generated will be greater still. Large volumes of melt increase the pore pressure in the peridotite, this eventually exceeds the confining pressure (*Nicolas & Jackson, 1982*) leading to melt extraction from the mantle. Melt migration pathways will be orientated perpendicular to the direction of principal stress, forming extensional dykes.

The fluid-rich boninite melts generated in the extensional tectonic setting of a SSZ fore arc, possess all the attributes that facilitate hydraulic fracturing in the mantle; i.e. large volumes of melt and high pressures resulting in the formation of brittle fractures in the mantle. The melt migration preferentially focuses along the brittle fracture network that is aligned perpendicular to the orientation of principal stress (the mantle minerals aligned parallel to the direction of principal stress), forming discordantly orientated dykes. The crystallisation of chromite and olivine from the melt fills the dyke conduits and forms podiform chromitite. Late-stage plastic flow deformation may cause the dykes to become aligned with the peridotite mineral foliation, forming concordant chromitite pods (*Cassard et al., 1981*).

Alternatively, in the event that the melt pressure was insufficient to induce brittle fracturing of the mantle, it has been proposed that kinked, shear zone regions may be exploited by melts percolating through the mantle (*Nicolas & Jackson, 1982; Python & Ceuleneer, 2003*).

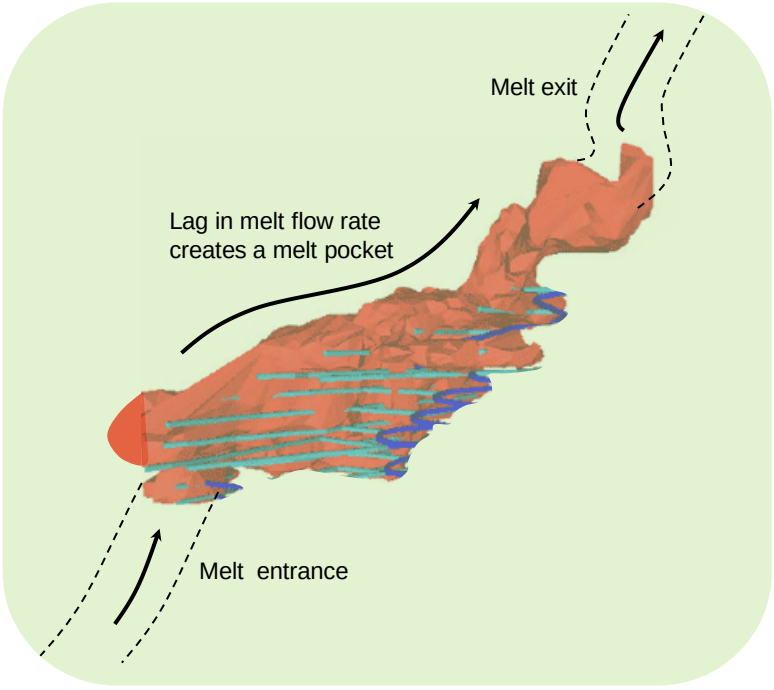

Figure 9.3.1: A 3.D model of the Voskhod chromite deposit

The red mass identifies the ore body. The blue lines indicate the levels planned for mining. Black arrows are drawn to indicate the movement of melt through the region, identifying hypothetical entrance and exit points of the melt flow. Image created with Gemcom software (*Matt Boyes, 2006*) using data collected by the author.

The detailed 3.D ore body model generated by block modelling of the drilling data provides new information on the structure of chromitite pods (Figure 9.3.1). Such regions form sites of focused melt flow during ascent to the crust. The ore body morphology of the Voskhod deposit, is interpreted to be a preserved site of focused melt flow.

9.3.2 Genesis of ore zone dunite and the dunite halo

The multiple stacked chromitite lenses that comprise the ore body are separated by barren dunite units. It is proposed that the interleaved barren dunite units formed from the accumulation of interstitial olivine that was squeezed out from between the chromite grains during densification of the chromite. The evidence of densification, by a process analogous to sintering, is seen preserved in the massive chromite textures i.e. chain textures, grain boundary intergrowths, compaction and annealing textures, corrosion features, triple junctions and grain boundary voids. These features indicate that an unknown volume of olivine was, at one point during the chromitite genesis, present between chromite grains. During chromite densification the olivine migrated, becoming physically separated from the chromite, a process that could explain the barren ore zone dunite. This process may also account, at least in part, for the formation of the dunite halo that characteristically surrounds a podiform chromitite. The deposit could be considered as being comprised of a series of stacked chromitite lenses, each surrounded by a dunite halo and that internally juxtaposing dunite halos form the separating ore zone barren dunite intervals.

It is acknowledged that the formation of the dunite halo by melt-rock reaction between a percolating melt and the host harzburgite, resulting in the dissolution of orthopyroxene and formation of dunite, is also plausible (*Quick, 1981; Fisk, 1986; Kelemen, 1990; Arai & Yurimoto, 1994; Arai, 1997*). However, the proposed model that localised high degrees of partial melting of harzburgite during the orebody formation (*Boudier & Nicola, 1972; Boudier, 1978; Cassard et al., 1981*) produces the dunite halo is improbable in the case of the Voskhod deposit where the Cr# of chromite in the dunite halo reaches 0.76. The degree of partial melting required to achieve a Cr# of 0.76 would have to be greater than 40% (*Jacques & Green, 1980*). Additionally, if high degrees of partial melting were responsible highly depleted LREE profiles would be expected from the dunite halo rocks and these are not seen.

The composition of chromite present in the ore zone dunite is the same as that comprising the chromitite (ore). These chromites may have crystallised from the inter-granular melt. Alternatively the compositions could be achieved by chemical

equilibration between interstitial melt and the chromite in the chromitites and dunites respectively. In contrast, the peripheral dunite halo chromite has a slightly lower Cr# than chromite within the ore body, although the REE and spidergram profiles of the dunite halo and ore zone dunite are similar. The chromite compositions and REE patterns result from equilibration (or melt-rock interaction) between the host harzburgite and small amounts of interstitial melt percolating outwards into the wall-rock away from the ore zone (that is the focus of the melt pathway).

9.4 Compositional variations in chromite from the ore zone

Down hole sampling of massive chromite from drill core V05-13 identified compositional variations in the chromite. The compositional differences are controlled by variations in the MgO%, FeO% and Fe_2O_3% contents of the chromites. It has previously been documented that within a chromitite ore body the chromite composition is essentially homogenous (*Golding, 1975; Melcher et al., 1997*). The findings of this study, in a broad context, support this statement. However, the minor variations identified reveal important information on the genesis of the chromite.

9.4.1 Massive chromite composition variations

MgO>$FeO_{(t)}$ Chromite

The majority of the V05-13 chromites have compositions characterised by MgO% being greater than $FeO_{(t)}$% (classified as MgO>$FeO_{(t)}$ chromites). On the FeO%-Fe_2O_3% diagram these chromites form a negative trend, as FeO% increases Fe_2O_3% decreases. This trend reflects the oxidising conditions that the chromites have been subject to during crystallisation. Under more oxidising conditions FeO will convert to Fe_2O_3 to accommodate the increased availability of oxygen present in the system, under more reducing conditions FeO is favoured. The oxidising conditions are controlled by the chemistry, principally the water content, of the melt. Changes at the source of melting resulting from; the introduction of crustal contaminants (e.g. continental margin sediment), the dehydration of minerals and subsequent production of volatile-rich liquids during slab subduction and/or

variations in the degree of partial melting of the mantle, affect the composition of the melt formed. In addition, the melt will also inherit chemical signatures from the composition of the mantle melted, these are determined by the fertility of the mantle being melted, the degree of partial melting and the composition of the mantle rock which the melt has percolated through and that is present at the site of chromite crystallisation.

The chromites crystallised with greater Fe_2O_3% compositions, under more oxidising conditions, do so from melt pulses that are comparatively more water-rich than melts which crystallise chromites with higher FeO% contents (and lower Fe_2O_3% contents). The trend formed by the MgO>$FeO_{(t)}$ chromites is interpreted to reflect variations in oxygen fugacity conditions within a melt.

The role of water in a melt is two fold. As stated, it will promote the oxidation of FeO to Fe_2O_3. In addition, water also lowers the SiO_2 content of the melt (*Wood & Fraser, 1984; Lange, 1994; McMillan, 1994; Richet et al., 1996*). Lower SiO_2 contents lead to decreased polymerisation of the melt, this increases the availability of octahedral sites causing Cr^{3+} to be more soluble and partition into the melt (*Hess, 1971; 1980; Dick & Bullen, 1984; Murck & Campbell, 1986; Peck & Keays, 1990; Melcher et al., 1997; Edwards et al., 2000*). Consequently, the crystallisation of chromite is inhibited. The retention of Cr^{3+} in the melt results in Al^{3+} and/or Fe^{3+} substituting into the chromite lattice.

$FeO_{(t)}$>MgO Chromite

In the V05-13 chromite dataset a second chromite group was identified with $FeO_{(t)}$% contents greater than MgO% ($FeO_{(t)}$>MgO chromites). These chromites do not form a trend, but plot scattered away from the main MgO>$FeO_{(t)}$ chromite trend to higher FeO% and/or higher Fe_2O_3% values. The higher iron contents of these chromites could result for several reasons;

(i) Subsolidus re-equilibration with interstitial residual olivine
(ii) Contemporaneous crystallisation of olivine and chromite from the melt
(iii) The introduction of a new water-rich pulse of melt interacts with a comparatively reduced (Fe^{2+}-rich) previous melt pulse.

(iv) Chromite composition variation resulting from the melt source and/or mantle heterogeneities

The rationale behind each of these proposed genesis models follows:

Crystallisation of olivine from the melt increases the Fe^{2+}# of the melt and consequently the Fe^{2+}# of contemporaneously crystallised chromite (*Roeder & Reynolds, 1991*). Two mechanisms are proposed that involve chromite and olivine co-existing (i) and (ii).

(i) Subsolidus re-equilibration of chromite with interstitial residual olivine

It is seen from the OSMA plot that harzburgite and distal dunite olivine Fo contents are lower than ore zone dunite olivine Fo contents, which are more magnesium rich. From this it is deduced that residual mantle olivine is more fayalitic than olivine crystallised from the magnesium-rich boninite melt. Alternatively, it may be that olivine is not crystallised directly from the melt, but that in the melt saturated region of the mantle (where chromite crystallisation is most intense) the residual olivine (around which the melt percolates) equilibrates with the melt. This would cause the magnesium content of the residual olivine to increase and the iron content of the melt to be increased, owing to the reciprocal exchange of Fe^{2+}-Mg that occurs during equilibration. Chromite crystallised in the presence of the equilibrated melt would be more comparatively iron-rich. Furthermore, this process would also account for the higher Fo contents of the olivine present within the ore zone.

(ii) Contemporaneous crystallisation of olivine and chromite from the melt

Similar to the process invoked for the subsolidus re-equilibration with interstitial residual olivine, the contemporaneous crystallisation of chromite and olivine will have a similar affect on the melt composition. It is possible for the onset of olivine crystallisation to drive chromite crystallisation. Crystallisation of olivine lowers the SiO_2 content of the melt (*Murase & McBirney, 1973*), causing a decrease in the polymerisation of the melt and in turn the number of octahedral sites available to accommodate Cr in the melt (*Hess, 1971, 1980*). Subsequently the solubility of Cr^{3+} decreases resulting in the crystallisation of chromite (*Dick & Bullen, 1984,*

Murck & Campbell, 1986; Peck & Keays, 1990; Melcher et al., 1997, Edwards et al., 2000). The contemporaneous crystallisation of the two mineral phases, which both incorporate Fe^{2+} and Mg into their respective lattice structures, results in competition for magnesium as well as to obtain chemical equilibrium. This will cause the chromite to have a lower Mg# (be more iron-rich) than if it were the only phase crystallising. The increased availability of iron in the melt explains the compositions of the $FeO_{(t)}$>MgO chromites. Furthermore, a hydrous melt would promote the oxidation of FeO increasing the Fe_2O_3 content of the melt, which could increase the availability of Fe^{3+} to partition into the chromite lattice.

(iii) Melt mixing: The introduction of a new water-rich pulse of melt interacts with a comparatively reduced earlier stage melt.

This model requires that melt is introduced to the mantle in batches, rather than as a continuous flow. If a hydrous (more oxidising, Fe^{3+}-rich) melt batch interacts with a comparatively reduced (Fe^{2+}-rich) melt pulse, the chromite crystallised will have higher FeO% and Fe_2O_3% contents than if chromite crystallised from either of the unmixed melts.

(iv) Chromite composition variation resulting from the melt source and/or mantle heterogeneities

A more simplistic explanation for the differences in the FeO and Fe_2O_3 contents of the chromites could result from compositional differences between melt pulses. Possible causes of compositional difference include ;

- the introduction of a crustal component from the subducting slab (*Gill, 1981; Crawford et al., 1981; Hickey and Frey, 1982; Cameron et al., 1983; Tatsumi et al., 1986; Taylor & Nesbitt,1992; Stolper & Newman, 1994; Schiano & Clocchiati, 1995; Olive et al.,1997*)
- the addition of fluids, derived from the devolatilisation and melting of hydrous minerals (e.g. amphibole) present in the subducting slab to the site of mantle melting (*Gill, 1981; Pearce, 1982; Saunders et al., 1991; Bédard, 1999, Page et al., 2009*)
- the melting of heterogeneous mantle (*Hart, 1988; Van Keken et al., 2002*), could feasibly produce melts with varying compositions.

Chromite crystallising from and equilibrating with these melts will record the chemical difference. The results of sample F1925 help to determine which of these genesis models best fits the Voskhod chromite.

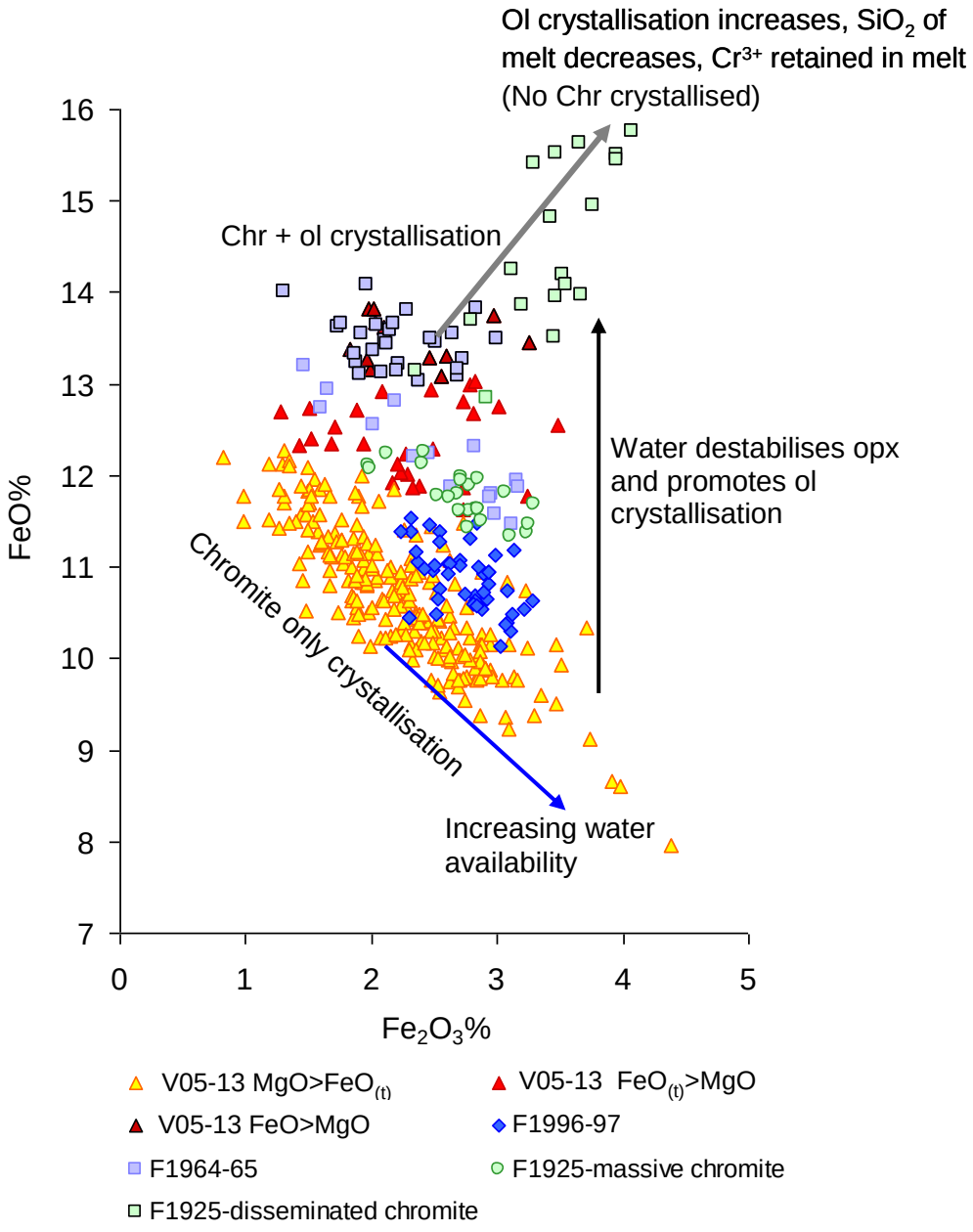

Figure 9.4.1: FeO% against Fe_2O_3% annotated with processes that control chromite and olivine crystallisation from a melt.

Massive chromite grading into disseminated chromite

The chromites in sample F1925 have $FeO_{(t)}$>MgO compositions. However, when viewed in terms of MgO% and FeO% it is seen that the massive chromite sections have MgO% contents greater than FeO and the disseminated chromites have FeO% contents greater than MgO%. The change in composition occurs when the olivine content increases from 18% to 60%, this happens over a 1 cm interval. Simultaneously, the Cr# of chromite decreases with both Cr^{3+} and Al^{3+} decreasing as Fe^{3+} increases. The increase in Fe^{3+} implies that the crystallisation conditions are more oxidising, indicating a more water-rich melt. As the proportion of olivine increases from 60% to 97% the Cr# and Mg# of the co-existing chromite decrease (and FeO% and Fe_2O_3% increase). These observations are consistent with the findings of Roeder & Reynolds (1991) that the crystallisation of olivine increases the Fe^{2+}# of the melt and consequently the Fe^{2+}# of contemporaneously crystallised chromite.

It is possible that the olivine is residual olivine from the host rocks (proposed genesis model (i). The progressive increase in olivine content (into the disseminated section of sample F1925) and cessation of chromite crystallisation could indicate the limit of melt percolation into the host rock. The absence of clino- and orthopyroxene can be explained by melt-rock reaction owing to the presence of water in the melt which would destabilise these minerals and at the same time increases the olivine stability field (*Nicholls & Ringwood, 1973; Kushiro, 1975; Ulmer, 1989*). The decrease in Mg# of the chromite is the result of equilibration between the comparatively iron-rich residual mantle olivine and the magnesium-rich boninitic melt. Equilibration between the melt and olivine raises the Fe^{2+} content of the melt at the expense of Mg which is incorporated into the olivine. The increase in Fe^{2+} in the melt is recorded in the chromite crystallised (hence disseminated chromite has a lower Mg# than massive chromite where no olivine was present to alter the melt composition). Furthermore, the increased abundance of Fe^{2+} in the melt combined with the oxidising conditions (the presence of water) results in Fe^{3+}. The increased availability of Fe^{3+} competes with Al^{3+} and Cr^{3+} for octahedral sites in the chromite lattice. Consequently, the Fe^{3+} content of the chromite also increases.

An alternative model is that olivine crystallises from the melt with chromite (proposed genesis model (ii). In terms of Fe^{2+}-Mg exchange between coexisting melt, chromite and olivine phases, and the potential for the oxidising conditions of the boninite melt to convert Fe^{2+} to Fe^{3+} that subsequently partitions into the chromite lattice, this model is chemically the same as genesis model (i). However, there is one observation that this model (ii) satisfies, that genesis model (i) does not and that is the notable increase in Fe^{3+} in the massive chromite immediately prior to the increase in the modal proportion of olivine. This implies that the conditions of chromite crystallisation become increasingly more oxidising prior to the onset of disseminated chromite, interpreted to reflect an increase in the availability of water in the melt. This would increase the stability field of olivine (and suppress orthopyroxene) and consequently promote olivine crystallisation. The increase in olivine crystallisation would consume SiO_2 from the melt. This would reduce the polymerisation of the melt and increase the availability of octahedral sites in the melt to accommodate Cr^{3+}, causing Cr^{3+} to become more soluble in the melt and consequently inhibit the crystallisation of chromite. As a consequence the crystallisation of chromite would decrease (Figure 9.4.1).

Although this interpretation does not discredit genesis model (i) it is apparent that the observations, both chemical and mineralogical, are better supported by genesis model (ii).

The formation of massive chromite

The crystallisation, or formation, of monomineralic, massive chromite in podiform chromitites has been explained by;

- Cotectic crystallisation of chromite and olivine followed by mechanical separation (*e.g., Thayer, 1969; Lago et al., 1982*).
- Magma mixing resulting in chromite being the only phase to crystallise (*Arai and Yurimoto, 1994; Zhou et al., 1996; Zhou and Robinson, 1997*).
- Variations in the oxygen fugacity of a vapour-rich parent melt and volatile-rich fluids/liquids (*Johan et al., 1983; McElduff and Stumpfl, 1991; Melcher et al., 1997*).

- Post-crystallisation densification by a process similar to that of sintering resulting in the transfer of interstitial minerals (olivine) away from chromite grain boundaries (*Golding, 1975; Hulbert & Von Gruenewaldt, 1985).*

Proenza et al. (1999) state that coevally crystallised chromite and olivine, which is subsequently separated by physical processes, should produce dunite rocks containing chromite with the same composition as that in the chromitite. Further to this statement it is proposed that massive chromite with chromite compositions $FeO_{(t)}$>MgO (formed when both chromite and olivine crystallise from a melt) results from the post-crystallisation separation of chromite and olivine. This being the case the question is, where is the olivine now? The mechanism for chromite-olivine phase separation is unclear, however some suggestions can be made.

The explanations for massive chromite formation by magma mixing (*Arai and Yurimoto, 1994; Zhou et al., 1996; Zhou and Robinson, 1997*) and vapour-rich melt (*Johan et al., 1983; McElduff and Stumpfl, 1991; Melcher et al., 1997*) propose that changes to the composition or oxygen fugacity conditions of the melt result in chromite crystallisation. Consequently, this model is not applicable when addressing the separation of coevally formed chromite and olivine.

The mechanical separation model (*e.g., Thayer, 1969; Lago et al., 1982*) addresses the requirement of contemporaneous chromite-olivine crystallisation from a melt. The process is driven by active melt flow through a conduit as well as convection within the conduit resulting in the separation and dispersion of the chromite and olivine minerals. The samples analysed were collected from drill core where the surrounding three dimensional variations in mineralogy are unknown. It is possible that the co-crystallised olivine may be present nearby.

The effect of post-crystallisation densification (*Golding, 1975; Hulbert & Von Gruenewaldt, 1985)* causes the ore to be exposed to high pressures at temperatures that are not sufficient to cause melting. The result is that co-crystallised, interstitial olivine is squeezed out leaving only chromite. Textural evidence to support densification is preserved in the textures of the massive chromite samples. Furthermore, this model provides an explanation for the composition of the $FeO_{(t)}$>MgO chromites as well as an explanation for the

formation of the dunite halo and inter-layered barren dunite horizons present in the ore zone (see Section 9.3.2). The near constant trivalent cation geochemistry accompanied by the varied divalent geochemistry (changes in Mg#) indicate that the geochemical signature of chromite crystallised with olivine has been preserved, despite the present mineralogy inferring that only chromite crystallised.

Evidence for fine scale cryptic layering within massive chromite

The chromite composition of massive chromite sample F1964-65 changed with depth. The upper and lower 4 cms of the sample recorded lower FeO% values than the middle 5 cms of chromite, where the FeO% was higher (Figure 9.4.4, purple squares). When viewed in comparison with all of the massive chromite data collected (samples V05-13, F1996-97 and F1925, Figure 9.4.4) it appears that the shift to higher FeO% can be explained by a change in the melt conditions towards a phase where chromite and olivine crystallised together. In contrast the upper and lower 4 cms of chromite crystallised from a melt where less or no olivine was contemporaneously crystallising. In terms of the sample mineralogical composition, there is no noticeable increase in the olivine content of the middle 5 cms, meaning that the coevally crystallised olivine has been removed to produce the massive chromite (>80% modal chromite) composition seen.

Similar scale, fine cryptic layering has been reported in massive chromite segregations from the Bushveld Complex (*Naldrett et al., 2009*). The layers were distinguished between using the Mg#-Cr# diagram and resulted in the identification of two compositional trends, termed Trend A and Trend B. These trendlines have been annotated on the Mg#-Cr# diagram for the Voskhod massive chromite data (Figure 9.4.2).

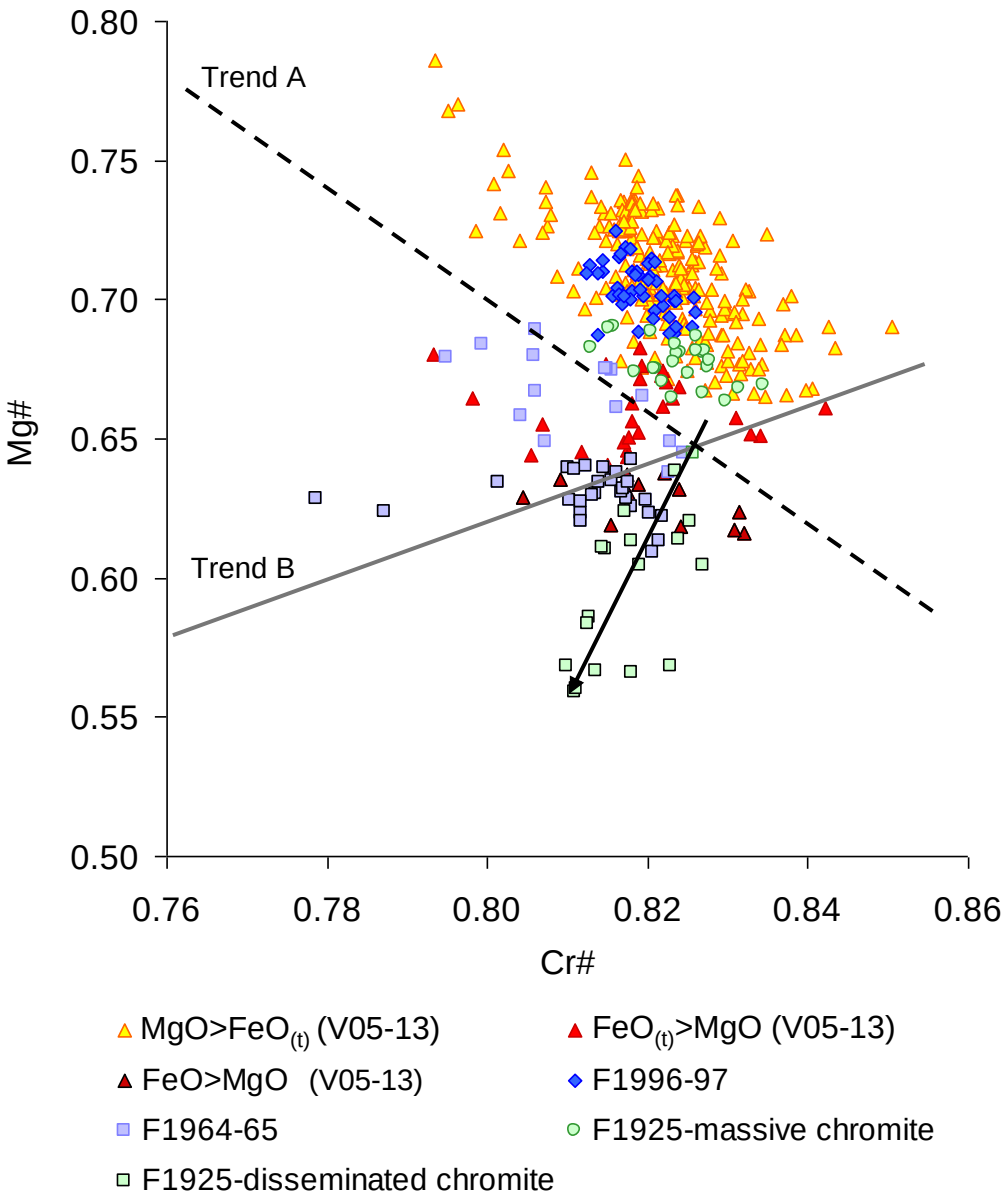

Figure 9.4.2 : Mg# against Cr# for all massive chromite data collected from the Voskhod deposit.

Annotated with trendlines, Trend A (broken black line) and Trend B (solid grey line) after Naldrett et al. (2009). Black arrow indicates the progression of the chromite compositions across sample F1925-disseminated chromite.

Trend A was interpreted to form as a result of the equilibration between chromite and melt only, while Trend B resulted from equilibration between chromite, melt and silicate minerals (namely, olivine and/or orthopyroxene, with/without plagioclase). The principal data trend of the Voskhod massive chromites (formed by datasets V05-13, F1996-97, and F1925-massive chromite) aligns with the orientation of Trend A. This compares favourably with the interpretation presented

in this study where it is proposed that these chromite compositions result from the crystallisation of chromite only from the melt. Furthermore, it is noted that the chromites with lower Mg# values (V05-13 $FeO_{(t)}$>MgO chromites and sample F1964-65) that it is proposed have crystallised out of a melt from which olivine was also crystallising, plot nearly parallel to the orientation of the Trend A trendline as well. This relationship reflects the preferential cation pairing of Cr^{3+} and Fe^{2+} that is complimented by the pairing of Al^{3+} and Mg^{2+} (*Henderson , 1975; Henderson & Wood, 1981; Barnes & Roeder, 2001; Naldrett et al., 2009*)

None of the Voskhod chromite samples align with Trend B, although the chromites from the disseminated chromite section of sample F1925 (green squares, Figure 9.4.2) plot to form a weak negatively correlated trend. The principal control on the formation of Trend B requires that a co-existing trivalent cation-bearing mineral (orthopyroxene or plagioclase) is crystallised contemporaneously from the melt with chromite. The addition to the chromite crystallising system of a mineral into which trivalent cations can partition, introduces another control on the chromite composition (the introduction of olivine controls the Mg-Fe^{2+} composition). In the case of the Voskhod chromite genesis, no other mineral phase present can accommodate trivalent cations and consequently there is no competition for these components. As a result, the controls governing the formation of Trend B are not applicable to the formation of the Voskhod chromite. Instead, the variation in Cr# is interpreted to be controlled solely by the presence of water and the potential this has to increase in Fe_2O_3 in the melt system (which could lower the chromite Cr#). Water will also promote olivine stabilisation at the expense of orthopyroxene; an increase in olivine would lower the Mg# of chromite. The addition of water alone to the system can potentially explain the weak negative trend produced by F1925-disseminated chromite.

9.4.2 A rationale for the genesis of co-existing MgO>$FeO_{(t)}$ and $FeO_{(t)}$>MgO chromites in massive chromite

In dataset V05-13, nine samples were found to contain a mixture of both MgO>$FeO_{(t)}$ and $FeO_{(t)}$>MgO chromites.

Melt-crystallisation models have been proposed to explain the genesis of each chromite group defined (i.e. $MgO>FeO_{(t)}$ and $FeO_{(t)}>MgO$ chromites). The models are independent of one another, such that the two types of chromite cannot crystallise simultaneously from the same parent melt. Consequently, the observation that both types of chromite are present in a single sample (of millimetre dimension) requires explanation.

The post-crystallisation densification model does not explain the mixed chromite compositions, however, the mechanical separation model can (e.g. *Thayer, 1969; Lago et al., 1982*). It allows for the accumulation of chromite grains some of which may have crystallised from melts with olivine. In addition to the chromite and olivine minerals separating, it seems feasible that the accumulating chromite grains could become mixed together. After all, the region of melt flow is not a stagnant environment. This could result in chromite grains crystallised from different melt batches to settle in close proximity to one another and become mixed.

An alternative explanation centres on subsolidus equilibration and the interaction of small quantities of interstitial olivine with chromite grain boundaries.

Subsolidus re-equilibration: Interstitial olivine and chromite grain boundaries

During post-crystallisation cooling of a system where chromite and olivine coexist, subsolidus re-equilibration can take place. When chromite is the dominant mineral phase substitution of Mg (from chromite) into olivine occurs at the expense of Fe^{2+}. Although the effect will be most notable in the composition of the minor mineral phase present (i.e. olivine) the process can potentially cause the Mg# of the chromite to decrease while the trivalent cations remain essentially unaffected (*Kamenetsky et al., 2001*). It was stated in the analytical procedure that during data acquisition the centre of grains were analysed so as to avoid any grain boundary, alteration-induced, compositional variations that might be present. The study of the massive chromite textures found small amounts of interstitial olivine present between grains, trapped along grain boundaries and as inclusions within some grains. Despite the efforts taken to avoid grain boundary edges there is no way on knowing the proximity of a grain boundary edge with depth from the sample surface. Consequently, it is feasible that some analyses may have been

acquired from some grains where a sub-surface grain boundary was present and where it is possible that subsolidus equilibration could have taken place between the trapped olivine and the chromite grain boundary. If this were the case, the composition of chromite at the grain boundary edge would be expected to have a lower Mg# (Figure 9.4.4).

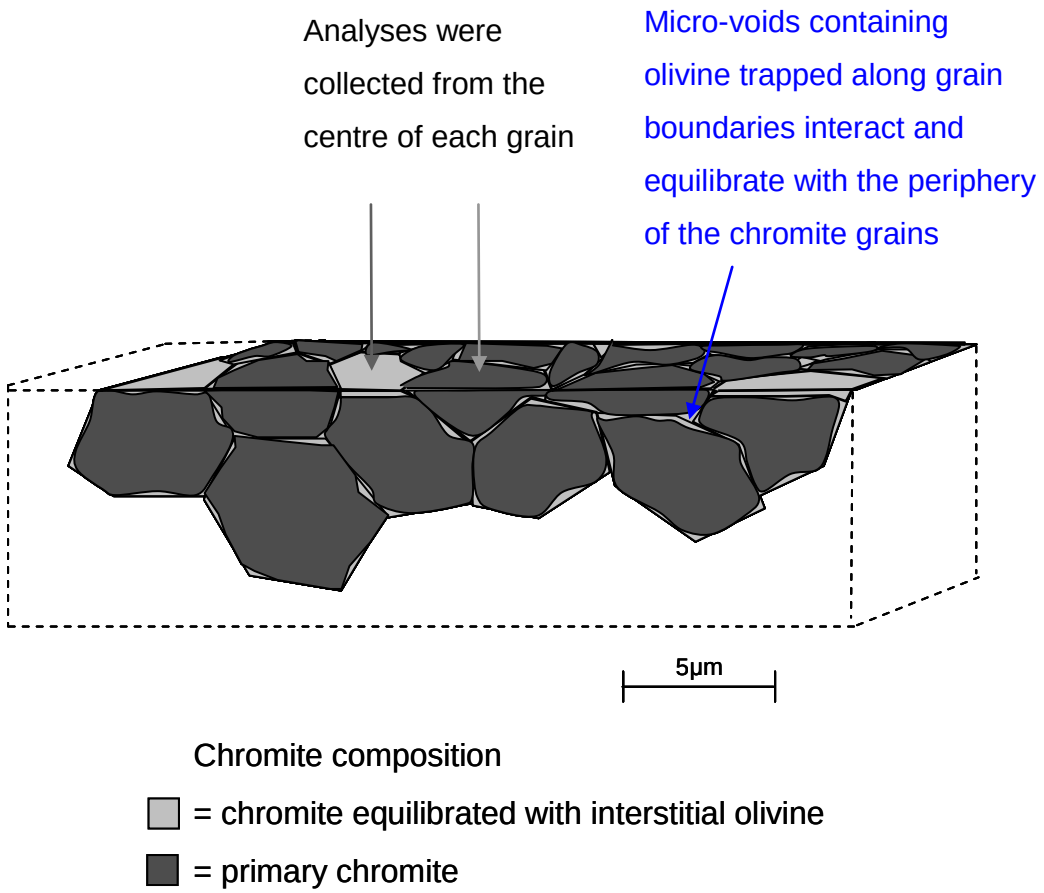

Figure 9.4.3: A schematic cross section profile of a massive chromite sample illustrating the unknown proximity of a grain boundary with depth.

It is not possible to determine whether or not subsolidus re-equilibration at chromite grain boundary edges has occurred. However, the process could explain the formation of sections that are comprised of mixed $FeO_{(t)}$>MgO and MgO>$FeO_{(t)}$ chromite compositions (as seen in dataset V05-13), in particular when only FeO% is increased and Fe_2O_3% values are maintained in a range characteristic of the MgO>$FeO_{(t)}$ chromites. Similarly this mechanism would explain the close proximity of the V05-13 $FeO_{(t)}$>MgO chromites (from mixed chromite composition samples)

to the main data trend (formed by the MgO>$FeO_{(t)}$ chromites) on the Mg#-Cr# plot (Figure 9.4.4).

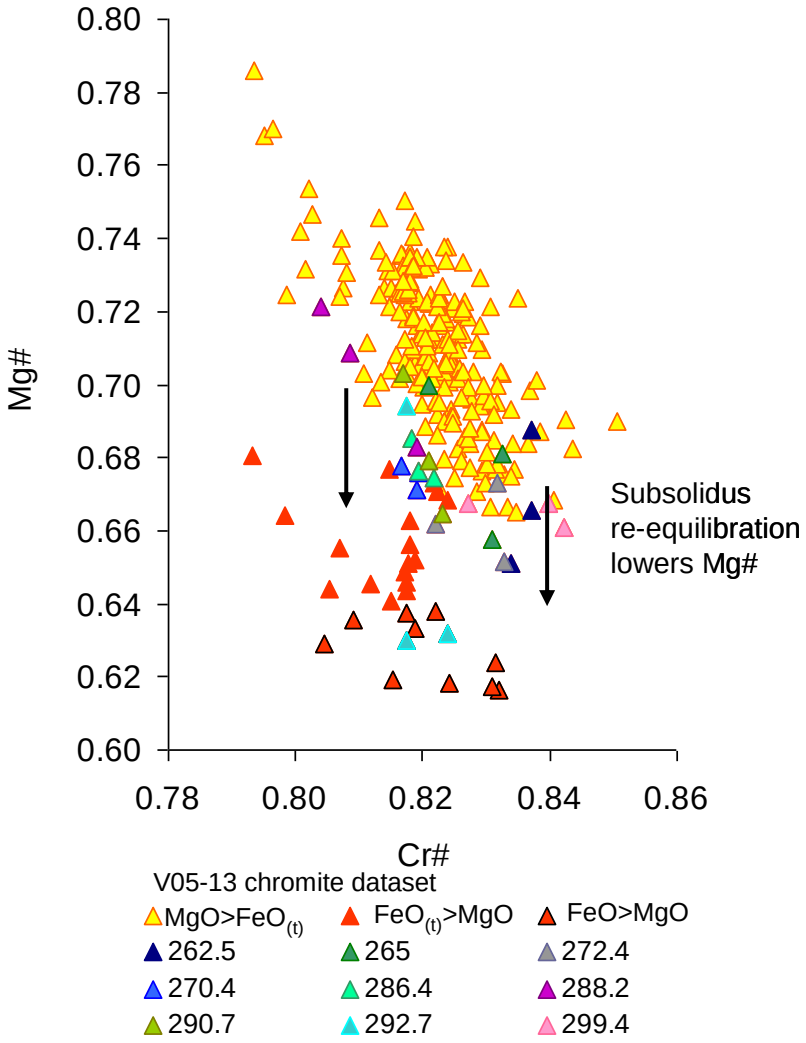

Figure 9.4.4: Mg# against Cr# indicating the proposed geochemical change in chromite composition resulting from subsolidus re-equilibration between chromite with interstitial olivine.

The coloured triangles correspond to the 9 samples in dataset V05-13 with results of mixed $FeO_{(t)}$>MgO and MgO>$FeO_{(t)}$ chromite compositions. With the exception of sample 292.7, the $FeO_{(t)}$>MgO chromites plot close to the main data trend formed by the MgO>$FeO_{(t)}$ chromites.

Corrosion textures in massive chromite

Irregular, cuspate grain morphologies present in the massive chromite samples are evidence of disequilibrium, indicating that the grains were not in chemical equilibrium with the melt, crystallised olivine and/or host rock they were

crystallising from and/or within (Chapter 5, Section 5.5.6). Two theories are proposed:

1) It is possible that olivine was not necessarily squeezed out, but could have been squeezed in, as a melt from which olivine later crystallised. It is possible that a later stage melt could have percolated been between chromite grains before the grains had fully consolidated. An influx of new melt of a different composition could feasibly be out of equilibrium with the compositions of the chromite grains, resulting in the development of the corrosion textures seen.

2) Is the olivine a product of crystallisation from a melt or a constituent of mantle residue host? If it is sourced from the mantle residue then it is feasible that the chromite Mg# will be out of equilibrium with that of the mantle olivine. In contrast, contemporaneously crystallised chromite and olivine, derived from the same parent melt, would be expected to be in equilibrium with one another and corrosion textures would not be expected to form.

A proposed source of chromium and other unique conditions that contributed to the formation of the Voskhod deposit

The source of the chromium that has formed the Voskhod deposit is an enigmatic point. It seems that to generate the volume of chromite contained in the Voskhod pod (18 Mt), (remembering that an additional 220 Mt is present close by in the MOF), an extraordinary amount of chromium must first be concentrated in the melt. It does not seem realistic for such quantities to have been solely scavenged from clinopyroxene present in depleted mantle harzburgite. However, the geochemical evidence indicates that the mantle may not have been a depleted harzburgite, at least not in the usual sense, given the low Cr# values (0.2) and LREE-depleted REE profiles are analogous with fertile mantle lherzolite. Yet the modal mineral proportions of olivine, clino- and orthopyroxene are analogous with harzburgite. It seems that the contrasting and unusual geochemistry and mineralogy is key to understanding the unique processes that resulted in such an enormous amount of chromite to crystallise. If an exceptionally water-rich boninite melt had percolated through a section of fertile mantle, the unusually high water content would be favourable for the destabilisation and dissolution of the pyroxene phases, which would be abundant in a fertile mantle section. It is possible that the

initial stage did not involve a melt but was a fluid driven event and that the resulting chromium-enriched fluid contemporaneously traversed the same conduit pathways through the mantle as the boninite melts. This would effectively "upgrade" the boninite chromium content.

Also in support of the unique setting conditions required for the genesis of the Voskhod deposit, it seems that the melt flow was particularly well focused as demonstrated by the change in Cr# from 0.84 to 0.2 over a distance of 142 m. It is possible that reports of other high-Cr podiform chromite deposits being set in depleted harzburgite result from widespread, diffuse melt percolation. Depleted harzburgite host rocks with Cr# of ~0.5 that typically host the high-Cr podiform chromitites (e.g. *Arai, 1994a*) may in fact be an extension of melt percolation resulting in melt-rock interaction and the incomplete re-equilibration of residual mantle chromite, in mantle regions where melt channel-ways are not well established. The typical U-shaped REE profiles of harzburgite rocks support this concept. The U-shaped REE profiles resulting from LREE-depletion followed by an LREE-enrichment event could be explained by late-stage boninite melt infiltrating a mantle residue. The pervasive infiltration of the boninite would also account for the widespread intermediate Cr# values that typify depleted harzburgite. A diffused, percolating boninite will not crystallise mass concentrations of chromite in localised pockets. It is proposed that the low Cr# values seen at Voskhod represent the limit of the diffusion of the boninite (and/or melt associated fluids) into the mantle. If this scenario is correct, then the intense focused flow of the boninite melt would also contribute to the favourable conditions that permitted the crystallisation and concentration of chromite that forms the Voskhod ore body.

Conditions that would favour the formation of a large accumulation of chromium-rich chromite would be:

- A fertile source from which large amounts of chromium could be acquired/extracted.
- A suitable fluid-rich melt that could accommodate and transport the chromium at high concentrations.
- A source of the fluid-rich melt that could be sustained for a long time period.
- A localised site where conditions promoted the crystallisation and accumulation of chromite.

- A focused melt flow, such that melt does not diffuse into the mantle wall rock being ‘lost’.

10. Conclusions

Since the early attempts to develop a podiform chromitite genesis model (e.g. *Thayer, 1964, 1969, 1970; Dickey, 1975; Greenbaum, 1977*) to those of more recent times (e.g*. Rollinson, 2005, 2008; Page & Barnes. 2009; Page et al., 2009; Merlini et al., 2011*) the research conducted frequently propose models substantiated on the basis of a relatively one dimensional investigative approach. Studies have been conducted to assess the;

- Ore body chromite compositions
- Mineralogy inclusions trapped in chromite ores
- Whole rock geochemistry of the host peridotite and dunite assemblages
- Mineralogy and ore textures

The results of each study have provided new insights and developed new concepts that have helped to determine the processes responsible for podiform chromitite formation. However, as yet, no one study has provided a coherent model to satisfy all podiform chromitite deposits.

The samples analysed from the Voskhod deposit ore zone and the hanging wall and footwall, form a unique dataset acquired from an orebody that forms part of the world's largest podiform chromitite ore field, the MOF. As part of a world class ore field it is likely that the genesis of the Voskhod deposit resulted from unique processes. None-the-less, the detailed study of the mantle host-rocks and ores; mineralogy, textures, whole rock geochemistry, spatial relationships, as well as grain specific chromite and olivine composition studies, combine the approaches taken by previous workers to create a genesis model for the Voskhod deposit.

Geological setting, deposit morphology and internal variation

The Voskhod deposit is a podiform chromitite deposit hosted in the upper mantle of the Kempirsai Massif. The mantle host lithologies are dominantly comprised of fertile MOR harzburgite and depleted harzburgite that has undergone between 15-18% partial melting. Dunites (termed distal dunites) are also present in the hanging wall

and foot wall units. These possess a transitional MOR-SSZ setting geochemical signature the result of mantle that has interacted with MORB and boninite melts.

The ore body has an elongate, kinked, pod morphology that narrows at either end. It is orientated at ~35°, being closest to surface in the south west, deepening to the north. The internal structure of the ore body is comprised of a series of stacked chromitite lenses. In some cases these appear to be interconnected forming a chromitite network. Chromitite lenses are separated by barren or weakly mineralised intensely serpentinised dunite units. The style of chromite mineralisation varies, massive chromite is most prevalent at the centre and to the north of the ore body where layers of massive chromitite (>80% chromite) reach up to 45 m in thickness. To the south of the centre and south west mineralisation is less intense; lenses become thinner and are often comprised of disseminated chromite.

Chromite grain morphologies

The holly-leaf shape and subidiomorphic chromite grain morphologies indicate that the most recent chromite and melt interaction event did not reach equilibrium. These grain shapes are found in the hanging wall and footwall host harzburgite and distal dunite units where evidence of MORB and SSZ melt percolation is recorded.

Euhedral grains are found in the dunite halo and ore zone. The shape is consistent with full equilibration between melt and residual chromite. Alternatively these grains may have crystallised directly from the melt. A SSZ melt signature is recorded in the composition of these chromites. It is not feasible for the exceptionally large volume of chromite that comprises the ore body to have formed from equilibrated residual chromite, rather the ore zone chromite has crystallised directly from the SSZ melt.

Whole rock geochemistry

REE profiles indicate that the host units have been subject to multiple melt (and or fluid) events which caused element mobilisation. The first phase resulted in the depletion of the host rocks forming LREE-depleted profiles, this event is associated with partial melting of the mantle. The second, a later stage event, resulted in refertilisation of the mantle by a LREE-enriched boninite melt. There is some

indication that there has been a late stage fluid remobilisation event, this would have occurred during ophiolite emplacement. However, the evidence to support this theory is inconclusive.

Spider diagrams show the Voskhod host and ore zone rocks have strong positive Ba, Nb-Ta (±Th), Zr-Hf signatures. The Nb-Ta (±Th) and Zr-Hf positive anomalies are independent of one another; each signature is the result of a different melt or fluid event, neither is associated with LREE-enrichment or LREE-depletion. The Nb-Ta (±Th) and Zr-Hf anomalies are identical to those identified of the TMO Quebec, Canada (*Page et al., 2009*). In addition, comparison of the TMO boninites with the TMO mantle rock signatures and the Voskhod mantle rocks with the BBC boninite signatures shows remarkable similarities. It is thought that the BBC boninites are the surface expression of the boninite melt which when percolating the upper mantle formed the Voskhod podiform chromite. The anomalous trace element signatures are attributed to the addition of a continental margin derived sediment contaminant at the site of melting. It is proposed that the addition of fluids or water associated with the sediment component have enhanced the melt's capability to carry chromium.

Tectonic evolution recorded by the Voskhod host and ore rocks

A complex tectonic evolution is evident from the multiple geochemical signatures recorded in the host harzburgite and dunite rocks. These are interpreted to result from subduction beneath an oceanic ridge system, i.e. the initiation of subduction along a transform fault (*Meijer, 1980*). In this scenario boninite melts would have formed when slab-derived fluids percolated the former MOR spreading region while a MORB-type geotherm was still present, causing shallow melting of a refractory source. This model explains the presence of:

i) Residual-MOR harzburgite; the result of dry partial melting of a fertile mantle source. This is remnant of the uprising mantle diapir that formed during the opening of the palaeo-Uralian ocean basin, marking the transition from a passive continental margin to a mid ocean ridge setting.

ii) MOR-reacted dunite; MORB melt-rock reaction pathways that are the remnant conduit feeders previously supplying the mid ocean ridge spreading site in the palaeo-Uralian ocean basin.

iii) SSZ-reacted harzburgite and dunite; record a boninite melt-rock reaction pathway. The initiation of subduction instigated by the onset of the palaeo-Uralian ocean basin closure resulted in hydrous melting of the depleted mantle. This formed boninite melts that ascended and erupted in a forearc setting. The BBC boninite lavas are the preserved crustal expression of the erupted boninite melts. The forearc was the tectonic setting precursor to the development of the Magnitgorsk island arc.

A modern day tectonic setting which is analogous to that recorded by the Voskhod deposit and its surrounding host rocks would be the Conical Seamount in the Izu-Bonin-Mariana forearc system (*Pearce et al., 2000*). It is a site where reaction between a mantle residue of ~15% partial melting and a boninite melt is taking place.

Conditions required for the formation of a super-sized podiform chromitite deposit

A boninite melt enriched with fluids, contaminated by distal continental margin sediments, provided the source of chromium that formed the deposit. The continental margin sediment component may well have contributed significantly to enhancing the chromium content of the melt. Boninites are typically water-rich melts and high water contents are favourable for the transport of chromium in the melt promoting chromium solubility. The initiation of orthopyroxene dissolution, induced by the reaction between water and the mantle, would have increased the SiO_2 content of the melt and caused a reduction in the number of octahedral sites available in the melt to accommodate chromium. Consequently chromite crystallised.

To form an 18 Mt chromite deposit where the average Cr_2O_3% composition of chromite is ~ 58% Cr_2O_3%, not only must the chromium concentration of the melt be high, exceptionally large quantities of melt are also needed. This is likely to have been achieved by a long lived subduction event. The hydrous nature of the boninite melt resulted in high fluid pressures in the melt that exceeded the confining pressure of the mantle rock. The high pressure difference led to hydraulic fracturing and brittle failure

of the mantle creating a conduit pathway that the boninite melt exploited and migrated through. This conduit must have been open and subjected to large volumes of melt through-flow, without redirection, to allow such massive volumes of chromite to accumulate in one place. The short distance (142 m) between the ore zone and occurrence of residual MOR harzburgite indicates that little melt was lost from the melt conduit by outward melt percolation into the wallrock. This is additional evidence of the contrasting pressure difference between the melt and the host mantle.

A theory to explain the genesis of massive chromite

The study of massive chromite identified two chromite groups on the basis of MgO and $FeO_{(t)}$ contents termed MgO>$FeO_{(tot)}$ and $FeO_{(tot)}$>MgO chromites. The MgO>$FeO_{(t)}$ chromite composition was dominant throughout the 45 m V05-13 drill core section, while $FeO_{(t)}$>MgO chromite was identified at irregular intervals. The $FeO_{(t)}$>MgO chromites occurred either as a single anomalous grain within a sample otherwise comprised of MgO>$FeO_{(t)}$ or as the composition of all three grains analysed in a sample. The MgO>$FeO_{(t)}$ chromite forms when chromite is the only phase crystallizing from a melt. In contrast, the $FeO_{(t)}$>MgO chromites form from another process involving the co-existence of olivine, either by contemporaneous crystallisation of olivine with chromite from the melt, or as a re-equilibration effect resulting from the interaction of chromite grain boundaries and small amounts of interstitially trapped olivine. The olivine involved in the latter scenario may either have crystallised contemporaneously from the melt with chromite, or alternatively be olivine from the mantle that was interstitially trapped between crystallising chromite grains during melt percolation. $FeO_{(t)}$>MgO chromites that crystallised with olivine from a melt have lower Mg# than chromite that re-equilibrated with interstitial olivine.

The formation of $FeO_{(t)}$>MgO massive chromite (that is interpreted to have crystallised with olivine from the melt) is explained to result either from mechanical sorting (by models such as that proposed by Lago et al. (1982) or, and the more favourable explanation, by the densification of chromite (*Golding, 1975*). Densification occurs as a post crystallisation process, similar to sintering, which results in the separation of the olivine and chromite phases. Olivine is effectively squeezed out from between the chromite grains and relocated away from the chromite. The separation of olivine by

this process explains the inter-layered barren dunite intervals that exist between the mineralized chromitite horizons, as well as possibly contributing the formation of the dunite halo. The interpretation is supported by the evidence of densification features; e.g. grain boundary merger, annealing textures, chain textures and olivine filled micro-voids along chromite-chromite grain boundaries that are seen in the massive chromite sections.

Fine scale cryptic layering

There is some indication that fine scale layering (4-5 cm scale layers) has been preserved in the chromite (sample F1964-65), however further work is required to substantiate this as the evidence to date is limited.

Grading from massive chromite to disseminated chromite: Changes in melt conditions

Grading from massive chromite into disseminated chromite is driven by the addition of water-rich fluids to the melt. This results in the destabilisation of orthopyroxene, the stabilisation and crystallisation of olivine from the melt. The SiO_2 content of the melt is lowered, reducing the polymerisation of the melt and increasing the availability of octahedral sites in the melt that accommodate chromium. Consequently chromium is retained in the melt, chromite crystallisation is inhibited and the modal chromite content decreases. For contemporaneous chromite and olivine crystallisation to be sustained the abundance of chromium in the melt must exceed the ability of the melt to carry incorporate chromium, so forcing chromite to crystallise. This might be achieved by fluctuations in the introduction of water-rich melt pulses.

Appendix A- Methods

Sample Preparation of powders

Rock samples collected from the Voskhod drill core were prepared following the standard procedures of the analytical geochemical facilities at Cardiff University during 2008-2010. Specimens weighing between 100 – 150 g were cut to size, weathered surfaces and vein material was removed using a diamond saw. The specimens were crushed to chip size using a clean steel jaw crusher and then milled to a fine powder using an agate planetary ball mill. The powders produced were collected and stored in clean plastic bags.

Loss on Ignition (LOI) analysis

Of the powders produced approximately 2g was placed in a small ceramic crucible and heated for two hours in a muffle furnace at 900°C to drive off volatiles, CO_2 and H_2O. After 2 hours the sample residues were removed from the furnace, allowed to cool and re-weighed to calculate the loss on ignition (LOI). The ignited powders were placed in sealed plastic bags and stored in a desiccator.

The LOI was calculated using the equation

LOI (wt.%) = 100 x (Mass of wet powder-Mass of ignited powder)/Mass of wet powder

The process of heating in the furnace resulted in all iron being oxidised from Fe^{2+} to Fe^{3+} hence all iron in analyses obtained from the ignited powders was reported as Fe_2O_3.

Sample preparation for dissolution of peridotites by $LiBO_2$ fusion:

1 – 0.1 g (± 0.001 g) of the ignited sample was mixed with 0.6 g (± 0.005g) of lithium metaborate flux (Alfa Aesar Spectroflux 100B) in acid washed platinum-rhodium crucibles.

2- 10-15 drops of lithium iodide wetting agent (20% vol LiI) was added to the sample/flux mixture.

3- The crucibles were then placed on a Claisse FLUXY automated fusion system and heated at 900°C over a propane burner fusing the sample/flux mixture.
4- After fusion the melt was poured into a 250 ml Teflon beaker containing 30 ml of 10% HNO_3 and 20 ml 18.2 MΩ deionised water.
5- The solution was stirred on a hotplate using a magnetic stirrer until the entire fused glass sample dissolved.
6- The resulting clear solution was spiked with 1ml of 100 ppm Rh solution as an internal standard.
7- Using deionised water (18.2 MΩ) the solution volume was made up to 100 ml.
Certified reference materials JB-1A and BIR-1 as well as a blank were prepared and run with each round of analyses. These samples were used for calibration and monitoring data quality.

Analysis of fusion solutions on ICP-OES

The major element components (Si, Ti, Al, Fe, Mn, Mg, Ca, K, Na and P reported as oxides wt %) and minor elements (Sc, V, Cr, Co, ni, Cu, Sr, Zr, Y and Ba reported as elements in ppm) were measured using the Jobin Yvon Horiba ULTIMA 2 ICP-OES instrument at Cardiff University operated by Dr. I. McDonald and Dr. L. Woolley.

Calibration was performed using a procedural blank and solutions of the international certified materials JB-1A and BIR-1. The addition of 1 ppm Rh spike to the fusion solution was used as an internal standard to allow for correction of drift over the course of the run. Analysis of JB-1A solution was repeated every 6 unknowns as an external check on instrumental drift and corrected by interpolation. Each analysis of a solution was the average of 3 repeat measurements of intensity from which the standard deviation was used to calculate the limits of detection and quantification. Accuracy was assessed by routine analysis of certified reference materials JB-1A (basalt) and BIR-1 (peridotite) as unknowns.

Analysis of Fusion Solutions by ICP-MS

The rare earth elements (REE), Ti, V, Cr, Mn, Co, Fe, Ni, Cu, Zn, Ga, Rb, Sr, Y, Zr, Nb, Ba, Hf, Ta, Pb, Th and U were analysed on the Thermo Elemental X Series (X7) ICP-MS system at Cardiff University, operated by Dr. I. McDonald.

The same rock solutions including standards and blanks used in calibration and monitoring, that were used for the ICP-OES were diluted for the ICP-MS using 1 ml of a Rh spike was added as an internal standard to 1 ml of sample solution to correct for instrumental drift at high masses. This was diluted with 8 ml of 2 % HNO_3 to produce a working volume of 10 ml solution, calibration was performed using the procedural blank reference materials, BIR-1 and JB-1A. Analysis of solution X was repeated every six unknown analyses as an external check on instrumental drift. Each analysis of a solution was the average of 4 repeat measurement of counts per second from which the standard deviation was used to calculate limits of detection and quantification (see section X). Accuracy was assessed by routine analysis of certified reference materials JB-1A (basalt) and BIR-1 (peridotite) as unknowns.

Procedure: SEM analysis

The 46 chromite samples selected were analysed at Cardiff University using an analytical LEO S360 scanning electron microscope (A-S.E.M) using wave-dispersive (W.D) analysis.

The A-SEM comprises; a Cambridge Instruments (ZEISS SMT) LEO S360 scanning electron microscope, an Oxford Instruments INCA ENERGY X-ray analyser, for energy dispersive X-ray analysis (EDX) and an Oxford Instruments INCA WAVE X-ray analyser, for wave dispersive X-ray analysis (WDX).

Registered standards (No. 2399) from Micro-Analysis Consultants Ltd. provided a range of natural and artificial standards used to calibrate the SEM. A cobalt standard was used for quantitative optimisation to correct for machine drift. When conducting W.DX analysis an automated screen prompt from the INCA software to quantitatively optimise appeared every 20 minutes. Additionally when changing between samples quantitative analysis was carried out on the cobalt standard.

During quantitative optimisation a count time of 70 s was selected and a dead time of 40-45% was run. The major and minor element compositions of the chromite samples were determined using in-situ microbeam techniques. Major elements Cr, Al, Fe and Mg and trace elements Ti, V, Mn, Co, Ni and Zn were analysed by WDX with count times of 20 s and an additional 15 s background count. Chromites were analysed using an electron gun to generate an electron beam. The electron beam was accelerated to 20 kV, having a 20 nA beam current and a uniform beam diameter (approximately 10-15 nm). Result totals exceeding 100 $\pm$ 1.0 % were discarded.

Procedure: Standard EMP

Chromite and olivine were analysed for the major and minor element compositions using a wavelength dispersive electron microprobe on the three – spectrometer CAMECA SX50 at the Open University, Milton Keynes. Samples were analysed with a 15kV accelerating voltage, 20nA beam current and a fixed beam size of approximately 1µm. Calibration was carried out on metals (Cr, Fe, Ti, V, Mn, Ni and Zn), synthetic oxides (Al_2O_3, Cr_2O_3 and Fe_2O_3). Counting times for the analysis of chromite were 15s for Si, Fe, Mg, Al, Cr, Ni, Mn and Zn. The analysis of the minor element Ti, integral to the study and work of this chapter, was analysed for a longer count time of 50s. The detection limit was 0.02 wt %.

PAP Φ – ρ – Z corrections were used in the data reduction (Pouchou & Pichoir, 1991). FeO and Fe_2O_3 in chromite were determined using the charge balance and stoichiometry calculations of Carmichael, 1967.

The standard EMP procedure was carried out on 3 chromites and 3 olivines per sample to enable oxygen fugacity and Cr# values to be calculated and an average value obtained for each slide.

Oxygen fugacity: detailed procedure for accurate ferric iron

The method for determining oxygen fugacity (fO_2) from chromite in this study follows the procedure employed by the authors whose data are used to define the discrimination fields MOR, arc and SSZ peridotites in Chapter 6 (i.e. Bryndzia & Wood, 1990; Parkinson & Pearce, 1998; Parkinson & Arculus, 1999; Pearce et al., 2000). This ensures that the data from this study is directly comparable to their data.

Oxygen fugacity (fO_2) was determined from the Fe^{2+}-Fe^{3+} equilibria between olivine, orthopyroxene and spinel based on the reaction $6Fe_2SiO_4 + O_2 = 3 Fe_2Si_2O_6 + 2Fe_3O_4$. Oxygen fugacity is presented as $\Delta\log fO_2$(FMQ), which refers to the deviation from the quartz-fayalite-magnetite (QFM) buffer at a specified temperature and pressure and is expressed in log units. Temperatures are calculated using the Fe-Mg olivine spinel exchange thermometer of Ballhaus et al.

(1991). The lack of a suitable barometer for spinel peridotites means that 1GPa was used in the calculation following Parkinson and Pearce (1998) and Parkinson & Arculus (1999). Calibrations using ol-opx-sp equilibria (Nell & Wood, 1991) and ol-sp equilibria (Ballhaus et al., 1991) five fO_2 values within 0.2-0.3 log units of each other (Parkinson & Arculus, 1999). The calibration of Ballhaus et al. (1991) was used in this study so that it could be applied to both harzburgite and dunite samples.

Accurate and precise determination of ferric iron content of chromite is required to calculate fO_2. This was achieved using the method of Wood & Virgo (1989) which is based on chromite standards that have well characterised $Fe^{3+}/\Sigma Fe$ ratios (by Mossbauer spectroscopy) to correct the EMP data. Wood & Virgo (1989) argue that ferric iron concentrations calculated by EMP analysis using charge balance and assuming spinel stoichiometry is not accurate enough for fO_2 calculations because they are sensitive to errors in Al_2O_3 in the spinel analyses. Wood & Virgo (1989) utilise the systematic errors imparted by Al_2O_3 on the calculated $Fe^{3+}/\Sigma Fe$ ratios are the basis for a correction scheme for EMP analyses. The difference between $Fe^{3+}/\Sigma Fe$ measured by Mossbauer and $Fe^{3+}/\Sigma Fe$ measured by electron microprobe is proportional to the Cr# of chromite. Thus, using secondary standards (analysed by Mossbauer) allows an effective correction of the spinel ferric iron contents and results in a consistent data set of chromite analyses (e.g. Wood & Virgo, 1989; Parkinson & Arculus, 1999).

This detailed procedure for fO_2 of chromite was carried out on 3 chromites and 3 olivines per sample for precise determination of ferric iron. The resulting dataset was corrected using the secondary internal natural standards with known Fe^{3+} contents from Mossbauer analysis (Wood & Virgo, 1989) and three additional samples (Pearce samples that had been previously analysed). The Cr-rich standards plot on the same trend as that defined by the Wood & Virgo (1989) standards. These standards were analysed 10 times each at the start and end of each run to correct the EMP data collected from that analytical session. Typical errors in fO_2 calculations are given in Parkinson & Arculus (1999).

Laser Ablation Induced Coupled Plasma Mass Spectroscopy

The laser ablation induced coupled plasma mass spectroscopy (LA-ICP-MS) methodology implemented follows the procedure of Dare et al., 2008.

The chromites were analysed for Al_2O_3, TiO_2, Cr_2O_3, V, FeO, Co, Ni, Zn and Ga by LA-ICP-MS using a New Wave 213 nm UV laser at Cardiff University and matrix-matched chromite standards. Isotope ^{71}Ga has been documented (Dare et al., 2008) to provide relatively interference free data and is preferential to use over isotope ^{69}Ga. The isotopes Mg^{24}, Al^{27}, V^{51}, Cr^{53}, Co^{59}, Ni^{60} and Zn^{66} were also measured to establish the chromite compositions of the grains analysed to could be monitored throughout the analysis of Ga and compared with the SEM and EMP data collected. Ablation of the chromites was undertaken at 15 Hz using helium in the sealed laser cell. The vapour produced was combined with argon prior to delivery into the ICP-MS. Time intervals of 250 ms were allowed for data acquisition in the time-resolved analysis (TRA) mode. The ablation process was initiated with a 20 s measurement of the gas blank prior to a 50 s interval of sample ablation by rastering along a line (40 µm wide, 10 µm deep and ~ 250 µm long) instead of spot analysis.

Each run analysed 6 unknown samples. Three grains from each sample were analysed (the same three grains had been analysed using the EMP) and one line per grain was analysed. Typically two runs were conducted daily. Following background correction of the data, the average signals were normalised to Mg, which had previously been analysed for, in each grain, using the EMP analytical method. This enabled differences in the absolute amount of material ablated and transported during individual analysis to be corrected for.

Appendix B

Drill Core Logs

Drill core log V06-48

Drill Core V06-48						
From	**To**	**Rep (m)**	**Rec (m)**	**Litho code**	**Min Code**	**Description**
0.00	0.20	0.20	0.20	OVB		Dark brown TOPSOIL, with rootlets.
0.20	1.80	1.60	1.40	OXY		Pale yellowish-brown, becoming greenish-brown weathered CLAY, with minor weathered rock/rubble fragments.
1.80	6.20	4.40	3.80	AHRTZ		Pale brownish-green weathered AHRTZ/HRTZ, with extensive fracturing along whitish lizardite stockwork veins.
6.20	7.30	1.10	0.85	FZ		AHRTZ/HRTZ, as above - rubble zone.
7.30	15.30	8.00	7.30	AHRTZ		Generally pale brownish-green, with occasionally dark grey patches, AHRTZ/HRTZ, with relict rounded porphyroblastic texture. Whitish lizardite stockwork veins, up to 8mm thickness, very strongly fractured. Occasionally broken entirely to rubble.
15.30	26.60	11.30	9.80	AHRTZ/FZ		As above, almost entirely reduced to rubble - fault zone? More intact between 16.2-16.8m, 20.7-21.1m, 21.5-22.0m, and 23.5-24.0m.
26.60	32.50	5.90	5.80	AHRTZ		Generally pale brownish-green, with occasionally dark grey patches, AHRTZ/HRTZ, with relict rounded porphyroblastic texture. Whitish lizardite stockwork veins, up to 8mm thickness, strongly fractured with occasional rubble.
32.50	39.20	6.70	6.50	AHRTZ/FZ		As above, almost entirely reduced to rubble - fault zone? More intact between 33.6-34.6m, 34.9-35.5m, 37.0-37.6m, and 38.2-38.4m.
39.20	64.00	24.80	22.00	AHRTZ		AHRTZ as above, very strongly fractured/broken, ~50% rubble. *[About 50% of core is rubble between 1.6-64.0m, rest is very strongly broken].*
64.00	94.20	30.20	26.30	PDUN		Sharp weathering transition into dark greenish-black porphyroblastic PDUN, with about 2-10% porphyroblasts (variable). Irregular whitish lizardite/pale green serpentine veins/veinlets throughout. Core is quite strongly broken between 75-90.5m (possibly drilling-induced?).
94.20	96.50	2.30	2.10	SDUN		As above, more serpentinised, dark greenish-grey colour.
96.50	101.00	4.50	3.90	PDUN		Dark greenish-black porphyroblastic PDUN, with about 2-10% porphyroblasts (variable). Irregular whitish lizardite/pale green serpentine veins/veinlets throughout.
101.00	103.65	2.65	2.45	SDUN		As above, more serpentinised, dark greenish-grey colour.
103.65	120.80	17.15	15.70	PDUN		Dark greenish-black porphyroblastic PDUN, with about 2-10% porphyroblasts (variable). Irregular whitish lizardite/pale green serpentine veins/veinlets throughout, occasional bleaching around veins.
120.80	122.75	1.95	1.55	SDUN		As above, more serpentinised, dark greenish-grey colour.
122.75	143.20	20.45	18.10	PDUN		Dark greenish-black porphyroblastic PDUN, with about 2-10% porphyroblasts (variable). Irregular whitish lizardite/pale green serpentine veins/veinlets throughout, occasional bleaching around veins. Strongly broken to rubble between 133.7-136.3m. With gradual loss of porphyroblasts grades into…
143.20	159.55	16.35	14.50	CDUN		Quite massive dark greenish-black serpentinised CDUN, with relatively few porphyroblasts, but patchily more porphyroblastic. Minor whitish lizardite/pale green serpentine veins/fractures. 151.2-153.7m : quite fractured, altered to paler greenish-grey colour (possible FZ?).
159.55	168.50	8.95	8.20	HRTZ		In places very coarsely porphyroblastic HRTZ, porphyroblasts up to 10-30mm in size, up to 50% in places, sometimes showing shearing? alignment at about 45o to core. Pale green serpentine veinlets, with associated wallrock bleaching/serpentinisation. Grades into less porphyroblastic…

Drill Core V06-48						
From	To	Rep (m)	Rec (m)	Litho code	Min Code	Description
168.50	185.40	16.90	15.40	PDUN		Finer-grained, quite massive, dark greenish-black PDUN, 0-5% porphyroblasts. Minor whitish lizardite and veins/veinlets/fractures and pale apple green serpentine veinlets. Occasional rubbly zones.
185.40	191.10	5.70	5.20	CDUN		Transition to dark greenish-black strongly serpentinitic CDUN. Minor whitish lizardite and veinlets/fractures and pale apple green serpentine veinlets. Rubble zones at 187.1m, 189.2-189.6m, paler greyish-green, altered between 188.5-189.6m (FZ?).
191.10	193.60	2.50	1.80	FZ		Rubble zone - FZ? Broken CDUN, as above, pale greenish-grey, serpentinised in places.
193.60	199.00	5.40	4.95	CDUN		Dark greenish-black strongly serpentinitic CDUN. Minor whitish lizardite and veinlets/fractures and pale apple green serpentine veinlets. Rubble zones (possibly drilling -induced?) at 194.2m, 197.6-198.2m.
199.00	201.40	2.40	2.20	FZ		Weakly to moderately weathered rubbly CDUN, more intact between 199.2-200.2m. Biotite (possible bronzite?) on undulating, slickensided, serpentine fractures. Sheared hangingwall contact to mineralisation.
201.40	201.80	0.40	0.35		MCR	Moderately weathered MCR : brown, reasonably intact
201.80	201.95	0.15	0.15	CDUN		Dark greenish-black, very serpentinised SDUN.
201.95	204.30	2.35	2.15		OCR	Variable zone of mostly OCR - rounded 1mm diameter grains in whitish/pale green serpentine matrix. Some lenses of MCR, with about 90% chromite; gritty/powdery PCR; and quite fresh SDUN. Partially weathered to clay in places. A few white lizardite veins throughout.
204.30	204.90	0.60	0.60	SDUN		Dark greenish-black, very serpentinised SDUN.
204.90	205.75	0.85	0.81		OCR	Variable zone of mostly OCR - rounded 1mm diameter grains in whitish/pale green serpentine matrix. Some lenses of MCR, with about 90% chromite, which are about 60% weathered to gritty/powdery PCR; and some quite fresh SDUN. Partially weathered to clay in places. A few white lizardite veins throughout.
205.75	214.95	9.20	8.75	TDUN		Dark greyish-green fine-grained serpentinised DUN, quite massive. Virtually no lizardite or serpentine veining. Minor anastomosing chlorite veinlets - typical of TDUN. Patchily more serpentinised to a paler green colour.
214.95	215.80	0.85	0.85	ADUN		Pale green bleached/altered TDUN, as above, with chlorite veinlets.
215.80	219.75	3.95	3.65	TDUN		Dark greyish-green fine-grained serpentinised DUN, quite massive. Virtually no lizardite or serpentine veining. Minor anastomosing chlorite veinlets - typical of TDUN. Patchily more serpentinised to a paler green colour. 217.2-217.65m : FZ, broken, rubbly, bleached, some clay gouge.
219.75	222.40	2.65	2.25		OCR	Sharp contacts to variable zone of mostly OCR - rounded 1mm diameter grains in whitish/pale green serpentine matrix. Some lenses of MCR, with about 90% chromite; these zones about 30% weathered to gritty/powdery PCR. Partially weathered to clay in places. A few white lizardite veins throughout. Zone very broken and rubbly.
222.40	225.50	3.10	2.75	TDUN		Quite broken, dark greenish-black serpentinised TDUN. Moderately altered. Fractured, with minor white lizardite, and pale apple green serpentine filled micro-fractures.
225.50	226.30	0.80	0.65	TDUN	VCR	Quite strongly altered TDUN, as above, with veins/aggregates of brown weathered chromite. Some minor disseminated and 'ryabchik' textured DCR.
226.30	227.30	1.00	0.85		PCR	Weathered brown PCR, about 25% grit, ~75% fine-grained powder. Intact core in places.
227.30	231.05	3.75	3.35		OCR	Quite massive OCR, with specular chromite grains in fine-grained pale green serpentine matrix. 229.0-229.3m : lens of TDUN.
231.05	231.70	0.65	0.60	TDUN		Massive dark greenish-black TDUN, with anastomosing chlorite veins.
231.70	242.10	10.40	9.40		OCR	Quite massive OCR, with specular chromite grains in fine-grained pale green serpentine matrix, in places almost lensoidal/vein-like in form. Occasional minor PCR grit/powder, and lenses of TDUN. Grades into...
242.10	244.70	2.60	2.25	TDUN	VCR	Massive green TDUN, with anastomosing chlorite veins. Chromite veins/aggregates decreasing towards the base of the interval.
244.70	246.40	1.70	1.65	TDUN	VCR	Massive green TDUN, with anastomosing chlorite veins. Only minor chromite veins/aggregates.

246.40	248.80	2.40	2.20	BX		Massive green TDUN, with anastomosing chlorite veins. In places quite strongly brecciated, with dark green chloritic matrix infill between wallrock fragments.
248.80	271.50	22.70	20.90	TDUN		Green to dark greenish-black serpentinitic TDUN, with minor chlorite veining. Weak brecciation between 251.0-251.5m. Minor VCR/DCR aggregates at 259.5-259.7m, 260.6-260.8m, and 267.2-267.4m.
271.50	285.30	13.80	12.30		OCR	Generally quite massive OCR, as above. Rounded ~1mm grains in fine-grained white/pale green serpentine matrix. Rubbly in places with very limited PCR grit/powder, <5%. Sharp hanging and footwall contacts. Very occasional fracture-controlled lenses of unmineralised TDUN. Relatively minor white lizardite filled fractures.
285.30	290.10	4.80	4.45	TDUN		Green massive TDUN, with chlorite veining. Minor pale apple green serpentine veining, and whitish lizardite veining/fractures. Small OCR aggregate at 289.5m.
290.10	297.00	6.90	6.55		OCR	Generally quite massive OCR, as above. Rounded ~1mm grains in fine-grained white/pale green serpentine matrix. Rubbly in places with very limited PCR grit/powder, <5%. Sharp brecciated footwall contact into unmineralised TDUN. Very occasional fracture-controlled lenses of unmineralised TDUN. Relatively minor white lizardite filled fractures.
297.00	301.55	4.55	4.10	TDUN		Green massive TDUN, with chlorite veining. Minor pale apple green serpentine veining, and whitish lizardite veining/fractures. Strongly fractured/brecciated in places with chloritic fracture infill. Small VCR/DCR aggregate at 299.5m.
301.55	303.15	1.60	1.30	BX		Zone of strongly brecciated TDUN. Dark green chloritic infill, and well developed clay gouge in places.
303.15	316.00	12.85	12.45	TDUN		Massive green to dark greenish-grey TDUN, with chloritic veinlets/micro-fractures.
316.00	320.10	4.10	4.10	TDUN		Massive green to dark greenish-grey TDUN, with chloritic veinlets/micro-fractures, with some VCR/DCR aggregates. Becomes paler/bleached/serpentinised ADUN between 319.0-320.1m.
320.10	323.10	3.00	3.00	TDUN		Dark green massive TDUN, with chloritic veinlets.

Drill core log VS6-06

Drill Core VS6-06						
From	**To**	**Rep (m)**	**Rec (m)**	**Litho code**	**Min Code**	**Description**
0.00	0.35	0.35	0.35	OVB		Dark brown silty, gritty CLAY with rock fragments (possibly weathered AHRTZ?).
0.35	2.50	2.15	1.80	OXY		Pale cream/pale brown gritty, silty CLAY with weathered rock fragments - weathered AHRTZ.
2.50	4.90	2.40	2.10	OXY		Khaki-green gritty, silty CLAY with weathered rock fragments, and in places intact core fragments - weathered AHRTZ.
4.90	5.65	0.75	0.70	OXY		Brownish-green sticky silty CLAY - weathered AHRTZ.
5.65	7.20	1.55	1.40	OXY		Dark brown sticky silty, gritty pisolitic CLAY - weathered AHRTZ (or possibly transported lacustrine clays?).
7.20	20.80	13.60	12.85	AHRTZ		Greyish-green moderately weathered AHRTZ, with minor relict porphyroblastic texture. Extensive whitish stockwork lizardite veining. Core generally intact, with minor rubble zones.
20.80	26.00	5.20	4.75	AHRTZ		Greyish-green moderately weathered AHRTZ, with minor relict porphyroblastic texture. Extensive whitish stockwork lizardite veining. ~50% rubble zones.
26.00	40.70	14.70	13.40	AHRTZ		Greyish-green moderately weathered AHRTZ, with minor relict porphyroblastic texture. Extensive whitish stockwork lizardite veining. Core more intact with ~20% rubble from about 34m.
40.70	47.50	6.80	6.20	AHRTZ		Greyish-green moderately weathered AHRTZ, with minor relict porphyroblastic texture. Extensive whitish stockwork lizardite veining. ~50% rubble zones, weathered along fractures to clay in places.
47.50	66.00	18.50	17.40	AHRTZ		Greyish-green moderately weathered AHRTZ, with minor relict porphyroblastic texture, becoming more porphyroblastic towards base of interval. Extensive whitish stockwork lizardite veining. Core more intact, ~20% rubble.
66.00	67.00	1.00	0.95	AHRTZ		Dark brownish-grey, less weathered AHRTZ, with strong porphyroblastic texture. Whitish stockwork lizardite veining, as above. Core mostly intact.
67.00	72.50	5.50	5.10	FZ	DCR	Very broken zone, especially from 70m onwards, heavily veined with lizardite and serpentine, with minor associated bleaching/alteration in places, and brecciated texture. Trace DCR/VCR aggregates/disseminations/blebs in places from 71.5m onwards.
72.50	75.80	3.30	3.10	CDUN	DCR	More intact darker greenish-black massive CDUN, altered and weathered along fractures to pale greyish-green colour. About 50% rubble. Trace DCR only.
75.80	78.10	2.30	2.10	CDUN/FZ	DCR	Very rubbly/broken interval - apparently more weathered CDUN, as above. Partially weathered to clay along fractures (possible gouge?).
78.10	88.90	10.80	10.10	CDUN/PDUN	DCR	Dark greenish-black CDUN, in places with strong porphyroblastic texture - PDUN. Minor white lizardite veining/fractures. Core is ~75% intact, in places weathered/broken to rubble, sometimes to clay, and broken along fractures, in zones up to 30cm thick. Very minor trace DCR seen throughout the interval, generally in greenish serpentinised patches.
88.90	94.10	5.20	4.80	PDUN		Massive dark greyish-green serpentinitic PDUN, with ~5% relict orthopyroxene porphyroblasts throughout. Minor white lizardite/pale apple green serpentine veinlets. Fresh.
94.10	95.10	1.00	0.90	FZ		Weathered rubble zone, clay weathering/gouge in fractures.
95.10	96.80	1.70	1.53	CDUN		Massive dark greenish-black serpentinitic CDUN, with minor clay-filled broken fractures.
96.80	98.70	1.90	1.80	CDUN		Massive dark greenish-black serpentinitic CDUN, with minor clay-filled broken fractures. More broken, ~30% clay-filled/rubbly fractures, and strong pale apple green stockwork serpentine veining, up to 30mm thick, with minor weak bleaching of wallrock.
98.70	104.10	5.40	5.30	PDUN/CDUN		More massive dark greenish-black CDUN, patchily PDUN with well developed porphyroblastic texture. Minor lizardite/serpentine veining, with weak associated alteration in places. Core is generally intact, with only minor clay/rubbly fractures.
104.10	110.10	6.00	5.45	PDUN/CDUN		More massive dark greenish-black CDUN, patchily PDUN with well developed porphyroblastic texture. Minor lizardite/serpentine veining, with weak associated alteration in places. Core more broken, ~40% rubble zones.
110.10	123.70	13.60	13.60	PDUN		Dark greenish-black massive PDUN, with ~2-5% relict porphyroblasts. Minor white lizardite veins. Core is generally intact, only minor broken/rubble zones.
123.70	127.90	4.20	3.80	PDUN		Dark greenish-black massive PDUN, with ~2-5% Minor white lizardite veins. Core is ~50% broken to rubble.
127.90	150.50	22.60	22.10	PDUN/CDUN		More massive dark greenish-black CDUN, patchily PDUN with well developed porphyroblastic texture. Minor lizardite/serpentine veining, with weak associated alteration in places. Core is generally intact, with only minor broken/rubble zones.

Drill core V05-28

Drill core V05-28				
From	To	Litho code	Min code	Description
0.00	0.19	OVB		Dark brown - Organic rich soil
0.19	0.70	OVB/HRTZ		Brown stained hartzburgite fragments - Grey colour
0.70	10.70	HRTZ		Highly weathered and fragmented hartzburgite - Microfractures - Little lizardite
10.70	13.00	HRTZ		Much less fragmentation - 'Spidery' lizardite veining - Bleached due to weathering
13.00	24.10	HRTZ		Weakening alteration - Mixture of fragmented/rubbly rock and solid core 60:40 - Lizardite veining throughout up to 1cm thick - Light grey colour to darker grey downhole
24.10	26.00	HRTZ		Bleached hartzburgite - Difficult to determine if it's HRTZ - Light green - Fine grained - Reasonbly competent - No visible phenocrysts
26.00	36.10	HRTZ		Weakening alteration - Mixture of fragmented/rubbly rock and solid core 60:40 - Lizardite veining throughout up to 1cm thick - Light grey colour to darker grey downhole
36.10	39.60	HRTZ		Mostly competent - Darker grey colour - Fresher hartzburgite - Some black microfractures - Lizardite/Green mineral veining - Some alteration halos on some veins
39.60	45.60	HRTZ		Mainly rubble and small rock fragments - Powdery in places possibly fault gauge - Some lizardite veining
45.60	52.40	HRTZ		Darker grey - Looks less altered - Fractured core - Pink/orange phenocrysts in a darker blue/black groundmass
52.40	56.60	HRTZ		Core is rubble - Fragments 1-6cm
56.60	65.90	HRTZ		Mixture of rubble and solid core - Little lizardite veining - Green colour with brown/orange altered phenocrysts
65.90	77.00	HRTZ		Fresh harzburgite - Some small areas of rubble/fractured rock - Phenocrysts approx 4mm
77.00	89.60	HRTZ		Spidery' lizardite veining - Most of the core is bleached a light grey/green - Some areas of rubble - Small patches of darker/fresher HRTZ approx. 30cm - Alteration of core
89.60	104.50	CDUN		Lizardite veining spread throughout - Some bleaching - Green/grey fine to medium grained - Not fractured - Very competent
104.50	146.65	PDUN		Grey/green - Slightly porphyritic - Core is mostly competent and fresh - Intermittent zones of strongly fractured/high angle lizardite veins
146.65	155.55	CDUN		Black/green - Fine grained - Weakly serpentinised - Very competent - Not fractured - 20-30cm of slighlty porphyritic rock with brown/orange altered phenocrysts
155.55	156.30	CDUN		Black/grey
156.30	161.80	PDUN		Faulted - Grey/green - Moderately bleached - 20/30cm segments are fresh PDUN - Core is rubble with predominantly clay infill
161.80	194.20	PDUN		Black/grey - Minor lizardite veining - Mostly competent - Intermittent zones of bleaching with altered lizardite/clay infill
194.20	227.30	CDUN		Grey/black - Fine grained CDUN - Broken core/rubble intervals
227.30	229.00	BRZ		Emerald green - Appears brecciated -Lizardite/silica/green mineral vein infill with browny/red altered phenocrysts close to vein boundaries - Interval mostly competent with 10cm of broken core/rubble
229.00	231.70	PDUN		Black/green - 4/5 zones of strongly microfractured PDUN - Weathered lizardite/green mineral veins - Core broken at these points - Solid core between fractures is very competent
231.70	242.05	PDUN		Green/grey - Massive - Very minor fracturing almost devoid
242.05	242.11	PER		White/grey completely bleached dunite - Intensely fractured - Lizardite/chlorite infill
242.11	242.92	PDUN		Green/black with minor fracturing with lizardite infill
242.92	243.32	PER		Light green/grey strongly fractured/broken dunite - Moderately bleached with lizardite veinlets
243.32	247.20	PDUN		Green/grey - Fresh - Very minor fracturing with lizardite infill
247.20	247.40	FL		Fault - Light green - 10cm of lizardite infill - Broken core - Minor clay
247.40	252.30	PDUN		Green/grey predominantly competent
252.30	252.70	BRZ		Strongly brecciated - Lizardite veinlet/weathered clay - Light green - Talc smooth fracture planes - Very soft core
252.70	281.70	PDUN		Green/grey - Intermittent medium angled faults approx. 1cm wide with green lizardite infill - Core predominantly very competent
281.70	282.50	TDUN		Light green/grey - Multiple microfractures - Moderately bleached groundmass - Approx. 10cm of broken core
282.50	302.70	PDUN		Green/grey moderately fractured - With frequent high angle fractures/faults often broken due to weathered lizardite/clay fault gauge - Unbroken core lengths no greater than 30cm

Drill core V05-28				
From	**To**	**Litho code**	**Min code**	**Description**
302.70	314.60	PDUN		Grey/green - Mostly competent - Infrequent lizardite veinlets - Mostly unbroken - Weakly tectonised
314.60	327.10	TDUN		Green/grey strongly tectonised dunite - Core moderately broken - Frequently weathered fractures leading to broken core
327.10	330.84	MCR	MCR	Reddy/brown - Weak orbicular texture - Short intervals of oxidised chromite less than 10cm
330.84	333.35	OCR	OCR	Lime green serpentinised matrix
333.35	335.65	SDUN		Weakly tectonised
335.65	336.46	OCR	OCR	Serpentinised matrix - Fragments of bleached dunite
336.46	336.60	PCR	PCR	Dark brown PCR
336.60	341.17	OCR	OCR	
341.17	342.60	MCR	MCR	Strong lizardite veining - Weak orbicular texture in last 5cm
342.60	343.20	TDUN		Green - Moderately serpentinised and tectonised dunite
343.20	347.75	OCR	OCR	Brown with lime green serpentinised matrix
347.75	348.30	OCR	OCR	Interlayered OCR with serpentinised dunite
348.30	355.70	TDUN	DCR	Light grey/green tectonised dunite - Blebs of DCR - Strongly fractured in places with pale green lizardite/chlorite infill - Core is predominantly not broken
355.70	357.40	MCR	MCR	Last 10cm is interlayered MCR with SDUN/bleached dunite
357.40	372.60	SDUN	DCR	Light green - Strongly serpentinised - DCR blebs - Core is competent - Low level of fracturing - Weakly tectonised
372.60	373.50	TDUN	DCR	Green/grey - Minor DCR - Relatively unaltered
373.50	380.30	TDUN	DCR	Green/grey - Strongly tectonised dunite - Minor DCR - 10cm of chromite blebs at 377.0m
380.30	382.40	SDUN	DCR	Lime green - Strongly serpentinised and tectonised dunite - Cut by large low angle fault with weathered lizardite/talc chlorite infill - 10% DCR
382.40	392.70	TDUN	DCR	Light green/grey - Less than 1% DCR - Core predominantly unbroken
392.70	394.45	TDUN	DCR	Bleached TDUN - Light grey/green - Moderately broken/fractured - Lizardite fracture infill weathered to clay - Dunite relatively soft - Minot DCR less than 1%
394.45	399.28	OCR	OCR	Light lime green serpentinised matrix
399.28	400.10	TDUN	DCR	Light grey/green - DCR blebs approx. 2%
400.10	400.27	OCR	OCR	Lime green serpentinised matrix - Chromite blebs show layering at low angle to the core axis
400.27	406.80	TDUN	DCR	Strongly tectonised and bleached dunite - Low angle fracturing interlayered with DCR approx. 25 degrees to core axis - DCR blebs 5%
406.80	410.90	TDUN		Grey/light green - Minor lizardite veining - Large bleb of chromite at 409.1m
410.90	412.50	OCR	OCR	Interlayered OCR with serpentinised dunite/lizardite - Multiple lizardite veinlets
412.50	415.30	TDUN	DCR	Light green/grey - Very broken core - Large sub-vertical lizardite/chlorite filled structure - Strongly fractured - Weathered to clay in places - Very smooth - Minor DCR
415.30	417.40	TDUN	DCR	Grey/green - Strongly altered with multiple low angle fractures infilled with lizardite/chlorite/green mineral - Significant amounts of DCR approx. 20% aligned with fractures - Core weak
417.40	424.60	TDUN	DCR	Green/grey - Minor blebs of DCR - Several large low angle structures - Core compentcy decreases in final metre becoming poor - Considerable bleaching
424.60	427.30	OCR	OCR	Serpentinised matrix
427.30	428.60	TDUN		Multiple lizardite veinlets - Light green/grey - Very broken
428.60	430.30	OCR	OCR	Serpentinised matrix
430.30	430.52	TDUN	DCR	Green/grey - Minor DCR
430.52	430.90	OCR	OCR	5cm band of bleached dunite within OCR
430.90	433.20	TDUN	DCR	Green/grey with minor DCR, less than 1%
433.20	433.65	OCR/MCR	OCR/PCR	Multiple high angle fractures with lizardite infill
433.65	433.98	BRZ		Light green/cream/grey - Seemingly brecciated dunite - Completely serpentinised breccia matrix made up of lizardite/green mineral
433.98	434.30	OCR/PCR	OCR/PCR	Light brown - Strongly oxidised OCR - Rubble - 10cm core loss approx.
434.30	435.40	TDUN		Green/grey
435.40	439.85	MCR	MCR	Dark brown metallic MCR - Weak orbicular texture in places - Multiple sub-parallel and high angle lizardite veinlets
439.85	441.50	TDUN	DCR	Minor DCR
441.50	442.10	TDUN	DCR	Light grey/green - Multiple blebs of disseminated chromite
442.10	465.50	TDUN	DCR	Black/grey - Filled with black microfractures - 455.7m is a 2cm wide large fracture which is broken, and very smooth
465.50	466.10	FL		Light green/light brown - Large brecciated fault zone - Strongly serpentinised - Angular clasts of dunite caught up in a lizardite/green mineral infill - Very broken - Smooth fracture planes
466.10	503.90	TDUN		Light green/grey - Very competent
503.90	523.50	PDUN/TDUN		Grey/green - Competent - Widely spaced lizardite veinlets
523.50	539.50	TDUN		Light grey - Slightly bleached TDUN
539.50	549.80	TDUN		Strongly tectonised - Porphyritic in places - Intensely fractured at 540.4m - Multiple lizardite veinlets - Core less competent

Drill core V05-24

Drill core V05-24						
From	**To**	**Rep (m)**	**Litho code**	**Min code**	**Chromite%**	**Description**
0.00	0.20	0.20	OVB			Dark brown soil with organic material
0.20	1.70	1.50	OVB			Light yellow-brown saprolitic clay fragments roughly 1-2cm of weathered Hartzburgite
1.70	4.30	2.60	OVB			Extremely weathered Hartzburgite rubble with some saprolitic clay Gravel for 1m with some Hartzburgite fragments up to 3-4cm maximum size
4.30	10.80	6.50	HRTZ			Light grey strongly weathered/altered Hartzburgite all interval is rubble with several sections of core roughly 10cm in length becoming more competent towards end interval
10.80	19.40	8.60	HRTZ			Light grey more competent than above with roughly 50% interval still rubble Moderate level of Lizardite veining some microfractures
19.40	29.70	10.30	HRTZ			Characteristic light grey altered Hartzburgite 'Spidery' stockwork texture of Lizardite veining rock is moderately competent with sections of SCR up to 30cm in length Some small sections of rubble still evident usually < than 10cm in length, Some apple green Lizardite veining visible
29.70	34.10	4.40	HRTZ			Dark brown fresher looking Hartzburgite with intense green mineral (Tremolite ferro) veining giving rock an almost brecciated appearance Moderate Lizardite veining also present with roughly 30% core reduced to rubble
34.10	73.40	39.30	HRTZ			Light to Dark brown Hartzburgite with very well defined phenocrysts roughly 5mm in diameter, Moderate to abundant Lizardite and apple green Lizardite veining, Roughly 40% of interval is rubble with 3-5cm fragments of semi fresh Hartzburgite Rock becoming far more competent towards end of interval
73.40	80.80	7.40	PDUN/HRTZ			Dark grey-black porphyritic Dunite/Hartzburgite minor Lizardite veinlets some white Lizardite infilled microfractures, some phenocrysts are altered to an orange-brown colour, rock is moderately competent although core is often broken
80.80	86.70	5.90	BRZ			Intensely altered bleached and in places brecciated Dunite all centred upon a large Shear/Fault structure @ 81.5m-81.8m within this zone rounded clasts of dunite are set in a bleached white clay matrix. Shear zone contact sits @ roughly 45 deg to core axis Core is generally solid with some rubble with moderate to strong white and green varieties of Lizardite veining
86.70	139.40	52.70	PDUN			Dark grey-black Pdun moderate Lizardite veining and fractures core usually competent, phenocrysts have a sunken glassy almost transparent Small sections of rubble after alteration/weathering of Lizardite to clay, Short sections exhibit zones of microfracturing and possible tectonisation
139.40	158.50	19.10	PDUN			Dark grey to black Pdun some bleaching and intense microfracturing minor white/apple green Lizardite veining
158.50	206.90	48.40	PDUN			Dark grey to black Pdun competent with only small sections of rubble Moderately fractured in places with very minor Lizardite veining some sections are weakly bleached adjacent to larger joints/faults
206.90	208.70	1.80	ADUN			Light grey bleached Dunite loss or destruction of rock fabric due to intense alteration, half of the interval is rubble very minor veining with a small section that appears to be brecciated
208.70	266.40	57.70	PDUN			Light grey to dark grey mostly competent Pdun, Increasing tectonised with weak bleaching and serpentinisation in places becoming less porphyritic and more tectonised towards end of interval
266.40	273.80	7.40	CDUN	DCR	<5%	Tectonised grey-black Cumulate dunite small intervals of rubble no greater then 10cm with core being badly broken in places although predominantly solid,Black microfractures abundant with some apple green Lizardite veining Minor blebs of DCR
273.80	287.60	13.80	CDUN		<5%	Dark grey-black tectonised cumulate Dunite, zones of moderate serpentinisation Minor Lizardite both white and apple green variety Minor DCR present in more bleached zones of core, Core is generally competent but broken in places becoming more porphyritic towards end of interval

Drill core V05-24						
From	To	Rep (m)	Litho code	Min code	Chromite%	Description
287.60	290.30	2.70		MCR	0.9	Chocolate brown intensely oxidised massive Chromite Very soft and badly broken with fianl 30cm a brown Chromite clay, 2 Fragments of bleached Serpentinised Dunite interlayered within Massive Chromite @ 287.7m and 289.85 both <10cm in length
290.30	291.00	0.70	SDUN			Light grey-green sheared/brecciated serpentinised Dunite 15cm of light grey clay with sub angular clasts of Dunite plus or minus altered Lizardite, @ 291.0m 2cm of fault gauge
291.00	299.20	8.20	SDUN	DCR	<2%	Green fine grained moderately jointed serpentinised Dunite, Joint planes usually have green Lizardite infill roughly 2mm in width Joint planes are very smooth when broken, Multiple blebs of Disseminated Chromite as small black flecks with one large bleb @ 296.2m
299.20	302.35	3.15		MCR	>90%	Chocolate brown to dark brown extremely oxidised very massive Chromite, predominantly reduced to rubble with some minor powdery Chromite 95cm of core is still solid
302.35	304.00	1.65		PCR	>90%	Light to dark brown strongly oxidised/weathered massive Chromite with fragments of semi fresh MCR
304.00	305.00	1.00		MCR	>90%	Dark brown massive Chromite exhibits a weakly orbicular texture in places
305.00	305.45	0.45		PCR	>90%	Dark brown powdery Chromite
305.45	308.10	2.65		MCR	>90%	Light to dark brown weakly orbicular Chromite strongly oxidised @ 305.7m 10cm is powder, core is badly broken with possible core loss
308.10	308.70	0.60		PCR	>90%	Dark brown powdery Chromite with sub angular fragments of massive Chromite
308.70	317.90	9.20		MCR	>90%	Dark brown to light brown strongly oxidised badly broken and crumbly massive Chromite, rubble in places 4-5 short sections of Powdery Chromite < 15cm in length distributed throughout interval
307.90	318.86	10.96		MCR	0.75	Dark brown massive Chromite with angular fragments of serpentinised dunite
318.86	320.00	1.14		PCR	>90%	Dark brown powdery Chromite with 20cm of massive Chromite rubble
320.00	326.60	6.60		MCR	>90%	Dark brown strongly jointed weakly oxidised massive Chromite, predominantly rubble solid core recoveries are usually no greater than 5-15cm in length
326.60	327.90	1.30		PCR	>90%	Very dark brown to Black fine grained powdery Chromite, possible 'sulphides' present non characteristic PCR
327.90	330.20	2.30		OCR	0.75	Not classic orbicular texture as Chromite is near massive with intense apple green serpentinised matrix plus 25cm of serpentinised Dunite @ 329.5m
330.20	331.85	1.65		PCR/MCR	>90%	Dark brown Metallic/Specular massive Chromite grading into a gritty powdery Chromite at end of interval
331.85	333.50	1.65		MCR	>90%	Dark brown massive Chromite with 10cm of Black powdery Chromite @ 332.15m
333.50	334.45	0.95		PCR	>90%	Dark brown to Black gritty powdery Chromite
334.45	340.90	6.45		MCR	>90%	Dark brown weakly oxidised badly broken Massive Chromite with 6 intervals of powdery Chromite roughly 10cm in length evenly spaced throughout interval, 90% is MCR
340.90	341.80	0.90		DCR	0.35	Light brown to brown disseminated Chromite within an intensely bleached serpentinsed Dunite, core is predominantly competent with several low angle planes being smooth when broken
341.80	349.20	7.40	SDUN	DCR	<5%	Light green to grey weakly tectonised serpentinised Dunite, weakly jointed with joint planes often infilled by aplle green Lizardite, Disseminated Chromite is present throughout interval <5%
349.20	349.90	0.70		MCR	0.85	Dark brown massive Chromite exhibits low angle tension fractures perpendicular to joint planes infilled predominantly with Lizardite
349.90	353.75	3.85	SDUN		<5%	Lime green to grey serpentinised Dunite moderately bleached in places with blebs of disseminated Chromite throughout interval Rock becoming more strongly serpentinsed towards Hanging wall contact with second Chromite lense

Drill core V05-24						
From	To	Rep (m)	Litho code	Min code	Chromite%	Description
360.60	361.60	1.00		DCR	0.3	Dark brown disseminated Chromite as rounded blebs within an intensely bleached serpentinised Dunite core is badly broken
361.60	367.30	5.70		MCR	0.9	Dark brown specular massive Chromite weakly oxidised very hard and moderately fractured
367.30	367.60	0.30		PCR	0.9	Muddy brown powdery Chromite clay
367.60	368.10	0.50		DCR	60-70%	Light brown to brown disseminated Chromite within a matrix of Lizardite, associated with a large low angle structure running parallel to core axis, very smooth when broken
368.10	372.95	4.85		MCR	>90%	Chocolate brown intensely oxidised weakly orbicular massive Chromite, very soft in places 25cm is reduced to mud caused by drilling, Badly broken in places but predominantly whole, Footwall contact is characterised by large Lizardite vein cutting the core axis @ roughly 45 degrees
372.95	377.50	4.55	TDUN	DCR	<1%	Dark grey-green moderately jointed tectonised Dunite with very minor disseminated Chromite
377.50	383.80	6.30	TDUN			Light grey-green intensely fractured/brecciated tectonised Dunite, large rounded clasts of serpentinised Dunite are evident within a green fibrous possibly Lizardite matrix, Core is moderately broken with 1m of rubble @ 380.85m becoming less fractured and tectonised
383.80	403.00	19.20	TDUN			Light grey-green fine grained very competent classic tectonised Dunite almost devoid of joint planes

Drill core V05-21

Drill core V05-21					
From	**To**	**Rep (m)**	**Min code**	**Litho code**	**Description**
0.00	1.00	1.00		OVB	Organic rich - Brown colour
1.00	3.00	2.00		OVB	Saprolitic clay - Hartzburgite fragments - last 10cm is oxidised
3.00	36.40	33.40		HRTZ	Thick, chaotic lizardite veining 0.5/3cm thick- Light green to brown colour - Rock generally competent - Minor brecciation in places
36.40	41.00	4.60		HRTZ	Large low angle fault, 1cm wide, infilled with green mineral
41.00	42.10	1.10		BRZ	Brecciated Harzburgite - Multiple microfractures with violet/green colour
42.10	51.70	9.60		HRTZ	Reddy-Brown-Light green colour - Phenocrysts are altered - Less frequent fracturing - Lizardite infill ususally less than 0.5cm thick
51.70	52.00	0.30		HRTZ	Green to light green - Lizardite and Green mineral altered to clay
52.00	58.40	6.40		HRTZ	Brown/Red/Green colour - Competent
58.40	61.60	3.20		SDUN	Green - Stongly serpentinised and altered dunite, no rock fabric is visible
61.60	108.20	46.60		PDUN	Porphyritic - Moderately fractured becoming fresh and more competent - Minor faulting - weathered/oxidised lizardite - Rubble in places
108.20	111.40	3.20		CDUN	Green/Grey - Strongly sheared/faulted dunite with moderate serpentinisation - Clay alteration in fracture infill - Core is rubble
111.40	130.20	18.80		TDUN/PDUN	Grey/Black tectonised porphyritic CDUN - Strongly fractured - Fractures about 1/2mm with chlorite+green mineral+lizardite infill - 129.6m-130.2m core is brecciated with carbonate alteration - About 20cm rubble
130.20	133.50	3.30		CDUN	Black/Grey fine grained CDUN - Predominantly no fractures - Very competent
133.50	136.60	3.10		TDUN	Green/Grey tectonised dunite - Moderately altered, possible serpentinisation - Microfractures abundant, high angle
136.60	143.30	6.70		CDUN/TDUN	Grey/Black - Weakly altered, bleached in parts - Competent
143.30	195.30	52.00		PDUN	Medium grained porphyritic dunite - Generally competent - Moderate to little fracturing - Infill predominantly lizardite - Some bleaching next to fractures
195.30	209.90	14.60		PDUN	Lots of the core is rubble - Intense alteration adjacent to fractures - Some carbonate - Green mineral is common infill - Small brecciated zones - Core competent only in short lenghts, 30cm max.
209.90	241.40	31.50		PDUN	Strongly porphyritic dunite - Very competent - Green/Black - Few fractures - Very weak serpentinisation in places - Minor areas of total bleaching
241.40	241.85	0.45	VCR	PDUN	Brown/Green low angle chromite veinlet
241.85	241.95	0.10		PDUN	10cm of porphyritic dunite
241.95	242.00	0.05	VCR	PDUN	5cm green chromite veinlet
242.00	242.20	0.20		PDUN	Fresh and non altered
242.20	242.50	0.30	OCR	OCR	Weakly obicular chromite
242.50	243.05	0.55		PDUN	
243.05	243.15	0.10	OCR	OCR	10cm of obicular chromite rubble
243.15	249.06	5.91		CDUN	Grey/Green CDUN - 1 high angle chromite veinlet at 244.8m
249.06	249.80	0.74	MCR	MCR	Loss of chromite at hanging wall contact, approximately 30cm
249.80	250.40	0.60		TDUN	Green/Grey TDUN/CDUN - Strongly fractured - Microfractures less than 1mm - Lizardite+Green mineral infill
250.40	250.90	0.50		PCR	Dark brown - Significant core loss approx. 50% - All rubble
250.90	251.23	0.33	DCR	CDUN	Light green/grey moderately altered - Has disseminated chromite within core
251.23	251.46	0.23	MCR	MCR	
251.46	251.80	0.34	PCR	PCR	Probable core loss approx. 40%
251.80	256.10	4.30	MCR	MCR	Roughly 20cm oxidised/powdery material
256.10	256.21	0.11		SDUN	Stongly serpentinised porphyritic dunite
256.21	256.90	0.69	PCR	PCR	Light brown highly oxidised - Approx. 20cm core loss
256.90	258.28	1.38	MCR	MCR	Strongly fractured - Low oxidisation - 50% rubble
258.28	258.90	0.62	PCR	PCR	Light brown, strongly oxidised and highly fractured - Possible core loss
258.90	261.30	2.40		TDUN	Weakly serpentinised - Brecciated in places - Core broken - Talc/chlorite infill - Minor infill with disseminated chromite
261.30	263.85	2.55		CDUN	Very competent, no fractures - Green/Black fine grained CDUN - Fresh - 5cm bleb of chromite
263.85	274.36	10.51		TDUN	Weakly serpentinised - Strongly microfractured - Green/Grey
274.36	274.86	0.50		TDUN	Green/Brown/Grey - 20% disseminated chromite blebs
274.86	275.34	0.48		TDUN	Grey/Green - Weakly altered
275.34	276.06	0.72		TDUN	Sheared approx. 45 degrees - Light green/white/grey -Strongly altered green mineral+clay+carbonate
276.06	278.10	2.04		TDUN	Green/Black/Grey - Very weakly altered - 20% core is rubble
278.10	280.80	2.70		TDUN	Light green/grey - Intensely fractured/altered tectonised dunite - Core very broken - Lizardite/Green mineral fracture infill - Minor brecciation+carbonates
280.80	280.90	0.10	MCR	MCR	Massive chromite only
280.90	282.80	1.90		TDUN	Grey/Black TDUN - Moderate fracturing - Very weak alteration
282.80	283.40	0.60	DCR	TDUN	Green/Brown/Grey TDUN with approx. 15% chromite blebs
283.40	287.70	4.30		TDUN	Green/Black unbroken fine to medium grained TDUN
287.70	288.40	0.70		SDUN	Light green strongly serpentinised, fractured non-competent - 90% interval is rubble - Green mineral+Lizardite fracture infill
288.40	288.50	0.10	MCR	MCR	Brown - Rubble
288.50	288.60	0.10		SDUN	Rubble

					Core Loss
289.02	289.10	0.08		TDUN	Unaltered - Light green colour
289.10	289.29	0.19	DCR	TDUN	60% chromite blebs
289.29	296.10	6.81		TDUN	Grey/Black TDUN - High level of microfracturing with no infill
296.10	296.15	0.05	DCR	TDUN	5cm disseminated chromite
296.15	298.38	2.23		TDUN	Black/Grey
298.38	298.48	0.10	DCR	TDUN	10cm disseminated chromite in a TDUN
298.48	300.00	1.52			

Drill core V05-13

Drill Core V05-13						
From	To	Rep (m)	Rec (m)	Litho code	Min	Description
0.00	0.15	0.15	0.15	OVB		BROWN CLAY
0.15	1.00	0.85	0.65	OVB		LIGHT BROWN CLAY AND GRAVEL
1.00	3.90	2.90	2.40	OVB		LIGHT BROWN - GREEN FIRM CLAY
3.90	5.10	1.20	1.00	HRTZ		WEATHERED PYROXENITE, LIME GREEN, SERPENTINIZED
5.10	10.80	5.70	5.47	HRTZ		LIGHT GREEN WITH KAOLIN VEINING
10.80	16.40	5.60	5.60	HRTZ		THICK KAOLIN VEINING AND GREENISH CARBONATE ALTERATION
16.40	21.60	5.20	5.20	HRTZ		THICK KAOLIN VEINING AND GREENISH CARBONATE ALTERATION
21.60	27.50	5.90	5.47	HRTZ		KAOLIN STOCKWORK
27.50	33.00	5.50	5.70	HRTZ		KAOLIN STOCKWORK BECOMING LESS STOCKWORKED IN FINAL 3M
33.00	38.60	5.60	5.70	HRTZ		THICK KAOLIN VEINING BECOMING STOCKWORK - SOME BROKEN GROUND
38.60	44.70	6.10	5.73	HRTZ		LIGHT GREEN KAOLIN AND SERPENTINITE VEINING
44.70	46.00	1.30	1.27	HRTZ		DARK GREEN SLIGHTLY SERPENTIZED FINE GRAINED WITH A FEATHERY TEXTURE
46.00	50.40	4.40	4.40	HRTZ		LIGHT GREEN WEAKLY KAOLIN VEINED
50.40	55.90	5.50	5.50	HRTZ		LIGHT - DARK GREY GREEN PATCHY KAOLIN VEINING
55.90	61.30	5.40	5.38	HRTZ		LIGHT - DARK GREY GREEN FINE KAOLIN STOCKWORK SOME CARBONATE ALTERATION
61.30	66.80	5.50	5.50	HRTZ		DARK GREY WITH GRANULAR BLUISH INTRUSIONS, KAOLIN AND SERPENTINITE VEINS
66.80	72.60	5.80	5.76	HRTZ		DARK GREY BECOMING FRESHER, PATCHY SERPENTINITE AND KAOLIN VEINING
72.60	78.60	6.00	5.77	HRTZ		DARK GREEN, REDUCED VEINING
78.60	84.80	6.20	5.74	HRTZ		DARK GREEN, REDUCED VEINING BECOMING FRESHER AND HARDER, SOME SOFT GROUND
84.80	90.60	5.80	5.62	HRTZ		DARK GREEN, REDUCED VEINING BECOMING FRESHER AND HARDER, SOME SOFT GROUND
90.60	96.00	5.40	5.40	HRTZ		DARK AND FINE GRAINED WITH KAOLIN VEINLETS
96.00	101.80	5.80	5.64	HRTZ		DARK AND FINE GRAINED WITH KAOLIN VEINLETS AND PATCHY SERPENTINITE
101.80	107.40	5.60	5.60	HRTZ		DARK AND FINE GRAINED WITH KAOLIN VEINLETS AND SERPENTINITE IN FIRST 2M
107.40	113.00	5.60	5.60	HRTZ		DARK AND FINE GRAINED WITH KAOLIN VEINLETS AND SLIGHT SERPENTINITE
113.00	118.80	5.80	5.77	HRTZ		DARK AND FINE GRAINED WITH KAOLIN VEINLETS AND SERPENTINITE VEINING
118.80	124.70	5.90	5.71	HRTZ		VERY DARK FINE GRAINED, SERPENTINITE AROUND LARGER JOINTS
124.70	130.40	5.70	5.41	HRTZ		VERY DARK FINE GRAINED INCREASING KAOLIN VEINLETS, BROKEN GROUND AROUND 128.5M
130.40	136.40	6.00	5.86	HRTZ		VERY DARK FINE GRAINED, SERPENTINITE AROUND LARGER JOINTS
136.40	142.60	6.20	5.74	HRTZ		DARK TO MID GREEN, INCREASING SERPENTINITE CONTENT AND WEAKENING GROUND CONDITIONS
142.60	149.00	6.40	5.74	HRTZ		DARK TO MID GREEN, INCREASING SERPENTINITE CONTENT AND WEAKENING GROUND CONDITIONS
149.00	154.80	5.80	8.20	HRTZ		FINE GRAINED DARK GREEN/BLACK WITH SMALL ZONES OF KAOLINIZATION
154.80	162.00	7.20	7.10	HRTZ		BECOMING MORE APPLE GREEN (DUNITE?) PATCHY KAOLIN, MINOR SERPENTINITE
162.00	167.10	5.10	4.90	HRTZ		VERY DARK FINE GRAINED, MINOR SERPENTINITE ON JOINTS
167.10	176.70	9.60	8.30	HRTZ		WEAKER ROCK WITH INCREASED SERPENTINITE VEINING
176.70	181.40	4.70	4.00	HRTZ		WELL BROKEN UP ~205, SERPENTINITE VEINING
181.40	194.10	12.70	11.30	HRTZ		MODERATE KAOLIN VEINING WITH BROKEN SECTIONS
194.10	206.70	12.60	12.00	DUN		MORE COMPETENT DARK TO APPLE GREEN POSSIBLY DUNITE TILL 197m
206.70	212.00	5.30	5.10	HRTZ		DARK GREEN WITH LARGE (5cm) MIXED KAOLIN/SERPENTINITE VEINING (WEAKLY LAYERED)
212.00	223.10	11.10	11.10	HRTZ		COMPETENT ROCK WITH FEW DISCONTINUITIES, APPLE GREEN BETWEEN 220-223m
223.10	237.80	14.70	14.20	HRTZ		DARK, FINE GRAINED BECOMING BRECCIATED WITH MICRO FRACTURES AND SERPENTINITE VEINING
237.80	243.80	6.00	5.90	HRTZ		LESS BROKEN UP, SERPENTINITE VEINS/VEINLETS AT NORMAL TO CORE AXIS
243.80	249.90	6.10	6.10	HRTZ		DARK GREEN WITH KAOLIN/SERPENTINITE VEINS NORMAL TO CORE AXIS
249.90	255.70	5.80	5.50	DUN		SLIGHTLY SERPENTINIZED APPLE GREEN, WELL BROKEN IN LAST 3M
255.70	264.10	8.40	8.05		MCR	MASSIVE BROWN/BLACK CHROMITE WITH SMALL PATCHES OF POWDERY CHROMITE @ 258m
264.10	271.70	7.60	7.60		MCR	MASSIVE CHROMITE WITH KAOLIN/CHALCEDONIC VEINS AND INCLUSIONS OF SERPENTINIZED HOST
271.70	277.60	5.90	5.90		MCR	MASSIVE CHROMITE WITH SLIGHTLY LESS VEINING
277.60	285.50	7.90	7.90		MCR	MASSIVE CHROMITE WITH SLIGHTLY LESS VEINING
285.50	290.00	4.50	4.50		MCR	MASSIVE CHROMITE WITH SERPENTINITE VEIN PARALLEL TO CORE AXIS
290.00	296.40	6.40	6.30		MCR	MASSIVE CHROMITE WITH SUB-PARALLEL VEINING AND BECOMING BROKEN
296.40	298.70	2.30	2.10		PCR	DARK SANDY/POWDERY CHROMITE
298.70	299.30	0.60	0.60		MCR	MASSIVE CHROMITE
299.30	301.20	1.90	1.10		MCR	WITH PATCHY SECTIONS OF MASSIVE CHROMITE, IRREGULAR CONTACTS, HOST INTRUDING CHROMITE?
301.20	306.20	5.00	5.00	SDUN		PROGRESSIVELY LESS SERPENTINITE, APPLE GREEN DUNITES
306.20	312.40	6.20	6.00	DUN		SLIGHT SERPENTINITE AND MINOR CHROMITE VEINING
312.40	315.40	3.00	3.00	DUN		FINE GRAINED SERPENTINITE DUNITE

315.40	318.50	3.10	3.10	SDUN		FINE GRAINED SERPENTINITE DUNITE WITH CHROMITE VEINS
318.50	321.50	3.00	3.00	SDUN		SERPENTINITE DUNITE WITH SPOTTED CHROMITE
321.50	330.40	8.90	8.70	SDUN		PROGRESSIVELY LESS SERPENTINITE AND PATCH SPOTTED CHROMITE
330.40	336.50	6.10	6.00	DUN		SLIGHT SERPENTINIZATION, PATCHY SPOTTED CHROMITE AND MASSIVE CHROMITE @ 333.5m (3m)
336.50	339.60	3.10	3.10	DUN		DARK GREEN, WITH SERPENTINITE VEINS
339.60	345.70	6.10	6.10	DUN		DARK GREEN, WITH SERPENTINITE VEINS, SOME SPOTTED CHROMITE AND CEMENTED JOINTS
345.70	351.50	5.80	5.70	SDUN		MILD TO STRONG SERPENTINIZATION OF LIGHT GREEN DUNITE WITH PATCHY SPOTTED AND MASSIVE CHROMITE
351.50	361.30	9.80	9.60	SDUN		2m OF MILD SERPENTINITE DUNITE BECOMING SERPENTINITE VEINED WITH DISSEMINATED CHROMITE. MCR @ 359.8
361.30	366.40	5.10	5.10	SDUN		PROGRESSIVELY LESS SERPENTINITE AND MILDLY BROKEN UP
366.40	375.10	8.70	8.00	DUN		MORE COMPETENT PYROXENE DUNITE WITH MINOR SERPENTINITE RUNNING @ HIGH ANGLES. BRECCIA AT 373.5 + SERPENTINITE
375.10	382.90	7.80	7.80	DUN		VERY DARK PYROXENE WITH SOME SERPENTINITE/CHALCEDONIC VEINING WITH POSSIBLE SHEARING
382.90	391.00	8.10	8.00	DUN		VERY DARK PYROXENE WITH SOME SERPENTINITE/CHALCEDONIC VEINING WITH POSSIBLE SHEARING

Appendix C – Whole Rock Analyses

Table A 1: Results for whole rock analyses of Voskhod rocks

Sample			**G1742**	**G1777**	**G1795**	**G1798**	**Vos 301**
Drillcore			V05-24	V05-24	V05-24	V05-24	V05-24
Depth (m)			141.28	185.64	231.90	239.50	249.53
Zone			Hanging wall	Hanging wall	Hanging wall	Hanging wall	Hanging wall
Rock Type			**Harzburgite**	**Dunite**	**Harzburgite**	**Dunite**	**Dunite**
SiO_2	wt%	OES	42.11	37.94	39.25	38.86	39.51
TiO_2	wt%	OES	0.032	0.008	0.011	0.007	0.045
Al_2O_3	wt%	OES	1.31	0.11	0.76	0.51	0.77
Fe_2O_3	wt%	OES	7.28	5.76	6.94	6.66	8.03
MnO	wt%	OES	0.11	0.08	0.10	0.09	0.10
MgO	wt%	OES	33.51	39.22	35.40	35.71	33.51
CaO	wt%	OES	0.93	0.16	0.15	0.04	0.42
Na_2O	wt%	OES	0.053	0.087	0.032	0.067	0.024
K_2O	wt%	OES	0.0038	0.0102	0.0089	0.0076	0.0322
P_2O_5	wt%	OES	0.003	0.001	0.005	0.003	0.003
Cr_2O_3	wt%	OES	0.35	0.67	0.32	0.39	0.41
LOI	wt%	OES	13.53	15.63	16.34	16.34	16.25
Total	wt%	OES	99.22	99.68	99.31	98.68	99.11
Sc	ppm	OES	11.37	2.46	7.44	5.57	5.81
V	ppm	OES/MS (ave)	59.23	19.50	34.43	29.56	19.43
Cr	ppm	OES/MS (ave)	2368	4610	2194	2670	2756
Co	ppm	OES/MS (ave)	86.62	87.78	83.24	86.39	104.01
Ni	ppm	OES/MS (ave)	1981	2710	2130	2115	1848
Cu	ppm	OES/MS (ave)	25.27	17.21	17.86	23.40	49.07
Zn	ppm	OES/MS (ave)	79.97	26.68	35.49	33.65	168.16
Sr	ppm	OES/MS (ave)	2.48	2.07	1.98	1.15	1.80
Y	ppm	OES/MS (ave)	0.82	0.10	0.25	0.05	0.56
Zr	ppm	OES/MS (ave)	1.05	1.14	0.58	1.08	1.46
Ba	ppm	OES/MS (ave)	16.74	8.94	13.68	5.86	9.13
Ti	ppm	OES/MS (ave)	192.36	49.17	67.08	44.35	272.85
Mn	ppm	OES/MS (ave)	857.81	643.35	802.40	710.13	742.24
Ga	ppm	MS	1.33	0.29	0.69	0.45	0.50
Rb	ppm	MS	0.29	0.15	0.29	0.25	0.45
Nb	ppm	MS	0.03	0.04	0.05	0.02	0.20
Cs	ppm	MS	0.02	0.02	0.02	0.01	0.02
La	ppm	MS	0.1212	0.0109	0.0282	0.0095	0.2239
Ce	ppm	MS	0.2027	0.0641	0.1033	0.0431	0.3770
Pr	ppm	MS	0.0290	0.0110	0.0160	0.0079	0.0459
Nd	ppm	MS	0.0945	0.0211	0.0498	0.0314	0.1274
Sm	ppm	MS	0.0238	0.0083	0.0139	0.0097	0.0259
Eu	ppm	MS	0.0139	0.0031	0.0050	0.0031	0.0076
Gd	ppm	MS	0.0508	0.0141	0.0191	0.0119	0.0414
Tb	ppm	MS	0.0126	0.0020	0.0029	0.0021	0.0091
Dy	ppm	MS	0.1135	0.0123	0.0289	0.0109	0.0481
Ho	ppm	MS	0.0275	0.0021	0.0049	0.0027	0.0092
Er	ppm	MS	0.0899	0.0063	0.0217	0.0073	0.0262
Tm	ppm	MS	0.0148	0.0011	0.0039	0.0018	0.0033
Yb	ppm	MS	0.1117	0.0102	0.0353	0.0132	0.0398
Lu	ppm	MS	0.0188	0.0010	0.0046	0.0025	0.0039
Hf	ppm	MS	0.0287	0.0211	0.0187	0.0201	0.0356
Ta	ppm	MS	0.0028	0.0021	0.0029	0.0010	0.0126
Th	ppm	MS	0.0130	0.0109	0.0173	0.0099	0.0138

Sample	Vos 303	Vos 306	Vos 312	Vos 315	Vos 322	Vos 327	F1907
Drillcore	V05-24	V05-24	V05-24	V05-24	V05-24	V05-24	V05-24
Depth (m)	251.70	258.94	266.88	270.10	276.80	282.72	282.80
Zone	Hanging wall	Upper Contact	Stringer (Hanging wall)	Stringer (Hanging wall)	Hanging wall	Hanging wall	Ore Zone
Rock Type	Dunite	Dunite	DCR (~40%)	DCR (~10%) + 0.5cm wide vein of chromite	Harzburgite	Harzburgite	Dunite
SiO_2	39.35	42.63	39.28	32.99	39.66	39.53	41.43
TiO_2	0.009	0.033	0.053	0.052	0.040	0.011	0.047
Al_2O_3	0.42	0.38	1.10	1.01	0.78	0.74	0.88
Fe_2O_3	7.13	7.28	10.79	9.13	7.12	6.93	8.14
MnO	0.10	0.09	0.14	0.12	0.09	0.10	0.12
MgO	35.09	32.91	39.24	34.56	34.24	36.12	33.49
CaO	0.08	0.04	0.09	0.07	0.17	0.11	0.11
Na_2O	0.031	0.017	0.001	0.003	0.016	0.029	0.012
K_2O	0.0064	0.0279	0.0174	0.0183	0.0299	0.0101	0.0203
P_2O_5	0.003	0.003	0.004	0.003	0.003	0.002	0.003
Cr_2O_3	0.37	0.32	9.55	6.43	0.42	0.36	0.47
LOI	16.50	16.22	-0.21	15.79	16.85	15.95	16.41
Total	99.10	99.94	100.06	100.16	99.42	99.89	101.12
Sc	5.12	3.55	3.86	3.30	6.53	8.65	7.43
V	25.39	23.06	124.83	64.34	31.48	49.18	35.58
Cr	2560	2436	66560	43636	2864	2511	3073
Co	87.64	134.83	151.34	110.02	102.49	84.62	94.90
Ni	2459	2443	1988	1981	1660	2184	1830
Cu	14.24	75.20	40.92	74.50	24.53	16.16	19.33
Zn	35.24	77.10	117.29	83.81	97.98	40.78	45.57
Sr	1.76	3.39	1.11	0.79	1.47	1.47	0.65
Y	0.11	0.44	0.49	0.32	0.44	0.21	0.36
Zr	0.57	1.29	1.04	1.49	1.00	4.03	0.64
Ba	11.08	11.54	8.27	6.13	7.40	7.44	9.21
Ti	54.72	195.66	317.00	314.52	242.70	68.33	283.46
Mn	777.84	683.04	1097.90	925.80	725.22	783.03	899.77
Ga	0.48	1.25	2.08	1.36	0.57	0.72	0.66
Rb	0.19	0.50	0.81	0.34	0.76	0.41	0.41
Nb	0.03	0.19	0.15	0.32	0.29	0.05	0.45
Cs	0.01	0.04	0.03	0.03	0.03	0.02	0.05
La	0.1361	0.1733	0.0320	0.0083	0.0098	0.0089	0.0086
Ce	0.2596	0.3384	0.0597	0.0188	0.0225	0.0186	0.0193
Pr	0.0335	0.0367	0.0088	0.0047	0.0044	0.0025	0.0034
Nd	0.0871	0.1551	0.0498	0.0152	0.0230	0.0129	0.0185
Sm	0.0131	0.0277	0.0094	0.0084	0.0165	0.0040	0.0102
Eu	0.0050	0.0067	0.0110	0.0049	0.0038	0.0020	0.0030
Gd	0.0144	0.0295	0.0218	0.0121	0.0181	0.0086	0.0257
Tb	0.0032	0.0035	0.0066	0.0036	0.0053	0.0019	0.0054
Dy	0.0165	0.0334	0.0199	0.0196	0.0523	0.0272	0.0406
Ho	0.0030	0.0065	0.0052	0.0037	0.0119	0.0060	0.0083
Er	0.0165	0.0197	0.0276	0.0162	0.0324	0.0162	0.0280
Tm	0.0027	0.0024	0.0064	0.0050	0.0060	0.0028	0.0052
Yb	0.0210	0.0352	0.0212	0.0196	0.0505	0.0230	0.0388
Lu	0.0028	0.0030	0.0033	0.0031	0.0066	0.0043	0.0057
Hf	0.0169	0.0412	0.0321	0.0269	0.0320	0.1028	0.0166
Ta	0.0019	0.0121	0.0127	0.0229	0.0189	0.0029	0.0299
Th	0.0147	0.0294	0.0143	0.0027	0.0064	0.0139	0.0018

Sample	F1971	G1908	Vos 328	Vos 341	Vos 345	Vos 348	Vos 350
Drillcore	V05-24	V05-24	V05-24	V05-24	V05-24	V05-24	V05-24
Depth (m)	343.55	373.42	375.00	389.23	394.11	398.63	403.00
Zone	Ore Zone	Ore Zone	Lower Contact	Footwall	Footwall	Footwall	Footwall
Rock Type	Dunite	Dunite	Dunite	Harzburgite	Harzburgite	Dunite	Dunite
SiO_2	36.94	38.66	37.94	39.03	40.51	44.20	39.89
TiO_2	0.036	0.029	0.013	0.024	0.029	0.009	0.009
Al_2O_3	0.57	0.30	0.24	1.09	1.27	0.27	0.35
Fe_2O_3	6.64	7.81	6.89	7.23	7.35	6.61	7.90
MnO	0.08	0.10	0.10	0.11	0.11	0.10	0.12
MgO	34.44	35.88	37.72	35.96	36.34	32.73	37.56
CaO	0.02	0.02	0.06	0.54	1.42	1.00	0.33
Na_2O	0.014	0.029	0.022	0.054	0.046	0.019	0.035
K_2O	0.0223	0.0295	0.0107	0.0066	0.0054	0.0074	0.0063
P_2O_5	0.004	0.002	0.002	0.002	0.004	0.003	0.002
Cr_2O_3	4.30	1.05	0.43	0.35	0.35	0.31	0.29
LOI	16.29	16.43	15.71	14.48	12.18	13.36	13.08
Total	99.36	100.34	99.14	98.86	99.61	98.61	99.58
Sc	1.63	2.56	3.37	8.20	9.59	7.48	6.09
V	42.65	26.29	20.33	41.15	47.09	40.34	27.93
Cr	29839	7286	2987	2408	2413	2109	1979
Co	110.36	120.42	93.50	87.74	84.38	82.16	93.52
Ni	2493	1822	2403	2162	2135	2250	2113
Cu	20.39	26.81	12.70	25.93	16.66	31.76	23.45
Zn	64.77	53.00	49.77	77.33	39.99	43.52	37.21
Sr	1.64	3.82	1.40	2.32	3.42	3.09	3.25
Y	0.29	0.52	0.35	0.69	0.96	0.11	0.14
Zr	0.55	1.33	1.66	3.79	9.21	0.96	1.69
Ba	7.41	11.33	9.41	6.44	9.36	7.48	12.37
Ti	217.10	171.20	80.01	143.74	171.95	52.54	54.51
Mn	641.95	768.76	753.43	852.88	849.06	763.83	899.58
Ga	1.04	0.61	0.34	1.10	1.16	0.47	0.51
Rb	0.47	0.55	0.17	0.28	0.29	0.14	0.30
Nb	0.37	0.25	0.04	0.29	0.05	0.03	0.08
Cs	0.08	0.09	0.01	0.02	0.03	0.01	0.03
La	0.0175	0.1075	0.1442	0.0349	0.0839	0.0243	0.1370
Ce	0.0415	0.1940	0.2616	0.0745	0.1940	0.0852	0.2610
Pr	0.0054	0.0191	0.0325	0.0150	0.0301	0.0130	0.0340
Nd	0.0279	0.0765	0.1085	0.0706	0.1161	0.0200	0.1030
Sm	0.0083	0.0194	0.0303	0.0340	0.0500	0.0060	0.0190
Eu	0.0030	0.0039	0.0100	0.0156	0.0204	0.0020	0.0040
Gd	0.0101	0.0202	0.0377	0.0534	0.0687	0.0075	0.0090
Tb	0.0026	0.0026	0.0058	0.0117	0.0176	0.0022	0.0015
Dy	0.0117	0.0158	0.0553	0.1047	0.1481	0.0179	0.0160
Ho	0.0028	0.0028	0.0110	0.0205	0.0293	0.0036	0.0027
Er	0.0087	0.0096	0.0359	0.0783	0.1067	0.0148	0.0094
Tm	0.0025	0.0015	0.0057	0.0116	0.0145	0.0022	0.0010
Yb	0.0103	0.0149	0.0392	0.1007	0.1235	0.0208	0.0146
Lu	0.0027	0.0016	0.0037	0.0141	0.0179	0.0027	0.0020
Hf	0.0180	0.0286	0.0407	0.1106	0.2361	0.0267	0.0360
Ta	0.0249	0.0150	0.0029	0.0289	0.0028	0.0019	0.0040
Th	0.0092	0.0248	0.0182	0.0193	0.0317	0.0165	0.0370

Appendix D – Voskhod Chromite – SEM Analyses

Table D 1: Chromite Analyses by Scanning Electron Microscope using Wave- Dispersive Spectroscopy

Sample	**Vos 174**	**Vos-179**	**G1742**	**G1777**	**G1910**	**G1791**	**G1941**
Drill Core	**V06-S6**	**V06-S6**	**V05-24**	**V05-24**	**V06-48**	**V05-24**	**V06-48**
Depth (m)	**66.45**	**79.50**	**141.28**	**185.64**	**200.75**	**221.03**	**231.35**
Zone	**Upper Contact**	**Upper Contact**	**Hanging wall**	**Hanging wall**	**Hanging wall**	**Hanging wall**	**Ore Zone**
Rock Type	**Dunite**	**Dunite**	**Harzburgite**	**Dunite**	**Dunite**	**Harzburgite**	**Dunite**
% Chromite	**<5%**	**<10%**	**<5%**	**<5%**	**<5%**	**<5%**	**<5%**
Chromite Morphology	Sl	Sl	HL/Sl	HL/Sl	Sl/Eu	HL/Sl	Sl/Eu
Chromite (n)=	3	3	3	3	3	3	3
Analyses per sample (n) =	9	9	9	9	9	9	9
Cr_2O_3	35.28	41.83	20.94	36.38	44.84	31.21	60.92
Al_2O_3	**30.84**	**25.76**	**46.08**	**30.94**	**15.44**	**37.58**	**6.66**
FeO	19.10	17.98	13.67	17.25	32.13	14.81	21.29
MgO	13.74	13.62	17.97	14.55	6.24	15.29	10.31
TiO_2	**0.15**	**0.12**	**0.06**	**0.17**	**0.16**	**0.04**	**0.13**
V_2O_5	0.18	0.25	0.17	0.30	0.19	0.15	0.11
MnO	0.25	0.26	0.14	0.23	0.33	0.18	0.32
CoO	0.08	0.08	0.06	0.08	0.06	0.07	0.08
NiO	0.12	0.09	0.25	0.13	0.08	0.15	0.05
ZnO	0.20	0.21	0.17	0.20	0.13	0.20	0.07
Total	**99.94**	**100.20**	**99.50**	**100.21**	**99.58**	**99.68**	**99.96**
Cr# **[Cr/(Cr+Al)]**	**0.434**	**0.521**	**0.234**	**0.441**	**0.661**	**0.358**	**0.860**
Cr#[1] **[Cr/(Cr+Al+Fe^{3+})]**	0.415	0.502	0.227	0.426	0.592	0.354	0.809
Al#	0.541	0.461	0.746	0.540	0.304	0.637	0.132
Fe^{3+}#	0.044	0.037	0.027	0.033	0.104	0.009	0.059
Mg#	**0.611**	**0.617**	**0.739**	**0.640**	**0.311**	**0.659**	**0.518**
Fe^{2+}#	**0.389**	**0.383**	**0.261**	**0.360**	**0.689**	**0.341**	**0.482**
Fe^{2+}/Fe^{3+}	**4.437**	**5.153**	**4.753**	**5.421**	**3.296**	**19.021**	**4.072**
Fo (Olivine)	**0.910**	**0.915**	**0.902**	**0.909**	**0.923**	**0.920**	n.d

Sample	**G1795**	**G1798**	**G1989**	**G1991**	**Vos 301**	**Vos 303**	**Vos 306**
Drill Core	**V05-24**	**V05-24**	**V05-21**	**V05-21**	**V05-24**	**V05-24**	**V05-24**
Depth (m)	**231.90**	**239.50**	**246.45**	**247.40**	**249.53**	**251.70**	**258.94**
Zone	**Hanging wall**	**Hanging wall**	**Hanging wall**	**Hanging wall**	**Hanging wall**	**Hanging wall**	**Upper Contact**
Rock Type	**Harzburgite**	**Dunite**	**Dunite**	**Dunite**	**Dunite**	**Dunite**	**Dunite**
% Chromite	**<5%**	**<5%**	**<5%**	**<5%**	**<5%**	**<5%**	**<5%**
Chromite Morphology	An/Sl	HL/Sl	Sl/Eu	Sl/Eu	HL/Sl	Sl	HL/Sl
Chromite (n)=	3	3	3	3	3	3	3
Analyses per sample (n) =	9	9	9	9	9	9	9
Cr_2O_3	29.62	35.72	47.26	57.97	40.61	41.10	44.41
Al_2O_3	**38.34**	**32.22**	**19.74**	**8.96**	**26.96**	**26.18**	**22.67**
FeO	14.80	16.58	20.52	21.94	18.35	18.37	20.37
MgO	16.22	14.27	11.60	9.93	13.21	12.88	11.66
TiO_2	**0.03**	**0.03**	**0.06**	**0.17**	**0.12**	**0.12**	**0.16**
V_2O_5	0.16	0.28	0.29	0.20	0.16	0.28	0.19
MnO	0.16	0.22	0.29	0.37	0.26	0.27	0.31
CoO	0.08	0.08	0.09	0.08	0.07	0.07	0.07
NiO	0.15	0.19	0.07	0.05	0.11	0.13	0.15
ZnO	0.21	0.20	0.17	0.12	0.19	0.19	0.12
Total	**99.76**	**99.80**	**100.08**	**99.78**	**100.05**	**99.60**	**100.11**
Cr# **[Cr/(Cr+Al)]**	**0.341**	**0.426**	**0.616**	**0.813**	**0.503**	**0.513**	**0.568**
Cr#[1] **[Cr/(Cr+Al+Fe^{3+})]**	0.333	0.417	0.589	0.768	0.486	0.498	0.547
Al#	0.643	0.561	0.367	0.177	0.481	0.473	0.416
Fe^{3+}#	0.024	0.022	0.044	0.055	0.033	0.030	0.037
Mg#	**0.693**	**0.632**	**0.546**	**0.496**	**0.599**	**0.589**	**0.542**
Fe^{2+}#	**0.307**	**0.368**	**0.454**	**0.504**	**0.401**	**0.411**	**0.458**
Fe^{2+}/Fe^{3+}	**6.389**	**8.888**	**5.114**	**4.541**	**6.105**	**7.341**	**6.208**
Fo (Olivine)	**0.912**	**0.916**	n.d	n.d	**0.910**	n.d	**0.911**

Sample	Vos 309	Vos 312	Vos 315	Vos 322	Vos 327	F1901	F1907
Drill Core	V05-24	V05-24	V05-24	V05-24	V05-24	V05-24	V05-24
Depth (m)	265.80	266.88	270.10	276.80	282.72	284.20	285.80
Zone	Upper Contact	Ore Zone	Ore Zone	Hanging wall	Hanging wall	Upper Contact	Upper Contact
Rock Type	Dunite	DCR	DCR	Harzburgite	Harzburgite	Dunite	Dunite
% Chromite	<5%	~30%	~50%	<5%	<5%	<5%	<5%
Chromite Morphology	Sl/Eu	Sl/Eu	Sl/Eu	An/Sl	An/Sl	Sl/Eu	Sl
Chromite (n)=	3	3	3	3	3	3	3
Analyses per sample (n) =	9	9	9	9	9	9	9
Cr_2O_3	44.66	60.25	60.56	37.21	31.14	59.98	33.87
Al_2O_3	**22.51**	**7.01**	**7.32**	**28.40**	**34.24**	**6.79**	**31.90**
FeO	19.81	22.77	20.68	19.86	18.52	22.19	19.09
MgO	12.27	8.98	10.27	13.22	14.79	9.94	14.15
TiO_2	**0.17**	**0.15**	**0.18**	**0.12**	**0.07**	**0.16**	**0.13**
V_2O_5	0.24	0.11	0.11	0.29	0.20	0.11	0.28
MnO	0.28	0.38	0.35	0.26	0.22	0.35	0.21
CoO	0.07	0.07	0.07	0.07	0.07	0.07	0.07
NiO	0.09	0.04	0.04	0.13	0.19	0.05	0.14
ZnO	0.21	0.05	0.03	0.19	0.19	0.05	0.21
Total	**100.30**	**99.82**	**99.61**	**99.75**	**99.63**	**99.69**	**100.07**
Cr# [Cr/(Cr+Al)]	**0.571**	**0.852**	**0.847**	**0.468**	**0.379**	**0.856**	**0.416**
Cr#[1] [Cr/(Cr+Al+Fe^{3+})]	0.548	0.808	0.806	0.445	0.359	0.800	0.396
Al#	0.412	0.140	0.145	0.506	0.589	0.135	0.556
Fe^{3+}#	0.040	0.052	0.049	0.049	0.051	0.064	0.048
Mg#	**0.567**	**0.456**	**0.516**	**0.596**	**0.648**	**0.501**	**0.624**
Fe^{2+}#	**0.433**	**0.544**	**0.484**	**0.404**	**0.352**	**0.499**	**0.376**
Fe^{2+}/Fe^{3+}	**5.361**	**5.898**	**4.731**	**4.097**	**3.568**	**3.856**	**3.937**
Fo (Olivine)	n.d	n.d	**0.927**	**0.913**	**0.909**	n.d	**0.913**

Sample	G1956	F1920	F1925	F1925	F1935	F1964/65	F1967
Drill Core	V06-48	V05-24	V05-24	V05-24	V05-24	V05-24	V05-24
Depth (m)	288.55	290.30	296.05	296.18	311.24	341.46	342.36
Zone	Ore Zone	Ore Zone	Ore Zone	Ore Zone	Ore Zone	Ore Zone	Ore Zone
Rock Type	Dunite	Dunite	HMCR	DCR	HMCR	HMCR	DCR
% Chromite	~15%	~10%	>95%	~30%	>90%	>95%	~50%
Chromite Morphology	Sl/Eu	Sl/Eu	Eu	Eu	Eu	Eu	Sl/Eu
Chromite (n)=	3	3	3	3	3	3	3
Analyses per sample (n) =	9	9	9	9	9	9	9
Cr_2O_3	60.57	61.31	**63.69**	**61.41**	63.07	62.77	61.78
Al_2O_3	**7.66**	**7.30**	7.23	7.10	**7.97**	**8.25**	**7.23**
FeO	19.50	17.97	13.80	11.31	12.86	15.10	18.04
MgO	11.39	12.40	**14.24**	**18.99**	15.21	13.13	11.98
TiO_2	**0.16**	**0.16**	0.17	0.15	**0.17**	**0.12**	**0.14**
V_2O_5	0.10	0.12	0.10	0.09	0.13	0.10	0.10
MnO	0.32	0.31	0.28	0.33	0.24	0.30	0.30
CoO	0.07	0.06	0.05	0.06	0.04	0.04	0.06
NiO	0.06	0.07	0.10	0.07	0.17	0.10	0.08
ZnO	0.07	0.05	0.00	0.02	0.01	0.03	0.02
Total	**99.91**	**99.74**	**28.73**	**31.02**	**99.86**	**99.94**	**99.74**
Cr# [Cr/(Cr+Al)]	**0.841**	**0.849**	**0.855**	**0.853**	**0.841**	**0.836**	**0.851**
Cr#[1] [Cr/(Cr+Al+Fe^{3+})]	0.796	0.802	0.827	0.812	0.807	0.812	0.811
Al#	0.150	0.142	0.140	0.140	0.152	0.159	0.142
Fe^{3+}#	0.054	0.055	0.033	0.048	0.041	0.029	0.048
Mg#	**0.565**	**0.612**	**0.675**	**0.565**	**0.733**	**0.643**	**0.594**
Fe^{2+}#	**0.435**	**0.388**	**0.325**	**0.435**	**0.267**	**0.357**	**0.406**
Fe^{2+}/Fe^{3+}	**3.996**	**3.507**	**4.909**	**4.483**	**3.297**	**3.884**	**4.251**
Fo (Olivine)	n.d	n.d	n.d	n.d	n.d	n.d	n.d

Sample	F1971	F1978	F1996/97	G1908	Vos 328	Vos 341	G1964
Drill Core	V05-24	V05-24	V05-24	V05-24	V05-24	V05-24	V06-48
Depth (m)	343.55	348.34	359.01	373.42	375.00	389.23	291.35
Zone	Ore Zone	Ore Zone	Ore Zone	Ore Zone	Lower Contact	Footwall	Ore Zone
Rock Type	DCR	DCR	HMCR	DCR	Dunite	Harzburgite	Chromitite
% Chromite	~15%	~35%	>95%	<5%	<5%	<5%	~70%
Chromite Morphology	Sl/Eu	Sl/Eu	Eu	Sl/Eu	Sl/Eu	HL	Sl/Eu
Chromite (n)=	3	3	3	3	3	3	3
Analyses per sample (n) =	9	9	9	9	9	9	9
Cr_2O_3	62.02	60.95	63.59	54.40	47.14	20.66	62.19
Al_2O_3	**6.80**	**7.05**	**7.66**	**11.39**	**17.46**	**47.68**	**7.23**
FeO	18.73	18.82	13.35	22.89	23.70	13.07	17.36
MgO	11.43	12.19	14.52	10.29	10.86	17.66	12.55
TiO_2	**0.14**	**0.15**	**0.16**	**0.16**	**0.24**	**0.05**	**0.15**
V_2O_5	0.09	0.11	0.11	0.18	0.17	0.12	0.09
MnO	0.33	0.32	0.24	0.34	0.32	0.15	0.33
CoO	0.07	0.06	0.04	0.06	0.09	0.07	0.07
NiO	0.04	0.05	0.11	0.07	0.08	0.18	0.04
ZnO	0.05	0.05	0.01	0.12	0.15	0.26	0.05
Total	**99.70**	**99.76**	**99.80**	**99.89**	**100.21**	**99.89**	**100.05**
Cr# [Cr/(Cr+Al)]	**0.860**	**0.853**	**0.848**	**0.762**	**0.644**	**0.225**	**0.852**
Cr#[1] [Cr/(Cr+Al+Fe^{3+})]	0.819	0.799	0.819	0.709	0.596	0.223	0.811
Al#	0.134	0.138	0.147	0.221	0.329	0.766	0.140
Fe^{3+}#	0.048	0.063	0.034	0.069	0.075	0.011	0.049
Mg#	**0.570**	**0.604**	**0.704**	**0.506**	**0.517**	**0.723**	**0.618**
Fe^{2+}#	**0.430**	**0.396**	**0.296**	**0.494**	**0.483**	**0.277**	**0.382**
Fe^{2+}/Fe^{3+}	**4.506**	**3.199**	**4.404**	**3.563**	**3.273**	**12.013**	**3.884**
Fo (Olivine)	n.d	n.d	n.d	**0.922**	**0.924**	**0.908**	n.d

Sample	G1979	G1983	G1988	G1601	G1608	G1605	G1623
Drill Core	V06-48	V06-48	V06-48	V05-28	V05-28	V05-28	V05-28
Depth (m)	296.70	298.45	300.15	322.09	328.70	325.52	354.67
Zone	Ore Zone	Lower Contact	Lower Contact	Hanging wall	Ore Zone	Upper Contact	Ore Zone
Rock Type	Chromitite	Dunite	Dunite	Dunite	Chromitite	Dunite	Dunite
% Chromite	~70%	<5%	<5%	<5%	~50%	<5%	<5%
Chromite Morphology	Sl/Eu	Sl/Eu	Sl/Eu	An/Sl	Eu	An/Sl	Sl/Eu
Chromite (n)=	3	3	3	3	3	3	3
Analyses per sample (n) =	9	9	9	9	9	9	9
Cr_2O_3	62.77	58.98	59.03	40.18	64.03	42.40	58.07
Al_2O_3	**7.45**	**7.50**	**8.18**	**27.67**	**7.20**	**24.78**	**7.20**
FeO	15.25	22.58	21.68	16.72	13.56	18.99	24.27
MgO	13.74	9.95	10.34	14.62	14.63	12.98	9.32
TiO_2	**0.16**	**0.18**	**0.15**	**0.12**	**0.16**	**0.20**	**0.15**
V_2O_5	0.09	0.14	0.15	0.18	0.10	0.23	0.16
MnO	0.26	0.37	0.37	0.22	0.26	0.28	0.39
CoO	0.05	0.09	0.08	0.07	0.03	0.09	0.09
NiO	0.08	0.06	0.03	0.11	0.09	0.08	0.05
ZnO	0.02	0.16	0.10	0.17	0.02	0.21	0.11
Total	**99.87**	**100.02**	**100.10**	**100.07**	**100.09**	**100.24**	**99.81**
Cr# [Cr/(Cr+Al)]	**0.850**	**0.841**	**0.829**	**0.493**	**0.856**	**0.534**	**0.844**
Cr#[1] [Cr/(Cr+Al+Fe^{3+})]	0.812	0.783	0.778	0.475	0.823	0.514	0.776
Al#	0.144	0.148	0.161	0.488	0.138	0.448	0.144
Fe^{3+}#	0.044	0.068	0.061	0.036	0.039	0.039	0.080
Mg#	**0.670**	**0.500**	**0.515**	**0.654**	**0.709**	**0.592**	**0.471**
Fe^{2+}#	**0.330**	**0.500**	**0.485**	**0.346**	**0.291**	**0.408**	**0.529**
Fe^{2+}/Fe^{3+}	**3.759**	**3.649**	**3.983**	**4.746**	**3.771**	**5.250**	**3.288**
Fo (Olivine)	n.d	**0.932**	**0.935**	**0.919**	n.d	**0.916**	**0.917**

Sample	Vos 345	Vos 348	Vos 350	G1624	G1631
Drill Core	V05-24	V05-24	V05-24	V05-28	V05-28
Depth (m)	394.11	398.63	402.92	432.97	434.40
Zone	Footwall	Footwall	Footwall	Ore Zone	Ore Zone
Rock Type	Harzburgite	Dunite	Dunite	Dunite	Dunite
% Chromite	<5%	<5%	<5%	<10%	<5%
Chromite Morphology	HL/Sl	HL/Sl/Eu	HL/Sl	Sl/Eu	Sl/Eu
Chromite (n)=	3	3	3	3	3
Analyses per sample (n) =	9	9	9	9	9
Cr_2O_3	20.15	46.33	42.94	59.15	54.98
Al_2O_3	**47.35**	**20.76**	**23.95**	**7.57**	**11.13**
FeO	12.74	21.02	20.23	22.24	21.14
MgO	18.71	10.79	11.77	10.24	11.59
TiO_2	**0.05**	**0.15**	**0.14**	**0.17**	**0.25**
V_2O_5	0.15	0.42	0.30	0.11	0.15
MnO	0.15	0.31	0.28	0.37	0.28
CoO	0.07	0.09	0.08	0.09	0.08
NiO	0.26	0.06	0.07	0.06	0.13
ZnO	0.16	0.19	0.23	0.09	0.19
Total	**99.79**	**100.11**	**100.00**	**100.08**	**99.93**
Cr# [Cr/(Cr+Al)]	**0.222**	**0.599**	**0.546**	**0.840**	**0.768**
Cr#[1] [Cr/(Cr+Al+Fe^{3+})]	0.216	0.581	0.527	0.782	0.712
Al#	0.757	0.388	0.438	0.149	0.215
Fe^{3+}#	0.027	0.031	0.035	0.068	0.073
Mg#	**0.762**	**0.507**	**0.544**	**0.513**	**0.566**
Fe^{2+}#	**0.238**	**0.493**	**0.456**	**0.487**	**0.434**
Fe^{2+}/Fe^{3+}	**4.427**	**7.964**	**6.589**	**3.552**	**2.981**
Fo (Olivine)	n.d	**0.909**	**0.908**	**0.935**	**0.933**

Table D 2: Drill core V05-13 $FeO_{(t)}$>MgO Chromite Group - Chromite Analyses by Scanning Electron Microscope using Wave- Dispersive Spectroscopy

Sample Ref	**259.5**	**259.5**	**259.5**	**261.5**	**261.5**	**261.5**	**261.5**	**262.5**	**265**	**268.9**	**268.9**	**268.9**	**270.4**
Drill Core	V05-13	V05-13	V05-13	V05-13	V05-13	V05-13	V05-13	V05-13	V05-13	V05-13	V05-13	V05-13	V05-13
Depth (m)	259.5	259.5	259.5	261.5	261.5	Ore Zone	Ore Zone	Ore Zone	265	268.9	268.9	268.9	270.4
Zone	Ore Zone	Ore Zone	Ore Zone	Ore Zone	Ore Zone	Chromitite	Chromitite	Chromitite	Ore Zone	Ore Zone	Ore Zone	Ore Zone	Ore Zone
Rock Type	Chromitite	Chromitite	Chromitite	Chromitite	Chromitite	MCR	MCR	MCR	Chromitite	Chromitite	Chromitite	Chromitite	Chromitite
Ore type	MCR	MCR	MCR	MCR	MCR	>95%	>95%	>95%	MCR	MCR	MCR	MCR	MCR
% Chromite	>95%	>95%	>95%	>95%	>95%	Euhedral	Euhedral	Euhedral	>95%	>95%	>95%	>95%	>95%
Morphology	Euhedral	Euhedral	Euhedral	Euhedral	Euhedral	1	1	1	Euhedral	Euhedral	Euhedral	Euhedral	Euhedral
Chromite (n) = Analyses per grain (n)=	1	1	1	1	1	1	1	1	1	1	1	1	1
	2	2	2	2	2	2	2	2	2	2	2	2	2
SiO_2	0.00	0.00	0.00	0.00	0.00	0.00	0.00	0.00	0.00	0.00	0.00	0.00	0.00
Cr_2O_3	63.44	63.32	63.20	62.44	62.50	62.99	64.40	63.96	63.02	62.89	63.23	63.47	63.47
Al_2O_3	8.23	8.36	8.18	7.73	7.74	7.69	7.79	7.75	7.54	7.67	7.67	7.95	7.95
FeO(t)	14.09	14.07	14.41	15.49	15.39	15.63	13.84	13.78	15.46	15.27	15.20	14.06	14.06
MgO	13.62	13.44	13.38	12.99	12.91	12.90	13.28	13.38	13.22	13.12	13.26	13.77	13.77
FeO	11.78	12.30	13.45	13.03	12.55	13.29	12.93	11.86	12.98	13.74	12.75	13.09	13.09
Fe_2O_3	3.23	2.48	3.25	2.82	3.48	2.45	2.09	2.72	2.78	2.97	3.02	2.56	2.56
TiO_2	0.14	0.14	0.21	0.14	0.15	0.15	0.14	0.14	0.14	0.16	0.14	0.16	0.16
V_2O_5	0.10	0.10	0.10	0.10	0.11	0.08	0.07	0.12	0.11	0.13	0.10	0.11	0.11
MnO	0.25	0.29	0.27	0.28	0.31	0.29	0.26	0.24	0.31	0.34	0.34	0.25	0.25
CoO	0.00	0.03	0.05	0.03	0.03	0.05	0.06	0.06	0.04	0.05	0.05	0.04	0.04
NiO	0.19	0.11	0.12	0.16	0.13	0.11	0.18	0.18	0.18	0.19	0.22	0.18	0.18
ZnO	0.00	0.06	0.00	0.00	0.00	0.00	0.00	0.07	0.05	0.04	0.04	0.05	0.05
Total	100.07	99.91	99.90	99.35	99.27	99.89	100.01	99.68	100.07	99.88	100.26	100.06	100.06
Cr#	0.838	0.836	0.838	0.844	0.844	0.846	0.847	0.847	0.849	0.846	0.847	0.843	0.843
Cr/3+	0.818	0.818	0.819	0.815	0.817	0.819	0.834	0.831	0.817	0.817	0.818	0.819	0.819
Al/3+	0.158	0.161	0.158	0.150	0.151	0.149	0.150	0.150	0.146	0.149	0.148	0.153	0.153
$Fe^{3+}/3+$	0.024	0.021	0.023	0.035	0.032	0.032	0.016	0.019	0.037	0.034	0.035	0.028	0.028
Mg#	0.663	0.656	0.652	0.641	0.637	0.633	0.651	0.658	0.649	0.646	0.651	0.671	0.671
Fe^{2+}#	0.337	0.344	0.348	0.359	0.363	0.367	0.349	0.342	0.351	0.354	0.349	0.329	0.329

Sample Ref	**271.9**	**271.9**	**271.9**	**272.4**	**272.4**	**275.7**	**275.7**	**275.7**	**280.1**	**280.1**	**280.1**	**282.3**
Drill Core	V05-13	V05-13	V05-13	V05-13	V05-13	V05-13	V05-13	V05-13	V05-13	V05-13	V05-13	V05-13
Depth (m)	271.9	271.9	271.9	272.4	272.4	275.7	275.7	275.7	280.1	280.1	280.1	282.3
Zone	Ore Zone	Ore Zone	Ore Zone	Ore Zone	Ore Zone	Ore Zone	Ore Zone	Ore Zone	Ore Zone	Ore Zone	Ore Zone	Ore Zone
Rock Type	Chromitite	Chromitite	Chromitite	Chromitite	Chromitite	Chromitite	Chromitite	Chromitite	Chromitite	Chromitite	Chromitite	Chromitite
Ore type	MCR	MCR	MCR	MCR	MCR	MCR	MCR	MCR	MCR	MCR	MCR	MCR
% Chromite	>95%	>95%	>95%	>95%	>95%	>95%	>95%	>95%	>95%	>95%	>95%	>95%
Morphology	Euhedral	Euhedral	Euhedral	Euhedral	Euhedral	Euhedral	Euhedral	Euhedral	Euhedral	Euhedral	Euhedral	Euhedral
Chromite (n) =	1	1	1	1	1	1	1	1	1	1	1	1
Analyses per grain (n)=	2	2	2	2	2	2	2	2	2	2	2	2
SiO_2	0.00	0.00	0.00	0.00	0.00	0.00	0.00	0.00	0.00	0.00	0.00	0.00
Cr_2O_3	63.48	63.60	63.74	63.57	64.62	62.03	62.52	62.42	63.30	63.73	63.40	63.10
Al_2O_3	7.94	7.87	7.82	8.16	7.74	8.04	7.81	7.59	7.91	7.73	7.81	7.31
FeO(t)	14.31	13.88	14.04	13.86	14.09	16.37	15.68	16.41	14.95	14.11	15.60	15.50
MgO	13.94	13.77	13.74	13.56	13.37	12.79	13.39	12.53	13.01	13.72	12.57	12.37
FeO	12.94	12.82	13.39	12.68	12.34	12.54	12.72	13.30	11.64	12.01	11.87	11.92
Fe_2O_3	2.48	2.73	1.83	2.80	1.94	1.70	1.88	2.59	2.73	2.28	2.32	2.17
TiO_2	0.14	0.15	0.13	0.14	0.14	0.14	0.17	0.15	0.18	0.18	0.14	0.13
V_2O_5	0.06	0.10	0.09	0.09	0.08	0.09	0.07	0.13	0.08	0.11	0.08	0.11
MnO	0.26	0.28	0.24	0.25	0.27	0.30	0.32	0.33	0.29	0.27	0.26	0.32
CoO	0.03	0.04	0.04	0.04	0.05	0.06	0.04	0.05	0.05	0.05	0.04	0.04
NiO	0.18	0.16	0.14	0.14	0.12	0.15	0.18	0.16	0.07	0.15	0.13	0.16
ZnO	0.00	0.05	0.06	0.00	0.04	0.06	0.08	0.05	0.08	0.00	0.09	0.04
Total	100.36	99.89	100.03	99.82	100.52	100.03	100.27	99.82	99.93	100.05	100.13	99.08
Cr#	0.843	0.844	0.845	0.839	0.848	0.838	0.843	0.847	0.843	0.847	0.845	0.853
Cr/3+	0.815	0.822	0.822	0.822	0.833	0.804	0.807	0.815	0.822	0.824	0.824	0.831
Al/3+	0.152	0.152	0.150	0.157	0.149	0.155	0.150	0.148	0.153	0.149	0.151	0.144
Fe^{3+}/3+	0.033	0.027	0.027	0.021	0.018	0.040	0.043	0.037	0.025	0.027	0.024	0.026
Mg#	0.677	0.673	0.671	0.662	0.652	0.629	0.655	0.619	0.638	0.668	0.618	0.617
Fe^{2+}#	0.323	0.327	0.329	0.338	0.348	0.371	0.345	0.381	0.362	0.332	0.382	0.383

Sample Ref	**282.3**	**282.3**	**286.4**	**286.4**	**288.2**	**290.7**	**292.7**	**292.7**	**295.9**	**295.9**	**295.9**	**297.9**
Drill Core	V05-13	V05-13	V05-13	V05-13	V05-13	V05-13	V05-13	V05-13	V05-13	V05-13	V05-13	V05-13
Depth (m)	282.3	282.3	286.4	286.4	288.2	290.7	292.7	292.7	295.9	295.9	295.9	297.9
Zone	Ore Zone	Ore Zone	Ore Zone	Ore Zone	Ore Zone	Ore Zone	Ore Zone	Ore Zone	Ore Zone	Ore Zone	Ore Zone	Ore Zone
Rock Type	Chromitite	Chromitite	Chromitite	Chromitite	Chromitite	Chromitite	Chromitite	Chromitite	Chromitite	Chromitite	Chromitite	Chromitite
Ore type	MCR	MCR	MCR	MCR	MCR	MCR	MCR	MCR	MCR	MCR	MCR	MCR
% Chromite	>95%	>95%	>95%	>95%	>95%	>95%	>95%	>95%	>95%	>95%	>95%	>95%
Morphology	Euhedral	Euhedral	Euhedral	Euhedral	Euhedral	Euhedral	Euhedral	Euhedral	Euhedral	Euhedral	Euhedral	Euhedral
Chromite (n) =	1	1	1	1	1	1	1	1	1	1	1	1
Analyses per grain (n)=	2	2	2	2	2	2	2	2	2	2	2	2
SiO_2	0.00	0.00	0.00	0.00	0.00	0.00	0.00	0.00	0.00	0.00	0.00	0.00
Cr_2O_3	63.82	63.64	63.66	63.56	63.42	63.64	62.86	63.02	62.41	62.61	62.91	62.06
Al_2O_3	7.34	7.33	7.94	7.72	7.65	7.72	8.24	7.77	8.31	8.34	7.84	8.78
FeO(t)	15.50	15.63	13.96	14.03	14.10	14.29	15.03	15.04	15.57	15.50	15.17	14.69
MgO	12.68	12.46	13.93	13.81	14.07	13.61	12.79	12.78	13.23	13.01	13.11	14.09
FeO	11.88	12.34	13.156744	12.03	12.24	12.13	13.27	13.82	13.67	12.41	13.62	13.82
Fe_2O_3	2.38	1.68	1.99	2.23	2.27	2.21	1.97	1.98	2.03	1.53	2.09	2.02
TiO_2	0.16	0.15	0.17	0.17	0.17	0.12	0.10	0.09	0.18	0.18	0.17	0.14
V_2O_5	0.08	0.09	0.12	0.10	0.13	0.13	0.07	0.09	0.10	0.13	0.10	0.09
MnO	0.30	0.31	0.25	0.28	0.25	0.26	0.22	0.24	0.28	0.28	0.28	0.27
CoO	0.04	0.06	0.02	0.04	0.04	0.03	0.04	0.04	0.05	0.03	0.06	0.03
NiO	0.14	0.17	0.17	0.16	0.09	0.14	0.12	0.07	0.16	0.23	0.14	0.12
ZnO	0.00	0.00	0.05	0.04	0.00	0.00	0.08	0.05	0.00	0.05	0.06	0.05
Total	100.05	99.84	100.27	99.90	99.91	99.92	99.55	99.18	100.29	100.36	99.83	100.33
Cr#	0.854	0.853	0.843	0.847	0.847	0.847	0.836	0.845	0.834	0.834	0.843	0.826
Cr/3+	0.831	0.832	0.819	0.822	0.819	0.823	0.818	0.824	0.805	0.809	0.817	0.793
Al/3+	0.143	0.143	0.152	0.149	0.147	0.149	0.160	0.152	0.160	0.161	0.152	0.167
Fe^{3+}/3+	0.026	0.025	0.028	0.029	0.034	0.028	0.023	0.025	0.035	0.030	0.031	0.039
Mg#	0.624	0.616	0.677	0.674	0.683	0.665	0.630	0.632	0.644	0.636	0.643	0.681
Fe^{2+}#	0.376	0.384	0.323	0.326	0.317	0.335	0.370	0.368	0.356	0.364	0.357	0.319

Sample Ref	**297.9**	**297.9**	**299.4**
Drill Core	V05-13	V05-13	V05-13
Depth (m)	297.9	297.9	299.4
Zone	Ore Zone	Ore Zone	Ore Zone
Rock Type	Chromitite	Chromitite	Chromitite
Ore type	MCR	MCR	MCR
% Chromite	>95%	>95%	>95%
Morphology	Euhedral	Euhedral	Euhedral
Chromite (n) =	1	1	1
Analyses per grain (n)=	2	2	2
SiO_2	0.00	0.00	0.00
Cr_2O_3	62.11	62.73	64.97
Al_2O_3	8.95	8.42	7.25
FeO(t)	14.53	14.81	13.61
MgO	13.66	13.22	13.49
FeO	12.74	12.69	12.326127
Fe_2O_3	1.50	1.27	1.42
TiO_2	0.15	0.14	0.11
V_2O_5	0.10	0.11	0.09
MnO	0.28	0.26	0.24
CoO	0.05	0.03	0.05
NiO	0.16	0.15	0.12
ZnO	0.05	0.00	0.00
Total	100.05	99.86	99.93
Cr#	0.823	0.833	0.86
Cr/3+	0.798	0.812	0.84
Al/3+	0.171	0.162	0.14
Fe^{3+}/3+	0.030	0.026	0.02
Mg#	0.664	0.646	0.66
Fe^{2+}#	0.336	0.354	0.34

Table D 3: Drill core V05-13 MgO>$FeO_{(t)}$ Chromite Group - Chromite Analyses by Scanning Electron Microscope using Wave- Dispersive Spectroscopy

Sample Ref	**256.50**	**256.50**	**256.50**	**257.00**	**257.00**	**257.00**	**257.50**	**257.50**	**257.50**	**258.00**	**258.00**
Drill Core	V05-13	V05-13	V05-13	V05-13	V05-13	V05-13	V05-13	V05-13	V05-13	V05-13	V05-13
Depth (m)	256.50	256.50	256.50	257.00	257.00	257.00	257.50	257.50	257.50	258.00	258.00
Zone	Ore Zone	Ore Zone	Ore Zone	Ore Zone	Ore Zone	Ore Zone	Ore Zone	Ore Zone	Ore Zone	Ore Zone	Ore Zone
Rock Type	Chromitite	Chromitite	Chromitite	Chromitite	Chromitite	Chromitite	Chromitite	Chromitite	Chromitite	Chromitite	Chromitite
Ore type	MCR	MCR	MCR	MCR	MCR	MCR	MCR	MCR	MCR	MCR	MCR
% Chromite	>95%	>95%	>95%	>95%	>95%	>95%	>95%	>95%	>95%	>95%	>95%
Morphology	Euhedral	Euhedral	Euhedral	Euhedral	Euhedral	Euhedral	Euhedral	Euhedral	Euhedral	Euhedral	Euhedral
Chromite (n) = Analyses per grain (n)=	2	2	2	2	2	2	2	2	2	2	2
SiO_2	0.00	0.00	0.00	0.00	0.00	0.00	0.00	0.00	0.00	0.00	0.00
Cr_2O_3	64.04	63.69	63.83	63.75	63.83	63.75	64.06	64.19	63.64	64.24	64.95
Al_2O_3	7.71	8.22	7.87	7.77	7.78	7.71	7.57	7.32	7.82	7.86	7.59
FeO(t)	12.33	12.58	12.63	12.79	12.83	13.03	11.92	12.21	12.23	12.51	12.56
MgO	14.93	14.59	14.70	15.02	14.83	15.09	15.20	15.11	14.81	14.26	14.08
FeO	10.18	10.84	10.58	10.15	10.48	10.12	9.63	9.77	10.15	11.17	11.42
Fe_2O_3	2.39	1.93	2.27	2.94	2.62	3.24	2.54	2.70	2.31	1.49	1.26
TiO_2	0.15	0.18	0.16	0.17	0.19	0.19	0.15	0.15	0.16	0.15	0.15
V_2O_5	0.14	0.10	0.12	0.10	0.09	0.09	0.10	0.09	0.07	0.11	0.11
MnO	0.22	0.21	0.22	0.23	0.23	0.26	0.23	0.22	0.23	0.21	0.25
CoO	0.06	0.02	0.05	0.05	0.03	0.02	0.04	0.03	0.03	0.03	0.03
NiO	0.18	0.15	0.15	0.18	0.15	0.20	0.20	0.18	0.18	0.15	0.19
ZnO	0.00	0.00	0.00	0.00	0.00	0.00	0.00	0.00	0.06	0.00	0.04
Total											
Cr#	0.848	0.839	0.845	0.846	0.846	0.847	0.850	0.855	0.845	0.846	0.852
Cr/3+	0.823	0.819	0.821	0.816	0.819	0.814	0.824	0.826	0.821	0.830	0.838
Al/3+	0.148	0.158	0.151	0.148	0.149	0.147	0.145	0.141	0.150	0.151	0.146
$Fe^{3+}/3+$	0.029	0.024	0.028	0.036	0.032	0.039	0.031	0.033	0.028	0.018	0.016
Mg#	0.723	0.706	0.712	0.725	0.716	0.727	0.738	0.734	0.722	0.695	0.687
Fe^{2+}#	0.277	0.294	0.288	0.275	0.284	0.273	0.262	0.266	0.278	0.305	0.313

Sample Ref	**258.00**	**258.50**	**258.50**	**258.50**	**259.00**	**259.00**	**259.00**	**260.00**	**260.00**	**260.00**	**260.50**	**260.50**
Drill Core	V05-13	V05-13	V05-13	V05-13	V05-13	V05-13	V05-13	V05-13	V05-13	V05-13	V05-13	V05-13
Depth (m)	258.00	258.50	258.50	258.50	259.00	259.00	259.00	260.00	260.00	260.00	260.50	260.50
Zone	Ore Zone	Ore Zone	Ore Zone	Ore Zone	Ore Zone	Ore Zone	Ore Zone	Ore Zone	Ore Zone	Ore Zone	Ore Zone	Ore Zone
Rock Type	Chromitite	Chromitite	Chromitite	Chromitite	Chromitite	Chromitite	Chromitite	Chromitite	Chromitite	Chromitite	Chromitite	Chromitite
Ore type	MCR	MCR	MCR	MCR	MCR	MCR	MCR	MCR	MCR	MCR	MCR	MCR
% Chromite	>95%	>95%	>95%	>95%	>95%	>95%	>95%	>95%	>95%	>95%	>95%	>95%
Morphology	Euhedral	Euhedral	Euhedral	Euhedral	Euhedral	Euhedral	Euhedral	Euhedral	Euhedral	Euhedral	Euhedral	Euhedral
Chromite (n) =	1	1	1	1	1	1	1	1	1	1	1	1
Analyses per grain (n)=	2	2	2	2	2	2	2	2	2	2	2	2
SiO_2	0.00	0.00	0.00	0.00	0.00	0.00	0.00	0.00	0.00	0.00	0.00	0.00
Cr_2O_3	64.21	63.65	63.75	63.81	62.80	62.82	62.50	64.44	63.93	63.70	63.86	64.84
Al_2O_3	8.00	7.89	7.94	7.50	8.26	8.01	8.22	7.72	7.76	7.86	7.55	7.34
FeO(t)	12.57	12.11	12.28	12.35	12.35	12.49	12.63	13.17	13.28	13.36	12.63	12.64
MgO	14.02	15.20	15.05	15.09	15.52	15.67	15.35	13.80	13.81	13.66	14.63	14.36
FeO	11.51	9.74	10.03	9.80	9.39	9.13	9.52	11.83	11.78	11.96	10.51	11.04
Fe_2O_3	1.18	2.62	2.50	2.83	3.30	3.73	3.47	1.50	1.67	1.55	2.35	1.78
TiO_2	0.17	0.16	0.15	0.14	0.15	0.19	0.15	0.15	0.13	0.16	0.17	0.17
V_2O_5	0.12	0.11	0.10	0.09	0.12	0.12	0.10	0.08	0.10	0.10	0.08	0.12
MnO	0.22	0.21	0.23	0.21	0.22	0.25	0.25	0.24	0.25	0.23	0.21	0.23
CoO	0.03	0.05	0.02	0.02	0.03	0.06	0.03	0.04	0.05	0.05	0.03	0.05
NiO	0.20	0.18	0.15	0.16	0.14	0.17	0.17	0.18	0.13	0.14	0.16	0.16
ZnO	0.05	0.00	0.00	0.05	0.00	0.00	0.00	0.06	0.00	0.05	0.00	0.05
Total												
Cr#	0.843	0.844	0.843	0.851	0.836	0.840	0.836	0.848	0.847	0.845	0.850	0.856
Cr/3+	0.831	0.817	0.818	0.821	0.803	0.802	0.801	0.833	0.829	0.828	0.826	0.837
Al/3+	0.154	0.151	0.152	0.144	0.157	0.153	0.157	0.149	0.150	0.152	0.146	0.141
Fe^{3+}/3+	0.015	0.032	0.031	0.035	0.040	0.045	0.042	0.018	0.021	0.019	0.029	0.022
Mg#	0.685	0.735	0.728	0.733	0.747	0.754	0.742	0.675	0.676	0.671	0.713	0.699
Fe^{2+}#	0.315	0.265	0.272	0.267	0.253	0.246	0.258	0.325	0.324	0.329	0.287	0.301

Sample Ref	**260.50**	**261.00**	**261.00**	**261.00**	**262.00**	**262.00**	**262.00**	**262.50**	**262.50**	**263.00**	**263.00**	**263.00**
Drill Core	V05-13	V05-13	V05-13	V05-13	V05-13	V05-13	V05-13	V05-13	V05-13	V05-13	V05-13	V05-13
Depth (m)	260.50	261.00	261.00	261.00	262.00	262.00	262.00	262.50	262.50	263.00	263.00	263.00
Zone	Ore Zone	Ore Zone	Ore Zone	Ore Zone	Ore Zone	Ore Zone	Ore Zone	Ore Zone	Ore Zone	Ore Zone	Ore Zone	Ore Zone
Rock Type	Chromitite	Chromitite	Chromitite	Chromitite	Chromitite	Chromitite	Chromitite	Chromitite	Chromitite	Chromitite	Chromitite	Chromitite
Ore type	MCR	MCR	MCR	MCR	MCR	MCR	MCR	MCR	MCR	MCR	MCR	MCR
% Chromite	>95%	>95%	>95%	>95%	>95%	>95%	>95%	>95%	>95%	>95%	>95%	>95%
Morphology	Euhedral	Euhedral	Euhedral	Euhedral	Euhedral	Euhedral	Euhedral	Euhedral	Euhedral	Euhedral	Euhedral	Euhedral
Chromite (n) =	1	1	1	1	1	1	1	1	1	1	1	1
Analyses per grain (n)=	2	2	2	2	2	2	2	2	2	2	2	2
SiO_2	0.00	0.00	0.00	0.00	0.00	0.00	0.00	0.00	0.00	0.00	0.00	0.00
Cr_2O_3	64.39	63.58	63.60	63.83	64.24	64.08	63.97	64.68	64.30	65.03	63.99	64.35
Al_2O_3	7.39	7.87	7.83	7.75	7.88	7.69	7.96	7.44	7.63	7.37	7.79	7.56
FeO(t)	12.69	12.33	12.33	12.73	12.52	12.60	12.71	12.81	13.19	12.48	12.49	12.52
MgO	14.41	15.05	15.04	14.95	15.02	14.78	14.90	14.07	13.56	14.45	14.78	14.61
FeO	10.86	9.96	9.99	10.23	10.22	10.39	10.42	11.40	12.13	10.97	10.43	10.65
Fe_2O_3	2.03	2.63	2.61	2.78	2.56	2.45	2.55	1.57	1.19	1.67	2.29	2.08
TiO_2	0.17	0.15	0.16	0.16	0.15	0.14	0.15	0.14	0.14	0.17	0.16	0.16
V_2O_5	0.10	0.10	0.10	0.10	0.10	0.07	0.08	0.09	0.12	0.10	0.11	0.10
MnO	0.23	0.23	0.23	0.25	0.23	0.21	0.20	0.22	0.24	0.23	0.23	0.22
CoO	0.03	0.03	0.02	0.06	0.06	0.04	0.04	0.05	0.05	0.03	0.03	0.04
NiO	0.16	0.16	0.15	0.15	0.16	0.15	0.17	0.17	0.16	0.15	0.18	0.17
ZnO	0.04	0.00	0.00	0.00	0.04	0.04	0.00	0.00	0.00	0.00	0.00	0.00
Total												
Cr#	0.854	0.844	0.845	0.847	0.845	0.848	0.843	0.854	0.850	0.855	0.846	0.851
Cr/3+	0.833	0.817	0.818	0.818	0.819	0.823	0.817	0.837	0.837	0.838	0.823	0.829
Al/3+	0.142	0.151	0.150	0.148	0.150	0.147	0.152	0.144	0.148	0.142	0.149	0.145
Fe^{3+}/3+	0.025	0.032	0.032	0.034	0.031	0.030	0.031	0.019	0.015	0.021	0.028	0.026
Mg#	0.703	0.729	0.729	0.723	0.724	0.717	0.718	0.687	0.666	0.701	0.716	0.710
Fe^{2+}#	0.297	0.271	0.271	0.277	0.276	0.283	0.282	0.313	0.334	0.299	0.284	0.290

Sample Ref	263.50	263.50	263.50	264.00	264.00	264.00	264.50	264.50	264.50	265.00	265.00	265.40
Drill Core	V05-13	V05-13	V05-13	V05-13	V05-13	V05-13	V05-13	V05-13	V05-13	V05-13	V05-13	V05-13
Depth (m)	263.50	263.50	263.50	264.00	264.00	264.00	264.50	264.50	264.50	265.00	265.00	265.40
Zone	Ore Zone	Ore Zone	Ore Zone	Ore Zone	Ore Zone	Ore Zone	Ore Zone	Ore Zone	Ore Zone	Ore Zone	Ore Zone	Ore Zone
Rock Type	Chromitite	Chromitite	Chromitite	Chromitite	Chromitite	Chromitite	Chromitite	Chromitite	Chromitite	Chromitite	Chromitite	Chromitite
Ore type	MCR	MCR	MCR	MCR	MCR	MCR	MCR	MCR	MCR	MCR	MCR	MCR
% Chromite	>95%	>95%	>95%	>95%	>95%	>95%	>95%	>95%	>95%	>95%	>95%	>95%
Morphology	Euhedral	Euhedral	Euhedral	Euhedral	Euhedral	Euhedral	Euhedral	Euhedral	Euhedral	Euhedral	Euhedral	Euhedral
Chromite (n) =	1	1	1	1	1	1	1	1	1	1	1	1
Analyses per grain (n)=	2	2	2	2	2	2	2	2	2	2	2	2
SiO_2	0.00	0.00	0.00	0.00	0.00	0.00	0.00	0.00	0.00	0.00	0.00	0.00
Cr_2O_3	64.24	64.03	63.99	64.28	63.96	64.61	64.29	63.42	62.96	64.61	64.05	63.96
Al_2O_3	8.08	7.95	7.91	7.63	7.88	7.51	7.62	7.84	8.77	7.75	7.89	7.84
FeO(t)	12.48	12.73	12.98	12.34	12.58	12.72	12.70	12.86	12.92	13.05	13.18	12.57
MgO	14.60	14.65	14.70	14.85	14.70	14.99	14.85	14.90	15.16	14.01	14.52	14.44
FeO	10.85	10.74	10.72	10.32	10.58	10.34	10.43	10.27	10.27	11.70	11.09	10.81
Fe_2O_3	1.81	2.22	2.51	2.25	2.23	2.65	2.53	2.88	2.95	1.50	2.32	1.96
TiO_2	0.16	0.15	0.15	0.17	0.15	0.16	0.16	0.15	0.17	0.14	0.14	0.15
V_2O_5	0.08	0.09	0.10	0.08	0.13	0.10	0.09	0.11	0.11	0.14	0.17	0.11
MnO	0.21	0.22	0.21	0.23	0.24	0.23	0.23	0.22	0.23	0.25	0.26	0.25
CoO	0.04	0.04	0.06	0.03	0.05	0.03	0.03	0.04	0.05	0.04	0.00	0.04
NiO	0.17	0.16	0.18	0.14	0.17	0.13	0.15	0.13	0.11	0.17	0.14	0.20
ZnO	0.00	0.00	0.00	0.00	0.00	0.00	0.00	0.00	0.05	0.00	0.00	0.05
Total												
Cr#	0.842	0.844	0.844	0.850	0.845	0.852	0.850	0.844	0.828	0.848	0.845	0.846
Cr/3+	0.823	0.821	0.819	0.826	0.822	0.825	0.824	0.815	0.799	0.833	0.821	0.825
Al/3+	0.155	0.152	0.151	0.146	0.151	0.143	0.146	0.150	0.166	0.149	0.151	0.151
Fe^{3+}/3+	0.022	0.027	0.031	0.027	0.027	0.032	0.031	0.035	0.036	0.018	0.028	0.024
Mg#	0.706	0.709	0.709	0.719	0.712	0.721	0.717	0.721	0.725	0.681	0.700	0.704
Fe^{2+}#	0.294	0.291	0.291	0.281	0.288	0.279	0.283	0.279	0.275	0.319	0.300	0.296

Sample Ref	265.40	265.40	265.90	265.90	265.90	266.40	266.40	266.40	266.90	266.90	266.90	267.40
Drill Core	V05-13	V05-13	V05-13	V05-13	V05-13	V05-13	V05-13	V05-13	V05-13	V05-13	V05-13	V05-13
Depth (m)	265.40	265.40	265.90	265.90	265.90	266.40	266.40	266.40	266.90	266.90	266.90	267.40
Zone	Ore Zone	Ore Zone	Ore Zone	Ore Zone	Ore Zone	Ore Zone	Ore Zone	Ore Zone	Ore Zone	Ore Zone	Ore Zone	Ore Zone
Rock Type	Chromitite	Chromitite	Chromitite	Chromitite	Chromitite	Chromitite	Chromitite	Chromitite	Chromitite	Chromitite	Chromitite	Chromitite
Ore type	MCR	MCR	MCR	MCR	MCR	MCR	MCR	MCR	MCR	MCR	MCR	MCR
% Chromite	>95%	>95%	>95%	>95%	>95%	>95%	>95%	>95%	>95%	>95%	>95%	>95%
Morphology	Euhedral	Euhedral	Euhedral	Euhedral	Euhedral	Euhedral	Euhedral	Euhedral	Euhedral	Euhedral	Euhedral	Euhedral
Chromite (n) =	1	1	1	1	1	1	1	1	1	1	1	1
Analyses per grain (n)=	2	2	2	2	2	2	2	2	2	2	2	2
SiO_2	0.00	0.00	0.00	0.00	0.00	0.00	0.00	0.00	0.00	0.00	0.00	0.00
Cr_2O_3	64.29	63.82	63.50	63.34	63.11	64.21	64.21	63.93	63.71	63.78	63.57	63.04
Al_2O_3	7.60	8.13	7.87	7.82	8.11	7.98	8.26	8.13	8.17	8.39	8.23	7.96
FeO(t)	12.71	12.89	12.48	12.59	12.61	12.07	12.17	12.27	12.57	12.67	12.70	12.60
MgO	14.22	14.23	15.12	14.94	15.26	14.71	15.12	14.77	14.55	14.35	14.64	15.34
FeO	11.12	11.31	9.91	10.03	9.80	10.51	10.24	10.50	10.83	11.25	10.75	9.59
Fe_2O_3	1.76	1.76	2.86	2.84	3.13	1.73	2.15	1.97	1.93	1.59	2.17	3.34
TiO_2	0.14	0.15	0.16	0.15	0.16	0.15	0.15	0.16	0.17	0.18	0.18	0.15
V_2O_5	0.09	0.11	0.10	0.10	0.10	0.09	0.12	0.08	0.09	0.12	0.10	0.10
MnO	0.26	0.20	0.21	0.22	0.24	0.21	0.22	0.20	0.23	0.23	0.22	0.22
CoO	0.03	0.04	0.02	0.07	0.00	0.03	0.03	0.04	0.03	0.04	0.05	0.00
NiO	0.16	0.17	0.16	0.13	0.15	0.17	0.16	0.17	0.15	0.17	0.16	0.18
ZnO	0.00	0.04	0.04	0.06	0.00	0.00	0.00	0.00	0.00	0.00	0.00	0.00
Total												
Cr#	0.850	0.840	0.844	0.845	0.839	0.844	0.839	0.841	0.839	0.836	0.838	0.842
Cr/3+	0.832	0.822	0.814	0.815	0.807	0.826	0.817	0.820	0.820	0.820	0.816	0.807
Al/3+	0.147	0.156	0.151	0.150	0.155	0.153	0.157	0.156	0.157	0.161	0.158	0.152
Fe^{3+}/3+	0.022	0.022	0.035	0.035	0.038	0.021	0.026	0.024	0.024	0.019	0.026	0.041
Mg#	0.695	0.692	0.731	0.726	0.735	0.714	0.725	0.715	0.705	0.694	0.708	0.740
Fe^{2+}#	0.305	0.308	0.269	0.274	0.265	0.286	0.275	0.285	0.295	0.306	0.292	0.260

Sample Ref	267.40	267.40	267.90	267.90	267.90	268.40	268.40	268.40	269.40	269.40	269.40	269.90
Drill Core	V05-13	V05-13	V05-13	V05-13	V05-13	V05-13	V05-13	V05-13	V05-13	V05-13	V05-13	V05-13
Depth (m)	267.40	267.40	267.90	267.90	267.90	268.40	268.40	268.40	269.40	269.40	269.40	269.90
Zone	Ore Zone	Ore Zone	Ore Zone	Ore Zone	Ore Zone	Ore Zone	Ore Zone	Ore Zone	Ore Zone	Ore Zone	Ore Zone	Ore Zone
Rock Type	Chromitite	Chromitite	Chromitite	Chromitite	Chromitite	Chromitite	Chromitite	Chromitite	Chromitite	Chromitite	Chromitite	Chromitite
Ore type	MCR	MCR	MCR	MCR	MCR	MCR	MCR	MCR	MCR	MCR	MCR	MCR
% Chromite	>95%	>95%	>95%	>95%	>95%	>95%	>95%	>95%	>95%	>95%	>95%	>95%
Morphology	Euhedral	Euhedral	Euhedral	Euhedral	Euhedral	Euhedral	Euhedral	Euhedral	Euhedral	Euhedral	Euhedral	Euhedral
Chromite (n) =	1	1	1	1	1	1	1	1	1	1	1	1
Analyses per grain (n)=	2	2	2	2	2	2	2	2	2	2	2	2
SiO_2	0.00	0.00	0.00	0.00	0.00	0.00	0.00	0.00	0.00	0.00	0.00	0.00
Cr_2O_3	64.12	64.22	64.31	64.14	64.39	64.48	64.88	65.24	64.15	64.14	63.19	64.42
Al_2O_3	8.14	8.07	8.08	8.10	8.29	8.28	7.58	7.18	7.76	7.99	8.39	7.94
FeO(t)	12.70	12.92	12.73	12.82	12.89	12.39	12.86	12.91	12.55	12.67	12.71	12.73
MgO	14.30	14.31	14.54	14.26	14.13	14.21	14.04	13.96	14.47	14.45	14.71	14.64
FeO	11.27	11.38	10.98	11.33	11.71	11.50	11.57	11.58	10.87	11.01	10.64	10.89
Fe_2O_3	1.60	1.71	1.94	1.65	1.31	0.99	1.44	1.48	1.86	1.85	2.30	2.04
TiO_2	0.16	0.17	0.14	0.16	0.16	0.17	0.15	0.13	0.15	0.15	0.18	0.16
V_2O_5	0.10	0.10	0.11	0.10	0.11	0.12	0.09	0.08	0.08	0.10	0.12	0.12
MnO	0.23	0.22	0.22	0.26	0.22	0.22	0.25	0.27	0.20	0.24	0.22	0.26
CoO	0.03	0.00	0.05	0.06	0.05	0.03	0.05	0.05	0.04	0.04	0.06	0.00
NiO	0.15	0.16	0.15	0.15	0.15	0.16	0.15	0.13	0.13	0.15	0.17	0.18
ZnO	0.04	0.00	0.08	0.00	0.00	0.00	0.00	0.00	0.00	0.00	0.00	0.00
Total												
Cr#	0.841	0.842	0.842	0.842	0.839	0.839	0.852	0.859	0.847	0.843	0.835	0.845
Cr/3+	0.824	0.825	0.822	0.825	0.826	0.829	0.837	0.843	0.828	0.824	0.811	0.824
Al/3+	0.156	0.155	0.154	0.155	0.158	0.159	0.146	0.138	0.149	0.153	0.161	0.151
Fe^{3+}/3+	0.020	0.021	0.024	0.020	0.016	0.012	0.018	0.018	0.023	0.023	0.028	0.025
Mg#	0.693	0.691	0.702	0.691	0.683	0.688	0.684	0.682	0.703	0.701	0.711	0.705
Fe^{2+}#	0.307	0.309	0.298	0.309	0.317	0.312	0.316	0.318	0.297	0.299	0.289	0.295

Sample Ref	269.90	269.90	270.40	270.40	270.90	270.90	270.90	271.40	271.40	271.40	272.40	272.90
Drill Core	V05-13	V05-13	V05-13	V05-13	V05-13	V05-13	V05-13	V05-13	V05-13	V05-13	V05-13	V05-13
Depth (m)	269.90	269.90	270.40	270.40	270.90	270.90	270.90	271.40	271.40	271.40	272.40	272.90
Zone	Ore Zone	Ore Zone	Ore Zone	Ore Zone	Ore Zone	Ore Zone	Ore Zone	Ore Zone	Ore Zone	Ore Zone	Ore Zone	Ore Zone
Rock Type	Chromitite	Chromitite	Chromitite	Chromitite	Chromitite	Chromitite	Chromitite	Chromitite	Chromitite	Chromitite	Chromitite	Chromitite
Ore type	MCR	MCR	MCR	MCR	MCR	MCR	MCR	MCR	MCR	MCR	MCR	MCR
% Chromite	>95%	>95%	>95%	>95%	>95%	>95%	>95%	>95%	>95%	>95%	>95%	>95%
Morphology	Euhedral	Euhedral	Euhedral	Euhedral	Euhedral	Euhedral	Euhedral	Euhedral	Euhedral	Euhedral	Euhedral	Euhedral
Chromite (n) =	1	1	1	1	1	1	1	1	1	1	1	1
Analyses per grain (n)=	2	2	2	2	2	2	2	2	2	2	2	2
SiO_2	0.00	0.00	0.00	0.00	0.00	0.00	0.00	0.00	0.00	0.00	0.00	0.00
Cr_2O_3	63.88	63.76	63.17	63.62	64.09	64.26	64.01	63.67	63.84	63.83	63.95	64.32
Al_2O_3	8.16	8.25	8.20	8.02	7.80	7.68	7.98	7.94	7.56	7.90	7.68	7.63
FeO(t)	12.81	12.93	13.57	13.81	12.72	12.76	12.89	12.28	12.52	12.59	13.28	12.31
MgO	14.45	14.52	13.85	13.87	14.28	13.96	13.97	14.50	15.11	14.73	13.70	14.40
FeO	11.07	11.00	11.73	11.85	11.11	11.50	11.51	10.63	9.87	10.48	11.85	10.81
Fe_2O_3	1.93	2.14	2.05	2.17	1.79	1.40	1.54	1.84	2.94	2.35	1.58	1.67
TiO_2	0.17	0.16	0.15	0.15	0.14	0.12	0.15	0.16	0.14	0.14	0.16	0.15
V_2O_5	0.09	0.07	0.09	0.10	0.09	0.09	0.06	0.11	0.10	0.13	0.13	0.08
MnO	0.23	0.22	0.29	0.26	0.22	0.22	0.22	0.24	0.24	0.24	0.28	0.22
CoO	0.04	0.04	0.04	0.05	0.02	0.00	0.04	0.05	0.03	0.02	0.04	0.05
NiO	0.16	0.15	0.17	0.18	0.16	0.15	0.18	0.17	0.17	0.21	0.16	0.14
ZnO	0.00	0.00	0.06	0.06	0.00	0.00	0.10	0.05	0.00	0.04	0.08	0.05
Total												
Cr#	0.840	0.838	0.838	0.842	0.846	0.849	0.843	0.843	0.850	0.844	0.848	0.850
Cr/3+	0.820	0.816	0.817	0.819	0.828	0.834	0.827	0.824	0.819	0.820	0.832	0.832
Al/3+	0.156	0.157	0.158	0.154	0.150	0.149	0.154	0.153	0.145	0.151	0.149	0.147
Fe^{3+}/3+	0.024	0.026	0.025	0.027	0.022	0.017	0.019	0.023	0.036	0.029	0.020	0.021
Mg#	0.699	0.702	0.678	0.676	0.696	0.684	0.684	0.709	0.732	0.715	0.673	0.704
Fe^{2+}#	0.301	0.298	0.322	0.324	0.304	0.316	0.316	0.291	0.268	0.285	0.327	0.296

Sample Ref	272.90	272.90	273.40	273.40	273.40	273.90	273.90	273.90	274.30	274.30	274.30	274.80
Drill Core	V05-13	V05-13	V05-13	V05-13	V05-13	V05-13	V05-13	V05-13	V05-13	V05-13	V05-13	V05-13
Depth (m)	272.90	272.90	273.40	273.40	273.40	273.90	273.90	273.90	274.30	274.30	274.30	274.80
Zone	Ore Zone	Ore Zone	Ore Zone	Ore Zone	Ore Zone	Ore Zone	Ore Zone	Ore Zone	Ore Zone	Ore Zone	Ore Zone	Ore Zone
Rock Type	Chromitite	Chromitite	Chromitite	Chromitite	Chromitite	Chromitite	Chromitite	Chromitite	Chromitite	Chromitite	Chromitite	Chromitite
Ore type	MCR	MCR	MCR	MCR	MCR	MCR	MCR	MCR	MCR	MCR	MCR	MCR
% Chromite	>95%	>95%	>95%	>95%	>95%	>95%	>95%	>95%	>95%	>95%	>95%	>95%
Morphology	Euhedral	Euhedral	Euhedral	Euhedral	Euhedral	Euhedral	Euhedral	Euhedral	Euhedral	Euhedral	Euhedral	Euhedral
Chromite (n) =	1	1	1	1	1	1	1	1	1	1	1	1
Analyses per grain (n)=	2	2	2	2	2	2	2	2	2	2	2	2
SiO_2	0.00	0.00	0.00	0.00	0.00	0.00	0.00	0.00	0.00	0.00	0.00	0.00
Cr_2O_3	64.41	64.28	63.98	64.37	63.72	63.90	63.38	63.78	63.66	63.97	64.53	63.77
Al_2O_3	7.83	7.67	7.88	7.72	7.86	7.93	7.82	7.68	7.61	7.63	7.56	7.90
FeO(t)	12.55	12.60	12.52	12.77	12.82	11.99	12.11	12.22	11.96	12.02	12.10	11.98
MgO	15.04	14.86	14.68	14.67	14.91	15.24	15.41	15.09	15.35	15.60	15.28	15.22
FeO	10.31	10.41	10.63	10.70	10.34	9.76	9.36	9.84	9.38	9.24	9.68	9.72
Fe_2O_3	2.50	2.43	2.10	2.30	2.76	2.48	3.06	2.64	2.87	3.09	2.68	2.52
TiO_2	0.16	0.16	0.16	0.15	0.17	0.17	0.15	0.15	0.16	0.14	0.15	0.15
V_2O_5	0.10	0.09	0.10	0.09	0.09	0.11	0.08	0.12	0.11	0.11	0.06	0.09
MnO	0.23	0.22	0.23	0.22	0.26	0.24	0.21	0.22	0.23	0.23	0.20	0.22
CoO	0.04	0.04	0.04	0.04	0.04	0.06	0.06	0.05	0.04	0.03	0.04	0.05
NiO	0.15	0.14	0.11	0.14	0.14	0.15	0.15	0.15	0.18	0.12	0.21	0.15
ZnO	0.00	0.00	0.00	0.06	0.00	0.00	0.00	0.04	0.00	0.00	0.04	0.00
Total												
Cr#	0.847	0.849	0.845	0.848	0.845	0.844	0.845	0.848	0.849	0.849	0.851	0.844
Cr/3+	0.821	0.824	0.823	0.824	0.816	0.818	0.813	0.820	0.819	0.817	0.823	0.818
Al/3+	0.149	0.147	0.151	0.148	0.150	0.151	0.150	0.147	0.146	0.145	0.144	0.151
Fe^{3+}/3+	0.030	0.030	0.026	0.028	0.034	0.030	0.037	0.032	0.035	0.038	0.033	0.031
Mg#	0.722	0.718	0.711	0.710	0.720	0.736	0.746	0.732	0.745	0.751	0.738	0.736
Fe^{2+}#	0.278	0.282	0.289	0.290	0.280	0.264	0.254	0.268	0.255	0.249	0.262	0.264

Sample Ref	274.80	274.80	275.20	275.20	275.20	276.10	276.10	276.10	276.60	276.60	276.60	277.10
Drill Core	V05-13	V05-13	V05-13	V05-13	V05-13	V05-13	V05-13	V05-13	V05-13	V05-13	V05-13	V05-13
Depth (m)	274.80	274.80	275.20	275.20	275.20	276.10	276.10	276.10	276.60	276.60	276.60	277.10
Zone	Ore Zone	Ore Zone	Ore Zone	Ore Zone	Ore Zone	Ore Zone	Ore Zone	Ore Zone	Ore Zone	Ore Zone	Ore Zone	Ore Zone
Rock Type	Chromitite	Chromitite	Chromitite	Chromitite	Chromitite	Chromitite	Chromitite	Chromitite	Chromitite	Chromitite	Chromitite	Chromitite
Ore type	MCR	MCR	MCR	MCR	MCR	MCR	MCR	MCR	MCR	MCR	MCR	MCR
% Chromite	>95%	>95%	>95%	>95%	>95%	>95%	>95%	>95%	>95%	>95%	>95%	>95%
Morphology	Euhedral	Euhedral	Euhedral	Euhedral	Euhedral	Euhedral	Euhedral	Euhedral	Euhedral	Euhedral	Euhedral	Euhedral
Chromite (n) =	1	1	1	1	1	1	1	1	1	1	1	1
Analyses per grain (n)=	2	2	2	2	2	2	2	2	2	2	2	2
SiO_2	0.00	0.00	0.00	0.00	0.00	0.00	0.00	0.00	0.00	0.00	0.00	0.00
Cr_2O_3	63.79	63.62	64.44	63.88	64.57	63.21	62.73	63.45	64.16	64.14	64.74	64.24
Al_2O_3	7.72	7.85	7.46	7.57	7.60	8.02	8.57	8.43	7.92	7.88	7.81	7.59
FeO(t)	12.02	12.09	12.77	12.93	12.98	12.53	12.59	12.63	12.66	12.95	13.20	12.82
MgO	15.29	14.73	14.37	14.21	14.38	14.92	14.39	14.53	13.86	13.83	14.01	14.28
FeO	9.54	10.23	10.98	11.16	11.15	10.11	10.82	10.88	11.78	11.77	11.84	11.15
Fe_2O_3	2.75	2.07	2.00	1.97	2.04	2.68	1.97	1.95	0.98	1.31	1.51	1.86
TiO_2	0.15	0.16	0.18	0.17	0.16	0.16	0.13	0.15	0.17	0.15	0.16	0.17
V_2O_5	0.09	0.08	0.11	0.13	0.10	0.09	0.10	0.11	0.14	0.11	0.11	0.15
MnO	0.23	0.19	0.22	0.20	0.24	0.23	0.22	0.25	0.20	0.25	0.22	0.22
CoO	0.06	0.03	0.05	0.04	0.00	0.07	0.04	0.04	0.04	0.03	0.04	0.06
NiO	0.16	0.20	0.19	0.20	0.21	0.14	0.19	0.17	0.13	0.16	0.15	0.16
ZnO	0.00	0.04	0.06	0.00	0.00	0.00	0.05	0.00	0.00	0.04	0.00	0.05
Total												
Cr#	0.847	0.845	0.853	0.850	0.851	0.841	0.831	0.835	0.845	0.845	0.847	0.850
Cr/3+	0.819	0.823	0.832	0.829	0.829	0.813	0.811	0.815	0.834	0.831	0.832	0.831
Al/3+	0.148	0.151	0.144	0.147	0.146	0.154	0.165	0.161	0.154	0.152	0.150	0.146
Fe^{3+}/3+	0.034	0.025	0.025	0.024	0.025	0.033	0.024	0.024	0.012	0.016	0.018	0.023
Mg#	0.741	0.720	0.700	0.694	0.697	0.724	0.703	0.704	0.677	0.677	0.678	0.695
Fe^{2+}#	0.259	0.280	0.300	0.306	0.303	0.276	0.297	0.296	0.323	0.323	0.322	0.305

Sample Ref	277.10	277.10	277.60	277.60	277.60	278.10	278.10	278.10	278.60	278.60	278.60	279.10
Drill Core	V05-13	V05-13	V05-13	V05-13	V05-13	V05-13	V05-13	V05-13	V05-13	V05-13	V05-13	V05-13
Depth (m)	277.10	277.10	277.60	277.60	277.60	278.10	278.10	278.10	278.60	278.60	278.60	279.10
Zone	Ore Zone	Ore Zone	Ore Zone	Ore Zone	Ore Zone	Ore Zone	Ore Zone	Ore Zone	Ore Zone	Ore Zone	Ore Zone	Ore Zone
Rock Type	Chromitite	Chromitite	Chromitite	Chromitite	Chromitite	Chromitite	Chromitite	Chromitite	Chromitite	Chromitite	Chromitite	Chromitite
Ore type	MCR	MCR	MCR	MCR	MCR	MCR	MCR	MCR	MCR	MCR	MCR	MCR
% Chromite	>95%	>95%	>95%	>95%	>95%	>95%	>95%	>95%	>95%	>95%	>95%	>95%
Morphology	Euhedral	Euhedral	Euhedral	Euhedral	Euhedral	Euhedral	Euhedral	Euhedral	Euhedral	Euhedral	Euhedral	Euhedral
Chromite (n) =	1	1	1	1	1	1	1	1	1	1	1	1
Analyses per grain (n)=	2	2	2	2	2	2	2	2	2	2	2	2
SiO_2	0.00	0.00	0.00	0.00	0.00	0.00	0.00	0.00	0.00	0.00	0.00	0.00
Cr_2O_3	65.18	63.80	63.99	64.01	64.26	64.33	63.87	64.42	63.80	63.24	63.28	64.59
Al_2O_3	6.99	7.43	7.76	7.79	7.85	7.99	7.90	8.19	8.20	8.59	8.06	7.93
FeO(t)	12.98	13.21	12.69	12.89	13.05	12.54	12.60	12.63	12.66	12.87	13.07	12.60
MgO	14.16	14.46	14.57	14.50	14.71	14.58	14.70	14.50	14.31	14.37	14.05	14.58
FeO	11.31	10.82	10.72	10.90	10.84	10.86	10.46	11.11	11.17	11.16	11.33	10.91
Fe_2O_3	1.85	2.66	2.19	2.21	2.47	1.86	2.38	1.68	1.66	1.91	1.94	1.88
TiO_2	0.15	0.16	0.16	0.16	0.16	0.16	0.17	0.16	0.16	0.16	0.14	0.15
V_2O_5	0.10	0.09	0.10	0.11	0.13	0.11	0.00	0.09	0.11	0.11	0.08	0.09
MnO	0.26	0.23	0.23	0.24	0.24	0.26	0.24	0.25	0.25	0.24	0.27	0.21
CoO	0.04	0.06	0.04	0.03	0.03	0.03	0.00	0.04	0.05	0.03	0.04	0.00
NiO	0.13	0.12	0.17	0.18	0.17	0.19	0.18	0.15	0.16	0.18	0.15	0.19
ZnO	0.00	0.00	0.00	0.00	0.00	0.00	0.04	0.00	0.00	0.04	0.00	0.07
Total												
Cr#	0.862	0.852	0.847	0.846	0.846	0.844	0.844	0.841	0.839	0.832	0.840	0.845
Cr/3+	0.843	0.824	0.824	0.823	0.820	0.824	0.820	0.823	0.822	0.812	0.820	0.826
Al/3+	0.135	0.143	0.149	0.149	0.150	0.153	0.151	0.156	0.158	0.165	0.156	0.151
Fe^{3+}/3+	0.023	0.033	0.027	0.027	0.030	0.023	0.029	0.020	0.020	0.023	0.024	0.023
Mg#	0.690	0.704	0.708	0.703	0.708	0.705	0.715	0.699	0.696	0.697	0.689	0.704
Fe^{2+}#	0.310	0.296	0.292	0.297	0.292	0.295	0.285	0.301	0.304	0.303	0.311	0.296

Sample Ref	279.10	279.10	279.60	279.60	279.60	280.60	280.60	280.60	281.10	281.10	281.10	281.60
Drill Core	V05-13	V05-13	V05-13	V05-13	V05-13	V05-13	V05-13	V05-13	V05-13	V05-13	V05-13	V05-13
Depth (m)	279.10	279.10	279.60	279.60	279.60	280.60	280.60	280.60	281.10	281.10	281.10	281.60
Zone	Ore Zone	Ore Zone	Ore Zone	Ore Zone	Ore Zone	Ore Zone	Ore Zone	Ore Zone	Ore Zone	Ore Zone	Ore Zone	Ore Zone
Rock Type	Chromitite	Chromitite	Chromitite	Chromitite	Chromitite	Chromitite	Chromitite	Chromitite	Chromitite	Chromitite	Chromitite	Chromitite
Ore type	MCR	MCR	MCR	MCR	MCR	MCR	MCR	MCR	MCR	MCR	MCR	MCR
% Chromite	>95%	>95%	>95%	>95%	>95%	>95%	>95%	>95%	>95%	>95%	>95%	>95%
Morphology	Euhedral	Euhedral	Euhedral	Euhedral	Euhedral	Euhedral	Euhedral	Euhedral	Euhedral	Euhedral	Euhedral	Euhedral
Chromite (n) =	1	1	1	1	1	1	1	1	1	1	1	1
Analyses per grain (n)=	2	2	2	2	2	2	2	2	2	2	2	2
SiO_2	0.00	0.00	0.00	0.00	0.00	0.00	0.00	0.00	0.00	0.00	0.00	0.00
Cr_2O_3	63.96	64.04	64.64	63.86	64.06	64.26	64.34	64.70	64.10	63.82	64.20	63.70
Al_2O_3	8.02	8.14	7.45	7.84	7.83	7.88	7.65	8.08	7.89	7.74	8.03	8.05
FeO(t)	12.83	12.83	12.09	12.60	12.73	12.81	12.87	13.00	13.10	13.16	13.48	13.04
MgO	14.55	14.56	15.11	15.33	15.12	14.27	14.22	14.01	14.11	14.01	14.04	13.89
FeO	10.90	11.03	9.99	9.76	10.15	11.27	11.29	11.85	11.51	11.47	11.78	11.69
Fe_2O_3	2.15	2.00	2.33	3.15	2.86	1.71	1.76	1.27	1.76	1.88	1.89	1.49
TiO_2	0.16	0.15	0.17	0.15	0.15	0.14	0.16	0.14	0.16	0.15	0.15	0.15
V_2O_5	0.10	0.09	0.12	0.11	0.10	0.09	0.11	0.11	0.12	0.08	0.07	0.11
MnO	0.22	0.23	0.23	0.23	0.22	0.22	0.22	0.22	0.21	0.24	0.25	0.23
CoO	0.05	0.00	0.00	0.07	0.03	0.03	0.05	0.04	0.03	0.04	0.03	0.06
NiO	0.19	0.10	0.17	0.17	0.15	0.15	0.14	0.16	0.15	0.13	0.14	0.14
ZnO	0.00	0.00	0.00	0.00	0.00	0.00	0.00	0.00	0.07	0.00	0.00	0.00
Total												
Cr#	0.842	0.841	0.853	0.845	0.846	0.845	0.849	0.843	0.845	0.847	0.843	0.841
Cr/3+	0.820	0.820	0.829	0.813	0.816	0.828	0.831	0.830	0.827	0.827	0.823	0.826
Al/3+	0.153	0.155	0.143	0.149	0.149	0.151	0.147	0.154	0.152	0.150	0.154	0.156
Fe^{3+}/3+	0.026	0.024	0.028	0.038	0.035	0.021	0.022	0.015	0.022	0.023	0.023	0.018
Mg#	0.704	0.702	0.729	0.737	0.726	0.693	0.692	0.678	0.686	0.685	0.680	0.679
Fe^{2+}#	0.296	0.298	0.271	0.263	0.274	0.307	0.308	0.322	0.314	0.315	0.320	0.321

Sample Ref	281.60	281.60	282.00	282.00	282.00	282.90	282.90	282.90	283.40	283.40	283.40	283.90
Drill Core	V05-13	V05-13	V05-13	V05-13	V05-13	V05-13	V05-13	V05-13	V05-13	V05-13	V05-13	V05-13
Depth (m)	281.60	281.60	282.00	282.00	282.00	282.90	282.90	282.90	283.40	283.40	283.40	283.90
Zone	Ore Zone	Ore Zone	Ore Zone	Ore Zone	Ore Zone	Ore Zone	Ore Zone	Ore Zone	Ore Zone	Ore Zone	Ore Zone	Ore Zone
Rock Type	Chromitite	Chromitite	Chromitite	Chromitite	Chromitite	Chromitite	Chromitite	Chromitite	Chromitite	Chromitite	Chromitite	Chromitite
Ore type	MCR	MCR	MCR	MCR	MCR	MCR	MCR	MCR	MCR	MCR	MCR	MCR
% Chromite	>95%	>95%	>95%	>95%	>95%	>95%	>95%	>95%	>95%	>95%	>95%	>95%
Morphology	Euhedral	Euhedral	Euhedral	Euhedral	Euhedral	Euhedral	Euhedral	Euhedral	Euhedral	Euhedral	Euhedral	Euhedral
Chromite (n) =	1	1	1	1	1	1	1	1	1	1	1	1
Analyses per grain (n)=	2	2	2	2	2	2	2	2	2	2	2	2
SiO_2	0.00	0.00	0.00	0.00	0.00	0.00	0.00	0.00	0.00	0.00	0.00	0.00
Cr_2O_3	63.86	64.09	64.10	63.75	63.93	65.43	63.87	64.66	63.93	63.96	63.80	63.83
Al_2O_3	7.86	7.78	7.64	7.63	7.24	7.80	7.76	8.02	7.70	7.49	7.61	7.85
FeO(t)	13.18	13.29	12.28	12.31	12.49	12.94	13.01	13.45	13.47	13.53	13.59	13.03
MgO	13.72	13.60	15.24	15.17	15.11	13.80	13.91	13.77	14.20	14.45	14.60	14.16
FeO	11.88	12.13	9.80	9.76	9.76	12.20	11.58	12.28	11.36	10.94	10.83	11.26
Fe_2O_3	1.44	1.28	2.76	2.84	3.03	0.82	1.59	1.30	2.35	2.87	3.07	1.97
TiO_2	0.14	0.15	0.16	0.15	0.16	0.15	0.16	0.15	0.13	0.12	0.12	0.15
V_2O_5	0.11	0.09	0.10	0.11	0.11	0.10	0.11	0.11	0.07	0.05	0.05	0.09
MnO	0.25	0.24	0.22	0.22	0.20	0.24	0.26	0.25	0.22	0.21	0.17	0.23
CoO	0.04	0.04	0.03	0.05	0.05	0.04	0.04	0.04	0.03	0.05	0.03	0.04
NiO	0.17	0.12	0.13	0.17	0.15	0.14	0.15	0.14	0.13	0.15	0.14	0.16
ZnO	0.00	0.00	0.00	0.00	0.06	0.00	0.00	0.00	0.00	0.00	0.00	0.05
Total												
Cr#	0.845	0.847	0.849	0.849	0.855	0.849	0.847	0.844	0.848	0.851	0.849	0.845
Cr/3+	0.830	0.833	0.821	0.819	0.824	0.841	0.830	0.831	0.823	0.821	0.817	0.825
Al/3+	0.152	0.151	0.146	0.146	0.139	0.149	0.150	0.154	0.148	0.143	0.145	0.151
Fe^{3+}/3+	0.018	0.016	0.034	0.035	0.037	0.010	0.020	0.016	0.029	0.035	0.037	0.024
Mg#	0.673	0.666	0.735	0.735	0.734	0.668	0.682	0.666	0.690	0.702	0.706	0.691
Fe^{2+}#	0.327	0.334	0.265	0.265	0.266	0.332	0.318	0.334	0.310	0.298	0.294	0.309

Sample Ref	283.90	283.90	284.40	284.40	284.40	284.90	284.90	284.90	285.40	285.40	285.40	285.90
Drill Core	V05-13	V05-13	V05-13	V05-13	V05-13	V05-13	V05-13	V05-13	V05-13	V05-13	V05-13	V05-13
Depth (m)	283.90	283.90	284.40	284.40	284.40	284.90	284.90	284.90	285.40	285.40	285.40	285.90
Zone	Ore Zone	Ore Zone	Ore Zone	Ore Zone	Ore Zone	Ore Zone	Ore Zone	Ore Zone	Ore Zone	Ore Zone	Ore Zone	Ore Zone
Rock Type	Chromitite	Chromitite	Chromitite	Chromitite	Chromitite	Chromitite	Chromitite	Chromitite	Chromitite	Chromitite	Chromitite	Chromitite
Ore type	MCR	MCR	MCR	MCR	MCR	MCR	MCR	MCR	MCR	MCR	MCR	MCR
% Chromite	>95%	>95%	>95%	>95%	>95%	>95%	>95%	>95%	>95%	>95%	>95%	>95%
Morphology	Euhedral	Euhedral	Euhedral	Euhedral	Euhedral	Euhedral	Euhedral	Euhedral	Euhedral	Euhedral	Euhedral	Euhedral
Chromite (n) =	1	1	1	1	1	1	1	1	1	1	1	1
Analyses per grain (n)=	2	2	2	2	2	2	2	2	2	2	2	2
SiO_2	0.00	0.00	0.00	0.00	0.00	0.00	0.00	0.00	0.00	0.00	0.00	0.00
Cr_2O_3	63.74	63.56	64.21	63.51	63.85	64.83	64.46	64.31	62.52	62.68	62.99	63.74
Al_2O_3	7.96	7.98	7.42	7.83	7.61	7.33	7.97	8.21	8.11	8.33	8.26	8.18
FeO(t)	13.10	13.72	12.53	12.62	12.92	11.92	11.95	12.33	11.90	12.18	12.18	11.85
MgO	14.44	13.77	14.77	14.67	14.37	14.88	15.00	14.97	16.42	16.09	16.18	14.64
FeO	11.01	12.00	10.30	10.48	10.90	10.13	10.25	10.43	7.96	8.65	8.61	10.52
Fe_2O_3	2.32	1.92	2.48	2.38	2.25	1.98	1.90	2.12	4.38	3.92	3.98	1.48
TiO_2	0.16	0.14	0.18	0.18	0.18	0.15	0.17	0.16	0.14	0.15	0.16	0.15
V_2O_5	0.09	0.14	0.06	0.08	0.10	0.08	0.09	0.10	0.08	0.10	0.11	0.11
MnO	0.24	0.25	0.25	0.23	0.23	0.24	0.23	0.24	0.20	0.18	0.21	0.19
CoO	0.03	0.03	0.05	0.04	0.04	0.04	0.03	0.03	0.05	0.04	0.05	0.04
NiO	0.17	0.17	0.15	0.18	0.19	0.16	0.14	0.19	0.16	0.13	0.12	0.16
ZnO	0.00	0.00	0.04	0.00	0.05	0.00	0.00	0.00	0.00	0.00	0.00	0.00
Total												
Cr#	0.843	0.842	0.853	0.845	0.849	0.856	0.844	0.840	0.838	0.835	0.836	0.839
Cr/3+	0.819	0.822	0.827	0.820	0.826	0.835	0.825	0.819	0.794	0.795	0.796	0.824
Al/3+	0.153	0.154	0.142	0.151	0.147	0.141	0.152	0.156	0.154	0.158	0.156	0.158
Fe^{3+}/3+	0.028	0.024	0.030	0.029	0.028	0.024	0.023	0.026	0.053	0.047	0.048	0.018
Mg#	0.700	0.672	0.719	0.714	0.701	0.724	0.723	0.719	0.786	0.768	0.770	0.713
Fe^{2+}#	0.300	0.328	0.281	0.286	0.299	0.276	0.277	0.281	0.214	0.232	0.230	0.287

Sample Ref	285.90	285.90	286.40	286.90	286.90	286.90	287.40	287.40	287.40	287.80	287.80	287.80
Drill Core	V05-13	V05-13	V05-13	V05-13	V05-13	V05-13	V05-13	V05-13	V05-13	V05-13	V05-13	V05-13
Depth (m)	285.90	285.90	286.40	286.90	286.90	286.90	287.40	287.40	287.40	287.80	287.80	287.80
Zone	Ore Zone	Ore Zone	Ore Zone	Ore Zone	Ore Zone	Ore Zone	Ore Zone	Ore Zone	Ore Zone	Ore Zone	Ore Zone	Ore Zone
Rock Type	Chromitite	Chromitite	Chromitite	Chromitite	Chromitite	Chromitite	Chromitite	Chromitite	Chromitite	Chromitite	Chromitite	Chromitite
Ore type	MCR	MCR	MCR	MCR	MCR	MCR	MCR	MCR	MCR	MCR	MCR	MCR
% Chromite	>95%	>95%	>95%	>95%	>95%	>95%	>95%	>95%	>95%	>95%	>95%	>95%
Morphology	Euhedral	Euhedral	Euhedral	Euhedral	Euhedral	Euhedral	Euhedral	Euhedral	Euhedral	Euhedral	Euhedral	Euhedral
Chromite (n) =	1	1	1	1	1	1	1	1	1	1	1	1
Analyses per grain (n)=	2	2	2	2	2	2	2	2	2	2	2	2
SiO_2	0.00	0.00	0.00	0.00	0.00	0.00	0.00	0.00	0.00	0.00	0.00	0.00
Cr_2O_3	64.30	63.90	63.27	63.91	64.17	63.98	63.99	63.92	64.31	63.71	63.96	63.84
Al_2O_3	8.31	8.35	7.69	7.84	7.77	7.77	7.58	8.06	7.69	7.91	7.74	7.80
FeO(t)	12.16	12.35	13.95	12.22	12.46	12.50	13.13	13.37	13.37	12.41	12.50	12.74
MgO	14.62	14.72	14.04	14.92	15.30	15.19	13.71	13.85	13.55	14.97	15.16	15.02
FeO	10.86	10.69	11.49	10.11	9.80	9.89	11.77	11.91	12.17	10.09	9.89	10.15
Fe_2O_3	1.45	1.84	2.73	2.35	2.96	2.90	1.52	1.63	1.34	2.58	2.90	2.87
TiO_2	0.18	0.16	0.15	0.11	0.12	0.11	0.14	0.14	0.12	0.16	0.14	0.15
V_2O_5	0.10	0.10	0.11	0.06	0.07	0.07	0.10	0.10	0.09	0.11	0.09	0.08
MnO	0.24	0.21	0.27	0.19	0.18	0.16	0.24	0.24	0.24	0.23	0.23	0.22
CoO	0.03	0.04	0.04	0.05	0.04	0.04	0.04	0.03	0.04	0.05	0.03	0.05
NiO	0.17	0.17	0.18	0.14	0.15	0.16	0.14	0.15	0.16	0.19	0.21	0.18
ZnO	0.00	0.00	0.00	0.00	0.04	0.00	0.03	0.00	0.00	0.05	0.00	0.00
Total												
Cr#	0.838	0.837	0.847	0.845	0.847	0.847	0.850	0.842	0.849	0.844	0.847	0.846
Cr/3+	0.824	0.818	0.818	0.821	0.817	0.817	0.834	0.825	0.835	0.817	0.817	0.816
Al/3+	0.159	0.159	0.148	0.150	0.147	0.148	0.147	0.155	0.149	0.151	0.147	0.149
Fe^{3+}/3+	0.018	0.022	0.034	0.029	0.036	0.035	0.019	0.020	0.017	0.032	0.035	0.035
Mg#	0.706	0.710	0.685	0.725	0.736	0.732	0.675	0.675	0.665	0.725	0.732	0.725
Fe^{2+}#	0.294	0.290	0.315	0.275	0.264	0.268	0.325	0.325	0.335	0.275	0.268	0.275

Sample Ref	288.20	288.20	288.70	288.70	288.70	289.20	289.20	289.20	289.70	289.70	289.70	290.20
Drill Core	V05-13	V05-13	V05-13	V05-13	V05-13	V05-13	V05-13	V05-13	V05-13	V05-13	V05-13	V05-13
Depth (m)	288.20	288.20	288.70	288.70	288.70	289.20	289.20	289.20	289.70	289.70	289.70	290.20
Zone	Ore Zone	Ore Zone	Ore Zone	Ore Zone	Ore Zone	Ore Zone	Ore Zone	Ore Zone	Ore Zone	Ore Zone	Ore Zone	Ore Zone
Rock Type	Chromitite	Chromitite	Chromitite	Chromitite	Chromitite	Chromitite	Chromitite	Chromitite	Chromitite	Chromitite	Chromitite	Chromitite
Ore type	MCR	MCR	MCR	MCR	MCR	MCR	MCR	MCR	MCR	MCR	MCR	MCR
% Chromite	>95%	>95%	>95%	>95%	>95%	>95%	>95%	>95%	>95%	>95%	>95%	>95%
Morphology	Euhedral	Euhedral	Euhedral	Euhedral	Euhedral	Euhedral	Euhedral	Euhedral	Euhedral	Euhedral	Euhedral	Euhedral
Chromite (n) =	1	1	1	1	1	1	1	1	1	1	1	1
Analyses per grain (n)=	2	2	2	2	2	2	2	2	2	2	2	2
SiO_2	0.00	0.00	0.00	0.00	0.00	0.00	0.00	0.00	0.00	0.00	0.00	0.00
Cr_2O_3	63.05	63.01	63.89	63.77	63.89	63.95	64.02	63.88	64.27	64.22	64.18	63.62
Al_2O_3	7.95	7.93	7.82	7.84	7.90	8.06	7.57	7.58	8.09	8.21	7.97	7.75
FeO(t)	13.66	13.69	12.13	12.26	12.47	12.43	12.57	12.84	12.32	12.35	12.50	12.41
MgO	14.66	15.03	14.64	14.50	15.02	14.90	14.69	14.42	14.40	14.84	14.81	14.88
FeO	10.75	10.35	10.46	10.57	10.14	10.39	10.45	10.83	11.04	10.68	10.54	10.18
Fe_2O_3	3.23	3.71	1.86	1.88	2.59	2.26	2.36	2.23	1.42	1.86	2.17	2.48
TiO_2	0.17	0.18	0.17	0.17	0.18	0.16	0.17	0.16	0.17	0.19	0.17	0.15
V_2O_5	0.11	0.09	0.10	0.10	0.06	0.11	0.09	0.11	0.08	0.13	0.09	0.14
MnO	0.23	0.20	0.23	0.25	0.21	0.25	0.22	0.22	0.22	0.21	0.24	0.22
CoO	0.05	0.04	0.04	0.05	0.03	0.03	0.04	0.05	0.05	0.00	0.03	0.02
NiO	0.11	0.13	0.18	0.22	0.20	0.16	0.19	0.19	0.17	0.16	0.17	0.17
ZnO	0.05	0.00	0.00	0.04	0.00	0.00	0.00	0.00	0.00	0.00	0.00	0.00
Total												
Cr#	0.842	0.842	0.846	0.845	0.844	0.842	0.850	0.850	0.842	0.840	0.844	0.846
Cr/3+	0.809	0.804	0.826	0.825	0.818	0.819	0.825	0.826	0.827	0.821	0.821	0.821
Al/3+	0.152	0.151	0.151	0.151	0.151	0.154	0.146	0.146	0.155	0.157	0.152	0.149
Fe^{3+}/3+	0.039	0.045	0.023	0.023	0.032	0.028	0.029	0.027	0.017	0.023	0.026	0.030
Mg#	0.708	0.721	0.714	0.710	0.725	0.719	0.715	0.703	0.699	0.712	0.714	0.723
Fe^{2+}#	0.292	0.279	0.286	0.290	0.275	0.281	0.285	0.297	0.301	0.288	0.286	0.277

Sample Ref	290.20	290.20	290.70	290.70	291.20	291.20	291.20	291.70	291.70	291.70	292.20	292.20
Drill Core	V05-13	V05-13	V05-13	V05-13	V05-13	V05-13	V05-13	V05-13	V05-13	V05-13	V05-13	V05-13
Depth (m)	290.20	290.20	290.70	290.70	291.20	291.20	291.20	291.70	291.70	291.70	292.20	292.20
Zone	Ore Zone	Ore Zone	Ore Zone	Ore Zone	Ore Zone	Ore Zone	Ore Zone	Ore Zone	Ore Zone	Ore Zone	Ore Zone	Ore Zone
Rock Type	Chromitite	Chromitite	Chromitite	Chromitite	Chromitite	Chromitite	Chromitite	Chromitite	Chromitite	Chromitite	Chromitite	Chromitite
Ore type	MCR	MCR	MCR	MCR	MCR	MCR	MCR	MCR	MCR	MCR	MCR	MCR
% Chromite	>95%	>95%	>95%	>95%	>95%	>95%	>95%	>95%	>95%	>95%	>95%	>95%
Morphology	Euhedral	Euhedral	Euhedral	Euhedral	Euhedral	Euhedral	Euhedral	Euhedral	Euhedral	Euhedral	Euhedral	Euhedral
Chromite (n) =	1	1	1	1	1	1	1	1	1	1	1	1
Analyses per grain (n)=	2	2	2	2	2	2	2	2	2	2	2	2
SiO_2	0.00	0.00	0.00	0.00	0.00	0.00	0.00	0.00	0.00	0.00	0.00	0.00
Cr_2O_3	63.54	63.63	63.66	63.28	63.70	63.92	63.67	64.50	64.05	64.34	64.08	63.70
Al_2O_3	7.84	7.74	8.05	8.03	7.88	7.82	7.88	8.05	8.00	8.01	8.01	7.90
FeO(t)	12.45	12.66	13.09	13.39	12.79	12.94	13.03	12.69	12.75	13.07	12.65	12.91
MgO	15.12	14.95	14.53	13.86	14.54	14.54	14.44	14.16	14.13	14.38	14.74	14.72
FeO	9.90	10.08	10.95	11.66	10.77	10.87	10.92	11.49	11.41	11.25	10.69	10.58
Fe_2O_3	2.83	2.87	2.38	1.92	2.25	2.31	2.35	1.34	1.49	2.03	2.17	2.59
TiO_2	0.17	0.16	0.16	0.15	0.15	0.14	0.15	0.15	0.16	0.15	0.16	0.12
V_2O_5	0.11	0.07	0.11	0.08	0.11	0.12	0.10	0.11	0.10	0.07	0.12	0.09
MnO	0.22	0.24	0.24	0.24	0.24	0.22	0.23	0.25	0.23	0.23	0.23	0.17
CoO	0.00	0.05	0.04	0.04	0.04	0.04	0.06	0.03	0.04	0.05	0.03	0.04
NiO	0.17	0.19	0.15	0.15	0.15	0.14	0.18	0.20	0.14	0.18	0.15	0.12
ZnO	0.04	0.00	0.00	0.05	0.00	0.00	0.00	0.00	0.00	0.00	0.00	0.03
Total												
Cr#	0.845	0.846	0.841	0.841	0.844	0.846	0.844	0.843	0.843	0.843	0.843	0.844
Cr/3+	0.815	0.817	0.817	0.821	0.821	0.822	0.820	0.829	0.828	0.823	0.821	0.817
Al/3+	0.150	0.148	0.154	0.155	0.151	0.150	0.151	0.154	0.154	0.153	0.153	0.151
Fe^{3+}/3+	0.035	0.035	0.029	0.024	0.028	0.028	0.029	0.016	0.018	0.025	0.026	0.032
Mg#	0.731	0.725	0.703	0.679	0.706	0.704	0.702	0.687	0.688	0.695	0.711	0.713
Fe^{2+}#	0.269	0.275	0.297	0.321	0.294	0.296	0.298	0.313	0.312	0.305	0.289	0.287

Sample Ref	292.20	292.70	293.20	293.20	293.20	293.70	293.70	293.70	294.20	294.20	294.20	294.90
Drill Core	V05-13	V05-13	V05-13	V05-13	V05-13	V05-13	V05-13	V05-13	V05-13	V05-13	V05-13	V05-13
Depth (m)	292.20	292.70	293.20	293.20	293.20	293.70	293.70	293.70	294.20	294.20	294.20	294.90
Zone	Ore Zone	Ore Zone	Ore Zone	Ore Zone	Ore Zone	Ore Zone	Ore Zone	Ore Zone	Ore Zone	Ore Zone	Ore Zone	Ore Zone
Rock Type	Chromitite	Chromitite	Chromitite	Chromitite	Chromitite	Chromitite	Chromitite	Chromitite	Chromitite	Chromitite	Chromitite	Chromitite
Ore type	MCR	MCR	MCR	MCR	MCR	MCR	MCR	MCR	MCR	MCR	MCR	MCR
% Chromite	>95%	>95%	>95%	>95%	>95%	>95%	>95%	>95%	>95%	>95%	>95%	>95%
Morphology	Euhedral	Euhedral	Euhedral	Euhedral	Euhedral	Euhedral	Euhedral	Euhedral	Euhedral	Euhedral	Euhedral	Euhedral
Chromite (n) =	1	1	1	1	1	1	1	1	1	1	1	1
Analyses per grain (n)=	2	2	2	2	2	2	2	2	2	2	2	2
SiO_2	0.00	0.00	0.00	0.00	0.00	0.00	0.00	0.00	0.00	0.00	0.00	0.00
Cr_2O_3	63.45	63.60	63.93	63.34	64.98	63.68	64.03	63.66	64.56	63.72	63.95	63.68
Al_2O_3	8.17	7.89	7.79	7.87	7.39	8.19	7.97	8.11	7.73	7.79	7.88	7.84
FeO(t)	12.93	13.55	12.25	12.37	12.41	12.86	13.14	13.43	12.14	12.18	12.38	12.54
MgO	15.14	14.30	15.24	15.14	14.95	14.54	14.61	14.54	14.97	15.18	15.08	14.77
FeO	10.15	11.24	9.79	9.79	10.30	10.96	10.90	11.07	10.24	9.76	10.03	10.39
Fe_2O_3	3.09	2.56	2.73	2.87	2.34	2.12	2.49	2.62	2.11	2.68	2.62	2.38
TiO_2	0.17	0.12	0.17	0.16	0.15	0.19	0.14	0.15	0.16	0.17	0.15	0.17
V_2O_5	0.09	0.07	0.08	0.08	0.10	0.11	0.05	0.07	0.09	0.10	0.11	0.10
MnO	0.23	0.20	0.23	0.20	0.24	0.23	0.21	0.20	0.22	0.20	0.22	0.23
CoO	0.04	0.03	0.03	0.04	0.03	0.04	0.03	0.03	0.03	0.05	0.05	0.05
NiO	0.13	0.13	0.16	0.17	0.15	0.17	0.15	0.14	0.17	0.20	0.18	0.16
ZnO	0.05	0.00	0.00	0.00	0.04	0.00	0.00	0.00	0.00	0.00	0.05	0.00
Total												
Cr#	0.839	0.844	0.846	0.844	0.855	0.839	0.844	0.840	0.848	0.846	0.845	0.845
Cr/3+	0.807	0.817	0.818	0.814	0.831	0.817	0.818	0.814	0.827	0.818	0.818	0.820
Al/3+	0.155	0.151	0.149	0.151	0.141	0.157	0.152	0.155	0.148	0.149	0.150	0.151
Fe^{3+}/3+	0.037	0.031	0.033	0.035	0.028	0.026	0.030	0.032	0.026	0.033	0.032	0.029
Mg#	0.727	0.694	0.735	0.734	0.721	0.703	0.705	0.701	0.723	0.735	0.728	0.717
Fe^{2+}#	0.273	0.306	0.265	0.266	0.279	0.297	0.295	0.299	0.277	0.265	0.272	0.283

Sample Ref	294.90	294.90	295.40	295.40	295.40	296.40	296.40	296.40	296.90	296.90	296.90	297.40
Drill Core	V05-13	V05-13	V05-13	V05-13	V05-13	V05-13	V05-13	V05-13	V05-13	V05-13	V05-13	V05-13
Depth (m)	294.90	294.90	295.40	295.40	295.40	296.40	296.40	296.40	296.90	296.90	296.90	297.40
Zone	Ore Zone	Ore Zone	Ore Zone	Ore Zone	Ore Zone	Ore Zone	Ore Zone	Ore Zone	Ore Zone	Ore Zone	Ore Zone	Ore Zone
Rock Type	Chromitite	Chromitite	Chromitite	Chromitite	Chromitite	Chromitite	Chromitite	Chromitite	Chromitite	Chromitite	Chromitite	Chromitite
Ore type	MCR	MCR	MCR	MCR	MCR	MCR	MCR	MCR	MCR	MCR	MCR	MCR
% Chromite	>95%	>95%	>95%	>95%	>95%	>95%	>95%	>95%	>95%	>95%	>95%	>95%
Morphology	Euhedral	Euhedral	Euhedral	Euhedral	Euhedral	Euhedral	Euhedral	Euhedral	Euhedral	Euhedral	Euhedral	Euhedral
Chromite (n) =	1	1	1	1	1	1	1	1	1	1	1	1
Analyses per grain (n)=	2	2	2	2	2	2	2	2	2	2	2	2
SiO_2	0.00	0.00	0.00	0.00	0.00	0.00	0.00	0.00	0.00	0.00	0.00	0.00
Cr_2O_3	64.22	63.95	63.32	64.13	63.49	63.21	62.69	62.66	63.77	63.71	64.18	63.27
Al_2O_3	7.39	7.63	7.73	7.70	7.65	8.31	8.17	7.85	7.75	7.95	7.86	7.72
FeO(t)	12.63	13.05	12.46	12.52	12.56	12.48	13.09	13.28	12.17	12.28	12.31	13.45
MgO	14.83	14.72	14.91	15.20	14.99	15.19	15.18	14.95	14.90	15.06	14.90	14.02
FeO	10.27	10.57	10.02	9.90	9.97	9.98	9.94	10.16	10.10	10.00	10.27	11.42
Fe_2O_3	2.62	2.76	2.71	2.91	2.87	2.78	3.51	3.46	2.30	2.53	2.27	2.26
TiO_2	0.14	0.15	0.16	0.16	0.16	0.17	0.19	0.18	0.15	0.15	0.15	0.17
V_2O_5	0.08	0.10	0.09	0.05	0.09	0.11	0.08	0.15	0.11	0.11	0.11	0.12
MnO	0.23	0.21	0.20	0.23	0.23	0.22	0.25	0.24	0.20	0.21	0.24	0.22
CoO	0.04	0.05	0.03	0.03	0.04	0.03	0.05	0.03	0.04	0.04	0.05	0.06
NiO	0.15	0.16	0.19	0.16	0.15	0.15	0.14	0.16	0.18	0.15	0.20	0.13
ZnO	0.00	0.05	0.00	0.00	0.00	0.00	0.00	0.00	0.00	0.05	0.00	0.04
Total												
Cr#	0.853	0.849	0.846	0.848	0.848	0.836	0.837	0.843	0.847	0.843	0.846	0.846
Cr/3+	0.826	0.820	0.818	0.818	0.818	0.808	0.802	0.807	0.823	0.817	0.822	0.822
Al/3+	0.142	0.146	0.149	0.147	0.147	0.158	0.156	0.151	0.149	0.152	0.150	0.150
Fe^{3+}/3+	0.032	0.034	0.033	0.035	0.035	0.034	0.043	0.042	0.028	0.031	0.028	0.028
Mg#	0.720	0.713	0.726	0.732	0.728	0.731	0.731	0.724	0.724	0.728	0.721	0.686
Fe^{2+}#	0.280	0.287	0.274	0.268	0.272	0.269	0.269	0.276	0.276	0.272	0.279	0.314

Sample Ref	297.40	297.40	298.40	298.40	298.40	298.90	298.90	298.90	299.40	299.40	299.90	299.90
Drill Core	V05-13	V05-13	V05-13	V05-13	V05-13	V05-13	V05-13	V05-13	V05-13	V05-13	V05-13	V05-13
Depth (m)	297.40	297.40	298.40	298.40	298.40	298.90	298.90	298.90	299.40	299.40	299.90	299.90
Zone	Ore Zone	Ore Zone	Ore Zone	Ore Zone	Ore Zone	Ore Zone	Ore Zone	Ore Zone	Ore Zone	Ore Zone	Ore Zone	Ore Zone
Rock Type	Chromitite	Chromitite	Chromitite	Chromitite	Chromitite	Chromitite	Chromitite	Chromitite	Chromitite	Chromitite	Chromitite	Chromitite
Ore type	MCR	MCR	MCR	MCR	MCR	MCR	MCR	MCR	MCR	MCR	MCR	MCR
% Chromite	>95%	>95%	>95%	>95%	>95%	>95%	>95%	>95%	>95%	>95%	>95%	>95%
Morphology	Euhedral	Euhedral	Euhedral	Euhedral	Euhedral	Euhedral	Euhedral	Euhedral	Euhedral	Euhedral	Euhedral	Euhedral
Chromite (n) =	1	1	1	1	1	1	1	1	1	1	1	1
Analyses per grain (n)=	2	2	2	2	2	2	2	2	2	2	2	2
SiO_2	0.00	0.00	0.00	0.00	0.00	0.00	0.00	0.00	0.00	0.00	0.00	0.00
Cr_2O_3	64.09	64.14	64.85	64.28	64.62	63.85	63.97	64.44	64.92	63.75	64.00	63.98
Al_2O_3	7.78	7.57	7.76	7.66	7.77	7.86	7.98	7.80	7.45	7.98	7.71	7.67
FeO(t)	13.49	13.66	12.20	12.24	12.32	12.36	12.64	12.65	13.33	13.44	12.34	12.50
MgO	13.91	14.25	14.84	14.87	14.70	14.60	14.34	14.92	13.65	13.63	14.95	15.19
FeO	11.82	11.44	10.49	10.27	10.63	10.57	11.14	10.48	12.12	12.09	10.17	9.89
Fe_2O_3	1.86	2.47	1.90	2.19	1.88	2.00	1.67	2.40	1.34	1.49	2.41	2.90
TiO_2	0.16	0.18	0.15	0.16	0.14	0.15	0.18	0.17	0.15	0.15	0.16	0.16
V_2O_5	0.10	0.09	0.13	0.12	0.14	0.12	0.12	0.11	0.07	0.09	0.13	0.10
MnO	0.24	0.23	0.22	0.24	0.21	0.22	0.21	0.22	0.23	0.24	0.19	0.23
CoO	0.04	0.04	0.05	0.03	0.04	0.05	0.04	0.04	0.05	0.05	0.05	0.03
NiO	0.11	0.12	0.19	0.16	0.17	0.16	0.15	0.17	0.16	0.16	0.18	0.16
ZnO	0.05	0.00	0.04	0.00	0.06	0.04	0.00	0.00	0.04	0.00	0.00	0.00
Total												
Cr#	0.847	0.850	0.849	0.849	0.848	0.845	0.843	0.847	0.854	0.843	0.848	0.848
Cr/3+	0.827	0.825	0.829	0.826	0.828	0.824	0.826	0.822	0.840	0.827	0.823	0.818
Al/3+	0.150	0.145	0.148	0.147	0.149	0.151	0.154	0.148	0.144	0.154	0.148	0.146
Fe^{3+}/3+	0.023	0.030	0.023	0.027	0.023	0.025	0.021	0.029	0.017	0.018	0.030	0.035
Mg#	0.677	0.689	0.716	0.721	0.711	0.711	0.696	0.717	0.667	0.668	0.724	0.732
Fe^{2+}#	0.323	0.311	0.284	0.279	0.289	0.289	0.304	0.283	0.333	0.332	0.276	0.268

Sample Ref	299.90	300.40	300.40	300.40
Drill Core	V05-13	V05-13	V05-13	V05-13
Depth (m)	299.90	300.40	300.40	300.40
Zone	Ore Zone	Ore Zone	Ore Zone	Ore Zone
Rock Type	Chromitite	Chromitite	Chromitite	Chromitite
Ore type	MCR	MCR	MCR	MCR
% Chromite	>95%	>95%	>95%	>95%
Morphology	Euhedral	Euhedral	Euhedral	Euhedral
Chromite (n) =	1	1	1	1
Analyses per grain (n)=	2	2	2	2
SiO_2	0.00	0.00	0.00	0.00
Cr_2O_3	64.09	65.46	64.24	64.00
Al_2O_3	7.48	6.70	7.38	7.39
FeO(t)	12.52	12.73	12.85	12.95
MgO	15.03	14.10	14.15	14.31
FeO	10.05	11.29	11.17	10.94
Fe_2O_3	2.74	1.60	1.88	2.23
TiO_2	0.16	0.13	0.13	0.15
V_2O_5	0.12	0.11	0.09	0.09
MnO	0.22	0.23	0.19	0.22
CoO	0.04	0.00	0.03	0.05
NiO	0.16	0.13	0.14	0.15
ZnO	0.00	0.00	0.04	0.00
Total				
Cr#	0.852	0.868	0.854	0.853
Cr/3+	0.823	0.850	0.834	0.830
Al/3+	0.143	0.130	0.143	0.143
Fe^{3+}/3+	0.034	0.020	0.023	0.028
Mg#	0.727	0.690	0.693	0.700
Fe^{2+}#	0.273	0.310	0.307	0.300

Table D 4: Sample F1964-65 drill core V05-24. Chromite Analyses by Scanning Electron Microscope using Wave- Dispersive Spectroscopy

Sample	F1964-65		F1964-65		F1964-65		F1964-65		F1964-65		F1964-65	
Subsection I.D	P		Q		R		S		T		U		V	
Drill Core	V05-24		V05-24		V05-24		V05-24		V05-24		V05-24		V05-24	
Depth (m)	341.46		341.47		341.48		341.49		341.50		341.51		341.52	
Zone	Ore Zone		Ore Zone		Ore Zone		Ore Zone		Ore Zone		Ore Zone		Ore Zone	
Rock Type	Chromitite		Chromitite		Chromitite		Chromitite		Chromitite		Chromitite		Chromitite	
Ore Type	MCR		MCR		MCR		MCR		MCR		MCR		MCR	
% Chromite	>95%		>95%		>95%		>95%		>95%		>95%		>95%	
Chromite Morphology	Euhedral		Euhedral		Euhedral		Euhedral		Euhedral		Euhedral		Euhedral	
Chromite (n) =	3		3		3		3		3		3		3	
Analyses per sample (n) =	9		9		9		9		9		9		9	
		%RSD		*%RSD*		*%RSD*		*%RSD*		*%RSD*		*%RSD*		*%RSD*
SiO_2	0.000	-	0.000	-	0.000	-	0.000	-	0.000	-	0.000	-	0.000	-
Cr_2O_3	62.278	*1.232*	61.598	*2.279*	63.126	*0.213*	62.411	*1.118*	63.162	*0.284*	63.187	*0.331*	62.720	*0.488*
Al_2O_3	8.455	*8.956*	8.698	*8.239*	7.975	*0.892*	8.238	*2.811*	7.631	*0.985*	8.000	*1.990*	8.479	*2.113*
FeO	15.744	*3.470*	15.857	*2.104*	15.547	*2.202*	15.786	*0.799*	14.789	*0.420*	14.276	*0.261*	14.564	*1.272*
MgO	12.877	*0.966*	12.686	*0.834*	12.751	*3.157*	12.860	*0.402*	13.743	*1.711*	13.906	*2.299*	13.703	*2.795*
TiO_2	0.110	*39.985*	0.097	*14.297*	0.114	*35.666*	0.111	*18.892*	0.151	*7.485*	0.156	*3.598*	0.144	*15.915*
V_2O_5	0.096	*5.461*	0.097	*19.028*	0.088	*15.456*	0.104	*44.593*	0.105	*37.162*	0.080	*8.929*	0.104	*3.970*
MnO	0.295	*4.986*	0.300	*8.689*	0.303	*8.198*	0.320	*4.986*	0.305	*3.357*	0.272	*0.656*	0.269	*0.930*
CoO	0.044	*12.623*	0.037	*2.016*	0.035	*87.227*	0.053	*21.288*	0.044	*14.255*	0.045	*22.127*	0.057	*23.518*
NiO	0.088	*15.850*	0.079	*31.326*	0.116	*2.906*	0.086	*6.194*	0.125	*16.308*	0.114	*10.462*	0.118	*10.700*
ZnO	0.042	*96.407*	0.024	*173.205*	0.000	-	0.043	*87.169*	0.017	*173.205*	0.055	*10.612*	0.025	*173.205*
Total	100.03		99.47		100.06		100.02		100.07		100.09		100.18	
Cr^{3+}	1.603		1.594		1.630		1.609		1.621		1.618		1.603	
Al^{3+}	0.325		0.336		0.307		0.317		0.292		0.305		0.323	
Fe^{3+}	0.062		0.061		0.053		0.065		0.075		0.066		0.062	
Fe^{2+}	0.367		0.373		0.371		0.366		0.327		0.321		0.332	
Mg^{2+}	0.625		0.619		0.621		0.625		0.665		0.671		0.660	
Ti^{4+}	0.003		0.002		0.003		0.003		0.004		0.004		0.004	
V^{5+}	0.002		0.002		0.002		0.002		0.002		0.002		0.002	
Mn^{2+}	0.008		0.008		0.008		0.009		0.008		0.007		0.007	
Co^{2+}	0.001		0.001		0.001		0.001		0.001		0.001		0.001	
Ni^{2+}	0.002		0.002		0.003		0.002		0.003		0.003		0.003	
Zn^{2+}	0.001		0.001		0.000		0.001		0.000		0.001		0.001	
Cr#	0.832		0.826		0.841		0.836		0.847		0.841		0.832	
Cr/3+	0.806		0.801		0.819		0.808		0.816		0.813		0.806	
Al/3+	0.163		0.169		0.154		0.159		0.147		0.154		0.163	
$Fe^{3+}/3+$	0.031		0.031		0.027		0.032		0.037		0.033		0.031	
Mg#	0.630		0.624		0.626		0.631		0.670		0.677		0.665	
Fe^{2+}#	0.365		0.372		0.370		0.364		0.325		0.319		0.330	
MgO/FeO_{tot}	0.818		0.800		0.820		0.815		0.929		0.974		0.941	
Cr/Fe	3.482		3.419		3.574		3.480		3.759		3.896		3.791	
Fe^{3+}/Fe^{2+}	0.170		0.164		0.144		0.176		0.228		0.205		0.186	

Sample	**F1964-65**		**F1964-65**		**F1964-65**		**F1964-65**		**F1964-65**		**F1964-65**		**F1964-65**	
Subsection I.D	**W**		**X**		**Y**		**Z**		**AA**		**BB**		**CC**	
Drill Core	V05-24		V05-24		V05-24		V05-24		V05-24		V05-24		V05-24	
Depth (m)	341.53		341.54		341.55		341.56		341.57		341.58		341.59	
Zone	Ore Zone		Ore Zone		Ore Zone		Ore Zone		Ore Zone		Ore Zone		Ore Zone	
Rock Type	Chromitite		Chromitite		Chromitite		Chromitite		Chromitite		Chromitite		Chromitite	
Ore Type	**MCR**		**MCR**		**MCR**		**MCR**		**MCR**		**MCR**		**MCR**	
% Chromite	>95%		>95%		>95%		>95%		>95%		>95%		>95%	
Chromite Morphology	Euhedral		Euhedral		Euhedral		Euhedral		Euhedral		Euhedral		Euhedral	
Chromite (n)=	3		3		3		3		3		3		3	
Analyses per sample (n) =	9		9		9		9		9		9		9	
		%RSD		*%RSD*		*%RSD*		*%RSD*		*%RSD*		*%RSD*		*%RSD*
SiO_2	0.000	-	0.000	-	0.000	-	0.000	-	0.000	-	0.000	-	0.000	-
Cr_2O_3	63.489	*0.441*	62.116	*0.484*	62.995	*0.384*	62.930	*0.576*	63.017	*0.349*	62.853	*0.493*	62.885	*0.606*
Al_2O_3	8.126	*1.375*	8.754	*2.236*	8.097	*1.942*	8.376	*3.424*	8.065	*1.899*	8.484	*0.725*	8.115	*2.961*
FeO	14.374	*1.204*	14.344	*0.555*	15.495	*1.410*	15.102	*1.037*	15.372	*1.319*	14.939	*0.685*	15.180	*0.364*
MgO	13.140	*0.657*	13.865	*1.880*	12.788	*0.904*	12.943	*0.879*	12.962	*1.039*	13.020	*0.434*	12.625	*1.331*
TiO_2	0.133	*25.957*	0.131	*13.808*	0.108	*11.306*	0.106	*52.157*	0.138	*29.195*	0.088	*21.073*	0.125	*45.803*
V_2O_5	0.118	*21.274*	0.103	*41.512*	0.121	*12.234*	0.096	*24.745*	0.120	*12.143*	0.088	*11.619*	0.092	*5.909*
MnO	0.302	*5.900*	0.290	*0.999*	0.298	*5.984*	0.295	*3.764*	0.293	*4.536*	0.293	*2.595*	0.302	*3.592*
CoO	0.050	*34.662*	0.052	*38.167*	0.026	*86.717*	0.048	*12.441*	0.047	*17.149*	0.045	*19.357*	0.041	*86.855*
NiO	0.122	*11.105*	0.092	*33.000*	0.087	*13.776*	0.082	*27.960*	0.111	*12.030*	0.080	*24.632*	0.108	*44.477*
ZnO	0.000	-	0.000	-	0.058	*0.600*	0.000	-	0.046	*90.317*	0.053	*7.210*	0.039	*93.641*
Total	99.85		99.75		100.07		99.98		100.17		99.94		99.51	
Cr^{3+}	1.637		1.590		1.625		1.621		1.622		1.618		1.632	
Al^{3+}	0.312		0.334		0.311		0.322		0.310		0.326		0.314	
Fe^{3+}	0.039		0.065		0.053		0.048		0.056		0.048		0.043	
Fe^{2+}	0.353		0.324		0.370		0.364		0.363		0.359		0.373	
Mg^{2+}	0.639		0.669		0.622		0.629		0.629		0.632		0.618	
Ti^{4+}	0.003		0.003		0.003		0.003		0.003		0.002		0.003	
V^{5+}	0.003		0.002		0.003		0.002		0.003		0.002		0.002	
Mn^{2+}	0.008		0.008		0.008		0.008		0.008		0.008		0.008	
Co^{2+}	0.001		0.001		0.001		0.001		0.001		0.001		0.001	
Ni^{2+}	0.003		0.002		0.002		0.002		0.003		0.002		0.003	
Zn^{2+}	0.000		0.000		0.001		0.000		0.001		0.001		0.001	
Cr#	0.840		0.826		0.839		0.834		0.840		0.832		0.839	
Cr/3+	0.823		0.800		0.817		0.814		0.816		0.812		0.820	
Al/3+	0.157		0.168		0.157		0.162		0.156		0.164		0.158	
Fe^{3+}/3+	0.019		0.032		0.027		0.024		0.028		0.024		0.022	
Mg#	0.644		0.674		0.627		0.633		0.634		0.638		0.623	
Fe^{2+}#	0.352		0.322		0.368		0.362		0.361		0.358		0.372	
MgO/FeO_{tot}	0.914		0.967		0.825		0.857		0.843		0.872		0.832	
Cr/Fe	3.888		3.812		3.579		3.668		3.608		3.703		3.646	
Fe^{3+}/Fe^{2+}	0.109		0.199		0.143		0.131		0.154		0.133		0.116	

Table D 5: Sample F1996-97 drill core V05-24. Chromite Analyses by Scanning Electron Microscope using Wave- Dispersive Spectroscopy

Sample	F1996-97		F1996-97		F1996-97		F1996-97		F1996-97		F1996-97		F1996-97	
Subsection I.D	**O**		**N**		**M**		**L**		**K**		**J**		**I**	
Drill Core	V05-24		V05-24		V05-24		V05-24		V05-24		V05-24		V05-24	
Depth (m)	359.01		359.02		359.03		359.04		359.05		359.06		359.07	
Zone	Ore Zone		Ore Zone		Ore Zone		Ore Zone		Ore Zone		Ore Zone		Ore Zone	
Rock Type	Chromitite		Chromitite		Chromitite		Chromitite		Chromitite		Chromitite		Chromitite	
Ore Type	**MCR**		**MCR**		**MCR**		**MCR**		**MCR**		**MCR**		**MCR**	
% Chromite	>95%		>95%		>95%		>95%		>95%		>95%		>95%	
Chromite Morphology	Euhedral		Euhedral		Euhedral		Euhedral		Euhedral		Euhedral		Euhedral	
Chromite (n) =	3		3		3		3		3		3		3	
Analyses per sample (n) =	9		9		9		9		9		9		9	
		%RSD		*%RSD*		*%RSD*		*%RSD*		*%RSD*		*%RSD*		*%RSD*
SiO_2	0.000	-	0.000	-	0.000	-	0.000	-	0.000	-	0.000	-	0.000	-
Cr_2O_3	63.461	*0.400*	63.353	*0.070*	63.859	*0.359*	63.432	*0.650*	63.627	*0.276*	63.817	*0.728*	63.567	*0.091*
Al_2O_3	7.865	*2.816*	7.853	*2.603*	7.539	*0.521*	7.577	*0.066*	7.659	*1.063*	7.657	*2.898*	7.534	*2.560*
FeO	12.731	*1.601*	13.196	*0.806*	13.269	*1.622*	13.332	*1.724*	13.061	*1.555*	13.232	*1.128*	13.477	*1.205*
MgO	14.680	*1.035*	14.667	*0.487*	14.633	*1.200*	14.610	*1.614*	14.652	*1.982*	14.638	*0.865*	14.559	*1.066*
TiO_2	0.169	*2.328*	0.159	*2.158*	0.162	*2.753*	0.151	*0.788*	0.163	*3.601*	0.169	*7.507*	0.160	*6.656*
V_2O_5	0.112	*10.323*	0.102	*20.381*	0.129	*19.044*	0.110	*5.701*	0.139	*12.913*	0.121	*20.482*	0.116	*24.063*
MnO	0.229	*7.479*	0.236	*9.286*	0.228	*3.697*	0.250	*11.197*	0.242	*8.840*	0.249	*5.491*	0.241	*3.253*
CoO	0.036	*8.061*	0.045	*21.160*	0.047	*25.215*	0.059	*10.226*	0.053	*7.425*	0.052	*17.759*	0.039	*30.101*
NiO	0.136	*2.804*	0.135	*8.099*	0.114	*21.594*	0.097	*9.829*	0.125	*20.262*	0.109	*6.887*	0.088	*21.614*
ZnO	0.017	*173.205*	0.000	-	0.000	-	0.000	-	0.000	-	0.000	-	0.016	*173.205*
Total	99.43		99.75		99.98		99.62		99.72		100.04		99.80	
Cr^{3+}	1.626		1.619		1.631		1.625		1.628		1.629		1.627	
Al^{3+}	0.301		0.299		0.287		0.290		0.292		0.291		0.288	
Fe^{3+}	0.060		0.069		0.068		0.073		0.066		0.066		0.072	
Fe^{2+}	0.285		0.288		0.291		0.289		0.288		0.291		0.293	
Mg^{2+}	0.709		0.707		0.705		0.706		0.707		0.704		0.703	
Ti^{4+}	0.004		0.004		0.004		0.004		0.004		0.004		0.004	
V^{5+}	0.002		0.002		0.003		0.002		0.003		0.003		0.002	
Mn^{2+}	0.006		0.006		0.006		0.007		0.007		0.007		0.007	
Co^{2+}	0.001		0.001		0.001		0.002		0.001		0.001		0.001	
Ni^{2+}	0.004		0.004		0.003		0.003		0.003		0.003		0.002	
Zn^{2+}	0.000		0.000		0.000		0.000		0.000		0.000		0.000	
Cr#	0.844		0.844		0.850		0.849		0.848		0.848		0.850	
Cr/3+	0.819		0.815		0.821		0.818		0.820		0.820		0.819	
Al/3+	0.149		0.145		0.148		0.147		0.148		0.147		0.147	
Fe^{3+}/3+	0.030		0.035		0.034		0.037		0.033		0.033		0.036	
Mg#	0.713		0.711		0.708		0.710		0.710		0.708		0.706	
Fe^{2+}#	0.287		0.289		0.292		0.290		0.290		0.292		0.294	
MgO/FeO_{tot}	1.072		1.045		1.083		1.064		1.034		1.050		1.095	
Cr/Fe	4.209		4.121		4.149		4.151		4.058		4.090		4.188	
Fe^{3+}/Fe^{2+}	0.188		0.203		0.243		0.213		0.216		0.224		0.241	

Sample	F1996-97		F1996-97		F1996-97		F1996-97		F1996-97		F1996-97		F1996-97	
Subsection I.D	**H**		**G**		**F**		**E**		**D**		**C**		**B**	
Drill Core	V05-24		V05-24		V05-24		V05-24		V05-24		V05-24		V05-24	
Depth (m)	359.08		359.09		359.10		359.11		359.12		359.13		359.14	
Zone	Ore Zone		Ore Zone		Ore Zone		Ore Zone		Ore Zone		Ore Zone		Ore Zone	
Rock Type	Chromitite		Chromitite		Chromitite		Chromitite		Chromitite		Chromitite		Chromitite	
Ore Type	**MCR**		**MCR**		**MCR**		**MCR**		**MCR**		**MCR**		**MCR**	
% Chromite	>95%		>95%		>95%		>95%		>95%		>95%		>95%	
Chromite Morphology	Euhedral		Euhedral		Euhedral		Euhedral		Euhedral		Euhedral		Euhedral	
Chromite (n) =	3		3		3		3		3		3		3	
Analyses per sample (n) =	9		9		9		9		9		9		9	
		%RSD		*%RSD*		*%RSD*		*%RSD*		*%RSD*		*%RSD*		*%RSD*
SiO_2	0.000	-	0.000	-	0.000	-	0.000	-	0.000	-	0.000	-	0.000	-
Cr_2O_3	63.223	*0.162*	63.500	*0.033*	63.533	*0.573*	63.638	*0.863*	63.853	*0.594*	63.340	*0.526*	63.765	*0.629*
Al_2O_3	7.544	*0.500*	7.666	*1.935*	7.668	*0.160*	7.693	*2.363*	7.662	*2.627*	7.701	*1.349*	7.551	*2.341*
FeO	13.170	*0.082*	13.345	*0.825*	13.672	*1.086*	13.804	*1.746*	13.539	*0.843*	13.438	*1.124*	13.620	*2.418*
MgO	14.550	*0.691*	14.615	*1.118*	14.358	*1.113*	14.278	*0.828*	14.410	*0.963*	14.551	*0.664*	14.236	*0.959*
TiO_2	0.151	*1.519*	0.169	*6.436*	0.164	*3.497*	0.169	*5.431*	0.165	*6.830*	0.168	*3.749*	0.168	*5.096*
V_2O_5	0.103	*7.472*	0.114	*14.568*	0.100	*14.603*	0.100	*7.904*	0.107	*19.742*	0.124	*13.660*	0.117	*24.373*
MnO	0.247	*4.273*	0.244	*5.078*	0.227	*3.226*	0.243	*2.764*	0.231	*2.345*	0.257	*4.730*	0.245	*4.981*
CoO	0.058	*19.915*	0.038	*28.270*	0.036	*36.228*	0.034	*26.140*	0.039	*35.006*	0.036	*15.609*	0.035	*13.979*
NiO	0.099	*6.484*	0.092	*19.625*	0.083	*16.440*	0.093	*0.619*	0.097	*28.732*	0.107	*11.845*	0.096	*26.895*
ZnO	0.000	-	0.000	-	0.012	*173.205*	0.000	-	0.014	*173.205*	0.018	*173.205*	0.016	*173.205*
Total	99.15		99.78		99.85		100.05		100.12		99.74		99.85	
Cr^{3+}	1.628		1.624		1.627		1.628		1.631		1.621		1.635	
Al^{3+}	0.290		0.292		0.293		0.293		0.292		0.294		0.289	
Fe^{3+}	0.071		0.070		0.068		0.066		0.064		0.071		0.062	
Fe^{2+}	0.288		0.291		0.303		0.307		0.301		0.293		0.307	
Mg^{2+}	0.706		0.705		0.693		0.688		0.694		0.702		0.688	
Ti^{4+}	0.004		0.004		0.004		0.004		0.004		0.004		0.004	
V^{5+}	0.002		0.002		0.002		0.002		0.002		0.003		0.002	
Mn^{2+}	0.007		0.007		0.006		0.007		0.006		0.007		0.007	
Co^{2+}	0.002		0.001		0.001		0.001		0.001		0.001		0.001	
Ni^{2+}	0.003		0.002		0.002		0.002		0.003		0.003		0.003	
Zn^{2+}	0.000		0.000		0.000		0.000		0.000		0.000		0.000	
Cr#	0.849		0.847		0.847		0.847		0.848		0.847		0.850	
Cr/3+	0.819		0.818		0.819		0.819		0.821		0.816		0.823	
Al/3+	0.146		0.145		0.147		0.147		0.146		0.145		0.151	
Fe^{3+}/3+	0.036		0.035		0.034		0.033		0.032		0.036		0.031	
Mg#	0.710		0.708		0.696		0.691		0.697		0.706		0.691	
Fe^{2+}#	0.290		0.292		0.304		0.309		0.303		0.294		0.309	
MgO/FeO_{tot}	1.105		1.080		1.106		1.122		1.096		1.103		1.111	
Cr/Fe	4.226		4.152		4.245		4.288		4.188		4.236		4.226	
Fe^{3+}/Fe^{2+}	0.245		0.247		0.229		0.227		0.252		0.233		0.241	

Sample	**F1996-97**	
Subsection I.D	**A**	
Drill Core	V05-24	
Depth (m)	359.15	
Zone	Ore Zone	
Rock Type	Chromitite	
Ore Type	**MCR**	
% Chromite	>95%	
Chromite Morphology	Euhedral	
Chromite (n) =	3	
Analyses per sample (n) =	9	
		%RSD
SiO_2	0.000	-
Cr_2O_3	63.922	*0.397*
Al_2O_3	7.769	*3.049*
FeO	13.367	*1.724*
MgO	14.327	*0.109*
TiO_2	0.160	*2.767*
V_2O_5	0.111	*13.926*
MnO	0.234	*5.384*
CoO	0.041	*16.240*
NiO	0.108	*22.050*
ZnO	0.019	*173.205*
Total	100.06	
Cr^{3+}	1.634	
Al^{3+}	0.296	
Fe^{3+}	0.057	
Fe^{2+}	0.304	
Mg^{2+}	0.690	
Ti^{4+}	0.004	
V^{5+}	0.002	
Mn^{2+}	0.006	
Co^{2+}	0.001	
Ni^{2+}	0.003	
Zn^{2+}	0.000	
Cr#	0.847	
Cr/3+	0.822	
Al/3+	0.151	
Fe^{3+}/3+	0.029	
Mg#	0.694	
Fe^{2+}#	0.306	
MgO/FeO_{tot}	1.153	
Cr/Fe	4.388	
Fe^{3+}/Fe^{2+}	0.209	

Table D 6: Sample F1925 drill core V05-24. Chromite Analyses by Scanning Electron Microscope using Wave- Dispersive Spectroscopy

Sample Ref	F1925-DD		F1925-EE		F1925-FF		F1925-GG		F1925-HH		F1925-II		F1925-JJ	
Drill Core	V05-24		V05-24		V05-24		V05-24		V05-24		V05-24		V05-24	
Depth (m)	296.05		296.06		296.07		296.08		296.09		296.1		296.11	
Zone	Ore Zone		Ore Zone		Ore Zone		Ore Zone		Ore Zone		Ore Zone		Ore Zone	
Rock Type	Chromitite		Chromitite		Chromitite		Chromitite		Chromitite		Chromitite		Chromitite	
Ore Type	MCR		MCR		MCR		MCR		MCR		MCR		MCR	
% Chromite	>95%		>95%		>95%		>95%		>95%		>95%		>95%	
Chromite Morphology	Euhedral		Euhedral		Euhedral		Euhedral		Euhedral		Euhedral		Euhedral	
Chromite (n)=	3		3		3		3		3		3		3	
Analyses per sample (n) =	9		9		9		9		9		9		9	
		%RSD		*%RSD*		*%RSD*		*%RSD*		*%RSD*		*%RSD*		*%RSD*
SiO_2	0.000	-	0.000	-	0.000	-	0.000	-	0.000	-	0.000	-	0.000	-
Cr_2O_3	63.693	*0.405*	63.366	*0.281*	63.524	*0.286*	63.958	*0.351*	64.017	*0.271*	64.032	*0.380*	63.401	*0.637*
Al_2O_3	7.227	*1.134*	7.623	*0.848*	7.260	*0.547*	7.253	*1.015*	7.361	*1.279*	7.368	*3.295*	7.469	*3.222*
FeO	14.241	*1.201*	14.348	*1.852*	14.064	*0.904*	14.280	*1.508*	14.106	*1.773*	14.068	*1.323*	14.395	*1.230*
MgO	13.798	*1.595*	14.151	*0.447*	13.973	*0.581*	13.891	*0.385*	13.938	*1.886*	13.800	*1.083*	13.846	*0.621*
TiO_2	0.171	*9.465*	0.130	*11.405*	0.146	*6.435*	0.146	*3.278*	0.150	*5.389*	0.156	*4.583*	0.140	*6.766*
V_2O_5	0.096	*18.178*	0.093	*19.221*	0.111	*14.265*	0.113	*17.390*	0.111	*12.202*	0.136	*21.026*	0.110	*31.177*
MnO	0.282	*6.242*	0.262	*6.293*	0.241	*7.689*	0.265	*6.712*	0.252	*4.005*	0.251	*8.854*	0.248	*10.269*
CoO	0.048	*27.941*	0.049	*14.934*	0.048	*12.174*	0.058	*15.222*	0.047	*30.376*	0.046	*36.627*	0.032	*6.462*
NiO	0.096	*20.666*	0.109	*4.267*	0.102	*12.986*	0.091	*25.372*	0.100	*38.560*	0.080	*21.840*	0.100	*26.951*
ZnO	0.000	-	0.039	*91.752*	0.031	*88.069*	0.000	-	0.017	*173.205*	0.022	*173.205*	0.000	-
Total	99.65		100.17		99.50		100.05		100.10		99.96		99.74	
Cr^{3+}	1.643		1.621		1.639		1.643		1.643		1.647		1.632	
Al^{3+}	0.278		0.291		0.279		0.278		0.282		0.283		0.287	
Fe^{3+}	0.066		0.078		0.070		0.067		0.063		0.057		0.069	
Fe^{2+}	0.323		0.310		0.314		0.321		0.320		0.326		0.323	
Mg^{2+}	0.671		0.682		0.680		0.673		0.674		0.669		0.672	
Ti^{4+}	0.004		0.003		0.004		0.004		0.004		0.004		0.003	
V^{5+}	0.002		0.002		0.002		0.002		0.002		0.003		0.002	
Mn^{2+}	0.008		0.007		0.007		0.007		0.007		0.007		0.007	
Co^{2+}	0.001		0.001		0.001		0.002		0.001		0.001		0.001	
Ni^{2+}	0.003		0.003		0.003		0.002		0.003		0.002		0.003	
Zn^{2+}	0.000		0.001		0.001		0.000		0.000		0.001		0.000	
Cr#	0.855		0.848		0.854		0.855		0.854		0.854		0.851	
Cr/3+	0.827		0.815		0.824		0.827		0.827		0.829		0.821	
Al/3+	0.140		0.146		0.141		0.140		0.142		0.142		0.144	
$Fe^{3+}/3+$	0.033		0.039		0.035		0.034		0.032		0.029		0.035	
Mg#	0.675		0.688		0.684		0.677		0.678		0.672		0.675	
Fe^{2+}#	0.325		0.312		0.316		0.323		0.322		0.328		0.325	
MgO/FeO_{tot}	0.969		0.986		0.993		0.973		0.988		0.981		0.962	
Cr/Fe	3.937		3.887		3.976		3.942		3.995		4.006		3.877	
Fe^{3+}/Fe^{2+}	0.204		0.252		0.221		0.208		0.197		0.174		0.214	

Sample Ref	F1925-KK		F1925-LL		F1925-MM		F1925-NN		F1925-OO		F1925-PP		F1925-QQ	
Drill Core	V05-24		V05-24		V05-24		V05-24		V05-24		V05-24		V05-24	
Depth (m)	296.12		296.13		296.14		296.15		296.16		296.17		296.18	
Zone	Ore Zone		Ore Zone		Ore Zone		Ore Zone		Ore Zone		Ore Zone		Ore Zone	
Rock Type	Chromitite		Chromitite		Chromitite		Chromitite		Chromitite		Chromitite			
Ore Type	**MCR**		**DCR**		**DCR**		**DCR**		**DCR**		**DCR**		**DCR**	
% Chromite	>95%		~50%		~40%		~35%		~30%		~20%		~15%	
Chromite Morphology	Euhedral		Euhedral		Euhedral		Euhedral		Euhedral		Euhedral		Euhedral	
Chromite (n) =	3		3		3		3		3		3		3	
Analyses per sample (n) =	9		9		9		9		9		9		9	
		%RSD		*%RSD*		*%RSD*		*%RSD*		*%RSD*		*%RSD*		*%RSD*
SiO_2	0.000	-	0.000	-	0.000	-	0.000	-	0.000	-	0.000	-	0.000	-
Cr_2O_3	63.097	*0.190*	63.112	*0.129*	62.576	*0.727*	62.345	*0.495*	61.866	*1.045*	61.943	*0.353*	61.413	*0.486*
Al_2O_3	7.490	*1.310*	7.270	*3.790*	7.030	*2.056*	7.017	*1.307*	7.212	*2.583*	7.017	*1.958*	7.104	*1.889*
FeO	14.314	*1.388*	15.650	*3.201*	16.910	*1.509*	17.121	*1.979*	18.196	*6.105*	18.450	*0.888*	18.991	*0.346*
MgO	13.619	*0.906*	12.894	*2.346*	12.394	*1.416*	12.272	*0.784*	11.791	*5.004*	11.501	*1.866*	11.312	*1.089*
TiO_2	0.145	*6.587*	0.155	*12.909*	0.151	*4.481*	0.144	*12.691*	0.141	*9.469*	0.153	*1.342*	0.147	*7.733*
V_2O_5	0.099	*19.301*	0.121	*13.255*	0.085	*18.954*	0.092	*33.292*	0.105	*40.317*	0.135	*2.874*	0.094	*3.136*
MnO	0.258	*8.458*	0.256	*15.506*	0.297	*2.352*	0.293	*8.930*	0.314	*6.154*	0.307	*4.856*	0.331	*5.785*
CoO	0.056	*16.364*	0.052	*36.673*	0.063	*18.825*	0.073	*17.591*	0.076	*17.232*	0.069	*35.176*	0.056	*9.415*
NiO	0.093	*37.991*	0.057	*25.580*	0.079	*11.546*	0.058	*0.873*	0.049	*89.692*	0.069	*5.497*	0.067	*10.055*
ZnO	0.060	*30.762*	0.041	*94.513*	0.000	-	0.063	*19.370*	0.050	*92.981*	0.029	*94.650*	0.023	*173.205*
Total	99.23		99.61		99.58		99.48		99.80		99.67		99.54	
Cr^{3+}	1.634		1.639		1.632		1.629		1.616		1.624		1.614	
Al^{3+}	0.289		0.282		0.273		0.273		0.281		0.274		0.278	
Fe^{3+}	0.065		0.066		0.083		0.086		0.091		0.087		0.096	
Fe^{2+}	0.328		0.363		0.384		0.387		0.411		0.424		0.432	
Mg^{2+}	0.665		0.631		0.609		0.605		0.580		0.569		0.560	
Ti^{4+}	0.004		0.004		0.004		0.004		0.004		0.004		0.004	
V^{5+}	0.002		0.003		0.002		0.002		0.002		0.003		0.002	
Mn^{2+}	0.007		0.007		0.008		0.008		0.009		0.009		0.009	
Co^{2+}	0.001		0.001		0.002		0.002		0.002		0.002		0.001	
Ni^{2+}	0.002		0.002		0.002		0.002		0.001		0.002		0.002	
Zn^{2+}	0.001		0.001		0.000		0.002		0.001		0.001		0.001	
Cr#	0.850		0.853		0.857		0.856		0.852		0.855		0.853	
Cr/3+	0.822		0.825		0.821		0.819		0.813		0.818		0.812	
Al/3+	0.146		0.142		0.137		0.137		0.141		0.138		0.140	
Fe^{3+}/3+	0.033		0.033		0.042		0.043		0.046		0.044		0.048	
Mg#	0.670		0.635		0.614		0.610		0.585		0.573		0.565	
Fe^{2+}#	0.330		0.365		0.386		0.390		0.415		0.427		0.435	
MgO/FeO_{tot}	0.951		0.824		0.733		0.717		0.648		0.623		0.596	
Cr/Fe	3.880		3.550		3.257		3.205		2.993		2.955		2.846	
Fe^{3+}/Fe^{2+}	0.198		0.183		0.217		0.222		0.222		0.206		0.223	

Appendix E – EMPA and LA- ICP- MS Analyses

Table E 1: Chromite Analyses by Electron Microprobe and Laser Ablation (LA-ICP-MS)

Sample	G1742	G1777	G1795	G1798	V05-24-301	V05-24-303	V05-24-306
Drill Core	V05-24	V05-24	V05-24	V05-24	V05-24	V05-24	V05-24
Depth (m)	141.28	185.64	231.90	239.50	249.53	251.70	258.94
Zone	Hanging wall	Hanging wall	Hanging wall	Hanging wall	Hanging wall	Hanging wall	Upper Contact
Rock Type	Harzburgite	Dunite	Harzburgite	Dunite	Dunite	Dunite	Dunite Halo
% Chromite	<5%	<5%	<5%	<5%	<5%	<5%	<5%
Chromite Morphology	HL/SI	HL/SI	SI/An	HL/SI	HL/SI	SI	HL/SI
Spinel EMPA (n=)	3	3	3	3	3	3	3
SiO_2	0.04	0.07	0.06	0.10	0.06	0.09	0.08
TiO_2	0.06	0.18	0.02	0.03	0.07	0.06	0.16
Al_2O_3	47.60	31.38	39.02	33.73	26.95	26.76	23.01
V_2O_3	0.14	0.22	0.13	0.16	0.17	0.14	0.19
Cr_2O_3	20.16	35.99	29.79	33.53	40.57	40.45	44.74
FeO	14.14	17.89	15.24	17.73	18.36	18.40	20.11
MnO	0.15	0.27	0.20	0.23	0.26	0.29	0.30
MgO	17.58	13.87	15.64	14.23	13.21	13.52	11.57
CaO	0.00	0.00	0.01	0.01	0.01	0.01	0.01
Na_2O	0.01	0.01	0.02	0.01	0.01	0.01	0.00
ZnO	0.18	0.20	0.20	0.30	0.19	0.20	0.20
NiO	0.25	0.12	0.17	0.10	0.11	0.09	0.08
Total	100.32	100.21	100.49	100.16	99.97	100.02	100.45
Mg#	0.72	0.61	0.67	0.63	0.60	0.61	0.54
Cr# [Cr/(Cr+Al)]	**0.22**	**0.43**	**0.34**	**0.40**	**0.50**	**0.50**	**0.57**
Fe^{+3}#	0.01	0.02	0.06	0.02	0.04	0.02	0.10
$Fe^{3+}/\sum Fe$ (probe)	0.13	0.13	0.09	0.14	0.14	0.17	0.11
$Fe^{3+}/\sum Fe$ (corrected)	0.14	0.16	0.11	0.17	0.18	0.21	0.15
Fa (Ol)	0.098	0.091	0.088	nd	0.090	0.082	0.090
T°C (Balhaus)	637	651	690	nd	696	657	733
Δlog fO_2 (FMQ) (Balhaus)	-2.81	-0.46	1.36	nd	0.34	-1.05	1.87
T°C	1100	1100	1100	1100	1100	1100	1100
Δlog fO_2 (FMQ) (Balhaus)	**-3.20**	**-0.55**	**1.18**	**nd**	**0.32**	**-1.05**	**1.89**
Spinel LA-ICP-MS							
TiO_2 wt.%	0.06	0.22	0.02	0.02	0.08	0.06	0.12
Ga ppm	47.94	41.49	27.10	19.81	38.11	23.18	29.28
$100*TiO_2/Fe^{3+}$#	1161.38	866.31	37.67	116.87	181.97	335.95	110.61
Ga/Fe^{3+}#	8836.97	1669.33	450.39	964.66	896.73	1305.12	280.83

Sample	V05-24-312	V05-24-315	V05-24-322	V05-24-327	F1907	F1971	G1908
Drill Core	V05-24	V05-24	V05-24	V05-24	V05-24	V05-24	V05-24
Depth (m)	266.88	270.10	276.80	282.72	285.80	343.55	373.42
Zone	Ore Zone	Ore Zone	Hanging wall	Hanging wall	Upper Contact	Ore Zone	Ore Zone
Rock Type	Chromitite	Chromitite	Harzburgite	Harzburgite	Dunite Halo	Ore Zone Dunite	Dunite Halo
% Chromite	~30%	~50%	<5%	<5%	<5%	~15%	<5%
Chromite Morphology	SI/Eu	SI/Eu	SI/An	SI/Eu	SI	SI/Eu	SI/Eu
Spinel EMPA (n=)	3	3	3	3	3	3	3
SiO_2	0.07	0.12	0.07	0.06	0.05	0.11	0.08
TiO_2	0.13	0.14	0.10	0.07	0.10	0.13	0.17
Al_2O_3	7.09	7.56	29.44	34.03	33.72	7.03	13.16
V_2O_3	0.07	0.08	0.19	0.20	0.21	0.06	0.15
Cr_2O_3	61.30	61.00	37.30	31.22	31.85	62.43	50.74
FeO	22.71	20.78	19.49	18.63	18.91	19.62	24.28
MnO	0.42	0.38	0.26	0.23	0.24	0.37	0.37
MgO	8.57	10.01	13.06	14.88	14.39	10.67	10.49
CaO	0.00	0.02	0.01	0.00	0.01	0.02	0.00
Na_2O	0.01	0.01	0.01	0.02	0.01	0.01	0.00
ZnO	0.07	0.05	0.19	0.20	0.20	0.06	0.14
NiO	0.03	0.06	0.11	0.18	0.16	0.05	0.08
Total	100.47	100.20	100.23	99.72	99.86	100.55	99.65
Mg#	0.43	0.50	0.59	0.65	0.63	0.53	0.51
Cr# [Cr/(Cr+Al)]	**0.85**	**0.84**	**0.46**	**0.38**	**0.39**	**0.86**	**0.72**
Fe^{+3}#	0.14	0.15	0.07	0.04	0.05	0.15	0.10
$Fe^{3+}/\sum Fe$ (probe)	0.12	0.14	0.16	0.24	0.21	0.14	0.27
$Fe^{3+}/\sum Fe$ (corrected)	0.19	0.21	0.19	0.26	0.23	0.21	0.32
Fa (Ol)	nd	0.073	0.087	0.091	0.088	nd	0.078
T°C (Balhaus)	nd	846	665	671	649	nd	729
Δlog fO_2 (FMQ) (Balhaus)	nd	2.71	1.31	0.30	0.78	nd	1.77
T°C	1100	1100	1100	1100	1100	1100	1100
Δlog fO_2 (FMQ) (Balhaus)	**nd**	**2.81**	**1.26**	**0.18**	**0.66**	**nd**	**1.89**
Spinel LA-ICP-MS							
TiO_2 wt.%	0.15	0.15	nd	0.05	0.11	0.14	0.19
Ga ppm	11.06	11.43	nd	28.51	35.40	10.35	17.38
$100*TiO_2/Fe^{3+}$#	107.60	99.14	n.d	144.91	231.46	91.05	194.62
Ga/Fe^{3+}#	81.12	74.36	n.d	755.76	756.27	67.64	181.17

Sample	V05-24-328	V05-24-341	V05-24-345	V05-24-348	V05-24-350
Drill Core	V05-24	V05-24	V05-24	V05-24	V05-24
Depth (m)	375.00	389.23	394.11	398.63	402.92
Zone	Lower Contact	Footwall	Footwall	Footwall	Footwall
Rock Type	Dunite Halo	Harzburgite	Harzburgite	Dunite	Dunite
% Chromite	<5%	<5%	<5%	<5%	<5%
Chromite Morphology	Sl/Eu	HL	HL/Sl	HL/Sl/Eu	HL/Si
			SEM		
Spinel EMPA (n=)	3	3	3	3	3
SiO_2	0.08	0.05	0.00	0.07	0.07
TiO_2	0.24	0.03	0.05	0.14	0.12
Al_2O_3	14.78	47.88	47.35	20.95	24.20
V_2O_3	0.12	0.12	0.15	0.34	0.23
Cr_2O_3	48.90	20.96	20.15	46.07	42.62
FeO	24.83	13.14	12.74	21.46	20.66
MnO	0.36	0.16	0.15	0.34	0.31
MgO	10.01	17.65	18.71	10.82	11.75
CaO	0.02	0.00	0.00	0.00	0.00
Na_2O	0.01	0.01	0.00	0.02	0.01
ZnO	0.16	0.17	0.16	0.21	0.22
NiO	0.08	0.27	0.26	0.07	0.09
Total	99.59	100.45	99.72	100.49	100.29
Mg#	0.49	0.72	0.76	0.51	0.54
Cr# [Cr/(Cr+Al)]	**0.69**	**0.23**	**0.22**	**0.60**	**0.54**
Fe^{+3}#	0.12	0.06	0.03	0.06	0.05
$Fe^{3+}/\sum Fe$ (probe)	0.25	0.07	0.19	0.13	0.15
$Fe^{3+}/\sum Fe$ (corrected)	0.30	0.08		0.18	0.19
Fa (Ol)	0.076	0.092	nd	0.093	0.095
T°C (Balhaus)	699	710	nd	674	674
Δlog fO_2 (FMQ) (Balhaus)	2.28	1.51	nd	0.74	0.57
T°C	1100	1100	1100	1100	1100
Δlog fO_2 (FMQ) (Balhaus)	**2.40**	**1.22**	**nd**	**0.78**	**0.58**
Spinel LA-ICP-MS					
TiO_2 wt.%	0.27	0.07	0.06	0.14	0.15
Ga ppm	21.12	42.69	44.21	29.07	30.99
$100*TiO_2/Fe^{3+}$#	231.47	117.10	n.d	243.34	292.35
Ga/Fe^{3+}#	178.64	717.56	n.d	504.08	601.27

Appendix F – Voskhod Olivine (Fo) – SEM and EMPA Analyses

Table F 1: Olivine Forsterite Analyses by Scanning Electron Microscope

Sample	**G1601**	***RStd***	**G1605**	***RStd***	**G1623**	***RStd***	**G1624**	***RStd***	**G1631**	***RStd***
Drill Core	**V05-28**		**V05-28**		**V05-28**		**V05-28**		**V05-28**	
Depth (m)	322.09		325.52		354.67		432.97		434.40	
Rock Type	**Dunite**		**Dunite**		**Dunite**		**Dunite**		**Dunite**	
Zone	Upper Contact		Upper Contact		Ore Zone		Ore Zone		Ore Zone	
Proximity from Ore Zone (m)	5.15		1.72		n/a		n/a		n/a	
n=	3		6		3		3		3	
Si	13.391	*0.700*	13.380	*0.454*	13.367	*0.769*	13.352	*0.287*	13.351	*0.242*
Mg	**27.379**	*0.349*	**27.333**	*0.230*	**27.384**	*0.280*	**27.923**	*0.299*	**27.910**	*0.263*
Fe	**2.422**	*2.073*	**2.521**	*2.003*	**2.471**	*3.790*	**1.938**	*2.253*	**1.996**	*2.660*
Ni	0.112	*19.043*	0.076	*78.899*	0.095	*10.162*	0.112	*1.108*	0.068	*86.992*
Mn										
O	56.696	*0.083*	56.690	*0.054*	56.683	*0.091*	56.676	*0.034*	56.676	*0.029*
Fo	**0.919**		**0.916**		**0.917**		**0.935**		**0.933**	

Sample	**Vos 174**	***RStd***	**Vos 179**	***RStd***	**G1910**	***RStd***	**G1983**	***RStd***	**G1988**	***RStd***
Drill Core	**V06-S6**		**V06-S6**		**V06-48**		**V06-48**		**V06-48**	
Depth (m)	66.45		77.25		200.75		298.45		300.15	
Rock Type	**Dunite**		**Dunite**		**Dunite**		**Dunite**		**Dunite**	
Zone	Upper Contact		Upper Contact		Upper Contact		Lower Contact		Lower Contact	
Proximity from Ore Zone (m)	13.05		2.25		0.56		1.75		3.45	
n=	3		6		6		3		3	
Si	13.412	*0.342*	13.312	*0.425*	14.173	*0.295*	13.242	*0.435*	13.396	*0.555*
Mg	**27.133**	*0.190*	**27.370**	*0.255*	**26.403**	*0.353*	**27.961**	*0.259*	**27.899**	*0.437*
Fe	**2.680**	*1.785*	**2.556**	*1.900*	**2.198**	*2.107*	**2.029**	*1.383*	**1.942**	*3.630*
Ni	0.069	*86.637*	0.106	*8.428*	0.118	*17.277*	0.116	*2.355*	0.066	*86.606*
Mn					0.067	*22.163*	0.031			
O	56.706	*0.040*	56.656	*0.050*	57.086	*0.037*	56.621	*0.051*	56.698	*0.066*
Fo	**0.910**		**0.915**		**0.923**		**0.932**		**0.935**	

Sample	**G1742**	***RStd***	**G1777**	***RStd***	**G1791**	***RStd***	**G1795**	***RStd***	**G1798**	***RStd***
Drill Core	**V05-24**		**V05-24**		**V05-24**		**V05-24**		**V05-24**	
Depth (m)	141.30		185.60		221.03		231.90		239.50	
Rock Type	**Harzburgite**		**Dunite**		**Harzburgite**		**Harzburgite**		**Dunite**	
Zone	Hanging wall		Hanging wall		Hanging wall		Hanging wall		Hanging wall	
Proximity from Ore Zone (m)	142.92		98.56		63.17		52.30		44.70	
n=	3		3		4		3		1	
Si	14.153	*0.2368*	14.202	*0.3343*	14.189	*0.423*	13.867	*0.451*	14.159	-
Mg	**25.553**	*0.1186*	**25.853**	*0.0774*	**26.339**	*0.482*	**26.418**	*0.256*	**26.255**	**-**
Fe	**2.781**	*0.7532*	**2.587**	*1.3240*	**2.296**	*0.703*	**2.546**	*0.816*	**2.395**	**-**
Ni	0.120	*9.4791*	0.110	*7.5977*	0.081	*67.116*	0.115	*1.972*	0.112	-
Mn	0.039	*3.1115*	0.035	*6.1068*			0.033	*1.307*		
O	57.353	*0.0241*	57.213	*0.0162*	57.095	*0.053*	57.021	*0.035*	57.080	-
Fo	**0.902**		**0.909**		**0.920**		**0.912**		**0.916**	

Sample	**Vos 301**	***RStd***	**306**	***RStd***	**315**	***RStd***	**Vos 322**	***RStd***	**Vos 327**	***RStd***
Drill Core	**V05-24**		**V05-24**		**V05-24**		**V05-24**		**V05-24**	
Depth (m)	249.53		258.94		270.10		276.80		282.72	
Rock Type	**Dunite**		**Dunite**		**DCR**		**Harzburgite**		**Harzburgite**	
Zone	Hanging wall		Upper Contact		Stringer Mineralisation		Hanging wall		Hanging wall	
Proximity from Ore Zone (m)	34.67		25.26		14.10		7.40		1.48	
n=	3		3		3		3		3	
Si	14.127	*0.334*	14.007	*0.189*	13.948	*0.773*	13.873	*0.568*	13.993	*0.683*
Mg	**26.004**	*0.420*	**26.158**	*0.228*	**27.066**	*0.554*	**26.436**	*0.550*	**26.136**	*0.880*
Fe	**2.559**	*1.674*	**2.552**	*1.542*	**2.128**	*0.625*	**2.530**	*0.985*	**2.602**	*1.418*
Ni	0.116	*10.400*	0.132	*3.136*	0.104	*11.288*	0.114	*1.281*	0.109	*12.816*
Mn	0.035	*8.500*	0.039	*1.014*	0.032	*3.950*	0.036	*9.697*	0.037	*6.064*
O	57.160	*0.077*	57.112	*0.047*	56.723	*0.084*	57.012	*0.090*	57.124	*0.151*
Fo	**0.910**		**0.911**		**0.927**		**0.913**		**0.909**	

Sample	**F1907**	***RStd***	**G1908**	***RStd***	**Vos 328**	***RStd***	**Vos 341**	***RStd***	**Vos 348**	***RStd***
Drill Core	**V05-24**		**V05-24**		**V05-24**		**V05-24**		**V05-24**	
Depth (m)	285.50		372.00		375.00		389.23		398.63	
Rock Type	**Dunite**		**Dunite**		**Dunite**		**Harzburgite**		**Dunite**	
Zone	Upper Contact		Ore Zone		Lower Contact		Footwall		Footwall	
Proximity from Ore Zone (m)	1.60		n/a		1.58		15.81		25.21	
n=	3		3		3		3		3	
Si	14.322	*0.1810*	14.231	*0.642*	14.188	*0.304*	14.054	*0.6383*	14.027	*0.326*
Mg	**25.913**	*0.7424*	**26.437**	*0.752*	**26.625**	*0.074*	**26.003**	*0.4308*	**26.060**	*0.305*
Fe	**2.457**	*3.5000*	**2.248**	*2.247*	**2.184**	*1.641*	**2.625**	*1.1548*	**2.617**	*2.770*
Ni	0.108	*1.4071*	0.101	*2.895*	0.099	*3.029*	0.110	*7.2222*	0.107	*11.315*
Mn	0.032	*1.4293*	0.031	*9.140*	0.027	*4.504*	0.035	*3.9712*	0.039	*10.242*
O	57.168	*0.1404*	56.952	*0.130*	56.877	*0.016*	57.172	*0.0616*	57.151	*0.066*
Fo	**0.913**		**0.922**		**0.924**		**0.908**		**0.909**	

Sample	**Vos 350**	***RStd***
Drill Core	**V05-24**	
Depth (m)	403.00	
Rock Type	**Dunite**	
Zone	Footwall	
Proximity from Ore Zone (m)	29.50	
n=	3	
Si	13.975	*0.691*
Mg	**26.048**	*0.468*
Fe	**2.654**	*1.503*
Ni	0.119	*11.874*
Mn	0.038	*9.835*
O	57.166	*0.074*
Fo	**0.908**	

Table F 2: Olivine Forsterite Analyses by Electron Microprobe

Sample	G1742	*RStd*	G1777	*RStd*	G1795	*RStd*	Vos 301	*RStd*	306	*RStd*
Drill Core	**V05-24**		**V05-24**		**V05-24**		**V05-24**		**V05-24**	
Depth (m)	141.30		185.60		231.90		249.53		258.94	
Rock Type	**Harzburgite**		**Dunite**		**Harzburgite**		**Dunite**		**Dunite**	
Zone	Hanging wall		Hanging wall		Hanging wall		Hanging wall		Upper Contact	
Proximity from Ore Zone (m)	142.92		98.56		52.30		34.67		25.26	
n=	3		3		3		3		3	
Si	14.224	*0.197*	14.227	*0.266*	13.863	-	14.146	*0.338*	14.033	-
Mg	**25.690**	*0.101*	**25.906**	*0.109*	**26.486**	-	**26.048**	*0.368*	**26.152**	-
Fe	**2.796**	*0.809*	**2.591**	*1.396*	**2.540**	-	**2.562**	*1.744*	**2.594**	-
Ni	0.120	*9.526*	0.110	*7.638*	0.116	-	0.116	*10.431*	0.137	-
Mn	0.039	*3.113*	0.035	*6.060*	0.033	-	0.035	*8.541*	0.039	-
O	57.119	*0.025*	57.120	*0.038*	56.940	-	57.079	*0.042*	57.025	-
Fo	**0.902**		**0.909**		**0.912**		**0.910**		**0.910**	

Sample	315	*RStd*	Vos 322	*RStd*	Vos 327	*RStd*	F1907	*RStd*	G1908	*RStd*
Drill Core	**V05-24**		**V05-24**		**V05-24**		**V05-24**		**V05-24**	
Depth (m)	270.10		276.80		282.72		285.50		372.00	
Rock Type	**DCR**		**Harzburgite**		**Harzburgite**		**Dunite**		**Dunite**	
Zone	Stringer Mineralisation		Hanging wall		Hanging wall		Upper Contact		Ore Zone	
Proximity from Ore Zone (m)	14.10		7.40		1.48		1.60		n/a	
n=	3		3		3		3		3	
Si	13.869	*0.752*	13.885	*0.606*	14.019	*0.749*	14.317	-	14.172	*0.696*
Mg	**26.921**	*0.576*	**26.469**	*0.508*	**26.196**	*0.808*	**25.861**	-	**26.337**	*0.674*
Fe	**2.116**	*0.608*	**2.532**	*1.030*	**2.607**	*1.495*	**2.485**	-	**2.239**	*2.346*
Ni	0.103	*11.311*	0.114	*1.319*	0.109	*12.905*	0.106	-	0.100	*2.965*
Mn	0.031	*3.943*	0.036	*9.656*	0.037	*6.124*	0.033	-	0.031	*9.171*
O	56.942	*0.094*	56.949	*0.071*	57.017	*0.094*	57.170	-	57.096	*0.082*
Fo	**0.927**		**0.913**		**0.909**		**0.912**		**0.922**	

Sample	**Vos 328**	***RStd***	**Vos 341**	***RStd***	**Vos 348**	***RStd***	**Vos 350**	***RStd***
Drill Core	**V05-24**		**V05-24**		**V05-24**		**V05-24**	
Depth (m)	375.00		389.23		398.63		403.00	
Rock Type	**Dunite**		**Harzburgite**		**Dunite**		**Dunite**	
Zone	Lower Contact		Footwall		Footwall		Footwall	
Proximity from Ore Zone (m)	1.58		15.81		25.21		29.50	
n=	3		3		3		3	
Si	14.115	*0.240*	14.088	*0.614*	13.965	*0.258*	13.923	*0.645*
Mg	**26.496**	*0.104*	**26.073**	*0.449*	**26.192**	*0.224*	**26.198**	*0.487*
Fe	**2.173**	*1.707*	**2.632**	*1.196*	**2.693**	*2.865*	**2.734**	*1.566*
Ni	0.098	*2.984*	0.110	*7.184*	0.107	*11.400*	0.119	*12.084*
Mn	0.027	*4.527*	0.035	*3.932*	0.039	*10.404*	0.039	*9.974*
O	57.069	*0.033*	57.050	*0.077*	56.993	*0.029*	56.970	*0.082*
Fo	**0.924**		**0.908**		**0.907**		**0.906**	

Appendix G
Evaluation of precision

Graphs to show the relationship and strength of correlation (given as R^2) for the Al_2O_3, Cr_2O_3, FeO, V and TiO_2 contents of chromites analysed using LA-ICP-MS and EMPA techniques.

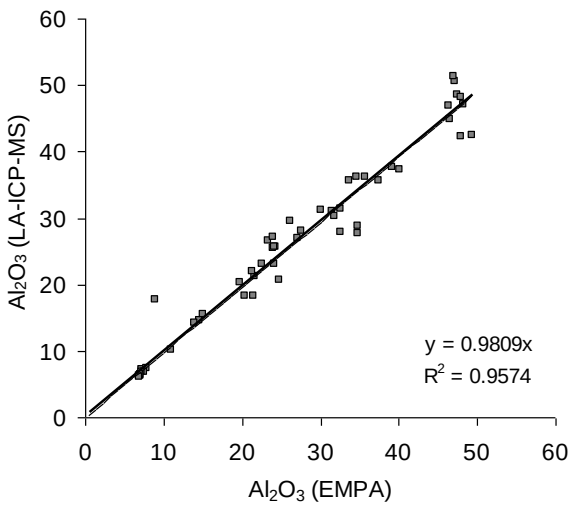

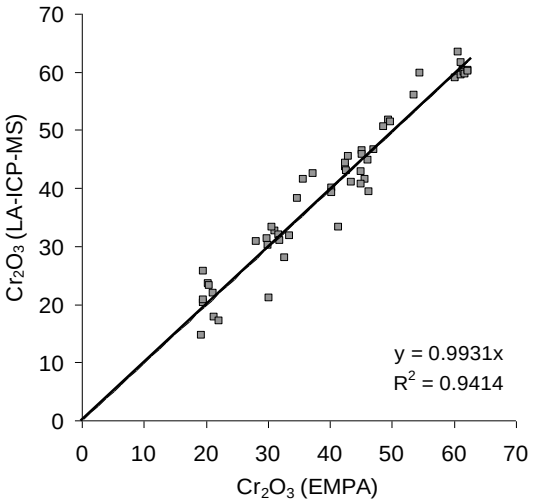

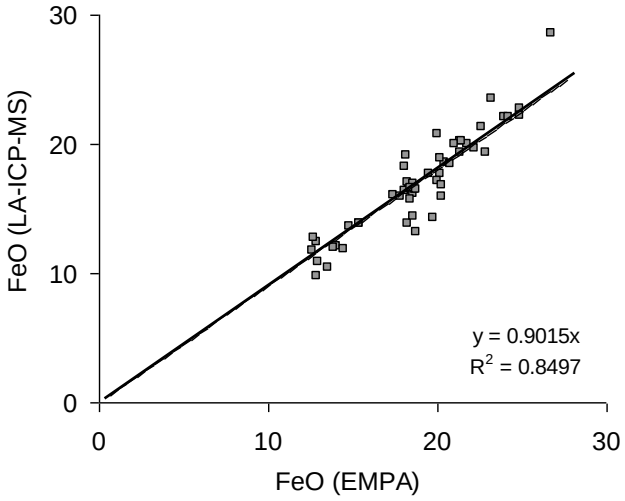

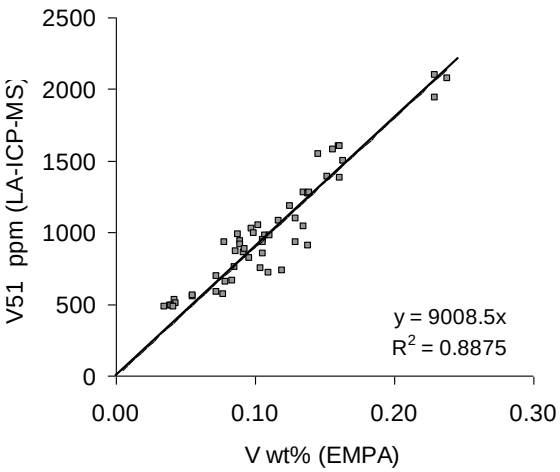

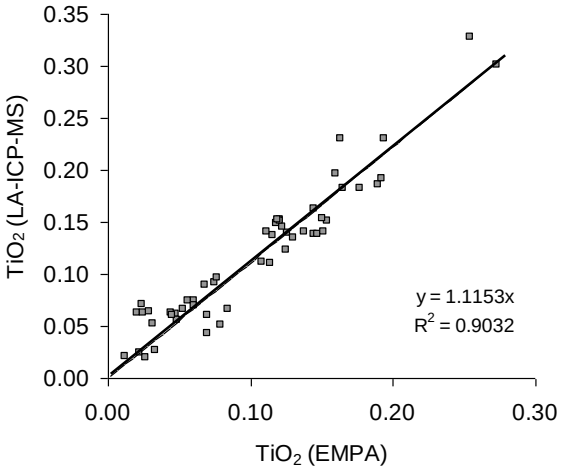

Graphs to show the relationship and strength of correlation (given as R^2) for the minor element oxides NiO, ZnO, V_2O_5, TiO_2 and MnO present in chromites analysed using the SEM and EMPA techniques. Error bars are given to 1.s.d. Where bars are not observed the symbol size exceeds the length of the bar.

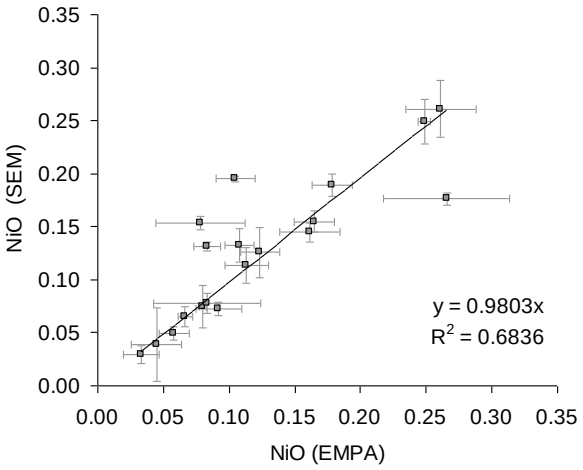

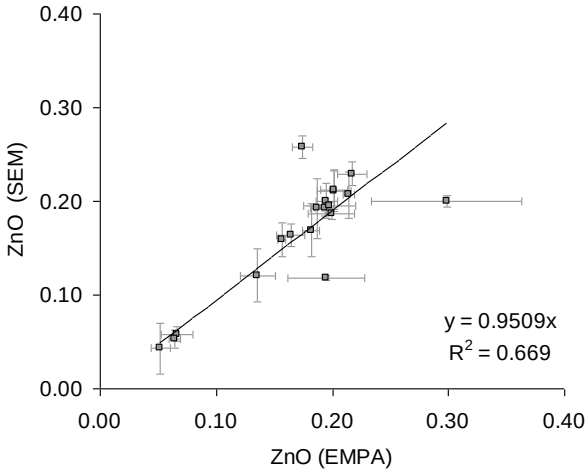

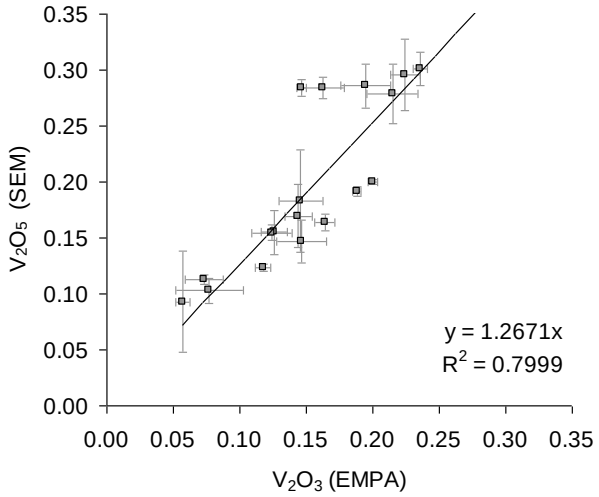

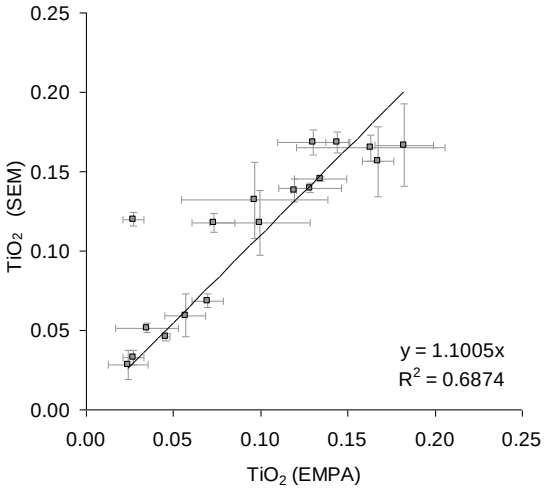

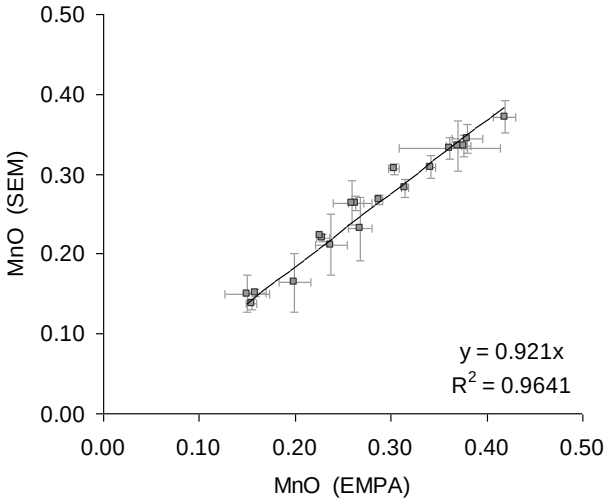

Graphs to show the relationship and strength of correlation (given as R^2) for the major element oxides Cr_2O_3, Al_2O_3, FeO and MgO present in chromites analysed using the SEM and EMPA techniques. Error bars are given to 1.s.d. Where bars are not observed the symbol size exceeds the length of the bar.

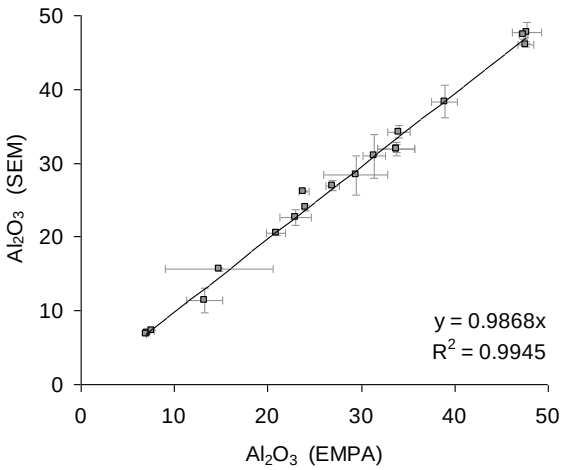

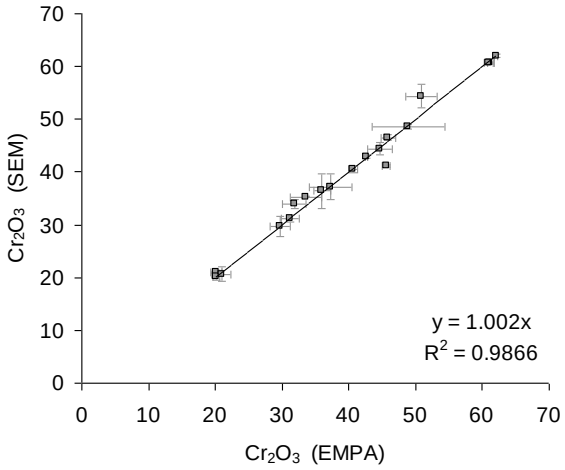

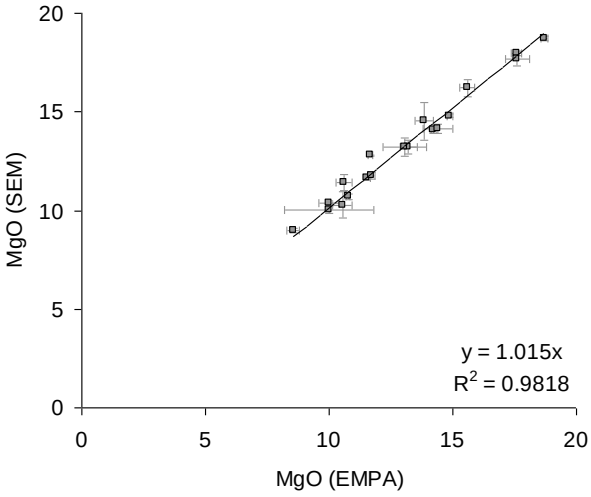

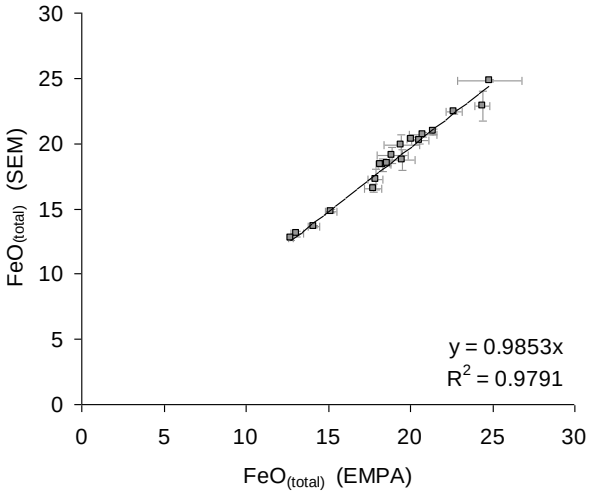

Graphs to show the relationship and strength of correlation (given as R^2) for the major element oxides FeO and MgO present in olivine analysed using the SEM and EMPA techniques. Error bars are given to 1.s.d. Where bars are not observed the symbol size exceeds the length of the bar.

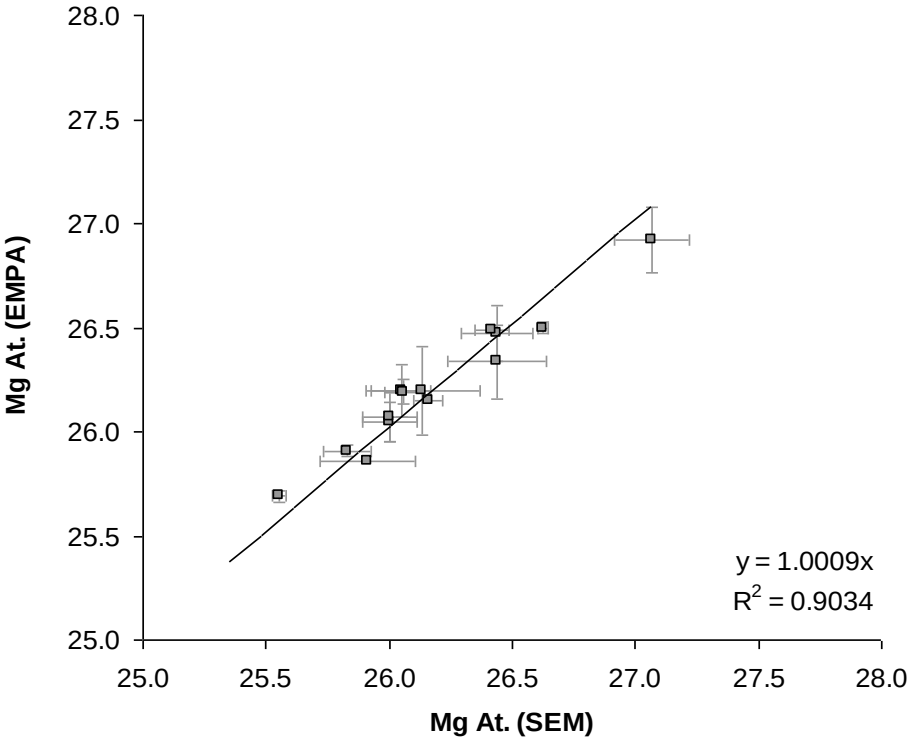

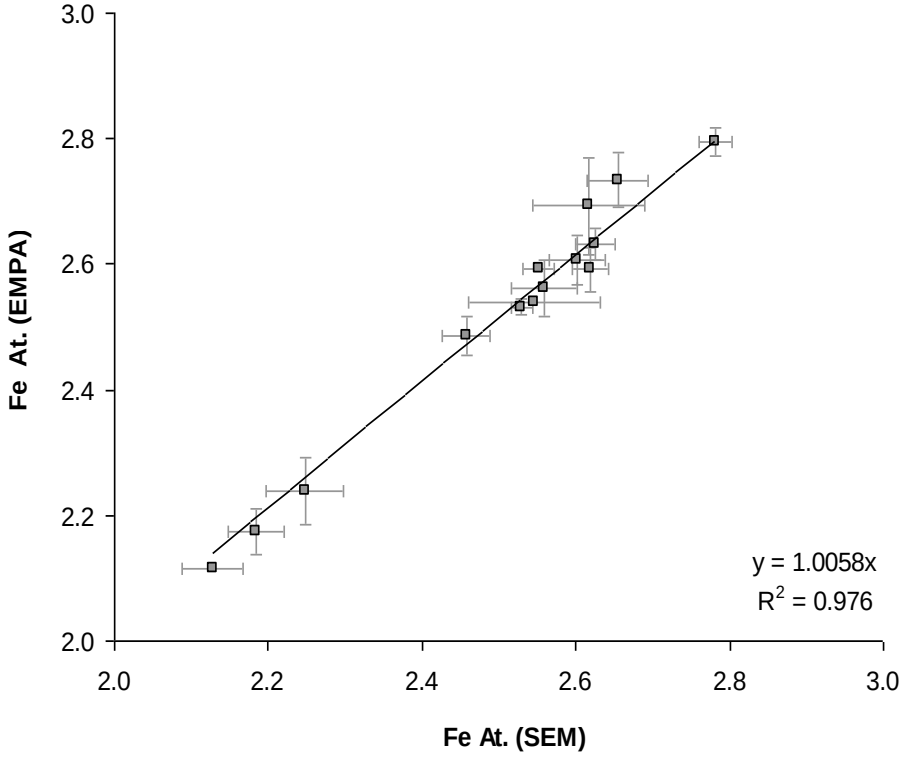

Appendix H

Voskhod Samples: Petrographic Tables

Table H 1: Petrography of Voskhod harzburgite, dunite, dunite halo and ore zone sample suite.

Sample I.D	Drill core I.D	Region in ore body	Depth down hole (m)	Distance from mineralisation (m)	Rock type	Chromite modal %	Grain Shape	Composition (%)				Serpentinisation %	LOI
								Olivine	Clinopyroxene	Orthopyroxene	Chromite		
G1815	V05-21	West	286.60	n/a	OZ Dun	< 5%		97			3	>90	
G1823	V05-21	West	297.65	48.80	Dist Dun	< 5%		95		2	3	~80	
G1742	V05-24	Centre	141.30	142.92	Harz	< 5%	HL/Sl	84	3	10	3	~70	13.53
G1763	V05-24	Centre	167.60	116.61	Harz	< 5%	HL/Sl	83	2	12	2	~70	
G1768	V05-24	Centre	176.94	107.26	Harz	<5%	HL/Sl	85	2	10	3	~70	
G1777	V05-24	Centre	185.60	98.56	Dist Dun	< 5%	HL/Sl	90	2	5	3	~70	15.63
G1791	V05-24	Centre	221.00	63.17	Harz	< 5%	HL/Sl	87	3	7	3	~70	
G1795	V05-24	Centre	231.90	52.30	Harz	< 5%	Sl/An	85	3	10	2	~80	16.34
G1798	V05-24	Centre	240.00	44.70	Dist Dun	< 5%	HL/Sl	92		5	3	~80	16.34
VOS-301	V05-24	Centre	249.53	34.67	Dist Dun	< 5%	HL/Sl	95		3	2	~75	16.25
VOS-303	V05-24	Centre	252.00	32.50	Dist Dun	< 5%	Sl	95		2	3	~75	16.5
VOS-306	V05-24	Centre	258.94	25.26	Dun Halo	< 5%	HL/Sl	97			3	~90	16.22
VOS-312	V05-24	Centre	266.88	n/a	Dun/Chr Stringer	~ 30%	Sl/Eu	70			30	~90	
VOS-315	V05-24	Centre	270.10	n/a	Dun/Chr Stringer	~ 50%	Sl/Eu	50			50	~90	-0.21
VOS-320	V05-24	Centre	274.59	9.61	Dist Dun	< 5%	Sl	97			3	~90	15.79
VOS-322	V05-24	Centre	276.80	7.40	Harz	< 5%	Sl/An	88	2	7	3	~90	16.85
VOS-327	V05-24	Centre	282.72	1.48	Harz	< 5%	Sl/Eu	86	1	8	3	~90	15.95
F1901	V05-24	Centre	284.2	n/a	Dun Halo	< 5%	Sl/Eu	97			3	~80	
F1907	V05-24	Centre	285.50	n/a	OZ Dun	<5%	Sl	97			3	>90	16.41
F1920	V05-24	Centre	290.3	n/a	DCR	10%	Eu	92			8	>90	
F1925	V05-24	Centre	296.05	n/a	HMCR	>95%	Eu	3			97	>90	
F1925	V05-24	Centre	296.18	n/a	DCR	~30%	Eu	70			30	>90	16.57
F1926	V05-24	Centre	296.70	n/a	OZ Dun	<5%	Eu	97			3	>90	
F1935	V05-24	Centre	311.24	n/a	HMCR	>90%	Eu	7			92	>90	
F1964/65	V05-24	Centre	341.46	n/a	HMCR	>95%	Eu	3			97	>90	
F1967	V05-24	Centre	342.36	n/a	DCR	~50%	Sl/Eu	50			50	>90	12.91
F1968	V05-24	Centre	341.70	n/a	OZ Dun	<5%	Eu	97			3	>90	
F1971	V05-24	Centre	343.00	n/a	DCR	~ 15%	Eu	85			15	>90	16.29
F1978	V05-24	Centre	348.00	n/a	DCR	~ 35%	Eu	65			35	>90	
F1996/97	V05-24	Centre	359.01	n/a	HMCR	>95%	Eu	3			97	>90	
G1908	V05-24	Centre	373.42	n/a	Dun Halo	< 5%	Sl/Eu	97			3	~90	16.43
VOS-328	V05-24	Centre	375.00	1.58	Dun Halo	< 5%	Sl/Eu	97			3	~90	15.71
VOS-341	V05-24	Centre	389.23	15.81	Harz	< 5%	HL	85	3	9	3	~70	14.48
VOS-345	V05-24	Centre	394.00	20.69	Harz	< 5%	HL/Sl	84	3	10	3	~65	12.18
VOS-348	V05-24	Centre	398.63	25.21	Dist Dun	< 5%	HL/Sl/Eu	95		2	3	~70	13.36
VOS-350	V05-24	Centre	403.00	29.50	Dist Dun	< 5%	HL/Sl	96		1	3	~65	13.08

Table H 2: (Cont) Petrography of Voskhod harzburgite, dunite, dunite halo and ore zone sample suite.

Sample I.D	Drill core I.D	Region in ore body	Depth down hole (m)	Distance from mineralisation (m)	Rock type	Chromite modal %	Grain Shape	Composition (%)				Serpentinisation %	LOI
								Olivine	Clinopyroxene	Orthopyroxene	Chromite		
G1601	V05-28	East	322.09	5.15	Dun Halo	< 5%	An/SI	97			3	~70	14.35
G1605	V05-28	East	325.52	1.72	Dun Halo	< 5%	An/SI	97			3	~70	14.28
G1608	V05-28	East	330.25	n/a	DCR	~50%	Eu	50			50	>90	16.4
G1609	V05-28	East	333.85	n/a	OZ Dun	< 5%	Eu	97			3	>90	
G1623	V05-28	East	354.67	n/a	OZ Dun	< 5%	SI/Eu	97			3	>90	14.1
G1654	V05-28	East	369.70	n/a	OZ Dun	< 5%	SI/Eu	97			3	>90	
G1624	V05-28	East	432.97	n/a	DCR	< 10%	SI/Eu	92			8	>90	
G1631	V05-28	East	434.40	n/a	OZ Dun	< 5%	SI/Eu	97			3	>90	
G1910	V06-48	S. Centre	200.75	0.56	Dun Halo	< 5%	SI/Eu	97			3	~70	
G1941	V06-48	S. Centre	231.35	n/a	OZ Dun	<5%	SI/Eu	97			3	>90	
G1956	V06-48	S. Centre	288.55	n/a	DCR	~15%	SI/Eu	85			15	>90	
G1964	V06-48	S. Centre	291.35	n/a	HMCR	~70%	SI/Eu	30			70	>90	
G1979	V06-48	S. Centre	296.7	n/a	HMCR	~70%	SI/Eu	30			70	>90	13.99
G1983	V06-48	S. Centre	298.45	1.75	Dun Halo	< 5%	SI/Eu	97			3	~80	16.97
G1988	V06-48	S. Centre	300.15	3.45	Dun Halo	< 5%	SI/Eu	97			3	~70	
VOS-174	V06-S6	South	66.45	13.05	Dist Dun	< 5%	SI	97		2	3	~70	
VOS-179	V06-S6	South	79.50	n/a	DCR	< 10%	SI	93			7	>90	
VOS-185	V06-S6	South	93.95	8.08	Harz	< 5%	An/SI	85	3	9	3	~75	

References

Ahmed, A.H. and Arai, S. (2002). Unexpectedly high PGE-chromitite from the deeper mantle section of the northern Oman ophiolite and its tectonic implications. Contributions to Mineralogy and Petrology, 143, 263 – 278.

Alabaster, T., Pearce, J.A. and Maplas, J. (1982). The volcanic stratigraphy and petrogenesis of the Oman ophiolite complex. Contributions to Mineralogy and Petrology, 81, 168 - 183.

Allan, J.F., and Dick, H.J.B. (1996). Cr-rich spinel as a tracer for melt migration and melt–wall rock interaction in the mantle: Hess Deep, Leg 147. In: Mével, C., Gillis, K.M., Allan, J.F., and Meyer, P.S. (Eds.), Proceedings of the Ocean Drilling Program, Scientific Results, 147, 157–172.

Allan, J.F., Sack, R.O. and Batiza, R. (1988). Cr-rich spinels as petrogenetic indicators: MORB-type lavas from the Lamont seamount chain, eastern Pacific. American Mineralogist, 73, 741-753.

Alvarez-Marron, J. (2002). Tectonic processes during collisional orogenesis from comparison of the Southern Urals with the Central Variscides. In: Brown, D., Juhlin, C., Puchkov, V. (Eds.), Mountain Building in the Uralides: Pangea to Present. American Geophysical Union, Geophysical Monograph, vol. 132, pp. 83–100.

Alvarez-Marron, J., Brown, D., Perez-Estaun, A., Puchkov, V., Gorozhanina, Y. (2000). Accretionary complex structure and kinematics during Paleozoic arc–continent collision in the Southern Urals. Tectonophysics v.325, p.175–191.

Amstutz, G.C., 1980. The early history of the term Ophiolites and its evolution until 1945. In: Panayiotou, A. (Ed.), Ophiolites: Proceedings International Symposium Cyprus 1979. Cyprus Geological Survey Department, pp. 49– 143.

Anonymous, 1972. Penrose field conference report: Geotimes, v. 17, no. 12, p. 24-25.

Antsigin, N.I., Zoloev, K.K., Kluzina, M.L., Nasedkina, V.A., Popov, B.A., Chuvashov, B.I., Shurigina, M.V., Sherbakov, O.A., and Iackusev, V.M., (1994). Descriptions of the stratigraphic schemes of the Urals: Ekaterinburg, Urals Stratigraphic Committee (in Russian).

Arai, S. (1980). Dunite-harzburgite-chromitite complexes as refractory residue in the Sangun-Yamaguchi zone, Western Japan, Journal of Petrology, v.21, 141-165

Arai, S. (1992). Chemistry of chromian spinel in volcanic rocks as a potential guide to magma chemistry. Mineralogical Magazine, 56, 173-184.

Arai, S. (1994a). Characterization of spinel peridotites by olivine-spinel compositional relationships: Review and interpretation. Chemical Geology, 113, 191-204.

Arai, S. (1997) Control of wall-rock composition on the formation of podiform chromitites as a result of magma/peridotite interaction. Resour Geol 47:177–187

Arai, S., Schimizu, Y., Ismail, S.A. & Ahmed, A.H (2006). Low-T formation of high-Cr spinel with apparently primary chemical characteristics within podiform chromitite from Rayat, northeastern Iraq. Min Mag. v70 (5) pp 499-508

Arai, S. & Abe, N. (1995) Reaction of orthopyroxene in peridotite xenoliths with alkali-basalt melt and its implication for of Alpine-type chromitite. American Mineralogist 80:1041–1047

Arai, S. & Matsukage, K. (1996). Petrology of gabbro-troctolite-peridotite complex from Hess Deep, equatorial Pacific: implications for mantle-melt interaction within the oceanic lithosphere. In: Mével, C., Gillis, K.M., Allan, J.F., and Meyer, P.S. (Eds.), Proceedings of the Ocean Drilling Program, Scientific Results, 147, 135–155.

Arai, S. & Matsukage, K. (1998). Petrology of a chromitite micropod from Hess Deep, equatorial Pacific: a comparison between abyssal and alpine-type podiform chromitites. Lithos 43: 1-14

Arai, S. & Yurimoto, H. (1994) Podiform chromitites from the Tari-Misaka ultramafic complex, southwestern Japan, as a melt mantle interaction products. Econ Geol 89:1279–1288

Arai, S., Uesugi, J. & Ahmed, A.H. (2004). Upper crustal podiform chromitite from the northern Oman ophiolite as the stratigraphically shallowest chromitite in ophiolite and its implication for Cr concentration. Contributions to Mineralogy and Petrology, 147, 145-154.

Arai, S., Kadoshima, K. & Morishita,T. (2006). Widespread arc-related melting in the mantle section of the northern Oman ophiolite as inferred from detrital chromian spinels. Journal of the Geological Society, 163, 869-879.

Arai, S., Schimizu, Y., Ismail, S.A. & Ahmed, A.H (2006). Low-T formation of high-Cr spinel with apparently primary chemical characteristics within podiform chromitite from Rayat, northeastern Iraq. Min Mag. v70 (5) pp 499-508

Augé, T. (1987). Chromite deposits in the northern Oman ophiolite: mineralogical constraints. Mineralium Deposita, 22, 1- 10.

Augé, T. and Roberts, S. (1982). Petrology and geochemistry of some chromitiferous bodies within the Oman ophiolite. Ofioliti , 7.

Ayarza, P., Brown, D., Alvarez-Marrón, J. & Juhlin, C. (2000). Contrasting tectonic history of the arc-continent suture in the Southern and Middle Urals: Implications for the evolution of the orogen: Journal of the Geological Society, v. 157, pp. 1065–1076.

Bai, W.J., Zhou M.F. & Robinson, P.T. (1993). Possibly diamond-bearing mantle peridotites and podiform chromitites in the Loubusa and Donqiao ophiolites, Tibet: Canadian Journal of Earth Sciences. v, 30, pp.1650-1659.

Bailey, E.B., 1936. Sedimentation in relation to tectonics. Geological Society of America Bulletin 47, 1713–1726.

Ballhaus, C., (1993). Redox states of lithospheric and asthenospheric upper mantle. Contributions to Mineralogy and Petrology 114, 331–348.

Ballhaus C (1998). Origin of podiform chromite deposits by magma mingling. Earth Planet Sci Lett 156:185–193

Ballhaus, C., Berry, R.F., Green, D.H., (1990). Oxygen fugacity controls in the Earth's upper mantle. Nature 348, 437–440.

Ballhaus, C., Berry, R.F. and Green D.H. (1991). High pressure experimental calibration of the olivine-orthopyroxene-spinel oxygen barometer: implications for the oxidation state for the upper mantle. Contributions to Mineralogy and Petrology, 107, 27-40.

Barnes, S.J., 1998. Chromite in komatiites, I. Magmatic controls on crystallization and composition: Journal of Petrology, v. 39, p. 1689–1720.

Barnes, S.J., 2000. Chromite in komatiites, II. Modification during greenschist to mid-amphibolite facies metamorphism: Journal of Petrology, v. 41, p. 387–409.

Barnes, S.J. and Maier, W.D (2002). Platinum-group elements and microstructures from Impala Platinum Mines, Bushveld Complex. Journal of Petrology, vol. 43, pp.171–198.

Barnes S.J. & Roeder P.L. (2001). The range of spinel compositions in terrestrial mafic and ultramafic rocks. Journal of Petrology, 42, 2279-2302.

Bashta, E.G., Kushkov, V.N., Shatornaya, L.N., Glushkov, A.N. & Sergeev, V.A., (1990). First results from the drilling and investigations of the Urals superdeep borehole (SG-4): Mineral Geology SSSR, pp. 19–30.

Bea, F., Fershtater, G.B., Montero, P., Whitehouse, M., Levin, V.Ya., Scarrow, J.H., Austrheim, H., and Pushkariev, E.V., 2001. Recycling of continental crust into the mantle as revealed by Kytlym dunite zircons, Ural Mts, Russia: Terra Nova, v. 13, p. 407–412.

Benoit, M., Ceuleneer, G. and Polvé, M. (1999). The remelting of hydrothermally altered peridotite at mid-ocean ridges by intruding mantle diapirs. Nature, 403, 514-518.

Benson, W.N. (1926). The tectonic conditions accompanying the intrusion of basic and ultrabasic igneous rocks. Nat. Acad. Sci. Mem., 19 (1), pp. 1–90.

Bédard, J.H., Pagé, P., Bécu, V., Schroetter, J.-M. & Tremblay, A. (2007). Overview of the geology and Cr-PGE potential of the southern Québec ophiolite belt: Geological Association of Canada, Mineral Deposits Division, Special Publication 5, p. 433−448.

Bischoff, J. L. (1969). Red Sea geothermal brine deposits: Their mineralogy, chemistry, and genesis, in Degens, D. T., and Ross, D. A., eds., Hot brines and recent heavy metal deposits in the Red Sea: New York, Springer-Verlag, p. 368-401.

Bizimis, M., Salters, V.J.M., Bonatti, E., (2000). Trace and REE content of clinopyroxenes from supra-subduction zone peridotites. Implications for melting and enrichment processes in islands arcs. Chemical Geology 165, 67–85.

Blome, C.D. & Irwin, W.P. (1985). Equivalent radiolarian ages from the ophiolite terrains of Cyprus and Oman. Geology 13, 401–404.

Bloomer, S. H. & Hawkins, J. W. (1987). Petrology and geochemistry of boninite series volcanic rocks from the Mariana Trench. Contrib. Mineral. Petrol. 97, 36 l-377.

Bloomer, S.H., Ewart, A., Bryan, W., Hergt, J. (1994). In: Hawkins, J., Parson, L., Allan, J., et al. (Eds.), Geochemistry and Origin of Igneous Rocks from the Outer Tonga Forearc. Proc. ODP, Sci. Results, vol. 135. OceanDrilling Program, College Station, Texas, pp. 625–646.

Bodinier, J.-L., Vasseur, G., Vernière, J., Dupuy, C., Fabries, J., (1990). Mechanisms of mantle metasomatism: geochemical evidence from the Lherz orogenic peridotite. Journal of Petrology 31, 597–628.

Bonatti, E. and Michael, P. J. (1989). Mantle peridotites from continental rifts to ocean basins to subduction zones. Earth and Planetary Science Letters 91, 297–311.

Bosch, D., Krasnobayev, A.A., Efimov, A., Savelieva, G. & Boudier, F. (1997). Early Silurian ages for the gabbroic section of the mafic-ultramafic zone from the Urals [abs.], in Oxburgh, E.R., ed., EUG 9, Terra Nova: Strasbourg, Cambridge Publications, p. 121.

Boudier, F. and Coleman, R.G. (1981). Cross-section through the peridotite in the Semail ophioite, southeastern Oman mountains. Journal of Geophysical Research, 86, 307 - 326.

Boudier, F. and Nicolas, A. (1995)**.** Nature of the Moho transition zone in the Oman ophiolite. Journal of Petrology, 36, 777–796.

Boudier, F., Ceuleneer, G. and Nicolas, A. (1988). Shear zones, thrusts and related magmatism in the Oman ophiolite: initiation of thrusting on an oceanic ridge. Tectonophysics, 151, 275-296.

Boudier, F., Godard, M. and Armbruster, C. (2000). Significance of noritic gabbros in the gabbro section of the Oman ophiolite. Marine Geophysical Researches, 21, 307 - 326 .

Boudier, F., Nicolas, A., and Ildefonse, B. (1996). Magma chambers in the Oman ophiolite: fed from the top and bottom. Earth and Planetary Science Letters, 144, 239 - 250.

Boyd, F.R. (1972). Zoned pyroxenes in rock 15555. Ann. Rep. Geophys. Lab., Yearb. 71, pp.459-463.

Boyd, F.R. & Smith, D. (1971). Compositional zoning in pyroxenes from lunar rock 12021, Oceanus Procellarum. J. Petrol. V.12, pp.439-464.

Brenan, J.M., Shaw, H.F., Ryerson, F.J., Phinney, D.L., (1995). Mineral-aqueous fluid partitioning of trace elements at 900 °C and 2.0 GPa: constraints on the trace element chemistry of mantle and deep crustal fluids. Geochimica et Cosmochimica Acta 59, 3331–3350.

Brown, D., Puchkov, V., Alvarez-Marron, J. & Perez-Estaun, A. (1996). The structural architecture of the footwall to the Main Uralian Fault, Southern Urals. Earth-Science Reviews 40, 125–147.

Brown, D., Alvarez-Marron, J., Perez-Estaun, A., Gorozhanina, Y., Baryshev, V. & Puchkov, V. (1997). Geometric and kinematic evolution of the foreland thrust and fold belt in the Southern Urals. Tectonics 16, 551–562.

Brown, D., Juhlin, C., Alvarez-Marron, J., Perez-Estaún, A. & Oslianski, A. (1998). Crustal-scale structure and evolution of an arc – continent collision zone in the southern Urals, Russia. Tectonics, 17, 158-171.

Brown, D. & Spadea, P. (1999). Processes of forearc and accretionary complex formation during arc–continent collision in the Southern Ural Mountains. Geology 27, 649–652.

Brown, D., Alvarez-Marron, J., Perez-Estaun, A., Puchkov, V., Ayarza, P., Gorozhanina, Y. (2001). Structure and evolution of the Magnitogorsk forearc basin: identifying upper crustal processes during arc–continent collision in the Southern Urals. Tectonics 20, 364–375.

Brown, D., Spadea, P., Puchkov, V., Alvarez-Marron, J., Herrington, R., Willner, A.P., Hetzel, R. & Gorozhanina, Y. (2006). Arc–continent collision in the Southern Urals. Earth-Science Reviews. 79:261–287.

Brown, M.A. (1980). Textural and geochemical evidence fro the origin of some chromite deposits in the Oman ophiolite. Panayiotou, A. (Eds.), Ophiolites: Proceedings Internat. Ophiolite Symposium 1979., Geological Survey Dept. Cyprus, 714-721.

Brown, M.A. (1982). Chromite Deposits and Their Ultramafic Host Rocks in the Oman Ophiolite. Ph.D. Thesis, Open University, Milton Keynes .

Browning, P. (1982). The petrology, geochemistry, and structure of the plutonic rocks of the Oman ophiolite. Ph.D. Thesis, Open University, Milton Keynes.

Bryan, W.B. (1983). Systematics of model phenocrysts assemblages in submarine basalts: Petrologic implications. Contrib. Mineral. Petrol., 83: pp. 62.

Bryndzia, L. T. and Wood, B. J. (1990). Oxygen thermobarometry of abyssal spinel peridotites: the redox state and C–O–H volatile composition of the Earth's sub-oceanic upper mantle. American Journal of Science, 290, 1093-1116.

Burke, K.C.A., Dewey, J.F. & Kidd, W.S.F. (1977). World distribution of sutures: the sites of former oceans: Techonophysics. 40, 69-99.

Burns, R.G. (1970). Mineralogical Applications of Crystal Field Theory. Cambridge University Press.

Burns, V.M. & Burns, R.G. (1975). Mineralogy of chromium. Geochimica et Cosmochimica Acta. V.39, pp.903-910.

Burton, J.D., Culkin, F. and Riley, J.P. (1959). The abundances of gallium and germanium in terrestrial materials. Geochimica et Cosmochimica Acta, 16, 151-180.

Cameron, E.N. (1980). Evolution of the Lower Critical zone, central sector, eastern Bushveld Complex, and its chromite deposits: Economic Geology, v. 75, p. 845–871.

Cameron, W.E. (1985). Petrology and origin of primitive lavas from Troodos ophiolitesCyprus. Contributions to Mineralogy and Petrology 89, 239–255.

Cameron, E.N. & Desborough, G.A. (1969). Occurrence and characteristics of chromite deposits—Eastern Bushveld Complex: Economic Geology Monograph 4, p. 23–40.

Cameron, W.E., McCulloch, M.T. & Walker, D.A. (1983). Boninite petrogenesis: chemical and Nd–Sr isotopic constraints. Earth and Planetary Science Letters 65, 75–89.

Campbell, I.H., and Murck, B.W., 1993. Petrology of the G and H chromitite zones in the Mountain View area of the Stillwater Complex: Journal of Petrology, v. 34, p. 291–316.

Caran, S., Coban, H., Flower, M.F.J., Ottley, C.J. and Yılmaz, K., (2010). Podiform chromitites and mantle peridotites of the Antalya ophiolite, Isparta Angle (SW Turkey): implications for partial melting and melt-rock interaction in oceanic and subduction-related settings. Lithos, 114, 307–326.

Carmichael, I.S.E. & Ghiorso, M.S. (1986). Oxidation-reduction relations in basic magma: a case for homogeneous equilibria. Earth Planet Sci Lett 78:200-210

Casey, J.F. and Karson, J.A., (1981). Magma chamber profiles from the Bay of Islands Gphiolite Complex: implications for crustal level magma chambers at mid-ocean ridges. Nature, 292: 295-301.

Cassard, D., Nicolas, A., Rabinovitch, M., Leblanc, M.and Prinzhofer, A. (1981). Structural classification of chromite pods in southern new Caledonia: Economic Geology, 76, 805 - 831.

Cawthorn, R.G. (1975). The amphibole peridotite-metagabbro complex Finero, Northern Italy. J. Geol. 83, pp.437-454.

Ceuleneer, G., Nicolas, A., and Boudier, F., 1988. Mantle flow paterns at an oceanic spreading centre: The Oman peridotites record. Tectonophysics, 151, 1-26.

Chemeneda A, Matte P, Sokolov V., 1997. A model of Palaeozoic obduction and exhumation of high-pressure/low-temperature rocks in the southern Urals. Tectonophysics 276: 217-227

Christiansen. F.G.. (1982). Structural analysis of some ophiolitic chromitites in Sultanate of Oman. Ofioliti. 7: 221-230.

Christie, D.M., Carmichael, I.S.E., Langmuir, C.H. (1986). Oxidation states of mid-ocean ridge basalt glasses. Earth Planet. Sci. Lett. 79, 397–411.

Church, W. R. & Stevens R. K. (1970). Mantle Peridotite and Early Ophiolite Complexes of the Newfoundland Appalachians. Progr. Intern. Symp. Mech. Properties and Processes of the Mantle, Flagstaff, Arizona, 38-39.

Clague, D., Rubin, J. and Brackett, R. (1981). The age and origin of garnet amphibolite underlying the Thetford Mines ophiolite, Que´bec, Can. J. Earth Sci., v.18, pp. 469 – 486.

Cloos, M. (1993). Lithospheric buoyancy and collisional orogenesis: subduction of oceanic plateaus, continental margins, island arcs, spreading ridges, and seamounts. Geological Society of America Bulletin 105, 715-737.

Cloos, M. & Shreve, R.L. (1996). Shear-zone thickness and seismicity of Chilean- and Marianas-type subduction zones. Geology, 24, 107-110.

Clynne, M.A. & Borg, L.E. (1997). Olivine and chromian spinel in primitive calc-alkaline and tholeiitic lavas from the southernmost Cascade Range, California: a reflection of relative fertility of the source. Canadian Mineralogist, v.35, pp.453-472.

Coish, R. A. (1989). Boninitic lavas in Appalachian ophiolites: A review. In Boninites (ed. A. J. Crawford), pp. 264-287. Unwin Hyman.

Coleman, R.G. (1971). Plate tectonic emplacement of upper mantle peridotites along continental edges. Journal of Geophysical Research, 76, 1212-1222.

Coleman, R. G. (1977). Ophiolites. Berlin-Heidelberg: Springer-Verlag.

Coleman, R.G. (1981). Tectonic setting of ophiolite obduction in Oman.Journal of Geophysical Research, 86, 2497-2508.

Crawford, A.J. (1989). Boninites and related rocks. London, Unwin Hyman, 465 pp.

Crawford, A.J. & Verbeeten, A. (1997). Adakite–high-Nb basalt association, Hunter Ridge, SW Pacific: Hot subduction and holes in the slab. In Materials Recycling Near Convergent Plate Boundaries Conference, Manila: Carnegie Institution of Washington, Abstracts, p. 16.

Crawford, A.J., Beccaluva, L. & Serri, G. (1981). Tectonomagmatic evolution of the West Philippine-Mariana Region and the origin of boninites. Earth Planet. Sci. Lett., 54: 3466356.

Crawford A. J. and Cameron W. E. (1985). Petrology and geochemistry of Cambrian boninites and low-Ti andesites from Heathcote. Victoria. Contrih. Mineral. Petrol. 91. 93-104.

Crawford, A.J., Falloon, T.J., Green, D.H. (1989). Classification, petrogenesis and tectonic setting of boninites. In: Crawford, A.J. (Ed.), Boninites and Related Rocks. Unwin Hyman, London, pp. 1–49.

Danyushevsky, L.V., Sobolev, A.V. & Dmitriev, L.V. (1987). Low-titanium orthopyroxene-bearing tholeiite, a new type of ocean-rift tholeiite. Transactions (Doklady) of the USSR Academy of Sciences. 292, 102-105

Dare, S.A.S., Pearce, J.A., McDonald, I. & Styles, M.T., (2009). Tectonic discrimination of peridotites using fO_2 – Cr and Ga-Ti-Fe^{3+} systematic in chrome-spinel., Chemical Geology, V.261, 199-216.

De Roever W. P. (1957). Sind die alpinotypen peridotitmassen vielleicht teknosch verfrachtete bruchstu¨ cke der Peridotitschale? Geol. Rundsch. V.46, pp.137–146.

Della-Pasqua, F.N., Kamenetesky, V.S., Gasparon, M., Crawford, A.J. & Varne, R (1995). Al-rich spinel in a primitive arc volcanics. Mineralogy & Petrology, v.53, pp.1-26.

Deschamps, A., & Lallemand, S. (2003). Geodynamic setting of Izu-Bonin-Mariana boninites. In: R.D. Larter, P.T. Leat (Eds.), Intra-Oceanic Subduction Systems: Tectonic & Magmatic Processes, Geol. Soc. London Spec. Publ. 219:163-185.

Dewey, J.F. (1976). Ophiolite obduction. Tectonophysics, 31, 93-120.

Dewey, J.F. & Bird, J.M. (1971). Origin and emplacement of the ophiolite suite: Appalachian ophiolites in Newfoundland. In: Gillis, K., Mevel, C., Allan, J., and al., e., (Eds.), Scientific Results: College Station, TX, Ocean Drilling Program, Texas AandM University, 103-134.

Dick, H.J.B. (1977). Partial melting in the Josephine peridotite I, the effect on mineral composition and its consequence for geobarometry and geothermometry. American Journal of Science, 277, 801-832.

Dick H.J. & Bullen T. (1984). Chromian spinel as a petrogenetic indicator in abyssal and alpine-type peridotites and spatially associated lavas. Contributions to Mineralogy and Petrology, 86, 54-76.

Dick, H.J.B., Fisher, R.L. & Bryan, W.B. (1984). Mineralogic variability of the uppermost mantle along mid-ocean ridges, Earth Planet. Sci. Lett. 69: 88 -106.

Dick, H.J.B., & Natland, J. H. (1996). Late stage melt evolution and transport in the shallow mantle beneath the East Pacific Rise, .In: Gillis, K., Mevel, C., Allan, J., and al., e., (Eds.), Scientific Results: College Station, TX, Ocean Drilling Program, Texas AandM University, 103-134.

Dickey, J.S. (1975) A hypothesis of origin for podiform chromite deposits. Geochim Cosmochim Acta 39:1061–1074

Dietz, R.S and Holden, J.C (1970). Reconstruction of Pangea: Breakup and Dispersion of Continents, Permian to Present. Journal of Geophysical Research, V.75, No.26, pp.4939-4956.

Dilek, Y. (2003). Ophiolite concept and its evolution. In:Ophiolite Concept and the evolution of geological thought. Eds. Dilek, Y and Newcomb, S. Geological Society of America Special Paper, 373, 1-16.

Dilek, Y., Moores, E.M. & Furnes, H. (1998). Structure of modern oceanic crust and ophiolites and implications for faulting and magmatism at oceanic spreading centres. In: Buck, R., Karson, J., Delaney, P., and Lagabrielle, Y., (Eds.), Faulting and magmatism at mid-ocean ridges: Washington, D.C., American Geophysical Union Monograph, 106, 219-266.

Dilek, Y., Moores, E., Elthon, D. & Nicolas, A. (Eds.) (2000). Ophiolites and Oceanic Crust: New Insights from Field Studies and the Ocean Drilling Program. Geological Society of America. Special Papers. 349.

Dilek, Y., and Flower, M.F.J. (2003). Arc-trench rollback and forearc accretion: 2. A Model Template for Ophiolites in Albania, Cyprus, and Oman, in Dilek, Y., and Robinson, P.T., eds., Ophiolites in Earth history: Geological Society [London] Special Publication 218, p. 43–68.

Distler, V.V., Kryachko, V.V. & Yudovskaya, M.A. (2003). Formation of platinum-group metals in chromite ores of the Kempirsai ore field. Geology of Ore Deposits. 45: 37-65.

Donath, I.M. (1962). Die Metallischen Rohstoffe. Band 14: Chrom, p.2 Ferdinand Enke, pp.371

Duke, J. M. (1983). Ore deposit models 7: Magmatic segregation deposits of chromite. Journal of the Geological Association of Canada. V.10, No.1, p. 15-24

Duncan, R.A. & Green, D.H. (1987). The genesis of refractory melts in the formation of oceanic crust. Contrib. Mineral. Petrol., 96: 326-342.

Eales, H.V. (2000). Implications of the chromium budget of the Western Limb of the Bushveld Complex, South African Journal of Geology, v.103, pp.141-150.

Eales, H.V., and Reynolds, I.M., (1986). Cryptic variations within chromitites of the Upper Critical zone, Northwestern Bushveld Complex: Economic Geology. V. 81, pp. 1056–1066.

Eales, H.V., Wilson, A.H., and Reynolds, I.M., (1988). Complex unmixed spinels in layered intrusions within an obducted ophiolite in the Natal-amaqua mobile belt: Mineralium Deposita, v.23, p. 150–157.

Edwards, R. L. & Wasserburg, G. J., (1985). The age and emplacement of obducted oceanic crust in the Urals from Sm–Nd and Rb–Sr systematics. Earth and Planetary Science Letters 72, 389–404.

Edwards, S.J., (1990). Harzburgites and refractory melts in the Lewis Hills massif, Bay of Islands ophiolite Complex: The base-metals and precious-metals story: Canadian Mineralogist. V.28, pp.537-552.

Edwards, S.J., (1991). Magmatic and fluid processes in the upper mantle: A study of the Bay of Islands ophiolite complex, Newfoundland [Ph.D. Thesis]. St. John's, Memorial University of Newfoundland.

Edwards, S. J. and Malpas, J. (1996). Melt-peridotite interactions in shallow mantle at the East Pacific Rise: evidence from ODP Site 895 (Hess Deep). Mineralogical Magazine, 60, 191–206.

Edwards, S. J., Falloon, T.J., Malpas, J. & Pedersen, R.B. (1996). A review of the petrology of harzburgites at Hess Deep & Garrett Deep: Implications for mantle processes beneath segments of the East Pacific Rise. Geol. Soc. London. Spec. Publication. 118: 143-156.

Edwards, S.J., Pearce, J.A. and Freeman, J. (2000). New insights concerning the influence of water during the formation of podiform chromitite. In: Dilek, Y., Moores, E.M., Elthon, D., and Nicolas, A., (Eds.), Ophiolites and Oceanic Crust: New Insights from Field Studies and the Ocean Drilling Program: Boulder, Colorado, Geological Society of America Special Paper 349,139-147.

Eggins, S.M., Rudnick, R.L. & McDonough W.F. (1998). The composition of peridotites and their minerals: a laser-ablation ICP-MS study. Earth and Planetary Science Letters, 154, 53-71.

Elburg, M.A. and Kamenetsky, V.S. (2007). Dehydration processes determine fO_2 of arc and intraplate magmas. Geochimica et Cosmochimica Acta, in press p.A252.

Elthon, D. (1992). Chemical trends in abyssal peridotites: refertilisation of depleted oceanic mantle. Journal of Geophysical Research. 97: 9015–9025.

Engel, A.E.J., Engel, C.G. & Havens RG (1965). Chemical characteristics of oceanic basalts and the upper mantle. Geol Soc Am Bull. 76:719-734

Evans, B. W. and Frost, B. R. (1975). Chrome-spinel in progressive metamorphism—a preliminary analysis. Geochimica et Cosmochimica Acta 39, 959–972.

Fabries, J. (1979). Spinel–olivine geothermometer in peridotites from ultramafic complex. Contributions to Mineralogy and Petrology, 69, 329–336.

Falloon, T. J., & Green, D. H. (1987). Anhydrous partial melting of MORB pyrolite and other peridotite compositions at 10-kb: implications for the origin of primitive MORB glasses. Miner. Petrol. V.37, pp.181-219

Feig, S., Koepke, J. and Snow, J. (2006). Effect of water on tholeiitic basalt phase equilibria: An experimental study under oxidizing conditions. Contributions to Mineralogy and Petrology, 152, 611.

Fischmeister, H.F. and Exner, H.E. (1965). Sintering in the presence of a liquid phase. Metall, V.19, pp.113, 941.

Fisk, M.R., (1986). Basalt-magma interactions with harzburgite and the formation of high-magnesian sndesites. Geophysical Research Letter, V.13, 467-470

Fisk, M.R. & Bence, A.E. (1980). Experimental crystallization of chrome spinel in FAMOUS basalt 527-1-1. Earth and Planetary Science Letters 48:111–123

Flower, M.F.J. (2003). Ophiolites, historical contingency, and the Wilson Cycle. In: Dilek, Y., Newcomb, S. (Eds.), Geological Society of America — Spec. Publ: Ophiolite Concept and the Evolution of Geological Thought, vol. 373, pp. 111–136.

Frey, F.A., Suen, J.C., Stockman, H.W., (1985). The Ronda high temperature peridotite: geochemistry and petrogenesis. Geochimica et Cosmochimica Acta 49, 2469–2491.

Friberg, M., Larionov, A., Petrov, G.A. & Gee, D.G. (2000). Paleozoic amphibolite-granulite facies magmatic complexes in the hinterland of the Uralide orogen: International Journal of Earth Science, v. 89, p. 21–39.

Frisch, T. (1971). Alteration of chrome spinel in a dunite nodule from Lanzarote, Canary Islands. Lithos v.4, pp.83-91.

Fujii, T. & Scarfe, C. M. (1985). Composition of liquids coexisting with spinel lherzolite at 10-kb and the genesis of MORBs. Contr. Miner. Petrol. V.90, pp.18-28.

Gaetani, G.A., Grove, T.L., (1998). The influence of water on melting of mantle peridotite. Contributions to Mineralogy and Petrology 131, 323–346.

Garuti, G., Pushkarev, E. & Zaccarini, F. (2002). Composition and paragenesis of Pt alloys from chromitites of the Uralian-Alaskantype Kytlym and Uktus complexes, northern and central Urals, Russia. Can. Mineral., 40, 357-376.

Gass, I.G. (1968). Is the Troodos massif of Cyprus a fragment of mesozoic ocean floor? Nature, 220, 39-42.

Gass, I.G. 1990. Ophiolites and oceanic lithosphere in Ophiolites and Oceanic Crustal Analogues Proceeding of the Symposium "Troodos 1987", edited by J.G. Malpas, et al., pp. 1-10, Geol. Sur. Dept., Nicosia, Cyprus, 1990.

Gass, I.G. and Masson-Smith, D. (1963). The geology and gravity anomolies of the Troodos massif, Cyprus. Philisophical Transaction of the Royal Society of London, A 225, 417-467.

Gauthier, M., Corrivaux, L., Trottier, L.J., Cabri, J., Laflamme, J.H.G. & Bergeron, M. (1990). Chromitites platinifères des complexes ophiolitiques de l'Estrie-Beauce, Appalaches du sud du Québec: Mineralium Deposita, v. 25, p. 169−178.

Genshaft, Y.S., & Ilupin, I.P. (2002). On genetic classification of chromian spinels in deep-seared rocks from continental structures. Russian Journal of Earth Sciences.

Georgiou, E. (1987). Geology, petrology and mineral chemistry of the Akapnou Forest plutonic complex and the associated chromite occurrences, Cyprus [Ph.D. Thesis]: Orleans, l'Universite d'Orleans.

Gervilla F. and Leblanc M. (1990). Magmatic ores in high-temperature alpine-type lherzolite massifs (Ronda, Spain. and Beni Bousera, Morocco). Econ. Geol. 85, 112-132.

Girardeau, J., Monnier, C., Le Mée, L. and Quatrevaux, F. (2002). The Wuqbah peridotite, central Oman ophiolite: Petrological characteristics of the mantle in a fossil overlapping ridge setting, Mar. Geophys. Res., 23 (1), 43-56.

Godard, M., Bodinier, J.L. & Vasseur, G. (1995). Effects of mineralogical reactions on trace element redistributions in mantle rocks during percolation processes: A chromatographic approach. Earth Planet. Sci. Lett. 133: 449-461.

Godard, M., Jousselin, D. and Bodinier, J-L. (2000). Relationships between geochemistry and structure beneath a palaeo-spreading centre: a study of the mantle section in the Oman ophiolite. Earth and Planetary Science Letters, 180, 133-148.

Godard, M., Dautria, J-M. and Perin, M. (2003). Geochemical variability of the Oman ophiolite lavas: Relationship with spatial distribution and paleomagnetic directions. Geochemistry, Geophysics, Geosystems, 4, 8609, doi:10.1029/2002GC000452.

Godard, M., Bosch, D. and Einaudi, F. (2006). A MORB source for low-Ti magmatism in the Semail ophiolite. Chemical Geology, 234, 58-78.

Godard, M., Lagabrielle, Y., Alard, O. & Harvey, J. (2008). Geochemistry of the highly depleted peridotites drilled at ODP Sites 1272 and 1274 (Fifteen–Twenty Fracture Zone, Mid-Atlantic Ridge): implications for mantle dynamics beneath a slow spreading ridge. Earth Planet. Sci. Lett. 267 (3–4), 410–425.

Golding, H.G. (1975). Relict textures of chromitite from New South Wales.- Geol. Soc. Australia. J, v. 22, pp.397--412.

Graham, I. T., Franklin, B. J. & Marshall, B., (1996). Chemistry and mineralogy of podiform chromitite deposits, southern NSW, Australia: a guide to their origin and evolution. Mineralogy and Petrology 57, 129–150.

Gruau, G., Bernard-Griffiths, J. & Lecuyer, C. (1998). The origin of U-shaped rare earth patterns in ophiolite peridotites: assessing the role of secondary alteration and melt/rock reaction, Geochim. Cosmochim. Acta. 62 (21–22), 3545-3560.

Green, D. H. (1973). Experimental melting studies on model upper mantle compositions at high pressure under both water-saturated and water-undersaturated conditions. Earth Planet. Sci. Lett. 19, pp.37-53.

Greenbaum, D. (1972). Magmatic processes at ocean ridges: evidence from the Troodos Massif, Cyprus. Nature, 238, 18-21.

Greenbaum, D. (1977a). The chromitiferous rocks of the Troodos ophiolite complex, Cyprus. Economic Geology and the Bulletin of the Society of Economic Geologists, Nature, 72, 1175-1194.

Greenbaum, D. (1977b). Magmatic processes at ocean ridges: Evidence from the Toodos massif, Cyprus. Nature, v.238, 18-21

Grégoire M., Moine B.N., O'Reilly S.Y., Cottin J.Y. and Giret A. (2000). Trace element residence and partitioning in mantle xenoliths metasomatized by highly alkaline, silicate- and carbonate- rich melts (Kerguelen Islands, Indian Ocean). Journal of Petrology, 41, 477-509.

Hamlyn, P.R. & Keays, R.R. (1979). Origin of chromite compositional variation in the Panton Sill, Western Australia. Contrib Mineral Petrol, 69:75 82

Henderson, P. (1975). Reaction trends shown by chrome-spinels of the Rhum layered intrusion. Geocheimica et Cosmochimica Acta 39, 1035-1044.

Henderson, P. & Wood, R.J. (1981). Reaction relationships of chrome-spinels in igneous rocks – further evidence from the layered intrusions of Rhum and Mull, Inner Hebrides, Scotland. Contributions to Mineralogy and Petrology, v.78, pp.225-229.

Gusev, G.S., Gushchin, A.V., Zaykov, V.V., Maslennikov, V.V., Mezhelovsky, N.V., Perevozchikov, B.V, Surin, T.N., Filatov, E.I.., and Shirai, E.P., (2000). Geology and metallogeny of island arcs, in Mezhelovsky N. V. et al., eds., Geodynamics and metallogeny: Theory and implications for applied geology: Moscow, Ministry of Natural Resources of the RF and GEOKART Ltd., p. 213–295.

Hacker, B.R., Wang, X., Eide, E.A. & Ratschbacher, L. (1996). The Qinling–Dabie ultra-high-pressure collisional orogen. In: Yin, A., Harrison, T.M. (Eds.), The Tectonic Evolution of Asia. Cambridge University Press, Cambridge, pp. 345–370.

Hawkins, J.W. & Castillo, P.R. (1998). Early history of the Izu-Bonin-Mariana arc system: evidence from Belau and the Palau Trench. The Island Arc, 7, 559-578.

Haggerty, S.E., Boyd, F.R., Bell, P.M., Finger, L.W. & Bryan, W.B. (1970). Opaque minerals and olivine in lavas and breccias from Mare Tranquillitatis. Proc. Apollo 11 Lunur Sci. Conf., Geochim. Cosmochim. Acta Suppl.1, Vol. 1, pp, 513-538. Pergamon Press.

Haggerty, S.E. (1976). Oxidation of opaque mineral oxides in basalts. In Oxide Minerals (ed. D. Rumble Ill): Reviews in Mineralogy 3, pp. H1-H100.

Haggerty, S.E., (1991). Oxide mineralogy of the upper mantle. Reviews in Mineralogy, v. 25, p. 355-407.

Hamlyn, P.R., and Bonatti, E. (1980). Petrology of mantle-derived ultramafics from the Owen fracture zone, northwest Indian Ocean: implications for the nature of the oceanic upper mantle. Earth and Planetary Science Letters, 48, 65-79.

Hamlyn, P.R., Keays, R.R., Cameron, W.E., Crawford, A.J., Waldron, H.M., (1985). Precious metals in magnesian low-Ti lavas: implications for metallogenesis and sulfur saturation in primary magmas. Geochimica et Cosmochimica Acta 49, 1797–1811.

Hatton, C.J. & Von Gruenewaldt G, (1987). The geological setting and petrogenesis of the Bushveld chromitite layers, in Stowe, C.W., ed., Evolution of chromium ore fields: New York, Van Nostrand-Reinholdp, pp.109-143.

Hellebrand, E., Snow, J.E., Dick, H.J.B., and Hofmann, A.W. (2001). Coupled major and trace elements as indicators of the extent of melting in mid-ocean-ridge peridotites. Nature, 410, 677-680.

Herrington, R.J., Armstrong, R.N., Zaykov, V.V., Maslennikov, V.V., Tessalina, S.G., Orgeval, J.-J., Taylor, R.N.A., (2002). Massive sulfide deposits in the South Urals: geological setting within the framework of the Uralide Orogen. In: Brown, D., Juhlin, C., Puchkov, V. (Eds.), Mountain Building in the Uralides: Pangea to Present. American Geophysical Union, Geophysical Monograph, vol. 132, pp. 155–182.

Herrington, R.J., Zaykov, V.V., Maslennikov, V.V., Brown, D & Puchkov, V.N. (2005). Mineral Deposits of the Urals and Links to Geodynamic Evolution. Econ. Geol. 100th Ann. Vol. pp. 1069-1095.

Hess, H.H. (1955). Serpentines, orogeny and epeirogeny. In: Poldevaart, A., (ed.), Crust of the Earth (A Symposium): New York, Geological Society of America Special Paper, 62, 391-408.

Hess, H.H. (1965). Mid-ocean ridges and tectonics of the sea floor. In: Whitard, W.F., and Bradshaw, R., (Eds.), Submarine geology and geophysics: Proceedings of the 17th Symposium of the Colston Research Society: London, Butterworths, 317-334.

Hickey R. L. and Frey F. A. (1982). Geochemical characteristics of boninite volcanics: Implications for their source. Geochim. Cosmochim. Acta 46, 2099-2115.

Hirschmann, M. (1995). Melt pathways in the mantle.Nature, 375, 737 - 738.

Hofmann, A.W. (1988). Chemical differentiation of the Earth: The relationship between mantle, continental crust, and oceanic crust. Earth Planet Sci Lett. 90:297 314

Holwell, D.A. and McDonald, I. (2007). Distribution of platinum-group elements in the Platreef at Overysel, northern Bushveld Copmlex: a combined PGM and LA-ICP-MS study.Contributions to Mineralogy and Petrology, DOI 10.1007/s00410-007-0185-9.

Hulbert, L.J., and Gruenewaldt, G., (1985). Textural and compositional features of chromite in the Lower and Critical zones of the Bushveld Complex south of Potgietersrus: ECONOMIC GEOLOGY, v. 80, p. 872–895.

Irvine, T.N., (1965). Chromian spinel as a petrogenetic indicator. 1. Theory: Canadian Journal of Earth Sciences, v. 2, p. 648–672.

Irvine, T. N., (1967). Chromian spinel as a petrogenetic indicator. Part 2. Petrologic applications. Canadian Journal of Earth Sciences 4, 71–104.

Irvine, T.N., (1974). Petrology of the Duke Island ultramafic complex, southeastern Alaska. Geol. Soc. Am, Mem., 138: pp.240.

Irvine, T.N., (1975). Crystallisation sequence of the Muskox Intrusion and other layered intrusions: II. Origin of the chromitite layers and similar deposits of other magmatic ores: Geochimica et Cosmochimica Acta, v. 39, p. 991-1020.

Irvine, T.N., (1977). Origin of chromitite layers in the Muskox intrusion and other stratiform intrusions: A new interpretation: Geology, v. 5, p. 272–277.

Irvine, T.N., (1977b). Chromite crystallization in the join Mg_2SiO_4-$CaMgSi_20_6$-$CaAl_2Si_2O_6$-$MgCr_2O_4$-SiO_2: Carnegie Inst. Washington Yearbook 76, pp. 465-472.

Ishii, T., Robinson, P.T., Maekawa, H. and Fiske, R. (1992). Petrological studies of Peridotites from Diapiric Serpentinite Seamounts in the Izu-Ogasawara-Mariana Forearc, Leg 125. In: Fryer, P., Pearce, J.A., Stokking, L.B., et al (Eds.), Proceeding of the Ocean Drilling Program. Scientific Results, 125, 445-485.

Ishikawa, T., Fujisawa, Nagaishi, K. and Masuda, T. (2005). Trace element characteristics of the fluid liberated from amphibolite-facies slab: Inference from the metamorphic sole beneath the Oman ophiolite and implication for boninite genesis. Earth and Planetary Science Letters, 240, 355-377.

Ishikawa, T., Nagaishi, K. and Umino, S. (2002). Boninitic volcanism in the Oman ophiolite: Implications for thermal condition during transition from spreading ridge to arc. Geology, 30, 899-902

Ishiwatari, A.; Sokolov, S. D.; and Vysotskiy, S. V. (2003). Petrological diversity and origin of ophiolites in Japan and Far East Russia with emphasis on depleted harzburgite. In Dilek, Y., and Robinson, P. T., eds. Ophiolites

in earth history. Geol. Soc. Lond. Spec. Publ. 128:597–617.

Ishiwatari, A., Yanagida, Y., Li, Y-B., Ishii, T., Haraguchi. S., Koizumi, K., Ichiyama. Y. and Umeka., M. (2006). Dredge petrology of the boninite- and adakite- bearing Hahajima Seamount of the Ogasawara (Basin) forearc: and ophiolite or a serpentinitite seamount? The Island Arc, 15, 102-118.

Ivanov, K.S., Puchkov, V.N., Nasedkina, V.A. & Pelevin, I.A. (1989). First results on revised stratigraphy of the Polyakovka Formation based on conodonts. In: Exhegodnik-88. Institute of Geology and Geochemistry, Uralian Department, Russion Academy of Science, Sverdlovsk, 12-13.

Jackson, E.D. (1961). Primary textures and mineral association in the ultramafic zone of the Stillwater Complex . In: Wilson, H.D.B (ed), Magmatic ore deposits, Economic Geology Monograph, 4, 41-71.

Jackson, E. D., (1969). Chemical variation in coexisting chromite and olivine in chromitite zones of the Stillwater Complex. Economic Geology Monograph Series 4, 41–71.

Jackson, E.D. & Thayer, T.P. (1982). Some criteria for distinguishing between stratiform concentric and alpine peridotite-gabbro complexes: International Geological Congress, 24th, Montreal, Proceedings v.2, pp. 289-296.

Jacques, J.L. and Green, D.H. (1980). Anhydrous melting of peridotites at 0-15kb pressure and the genesis of tholeiitic basalts. Contributions to Mineralogy and Petrology,73 287-310.

Jambon, A. (1994). Earth degassing and large-scale geochemical cycling of volatile elements, in Volatiles in Magmas. Edited by M. R. Carroll and J. R. Holloway, Mineral. Soc. Am., Washington, D. C., pp. 479 – 517

Jenner, G.A. (1981). Geochemistry of high-Mg andesites from Cape Vogel, PNG. Chem Geology, 33:307 332.

Johan, Z. (1986). Chromite deposits in the Massif du Sud ophiolite, New Caledonia: genetic consideration. In: Chromites. UNESCO's IGCP- 197 Project. Athens: Theophrastos, pp. 311–339.

Johan, Z., Robert, J.L. &Volfinger, M., (1982). Role of reducing fluids in the origin of chromite deposits in ophiolitic complexes. Abstracts, Geological Association of Canada, 7, 58.

Johan, Z., Dunlop, H., Le Bel, L., Robert, J. L. & Volfinger, M. (1983). Origin of chromite deposits in ophiolitic complexes: evidence for a volatile- and sodium-rich reducing fluid phase. Fortschritte der Mineralogie. 61: 105–107.

Johnson, K. T. M., Dick, H. J. B. & Shimizu, N. (1990). Melting in the oceanic upper mantle: An ion microprobe study of diopsides in abyssal peridotites. Journal of Geophysical Research. 95: 2661-2678.

Kamenetsky, V.S., Crawford. A.J., and Meffre, S. (2001). Factors controlling chemistry of magmatic spinel: an empirical study of associated olivine, Cr-spinel and melt inclusions from primitive rocks. Journal of Petrology. 42: 655-671.

Kamperman,M., Danyushevsky, L.V., Taylor,W.R. and Jablonski, W. (1996). Direct oxygen measurements of Cr-rich spinel; implications for spinel stoichiometry. American Mineralogist, 81,1186-1194.

Kelemen, P.B. (1990). Reaction between ultramafic rock and fractionating basaltic magma.I. Phase relations, the origin of calc-alkaline magma series, and the formation of discordant dunite. Journal of Petrology, 31, 51-98.

Kelemen, P.B. (1995). Genesis of high Mg# andesites and the continental crust. Contrib Mineral Petrol, 120:1-19.

Kelemen, P.B., Dick, H.J.B. & Quick, J.E., (1992). Formation of harzburgite by pervasive melt/rock reaction in the upper mantle. Nature 358, 635–641.

Kelemen, P.B., Shimizu, N. & Slaters, V.J.M. (1995). Extraction of mid-ocean-ridge basalt from the upwelling mantle by focused flow of melt in dunite channels. Nature, 375, 747 – 753.

Kelemen, P.B., Koga, K. & Shimizu, N. (1997a). Geochemistry of gabbro sills in the crust-mantle transition zone of the Oman ophiolite: implications for the origin of the oceanic lower crust.Earth and Planetary Science Letters, 146, 475-488.

Kelemen, P.B., Hirth, G., Shimizu, N., Spiegelman, M. & Dick, H.J.B. (1997b). A review of melt migration processes in the adiabatically upwelling mantle beneath oceanic spreading ridges. Philisophical Transaction of the Royal Society of London, A, 355, 283-318.

Kelemen, P. B., Braun, M. & Hirth, G. (2000). Spatial distribution of melt conduits in the mantle beneath oceanic spreading ridges: Observations from the Ingalls and Oman ophiolites. Geochemistry, Geophysics, Geosystems, 1, [Paper number 1999GC000012.

Keppler, H., (1996). Constraints from partitioning experiments on the composition of subduction-zone fluids. Nature 380, 237–240.

Kimball, K.L. (1990). Effects of hydrothermal alteration on the compositions of chromian spinel. Contributions to Mineralogy and Petrology, 105, 337-346.

Klein, E. M. & Langmuir, C. H. (1987). Global correlations of ocean ridge basalt chemistry with axial depth and crustal thickness. Journal of Geophysical Research. 92: 8089–8115.

Klingenberg, M.N.E.T. and Kushiro, I. (1996). Melting of chromite-bearing harzburgite and generation of boninitic melts at low pressures under controlled oxygen fugacity. Lithos, 37, 1–13.

Klusky, T.M., Abdelsalam, M., Stern, R.J. & Tucker, R.D. (2003). Evolution og the East African and related orogens, and the assembly of Gondwana. Precambrian Research. 123, 81-85.

Koepke, J., Feig, S.T., and Snow, J. (2005). Hydrous partial melting within the lower oceanic crust. Terra Nova, 17, 286–291.

Kuroda, N., Shiraki, K, & Urano, H. (1978). Boninite as a possible calc-alkalic primary magma. Bull. Vokanol. V.41, pp.563-75.

Kushiro I (1969). The system forsterite diopside silica with and without water at high pressures. Am J Sci 267A:269-294

Kushiro I (1972). Effect of water on the composition of magmas formed at high pressures. J Petrol 13:311-334.

Kushiro, I. (1990). Partial melting of mantle wedge and evolution of island arc crust. J Geophys Res 95: 15929-15939

Kushiro, I., Syono, Y. & Akimoto, S. (1968). Melting of peridotite nodule at high pressures and high water pressures. Journal of Geophysical Research 73, 6023–6029.

Kushiro I, Yoder HS, Mysen BO (1977). Viscosities of basalt and andesite melts at high pressures. J Geophys Res 81:6351-6356

Kuz'min, M.I. & Kabanova, L.Ya. (1991). Boninite Series of the Southern Urals: Geologic and Petrographic Description, Compositional Peculiarities and Problems of Origin. Nauka, Miass, pp. 156–173 (in Russian).

Lago, B.L., Rabinowicz, M. & Nicolas, A., (1982). Podiform chromite orebodies: A genetic model: Journal of Petrology, v. 23, p. 103–125.

Le Mée, L., Girardeau, J., and Monnier, C. (2004). Mantle segmentation along the Oman ophiolite fossil mid-ocean ridge. Nature, 432:167-172.

le Roex, A.P. (1987). Source regions of mid-ocean ridge basalts: Evidence for enrichment processes. In: Menzies MA, Hawkesworth CJ (eds) Mantle metasomatism. Academic Press, London, pp 389-419

Leblanc, M., (1987). Chromitc in oceanic arc environment: New Caledonia. In: Stowe, C. W. (ed.) Evolution of Chromium Ore Fields. New York: Van Nostrand-Reinhold, pp. 265-296.

Leblanc M. (1995). Chromitite and ultramafic rock compositional zoning through a paleotransform fault, Poum, New Caledonia. Economic Geology, V.90, pp. 2028-2039

Leblanc M,. (1997). Chromitite and ultramafic rock compositional zoning through a paleotransform fault, Poum, New Caledonia – A Reply. Economic Geology, V.92, pp. 503-504

Leblanc, M. and Ceuleneer, G. (1992). Chromite crystallization in a multicellular magma flow: Evidence from a chromitite dike in the Oman ophiolite. Lithos, 27, 231-257.

Leblanc M & Nicolas A (1992). Ophiolitic chromitite. Int Geol Rev. V.34, pp.653–686.

Leblanc M. and Timagoult A. (1989). Chromite pods in a lherzolite massif (Collo, Algeria): evidence of oceanic-type mantle rocks along the West Mediterranean Alpine Belt. Lithos 23, 153-162.

Lee, C.-T.A., Leeman, W.P., Canil, D., Li, Z.-X.A., (2005). Similar V/Sc systematics in MORB and arc basalts: implications for oxygen fugacities of their mantle source regions. Journal of Petrology 46, 2313–2336.

Lehmann, J., (1983). Diffusion between olivine and spinel: application to geothermometry. Earth and Planetary Science Letters 64, 123–138.

Li, Z., et al., (1993). Prospecting for the Chromite Ores in the Luobusa Ophiolite, Tibet (in Chinese). Wuhan: China Univ. GeoSciences Press..

Li, J.-P., O'Neill, H. St. C. & Seifert, F., (1995). Subsolidus phase relations in the system MgO–SiO2–Cr–O in equilibrium with metallic Cr, and their significance for the petrochemistry of chromium. Journal of Petrology 36, 107–132.

Lilly, R. (2006). The magmatic and crustal evolution of the northern Oman-United Arab Emirates ophiolite. PhD thesis, Cardiff University, 202pp.

Lippard, S.J., Shelton, A.W. and Gass, I.G. (1986). The Ophiolite of Northern Oman. Memoir Geological Society of London, 11, 178.

Lippard, S.J., Smewing, J.D.,Rothery, D.A., Browning, P. (1982). The geology of the Dibba zone, northern Oman mountains; a preliminary study. Journal of the Geological Society of London, 139, 59 - 66.

Lorand, J.P. & Ceuleneer, G. (1989). Silicate and base-metal sulfide inclusions in chromites from the Maqsad are (Oman ophiolite, Gulf of Oman): a model for entrapment. Lithos, 63, 161-173.

Lorand, J. P. & Cottin, J. Y., (1987). Na–Ti–Zr–H_2O-rich mineral inclusions indicating post-cumulus chrome-spinel dissolution and recrystallization in the Western Laouni mafic intrusion, Algeria. Contributions to Mineralogy and Petrology 86, 251–263.

Macpherson, C.G. & Hall, R. (2001). Tectonic setting of Eocene boninite magmatism in the Izu– Bonin– Mariana forearc. Earth Planet. Sci. Lett. 186, 215– 230.

Maier, W.D. & Barnes, S-J (2008). Platinum-group elements in the UG1 and UG2 chromitites, and the Bastard reef, at Impala platinum mine, western Bushveld Complex, South Africa: Evidence for late magmatic cumulate instability and reef constitution, South African Journal of Geology, v.111, pp.159-176

Malpas, J. (Editors), Ophiolites, Oceanic Crustal Analogues. Geol. Surv. Dept. Minist. Agric. Nat. Res., Nicosia, pp. 557-565

Malpas, J. and Strong, D.F. (1975). A comparison of chrome-spinels in ophiolites and mantle diapies of Newfoundland. Geochemicica et Cosmochimica Acta. 39, pp.1045-1060.

Malpas, J.G. & Robinson, P.T. (1987). Chromite mineralization in the Troodos ophiolite, Cyprus. In: Stowe, C.W. (ed.) Evolution of chromium orefields, Van Nostrand-Reinhold Publishers, New York, pp. 220-227

Mao, H.K., Bell, P.M. & Dickey, J.S., Jr. (1972). Comparison of the crystal field spectra of natural and synthetic chrome diopside. Ann. Rep. Geophys. Lab., Yearb. 71, pp.524-527.

Marsh, B.D., (1989). Magma Chambers. Annu. Rev. Earth Planet. Sci. 17, 439-474

Marsh, B.D., 1989. On convective style and vigor in sheet like magma chambers. J. Pet. 30, 479-530.

Maslov, V.A., Cherkasov, V.L., Tischchenko, V.T., Smirnova, I.A., Artyushkova, O.V. & Pavlov, V.V. (1993). On the stratigraphy and correlation of the middle Paleozoic complexes of the main copper-pyritic areas of the southern Urals: Ufa, Ufinian Science Centre, 217 p. (in Russian).

Matsukage, K. and Arai, S. (1996). Jadeite, Albite and Nepheline as inclusions in spinel of chromitite from Hess Deep, Equatorial Pacific: their genesis and implications for serpentinite diapir formation. Contributions to Mineralogy and Petrology, 131, 111-128.

Matsukage, K. Arai, S. Abe, N. and Yurimoto, H. (2001). Two contrasting melting styles of mantle peridotite in the northen Oman ophiolite: implications for the swich of their tectonic setting. Research Report of JSPS Grants-in Aid for Science Research, 11691121, 19-32.

Matsumoto, I., Arai, S. & Yamauchi, H. (1997). High-Al podiform chromitites in dunite-harzburgite complexes of the Sangun zone, central Chugoku district, Southwest Japan. J Asian Earth Sci 15: 295-302

Matveev, S., Ballhaus, C., (2002). Role of water in the origin of podiform chromitite deposits. Earth and Planetary Science Letters 203, 235–243.

Maurel, C. & Maurel, P. (1982a). Etude expérimentale de la solubilité du chrome dans les bains silicatés basiques et sa distribution entre liquide et minéraux coexistants: conditions d'existence du spinelle chromifére: Bulletin Mineralogie, v. 105, p. 197–202.

Maurel, C. & Maurel, P. (1982b). Etude experimentale de la solubilite du chrome dans les bains silicates basiques et de sa distribution entre liquide et mineraux coexistants: conditions d'existence du spinelle chromifere. Ibid 105, pp.640-7.

Maurel, C. (1984). Etude experimentale de la distribution du fer ferreux et du magnesium entre spinelle chromitfere et bain silicate basique – Bulletin Mineralogy. 107, 767-776.

Maxwell, J. C. (1969). "Alpine" mafic and ultramafic rocks: The ophiolite suite: Tectonophysics, v. 7, p. 489-494.

McDonald, I. (2005). Development of sulphide standards for the in-situ analysis of platinum-group elements by laser ablation inductively coupled plasma-mass spectrometry (LA-ICP-MS). Extended abstract of the 10th International Platinum Symposium, 468-471.

McDonough WF, Frey FA (1989). Rare earth elements in upper mantle rocks. Rev Mineral 21: 99±145

McDonough, W.F., Sun, S.S., (1995). The composition of the Earth. Chemical Geology 120, 223–253.

McElduff, B. & Stumpfl, E. F., (1991). The chromite deposits of the Troodos Complex, Cyprus—evidence for the role of a fluid phase, accompanying chromite formation. Mineralium Deposita 26, 307–318.

McKay D.B and Mitchell R.H. (1988). Abundance and distribution of gallium in some spinel and garnet lherzolites. Geochimica et Cosmochimia Acta, 52, 2867-2870.

Meffre, S., Aitchison, J.C. & Crawford, A.J. (1996). Geochemical stratigraphy of boninites and tholeiites from the Permo–Triassic Koh Ophiolite, New Caledonia. Tectonics. 15:67–83.

Meijer A. (1980). Primitive arc volcanism and a boninite series: examples from western Pacific island arcs. In: The Tectonic and Geologic Evolution of Southeast Asian Seas and Islands (ed. D. E. Hayes), Amer. Geophys. Union Monogr. 23, pp. 269-282.

Melcher, F., Stumpfl, E. F. & Distler, V., (1994). Chromite deposits of the Kempirsai massif, southern Urals, Kazakhstan. Transactions of the Institution of Mining and Metallurgy (Section B: Applied Earth Sciences) 103, B107–B120.

Melcher, F., Grum, W. & Stumpfl, E. F., (1996). Ophiolitic–podiform chromite giants in the southern Urals: implications from geo-chemistry and the role of fluids. Geological Society of America, Abstracts with Programs 28, A92–A93.

Melcher F, Grum W, Simon G, Thalhammer TV, Stumpfl EF., (1997). Petrogenesis of the giant ophiolitic chromite deposits of Kempirsai, Kazakhstan: a study of solid and fluid inclusions in chromite. J Petrol 38: 1419-1458

Melcher, F., Grum,W., Thalhammer, T.V., Thalhammer, O.A.R., (1999). The giant chromite deposits at Kempirsai, Urals: constraints from trace element (PGE, REE) and isotope data. Mineralium Deposita 34, 250–272.

Mellini, M., Rumori, C., Viti, C. (2005). Hydrothermally reset magmatic spinels in retrograde serpentinites: formation of “ferritchromit” rims and chlorite aureoles. Contributions to Mineralogy and Petrology, 149, 266-275.

Melson WG, Vallier TL, Wright TL, Byerly G, Nelson J (1976). Chemical diversity of abyssal volcanic glass erupted along Pacific, Atlantic, and Indian Ocean sea-floor spreading centers. In: The Geophysics of the Pacific Ocean Basin and Its Margin (AGU, Washington), pp. 351-367

Menzies, M.A. & Allen, C.R. (1974). Plagioclase lherzolite-residual mantle relationships within two eastern Mediterranean ophiolites. Contr. Miner. Petrol. 45, 197-213.

Mercier, J-C.C. (1972). Structure des péridotites en enclaves dans quelques basaltes d'Europe et d'Hawaii. Regards sur la constitution du manteau supérieur. Thèse 3ème cycle, Univ. Nantes.

Mercier, J-C.C. and Nicolas, A. (1974). Textures and fabrics of upper-mantle peridotites as illustrated by xenoliths from basalts. Journal of Petrology, 16, 454-487.

Merlini, A.E.M. (2008). Chromite in ophiolite complexes: genesis and alteration. Sociedad Espanola de Mineralogie Italian, Extended abstract, Plinius, n.34. pp 100-108

Metcalf, R.V. & Shervais, J.W. (2008). Supra-Subduction Zone (SSZ) Ophiolites: is there really an ‘‘Ophiolite Conundrum’’? In: Wright JE, Shervais JW (eds) Ophiolites, arcs, and batholiths: A tribute to Cliff Hopson. Geol Soc Am Spec Paper, vol 438, pp191–222.

Michael, P.J. & Bonatti, E. (1985). Peridotite composition from the North Atlantic: regional and tectonic variations and implications for partial melting. Earth and Planetary Science Letters, 73, 91-104.

Michel, J.C. (1993). Mineral occurrence and metallogenic map of the Sultanate of Oman, at scale 1:1,000,000 with Explanatory Notes. Directorate General of Minerals, Oman, pp.40.

Mondal, S.K. & Mathez, E.A. (2007). Origin of the UG2 Chromitite Layer, Bushveld Complex, Journal of Petrology, 48, pp.495–510.

Mondal, S.K., Ripley, E.M., Li, C., and Frei, R., (2006). The genesis of Archaean chromitites from the Nuasahi and Sukinda massifs in the Singhbhum craton, India: Precambrian Research, v. 148, p. 45–66.

Monnier, C., Girardeau, J., Le Mée, L. and Polvé, M. (2006). Along-ridge petrological segmentation of the mantle in the Oman ophiolite. Geochemistry, Geophysics, Geosystems, 7, Q11008, doi:10.1029/2006GC001320.

Monsef, I., Rahgoshay, M., Mohajjel, M. & Moghadam, S.H. (2010). Peridotites from the Khoy Ophiolitic Complex, NW Iran: Evidence of mantle dynamics in a suprasubduction-zone context. Journal of Asian Earth Science 38, 105–120.

Moores, E.M. (1969). Petrology and structure of the Vourinos ophiolite complex, northern Greece: Geol. Soc. America Spec. Paper 118, 74 p.

Moores, E.M. (1970). Ultramafics and orogeny, with models from the U.S. Cordillera and the Tethys: Nature, v. 228, p. 837-842.

Moores, E.M. & Vine, F.J. (1971). Troodos massif, Cyprus and other ophiolites as oceanic crust: Evaluation and implications: Royal Society of London Philosophical Transactions, ser. A, v. 268, p. 443-466.

Moores, E.M. & Jackson, E.D. (1974). Ophiolites and oceanic crust: Nature, v. 250, p. 136-139.

Moores, E., L. H. Kellogg, & Y. Dilek. (2000). Tethyan ophiolites, mantle convection, and tectonic ‘‘historical contingency’’: Ar esolution of the ‘‘ophiolite conundrum’’. In: Dilek, Y., Moores, E.M., Elthon, D., and Nicolas, A., (Eds.), Ophiolites and Oceanic Crust: New Insights from Field Studies and the Ocean Drilling Program: Boulder, Colorado, Geological Society of America Special Paper, 349, 3–12.

Morishita, T., Arai, S. & Ishida, Y. (2007). Trace element compositions of jadeite (+ omphacite) in jadeitites from the Itoigawa–Ohmi district, Japan: Implications for fluid processes in subduction zones. Island Arc, 16, 40–56.

Mudge, M.R. (1968). Depth controls of some concordant intrusions: Geological Society of America Bulletin, v. 79, pp. 315-332.

Müntener, O. & Piccardo, G.B. (2003). Melt migration in ophiolitic peridotites: The message from Alpine-Apennine peridotites and implications for embryonic ocean basins. In Y. Dilek, and P.T. Robinson, Eds., Ophiolites in Earth History, 218, p. 69–89. Geological Society of London Special Publication, U.K.

Murck, B.W., and Campbell, I.H., (1986). The effects of temperature, oxygen fugacity and melt composition on the behaviour of chromium in basic and ultrabasic melts: Geochimica et Cosmochimica Acta, v. 50, p. 1871–1888.

Naldrett, A.J., Kinnaird, J., Wilson, A., Yudovskaya, M., McQuade, S., Chunnerr, G. & Stanley, C., (2009). Chromite composition and PGE content of Bushveld chromitites: Part 1 – the Lower and Middle Groups. Applied Earth Science Trans. Inst. Min. Metall. B118, 131-161.

Narkisova, V.V., Sazonova, L.V. & Nosova, A.A. (1999). Magmatic bodies within the sequence of the Uralian ultradeep well, in Paleosubduction zones: Tectonics, Magmatism, Metamorphism, Sedimentology: Ekaterinburg, Urals Branch, Russian Academy of Sciences, p. 104–106 (in Russian).

Natland, J.H. (1981). Crystal morphologies and pyroxene compositions in boninites and tholeiitic basalts from Deep Sea Drilling Project Holes 458 and 459 in the Mariana fore-arc region. In: Hussong D, Uyeda S (eds) Initial Report of Deep Sea Drilling Project 60:681-709

Natland, J.H. & Tarney, J. (1981). Petrologic evolution of the Mariana arc and back-arc system - a synthesis of drilling results in the Southern Philippine Sea. Init. Rep. D.S.D.P., 60: 877-908.

Neary, C.R., & Brown, M.A. (1979). Chromitites from the Al'Ays complex Saudi Arabia, and the Semail complex, Oman. In Al-Shanti, A.M.S. ed., Evolution and mineralisation of the Arabian-Nubian Shield: Symposium Volume, Institute of Applied Geology (IAG) Bulletin 2, 193-205.

Nell, J. & Wood, B. J. (1991). High-temperature electrical measurements and thermodynamic properties of Fe_3O_4-$FeCr_2O_4$-$MgCr_2O_4$- $FeAl_2O_4$ spinels. American Mineralogist, 76, 405-426.

Neilson Pike, J.E. & Schwarzman, E.C. (1977): Classification of texturesin ultramafic xenoliths. J. Geol. V.85, pp.49-61

Nicolas, A. (1986a). A melt extraction model based on structural studies in mantle peridotites. American Mineralogist, 76, 405-426.

Nicolas, A. (1986b). Structure and petrology of peridotites: clues to their geodynamic environment. Reviews of Geophysics, 24, 875 - 895.

Nicolas, A. (1989). Structures of ophiolites and dynamics of oceanic lithosphere. Dordrecht, Netherlands, Kluwer Academic Publishers, 367 p.

Nicolas, A. (1990). Melt extraction from mantle peridotites: hydrofracturing and porous flow, with consequences for oceanic ridge activity. In: Ryan, M.P. (Ed.), Magma Transport and Storage. John Wiley and Sons, Chichester, pp. 159–173.

Nicolas, A. & Boudier, F. (1995). Mapping oceanic ridge segments in Oman ophiolites. Journal of Geophysical Research, 100, 6179–6197.

Nicolas, A. & Prinzhofer, A. (1983) Cumulative or residual origin for the Transition Zone in ophiolites: structural evidence. Journal of Petrology, 24, 188-206.

Nicolas, A. & A. Azri, H. (1991). Chromite-rich and chromite-poor ophiolites: The Oman case. In: Peters, T.J., Nicolas, A. and Coleman, R.G. (Eds.), Ophiolite genesis and evolution of the oceanic lithosphere, 261-274. Kluwer Academic, Dordrecht, the Netherlands.

Nicolas, A., Boudier, F., and Bouchez, J.L. (1980). Interpretation of peridotite structures from ophiolitic and oceanic environments. American Journal of Science, 280, 192-210.

Nicolas, A., Ceuleneer, G., Boudier, F., and Misseri, M. (1988). Structural mapping in the Oman ophiolite: Mantle diapirism along an oceanic ridge. Tectonophysics, 151, 27-54.

Nielson Pike, J.E. and Schwarzman, E.C. (1997). Classification of textures in ultramafic xenoliths. Journal of Geology, 85, 49-61.

Niida K. (1984). Petrology of the Horoman ultramafic rocks in the Hidaka metamorphic belt, Hokkaido, Japan. J. Pac. Sci. Hokkaido Univ. Ser. IV 21, 197-250.

Niu, Y. (1997). Mantle melting and melt extraction processes beneath ocean ridges:evidence from abyssal peridotites. Journal of Petrology 38, 1047–1074.

Niu, Y. (2004). Bulk-rock major and trace element compositions of abyssal peridotites: implications for mantle melting, melt extraction and post-melting processes beneath mid-ocean ridges. Journal of Petrology 45, 2423–2458.

Niu, Y. & Hékinian, R. (1997). Basaltic liquids and harzburgitic residues in the Garrett Transform: a case study at fast-spreading ridges. Earth and Planetary Science Letters 146, 243–258.

Niu, Y., Langmuir, C. H. & Kinzler, R. J. (1997). The origin of abyssal peridotites: a new perspective. Earth and Planetary Science Letters. 152: 251–265.

Noller J. S. and Carter B. (1986). The origin of various types of chromite schlieren in the Trinity Peridotite, Klamath Mountains, California. In Metallogeny of Basic and Ultrabasic Rocks (Regional Presentations) (edited by Carter B., Chowdhury M. K. R., Jankovic S., Marakushev A. A., Morten L., Onikhimovsky V. V., Raade G., Rocci g. and Augustithis S. S.), pp. 151-178. Theophrastus, Athens, Greece.

O'Hara, Y. and Ishii, T. (1998). Peridotites from the southern Mariana forearc: Heterogeneous fluid supply in mantle wedge. The Island Arc, 7, 541-558.

O'Hara, Y., Stern, R.J., Ishii, T., Yurimoto, Y. & Yamazaki, T. (2002). Peridotites from the Mariana Trough: First look at the mantle beneath an active back-arc basin. Contrib. Mineral. Petrol. 143: 1-18.

Okamura, H., Arai, S., & Kim, Y.U. (2006). Petrology of forearc peridotites from the Hahajima Seamount, the Izu Bonin arc, with special reference to chemical characteristics of chromian spinel. Mineralogical Magazine, 70, 15-26.

Olive, V., Hébert, R., Loubet, M., (1997). Isotopic and trace element constraints on the genesis of a boninitic sequence in the Thetford Mines ophiolitic complex, Québec, Canada. Canadian Journal of Earth Sciences 34, 1258–1271.

O'Reilly, S.Y., Griffin, W.L. and Ryan, C.G. (1991). Residence of trace elements in metasomatized spinel lherzolite xenoliths: a proton microprobe study. Contributions to Mineralogy and Petrology, 109, 98-113.

Ozawa K (1994). Melting and melt segregation in the mantle wedge above a subduction zone: evidence from the chromite-bearing peridotites of the Miyamori ophiolite complex, northeastern Japan. J Petrol 35: 647-678

Pagé, P., Bédard, J.H., Schroetter, J.-M. & Tremblay, A. (2008). Mantle petrology and mineralogy of the Thetford Mines Ophiolite Complex: Lithos, v. 100, p. 255−292.

Pagé, P., Bédard, J.H. & Tremblay, A. (2009a). Geochemical variations in a depleted fore-arc mantle: The Ordovician Thetford Mines Ophiolite: Lithos, v. 113, p. 21−47.

Pagé, P & Barnes, S-J, (2009b). Using trace elements in chromites to constrain the origin of podiform chromitites in the Thetford Mines Ophiolite, Québec, Canada. Econ Geol, 104, 997-1018.

Pagé, P., Bédard, J.H., Tremblay, T., (2009b). Geochemical variations in a depleted fore-arc mantle: The Ordovician Thetford Mines Ophiolite. Lithos, 113, 21-47.

Paktunc AD (1990). Origin of podiform chromite deposits by multistage melting, melt segregation and magma mixing in the upper mantle. Ore Geology Reviews. V.5, 3, 211-222

Paktunc, A.D. & Baysal, O. (1981). Mineralogy of Catalocak-Suluocak chromites. Yerbilimleri, Bull. Inst. Earth Sci. Hacettepe Univ., Turkey, 8: 31-40.

Paktunc A.D. and Cabri L.J. (1995). A proton- and electron-microprobe study of gallium, nickel and zinc distribution in chromian-spinel. Lithos, 35, 261-282.

Paktunc, A.D. and Hulbert, L.J. (1996). Mineralogy of the Sturgeon Lake 01 Kimberlite, Saskatchewan: a proton microprobe study of the macrocryst phases. Exploration Mining Geology, 5, 263-279.

Panayiotou, A., Michaelides, A.E. & Georgiou, E. (1986). The chromite deposits of the Troodos ophiolite complex, Cyprus, in Chromites, UNESCO's IGCP-197 Project on Metallogeny of Ophiolites: Athens, Theophrastus publications, pp.161-198.

Parkinson, I.J. and Pearce J. (1998). Peridotites from the Izu-Bonin-Mariana Forearc (ODP Leg 125): Evidence for Mantle Melting and Melt-Mantle Interaction in a Supra-Subduction Zone Setting. Journal of Petrology, 39, 1577-1618.

Parkinson, I.J. and Arculus, R.J. (1999). The redox state of subduction zones: insights from arc-peridotites. Chemical Geology, 160, 409–423.

Pavlov, N. V. & Grigoryeva, I. I., (1977). Deposits of chromium. In: massif in Smirnov, V. I. (ed.) Ore Deposits of the USSR, Vol. I. London: Pitman, pp. 179–236.

Peck, D.C. & Keays, R.R. (1990). Geology, geochemistry, and origin of platinum-group element-chromitite occurrences in the Heazlewood River complex, Tasmania. Economic Geology 85, 765-793.

Pearce, J.A. (1980). Geochemical evidence for the genesis and eruptive setting of lavas from Tethyan ophiolites. In: Ophiolites Proceedings International Ophiolite Symposium, Cyprus, 1979, edited by A. Panayiotou, Geological Survey Department, Nicosia, Cyprus. pp. 261-272.

Pearce, J.A., (2003). Supra-subduction zone ophiolites: the search for modern analogues. In Dilek, Y., and Newcomb, S., eds. Ophiolite concept and the evolution of geological thought. Geol. Soc. Am. Spec. Pap. 373:269–293.

Pearce, J.A., Alabaster, T., Shelton, A.W. & Searle, M.P. (1981). The Oman ophiolite as a Cretaceous arc-basin complex: evidence and implications. Philisophical Transaction of the Royal Society of London, A 300, 299 – 317.

Pearce, J.A., Lippard, S.J. & Roberts, S. (1984). Characteristics and tectonic significance of supra-subduction zone ophiolites. Geological Society of London, Special Publication, 16, 77-94.

Pearce, J.A., Van Der Lean, S.R., Arculus, R.J., Murton, B.J., Ishii, T (1992). Boninite and harzburgite from Leg 125 (Bonin-Marianan forearc): A case study of magma genesis during the initial stages of subduction. In Proc. ODP Sci. Results, ed. P Fryer, JA Pearce, LB Stokking, et al. College Station, TX: Ocean Drilling Program. pp. 623-59.

Pearce, J.A. & Parkinson, I.J. (1993). Trace element models for mantle melting: application to volcanic arc petrogenesis. In: Pritchard, H.M., Alabaster, T., Harris, N.N.W., Neary, C.R. (Eds.), Magmatic Processes and Plate Tectonics, Geological Society Special Publication No. 76, 373-403.

Pearce, J.A., Kempton, P.D., Nowell, G.M., Noble, R., (1999). Hf–Nd element and isotope perspective on the nature and provenance of mantle and subduction components in Western Pacific arc-basin systems. Journal of Petrology 40, 579–611.

Pearce J., Barker P.F., Edwards S.J., Parkinson I.J. and Leat, P.T. (2000). Geochemistry and tectonic significance of peridotites from the South Sandwich arc-basin system, South Atlantic. Contribution to Mineralogy and Petrology, 139, 36-53.

Penrose Conference Participants (1982). GSA Penrose field conference on ophiolite, Geotimes.

Peters, T. & Kramers, J.D. (1974). Chromite deposits in the ophiolite complex of Northern Oman: Mineralium Deposita, v. 9, p. 253-259.

Pike, J.E. & Schwarzman, E.C. (1977). Classification of textures in ultramafic xenoliths. J. Geol. V.85, pp.49-61.

Portnyagin, M. V., Danyushevsky, L. V. & Kamenetsky, V. S. (1997). Coexistence of two distinct mantle sources during formation of ophiolites: a case study of primitive pillow-lavas from the lowest part of the volcanic section of the Troodos Ophiolite, Cyprus. Contributions to Mineralogy and Petrology. 128, 287–301.

Poustovetov, A. (2000). Numerical Modeling of Chemical Equilibria Between Chromian Spinel, Olivine, and Basaltic Melt, with Petrologic Applications. Ph.D. thesis, Queen's Univ., Kingston, Ontario

Puchkov, V.N. (1997). Structure and geodynamics of the Uralian orogen. In: Burg, J.-P., Ford, M. (Eds.), Orogeny Through Time. Geological Society Special Publication, vol. 121, pp. 201–236.

Puchkov, V.N. (2000). Paleogeodynamics of the central and southern Urals: Ufa, Pauria, pp.145.

Puchkov, V. (2002). Paleozoic evolution of the East European continental margin involved in the Uralide orogeny. In: Brown, D., Juhlin, C., Puchkov, V. (Eds.), Mountain Building in the Uralides: Pangea to Present. American Geophysical Union, Geophysical Monograph, vol. 132, pp. 9–32.

Quick, J.E. (1981). The origin and significance of large, tabular dunite bodies in the Trinity Peridotite, northern California. Contributions to Mineralogy and Petrology 78, 413–422.

Rabinowicz, M., Ceuleneer, G. and Nicolas, A., (1987). Melt segregation and flow in mantle diapirs below spreading centers: evidence from the Oman ophiolite. J. Geophys. Res., 92: 3475-3486.

Rampone, E. & Piccardo, G. B. (2000). The ophiolite–oceanic lithosphere analogue: new insights from the Northern Apennines (Italy). In: Dilek, Y., Moores, E. M., Elthon, D. & Nicolas, A. (eds) Ophiolites and Oceanic Crust: New Insights from Field Studies and the Oceanic Drilling Program. Geological Society of America Special Papers 349, 21–34.

Rassios, A., Roberts, S., Vacondios, I. (Eds.), (1986). The Application of a Multidisciplinary Concept for Chromite Exploration in the Vourinos Complex (N. Greece). Institute of Mining and Mineral Exploration, Athens. 409 pp.

Reagan, M.K. & Meijer, A. (1984). Geology and geochemistry of early arc-volcanic rocks from Guam. Geological Society of America Bulletin, 95:701-713.

Reynolds, I.M., (1985). The nature and origin of titaniferous magnetite-rich layers in the upper zone of the Bushveld Complex. A: review and synthesis: Econ Geol, v.80, pp.1089-110

Ringwood, A.E. (1975). Composition and Petrology of the Earth's Mantle McGraw-Hill, New York, N.Y., p. 618.

Ringwood, A.E. (1982). Phase transformations and differentiation in subducted lithosphere - implications for mantle dynamics, basalt petrogenesis and crustal evolution J. Geol., 90, pp. 611–643.

Ringwood, A.E. (1986). Dynamics of subducted lithosphere and implications for basalt petrogenesis. Terra Cognita., 6, pp. 67–77

Ringwood A.E. & Irifune, T. (1988). Nature of the 650 km seismic discontinuity: implications for mantle dynamics and differentiation. Nature (London), 331, pp. 131–136

Roach, T.A., Roeder, P.L. & Hulbert L.J. (1998). Composition of chromite in the upper chromitite, Muskox layered intrusion, Northwest Territories. Canadian Mineralogist 36, 117–35.

Roberts, S. (1986). The role of igneous processes in the formation of ophiolitic chromitite. Ph.D. Thesis, Department of Earth Sciences, The Open University, 250 p.

Roberts, S. (1988). Ophiolitic chromitite formation: A marginal basin phenomenon? Econ Geol. V. 83, pp.1034–1036.

Roberts, S. (1992). Influence of the partial melting regime on the formation of ophiolitic chromitite. Geol. Sot. Spec. Publ. Lond. V.60, pp.203-217.

Roberts, S. & Neary, C. (1993). Petrogenesis of ophiolitic chromitite. In: Prichard, H.M., Alabaster, T., Harris, N.B.W. and Neary, C.R. (Eds.), Magmatic Processes and Plate Tectonics, Geological Society Special Publication, 76, 257-272.

Robertson, A.H.F., Blome, C.D., Cooper, D.W.J., Kemp, A.E.S., Roeder, P. L., Campbell, I. H. & Jamieson, H. E. (1979). A re-evaluation of the olivine-spinel geothermometer. Contributions to Mineralogy and Petrology, 68, 325-334.

Robinson, P. T., Melson, W. G., O'Hearn, T. & Schmincke, H.U. (1983). Volcanicg lassc ompositiono f the Troodoso phiolite, Cyprus: Geology, v. 11, p. 400-404.

Rocci, G., Ohnenstetter, D, & Ohnenstetter, M. (1975). La dualite des ophiolites tethysiennes. Petrologie, l, 172-4.

Roeder, P.L. & Campbel, I.H. (1985). The effect of postcumulus reations on compositions of chrome-spinels from the Jimberlana Intruision. Journal of Petrology, v.26, pp.763-786.

Roeder, P.L. & Reynolds, I., (1991). Crystallisation of chromite and chromium solubility in basaltic melts: Journal of Petrology, v. 32, p. 909–934.

Rollinson, C.L. (1973). Chromium, Molybdenum and Tungsten. Chapt. 36 In Comprehensive Inorganic Chemistry, (editors J. C. Bailar, H. J. EmelBus, R. Nyholm and A. F. Trotman-Dickenson), Vol. 3, Chapter 36, pp. 355-417. Pergamon Press.

Rollinson, H. (2005). Chromite in the mantle section of the Oman ophiolite: a new genetic model. The Island Arc, 14, 542-550.

Rollinson, H. (2008). The geochemistry of mantle chromitites from the northern part of the Oman ophiolite: inferred parental melt compositions. Contributions to Mineralogy and Petrology 156 (3), 273–288.

Sack, R.O. (1982). Spinels as petrogentic indicators: activity-composition relations at low pressures. Contributions to Mineralogy and Petrology, v.79, pp.169-186

Sack, R.O. & Ghiorso, M.S. (1991). Chromian spinels as petrogenetic indicators: thermodynamics and petrological application. American Mineralogist 76, 827–847.

Sakuyama, M. (1978). Evidence of magma mixing: petrological study of Shiroumaoike calc-alkaline andesite volcano, Japan. J. Volcanol. Geotherm. Res. 5:179-208.

Sampson, E. (1929). May chromite crystallize late? Econ. Geol., 24(6): 632-641.

Sampson, E. (1931). Varieties of chromite deposits. Econ. Geol. 26, 833-839.

Sampson, E. (1932). Magmatic chromite deposits in Southern Africa. Economic Geology. V. 27, pp.113-144.

Savelieva, G.N. & Saveliev, A.A. (1992). Relationship between peridotites and gabbroic sequences in the ophiolites of the Urals and the Lesser Caucasus. Ofioliti 17: 117-138

Savelieva, G. N. & Nesbitt, R. W., (1996). A synthesis of the stratigraphic and tectonic setting of the Uralian ophiolites. Journal of the Geologial Society, London 153, 525–538.

Savelieva, G.N., Sharaskin, A.Y., Saveliev, A.A., Spadea, P., Gaggero, L., (1997). Ophiolites of the southern Uralides adjacent to the East European continental margin. Tectonophysics 276, 117–138.

Savelieva, G.N., Pertsev, A.N., Astrakhantsev, O., Denisova, E.A., Boudier, F., Bosch, D. & Puchkova, A.V. (1999). The Kytlym Pluton, North Urals: structure and emplacement history. Geotectonics 33, 119–141.

Savelieva, G.N., Sharaskin, A.Y., Saveliev, A.A., Spadea, P., Pertsev, A.N., and Babarina, I.I., (2002). Ophiolites and zoned mafic-ultramafic massifs of the Urals: A comparative analysis and some tectonic implications: Geophysical Monograph 132, p.135–153.

Scarrow, J.H., Savelieva, G.N., Glodny, J., Montero, P., Pertsev, A., Cortesogno, L., Gaggero, L., (1999). The Mindyak Paleozoic lherzolite ophiolite, Southern Urals: geochemistry and geochronology. Ofioliti 24, 239–246.

Scowen, P.A.H., Poeder, P.L. & Helz, R.T. (1991). Re-equilibration of chromite within Kilauea Iki lava lake, Hawaii. Contributions to Mineralogy and Petrology, v.107, pp.8-20

Schiano, P., Clocchiati, R., (1995). Deep silicate melts in convergent and intraplate settings. EUG8 Abstract, Terra Nova 7, 334.

Schiano, P., Clocchiatti, R., Lorand, J.-P. Massare, D., Deloule, E. and Chaussidon M. (1997). Primitive basaltic melts included in podiform chromites from the Oman Ophiolite. Earth and Planetary Science Letters, 146, 489-497.

Schilling, J.-G., M. Zalac, R. Evans, T. Johnston, W. White, J. D. Devine, and R. Kingsley (1983). Petrologic and geochemical variations along the Mid-Atlantic Ridge from 29 degrees N to 73 degrees N. American Journal of Science. 238:510–586.

Schilling, J.G., H. Sigurdsson, A. N. Davis, & R. N. Hey (1985). Easter microplate evolution, Nature, 317, 325–331.

Schreiber, H. D., (1976). The experimental determination of redox states, properties, and distribution of chromium in synthetic silicate phases and application to basalt. Unpublished Ph.D. Thesis, University of Wisconsin, Madison.

Scowen, P., Roeder, P.L., and Helz, R., (1991). Reequilibration of chromite within Kilauea Iki lava lake, Hawaii. Contributions to Mineralogy and Petrology, 107, 8-20.

Searle, M. and Cox, J. (1999). Tectonic setting, origin, and obduction fo the Oman ophiolite. Geological Society of America Bulletin, 111,104-122.

Seravkin, I.B., Kosarev, A.M., Salikhov, D.M., Znamenskii, S.E., Rodicheva, Z.I., Rykus, M.V. & Snachev, V.I. (1992). Volcanism of the South Urals: Moscow, Nauka, 197 p. (in Russian).

Sharaskin, A.J., Dobretsov, N.L. & Sobolev, N.V. (1980). Marianites: The clinoenstatite bearing pillow-lavas associated with the ophiolite assemblage of Mariana trench. In: Panayiotou A (ed), Ophiolites. Cyprus Geol Survey, Nicosia. pp 473-479

Sharpe, M.R., Bahat, D. & Von Gruenewaldt, G. (1981). The concentric elliptical structure of feeder sites to the Bushveld Complex and possible economic implications: Geological Society of South Africa Transactions. v. 84, pp. 239-244.

Sharpe, M.R. & Irvine, T.N. (1988). Melting relations of two Bushveld chilled margin rocks and implications for the origin of chromitite: Carnegie Inst. Washington Year Book 82, in press.

Shaw, D.M., (1970). Trace element fractionation during anatexis. Geochimica et Cosmochimica Acta 34, 237–243.

Shervais, J.W. (2001). Birth, death, and resurrection: the life cycle of suprasubduction zone ophiolites. Geochemistry, Geophysics, Geosystems, 2, 2000GC000080.

Sigurdsson, I.A. & Schilling, J.G. (1976). Spinels in Mid-Atlantic Ridge basalts: chemistry and occurrence. Earth and Planetary Science Letters, v.29, pp. 7-20.

Sobolev, A.V. & Shimizu, N. (1993). Ultra-depleted primary melt included in an olivine from the Mid-Atlantic Ridge. Nature 363, 151-154

Spadea, P. & D'Antonio, M., (2006). Initiation and evolution of intraoceanic subduction in the Uralides: geochemical and isotopic constraints from Devonian oceanic rocks of the Southern Urals, Russia. Island Arc 15, 7–25.

Spadea, P. & Scarrow, J. H. (2000). Early Devonian boninites from the Magnitogorsk Arc, Southern Urals (Russia): Implications for early development of a collisional orogen. In Dilek Y., Moores E., Elthon D. & Nicolas A. (eds). Ophiolites and Oceanic Crust: New Insights from Field Studies and Ocean Drilling Program. Geological Society of America Special Paper. 349:461–72.

Spadea, P., Kabanova, L.Y., Scarrow, J.H., (1998). Petrology, geochemistry and geodynamic significance of Mid-Devonian boninitic rocks from the Baimak-Buribai area (Magnitogorsk Zone, southern Urals). Ofioliti 23, 17–36.

Spadea, P., D'Antonio, M., Kosarev, A., Gorozhanina, Y., Brown, D., (2002). Arc–continent collision in the Southern Urals: petrogenetic aspects of the forearc complex. In: Brown, D., Juhlin, C., Puchkov, V. (Eds.), Mountain Building in the Uralides: Pangea to Present. Geophysical Monograph, American Geophysical Union, vol. 132, pp. 101–134.

Spadea, P., Zanetti, A., Vannucci, R., (2003). Mineral chemistry of ultramafic massifs in the southern Uralides orogenic belt (Russia) and the petrogenesis of the Lower Paleozoic ophiolites of the Uralian Ocean. In: Dilek, Y., Robinson, P.T. (Eds.), Ophiolites in Earth History. Geological Society, Special Publication, vol. 218, pp. 567–596.

Spier, C.B. & Ferreira Filho, C.F. (2001). The chromite deposits of the Bacuri mafic-ultramafic layered complex, Guyana shield, Amapá State, Brazil: Economic Geology, v. 96, 817–835.

Steinmann, G. (1927). Die ophiolitische Zonen in der Mediterrananen Kettingebirgen, Int. Geol. Congr. 14th, 2, 638-667.

Stern, R. J. & S. H. Bloomer (1992). Subduction zone infancy; examples from the Eocene Izu-Bonin-Mariana and Jurassic California arcs. Geol. Soc. Am. Bull., 104:1621–1636

Stoffers, P., T. Worthington, R. Hekinian, S. Petersen, M. Hannington, M. Türkay, and SO 157 Shipboard Scientific Party (2002). Silicic volcanism and hydrothermal activity documented at Pacific-Antarctic Ridge, Eos Trans. AGU, 83(28), 301, doi:10.1029/2002EO000215.

Stolper, E., Newman, S., (1994). The role of water in the petrogenesis of Mariana Trough magmas. Earth and Planetary Science Letters 121, 293–325.

Stowe, C.W. 1987. ed., Evolution of chromium ore fields: New York, Van Nostrand Reinhold Company, p. 71–88.

Stowe, C.W. (1994). Compositions and tectonic settings of chromite deposits through time. Economic Geology. V.89, p. 528 – 546

Stracke, A. & Bourdon, B. (2009). The importance of melt extraction for tracing mantle heterogeneity. Geochimica et Cosmochimica Acta. 73, pp.218-238.

Suhr, G. (2003). Formation of large mantle dunites near lithospheric walls (Haylayn Massif, Oman): significance for melt transport. Geophysical Research Abstracts, 5, 07654.

Sun, S.S. (1982). Chemical composition and origin of the earth's primitive mantle. Geochimica et Cosmochimica Acta 46, 179–192.

Sun, S.S. & McDonough, W.F. (1989). Chemical and isotopic systematics of oceanic basalts: implications for mantle compositions and processes. In: Saunders, A.D., Norry, M.J. (Eds.), Magmatism in the ocean Basins. Geological Society, London, Special Publication, vol. 42, pp. 313–345.

Takazawa, E., Okayasu, T. and Satoh, K. (2003). Geochemistry and origin of the basal lherzolites from the northern Oman ophiolite (northern Fizh Block). Geochemistry, Geophysics, Geosystems, 2, 1021, doi:10.1029/2001GC000232.

Takahashi, E. and Kushiro, I., (1983). Melting of a dry peridotite at high pressures and basalt magma genesis. Am. Mineral., 68: 859-879.

Talkington, R. and Malpas, J. (1980). Spinel phases of the White Hills peridotite, St. Anthony Complex, Newfoundland: Part 1 occurrence and chemistry. Proceedings of the International Ophiolite Symposium, Cyprus, 607-619.

Talkington, R. W., Watkinson, D. H., Whittaker, P. J. & Jones, P. C. (1983). Platinum-group mineral inclusions in chromite from the Bird River sill, Manitoba: Mineralium Deposita, v. 18, pp. 245-255.

Tamura, A., and Arai, S. (2006). Harzburgite-dunite-orthopyroxenite suite as a record of supra-subduction zone setting for the Oman ophiolite mantle. Lithos, 90, 43-56.

Tankut, A., (1980). The Orhaneli massif Turkey. In: A. Panayiotou (Editor), Ophiolites. Proc. Int. Ophiolite Syrup., pp. 702-713.

Tatsumi, Y., Maruyama, S., (1989). Boninites and high-Mg andesites: tectonics and petrogenesis. In: Crawford, A.J. (Ed.), Boninites and Related Rocks. Unwin Hyman, London, pp. 112–132.

Thayer T.P., (1964). Principal features and origin of podiform chromite deposits, and some observations on the Guleman-Soridag district, Turkey. Econ Geol 59:1497–1524

Thayer, T.P. (1969). Gravity differentiation and magmatic re-emplacemant of podiform chromite deposits: Economic Geology Monograph 4, p.132–146.

Thayer T.P. (1970). Chromite segregations as petrogenetic indicators. Geol. Soc. S. Africa. Spec. Publ. 1, pp.380-390.

Thayer, T.P. (1973). Chromium. U.S.G.S. Prof. Pap., v.820, pp.111-121.

Thy, P. (1983). Phase relations in transitional and alkali basaltic glasses from Iceland. Contributions to Mineralogy and Petrology 82, 232-51.

Thy, P. (1987). Petrogenetic implications of mineral crystallization trends of Troodos cumulates. Cyprus Geol. Mag. 124, 1–11.

Ulmer, G.L., (1969). Experimental investigations of chromite spinels. In: H.D.B. Wilson (Editor), Magmatic Ore Deposits. Econ. Geol., Monogr., 4:114-131.

Ulmer, P. & Trommsdorff, V., (1995). Serpentine stability to mantle depths and subductionrelated magmatism. Science 268, 858–861.

Umino, S. (1986). Magma mixing in boninite sequence of Chichijima, Bonin Islands. J. Volcanol. Geotherm. Res. 29, 125-157.

Uysal, I., Sadiklar, M.B., Tarkian, M., Karsli, O. & Aydin, F. (2005). Mineralogy and composition of the chromitites and their platinum-group minerals from Ortaca (Mug¢la-SW Turkey): evidence for ophiolitic chromitite genesis. Mineral Petrol. 83:219–242.

van der Laan, S.R., Flower, M.F. & Koster van Gross, A.F. (1989). Experimental evidence for the origin of boninitcs: Near liquidus phase relations to 7.5 kbar. In: Crawford AJ (ed) Boninites. Unwin Hyman, London, pp.112 147.

Varfalvy, V., Hebert, R., Bedard, J.H., (1996). Interactions between melt and upper-mantle peridotites in the North Arm Mountain massif, Bay of islands ophiolite, Newfoundland, Canada: implications for the genesis of boninitic and related magmas. Chemical Geology 129, 71–90.

Varfalvy, V., Hébert, R., Bédard, J.H., Lafléche, M.R., (1997). Petrology and geochemistry of pyroxenite dykes in upper mantle peridotite of the North Arm Mountain massif, Bay of Islands ophiolite, Newfoundland: implications for the genesis of boninitic and related magmas. Canadian Mineralogist 35, 543–570.

Varne, R., Brown, A. V., Jenner, G. A. and Falloon, T., (2000). Macquarie Island: its geology and structural history, and the timing and tectonic setting of its N-MORB to E-MORB magmatism. In: Dilek, Y., Moores, E.M., Elthon, D., and Nicolas, A., (Eds.), Ophiolites and Oceanic Crust: New Insights from Field Studies and the Ocean Drilling Program: Boulder, Colorado, Geological Society of America Special Paper, 349, 301-320.

Verniéres, J, Godard, M, & Bodininier J.L. (1985). A plate Model for the simulation of trace element fractionation during partial melting and magma transport in the Earth's upper mantle. Journal of Geophysical Resources. V 102, No B11, pp 24,771-24,784,

Verniéres, J., Godard, M. & Bodinier, J.L. (1997). A plate model for the simulation of trace element fractionation during partial melting and magma transport in the Earth's upper mantle. Journal of Geophysical Research. 102: 24771- 24784.

Voll G. (1960). New work on petrofabrics. Geol. J. (Liverpool and Manchester) 2, 502-597.

Von Gruenewaldt, G., Sharpe, M. R. & Hatton, C. J., (1985). The Bushveld Complex: Introduction and Review. Economic Geology, v.80, pp.803-812.

Voordouw, R., Gutzmer, J. & Beukes, N. J. (2009). Intrusive origin for Upper Group (UG1, UG2) stratiform chromitite seams in the Dwars River area, Bushveld Complex, South Africa, Mineralogy and Petrology.

Wakabayashi, J., and Dilek, Y. (2000). Spatial and temporal relationships between ophiolites and their metamorphic soles: a test of models of forearc ophiolite genesis. In: Dilek, Y., Moores, E.M., Elthon, D., and Nicolas, A., (Eds.), Ophiolites and Oceanic Crust: New Insights from Field Studies and the Ocean Drilling Program: Boulder, Colorado, Geological Society of America Special Paper 34953 – 34964.

Walker, D. A. & Cameron, W.E, (1983). Boninite primary magmas: evidence from the Cape Vogel Peninsula, PNG. Contr. Miner. Petrol. 83, 150-8.

White, R. S. (1988). The earth's crust and lithosphere, J. Pet., Special Lithosphere Issue, 1, 1- 10.

White, J.C. & White, S.H. (1981). The structure of grain boundaries in tectonites.Tectonophysics. V.78, pp.613-628.

Wilson, A.H., **(1982)**. The geology of the great "Dyke", Zimbabwe: The ultramafic rocks. J. Pet. 42, 109-124.

Windley, B.F., (1995). The Evolving Continents. Wiley. pp.526

Wood, B. J. and Virgo, D., (1989). Upper mantle oxidation state: ferric iron contents of lherzolite spinels by ^{57}Fe Mössbauer spectroscopy and resultant oxygen fugacities. Geochimica et Cosmochimica Acta , 53, 1277–1291

Wood, B.J., Bryndzia, L.T., Johnson, K.E., (1990). Mantle oxidation state and its relationship to tectonic environment and fluid speciation. Science 248, 337–344.

Workman, R.K., Hart, S.R., (2005). Major and trace element composition of the depleted MORB mantle (DMM). Earth and Planetary Science Letters 231, 53–72.

Worst, B.G. (1958). The differentiation and structure of the Great Dyke of Southern Rhodesia. Trans. Geol. Soc. S. Afr. V.61, pp. 283-354

Yazeva, R.G. & Bocharev, V.V. (1994). Post-collisional Devonian magmatism of the northern Urals: Geotectonics, v. 27, pp. 316–325.

Yazeva, R.G. & Bochkarev, V.V. (1996). Silurian island arc of the Urals: structure, evolution and geodynamics. Geotectonics 29, 478–489.

Zhou, M.F. & Robinson, P.T. (1994). High-Cr and high-Al chromitites, western China: Relationship to partial melting and melt/rock interaction in the upper mantle. Internation Geological Reviews. 36: 678-686.

Zhou, M.F., Robinson, P.T. and Bai, W.J. (1994). Formation of podiform chromites by melt/rock interaction in the upper mantle. Mineralium Deposita, 29, 98-101.

Zhou, M.F., Robinson, P.T., Malpas, J. & Li, Z. (1996). Podiform chromitites in the Luobusa ophiolite (southern Tibet): Implications for melt-rock interaction and chromite segregation in the upper mantle. J Petrol 37:3–21

Zhou M-F, Robinson P.T. (1997). Origin and tectonic environment of podiform chromite deposits, Econ. Geol., 92, 259-262.

Zhou, M.-F., Robinson, P.T., Malpas, J., Aitchison, J., Sun, M., Bai, W.J., Hu, X.F. & Yang, J.S. (2001). Melt/rock interaction and melt evolution in the Sartohay high-Al chromite deposit of the Dalabute ophiolite (NW China). J. Asian Earth Sci. 19, 519– 536.